Nottingham Geospatial Institute (NGI)

THE USE OF TARGETS TO IMPROVE THE PRECISION OF MOBILE LASER SCANNING

Farsat Heeto Abdulrahman

BSc Eng., MSc Eng.

Thesis submitted to the University of Nottingham

for the degree of Doctor of Philosophy

August 2013

"In the name of ALLAH, the Entirely Merciful, the Especially Merciful"

DEDICATION

This thesis, which I have worked incredibly hard on, is dedicated to the ones who have been there for me every step of the way, who have been by my side through the ups and downs and that is to my family. My gorgeous wife (Nargiz Balata) has always had a helping out throughout these long years. I also dedicate this to my children "Rand, Amed, Aree and Alan." My brothers and sisters, who always tried there hardest to help me even though they lived all the way in Iraq,

Last but not least, I want to thank my mother and father for always being an inspiration to me and always believing that I could achieve anything if I dreamed big enough.
So I want to thank you all for helping me achieve this.

Farast Heeto
December 2012

DECLARATION

I declare that, except where cited in the text, all work contained within this thesis is my own original work, under the direction of my supervisor. The work presented herein was performed at Jubilee Campus, the University of Nottingham between October 2009 and December 2012. This thesis has not been submitted to any institution other than The University of Nottingham for the degree of Doctor of Philosophy.

Farast Heeto
Nottingham Geospatial Institute (NGI)
December 2012

ABSTRACT

A Mobile Laser Scanning System (MLSS) is a kinematic platform combining different sensors, namely: GPS, IMU and laser scanner. These sensors are integrated and synchronised to a common time base providing 3D geo-referenced data. MLSS is used in several areas; such as 3D urban and landscape modelling for visualisation in planning and road design, simulations for environmental management, and to support land use decision-making.

The accuracy of 3D geo-referenced points, achieved via Mobile Laser Scanning (MLS) under normal conditions, can reach the level of 3cm. However, this accuracy tends to be degraded in urban areas, because of trajectory errors of the laser scanner (IMU drift due to the limited availability of GPS signal). This, also, can be attributed to the difficulty of matching natural features in the point cloud.

Previous researches have tried to overcome the problems in urban laser scanning by focusing on enhancing the performance of the navigation system (NGS). This can be costly and may not achieve the high accuracy level required for some engineering application. When the navigation solution is degraded, the accuracy of the point cloud results will be degraded. Using different data sources is another way to improve accuracy in urban areas. For example using airborne LiDAR, terrestrial imagery, and unmanned aerial vehicle (UAV) but these are very time consuming as well as costly compared to MLS systems.

Targets are used in a number of ways in MLS and are often chosen from natural detail points. These can be difficult to define, particularly when high accuracy requirements need to be met, for example, when matching scans together or fitting scans to existing surveys as used in this project, and calibrating the system.

The accuracy of MLS in the urban area was tested using three methods, namely ground control points (GCPs), surface to surface comparing, and additional source of data. Also, the effect of range, incidence angle (IA), resolution and brightness on different types of targets (sphere, cone, pyramid and flat target) was studied to explore the optimal target design. Moreover, an algorithm for automatic target

detection was developed to detect the optimal target. Then, for each target in the point cloud, the centre/apex was calculated using least squares surface fitting.

Tests show that the accuracy of 3D coordinates, obtained from MLS in an urban area is about 2-5 cm. Tests also show that using targets with MLS can improve the quality of results reaching 5 mm levels of accuracy even in the urban area, based on the use of check points to assess the quality and reliability of the outputs

Almost all work on this project was carried out using the software packages available at the Nottingham Geospatial Institute (NGI) and MLS data provided by 3D Laser Mapping Ltd. (3DLM). Two terrestrial laser scanners, namely: HDS 3000 and Faro Focus^{3D} have been used for testing the designed targets.

The findings of this research will contribute easy, cost effective and improved accuracies in MLS data. This enhances usefulness in applications, such as change detection, deformation monitoring, cultural heritage and the process of 3D modelling, particularly in urban areas.

ACKNOWLEDGEMENTS

Firstly, and most importantly, thanks to ***ALLAH*** for making all this possible, ***HE*** is truly magnificent!

Secondly, I would like to acknowledge the Iraqi Ministry of Higher Education and Scientific Research for the financial support, and Department of Civil Engineering, Faculty of Engineering, Dohuk University, Kurdistan for providing me this great opportunity to pursue a PhD degree. I would like to thank 3DLM Ltd. for providing the MLS data of the test site. I would also like to acknowledge the contribution of the NGI, the University of Nottingham for fabrication of the designed targets for this project.

I would like to express my deepest gratitude to my supervisor, Dr.Martin J Smith., and Dr. Nikolaos Kokkas from the NGI for their valuable advice, considerable assistance and encouragement, received throughout the whole project. I am also grateful to the internal assessor, Professor Terry Moore and my previous internal assessor Dr. David Park, for their useful suggestions and recommendations. Without their constructive criticism, the past 3 years would not have been so productive and successful.

Furthermore, I would like to thank Dr Christopher Cox., who provided me with valuable information on their campaign survey in Jubilee Campus, and other members of the NGI, who helped and talked to me whenever I needed help.

My gratitude goes to former experimental officer, Mr. Joseph Ryding, and PhD student Mustafa Amami for their help, support and advice on mastering the software used in this work. I also would like to thanks Dr Lei Yang for his helping on this project.

Finally, I would like to dedicate this thesis to my parents, wife and children (Rand, Amed, Aree and Alan) who I am perpetually grateful to for all their patience and support.

TABLE OF CONTENTS

LIST OF FIGURES

LIST OF TABLES

LIST OF ABBREVIATIONS

AD.....	Average determination
ALS.....	Airborne laser scanning
AOI.....	Area of interest
3D.....	3- Dimensional
DEM.....	Digital elevation model
3DLM.....	3D Laser Mapping
EOP.....	Exterior Orientation parameters
EQ.....	External quality
GCPs.....	Ground control points
GN.....	Gauss Newton algorithm
GPS.....	Global positioning system
HRP.....	Heading Roll and Pitch
HRT.....	Highly Reflective Tape
ICP.....	Iterative closet point
IMU.....	Inertial measurement unit
IQ.....	Internal quality
IT.....	Information Technology
Laser.....	Light amplification by the simulated emission of radiation
LiDAR.....	Light detection and ranging
LM.....	Levenberg Marquardt algorithm
MLS.....	Mobile laser scanning
MMS.....	Mobile mapping system
NGI.....	Nottingham Geospatial Institute
OS.....	Ordnance Survey
PRR.....	Pulse repetition rate
RIA.....	Removing Incidence angle
RMSE.....	Root Mean Square Error
SD.....	Standard Deviation
TIN.....	Triangulated irregular network
TGO.....	Trimble Geomatic office software
TMP.....	Tranverse Mercator projection
TLS.....	Terrestrial laser scanning
TOF.....	Time of flight
TRTS.....	Trimble Robotic Total station
UAV.....	Unmanned aerial vehicle
WGS84.....	World geodetic system 1984

CHAPTER 1: INTRODUCTION

1.1 Introduction and motivation

The main objective of Mobile Laser Scanning MLS is to generate 3D geo-referencing data of the surrounding environment by combining different sensors, namely GPS, IMU and laser scanner. These sensors are integrated and synchronised to a common time base providing 3D geo-referenced data. These (3D) data are useful for various applications; for example, 3D urban and landscape modelling for visualisation in planning, simulations for environmental management, and to support land use decision-making. There is an increasing demand from a growing range of applications for improving the accuracy of MLS, particularly in urban areas.

There are many technologies and methods for 3D modelling, including aerial and terrestrial photogrammetry, airborne light detection and ranging (LiDAR), and mobile laser scanning. These technologies enable the geometry of models to be created, and the images enable textures to be used for creating photo realistic models. The technologies of terrestrial and airborne photogrammetry, laser scanning, high speed video cameras and their integration with kinematic GPS/IMU can provide high accuracy positioning. These have played a significant role in the progress of 3D urban modelling and increasing its applications.

Laser scanning has become a very important source of 3D data collection, producing clouds of 3D coordinated points and return intensities. Airborne and ground-based technologies are now available, but their full potential has not been exploited. This is because the quality of the derived point cloud from a LiDAR system is based on the random and systematic error in the measurement system (Habib and Van Rens, 2007; Barber et al., 2008).

The use of terrestrial laser scanning (TLS) for collecting high quality 3D urban data has increased tremendously. Haala et al. (2008) said that *"an airborne dataset provides the outline and roof shape of buildings, while terrestrial data set from ground-based views is useful for the geometric refinement of building facades. This*

is required especially to improve the quality of visualisation from pedestrian viewpoints. However, the complete coverage of spatially complex urban environments by TLS usually needs data to be collected from multiple viewpoints". This has major financial implications as collecting data particularly for creating 3D city modelling is costly and time consuming. In contrast, laser scanning from a moving vehicle (mobile laser scanning (MLS)) allows the rapid and cost effective capture of 3D data from larger street sections, including the point cloud coverage of building facades. For this reason, TLS are integrated in to ground-based mobile mapping systems, which have been actively researched and developed for a number of years (Grejner-Brzezinska et al., 2004).

The accuracy of MLS data has significantly improved hand in hand with advances in MLS technology. Today a typical laser scanner, Riegl VMX-450, can provide a pulse repetition rate (PRR) of up to 1100 kHz and range measurement accuracy of almost 8 mm (Riegl., 2011). This accuracy and resolution has great potential in assisting engineering surveying application using MLS. The parameters are limited by the complexity of this system, the different components and their spatial relationship which can introduce errors, thus degrading the accuracy, the same as in airborne laser scanning (ALS) (Csanyi, 2007).

Some errors can still be present in the data even after accurate system calibration. These errors are generally dominated by navigation error and can be reduced via introducing targets with known coordinate into the laser data (Csanyi and Toth, 2006; Csanyi, 2007). Therefore, to support engineering surveying applications that require very high accuracy, such as engineering scale mapping, road environment modelling, and road design, the error in MLS point cloud must be eliminated, as in ALS (Csanyi and Toth, 2006). This level of accuracy needed for such applications can be achieved using specific targets, specially designed for MLS.

Many key challenges have been identified from the background researches that need to be overcome in urban laser scanning. The accuracy of 3D geo-referenced points, achieved via MLS under normal conditions, can reach the level of 3cm (Hunter et al., 2006). On the other hand, Joshua (2011), France, Riegl VMX-250 USA applications-systems Engineer concluded that the absolute accuracy to ground control averaged

5mm horizontally and 15 mm vertically from a highway vehicle. However, this accuracy tends to be degraded in the urban areas up to (10 to 15) cm, because of trajectory errors of the laser scanner, due to degrading of the position and orientation solution (integrated system) when GPS is absent. The degraded results can, also, be attributed to the difficulty of matching natural features in the point cloud. The aim of this research is to improve the accuracy of Mobile Laser Scanner (MLS) data, especially in areas of difficult GPS reception, typically urban environments, by using designed targets instead of natural features targets for the purpose of achieving mm-level positioning accuracy in such areas.

However, the improvement of accuracy of MLS data has not yet been fully addressed in urban areas. This issue has been studied to some extent by various researchers (Barber et al., 2008; Haala et al., 2008; Graefe, 2007c; Hunter et al., 2006; Alamus et al., 2005), and many companies (Infoterra, StreetMapper system 1,2, Geomatic, TeleAtlas). All these studies on MLS, concentrated on the vertical and horizontal geometric accuracy of the position and orientation solution of the system.

Targets are used in a number of ways in MLS and are often chosen from natural detail points, such as point, line and area, and these can be detected automatically based on some specification chosen by the user to improve the quality result of MLS data by improving system calibration (Rieger et al., 2010b; TerraSolid., 2009; Graefe, 2007b). When high accuracy requirements need to be met, natural features can be difficult to define, particularly, for example, in calibrating the system, matching scans together or fitting scans to existing surveys.

High accuracy can be achieved in urban areas using different data sources, such as airborne LiDAR, and terrestrial imagery (video frames or still images). Using these additional sources could affect the result negatively, due to the potential occurrence of random and systematic error differences. This is in addition to increasing the cost, and processing complexity.

It is possible to improve efficiency by capturing the point cloud and aerial images from airborne laser scanning (Habib, 2010). However, these are very costly, and time

consuming compared to the MLS, and still need another data source to acquire the building facade as seen from the street level.

For higher accuracy, particularly in urban areas, a key strategy is to use identifiable specific 3D geometric targets for matching multiple scans from different runs in the opposite directions instead of natural feature, and the possibility of using these targets in the self-calibration procedure of a MLS system.

The high value of targets in MLS has led to research into target designs and algorithms to detect and coordinates their position. Experiments have been undertaken to test the algorithms with the use of Matlab functions.

The StreetMapper360 system from 3DLM Ltd. was used to measure data in two survey campaigns 2009 and 2012 at the Jubilee Campus, the University of Nottingham. The data from the first campaign in 2009 were used to assess the quality of MLS data, and the possibility of using designed targets for improving the MLS data in urban areas. Different areas of interest (AOI) within the campus have been chosen according to the GPS quality varying from open landscape to urban canyon. A program was produced, using Matlab functions, to split the AOI based on the GPS quality level as shown in Appendix A. The second campaign in 2012 allowed testing of the final targets design, specifically for MLS.

Several targets have been designed, dot, ring, pyramid and cone, in order to overcome the limitations of the other existing targets such as Leica circular flat and Faro sphere targets. The designed targets with different sizes, shapes and colours have been tested under different ranges, incidence angles and resolutions in order to evaluate the performance of the targets in each case to find out the optimal target suitable for testing with MLS in the field. Methods for defining the 3D target centre/apex are defined on a mathematical basis and potential limitations identified. The significant advantages of using proposed targets specifically made for MLS is to increase the accuracy of data collected by a MLS particularly in urban areas.

Overall, several methods (ground survey, surface to surface compare and additional source of data) have been used to assess the accuracy of MLS data in urban area in

the first instance. A number of trials were carried out using Faro focus and HDS 3000 TLS to provide test date sites for the optimal target design. Based on the trials, targets were fabricated at the University of Nottingham. This research gives a new approach to provide mm level of target positioning accuracy and 100% matching of multiple scans in any areas, that meet the research requirements.

1.2 Aim of the research

The main aim behind this research was to improve the accuracy of Mobile Laser Scanner (MLS) data, especially in areas of difficult GPS reception, typically urban environments, by using specially designed targets instead of natural features targets.

1.3 Research objectives

The main objectives of this research are as follows:

1. Assessing the quality of MLS measurements in urban areas.
2. Discussing the factors affecting the quality of MLS in urban areas.
3. Investigating the possibility of using targets instead of natural features for improving the data quality. This includes:

    a. Designing different types of targets and investigate the effect of range, incidence angles, the effect of brightness and point density on the positioning of the target.
    b. Investigating detecting targets automatically.
    c. Investigating the mathematics to determine the targets centre/apex.

4. Testing the designed target and checking the improvements that can be obtained from such a target in MLS data.

1.4 Methodology

To fulfil the objectives of this research, it was necessary to undertake the following work**:**

A literature review of principles and research already performed by others related to the different subjects covered in this research: This was an ongoing activity throughout the period of study and provided the opportunity to put this research project into context. This provides the material for the introduction, background and context to the project.

Objectives 1 and 2: Assessing the quality of MLS measurement. Three methods have been considered after a test site was chosen to give a range of features in difficult areas e.g., open sky to urban canyon

- Survey control points on natural features such as the corner of white road marking, building, manhole and etc., along the study area, where some highly accurate ground control points have been coordinated using traditional ground survey technique to enable a comparison with the laser scanner data. A program was created; using Matlab functions to split the area of interest (AOI) based on the GPS position quality level (see Appendix A).

- Using multiple scans of different areas. Quality was assessed through:
    - Creating a triangular irregular network (TIN) for road surfaces and geometric planes for building facades, then a 3D surface comparison and best fit algorithm were applied to identify any detectable tilt error between two or more surfaces from different runs of MLS, particularly in urban areas.

- Using Faro focus^{3D} TLS data in two areas.
    - MLS scanning data of two or more runs were compared with TLS of the same area using iterative closes point (ICP) approach via Geomagic software. This was performed through:
    - TLS data considered as a reference points for comparison with the point cloud obtained from each MLS run.
    - Some GCPs were also used to assess the external quality of each run with TLS.

Objective 3: Designing targets,

This was investigated by designing targets with different shapes. This was achieved through a number of trials to assess the optimal shape, size and colour of the target, range at which the target works and incidence angle (the orientation of the target relative to laser scanner).

From this the optimal target is chosen and an algorithm developed containing two parts, detection and computation. In the first part, for each target, the algorithm was designed to detect the targets automatically from the point cloud. This automatic detection is based on three criteria, namely intensity value, distance between points and point density. The next part of the program is to calculate the centre/apex of the target automatically. In this step, the least squares surface fitting approach was applied through different methods, namely average determination (AD), Gauss Newton (GN) and Levenberg Marquardt (LM) algorithms.

Objective 4: Testing the quality of coordinating targets specifically made for MLS, and checking the improvements obtained from such targets in MLS data. This was achieved through:

1. Comparing coordinates of targets using ground survey techniques with MLS coordinates of the target.
2. Comparing coordinates of targets from multiple pass scans
3. Analysing the optimal target with the different types of targets used.

The above tasks were achieved through:

- MLS scanning the selected test site including targets. Targets were measured to high accuracy using ground survey with total station and level. The quality of the measured values was assessed using network adjustment. The results were compared after applying automatic target detection and computing the apex in the same coordinate system.

- Matching point clouds using natural features and targets. The Matlab algorithm was used for automatic detection and to compute the target centre/apex based on the least squares surface fitting. Least squares matching

approach through the available software in NGI was used for matching using targets.

- Comparing the results statistically for optimal target with different target designs.

1.5 Contribution to knowledge

The scientific contribution of this work comes from the fact that, there have been no studies reported in the literature, on the design of specific 3D targets for use with MLS for example with matching multiple scans use in areas of poor GPS and for linking scans to traditional ground surveys, and for integrated sensor calibration.

3D targets have not been used with MLS with the aim of matching the multiple scans and improving the quality of the data collected by MLS. Therefore, using such targets with MLS and represents a contribution to knowledge, not yet explored in practice. Trials were carried out to determine the most favourable target design. Parameters included optimal target size, shape, signal response, colour coating, and methods to accurately determine the 3D target apex in the laser point cloud.

1.6 Outline of the thesis

This section summarises the contents of the nine chapters included in this thesis as follows:

Chapter one: Includes an introduction to research and its motivation, aims, objectives, as well as thesis outline.

Chapter two: Consists of an introduction to the applications of MLS, especially in urban areas. This includes the required level of accuracy in each case as MLS has produced enormous developments in the techniques for spatial data acquisition, which provides users with the possibilities of direct and automated 3D data capture. It then discusses the specification and problem of the calibration technique and solution detailed in the existing literature. Finally and before the conclusion, the

significance of quality assessment of urban data and brief detail about 3D target designed to overcome the limitations of MLS, are given.

Chapter three: Provides details about the principles and design concept of MLS and TLS. In addition, an overview about the error sources in MLS, including: Platform position and attitude errors, calibration errors, and other systematic error sources and models of MLS. This chapter also discusses the methods of registration and geo-referencing of point clouds. Different types of targets and their errors in practical application are discussed. This chapter covers partly fulfil objectives 1 and 2.

Chapter four: This chapter is divided into two main sections; the first: discusses test related issues, such as test planning, test sites, fixing GCPs, collecting data and data processing. In the second, the accuracy of the data collected by a MLS is evaluated, and the effective factors are studied. Also, the benefits and limitations of the methods, used for quality assessment, and checking calibration of the data are investigated. Finally, the results are discussed in detail before reaching the conclusion, and the importance of designing specific 3D targets for improving the accuracy of MLS data will be discussed. This chapter covers further understanding for the quality issues of objectives 1 and 2.

Chapter five: Addresses and describes the problem and solution for the different types of geometric targets, namely pyramids, cone, sphere, dots and circular flat targets. Designing the target includes choosing the size, shape and colours. Then, the targets are tested under different ranges, incidence angle and resolution in order to evaluate the performance of the target in each direction relative to the scanner. The advantages and disadvantages of targets within the point cloud, and analysis of result are presented.

The registration and geo-referencing of point clouds, and evaluating how the accuracy deteriorates from minimum to maximum scan resolution using target and natural features are also presented in this chapter. Then, the obtained results are discussed and general conclusion is given. This chapter covers the objective 3 part1.

Chapter six: Starts with a detailed description of the automated workflow used for detecting the target from the entire point cloud. This will include showing how the Matlab functions, written by the author, filters the points that represent the target from all other points, and how to find the coordinated point on the target. Finally, results and conclusion are presented. This chapter covers the objective 3 part2.

Chapter seven: Is complementary to the previous chapter, where different methods for identifying the target's centre/apex are introduced. This will include: Plan intersection, average determination, Gauss Newton and Levenberg Marquardt (LM). Some of these methods have been programmed using Matlab factions, and the rest applied using open source codes available on the Internet. Finally, the results comparisons of each method are given. This chapter covers the objective 3 part3.

Chapter eight: will present testing the optimal target with MLS in the field. This includes: a brief description of the test and the accuracy of the result using targets and both natural features and targets. Also, the advantages and disadvantages of the method used and analysis and conclusion of the result are given. This chapter covers the objective 4.

Chapter nine: Presents the general findings and conclusions of this research related to the objectives and the prospects of future research activities in this area. This chapter covers the all objectives.

Project work flow diagram

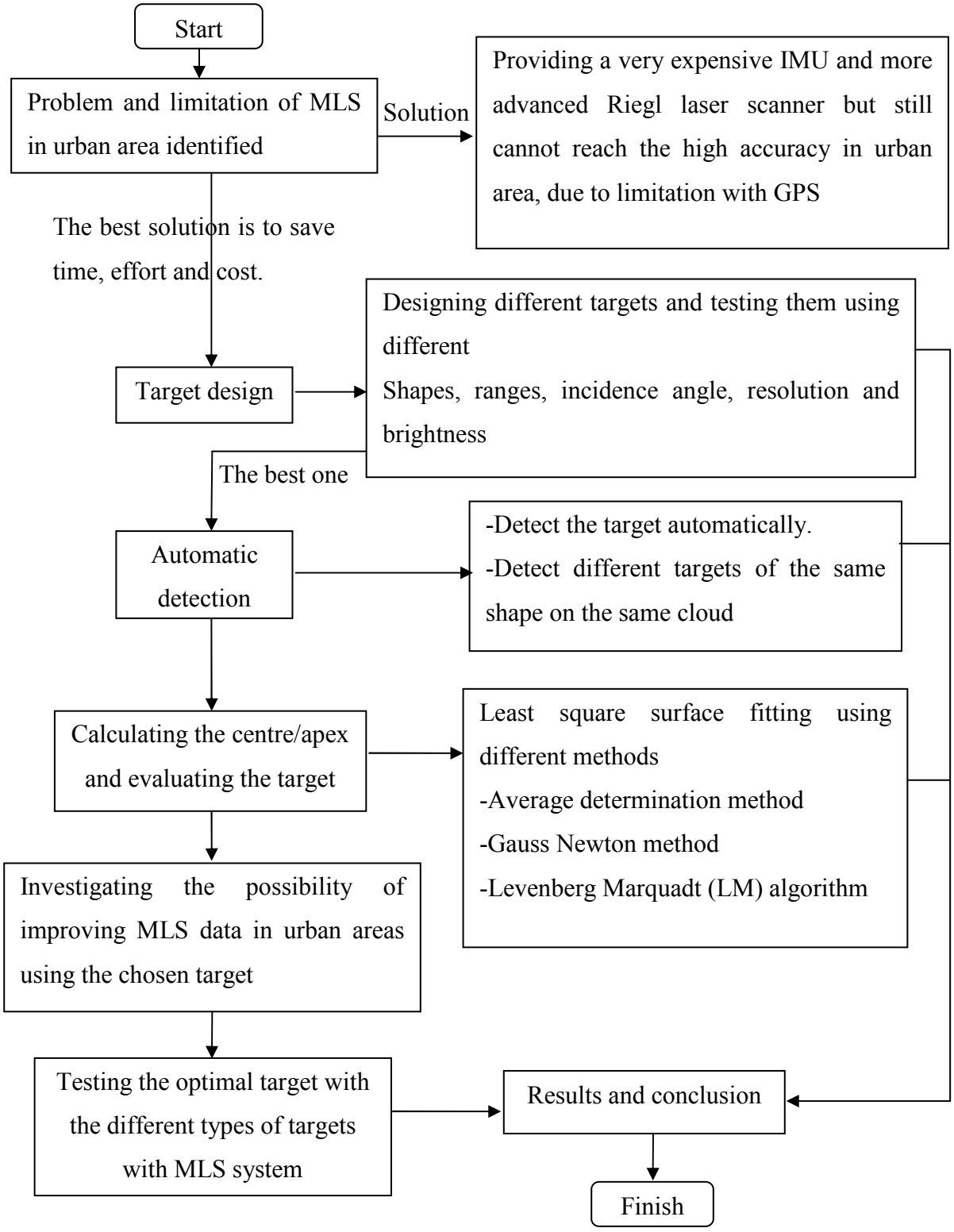

Figure 1-1: Project workflow diagram.

CHAPTER 2: BACKGROUND

2.1 History of mobile laser scanning

In this section, a brief overview about Mobile mapping system (MMS) or MLS will be given. Historical development of MMS, in the last two decades, has come from being designed for academic purposes to becoming a commercially viable industry (Tao and Li, 2007). The concept of MMS dates back to the late 1980s and early 1990s, when the Centre for Mapping at Ohio State University was the first to operate a terrestrial MMS. Their system used a van on which a GPS code receiver, two digital CCD cameras, two colour video cameras, two gyroscopes and sensor for measuring distance were mounted (Puente et al., 2011). Photogrammetric accuracy was at the level of decimetres using bundle adjustment method, but this was not the case in practice, where the accuracy degraded to the level of meters affected by the accuracy of navigation sensors, especially in the urban area.

Further developments on MMS based on GPSVan-including GIM ™ and GPSVision, all used same navigation sensors (Puente et al., 2011). Nearly all MMS depends on GPS as the absolute positioning system. Therefore, the accuracy of GPS plays an important role in the absolute geo-referencing accuracy for a MMS system. Based on that, positioning using dual frequencies carrier phase differential GPS, which can give better positioning accuracy, has been used instead of code positioning. In addition more accurate IMUs, high resolution cameras and more sophisticated processing techniques have been used more and more in MMS. Examples of such systems, include VISAT ™ system, designed by the University of Calgary together with GEOFIT Inc., for mobile highway mapping (Schwarz et al., 1993.), and KiSS ™ (Hock et al., 1995) designed by the institute of Geodesy at the Federal Armed forces University in Munich.

The historical developments of Terrestrial MMS technology in the last two decades are described in Ellum and El-Sheimy (2002). These days, laser scanning technology, often referred to as LiDAR (Light Detection and Ranging), has been

used more and more as a mapping sensor with and without the digital cameras. LiDAR has been operational for surface and object reconstruction since the mid-1990s. It is continuously evolving in the development sensors, as well as in aspects of data processing. High resolution of measurement, wider range spectrum, and extracting the properties of the target or object beyond the range are some of the developments in sensors (Pfeifer and Briese, 2007a).

Terrestrial MMS technology is based on laser range-finding measurements of the range between the sensor and targeted object and provides a considerable increase in data points of exceptional accuracy over conventional data capture methods (Puente et al., 2011). The development of laser technology, along with the improvement in the performance of GPS/IMU for direct geo-referencing, has expanded the range of applications of these MMS, which tend to be called mobile laser scanning systems (MLS). The difference between MLS and MMS is in the use of a laser scanner in the first, instead of cameras, as used in the second; however, in some systems, the laser scanner is used along with cameras. The term, MLS, will be used throughout the thesis.

The term, "Mobile LiDAR", is commonly used for a laser scanner mounted on any mobile platform. In general, the operation principles are similar to that of airborne and terrestrial mobile LiDAR systems, and the data processing workflows are the same or nearly identical in both cases, and the main advantages and disadvantages of MLS data over ALS data handling can be seen in section 2.5.

The majority of TLS and ALS systems use only the pulse time of flight (TOF) measurement principle for ranging (Riegl., 2011; Optech., 2011; Leica., 2011; TopEye., 2011; TopoSys., 2011; Fli-Map., 2011). The latter technologies have been extensively used for creating digital elevation model (DEMs) or dense surface model (DSM) and the estimation of forest inventories. They are quickly being adopted in operational forest management. The ALS technology has been extensively studied by many researchers, such us Habib and Van Rens (2007); Kersting et al. (2008.); etc., and also combined with the photogrammetric technique for realistic 3D city modelling and other application demands.

Locating the scanner on the ground gives some noticeable advantages for capturing isolated objects from multiple angles. TLS systems could be mounted on the tripod

or mobile scanning instruments and as point-scanning devices with a partial or complete curved field of view or frame-scanning devices. TLS are more convenient for capturing small irregular objects, such as buildings, earthworks, etc.

2.2 Calibration of MLS

All sensors GPS, IMU and laser scanner are synchronised using a pulse per second (PPS) which comes from the GPS receiver. The laser scanner has an internal clock and can accurately interpolate the timestamp. If the GPS signal is lost (no satellite visibility) the scanner can use its internal clock to keep the synchronisation. This procedure was carried out by 3DLM Ltd.

Transforming the point cloud in to usable data for system calibration typically requires several processing steps (TerraSolid., 2010). The first step in the process is the creation of a new project. It involves setting up the laser segment of data and beginning processing. The occurrence of any noise and error while establishing the different set up parameters will result in significant time spent on identifying the incorrect parameters or even repeating the entire work. Therefore, this step must be performed with greater responsibility to ensure smooth processing through the project workflow. This step involves defining project properties, such as the trajectories and raw point files, that will be processed and the coordinate system used. It also involves adding all the raw laser data that will be processed in the project.

For the purpose of this research, the following settings have been used in both software packages TerraScan and TerraMatch:

- Reference system: OSGB36.
- Map projection: Transverse Mercator (TM).
- Datum: Newlyn.
- Rotation system: Heading, Roll and Pitch.
- Scanner direction: X (forward), Y (right) and Z (down).
- Average range: vary depend on the objects from the scanner.
- Average height: approximately 3 m from the ground surface.

In order to perform a calibration, a suitable site drive with buildings should be made, ensuring good visibility to walls, smooth vertical walls, right driving pattern, search tie lines (section line) on the building walls automatically, and then HRP misalignment angles will be solved (Soininen, 2010). Figure 2.1 shows two examples of the calibration plan. First: Six driving passes see the same large building from different directions (Figure 2.1 left). Second: intersection with at least two buildings (Figure 2.1, right). Thus, the result of calibration, which is based on the line search, can be seen in Figure 2.2.

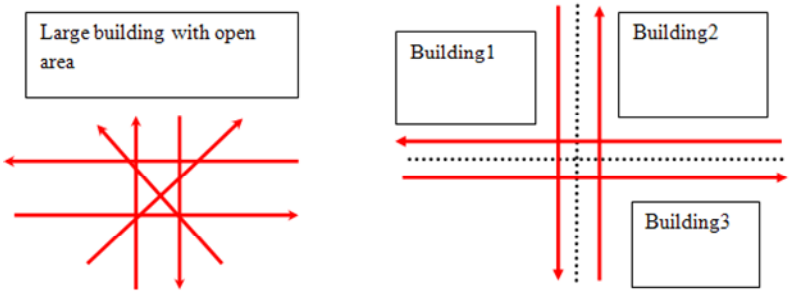

Figure 2-1: Calibration patterns: pattern1 (left); large buildings with open area: pattrn2 (right); Intersection with at least two buildings (Soininen, 2010).

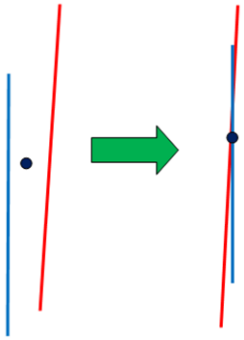

Figure 2-2: Mismatches of tie lines: (left), mismatch before correction; (right) matched after correction (pulls lines together) (Soininen, 2010)

The main procedure using TerraMatch software is data preparation, matching strips and applying corrections, and output of matching report (Burman, 2002). Data preparation includes managing trajectories and filtering laser data. The data needed for matching is:

- Trajectory data with time stamps, i.e. (Time, X, Y, Z, roll, pitch, and heading) for each profile line of the laser scanner..
- Laser data with time stamps (Time, X, Y, Z, I (intensity), profile line number).
- Ground control points (X, Y, Z) (optional).

Trajectory data is needed so that the laser data can be oriented, which is done by comparing time stamps. Trajectories are numbered and equivalent numbering is used for the laser data. As the matching procedure depends on continuous surfaces, laser data has to be filtered so that continuous surfaces belong to one class (Burman, 2002). (See Chapter 4, Table 4.4).

In the matching procedure, there are a number of settings to be made (Burman, 2002):

1. A priori standard deviation of unknowns (shifts and drifts parameters).
2. Convergence criteria.
3. Choosing point class to be matched.
4. Choosing unknowns to be solved.

Choosing how dense observations (measured elevation difference) should be made, from every laser point along the area of interest. The unknowns can be: shift and /or drift in easting, northing, height, roll, pitch and heading.

There is also an option to make the same correction for the entire data set or make the correction for individual strips. When calibrating misalignment between laser scanner and IMU, corrections for the entire data set are normally used (Burman, 2002; Soininen, 2010).

The output report has information about the number of laser points, number of observations, and standard error of unit weight and elapsed time in the matching procedure (Soininen, 2010). A sample of the calibration report of MLS carried out by the 3DLM Ltd. for the purpose of this project can be seen in Appendix B.

2.2.1 System calibration

In order to determine high quality and reliability for the data collected by MLS, the integrated sensors (GPS, IMU and laser scanner) forming the system should be calibrated (see Figure 2.3). During this step, the parameters which describe each sensor characteristics and those describing the relationship between the different sensors should be determined. This issue consists of:

- The internal calibrations of the laser scanner, which must be performed in advance. During this step, the parameters of the internal orientation of the scanner, which describes the scan geometry of the laser scanner, should be determined. These tend to be provided by the manufacturer.

- The misalignment between the IMU and the laser scanner, which can be determined by match and tie line principles (Rosell Polo et al., 2009). The first principle is surface to surface matching, and the second one is feature to feature matching of the two or more laser point clouds from the two or more separate drive passes in opposite directions (TerraSolid., 2009; Rieger et al., 2008) or between two strips or more in airborne laser scanning (Habib and Van Rens, 2007; Glennie, 2007; Burman, 2002).

MLS calibration can be performed using laboratory static calibration (Graefe, 2007b), stationary outdoor (Talaya et al., 2004), or via (Rieger et al., 2010b; TerraSolid, 2009), dynamic calibration.

The former methods need transformation parameters to measure the IMU and laser scanner position on the vehicle, which is based on target field indoors in the laboratory or outdoors. The best result from existing calibration static mode has been identified based on external reference surfaces such as targets (Graefe, 2007b).

Talaya et al. (2004), used control point (targets) observations between overlapping of several scenes captured while the van was stationary and GPS/IMU sensors were collecting data, and then run through a least squares adjustment to determine the best fit bore-sight angles. For improving the determination of the parameters, and separating their correlation, they used four scenes taken with different azimuth angles and used in the adjustment. The result of the calibration method for linear offset and misalignment matrix revealed formal accuracy of 6 mm and 12-34 arc-second respectively.

All MLS laser scanners need to be calibrated in terms of the laser scanner itself, GPS, lever arm and misalignment between laser scanner and IMU. But this is not sufficient for MLS to provide accurate results, where the error in Navigation Solution

(NS) cannot be eliminated in calibration processing. The calibration parameters of the system should be checked for each scanning project (TerraSolid., 2009).

In the literature, many papers discuss the bore-sight calibration of MLS, which is the one of the most recent methods in the automatic work flow for calibration procedure using TerraMatch software developed by TerraSolid (2009) and a variation of Riegl's RiProcess (Rieger et al., 2008). The idea is to scan a flat wall from different directions and distances. The software (either Riegl's RiProcess, or TerraSolid's TerraMatch) will then carry out the proper calibration finding the necessary parameters.

In TerraMatch software, the system calibration is based on natural feature, such as tie lines. The software searches for the tie line from the collected point cloud automatically. In the second phase, it calculates correction values for all ENH and Heading Roll and Pitch (HRP) or only for HRP angles, and finally will find out the misalignment between the laser scanner and the IMU. The outputs are correction values for HRP, which are applied for the entire data set (TerraSolid., 2004).

Rieger et al. (2008) determined the angular alignment between IMU/laser scanners while the vehicle is moving in an urban area. Their proposed method of data acquisition is based on scanning an object, e.g. a building with at least several planar surfaces oriented at different angles related to each other, obtained while driving the MLS system in the opposite direction. The distance of two corresponding surfaces was approximately proportional to twice the unknown angular deviation between the scanner and IMU with respect to the roll axis (Rieger et al., 2008).

The algorithm detects the corresponding planar surfaces of known flatness inside the point cloud. These surfaces are defined by the location of their centre of gravity, their normal vector and the size of the two correspondence surfaces areas. One in point cloud 1, and the other in point cloud 2, the author tested a total of 471 observations of corresponding planar surfaces for calculating bore-sight angles. The results for HRP obtained were **(**-0.032^{o}, 0.209^{o} and -0.868^{o}**),** respectively. The remaining error in standard deviation was around 14mm.

The drawback of this method is the ability to work, just in specific areas due to the difficulty of finding suitable planar surfaces from a high density point cloud.

There is a variety of approaches to bore-sight angle determination, but in general, all of these methods are reduced to two basic ways of solution for the unknown angles. Both approaches take advantage of overlapping LiDAR strips, usually flown in different direction and sometimes with different flying height (Glennie, 2007) (see Table 2.1). The two approaches are (Glennie, 2007):

1. Manual adjustment. The 3 misalignment angles are manually adjusted, and the data are processed until opposing runs visually match. Normally the edges of buildings were used to visually line up the data. The process can be fairly time consuming and is highly dependent upon the skill and visual bias of the operator performing the adjustment.

2. Least squares adjustment. Tie point and/or control point observation between overlapping LIDAR strips are collected, and then run through a least squares adjustment to determine the best fit bore-sight angles. This approach is detailed in Toth (2002), Morin (2002) and Talaya et al. (2004).

	Roll and pitch (deg.)	Heading (deg.)
Manual Bore-sight	0.005	0.008
Least squares Bore-sight	0.001	0.004

Table 2-1: Typical bore-sight angle determination errors (source (Glennie, 2007)).

Graefe (2007b) explained the calibration of a road mobile mapping system in the laboratory using a reference target consisting of at least 3 flat surfaces combined by a special target to measure the position of IMU system and laser scanner related to the vehicle coordinate system. He assessed the quality of calibration under practical survey conditions. The results of his approach show that: the laser scanner data accuracy reaches 3-4 mm for height of the scanned points even when using different scanners. Stereo-photogrammetric measurements fit to the laser scanner data within their measurement accuracy of less than 0.05 m (Graefe, 2007b).

The disadvantages of this approach are that: the calibration process in the laboratory does not reflect the actual field environment, although it is carried out in standard homogenous condition. The advantage of calibration in the laboratory gives initial values to start with in a self-calibration in the field. The actual parameters can be obtained during capturing data in dynamic environments.

2.2.2 Laser scanner calibration and performance investigation

High accuracy is required for various application, such as change detection and deformation monitoring using rigorous calibration procedure of the laser scanner (Tsakiri et al., 2006).

Boehler et al. (2003) at the Institute for Spatial Information and Survey Technology (i3mainz) in Germany was the first group to set up annual calibration tests allowing comparison between instruments from different manufacturers for the first time.
Gottwald (2008) proposed simplified and full calibration tests for laser scanners that could be adopted in an ISO standard. The simplified test was designed to be easily carried out by independent companies in less than an hour. The test quickly evaluates the angular and range accuracy of the laser scanner. The complete calibration test gives an estimation of accuracy and systematic deviations based on statistical methods.

In Kaasalainen et al. (2008), a new generation of practical calibration procedure for laser scanner intensity was developed with a TLS in the laboratory and field conditions using brightness targets and a calibrated reference panel. The result was compared with those obtained from ALS data, which used the same set of brightness targets. It revealed that the relative intensity calibration laser scanner is possible using a calibrated gray-scale, but requires background information of the targets and conditions in which the measurements are carried out.

The most recent research in the range and incidence angle effect on the intensity measurement for different TLS devices and targets were conducted by Kaasalainen et al. (2011a). The result showed that the distance effect is strongly dominated by instrument factors, whilst the incidence angle effect is mainly caused by the target

surface properties. This research test was essentially used to establish a correction scheme for range and incidence angle effects, e.g. in stationary TLS from multiple directions or a mobile application, which are constantly increased.

Schneider (2009) used two different calibration fields scanned with a terrestrial laser scanner, Riegl LMS-Z420i, from different positions. Signalised targets are used in the calibration fields, to be measured within the point cloud automatically. The measured spherical coordinates (distance, horizontal angle and vertical position) were used as observations in a multi-station adjustment, corresponding to a photogrammetric bundle adjustment. A number of additional parameters were used, determined within a self-calibration procedure. These additional parameters are partly derived from recognized error sources of geodetic instruments, such as errors of axes or eccentricities of axes and to some extent taken from the literature, where the calibration of other laser scanners is already explained, some of them can be found in Reshetyuk (2009).

The results of calibration (parameter values, standard deviations, significance), computed from the observations of both calibration fields are analysed and compared. The combination of adjustment procedure with variance in component estimation allows for the independent assessment of the precision of the different kinds of observations (distance, horizontal angle, vertical angle). Thus, the improvement of the precision of the adjusted observations as a result of a strip-wise addition of calibration parameters was studied. As object point coordinates were dealt with as unknowns within the adjustment, their standard deviations were computed and analysed (Schneider, 2009).

It could be revealed that the use of additional calibration parameters have the potential to enhance the object point precision. The drawback of this approach is that it is difficult to calculate reliable and comparable calibration values. Another reason is that the parameters are not only affected by the instruments, but also depend on the external measurement conditions, such as measurement range, target design, angle between laser beam and object surface and the chosen angular resolution.

Hiremagalur and colleagues created tests to determine range accuracy and noise. Flat surfaces with varying reflectivity were scanned at different known ranges up to 50 m; the scanned surfaces were modelled, and the point deviations from this were used to determine precision and range accuracies. The results showed that the error in range increased as the distance increased, the standard deviation was found to be between 1mm and 5mm over the 50 m range (Hiremagalur et al., 2007).

Boehler et al. (2003) also found a systematic range error when scanning targets with low reflectivity of the order of a few cm. For angular accuracy determination, they used two spherical targets and compared the angular distance separately as found by laser scanning with conventional methods to find the angular error. Boehler et al. (2003) also created a field test to find the scanner resolution by creating wheel spokes of changing thickness, a scanner with high resolution would be able to detect the thinnest section of the wheel spokes.

Kerstin and colleagues published a comprehensive comparison of seven laser scanners in a series of trials. The group tested the laser scanner 3D positional accuracy, range accuracy, target acquisition accuracy and the effects of incidence angle. The group evaluated the range accuracy of the seven laser scanners by comparing their ranges against ranges on a calibration baseline (Kersten et al., 2008). The accuracy of different target types were also tested over the same ranges and it was found that over shorter distances (up to 80 m) HDS blue and white targets were the most accurate. Over longer distance (over 120 m), spherical targets were the most accurate. The HDS black and white targets only work in the 200 m range, whereas, the HDS blue and white targets and the spherical targets can work in the 300 m range. When a Leica Scan Station2 was used, the incidence angle and surface type affected the accuracy of a point cloud; this was investigated by Kremen et al. (2006) at the University of Prague, and also by Clark and Robson (2004) from University College London.

A test of 3D positional accuracy was done by manually placing 30 spherical targets around a large hall and getting their accurate location by using a total station. Each scanner was then set up in different locations, and the positions of the targets from the laser scanning were compared to the total station coordinates. The tests found

that the Leica HDS 3000 used in this project had a positional error of around ± 6 mm while the Leica HDS 6000 had an error of ± 6.5 mm and Faro focus^{3D} 120 had an error ± 4mm (Kersten et al., 2008).

Kersten et al. (2008) found that phase based scanners have a large error (4mm) compared with time of flight scanner (1mm) when comparing them to a reference plane for an angles of incidence 45^{o}. Kremen et al. (2006) scanned many different types of surface at a variety of different angle of incidence. They found that at an incidence angle over 50^{o}, material with specular reflection and high absorbability, such as gloss black materials, recorded no return signal. Clark and Robson (2004) worked on scanned colour charts at a different angle to the laser scanner. They found that at an angle of 40^{o}, the point data was less noisy with less deviation away from the flat plane.

2.3 Accuracy assessment & performance

In this section, three related topics will be briefly addressed by Vosselman and Mass (2010).

- Testing and calibration as a requirement for the use of a mobile mapping system.
- Theoretical error and accuracy analysis.
- Experiential assessment of precision and accuracy.

The testing and calibration procedures generally include all system components. Particular emphasis has to be laid on the laser scanner regarding the reference point and axes, and the positioning and navigation sensors regarding offset and drift. In addition, temperature effects have to be studied. For more details, see Hesse (2008).

A theoretical error and accuracy analysis can be based on evaluation of the system configuration, the errors of the relevant components and the mathematical processing sequence during analysis of the captured data. Lichti et al. (2005) discusses error models and error propagation in directly geo-referencing terrestrial laser scanning networks. Glennie presents a rigorous first order error analysis of the TLS geo-referencing equations for mobile mapping systems. IMU attitude errors, laser scanner

error, lever-arm offset errors and positioning errors have been considered in the analysis. He, also, discusses different scenarios such as ground- based and kinematic terrestrial LiDAR. The derived horizontal and vertical errors are distance dependent and generally below 10 cm. The laser scanner errors are identified as the major effect quantity (Glennie, 2007).

A combination of a theoretical error analysis and empirical test in particular for the StreetMapper mobile mapping system is presented by Barber et al. (2008). They derived reference data from RTK GPS and short-term static differential GPS observation. Corner points of white road markings have been used as reference points, which could be easily identified in the scan data. Statistical analysis revealed that a precision of a few centimetres was less than the values of the theoretical analysis.

The quality and reliability of MLS data have not yet been fully addressed in urban areas. This issue has been studied to some extent by various researchers ((Barber et al., 2008; Haala et al., 2008; Graefe, 2007c; Hunter et al., 2006; Alamus et al., 2004), and many companies such as Infoterra, StreetMapper system, Geomatic, TeleAtlas, etc. All these studies on MLS concentrated on the vertical and horizontal geometric accuracy of the system.
In Barber et al. (2008), vertical and horizontal geometric accuracy of the SteetMapper MLS platform are analysed. Corresponding points are selected on target areas clearly identifiable by their intensity values. The planimetric accuracy ranged from 9 - 26 cm.

Haala et al. (2008) investigated the accuracies of MLS measurements from StreetMapper for architectural heritage collection and 3D city modelling. They compared estimated planes fitted on a selected number of building façade with walls from a 3D city model. They found constant errors between 12.6 up to 25.7 cm. Post-processing could reduce the errors to 7.4 - 9.0 cm. The remaining deviations are explained by the inaccuracies of the façade used as a reference.

In this thesis, the planimetric and vertical accuracy of the same MLS system has been measured from different areas within the Jubilee campus using 3D surface analysis

via Geomagic software v.10, and gave the result between 2 to 5 cm. In addition, the intersection of planes method has been used to evaluate the quality of the point cloud in the edge of building façades, and to accurately measure the points on the edge of walls, as illustrated in chapter 4, section 4.3.1.2.

In the work of Hunter et al. (2006), results from their first study showed that analysis should be based on continuous sections of scan data. The software, used for the manipulation of the data, was TerraScan (version 6) from TerraSolid. This allowed the data to be split into flight lines, i.e. continuous sections of point cloud data that begin and end where a change in vehicle direction approaches 180º. The same software but a new version (10.013) was used for checking the calibrated data from MLS blocks in two areas, blocks 67 and 55, and is presented in chapter 4, section 4.3.2.

Alamus et al. (2004) reported similar validation work to that performed by Barber et al. (2008), for the GEOMBLE system in two study areas: a small zone and a large zone, using five check points. In the small zone, the RMSE was 22 cm, 16 cm, and 26 cm in easting, northing, and height, respectively, based on image stereo pairs. In the second zone, the results obtained were 50 cm, 39cm in position and 48 cm in height.

In this thesis, the quality results of MLS data were assessed using different methods namely, ground survey point, multiple scans and additional source of data. The comparisons have been between laser points to a known control point in different areas with different GPS coverage, and is presented in chapter 4, section 4.3.1.1.

Soudarissanane et al. (2009) investigated the effect of incidence angle on the quality of TLS point. The quality of a scan point is influenced by four major factors, namely instrument calibration, atmospheric condition, object properties and scan geometry. They investigated the last factor focusing on the influence of incidence angle. They considered the impact of the angle on the signal-to-noise ratio, and modelled the increase in measurement noise with increasing incidence angle. Two experiments were performed; in the first, a reference panel was scanned at a fixed distance, but under different scan angles. The results of the first test showed that at angles above 60 degrees, the incident angle dominates the scan point precision. In their second

test, for a regular point cloud of a room, they found that 20% of the measurement noise was due to incident angle.

The importance of using targets for getting precise measurements can be found in Smith and Taha (2009). They used high resolution pictures acquired via SLR cameras, Canon EOS 5D MKII, where it was possible to measure the precise 3D coordinates for well-defined targets using close-range photogrammetric techniques. However, getting such precision is still challenging.

2.4 Importance of MLS over ALS

Precise road or rail corridor survey methods require sensors with complementary measurement characteristics. For example, Graefe (2007a) explained that the standard deviation of 4mm for height of the scanned points achieved on application for road infrastructure and road surface are the basis for planning and road design. This level of accuracy opens new potential in assisting engineering survey application using MLS.

On the other hand, Csanyi (2007) investigated the possibility of using LiDAR specific ground target to improve the LiDAR data accuracy for the application of the transportation corridor mapping to help engineering design and change detection of the road network requiring high spatial resolution and considerable, engineering scale mapping accuracy. Csanyi (2007) used two test flights, the Optech ALTM 30/70 LiDAR system operated by the Ohio Department of Transportation. The test shows that, the LiDAR-specific targets could make improvements to cm-level accuracy for the application of the transportation corridor mapping. The target circle centres were GPS surveyed with a horizontal accuracy of about 1-2 cm, and a vertical accuracy of 2-3 cm.

2.5 MLS applications

MLS has shown great potential to recreate 3D object geometric descriptions of the building facade and road surface models. Recently, the MLS system has been applied in erosion change mapping of the river Tenojoki (Tana) in Finland (Vaaja et al.,

2011) as well as in an application to assess snow cover roughness (Kaasalainen et al., 2011b).

Some surveys must take account of roof line not being the building footprint, such as ALS and Aerial photo; whereas MLS captures the wall and not roof line, and so directly provide a building footprint (see Figure 2.4). For example Shan and Toth (2008) identified problems as far as integrating ALS data into the cadastre map is concerned; for example, in photogrammetric research the position of the building wall cannot be correctly estimated with roof overhang. The extracted wall and the building footprints on the cadastral map have different representation (Vosselman and Mass, 2010b; Rutzinger et al., 2009; Oude El-Berink, 2008). The mobile or terrestrial laser scanning, which shows the advantage of providing details of building façade as required for the creation of realistic 3D city modeling, is also developed and widely applied in the use of field survey (Shan and Toth, 2008; Becker, 2009; Rutzinger et al., 2009; Oude El-Berink, 2010; Pu, 2010). The work of MLS mapping and accuracy assessment could be found in Barber et al. (2008) and Brenner (2009), where it is stated that 10 to 15 cm possible accuracy were reached respectively for the urban area mapping.

The needs for MLS data in urban areas are expanding and growing rapidly in a variety of applications in recent years, including mapping of urban areas, road surface models, forestry management, flood and risk assessment, transportation and pipeline corridor mapping, etc., All require high accuracy data. Therefore, the improvement of MLS accuracy is important.

The biggest advantage of MLS data in urban areas is its mobility and its realistic impact on users for future decision making processes. It has the potential to be used everywhere as scientists, engineers and planners require more detailed information about our environment. Also the requirement for accurate three-dimensional mapping of terrain and artificial structures is expected to increase significantly in the following years (Barber et al., 2008).

MLS data have some advantages over TLS and ALS data handling (Haala et al., 2008).

- As a result of its very large dense point clouds in urban areas, high resolution data for 3D city modelling can be obtained; building façade and road models can be supplemented and reconstructed from different environments by means of importing and exporting tools.

- MLS offer a new possibility to survey details, such as walls, road signs and other objects, which cannot be detected in ALS. In addition, modelling plants like trees from point cloud for visualisation purpose in 3D city models is an advantage as the tree trunks can be seen clearly in most cases, which is an important parameter for tree detection and modelling (Rutzinger et al., 2010).
- Urban models are already available for a large number of cities from aerial data like stereo images or airborne LiDAR. Ground based MLS is especially useful for accurate 3D mapping of other features and structures like road details, urban furniture or plants.
- Providing details of building façade as demanded for the production of realistic 3D city modeling. (See Figure 2.5, left).

The common advantages and disadvantages of MLS data over ALS data handling is summarised as follows.

	Airborne laser scanning (ALS)	Mobile Laser scanning (MLS)
Advantages	+ High performance to survey large area +Enough valuable information is available to determine the system's bore-sight alignment parameters + High satellite visibility + Fairly uniform positional accuracy	+ Fast operation and cost effective capturing of 3D data from larger street sections. + Similarities in data processing +Common technology with airborne. + Survey platform (car) is easier to be available
Disadvantages	- In general, do not survey vertical targets - Higher mobilization and operation costs. - Permission to fly, not always	- Satellite visibility in urban areas - Positional accuracy

Figure 2-3: StreetMapper360 with Riegl VQ-250 (left) and the system inside the vehicle with fixed frame (right) (source (Streetmapper360, 2009).

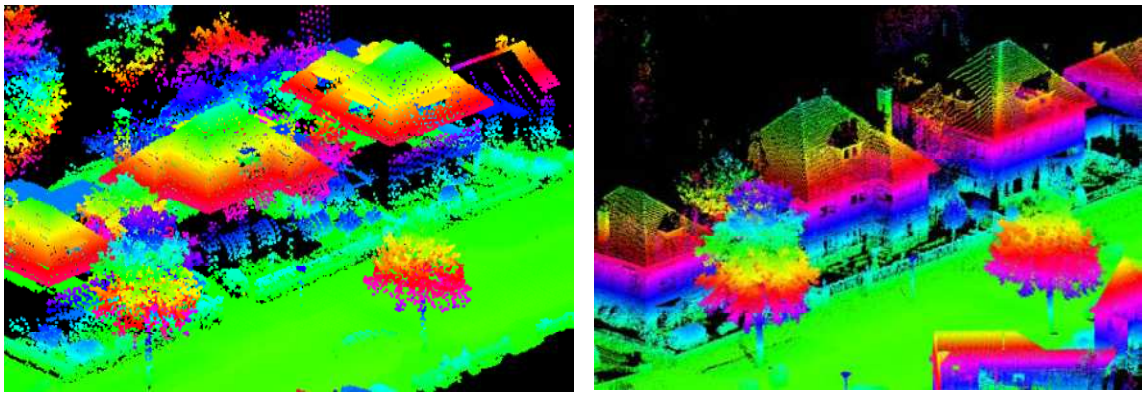

Figure 2-4: A detail of the test site acquired by airborne laser scanning (left) and mobile laser scanning (right) (source (Rutzinger et al., 2009)).

Three-dimensional data for MLS seem to be useful for other different applications such as:

- Most 3D format processing software such as AutoCAD could be used for handling and further analysis of the 3D point data, e.g. road design (see Figure 2.5, right).

- The geo-referenced point clouds data can be imported into different commercial software for the interested object detection and visualisation.

- Forensic uses to create 3D recreations of crime scenes.

- Cultural heritage documentation.

- Applications for road network survey, such as determination of geometric road parameters. The latter, especially, the roadway edges, lane structure and lane width were used by Graefe (2007b) to define the processing area of the digital surface model.

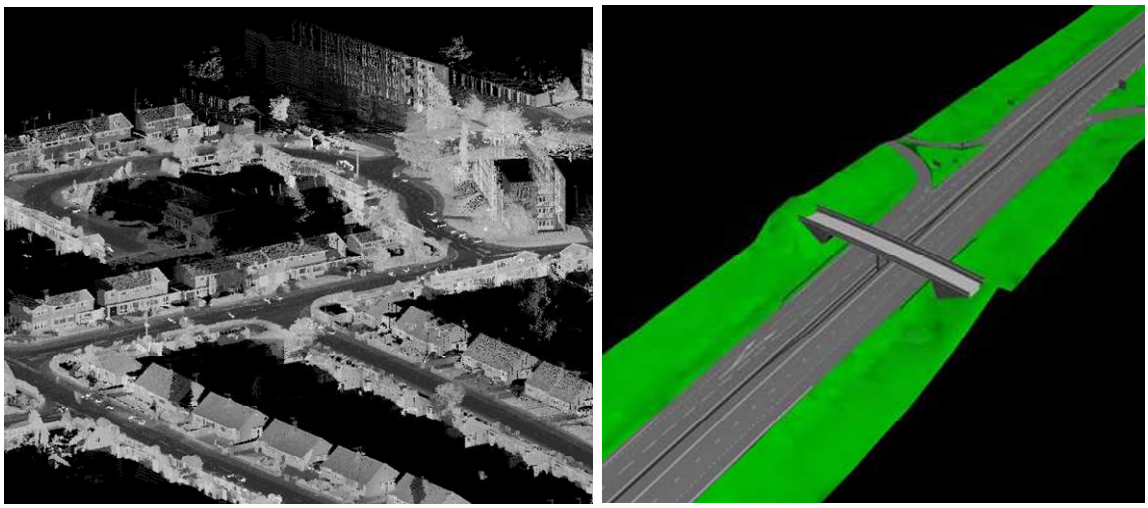

Figure 2-5: A typical point cloud of an urban area on the left, and perspective view of final 3D model created from StreetMapper highway data (right) (source (Hunter et al., 2006)).

Although the wide range of applications contributes to the common demand for three-dimension information, their spatial requirement differs significantly with regards to precision, and high quality and reliability of data capture by a MLS system in urban areas. There are many significant challenges that need to be overcome in urban laser scanning, which can be summarised as follows:

(1) Trajectory error of the laser scanner (IMU drift due to limited availability of GPS signal).
(2) Difficulty in accurately measuring natural detail points in the point cloud.

The above cases alter quality control and calibration of MLS data particularly, in urban areas.

As stated in the previous paragraphs, urban data has expanded into many application fields. It has been common for modelling urban areas including buildings, roads, road structures such as traffic signals and traffic signs, and vegetation. An example on the recent application of MLS is designing and planning of the Queen's Diamond Jubilee Concert. A RIEGL laser scanner was used to capture millions of individual measurements. The Bentley Pointools point-cloud software was then used for processing the collected dataset to create a 3D model of the area outside Buckingham Palace, London, UK, as shown in Figure (2.6, left) (GIM, 2012).

These days, low cost hand-held MLS, see Figure (2.6, right) has been used indoors and outdoors, even if GPS signals are not available. An example of this system was designed by Australian's national science agency, CSIRO- from the UK-based start-up GeoSLAM (GIM, 2013).

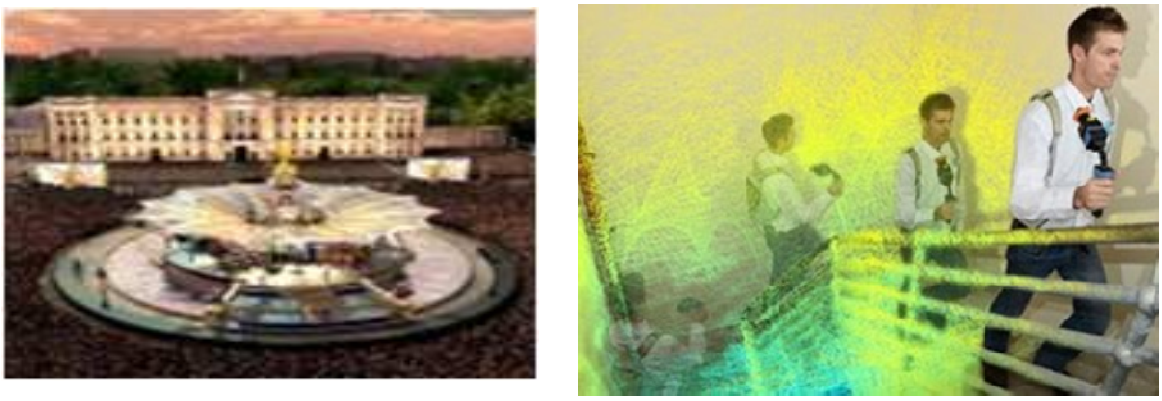

Figure 2-6: 3D Model for Queen's Jubilee Concert planning (left) (source (GIM, 2012)); New MLS hand-held system (right) (source (GIM,2013)).

2.6 Type of laser scanners

Currently, range measurements for MLS systems are divided mainly into two methods: time-of-flight and phase shift (see chapter 3). A time-of-flight (TOF) scanner uses the pulse emitted to the target, and the time it takes to return correlates to the range. Examples of laser scanners using this principle, include: Leica. (2011), Sick. (2011), Optech. (2011), Trimble. (2011), and Riegl. (2012).

Phase based laser scanners, e.g. (Faro 3DLS, 2011; Zoller+Frohlich., 2011; Leica., 2011), (Figure 2.8, left) deduce the range by measuring the phase difference between the signal transmitted, and the signal received back through an amplitude modulated continuous wave (AMCW). Although the measurement range is lower than TOF, phase based laser scanners have better accuracy. Ground coordinates of each laser pulse can be calculated highly accurately by combining the laser range, scan angle (mirror angles), laser position from GPS and orientation of the laser platform from IMU (Barber et al., 2008; Haala et al., 2008; Graefe, 2007c; Alamus et al., 2004).

The laser pulse repetition rate (PRR) in combination with the scanning mirror deflecting pattern determines the LiDAR data collection rate. (Puente et al., 2011). In the most advanced commercially available LiDAR systems, the rate of measuring data is normally 50 kHz – 550 kHz such as Riegl VQ-450 (see Figure 2.7, right), which allows the client to collect data in the required ground point density. This device (Riegl VQ-450) has been mounted on the StreetMapper system with a GPS/IMU operated by 3DLM Ltd. is used in this project for testing the quality of coordinating targets specifically made for MLS. The procedure and results are given in chapter 8.

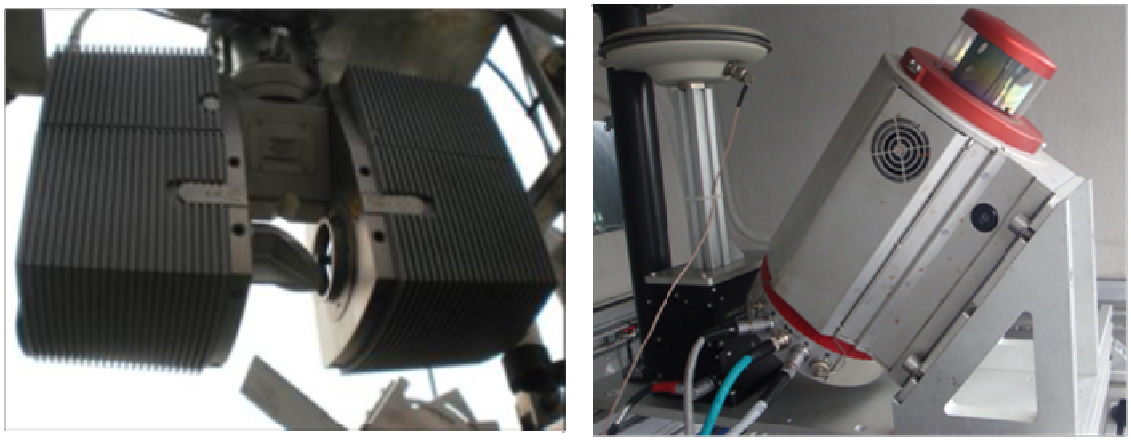

Figure 2-7: FARO Focus Photon 120 mounted on the ROAD-SCANNER system (left), (source (Puente et al., 2011)). Riegl VQ-450 latest version mounted on StreetMapper system with GPS/IMU (right).

Table 2.2 illustrates the most common laser scanning systems and their main specifications.

MLS System	Road scanner	IP-S2 Compact	StreetMapper 360 or Portable	VMX-250 and 450	Dynascan	Lynx Mobile Mapper
Scanner	Faro Photon 120	Sick LM 291	VQ-250 and VQ-450		MDL Scanner	Lynix LS
Maximum range	120m (ρ90%)	80m (ρ10%)	500m (ρ80%) and 800 m (ρ80%)		Up to 500m	200m (ρ80%)
Range precision	1mm@ 25m, (ρ90%)	10mm@20m	5mm@1-50m, (1σ)		-	8mm, 1σ
Range accuracy	±2mm@25m	±35mm	10 mm @1.5 to 50m, (1σ) 08 mm @1.5 to 50m, (1σ)		±5cm	±10mm (1σ)
PRR	122-976 kHz	40 kHz	Up to 600 kHz (2x300kHz) Up to 1100 kHz (2x550kHz)		36 kHz	1000 kHz (2x500 kHz)
Scan speed	48 Hz	75 Hz	200 Hz (2x100 Hz) 400 Hz (2x200 Hz)		Up to 30 Hz	200 Hz (2x100 Hz)
Scanner FOV.	H 360°/V 320°	180°(1) /90°(2)	360° without gabs		360°	360° without gabs
Angular resolution	H 0.00076°/V0.009°	1°(1) /0.5°(2)	0.001°		0.01°	0.001°
Weight	14.5kg	22.7kg	Approximate 11kg		11 kg	78 kg

(1) Sick LMS 291-S05 used in IP-S2 Compact system.
(2) Sick LMS 291-S14 used in IP-S2 Compact system.

Table 2-2: Laser scanner specifications of MLS systems.

2.7 Conclusion and Summary

Within this chapter, a general review of land-based mobile laser scanning (MLS) was discussed taking into account the development of both hardware and software, and the main applications of the system. Is it true that MLS systems have demonstrated their power in wide application areas and are gaining widespread acceptance. With the continuous advancement of mobile mapping technology, as well as the reduced costs of the system development, mobile mapping potential will be explored further.

3D data acquisition for road planning and 3D city modeling, and other applications such as change in detection cultural heritages can be acquired using a variety of terrestrial and non-terrestrial measurement techniques. Also, TLS and official cadastral information have been widely applied. ALS and aerial photogrammetry are currently the most used techniques in 3D data acquisition.

Road planning and 3D city modeling have been an active research area of MLS for more than a decade, and a number of methods and systems have been developed for improving 3D city models from digital images and other auxiliary data automatically or semi-automatically. Two key issues are involved for generating high quality data, which are: high performance of navigation sensors and advanced mapping sensors.

In order to improve the quality and reliability of the data in urban areas where the high dependence in navigation solution tends to be degraded, 3D targets have shown to have some potential but have not been fully explored. This is the focus of this research project.

Efforts to increase the level of accuracy have become essential in order to meet the increasing demand for accurate geo-referenced data in urban areas. However, the efforts to thoroughly automate the process from capturing data to providing outputs with high accuracy are still considered to be challenging.

CHAPTER 3: PRINCIPLES AND ERROR SOURCES OF LASER SCANNING

3.1 Introduction

The basic aim of a laser scanner is to create a cloud of 3D coordinated points that geometrically represent the object of interest. A laser beam is projected onto a rotating mirror, of which the horizontal and vertical angles are accurately measured. The laser beam is reflected on the object, and the returning signal (echo) is detected at the scanner, and the distance to the object is determined (Pfeifer and Briese, 2007b), see Figure 3.1. The range, horizontal and vertical angle are used to create an X, Y, Z coordinate of the point of reflection. Due to the rotating mirrors, the laser scanner is able to collect thousands of 3D points per/sec, making a dense and accurate 'point cloud' that can be visualised and analysed.

There are different types of beam deflection units used in TLS, such as "monogon" (flat) rotating mirrors, oscillating mirror and polygonal (Reshetyuk, 2009). These different types of beam deflection or scanning mechanisms, which are used in airborne and TLS, can be seen in Figure 3.2 (Vosselman and Mass, 2010). Scans can be geo-referenced to place the 'point cloud' into a local or global coordinate system this may be necessary for quality assessment of the derived point cloud and for some deformation projects where absolute movement is required.

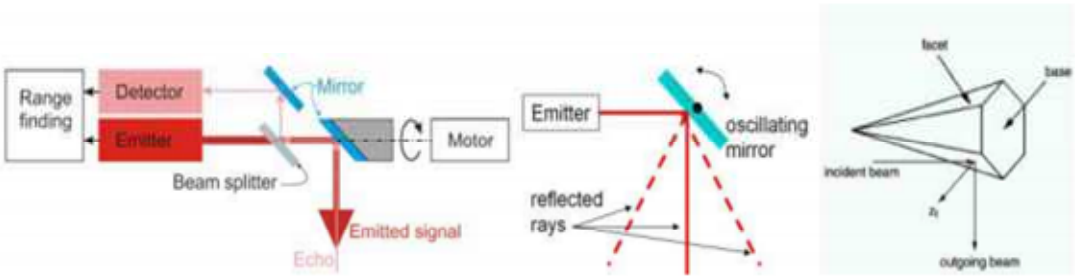

Figure 3-1: A schematic diagram of the basic internal working of a laser scanners of different mirrors: [Left: flat rotating mirror, middle: oscillating mirror, right multi-faceted (polygonal) mirror] (source (Pfeifer and Briese, 2007b)).

Laser scanners have been commercially available for the last two decades; from that time, significant advances have been made in this area. Enhancements in accuracy,

precision, ease and speed of use, size and weight of the equipment, as well as developments in software, have made laser scanning a valuable device in the surveying world. It is used for several applications in a variety of fields and as a tool for the highly accurate field of change detection, cultural heritage and structural deformation monitoring.

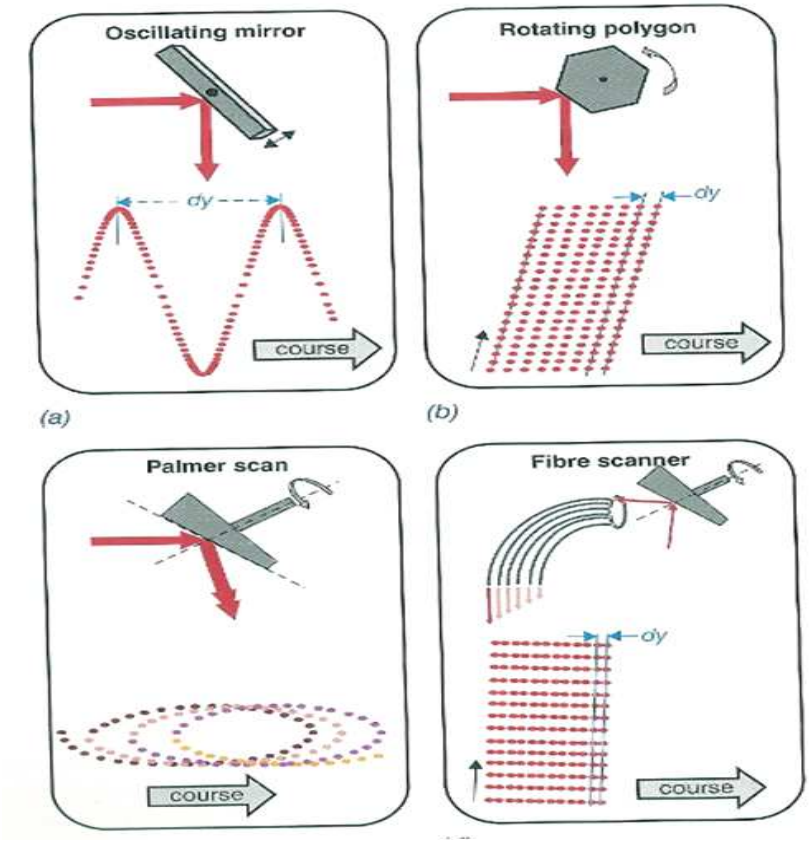

Figure 3-2: Scanner mechanisms and ground samples (Vosselman and Mass, 2010).

3.2 Classification

Most of the usual classification types, like precision, accuracy, range and speed of the data collection are primarily dependent on the object distance measurement used. There are three types of measuring systems, that are mainly applied to detect the distance between the target and the scanner; pulse round trip (TOF), and phase- and triangulation-based measurement, where each has different attributes.

TOF and phase based measurement can be categorized as “light transit time and estimation” which is based on the concept of the light wave and its propagation

velocity. The measurement of both can achieve mm level precision (Pfeifer and Briese, 2007b). With the character of continuous wave modulation, the phase based systems tend to have high data rate (pts/sec), but the range is shorter than TOF measurement. For example, the phase based Leica HDS 4500 has the scanning speed of 500 000 pts/sec, a range of 50 m and on accuracy of 5 mm / 50 m. Whereas the scanning speed is only 1800 per second for the pulse based (TOF) HDS 3000 (Leica., 2011).

The TOF measurement can be used for medium to long ranges 150 m- 2500 m; at medium ranges, these scanners can provide accuracy of around 6 mm at 100 m, but the accuracy decreases with increased range (less than 20 mm at 1000 m) (Leica., 2011). The main disadvantage of the TOF system is the relatively slow acquisition of points (up to 50,000 pts/second in the Leica ScanStation2) while the latest model of TOF (Riegl VQ-250 and VQ- 450) 2D laser scanner provides up to 300 000 and 550 000 pts/s respectively (Riegl., 2012).

The phase based measurement system can be used with short and medium ranges, up to 80 m. The accuracy is equivalent to the TOF system over close distances (6 mm at 80 m); nevertheless, the data tends to be nosier (Dimsdal, 2005). However, the capability of faro focus^{3D}120 laser scanner used in this project is 0.6m-120m indoor and outdoor with low surrounding light and normal incidence angle to a 90% reflective surface (Faro 3DLS, 2011). The major advantage of phase based scanners is the rapid point collection, which is ten times faster than TOF.

Another method of description that can help is the triangulation-based measurement following the cosine law, where the range is determined by angle measurement. This method normally has highly 3D precision which can achieve 1mm or less, but the range should be within a few meters (less than 5m) (Pfeifer and Briese, 2007b). For that reason, the triangular measurements is specified for the small products or artworks scanning (Pu, 2010).

The TLSs, used in the field trials of this project, are the Leica HDS 3000 a TOF scanner and the Faro focus^{3D}120, a phase-based scanner. Since both scanners have their advantages and disadvantages, the aim is to obtain the positive aspects of each,

in order to determine which scanner is suitable for a certain application. The next section contains further details on the operation of the two systems. This research will not use a laser scanner using optical triangulation for testing custom made 3D targets because they are not suited for long range measurement, and so will not be discussed further.

3.2.1 Time of flight measurement (TOF)

TOF laser scanners are based on pulse round trip measurements; each point is measured using a pulse of laser energy. The period of this pulse tends to have some nanoseconds (ns), most often specified for the full width half maximum (FWHM) of the pulse (see Figure 3.3, right), For example, a pulse duration of 5 ns corresponds to a length of about 1.5 m, as the speed of light is approximately $3*10^8$ m/s. Often the pulse is assumed to be Gaussian in shape, which is more factual than a rectangular pulse shape (Pfeifer and Briese, 2007a) (see Figure 3.4). The transmitted laser beam travels through the atmosphere and hits objects in its path. The spreading of the return pulse that travels back along the same path from the object to the scanner is taken by the scanner photo-detector. From emission of the laser beam, the timer is running, and it is stopped, once the return signal is received (see Figure 3.3, left). From this round trip time (Δt), the distance between the scanner and detected surface can be calculated by half of the time travel ($\Delta t/2$) and the average group velocity of light along the path from the sensor to the object is (C) as shown in the equation as follow (Pfeifer and Briese, 2007b).

$$r = C*\Delta t / 2 \quad \text{(3.2.1.1)}$$

Where r is the range, C is the speed of light and Δt (t_r-t_e); t_r is the time of the return signal and t_e is the time of the departing pulse.

The accuracy of this system depends on the accuracy of the time measurement, the accuracy of the shape of return signal, the wavelength of return signal and the accuracy of measuring angles. The reason that the TOF scanners have slow point collection is that the higher the pulse rate the lower the energy emitted, which limits the range, so a balance is made between maximum range and speed of point achievement (Pfeifer and Briese, 2007b).

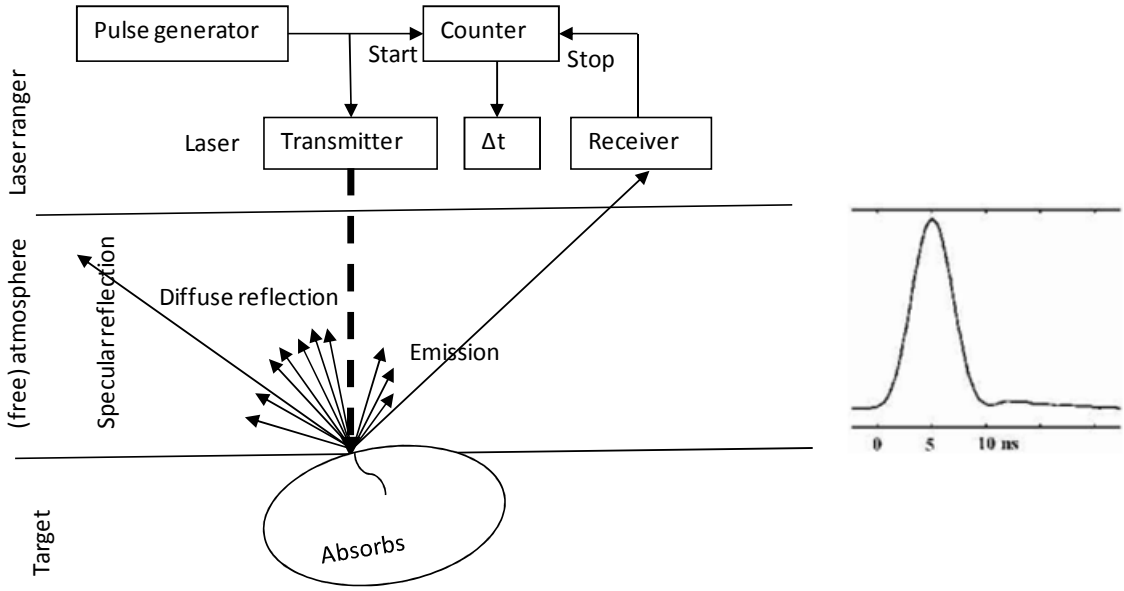

Figure 3-3: Principle of the pulsed time of flight measurement system (left) (updated from (Pfeifer and Briese, 2007b)). Right: Shape of a pulse emitted by a Riegl LMS-Q560 laser scanner, (source: (Wagner et al., 2006)).

3.2.2 Phase shift measurement

Unlike continually emitted laser pulses, mentioned in TOF, the phase based measurement applies two wavelengths, a continuous wave (CW) laser as the carrier wavelength and the modulation wavelength which is superimposed on to the carrier signal, similar to that of an EDM. The carrier signal is very short, a few μm, in order that the phase difference can be measured precisely. The carrier signal also governs the range, the shorter the wavelength the longer the range, while the modulation wave is longer by 10's of meters, and governs the precision of the scanner and is used to make the distance measurement (Uren and Price, 2006). The phase difference is measured by comparing the emitted laser beam and the return echo signal (see Figure 3.4). The distance is proportional to the phase difference and the wavelength of the amplitude modulated signal. The relationship between the phase difference $\Delta\varphi$ given in radians, and the one-way range (R) is given as: (Pfeifer and Briese, 2007b).

$$R = \Delta\varphi / (2\pi) \cdot \lambda/2 + \lambda/2 \cdot n \quad \text{.....(3.2.2.1)}$$

Where λ is the wavelength in meters of the modulation wave and n is the number of unknown full wavelengths between the scanners sensor and reflecting objects surface (Pfeifer and Briese, 2007b).

The accuracy of this system is dependent on how accurately the shift in phase is measured. Unlike the TOF approach, the accuracy depends on the horizontal and vertical angles measured.

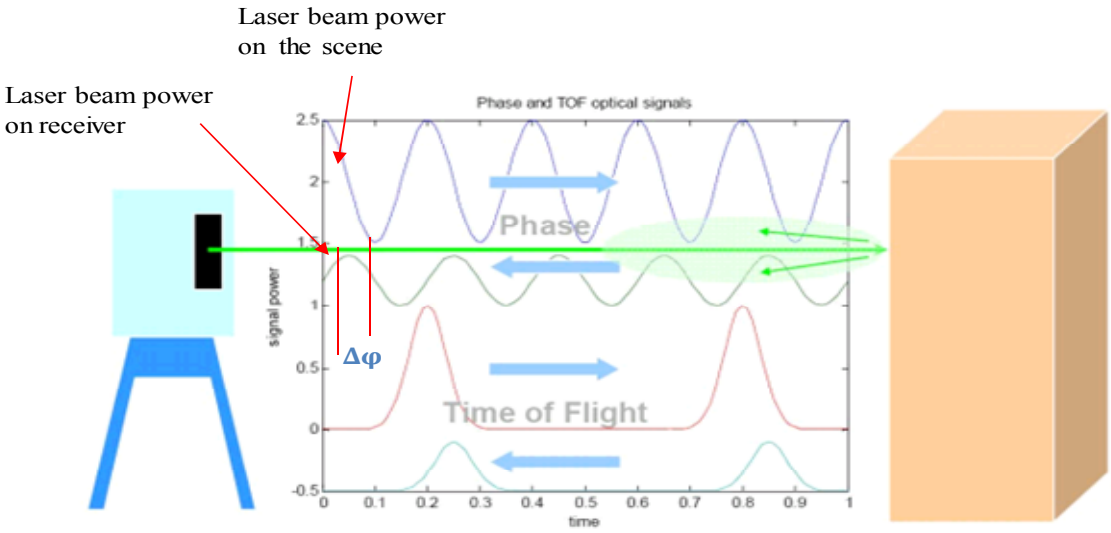

Figure 3-4: Principle of Phase based and time of flight laser scanner (updated from (Hiremagalur et al., 2007)).

The technical specifications for the both Faro focus^{3D}120 and Leica HDS3000 device that were used in this study are given (source: Manufacturer's literature and online; (Faro 3DLS, 2011; Leica., 2011).

	Faro focus 120 3D	Leica HDS3000
Accuracy (referred to 1σ sigma): range error	Uncertainty ±2 mm at 25 m distance.	Uncertainty ±8 mm at 100 m distance.
Resolution:	Up to 70 megapixel colour	64 megapixel
Effective range:	0.6 to 120m	1m-100m To 10% target reflectivity targets
Beam type:	Infrared (wavelength = 905nm).	Green (wavelength 532 nm)
Data capture speed: Measurement speed	up to 976000 pps	Up to 1800 points/second
Field of view:	360º horizontal by 305º vertical	360° x 270° field-of-view
Beam diameter:	3.8mm at the output	
Maximum Sample Density	1.2 mm	1.2 mm
Spot size	3.8 mm	From 0-50 m: 4mm (FwHH-based): 6mm [Gaussian- based]

Table 3-1: Specification of the Faro focus^{3D} 120 and Leica HDS3000 laser scanner (source (Faro 3DLS, 2011; Leica., 2011)).

3.3 Software Available

The post processing of the laser scanning data takes a long time, which might be about 10 times greater than the data capture duration. The time depends on the requirements of the result requested by the client (Sternberg et al., 2004).

In order to process the laser scanning data, a variety of commercial software are available. For example, each company that produces a laser scanning instruments usually has its own software packages. Leica Geosystem provides Cyclone, which is suitable for processing data from any laser scanner. RIEGL scanner provides a package of RISCAN and Faro provides Faro SCENE. Furthermore, scanner Imager 5003 from Zoller + Fröhlich (Z+F) (Germany) and Optich both provide LFM and Polyworks software, respectively. Several other software are available, for instance, Leica Cloudwork can be installed in order to make Autocad compatible with large point cloud. TerraScan/TerraMatch, coming under the TerraSolid software Packages, are specifically designed for calibration of MLS and ALS data. The data provided for this project was calibrated by 3DLM Company Ltd. using TerraScan / TerraMatch.
The latest RIEGL's RiACQUIRE software deals with the acquisition of precisely time-stamped images by the RIEGL VMX-450 with CS6 camera system. The RIEGL VMX-450 mobile scanning system consists of two RIEGL VQ-450 scanners on a mounted platform accompanied by GPS/IMU and up to 6 digital cameras or video equipment. In addition, the software controls the parameters of the camera that enables image monitoring during acquisition in real time.

Topcon. (2011) recently introduced ScanMaster v.2.0, which includes higher performance (visualisation and reproduction) billions of points with no lag, automatic edge extraction, volume computation, automatic noise filtering and automatic scan registration.

The problem of processing a huge amount of data remains largely unsolved and compounded by continual developments in the increased speed of data capture and size of the datasets, in order to reduce field time.

Unfortunately, available software is unable to detect and compute the centre/apex of the custom made target automatically from a laser point cloud. Therefore, an algorithm has been developed by the author using Matlab functions to detect and compute the optimal 3D target designed automatically. The procedure workflow is discussed in chapter 6.

3.4 Registration and geo-referencing in TLS

The first step in data processing from TLS is registration of multiple scans and geo-referencing. The latter procedure means conversion of the point clouds from the scanner coordinate system to absolute coordinate system, local or national. Geo-referencing is important for the integration of the TLS data and the products derived from it; for example, 3D models, with other geospatial data. The well-known method for geo-referencing in TLS in the recent years has been indirect geo-referencing. Therefore, the scans taken from multiple locations were first combined (registered) into one point cloud of the whole object or site. Afterwards, the "registered" point cloud was transformed to the external coordinate system using the coordinates of minimum 3 well-distributed control points, realised by means of special targets placed on or in the area of the object scanned (Barber, 2003; Harvey, 2004; Reshetyuk, 2009).

Objects being surveyed with a laser scanner are often quite large for example, high rise buildings and complex in shape such as a historical building. Therefore, several scans should be made from different setups of the instrument in order to capture the object completely (Heritage., 2007) see Figure 3.5.

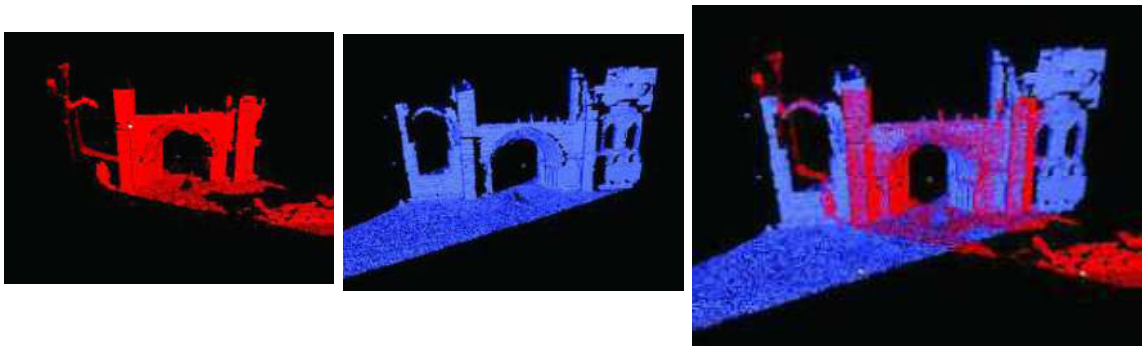

Figure 3-5: Registration (Heritage., 2007).

Point clouds obtained from each setup are referenced to the instrument-fixed, i.e. internal coordinate system of the scanner (see Figure 3.6). This coordinate system can be defined as follows (Balis et al., 2004):

- Origin – in the scanner electro-optical centre;
- z-axis – along the instrument vertical (rotation) axis;
- x-axis – following the instrument optical axis.
- y-axis – orthogonal to the two previous axes, completing a right-hand system.

The slope distance (s), horizontal angle (θ) and vertical angle (α) are measured. The instrument laser Cartesian coordinate X, Y and Z computed from the following equations.

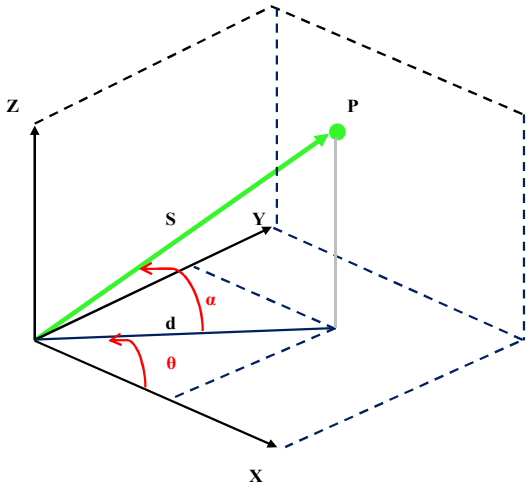

$d=s*\cos\alpha$ ……(3.2.1)

$X=d*\cos\theta$ ……(3.2.2)

$Y=d*\sin\theta$ ……...(3.2.3)

$Z= s*\sin\alpha$ ……..(3.2.4)

Where s is a slope distance, d horizontal distance, XYZ instrument laser Cartesian coordinate computed from polar coordinates measurements of the laser scanner.

Figure 3-6: Laser scanner coordinates system.

The above equations (3.2.1 to 3.2.4) can be illustrated in a matrix form as,

$$\begin{bmatrix} X_i \\ Y_i \\ Z_i \end{bmatrix} = \begin{bmatrix} s_i cos\alpha_i cos\theta_i \\ s_i cos\alpha_i sin\theta_i \\ s_i sin\alpha_i \end{bmatrix} \quad \text{(3.2.5)}$$

In the specifications of the manufacturer, there is usually insufficient amount of information about the type of mirror used in the scanner. Reshetyuk gives a comprehensive treatment of the design and performance of different scanning systems (Reshetyuk, 2009). The angle measurement system consists of angular encoders (normally binary rather than incremental) by which the horizontal and

vertical directions of the laser beam are measured [(Schulz, 2007) in (Reshetyuk, 2009)]. Hence, the deflections of the laser beam provide angular measurements; it is clear from Figure 3.6 that laser scanners operate in a similar way to reflector-less total stations: the range measurements are identical to those carried out by the total station.

Most scanners also record the intensity of the reflected laser signal at each point, which is thus the fourth observable (see Figure 3.7).

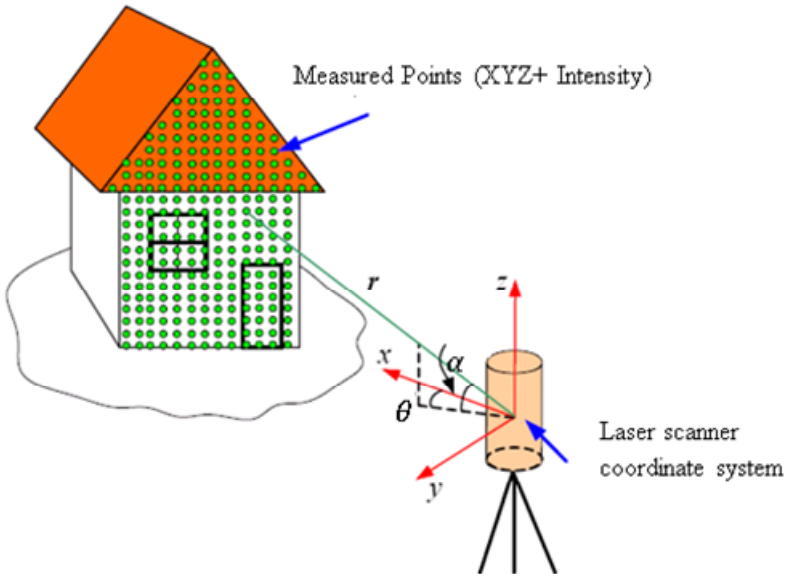

Figure 3-7: The principle of TLS and laser scanner observables (source: (Reshetyuk, 2009)).

The number of points achieved when scanning can be controlled by changing the distance between points in both the horizontal and vertical directions. For example, Leica HDS 2500 has maximum resolution of 0.25 mm at 50 m in. Other scanners have a range of pre-defined vertical and horizontal angular increments (steps) such as Faro focus^{3D}120 and Callidus CP 3200. The step size (vertical / horizontal) for Faro focus^{3D} used in this project is 0.009^{o} (40.960 3D pixels on 360^{o}) / 0.009^{o} (40.960 3D pixels on 360^{o}).

Registration can be achieved based on a minimum of three common coordinated points between the instrument and final coordinates system. The more common points, the more reliable registration can be achieved. It is important to add that the common points have to be well-distributed, normally at the extremities of the survey area, in order to achieve robust registration. Bae and Lichti (2008), state that *"once*

the common points were selected, the software rotates and translates the coordinate system of one of the point cloud to match the common points of the two or more point clouds together". Statistics are also produced regarding how well the point clouds fit together. The common points between the point clouds can be individual natural detail points in both point clouds, or in order to be more reliable, targets can be placed in the area of scanned object and used for registering the point clouds. This can be seen in section 3.5. There are several types of registration methods, which can be identified as follows:

- **Cloud to cloud registration**

The iterative closest point (ICP) algorithm is used to match two point clouds (scans), which are known as cloud to cloud registration. *The ICP is based on the search of pairs of nearest points in the two sets, and estimating the rigid transformation, which aligns them. Then, the rigid transformation is applied to the points of one set, and the procedure is iterated until convergence is achieved* (Besl and McKay, 1992). Barber (2003) stated that overlapping areas not only improve the resolution of the point cloud, but also, allows for a more accurate selection of common points between the scans.

- **Point to point registration**

This technique needs a careful selection and confirmation of a number of common target points between the two scans in the overlapping area. The suggested made targets can be used for this purpose but also, very clearly identifiable natural detail points can be selected. According to Wolf and Dewitt (2000), "*A 3D conformal transformation can be used to translate scans into a common reference system*". Also Barber (2003) stated that, if registration is made based on the targets used, the distinct point on the overlap can be used to improve the stability of the registration.

The automatic registration is regarded as one of the advanced techniques in the laser scanning processing software, which is based on target recognition and geometry recognition in the overlap of the point cloud.

Faro SCENE software can achieve such an accurate automatic registration via sphere targets. Also, Leica Cyclone can perform such registration, especially in the latest version 7.1.

Automatic registration of scanned points is one of the most significant advances in laser scanning history where, the data set can be completed and the registration can be performed in a few minutes.

The problem of this approach (automatic registration) is that the software only deals with a predefined target inside the software, and is unable to detect the custom made targets.

3.4.1 Registration of multiple scans

Normally, scans are considered in pairs, where a point cloud overlaps with the point cloud taken from the next scanner setup Figure 3.8. It is also possible to register more than two scans if they are overlapped. In order to transform the Scan 2 into the coordinate system of the Scan 1, similarity transformation (3 translations ΔX, ΔY, ΔZ; 3 rotations, ω, φ, κ.) is often performed.

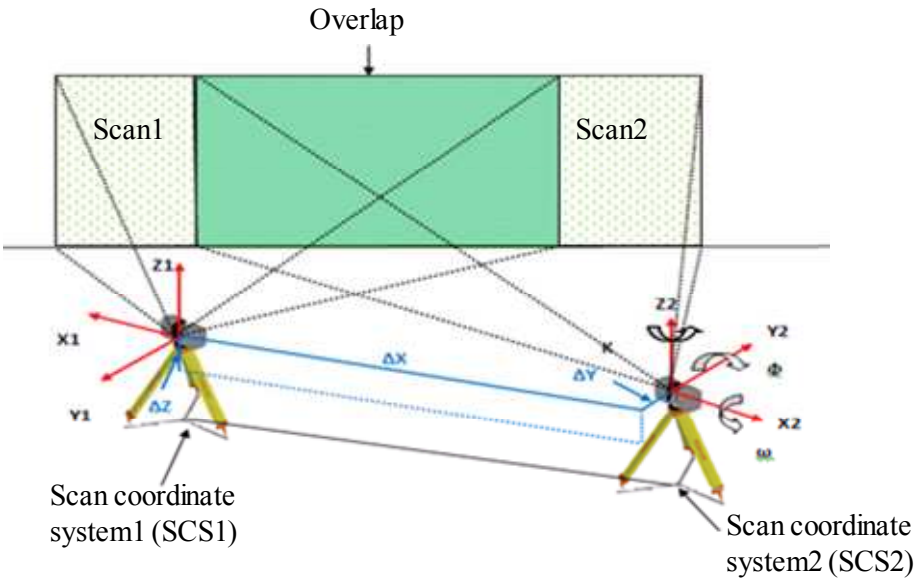

Figure 3-8: Registration of the two point cloud.

These parameters are also called the rigid-body transformation parameters (i.e. no scale factor) or "six degrees of freedom" and sometimes "*a 3D Helmert transformation without a scale factor*". The methods require the use of common points in both systems similar to the geo-referencing described in section 3.4.

3.4.2 Target based registration

This method is considered one of the most common registration approaches. To determine the 6 transformation parameters between any two scans, at least 6 coordinates must be found. This could be done via well distributed 3 points (not on the same line), in both scans. More than this number tends to be used, for more robust and reliable registration using least squares adjustment and enabling statistical quality analysis to be undertaken, see Figure 3.9.

The general equation of a 6 transformation parameters between any two scans as shown in Harvey (1998) is based on:

$$\begin{bmatrix} X_1 \\ Y_1 \\ Z_1 \end{bmatrix} = R \begin{bmatrix} X_2 \\ Y_2 \\ Z_2 \end{bmatrix} + \begin{bmatrix} Tx \\ Ty \\ Tz \end{bmatrix} \quad \text{.....(3.4.2)}$$

Where, (X_1, Y_1 and Z_1) are the scanner coordinates system1 (SCS1), and (X_2, Y_2 and Z_2) are the scanner coordinates system 2 (SCS2). The six parameters are the 3 translations and the 3 rotation angles between SCS1 and SCS2. Tx, Ty and Tz are the coordinates of the translation parameters between SCS1 and SCS2.

R is a 3x3 orthogonal rotation matrix that includes the 3 rotation angles (ω, φ, κ *about* the (X_2, Y_2 and Z_2) coordinate axes of the SCS 2. Each rotation matrix can be computed by Smith and Moore (2010)

Harvey (2004) said that "*determining scale factors between scanning distances and survey measurements is likely to be only required in research and testing situations and not usually in regular operational scanning survey*".

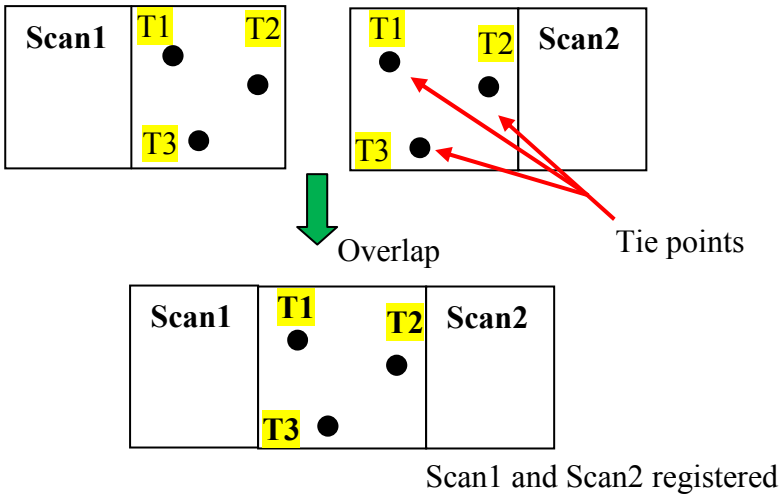

Figure 3-9: Registration using targets.

The targets used in the registration are commonly called tie-points. Different types of targets can be used (Balzani et al., 2001; Gordon and Lichti, 2004):

1. **Flat targets**. This is the most popular type of the targets. The problem of this target is that it may be impossible to correctly identify the centre of the target automatically with inclined scans, e.g. with incidence angles larger than 45°, or at large distances from the scanner (Balzani et al., 2001).

2. **3D shaped targets**. **Spherical** targets can be used and the centre of the sphere determined as the actual target point. Unlike flat targets, they can be easily identified from any scanning angle, and are suitable for use inside buildings (Balzani et al., 2001).

When using targets, the most important step is to determine their centres correctly to the required accuracy. The coordinates of the centres should be estimated from a number of laser returns covering the surface of the target. This estimation process is called "*target centroiding*" (Gordon, 2005), and called target reduction error (Gordon and Lichti, 2004), since the laser beam cannot be pointed exactly to the centre of the target (Figure 3.10). This error is proportional inversely at the point density on the surface of the target. For this reasons high point density is necessary (Jacobs, 2005a), which may be significantly higher than the point density of the main scan. This might not be useful with MLS, so new 3D shape targets must be considered.

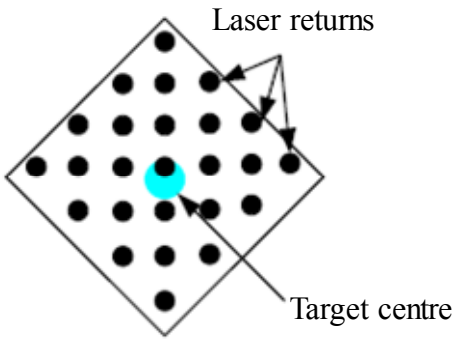

Figure 3-10: Target reduction errors.

3.4.3 Registration using natural point features

Natural point features can be used instead for registration, e.g. the edges of the steel, corners of buildings and windows, etc. as tie-points (Balzani et al., 2001; Jacobs, 2005a). The registration can be performed similarly to the case of using targets**.** Natural point features should be identified manually in the point clouds by the

operator. Like targets, these features should be scanned separately at high resolution, in order to secure their correct identification (Jacobs, 2005a). The results achieved via these methods are less accurate than those obtained using targets, which could be attributed to:

- No laser measurement accurately on the natural detail target point.
- Recognition of natural features is rather subjective, especially for scanning at large incident angles (Balzani et al., 2001).

English Heritage advises to avoid using natural point features for point cloud registration (Mills and Barber, 2003). The precision of the registration using targets or natural features depends mainly on the target geometry. When determining the positions of the tie-points for the registration, the following is recommended (Gordon and Lichti, 2004; Harvey, 2004) and (Jacobs, 2005a).

1. Regarding the overlap, the tie-points should be well distributed, and good variation in 3D (Tait et al., 2004).
2. An increase in the number of targets tends to improve the registration accuracy, although after adding the fourth target, the increase is not considerable (Gordon and Lichti, 2004). However, extra targets protect against gross errors and can also be used as an independent quality control of the registration as checkpoints (ibid.). In practical work, (Jacobs, 2005b) recommends using at least 4 targets.

In the tests performed by Bornaz et al. (2003) for the overlaps in the range between 10% and 90%, the minimal value of 30% has been found assuring that the registration accuracy is similar to the instrumental ranging precision.

3.4.4 Surface matching

The method of least squares 3D surface matching has been developed in the Swiss Federal Institute of Technology, Institute of Geodesy and Photogrammetry (e.g. (Akca and Gruen, 2005.)). Surface matching algorithms tend to be based on the Iterative Closest Point (ICP) method (Besl and McKay, 1992). Following this method, the reference point cloud is modelled with a surface and then registration is

implemented by minimizing the sum of the distances between the points of the other point cloud and the surface (Pfeifer and Lichti, 2004). The principle of registration with surface matching is shown in Figure 3.11.

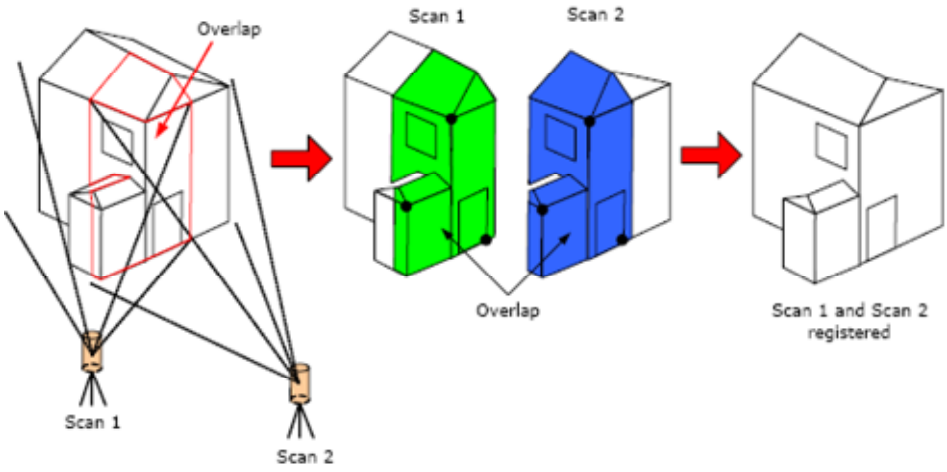

Figure 3-11: Surface matching (source (Reshetyuk, 2009)).

When matching a surface, it is necessary to have good 3D geometry in the overlap, that is, features oriented in different directions – along x, y and z-axes. Good examples are industrial facilities and buildings, and poor examples are flat roadways and walls (Jacobs, 2005a). Another factor that affects the registration accuracy is the area of overlap. Similar to the registration using targets or natural features, at least 30% overlap tends to be recommended. In order to be able to start the iterative registration process, the initial values for the transformation parameters have to be determined. For example, this can be done through the identification of at least 3 well-defined points (features) in the overlap, e.g. shown by dots in Figure 3.11 (Reshetyuk, 2009).

These points should be chosen to follow the same principles as for the registration using targets or natural point features. These points should be well distributed in the overlap with a good variation in depth and not on the same line. Based on these points, an initial alignment between the point clouds is computed, and refined during the iterations until an optimal alignment is achieved (Reshetyuk, 2009).

The same approach (ICP) has been used for MLS data, to determine the value of 3D deviation (tilt errors) between two or more surfaces obtained from different and opposite driving directions. The data were processed in Geomagic software. For more detail, the procedure is described in chapter 4, section 4.3.1.2.

3.4.5 Registration using common geometrical objects

Finally, it is also possible to carry out registration via geometrical objects, e.g. planes, cylinders etc., visible in both point clouds. These objects should be modelled firstly in the point clouds. This means that a plane should be fitted to the point cloud defining the object. The principle of registration using this method is shown in Figure 3.12.

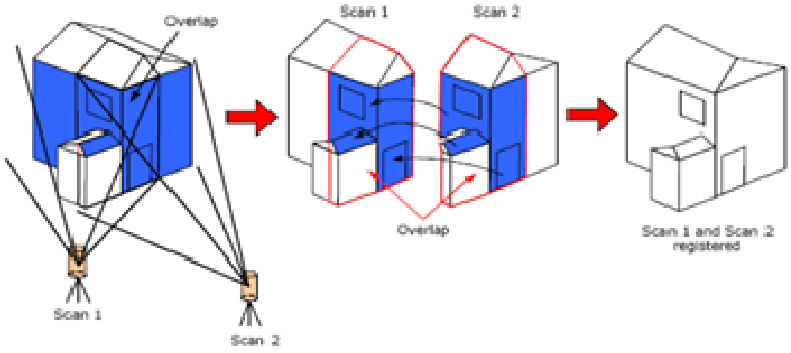

Figure 3-12: Registration using common geometrical object (source (Reshetyuk, 2009)).

During the registration process, is based on the best alignment between the point clouds based on the best fit of the common geometrical objects. The registration accuracy depends on the geometry of the overlap and the area of overlap. A clear example are three planes intersecting in a corner, e.g. a corner of the room or at an industrial facility with a set of pipes organised in different directions (Jacobs, 2005a).

3.5 Target

In laser scanning surveys, targets can be any distinct point that has been acquired by a laser scanner (TLS, MLS or ALS).

Targets can be known points with absolute coordinates, but they can also be put anywhere within the scanned area to be used as a tie point. This will ensure that corresponding points exist within the area of each scan. After the point clouds (scans) are registered, the scanned area can be registered with the coordinates of every available target. This will convert the registered point cloud to a required coordinate system (Gerber et al., 2010).

As stated in section 3.4, each laser scanner device is provided with specific targets. For example Leica scanners, tend to be use circular plane targets with a highly reflective area in the middle, while Faro scanner uses sphere targets. The sphere centre can be determined even if just a small part from the sphere is measured. This automatic detection is effective with the range of nearly 18 m (User manual, 2011). It is important to provide the sphere target with thread adaptor and magnetic mount (Figure 3.13); the offset value has to be considered. The prism is used for measuring the centre of sphere using total station.

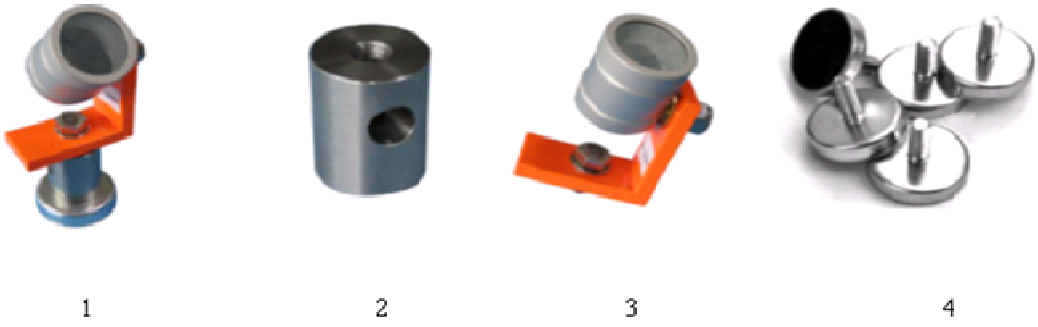

Figure 3-13: Prism kit including thread adaptor and magnetic mount (source (Faro 3DLS, 2011).

3.6 Error sources

There are two main sources, namely of errors geometric configuration and physical characteristics. Geometric configuration errors are internal errors inside the laser scanner; as discussed in section 3.2.1 and 3.2.2, the accuracy is dependent on the measuring system of angle and distance. In addition, the scanner accuracy is limited by the systematic instrumental errors, which means that it has to be properly calibrated. These errors are attributable to the scanner design and includes the scanner mechanism precision, mirror centre offset, rotation mechanism aberration, the beam width divergence and angular resolution and the detection process of the reflected signal (Soudarissanane et al., 2009).

The physical characteristic includes the measured surface and the environment (Kremen et al., 2006). There are several kinds of physical characteristics that could lead to positional errors; the main characteristics are discussed in the following sub-section.

3.6.1 Atmospheric condition

Uren and Price (2006) explained that, the atmosphere can change the speed of the laser light and can alter the power of the laser signal when passing through the atmosphere. This is caused by the temperature, pressure and relative humidity variations, defined by a change in refraction index (n).

$n = c/v$ .....(3.6.2.1)

Where, c is the speed of light and v is the velocity of light in that medium (atmosphere). The error is negligible over short distances, but over longer distances it needs to be taken into account. The accuracy is affected by the quality of these correction measurements.

Other factors affecting the laser beam propagating through the air are refraction and atmospheric disorder. As the beam propagates via the air at various temperatures, it bends (Price and Uren, 1989). The effect of this factor can be large in e.g. industrial environments. The atmospheric disorder, such as "Beam wander" has an effect on the TLS measurements, for the ranges of up to 1 km (Weichel, 1990). Figure 3.14, left shows displacement from the initial propagation direction, and is deflected in a random way. But the laser spot diameter remains the same without change. A test was carried out by Reshetyuk (2009) on the error introduced by the"beam wander" at strong turbulence for the scanner Leica HDS3000 over the range 10 to 100 m (see Figure 3.14, right). The result shows that the standard error ($\sigma_{\text{r-wander}}$) is 1.5 mm at 100 m range. This effect is neglected in the analysis of designed target.

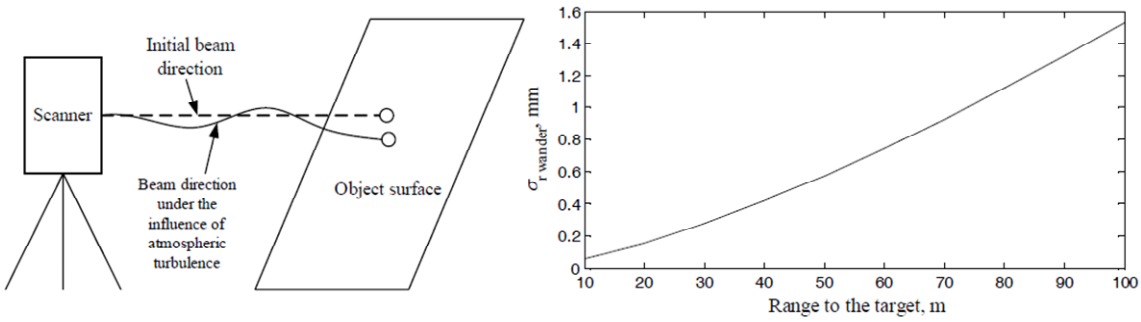

Figure 3-14: Beam wander(left) and (right), error introduced by the beam wander at strong turbulence for the scanner Leica HDS 3000 over the range *R* of 10 – 100 m. (source (Reshetyuk, 2009)).

3.6.2 Object properties

The main source of these errors is the reflectance of the object surface. Since TLS is a reflector-less surveying technique, the outcome of the range measurements are highly dependent on the reflectance from the surface, which affects the signal to noise ratio (SNR) (Thiel and Wehr, 2004). SNR can be defined as the power ratio between a signal (meaningful information) and the background noise (unwanted signal).

Reflectance can be defined as the relationship between reflected and incident laser power (Ingensand et al., 2003). It is a function of the following factors (Reshetyuk, 2009).

- Material properties of the object: such as electric permittivity, magnetic and etc.
- Permeability and conductivity.
- Surface colour.
- Wavelength of the laser.
- Laser beam incidence angle.
- Surface roughness, which, in turn, depends on the wavelength and the incidence angle (Kaasalainen et al., 2011a; Nayar et al., 1989).
- Temperature of the surface. When scanning a hot target, e.g. in an industrial environment, the background radiation introduced by the hot surface reduces the SNR and thus the precision of the range measurements (Määttä et al., 1993).
- Moisture of the surface.

The relationship between the transmitted signal power (Pt) and received (pr) of a laser power is describe by the radar range equation. It is important to analyse this relationship, since the amount of the received power influences the signal-to-noise ratio (SNR), (Soudarissanane et al., 2009).

3.6.3 Scanning geometry

The scanning geometry has a large effect on the error budget. Tests implemented by Schaer et al. (2007) shows the distribution of error modelled by error propagation without considering the scanning geometry. The errors were varying proportionally with the variation of the range on a steep slope from 500 to 1500m. In general, the accuracy progress tends to follow a very homogenous pattern with no unexpected changes. The situation changes significantly when considering the impact of incidence angle on target accuracy. The test shows with high incidence angles on a slope with rock faces, which causes strong deterioration in the accuracy, mainly in the vertical component (ibid).

Generally, the position of the TLS in a scene has an effect on the local IA, the local range and the local point densities of the scan points (Soudarissanane et al., 2009)
This thesis explores the effects of this factor on the point cloud quality, focusing on the incidence angle of the laser beam with respect to different types of target surfaces, namely cone, pyramid and flat target, as described in chapter 5 section 5.5.5.

3.6.4 Surface Reflectance

The return laser beams power can be affected by the physical characteristic and the angle of incidence of the surface it interacts with. The footprint (spot size) of the beam will increase, if a laser beam hits a surface at a high incidence angle. This will lead to decreasing the positional accuracy and the energy will be scattered over a larger area, so less energy is reflected back to the scanner.

Surface material has different physical characteristics in terms of reflectivity, absorbability and permeability. The amount of reflected energy returned to the scanner needs to be evaluated, not only affected by the surface absorbability and permeability, but also the direction of reflectance. There are three main kinds of reflectance (Kremen et al., 2006): diffusion, specular and chequered as shown in Figure 3.15.

- Diffusion, reflects the radiation proportionally in all directions; examples include chalk and plaster (Kremen et al., 2006).
- Specular, this follows the law of reflection that the angle of incidence is equal to the angle of reflection; examples are very shiny surfaces, such as polished silver (ibid).
- Chequered, this reflects most of the incoming radiation back in the direction it came from (ibid). Foil surfaces have this effect of reflection under special circumstance.

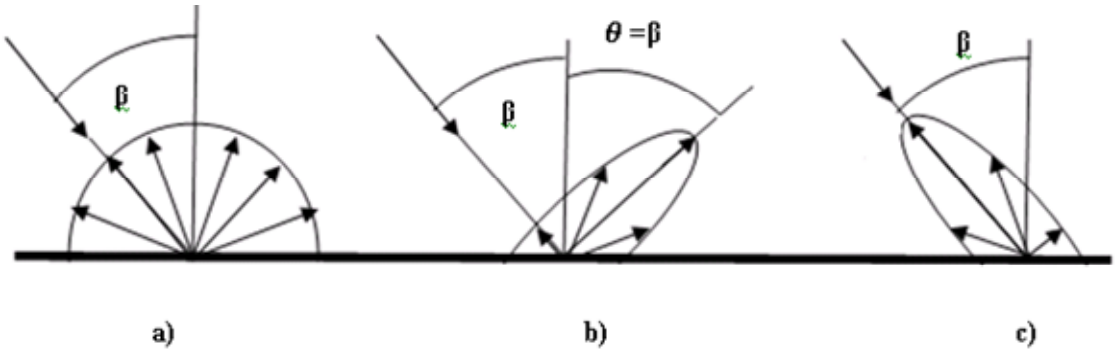

Figure 3-15: The main types of reflectance. Left (a): Diffusion. Middle (b): Specular. Right (c): Chquered (adapted from (Kremen et al., 2006)).

Most surfaces are a combination of these three types of reflectance. The most suitable surface for laser scanning is one that has diffusion with high reflectivity, where sufficient radiation will be reflected back to the scanner even with high incidence angles. The worst surfaces are those with high absorption such as black colours, with specular reflections (shiny surfaces), and with high permeability, such as glass (Boehler et al., 2003; Kremen et al., 2006).

The amount of backscatter may be recorded by the scanner software. This provides an intensity value, which is given as a digital number between 0 and 1. Values close to 1 indicate high reflectivity and 0 indicates that the energy is absorbed by the materials. The intensity can help to differentiate between objects when looking at a scan.

3.6.5 Beam Divergence

The diffraction of light is the reason behind expanding the diameter of beam when leaving the scanner. The increase in beam width is proportional to the travel distance

of the beam. This can affect the resolution of the "point cloud" giving positional uncertainties of point because of the large spot size of the beam at longer range. The foot print of the laser beam at normal and inclined incidence angle with the reflected laser light can be seen in Figure3.16 (Soudarissanane et al., 2009).

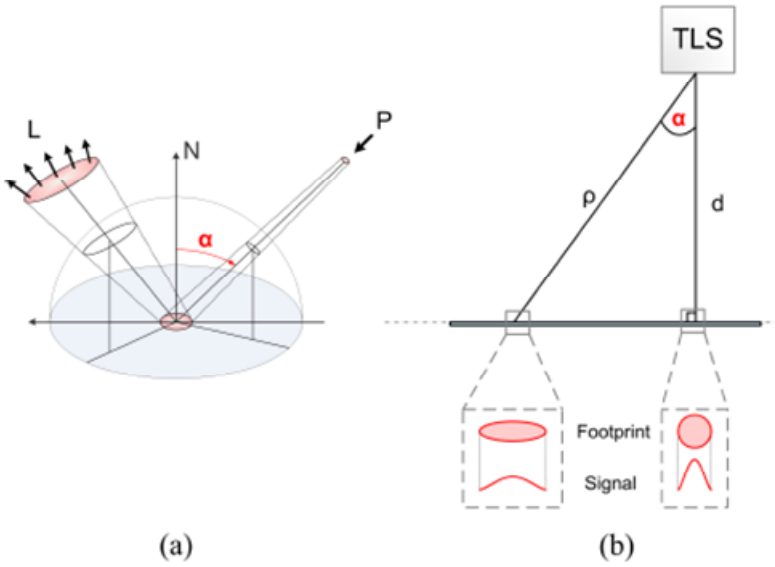

Figure 3-16: The reflection geometry. (a) Incidence angle of the transmitted laser beam with respect to a surface. (b) Perpendicular and incident laser (source (Soudarissanane et al., 2009)).

The divergence of the laser beam gives rise to doubt in the location of the target point of the measurement. This is the uncertainty in the angular position of the range measurement within the laser footprint on the object surface. The scanner records the apparent location of the point along the centerline of the emitted beam, but the actual location can be expected to lie anywhere within the projected beam footprint (Lichti and Gordon, 2004). The standard deviation for the position uncertainties due to the beam width as shown in Lichti and Gordon (2004) is ¼ of the beam diameter (i.e. $\sigma_{beam} = \pm\frac{\gamma}{4}$, where γ is the beam divergence).

The amplitude and the expectation centre of the signal power distribution are further modulated by the incidence angle, i.e. the relative alignment between the direction of the beam and the normal reflecting surfaces investigated by Glennie (2007), as shown in Figure 3.17.

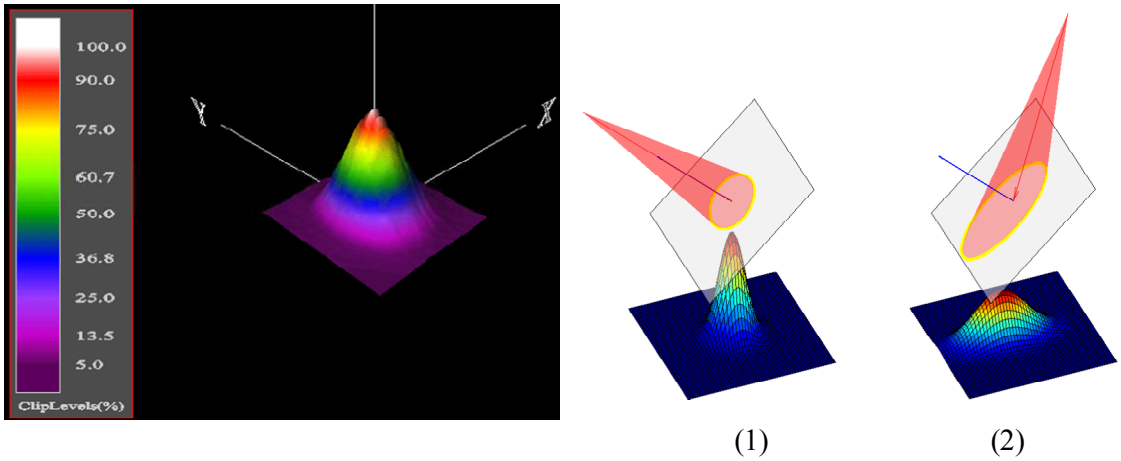

Figure 3-17: Influence of the incidence angle on relative power distribution: Left: An Optech ALTM LiDAR System [source (Glennie, 2007)]. Right (1): incidence angle = 0°. Right (2): incidence angle = 60° (Vosselman and Mass, 2010).

Laser beam incidence angle causes a systematic error in the pulsed ranging, which (Lichti et al., 2005) call the "range bias" (see Figure 3.18), and can be computed as follows:

$$\Delta R = \frac{R\gamma}{2} tan\beta \quad \text{.....(3.5.6.1)}$$

Where R is the range, γ is the beam divergence angle and β is the incidence angle. Figure 3.18 illustrated the above equation.

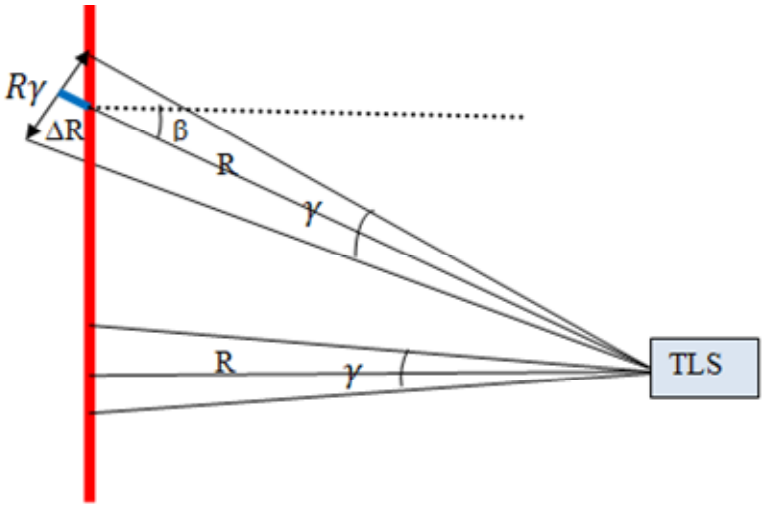

Figure 3-18: Range error ΔR due to the beam incidence angle.

The same error is present in ALS when scanning inclined surfaces, and referred to as "time walk" (Baltsavias, 1999b; Deems and Painter, 2006). The reason behind that is the spreading of the return pulse, leading to increase in the rise time of the received pulse to reach the threshold at which the timing is carried out. The recorded range will, therefore, be too long (Deems and Painter, 2006). This error depends also on the thresholding approach implemented in the laser rangefinder (Deems and Painter, 2006).

3.6.6 Materials

Highly reflective surfaces scanned at large incidence angles might cause "multipath" errors, when the laser beam is reflected from one surface to another before being reflected back to the scanner. The result is the wrong range measurement (up to several metres) in the correct direction (Gordon, 2005), because the measurement of angles is on the transmitted pulse.

Besides reflection, an incident laser beam may also penetrate some materials (e.g. normal wood, marble, Styrofoam) and be refracted more and more in the material itself, which introduces another addition constant to the range measurements (Ingensand et al., 2003) (see Figure 3.19). In Schulz (2007), the range errors of almost 15 mm and 5 mm were revealed for Styrofoam and wood, respectively, because of such effect. Therefore, such materials should be avoided in making targets.

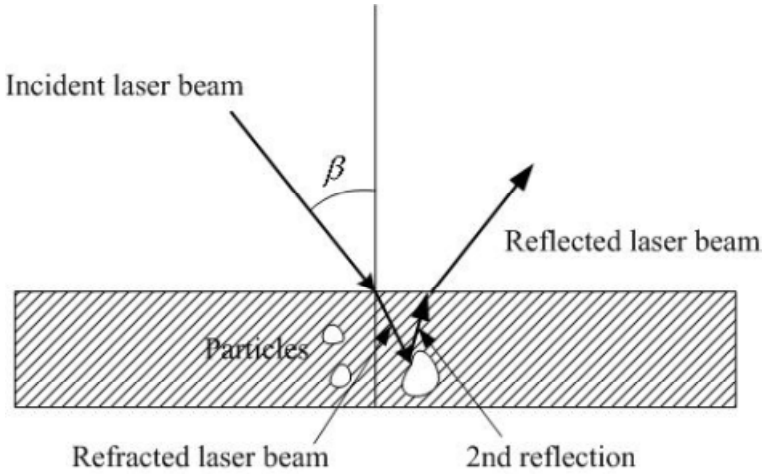

Figure 3-19: Penetration of the laser beam into some materials causing refraction and reflection in the material itself (from (Ingensand et al., 2003)).

3.7 Error sources specifically related to MLS

The sensors error (GPS, IMU and laser scanner) in MLS can be divided into the following groups:

3. Initialisation
4. Calibration
5. Manufacture calibration
6. Synchronisation between sensors.

Initialisation error: This error is attributed to the GPS position and IMU orientation.

Calibration error. This error is attributed to the position of the laser scanner in the IMU coordinates system and orientation of the laser scanner and the position of the GPS in the IMU coordinate system.

Manufacture calibration error. This error is attributed to the laser scanner distance and angular measurements.

Synchronisation error. This error attributes to the timestamp between sensors. All sensors GPS, IMU and laser scanner are synchronised using a pulse per second (PPS) which comes from the GPS receiver. The laser scanner has an internal clock and can accurately interpolate the timestamp so that each laser pulse has an accurate timestamps. If the GPS signal is lost (no satellite visibility) the scanner can use its internal clock to keep the synchronisation (3DLM Ltd.). These errors are discussed in an overview of basic relationship and error formula concerning MLS.

As stated in chapter 2, the measurement system, used by MLS includes GPS, IMU and laser scanner on a mobile platform.

The three main sensors, namely: GPS, IMU and laser scanner are highly integrated and mounted on the vehicle roof, fixed to a rigid frame. The StreetMapper360 system has been used for collecting data for this project. Figure (3.20) gives an example of the data collected for this study. Figure 3.21 shows the changing of velocity with time around the area of study “Jubilee campus”. It is clear from the Figure (3.21) that the vehicle speed and orientation changed in accordance with the road network in the campus, giving different point density. In an open area the vehicle moved quickly, and in a narrow street, the vehicle moved slowly.

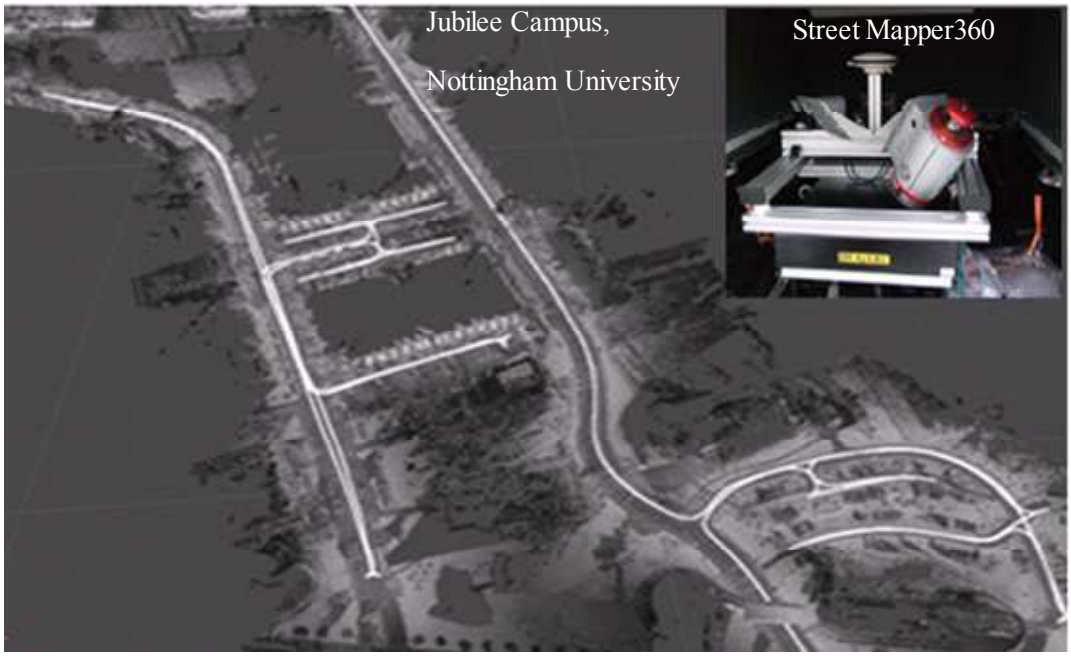

Figure 3-20: StreetMapper360, data collected in test area (Jubilee campus) overlain vehicle trajectory. Point shade represents the strength of the returned laser pulse. Right corner: MLS contains (Riegl VQ-250, IMU and GPS antenna).

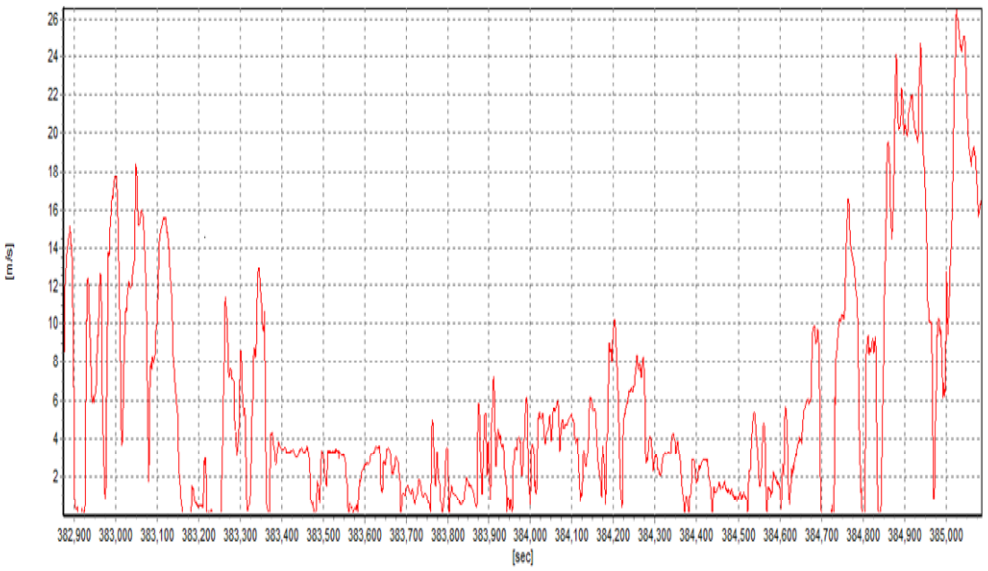

Figure 3-21: Shows time Vs. velocity m / second around the entire area.

Errors in laser scanning data can result from navigation sensors, individual sensor calibration, measurement errors, and the bore-sight alignment between the different sensors. Figure (3.22), Barbara et al (2008) and Graefe (2007) present an overview of basic relationship and error formula concerning MLS.

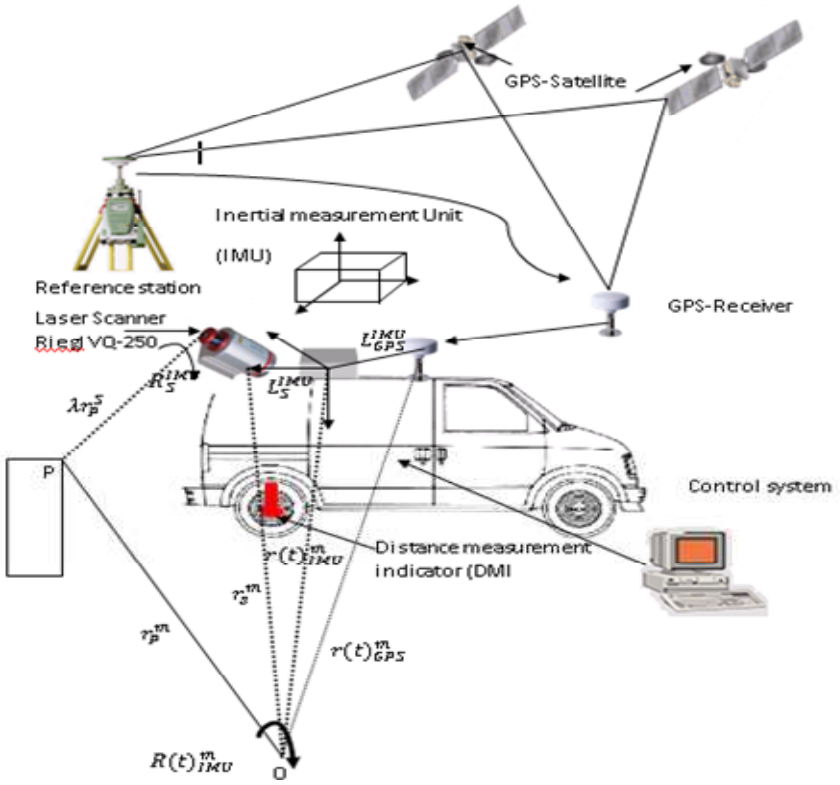

Figure 3-22: The configuration of muti-senor system on the van (adapted from (Graefe, 2008).

The following formulas are used for the geo-referencing procedure (Barber et al., 2008).

$$r_P^m = r(t)_{IMU}^m + R(t)_{IMU}^m \left(\lambda r_P^S R_S^{IMU} + L_S^{IMU}\right) \quad (3.7.1.1)$$

Where:

$$r(t)_{IMU}^m = r(t)_{GPS}^m - R(t)_{IMU}^m L_{GPS}^{IMU} \quad (3.7.1.2)$$

Thus:,

$$r_P^m = r(t)_{GPS}^m + R(t)_{IMU}^m \left(d_P^S R_S^{IMU} + L_S^{IMU} - L_{GPS}^{IMU}\right) \quad (3.7.1.3)$$

Where:

r_P^m : The position vector of the object point in the mapping coordinates system (m)

$r(t)_{GPS}^m$: The position vector of the GPS antenna in the mapping coordinates system at time t

$R(t)_{IMU}^m$: The rotation matrix between the IMU coordinates system and the mapping coordinates system at time t.

λ : The scale factor between the laser space and the object space.

d_P^S : The location of the point of interest represented in the laser coordinate system.

R_S^{IMU} : The rotation matrix between the sensor frame and the IMU frame.

L_{GPS}^{IMU} : The lever arm offset between the IMU and GPS.

L_S^{IMU} : The lever arm offset between the IMU and the laser scanner.

The above equation (3.7.1.3), can be expressed in a matrix form

$$\begin{bmatrix} X \\ Y \\ Z \end{bmatrix}_m^l = \begin{bmatrix} X \\ Y \\ Z \end{bmatrix}_{GPS}^l + R(t)_{IMU}^m(\omega\ \varphi\ k)\left(R_S^{IMU}(d\omega\ \ d\varphi\ \ dk).d_P^S(\theta\ r)\right) - \begin{bmatrix} lx \\ ly \\ lz \end{bmatrix}_l^{IMU}$$

.....(3.7.1.4)

The above formula shows that the mapping coordinate calculated for the laser return is dependent upon 14 observed parameters, namely:

- Coordinates (X, Y and Z) of GPS sensor.
- Orientations (ω φ k) measured by the IMU.
- Bore-sight angles(dω dφ dk), aligning the scanner frame with the IMU body frame.
- (θ , r), are the scan angle and range measured and returned by the laser scanner assembly denoted by λ.
- (Lx, Ly, Lz) are the lever arm offsets from the navigation origin to the measurement origin of the laser scan group.

The equation (3.7.1.4) is non-linear. The most common method of examining the effects of errors in parameters is to linearise the formula by expressing a Taylor series expansion after the first term. As a result, the effect of small differential errors in the measured parameters can be observed on the output mapping coordinates by the solution of a set of linear equations (Glennie, 2007). Differentiating equation (3.7.1.4) w.r.t. the 14 unknowns above leads to the overall error formula (ibid):

$$\begin{bmatrix}\delta x\\ \delta y\\ \delta z\end{bmatrix}_m^l = \begin{bmatrix}\delta x\\ \delta y\\ \delta z\end{bmatrix}_{GPS}^l + J\begin{bmatrix}\delta\omega\\ \delta\varphi\\ \delta k\end{bmatrix} + K\begin{bmatrix}\delta d\omega\\ \delta d\varphi\\ \delta dk\end{bmatrix} + B\begin{bmatrix}\delta\theta\\ \delta r\end{bmatrix} + C\begin{bmatrix}\delta lx\\ \delta ly\\ \delta lz\end{bmatrix}$$

The matrices, J, K, B, and C are the Jacobians of transformation, and are defined as:

$$J = \begin{bmatrix}\frac{\delta r_p^m}{\delta\omega} & \frac{\delta r_p^m}{\delta\varphi} & \frac{\delta r_p^m}{\delta k}\end{bmatrix}, K = \begin{bmatrix}\frac{\delta r_p^m}{\delta d\omega} & \frac{\delta r_p^m}{\delta d\varphi} & \frac{\delta r_p^m}{\delta dk}\end{bmatrix}, B = \begin{bmatrix}\frac{\delta r_p^m}{\delta\theta} & \frac{\delta r_p^m}{\delta r}\end{bmatrix},$$

$$C = \begin{bmatrix}\frac{\delta r_p^m}{\delta lx} & \frac{\delta r_p^m}{\delta ly} & \frac{\delta r_p^m}{\delta lz}\end{bmatrix}$$

The impact of the observed parameters on the determined ground coordinates was defined. The level of expected errors in each of the observations must be determined. Therefore, the typical error sizes for each group of observations were studied and discussed by (Glennie, 2007). Unless otherwise specified, all error values quoted are assumed to be one sigma values (Glennie, 2007). The typical sizes of each group can be summarised as follows:

- IMU attitude error

The typical accuracy of the IMU can be investigated by the manufacturer's technical specifications.

- Bore-sight error

According to Glennie (2007), the accuracy of the manual adjustment for bore-sight angles cannot be better; so normally, it is inappropriate that the IMU is used to measure attitude. He used the least squares approach, and statistics on the bore-sight angle accuracy were determined from the least squares adjustment. The accuracy on the level of 0.001^o degree in roll and pitch, and 0.004^o degree in yaw were normally observed. This level of accuracy seems to agree comparatively well with that shown in Morin (2002).

- Lever arm offset error ΔX

The system assembly errors are related to uncertainties in the position or the alignment between sensors (GPS, IMU and laser scanner). Since the magnitude of the lever-arm between IMU and laser scanner is small (at the dm level) and determined by the system manufacture, it tends not to be necessarily considered. On the other hand, the lever-arm between the body frame and GPS antenna varies per installation. Therefore, the accuracy of GPS/INS lever arm determination has the main effect on $\underline{\Delta X_{IMU}}^{L}$ (Vosselman and Mass, 2010).

On the other hand, Barbara et al (2008) used a calibration procedure based on repeated scanning passes to determine the three-dimensional offsets of the various sensors (known as a lever arm offsets). They investigated whether any errors in determining the orientation of these mountings will be propagated over the measurement range of the MLS system. "*By combining the range and scan angle from the laser profilers with GPS/IMU determined trajectory, a three-dimensional coordinate for the location at which the laser pulse was reflected can be calculated. By repeated measurement and calculation, a three-dimensional cloud of points can be generated and used to provide detailed positions and dimensions of the area over which the vehicle has driven"*.

The error analysis of their study shows that planimetric position of the laser point varies from approximately 5cm at 5m to 7cm at 25m range. While for elevation position, it is demonstrated that the predicted error were above 5cm at 5m, and vary with scan angle. This is explained by:

- Errors in the GPS positioning form the greatest single component of this error;
- Errors associated with determining the lever arm offsets between the GPS, laser profiler and the orientation of the profiler constitute a relatively small component of the error budget (less than 3 mm in plane) (Barber et al., 2008);
- Errors in the measurements taken by the profiler (range and scan angle) constitute the second largest error component after the GPS/IMU determined position while errors due to time synchronisation between sensors are relatively low (Barber et al., 2008).

Errors in the synchronisation of the laser profilers to the 1 pulse per second (pps) GPS signal dictate the extent to which the speed of the vehicle impacts upon the accuracy of the data collected (Barber et al., 2008). Given the relatively low estimate for time synchronisation error, the impact of vehicle speed is not significant in terms of geometric accuracy, although it is significant in the resolution of the data being collected, where higher speed leads to sparser point densities, which may impact on the accuracy of final products based upon them (Barber et al., 2008).

Rieger et al. (2008) stated that a necessary condition is to understand the internal calibration of the instrument, for example, precise information on how the actual measured range and mirror angles convert into coordinates within the coordinates of the laser scanner system. The internal calibration of the laser scanner is regularly achieved via a precisely surveyed test using targets.

Misalignment between the laser scanner and the IMU is widely recognized from the ALS system. While the principles of the algorithms used to calculate the misalignment, are the same in aligning ALS and MLS data, the process of data collection is certainly different (Rieger et al., 2010b). ALS survey scanned an area of interest from flight paths of different directions, from which the system's bore-sight alignment parameters can be computed (Habib and Van Rens, 2007).
In general, the misalignment errors are caused through orientation and position of the scanner in the IMU coordinates system. These errors can be reduced using the following points (Rieger et al., 2008).

- Installation on a rigid platform
    - On –site calibration.
    - Planar surfaces should be available on clean wall.
    - Need sufficient point density. For example choosing appropriate values of PRR, scan rate, and driving speed are necessary in order to ensure sufficient point density on the surface of the scanned objects.

- Urban and residential area, with a sufficient amount of useful information such as flat façade sections and buildings roofs along the road. This useful data is used as a basis for computing the misalignment parameters.

- At least two run passes.
- Opening the space (see Figure 3.23).

Figure (3.23, right) shows that the distance between the two surfaces is almost twice the angular deviation between the scanner and IMU. Rieger et al. (2008), stated that the procedure is: a semi-automated process, and to locate surfaces by location and normal vector, rotated in three axes, where best fit "(ICP) algorithm" indicates the optimum roll, pitch, and yaw.

The outcome of the adjustments of the scan data are three alignment angles according to the vehicle's roll, pitch and yaw axes (See Figure 3.23, left), and this is to be applied when combining scan data with position and orientation data.

For the purpose of this thesis, assessing the quality of the bore-sight calibration parameters determined by the StreetMapper 360 was undertaken with observations from two different types of environments; open landscape and typically urban canyon, according to the GPS positioning quality. The TerraScan / TerraMatch in TerraSolid software was used for checking the misalignment parameters (HRP). The iterative closet point (ICP) in Geomagic software was used to identify the 3D deviation (tilt error) between two surfaces based on the building façade and road surfaces. The workflows of these two procedures are given in chapter 4.

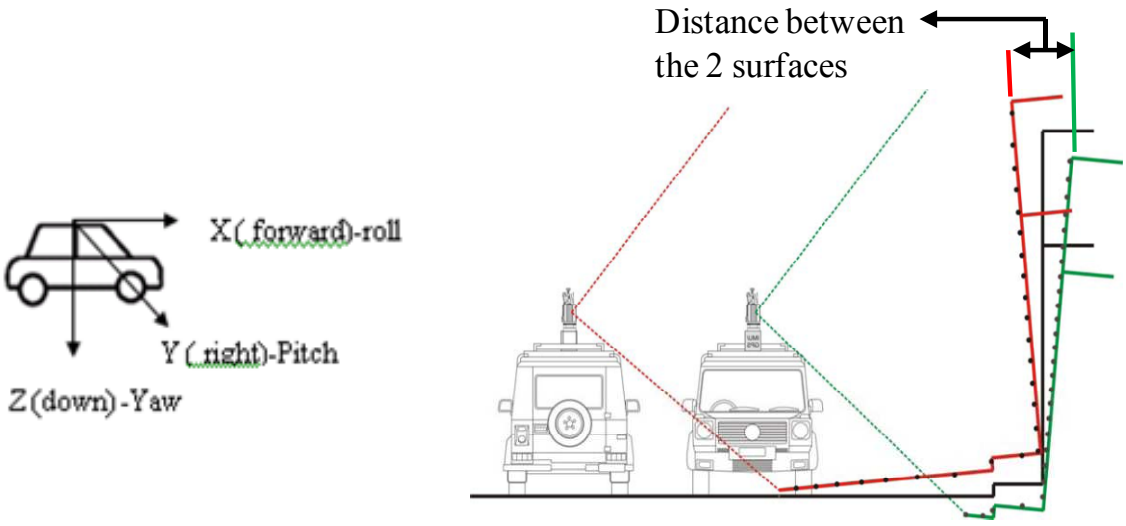

Figure 3-23: Appearance of bore-sight angles, e.g. the roll axis, in the three dimensional point clouds (Rieger et al., 2008).

3.8 Target accuracy error budget

The summation of the individual component errors and their projection by the geometry, the atmospheric effect and the target quality all affect the final accuracy of the target. The theoretical target accuracy can be expected by variance propagation. This analysis is presented in Glennie (2007) for various system and mission scenarios. When considering the relatively small performance gap between present airborne lasers scanners (see Table 3.2), the target error is largely controlled by angular uncertainty, which is in turn amplified by the flying height above the terrain. This amplification is nearly linear within the considered ranges and the upper limit of the error budget was extracted from (Table 3.2) (Glennie, 2007).

Glennie (2007), presented the analysis result of the relative distribution of the individual error elements for a fixed wing aircraft and a helicopter and a kinematic terrestrial laser scanning system. The result showed that the horizontal error for fixed-wing laser scanner are dominated by attitude error, the combined IMU and misalignment error make up from 60% to 75% of the overall horizontal error, depending on flight elevation. The vertical errors also show significant contribution by these two factors.

The attitude errors contribute 25% to over 50% of the error as a function of altitude. However, the error breakdown of a helicopter system is significantly different from that of a fixed-wing system. The dominant error for the helicopter system is clearly the scanner angle error, which is principally a result of the large beam divergence of the laser. Glennie (2007) also showed that the error budget for a helicopter is more uniform when a laser beam of lower divergence is used (0.5 mrad vs 2.7 mrad).

Finally, the situation changes again for a terrestrial based mobile scanning system, where range errors and scanning angle are the major error contribution (see Figure 3.23). For the purpose of this thesis, the range and incidence angle of the laser beam have been extensively addressed for the proposed designed targets specifically made for MLS.

	Vertical error per altitude (m)		Horizontal error per altitude (m)	
Attitude (m)	500	3000	500	3000
Tactical IMU	0.07	0.20	0.30	1.25
Navigation IMU	0.06	0.15	0.20	0.60

Table 3-2: Target accuracy in airborne laser scanning for a fixed-wing aircraft (source . (Vosselman and Mass, 2010).

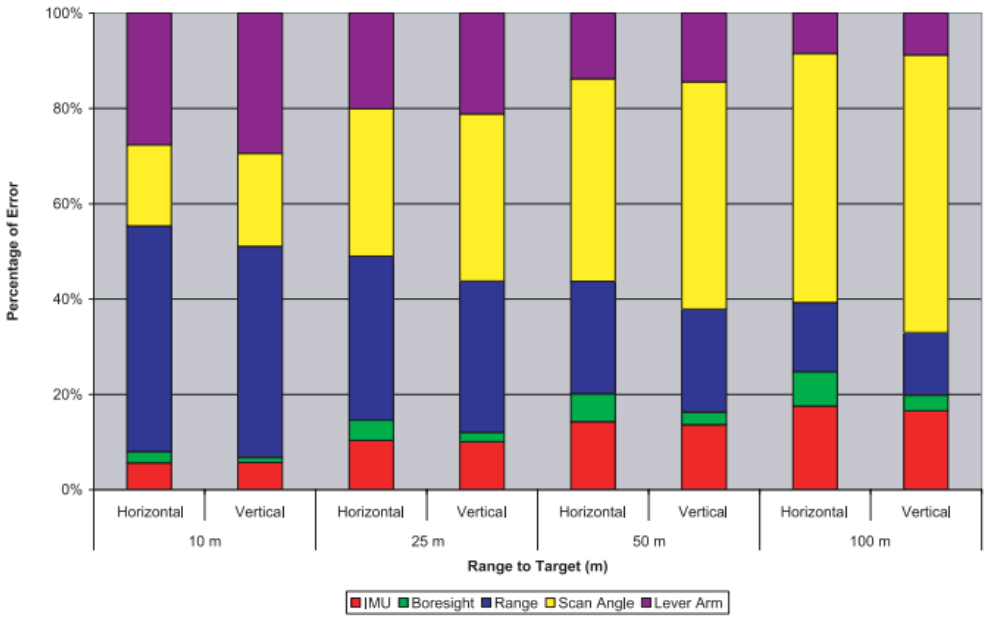

Figure 3-24: Subsystem error contribution by percentage (without GPS) to target error for a terrestrial vehicle system (LMS-Q240) (Vosselman and Mass, 2010).

3.9 Summary

In general, in this chapter, general concepts about laser scanning have been illustrated, including types of scanners, calibration and methods of registration. Also, error sources related to laser scanning were discussed in detail to partly fulfill objectives 1 and 2. In the following chapter, test planning and an understanding of the quality issues and calibration of MLS data in urban areas are studied to further understand quality issues related to objectives 1 and 2 of this work.

CHAPTER 4: TEST PLANNING AND AN UNDERSTANDING OF THE QUALITY ISSUES

4.1 Introduction

A theoretical study of errors was undertaken in chapter 3. This chapter looks at some practical trials to further understand quality issues. This will help fulfil objectives 1 and 2.

Any mobile laser scanning (MLS) project will involve two main stages: gathering and analysing data. Gathering data involves mission planning to produce the required 3D data acquisition (point cloud). The second stage involves preparing and processing the point cloud and associated data (GPS/IMU) to generate the required product (see section 2.4).

In general, the most important aspect of the quality of the data is the positional precision and accuracy of the collected data set, and the consistency of the data related to the time and position of data capture (i.e. time synchronisation between sensors).

4.2 Test planning

This section describes the test sites used in this research, the Jubilee Campus of the University of Nottingham and the several indoor trials performed in Nottingham Geospatial Building (NGB). In addition, this section presents an overview of the data provided for the purpose of this thesis**,** which has been collected using MLS and TLS described in the previous chapter. This will include describing the data collection stages, such as laser point data acquisition and ground control point along the study area. This section will also look at some details of the mission planning of MLS.

The accuracy requirements, set by the MLS user are the most critical factor in the planning stage and hence on the cost. The aim of the planning is to produce the architecture design for the sensors (GPS, IMU and laser scanner), which shows where the laser scanner unit is for each pulse, for the GPS/IMU and the method of data collection and other requirements, such as identifying the location of the GPS base station for kinematic DGPS, and alignment of the IMU by driving for a minimum of 10 minutes in excellent GPS conditions before capturing data. The plan includes optimal driving pattern (with contingency for periods of poor GPS

visibility) and determination of the driving speed for the required point density, and system calibration procedures for mounting parameters (bore-sight angles and offset) between sensors before capturing data. It will also require determination of the number of laser profiles per second, the number of scans and the direction of the vehicle. Rieger et al. (2010a) stated that, for MLS the achievable point density on the target's surface depends on:

- The measurement rate of the laser scanner profile.
- The speed of the scan, or line scan rate.
- The range from the surface of the object to the scanner.
- The vehicle driving speed.

According to Figure 4.1, the point spacing between two consecutive measurements on a flat surface at distance (*r)* from the instrument is $\frac{2\pi rLPS}{PRR}$, where LPS (line per second) is the scan rate and PRR is the laser pulse repetition rate. The spacing between two scan lines is v/LPS , where v is the vehicle driving speed. The average point density D, given in points per square meter, results from the reciprocal of the area of a parallelogram determined by these two distances and independent of the scan rate (Rieger et al., 2010a).

D = $\frac{LPS}{V}\frac{PRR}{2\pi r\ LPS}.= \frac{PRR}{2\pi rv}$

D = point density (points per m^2)

r = range to target (m)

v = speed of the vehicle (m/s)

PRR= pulse repetition rate (1/sec)

Example: $D = \frac{PRR}{2\pi rV}$

PRR	300 000 1/s
r	10 m
v	50 km / h
D	345 point per m^2

The actual point spacing within a single scan line is d = $\frac{1}{PRR}.\sqrt{v^2 + 4\pi^2r^2LPS^2}$. The point spacing within a scan line is calculated using Pythagoras law, where one side of the triangle is v/PRR (the along-track distance of consecutive laser shots) and the other side is $\frac{2\pi rLPS}{PRR}$ (the cross-track distance of consecutive laser shots (see Figure 4.1). The point density of each target can be obtained using the same equation. For example, using these parameters, about 73 points per target can be obtained using the designed targets such as a cone and square-based pyramid, which have surface areas of about 0.212 and 0.216 m^2 respectively.

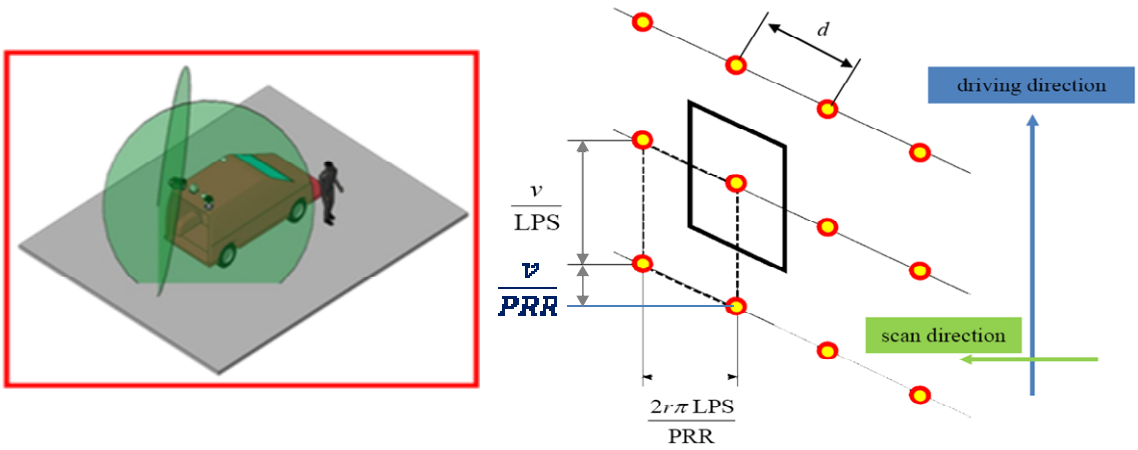

Figure 4-1: Representation of scan pattern on a flat surface (left), and with point space along the scan line and along driving direction (right), adapted from (Rieger et al., 2010a).

Often, a regular point pattern is needed at a given measurement distance. This means that the point spacing in each scan line is central to the spacing of a successive scan line (i.e., d = v / LPS). Rieger and his colleagues tested point densities over measurement distance, achieved by the Riegl VMX-250, at different driving speeds (Rieger et al., 2010a). Both scanners are operated at a PRR of 300 kHz as shown in Figure 4.2.

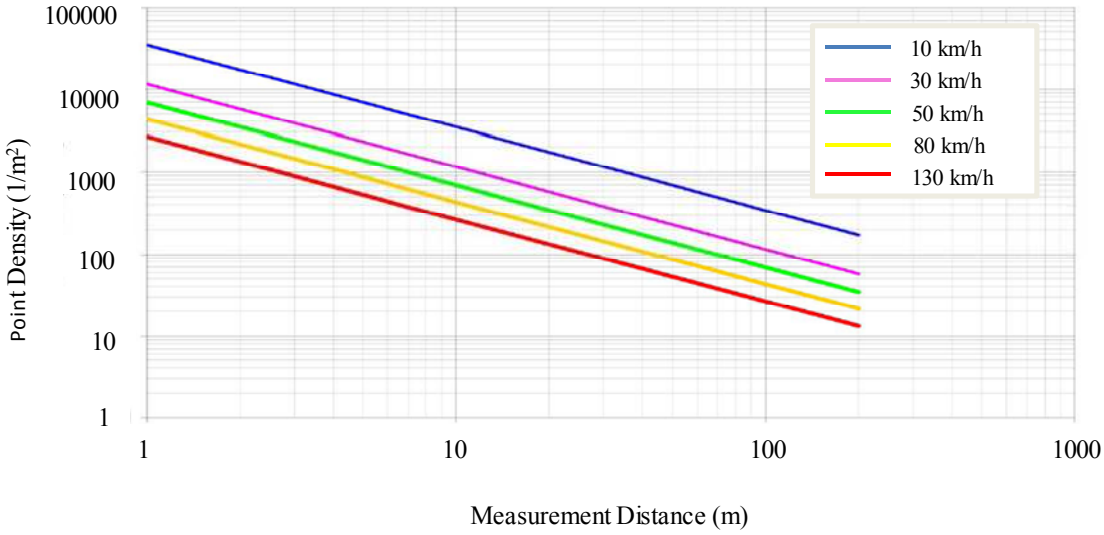

Figure 4-2: Point density vs measurement distance in dependence of the driving speed (source (Rieger et al., 2010a)).

As mentioned above, the point density changes considerably with the measurement range. This means that the MLS will deliver very high point densities on road surfaces, which are the closest objects in most surveys, resulting in a huge amount of data.

4.2.1 Test site

The StreetMapper mobile laser scanning system was used to provide a data set of the Jubilee Campus at the University of Nottingham. The system comprises a GPS, IMU and Riegl VQ-250 laser scanner. GCPs were established regularly every 10 m along the road of the study area for quality assessment and to check the calibration parameters of the data collected by 3DLM Ltd.

The Jubilee Campus at the University of Nottingham (Figure 4.3) is located about 2.5 km east of the main campus, with a total area of about 91,000 square meters. This study area consists of a mixture of buildings, with different heights, and street widths. The topography of the area is characterised by dense vegetation in front of buildings and tree clusters in many locations.

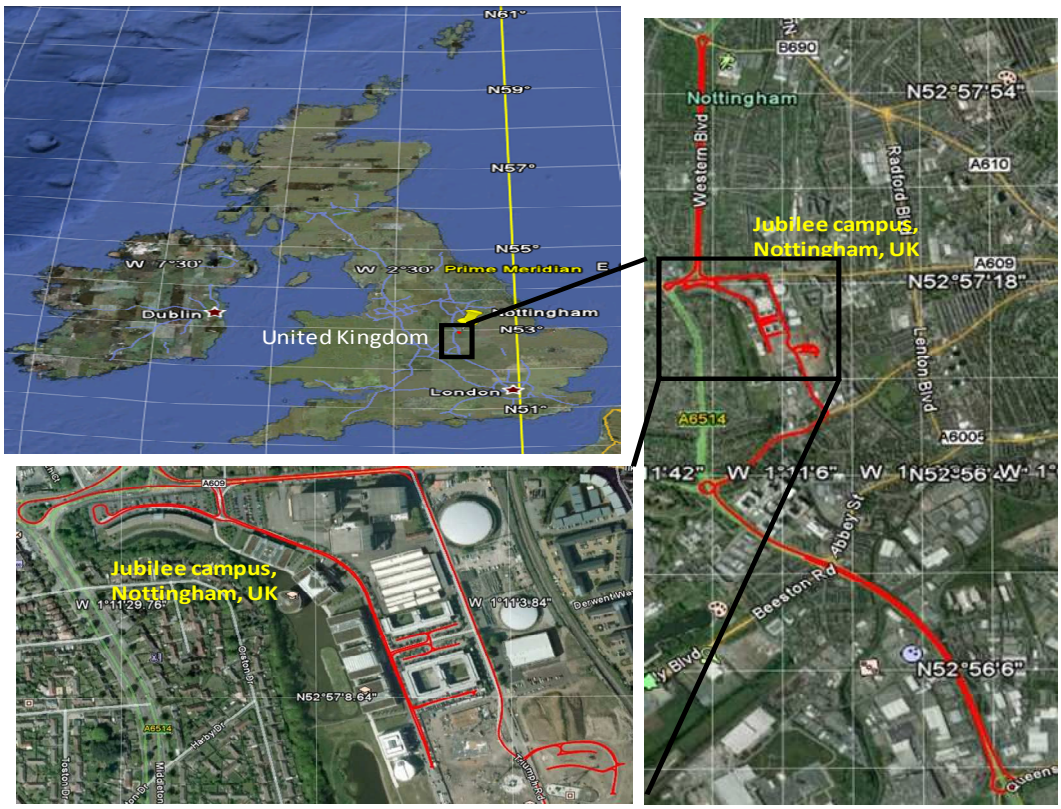

Figure 4-3: A block image of the first study area; Nottingham University, Jubilee Campus, upper, bottom and right images adapted from Google Earth.

The same area and the same MLS system were used for a number of trials. This test presented one of the most challenging environments, where improving the quality of MLS data using optimal targets will be investigated.

The optimal targets provide an excellent opportunity to improve the quality and reliability of the data collected by the system. Table 4.1 provides an overview of the test site data collected and the dates of the test.

MLS data and TLS

Test site	Point cloud collected	Point density	Date	GCPs / targets
Nottingham University Jubilee Campus	MLS	1400 pts / m^2	November 2009	277 GCPs
	MLS	Testing with the optimal target design	November 2012	28, diff. targets
Jubilee Campus	Faro Focus^{3D} TLS	(6x6) mm	July 2011	Sphere targets

TLS data for testing designed targets

Test site	Point cloud collected	Point density	Date	Target used
NGI-Experiments inside Lab.	HDS3000 TLS	Diff. pts., density	February 2011	Cardboard targets in 10 different sizes and shapes
	Faro Focus^{3D} TLS	Diff., resolutions between Min.to Max	April 2011	Targets, 20
	HDS3000 TLS and Faro Focus^{3D} TLS	(10x10) mm	August 2011	Different targets, 2D and 3D
NGI-Experiments outdoors	HDS3000 TLS	(10x10) mm	September 2011	Return intensity-analysis using colour
	HDS3000 and Faro Focus ^{3D}	(5x5; to 25x25) mm	October 2011	Optimal targets, designed by the UoN manufacture

Table 4-1: Overview of the test sites and data captured from MLS and Two TLS (HDS 3000 and Faro Focus^{3D} 120).

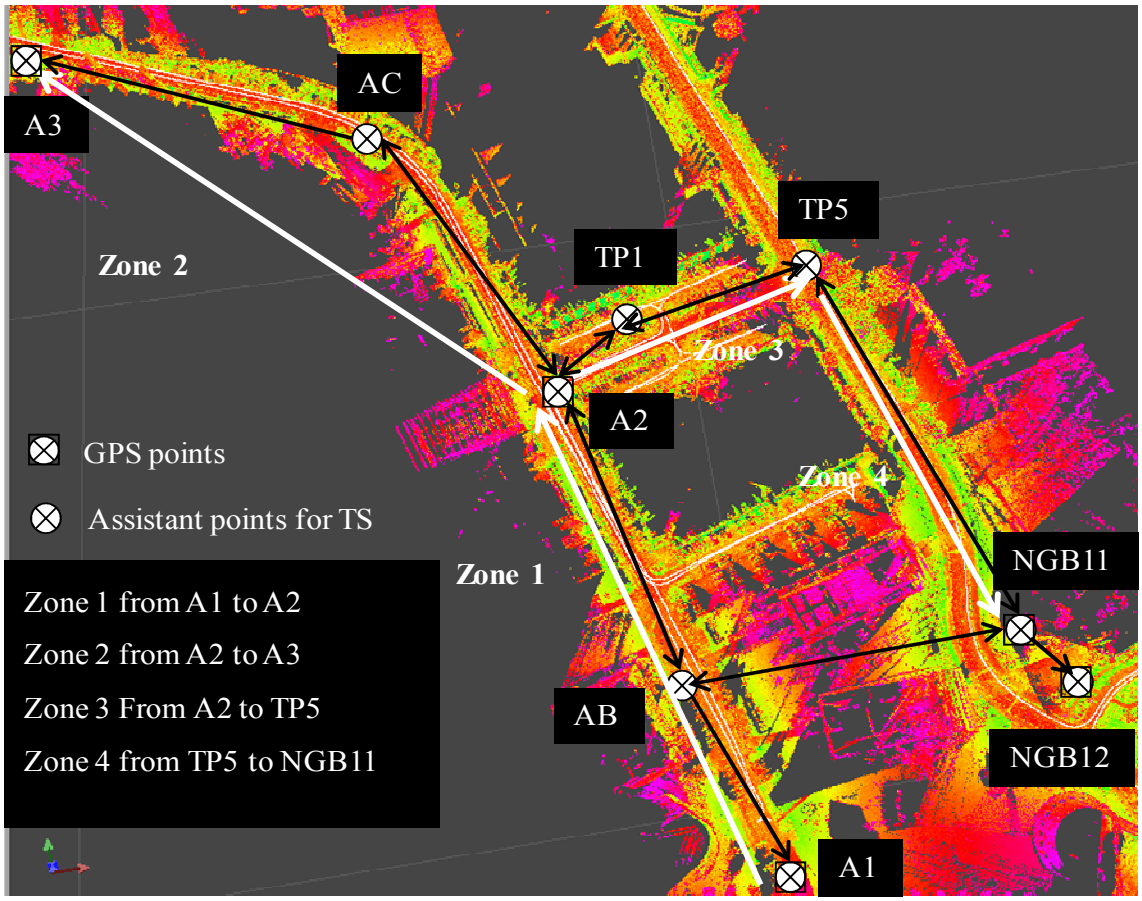

Figure 4-4: Survey work showing the four areas where the TS survey was performed overlain with the laser point and vehicle trajectory.

Figure 4.4 shows the four areas (zones) chosen with different GPS quality to test the MLS data and assess the accuracy of 3D points achieved from the system in such areas. The GPS quality of the entire area of the Jubilee Campus has been provided by 3DLM Ltd. in the form of E, N, H accuracy of the vehicle trajectory.

4.2.2 Ground Control Points (GCPs)

For quality assessment of MLS data, it is desirable to use ground control points. In general, there are two types of ground control points in common use. First is natural detail, which are normally plan and/or height coordinated points selected after taking the scan. A plan control is a sharp, definite piece of detail, such as a building corner, manhole cover corner or corner of white road markings. A height control is a flat

horizontal area near the other detail used for locating a position such as a road junction or a gateway. Second are pre-marks; these are targets that are put in position before the MLS takes place and they are normally three-dimensional coordinated points, with size, shape and colours selected depending on the range and signal response of the laser scanner. Targets are used in areas that lack natural objects or to improve the quality for registration and geo-referencing. Sometimes a combination of natural details and targets is used.

The density of control points and their optimum location depend on the purpose of the scanning regions. In general, to convert from one 3D system to another, three or more full GCPs are needed. Redundant control is recommended to enable quality assessment and is usually used also to increase the accuracy of the system (Smith, 2010).

According to Hunter et al. (2006), ground control points are to be collected within the project area using an appropriate survey method in a consistent manner on features visible in the laser point data, such as the corner of a white road marking.

The coordinates of the GCPs were provided by the use of GPS for some key reference points and then levelling and traversing was done to fix more points in the testing area.

Static GPS - Collection of GCPs as a reference

After careful study of the laser point cloud of the test area, the initial control points were selected, and the locations of the control points were chosen. The laser points selected were the corner of white road markings, a manhole and a building facade detail. To ensure that the chosen locations of the control points were valid, and did not occur in shadowed or confined areas, a reconnaissance survey was conducted, and all the locations were found to be accessible and visible.

After the reconnaissance survey, a field survey was carried out using static GPS with a cut-off angle of 10°. A static carrier phase of several hours was used with Leica Geo Office software to fix some GCPs in the testing area. Table 4.2 gives the

coordinates of points that were used as reference stations for digital levelling and the total station (TS), observations at selected points on flat ground and building facades along the road, as shown in Figures 4.4 and 4.5. A total of 277 (see Table 4.3) coordinated ground points were observed for the study area. These points were used for quality assessment of MLS data in different areas of interest. Some of these points were fixed as check points for the next test, and assessing the outputs of the test is discussed in section 4.3.1.3.

The NGB2 reference station at NGI, in addition to five other Ordnance Survey (OS) data stations, namely KEYW, LICF, LEE, BUXT and LINO, were used for the processing of GPS observations (see Appendix C). As the baseline length between the chosen GCPs and the active reference stations is a few kilometres, it can be seen from Figure 4.6 that 5 cm accuracy can be achieved when observing for a period of about 20 minutes (Ordnance Survey, 2012).

Troposphere and ionosphere corrections were performed. Regarding troposphere correction, the GPS signal is delayed by the troposphere. The amount of the delay varies with the temperature, humidity, pressure, the height of the station above sea level, and the GPS satellite elevation above the horizon (Leica, 2010). A correction can be made to the code and phase measurements using a tropo model to account for this delay (Leica, 2010). Two kinds of tropo model were applied to the observation, namely Hopfield and a computed model. Table 4.2 shows the results of processing data, and a graphical representation of the processing of the GPS observations of the selected point can be seen in Appendix C.

Points A1, A2 and A3 processed with NGB2-tropospheric type using Hopfield model.			
Station	**Easting (m)**	**Northing (m)**	**Height (m)**
NGB2	454920.9609	339703.9122	42.6826
A1	454806.5101	339624.4634	29.6673
A2	454749.3071	339810.2548	29.6562
A3	454541.2632	340012.4063	30.2502
The average of points of five nearby OS stations combined with A1, A2 and A3 troposphere type using Hopfield model.			
A1	454806.5138	339624.4641	29.6474
A2	454749.3113	339810.2570	29.6371
A3	454541.2692	340012.4098	30.2304
The average of points of five nearby OS stations combined with A1, A2 and A3 troposphere type using computed model.			
A1	454806.5135	339624.4638	29.6571
A2	454749.3108	339810.2567	29.6448
A3	454541.2688	340012.4101	30.2311
Using reference NGB2 with no-troposphere.			
A1	454806.5097	339624.4628	29.6794
A2	454749.3065	339810.2545	29.6665
A3	454541.2625	340012.4063	30.2616
The average of points, A1, A2, A3 of all methods excluding the no-troposphere model			
A1	454806.5125	339624.4638	29.6572
A2	454749.3097	339810.2561	29.6460
A3	454541.2671	340012.4087	30.2373

Table 4-2: The average horizontal and height coordinates of processing points A1, A2 and A3 from static GPS observation using Leica Geo Office software.

In the above table, the processed no-troposphere data were rejected where the results were very different from the other troposphere models. The results were quite similar to the Hopfield model when using only one base station (NGB2).

The digital level Topcon DL-101 was used for measuring the height of many of the selected points, and to check the height component of the GPS position. These points

are considered as benchmarks (BMs), to compare with the laser point data for assessing the quality of the point cloud from a different area within the AOI. A closed-loop levelling procedure was adopted. The measurement was repeated three times, and the average value was taken and stored automatically by the digital level device. The elevation errors obtained from the levelling process are within the allowable accuracy. Since the permissible closure for a level circuit (loop) is based upon the lengths of lines or the number of setups, it is logical to adjust the elevation on this basis. Appendix D shows a table including the accuracy, and a paragraph on the analysis request.

Traverse field work procedure around the study area

A traverse network was established around the area of interest on Jubilee Campus, starting from reference ground control point NGB11 and ending at the same point, as shown in Figure 4.7. In order to obtain a high-precision measurement, rounds of angles were measured using a Trimble robotic total station (TRTS). All natural points were observed as angle and distance along the study area. The reflector-less mode in TS was used to measure points on the building facades. Data processing and adjustment was performed using the Trimble Geomatic office application (TGO). Figure 4.5 shows the positions of the GCPs measured by a Total Station along the study area.

The process of determining and applying corrections to observations for the purpose of reducing error in a network adjustment is designed to achieve closure in a survey network by minimising the sum of the weighted squares of the observation. The adjustment technique employed by the TGO software is sometimes called variation of coordinates or the method of indirect observation (Geomatic, 2007). The adjustment processor performs the maximum number of iterations defined by the user.

After performing adjustment of the network using TGO software, the adjustment results for GCPs of the survey network around the study area show that the Chi-square test was passed with 95% confidence, with a maximum error ellipse of 3 mm for the adjusted coordinates. The standard deviation was found to be equal to 2.0

mm, 2.0 mm and 5.0 mm for the errors in northing, easting and height, respectively, and the accuracy was found to be equal to 5.0 mm, 5.0 mm and 13 mm for the errors in northing, easting and height, respectively (see Appendix E). It is worth mentioning that all the coordinates used in the adjustments are in the national Grid OSGB36 coordinate system.

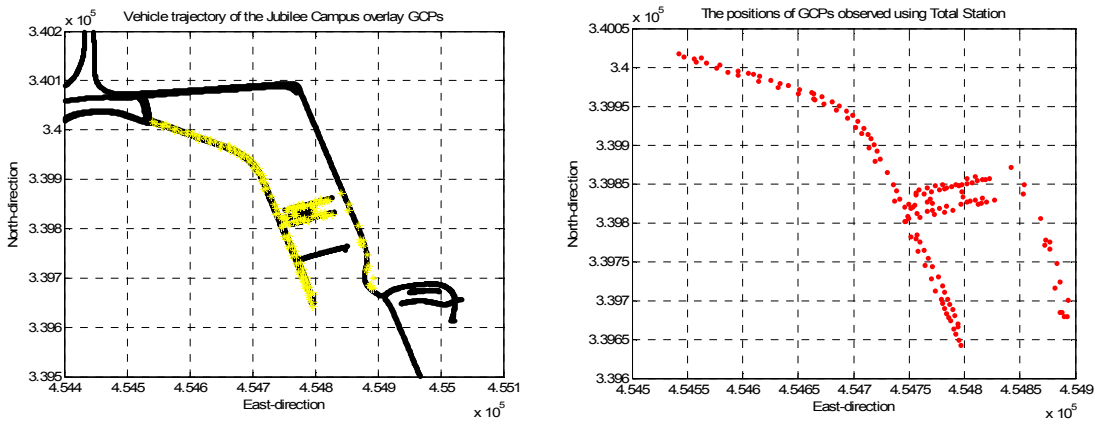

Figure 4-5: Vehicle trajectory of the Jubilee Campus. Left: GPS/IMU data overlain on TS data. Right: position of GCPs observed by TS data along the study area.

Zone	Point station	No. of points observed in each zone
1	From A1 to A2	34 on the road surface 31 on a building facade
2	From A2 to A3	50 on the road surface 54 on a building facade
3	From A2 TP5	50 on the road surface 30 on a building facade
4	From TP5 to NGB11	15 on the road surface 13 on a building facade

Table 4-3: Number of control points in each zone.

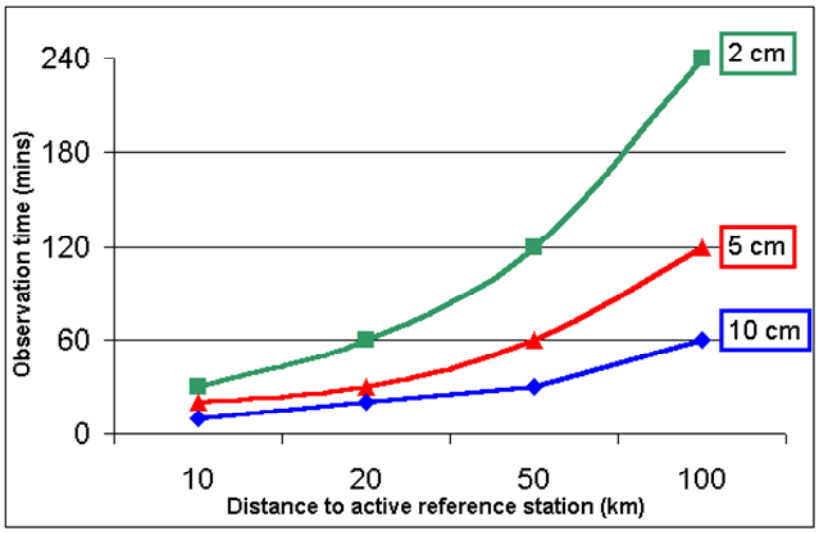

Figure 4-6: Typical GPS observation time as a function of distance to the active reference stations. Adapted from the Ordnance Survey website (Website, 2011).

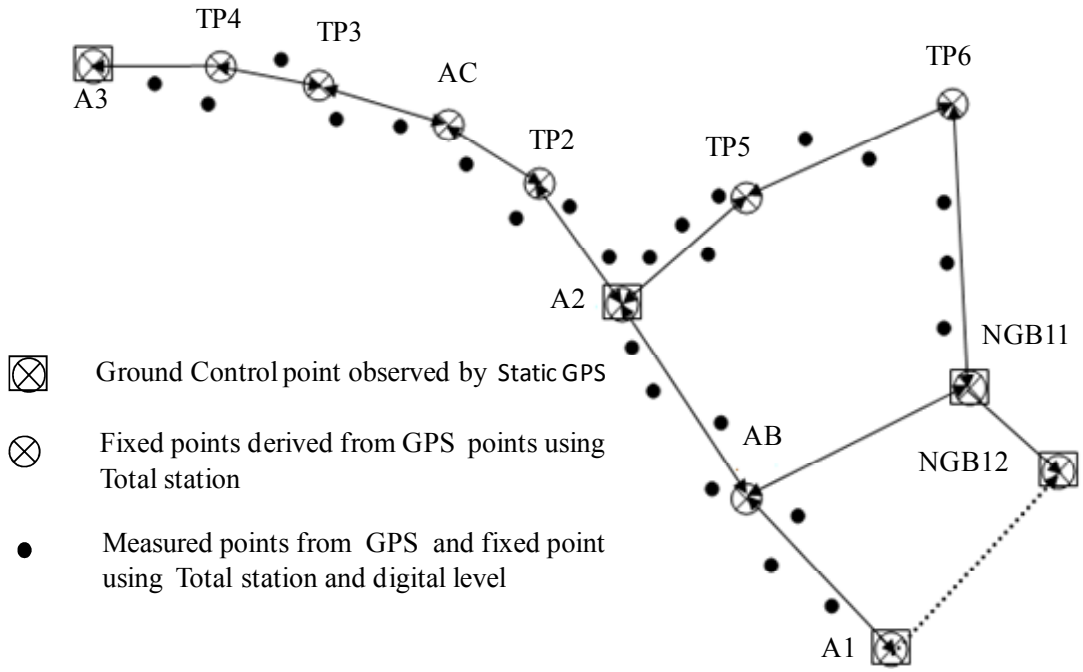

Figure 4-7: Traverse survey network around the study area.

4.2.3 MLS Data collection

The 3DLM data was acquired (Streetmapper360, 2009) in November 2009 on Jubilee Campus, University of Nottingham, starting from the south-west of the campus and ending in the north-west in the main Wollaton Road, as shown in Figure 4.3. The scanner was operating at 100 lines per second at a pulse repetition rate

(PRR) of 300 kHz in 37 minutes. The survey collected a total of approximately 111 million points in the test site at an average speed of no more than 20 km/h, given the urban location. This gives a very detailed laser survey, collecting data with a spot spacing of about 1 cm especially close to the driving path, and a density of over 1400 pts / m^2. This point density depends on the range of the laser beam and speed of the vehicle. The above information was provided by the 3DLM Ltd. In addition, the Riegl VQ-250 laser scanner used in this system was mounted 135 degrees from forward, and at -40 degrees pitch from the horizontal to provide a better ability to collect corner points.

A calibration report for the MLS system was also provided, as it was carried out some days before the data was collected at Jubilee. Appendix B contains the calibration report of the MLS system for the two test periods (2009, 2012).

In addition to the above, the processed GPS/IMU position and orientation data of the vehicle trajectory along the study area were provided as a text file in the format of easting, northing, elevation, heading, roll and pitch. The 'heading angle is the first rotation about the 'Z' axis, the 'roll' angle is the second rotation about the 'X' axis along the driving direction, and the 'pitch' angle is the third rotation about the 'Y' axis (see Figure 4.8).

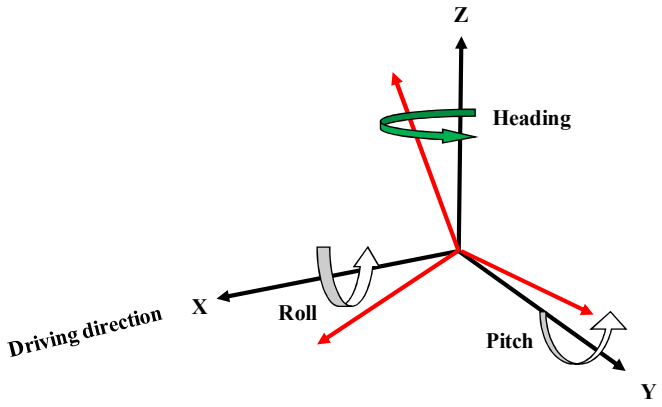

Figure 4-8: Rotation angles between actual and theoretical axes.

The 3D geometric objects extracted from the point cloud will be used as target points/ test surface objects and for the purpose of comparing the results of the TLS system. An example of the quality and point density of the MLS scenes is indicated in Figure 4.9.

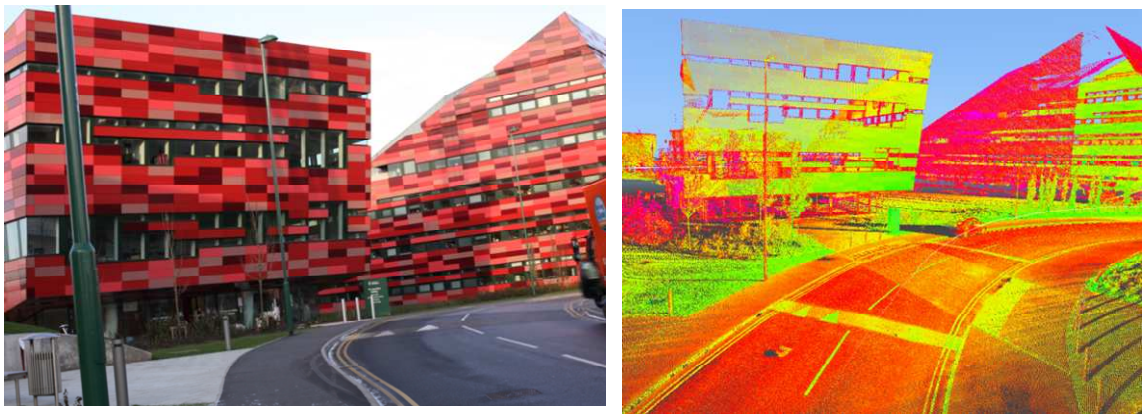

Figure 4-9: Left: image. Right: subset of point cloud captured by MLS in Jubilee Campus, Nottingham University test site (the International Office and Amenities buildings).

4.2.4 Data processing

In the process of data acquisition, three sub-systems record data as follows (Puente et al., 2011):

1. The GPS-IMU system calculates the vehicle trajectory and records each pulse of the laser scanner.

2. Line scanner data is transformed into three dimensions in the geo-referencing phase, where each laser point is assigned an appropriate time stamp, and then combined with the trajectory information of the location and altitude of the scanner to produce point data.

GPS data of MLS are processed by a kinematic differential GPS approach (3D Laser Mapping Ltd., 2011). This requires a reference station that should be located at a known position. StreetMapper360 used the base station at Nottingham (KEYW) for collecting data for this project. For the second survey operation in 2012, the permanent NGB2 reference station which is located on the Nottingham Geospatial Building (NGB) was used for differential correction. The second survey operated was used for testing the designed targets specifically made for MLS, as will be discussed in chapter 8.

Point classification is intended to determine the object for each laser point. This task is frequently the step that takes the most user time. Although automatic routines will carry out more than 90 % of the work, millions of points will still be left, for which the human operator has to make classification decisions. The survey whether in flight or on land, will frequently create data that may not be needed in the final product. The user will want to classify these points out of the active data set. Points might be excluded if they are (TerraSolid., 2004):

- Away from the project area.
- From the overlap area where points from another flight or vehicle pass will be kept.
- Of lower positional quality because of weather conditions or some other reason.

The level of classification detail varies significantly from one project to another. For example, in many airborne laser scanning projects, the only delivery product is a ground model and possibly contour drawings generated from the model. In those cases, 5-8 classes are all that is required (see Table 4.4).

Low, medium or high vegetation classes will not necessarily mean that the object is vegetation. Points in these classes will include hits on other surface objects too: cars, trains, lamp-posts, wires, etc. Some engineering projects may have more than 50 classes into which points need to be classified. The more detailed the classification point clouds, the greater the time required. Typically, classification is based on first running automatic routines and then performing interactive editing of the results (TerraSolid., 2004).

The density of mobile data decreases depending on the range. Additionally, the errors in misalignment angles reduce the x-y accuracy of points with increasing range. TerraScan software in option macros can filter out those points by repeating scanning several times and providing maximum distance. Furthermore, in places where the car stops and turns the point density tends to be higher than desired and such points also can be filtered and removed by TerraScan macros.

No.	Class	Description
1	Default	Not classified yet
2	Ground	Ground
3	Low vegetation	Objects < 0.3 m above ground
4	Medium vegetation	Objects 0.3 – 2.0 m above ground
5	High vegetation	Objects > 2.0 m above ground
6	Building	Building walls
7	Low point	Bad points
8	Model key point	Key points for ground model
9	Overlap	Points excluded from processing
10	Vector building	Building vector

Table 4-4: Classification of point cloud.

4.2.5 TLS dataset

The second set of data was captured using the Faro Focus^{3D} 120 TLS in July 2011. The system specification was discussed in section 3.2. The Faro Focus^{3D} 120 data was acquired with a "high" resolution setting, proving a point spacing of (6x6) mm on a target at 10 m distance from the scanner. The scanner was used to collect data from two areas of the University of Nottingham's Jubilee Campus. In each area, the scanner was positioned at a known point: the first area was under the open sky, where the GPS coverage is good, while the second was in a relatively urban canyon, in which the quality of GPS tends to be degraded. The data collected in the two selected areas were transformed to the UK national grid system and the precision of the referenced point clouds was better than 1cm.

The overall quality of the data captured by TLS is influenced by four major factors: instrument calibration, atmospheric condition, target properties and scan geometry, as described in section 3.6. These datasets present an excellent opportunity to evaluate the use of TLS data compared with other datasets such as MLS, as discussed in section 4.3.1.3.

4.3 Assessment of data quality

One of the primary objectives (see section 1.2) of this research is to evaluate the quality and reliability of MLS data in an urban area. Figure 4.10 shows the workflow of the methods used for undertaking the analysis. As stated in the literature review, the factors that affect the quality of MLS in urban areas are the GPS position, whose quality fluctuates from open areas to urban canyons, and IMU outputs, which drift over time. Obstruction of GPS signals by high buildings or tree shading reduces the positioning accuracy significantly. Therefore, the good areas and bad areas will need to be evaluated with respect to the quality and reliability of MLS data. The benchmark (GCPs) used to assess the accuracy of the mobile laser data was within a cm level of accuracy. This was a result of the network adjustment procedure, as can be seen in Appendix E.

This section will introduce the different methods used for assessing the quality, such as nearest points, iterative closest point (ICP) and additional sources of data. The TerraScan / TerraMatch approach is used for checking the system calibration results and for analysis of these results. Finally, the advantages and limitations of each method will be presented.

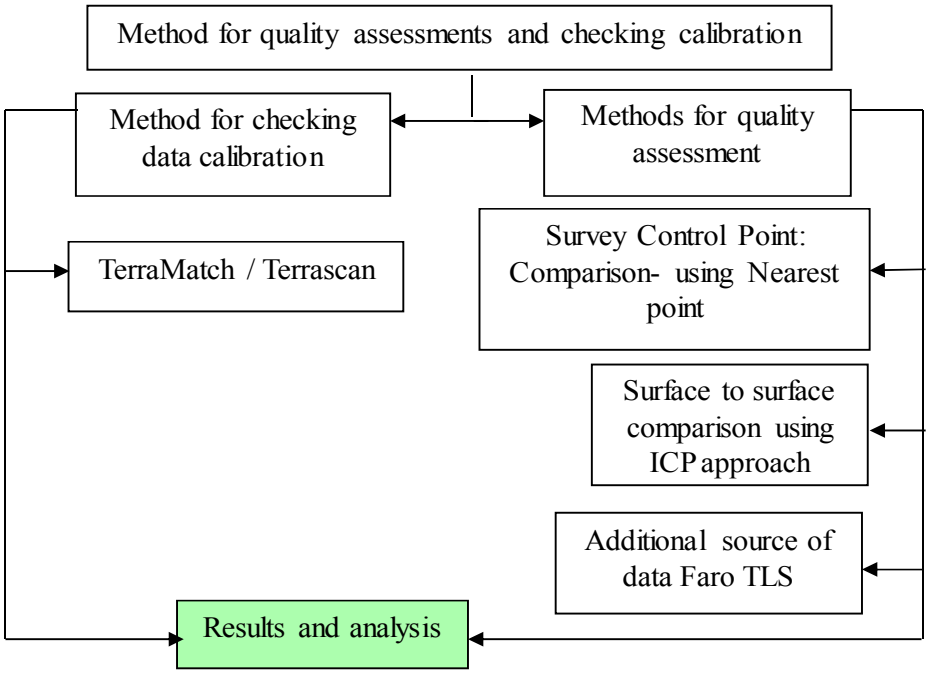

Figure 4-10: Flow diagram of the quality assessment and system calibration.

4.3.1 Methods for quality assessments

4.3.1.1 Using ground control points (GCPs)

In this section a large number of GCPs are used to assess the quality of data provided by 3DLM Ltd. for this research to achieve objectives 1 and 2 (section 1.2).

4.3.1.1.1 Assessing MLS point cloud of multiple scan using nearest point

Comparison of the MLS data and GCPs in coordinate measurement using the nearest point method will be the procedure adopted in this section.

The number of control points observed using the total station (TS) is 277 (see Table 4.3), and these were used for comparison between the MLS points and the known coordinates of the same points on the road surfaces and building facades.

In this trial, the area of interest (AOI) was divided into four different zones (see Figure 4.4). The trial is discussed, the accuracy of the MLS point cloud obtained from multiple scans will be assessed using GCPs, and the point coordinates achieved from MLS are compared with those of the TS along the study area. Figure 4.11 shows an example of ground points on the corner of a white road marking and a building used for comparison. The coordinates of these points are compared with the MLS coordinates from different zones, as mentioned above, in order to check the external quality of the data provided by 3DLM Ltd. for this project.

In other words, the planimetric and elevation accuracy will be evaluated by measuring reference targets within the MLS point cloud along the study area and then differences in the easting, northing and elevation will be computed. The reference targets observed were typically the corner of a white road marking, a building corner, a manhole cover corner and a kerb corner.

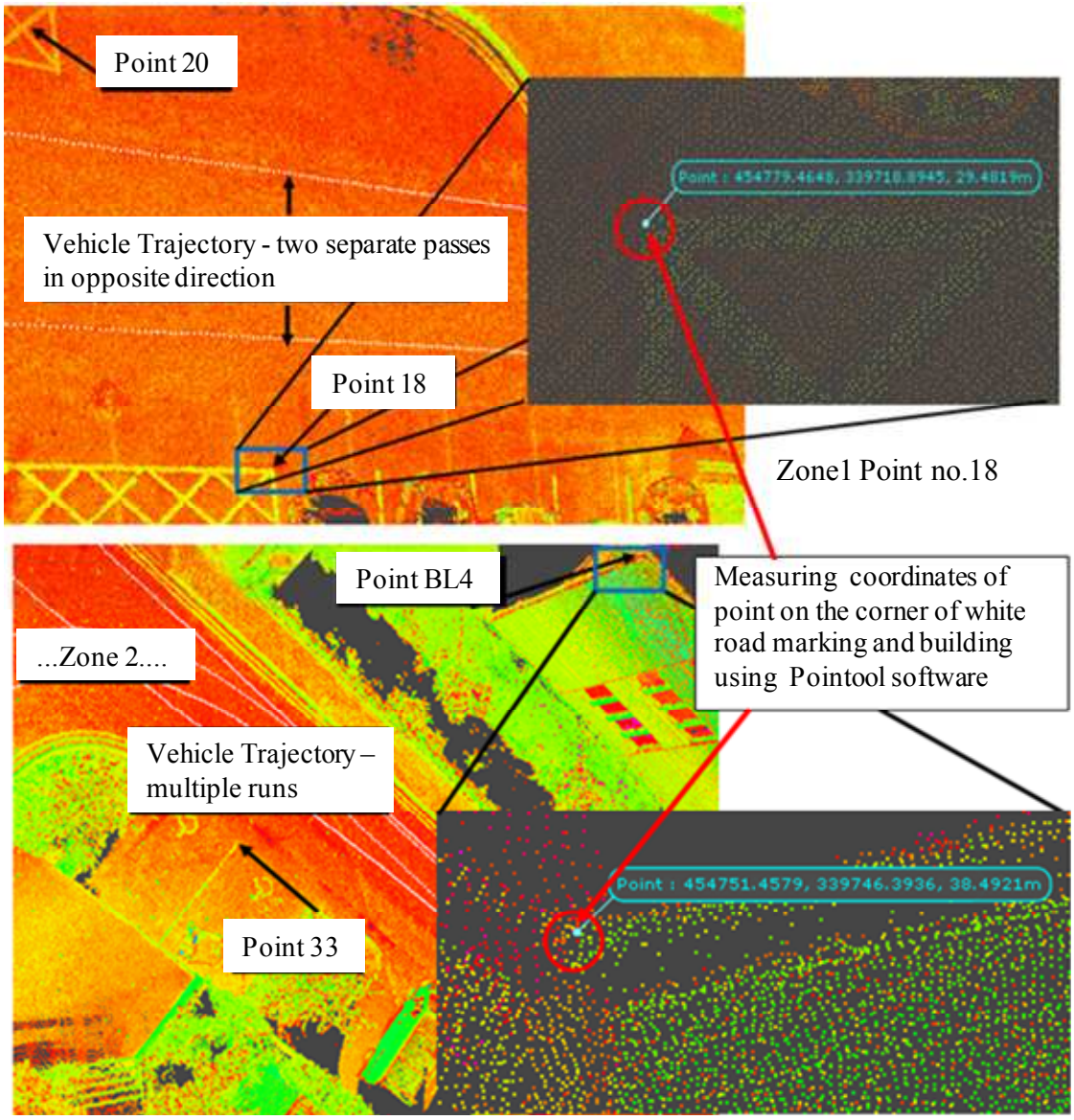

Figure 4-11: Measuring points manually on the road and building façades using Pointool software.

Result of comparisons of MLS coordinates from multiple scan with GCPs.

The aim of this comparison is to assess the quality of the data provided by 3DLM Ltd. on the road surfaces and building facades. Tables 4.5 and 4.6 show the RMS errors of vertical and horizontal positions between the points estimated from multiple passes of scans and the ground control points on the ground surfaces and building facades along the study area; the accuracy of the GPS position for every second in the entire area of Jubilee Campus was provided by 3DLM Ltd. The accuracy of the GPS position in each zone (see Appendix A) along the area of study is also presented in the table.

In order to assess the absolute accuracy of the entire area of study from all zones selected, the RMS errors of the data in each test area were combined, as shown in Table 4.7 and Figure 4.12.

Zone no.	Points	RMS (H)m	RMS (EN) m	Remarks	GPS quality position (ENH) m (3DLM Ltd.)
Zone1	34	0.0395	0.0286	From A1 to A2	0.0400 to over 0.1000
Zone2	50	0.0346	0.0284	From A2 to A3	0.0800 to 0.0300
Zone3	50	0.0484	0.0412	From A2 to TP 6	0.0400 to 0.0700
Zone4	16	0.0425	0.0415	From TP 6 to NGB11	0.0800 to 0.0400

Table 4-5: RMS error of vertical and horizontal position on ground surfaces.

Zone no.	Pts. No.	RMSE (H)m	RMS (EN) m	Remarks	GPS quality position (ENH) m (3DLM Ltd.)
Zone1	34	0.0560	0.0420	From A1 to A2	0.0400 to over 0.1000
Zone2	54	0.0600	0.0574	From A2 to A3	0.0800 to 0.0300
Zone3	32	0.0692	0.0560	From A2 to TP 6	0.0400 to 0.0700
Zone4	13	0.0213	0.0335	From TP 6 to NGB11	0.0800 to 0.0400

Table 4-6: RMS error of vertical and horizontal position on building facades.

The result of combining the RMS errors obtained from the points on the road surface and the building corners in a horizontal and vertical position of the same area are shown in Table 4.7 and Figure 4.12.

Zone no.	ΔE (m)	ΔN (m)	ΔH (m)	RMSE (ΔE, ΔN, ΔH) m
Zone1	0.0243	0.0252	0.0477	0.0592
Zone2	0.0286	0.0317	0.0473	0.0637
Zone3	0.0353	0.0322	0.0588	0.0758
Zone4	0.0277	0.0249	0.0319	0.0490

Table 4-7: The combined RMS error of each zone from points on the ground surface and building facades.

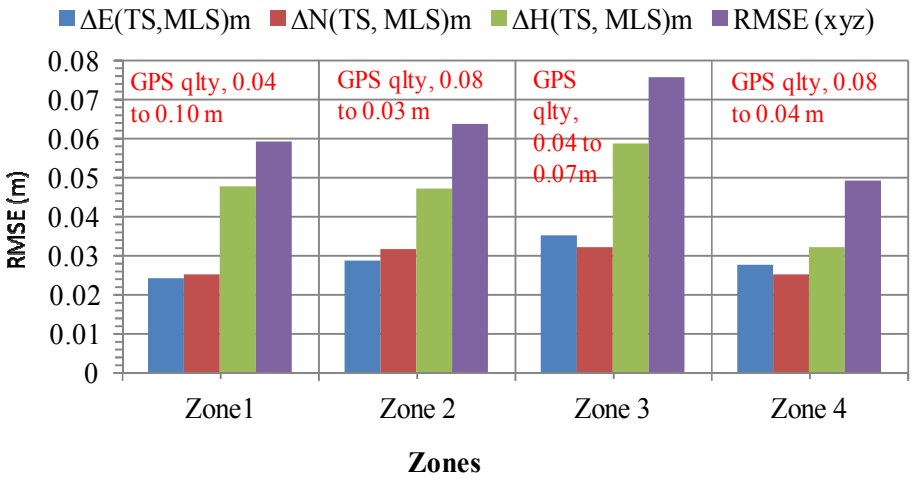

Figure 4-12: Combined RMS error of the ground surface and building facade in each zone.

Results analysis

Tables 4.5 and 4.6, show that the vertical position on the ground surfaces can be obtained with an accuracy of 3 to 5 cm. However, the accuracy of the vertical position on the building facades is within 2 to 7 cm. Meanwhile, the accuracy of the horizontal components on the ground surfaces and building facades is within 3 to 4 and 3 to 6 cm, respectively. The accuracy of each zone was comparable with or better than the GPS accuracy position, except for zone 3, where the ground surfaces and building facades positions showed less accuracy than was obtained using GPS. This is due to the misidentification of the estimated coordinates of points in MLS data compared to the Total Station (TS) measurements of those points.

Table 4.7 and Figure 4.12 show that combining the deviation errors of the horizontal and vertical components of the ground surfaces and building facades in each zone produces better results than when these are taken separately. Although the GPS quality seems to be very similar in zones 2, 3 and 4, the results fluctuated. For example, the best accuracy can be found in zone 4, 1, 2 and 3, in that order. This is because the GPS quality increases in zone 4 and is degraded in the other zones. The reason for obtaining the least accuracy in zones 2 and 3, which have the same GPS quality as zone 4, is the distribution of points in those zones. The number of selected points in zone 2 and 3 was greater than in the high GPS quality area.

In general, the method used for assessing the quality of the MLS data is the comparison of MLS data with ground control points. This approach is not accurate enough to be used for horizontal accuracy, unless specifically-designed targets are utilised (Habib and Van Rens, 2007). Because of that, the absolute accuracy of the MLS point cloud depends on the accuracy of the navigation solution. If the accuracy of the navigation solution is degraded in an urban area, the accuracy of the point cloud will likewise be degraded, due to degradation of the trajectory.

4.3.1.1.2 GCPs with separate scan using nearest points

In this test, the AOI was divided into five small zones. These small zones were represented by MLS blocks according to the GPS quality position, as obtained from 3DLM Ltd. (see Figure 4.13 and Table 4.8). The figure shows the vehicle trajectory plotted according to the GPS position quality (see Appendix A) and the five test areas. Table 4.8 shows the number of blocks used for this comparison. These point clouds of MLS blocks were collected from independent passes in opposite directions. Each pass was used for comparison with the TS (E, N) value along with the height value, in order to evaluate the accuracy of MLS in different GPS coverage.

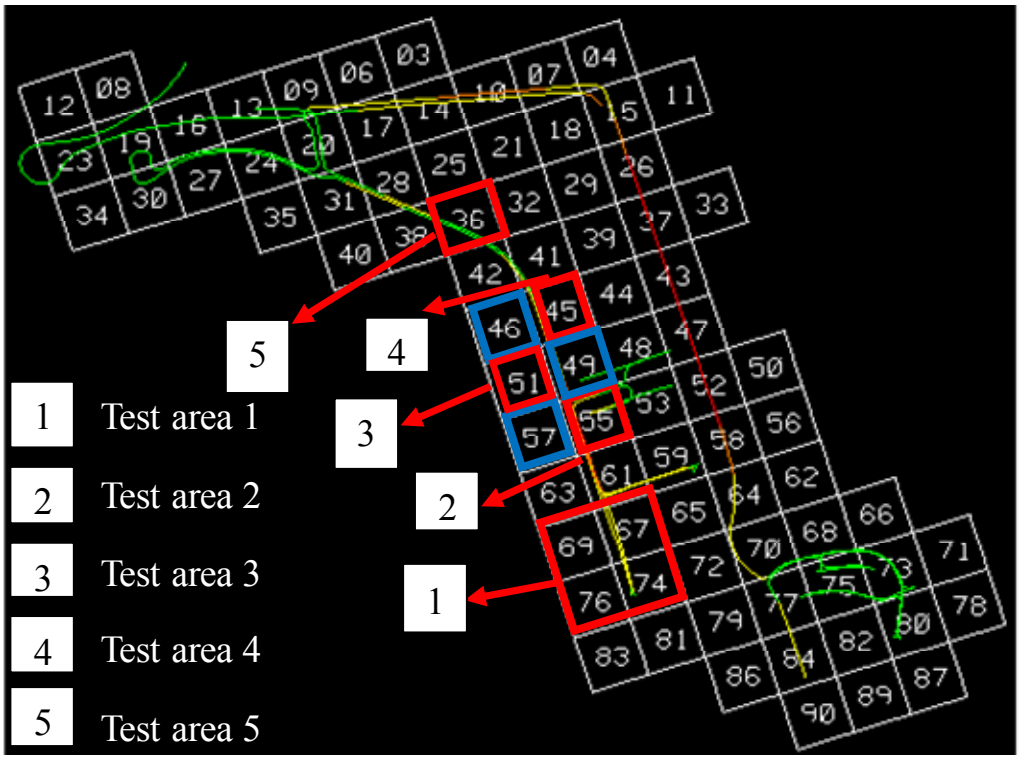

Figure 4-13: Trajectory of vehicle overlain with blocks boundary of the MLS point data.

Test	Block no.	GCPs used	GPS position quality (ENH) m	No. of runs
1	(67,69,74 and 76)	18	0.03	2 (LR)
2	45	10	0.04 to 0.07	3 (LR)
3	55	9	Over 0.1	7 (3L, 4R)
4	36	6	0.03	2 LR
5	51	15	0.08	8 (4L. 4R)

Table 4-8: Block numbers and the number of GCPs used for comparison with the MLS data.

Result of comparisons of single scan points with GCPs

The results for the horizontal and vertical position of the selected points on the ground surface and building façades obtained from two scans in opposite directions are as follows.

1. The RMS differences and standard deviation of the horizontal position for each scan separately compared with the known GCPs are shown in Table 4.9.
2. The RMS differences and standard deviation of the vertical position for each scan separately compared with the known GCPs are shown in Table 4.10.

Block no.	RMS (ΔE) (m)	RMS (ΔN) (m)	RMS (ΔE, ΔN)	Std Dev (ΔE) (m)	Std Dev (ΔN) (m)	Std Dev (ΔE, ΔN)	GPS Position quality (m)
Pass	**Scan point from left pass**						
(67,69)	0.0222	0.0162	0.0274	0.0159	0.0167	0.0226	0.0300
45	0.0256	0.0276	0.0376	0.0180	0.0174	0.0250	0.040 to 0.070
55	0.0294	0.0196	0.0353	0.0221	0.0224	0.0315	Over 0.1000
36	0.0143	0.0186	0.0235	0.0141	0.0132	0.0193	0.0300
51	0.0291	0.0345	0.0452	0.0256	0.0227	0.0342	0.0800
Pass	**scan point from right pass**						
(67,69)	0.0184	0.0197	0.0269	0.0147	0.0199	0.0247	0.0300
45	0.0281	0.0219	0.0356	0.0210	0.0219	0.0303	0.040 to 0.070
55	0.0267	0.0348	0.0439	0.0253	0.0271	0.0371	Over 0.1000
36	0.0263	0.0209	0.0336	0.0286	0.0181	0.0338	0.0300
51	0.0407	0.0225	0.0465	0.0267	0.0225	0.0349	0.0800

Table 4-9: RMS errors and standard deviation of horizontal position for each block of the point cloud compared with the known control points.

Block no.	Scan points of the left pass		GPS position quality (m) (3DLM Ltd.)
	RMSE (H) (m)	Std Dev (H) (m)	
d((67,69)	0.0359	0.0067	0.0300
45	0.192 / 0.0358	0.0070	0.040 to 0.070
55	0.0541	0.0019	Over 0.100
36	0.0332	0.0010	0.0300
51*	**x**	**x**	0.0800
Block no.	**Scan points of the right pass**		**GPS position quality (m)**
(67,69)	0.0392	0.0079	0.0300
45	0.184 / 0.0342	0.0128	0.040 to 0.070
55	0.0618	0.0116	Over 0.100
36	0.0309	0.0085	0.0300
51*	**x**	**x**	0.0800

Table 4-10 RMS errors and standard deviation of vertical position on the road surfaces for each block of the point cloud compared with known GCPs. Top: left passes. Bottom: right passes.

*The block 51 measurement was taken on the building facade; therefore, the height value acquired via the digital level is not available for comparing the height in the building facade.

.

Table 4.9 shows that the absolute accuracy that can be achieved from MLS data in the horizontal position is within 2-4 cm in each pass, and the standard deviation of the data is within 1-3 cm. The quality of the MLS point of the first pass was slightly better than the second one. This is because of the difficulty in accurately measuring natural point features in the point cloud. In addition, the geometry of satellites and the topology of the road also influence the horizontal position. Habib and Van Rens (2007) stated that this method is not accurate enough for verification of horizontal accuracy without the use of specifically-designed targets. Therefore, the absolute accuracy of the vertical position as shown in Table 4.10 fluctuated in both passes, and a large error on block 45 of 0.192 and 0.184 m in each scan respectively can be detected. After removing some unreliable points from the points of block 45, the resulting data was better; the RMSE was 0.036 m and 0.034 m for the first and second scan respectively and this is comparable with the accuracy of the other blocks in that area, except for block 55, which dominated due to the GPS position quality.

This method is unreliable for assessing the quality of the point cloud in any environments.

The planimetric and height RMSE between two scans for each block can also be estimated from the above tables. The results show that there are discrepancies between the two passes, as shown in Table 4.11, which vary according to the GPS position quality.

Blocks	RMSE (ΔE, ΔN)	RMSE (H) (m)
(67,69)	0.0052	0.0033
45	0.0062	0.0016
55	0.0154	0.0077
36	0.0122	0.0023
51	0.0170	---------

Table 4-11: RMSE of planimetric and height between two passes for each block.

4.3.1.1.3 General discussion

In order to provide a number of known points along the study area, TS and digital level reference data was collected for corresponding points in the laser scanning data. Data for other control points was tested in five small MLS blocks in the study area.
Although the white line road markings can be clearly seen in the scan data due to their highly reflective design, these control points still had to be manually determined with three points distributed across the width of the marking. This should include an assessment of the beam width uncertainty value, which at 10 m, is based on a beam diameter of around 7 mm (Lichti et al., 2005).

Logistical limitations did not allow testing to take place. Barber et al. (2008) suggested that routine implementation of such systems in the future will need an appropriate automated quality control method to ensure that the captured data meets the requirements for the work. This will be achieved by introducing a new target design located in the test area. The designed targets are discussed in Chapter 5.
The delivered point cloud data has been provided as a commercial product, which requires a general group of software tools for processing and verification. The main

commercial software package used in this test is Pointools for measuring points in MLS data, while TerraScan is used for classifying point cloud data and splitting scans into individual driving passes.

As mentioned, some areas (zones) or blocks were better than others in terms of accuracy. For example, the scan data in zone 2 through the urban canyons had a higher RMS error, while in the open areas it had many fewer RMS errors on the control point. While an analysis of the MLS blocks from repeated passes in the test area of the five blocks was highlighted in Figure 4.13, a lower standard deviation was found in the comparison of horizontal and vertical positions with other blocks (see Tables 4.9 and 4.10), and the RMS errors determined for the vertical position for those blocks were between 0.002 m and 0.007 m. However, the same blocks of point cloud data for a known control point in the vertical position used in block 45 in Table 4.10 had relatively high RMS errors, between 0.192 m for the first pass and 0.184 m for the second pass.

The GPS quality in that area was 0.08 m, after removing some unreliable points from the data for that block. The resulting data was better; the RMSE was 0.036 m and 0.034 m for the first and second pass respectively, which is comparable with the accuracy of the other blocks in that area, except for block 55, where the error were significant, due to the GPS position quality (see Table 4.10).

4.3.1.2 Surface to surface comparison using TIN approach

The analysis of the 3D data of an object (3D surface-to-surface comparison) depends on multiple scans, or at least the same object appearing in two scans. For the 3D data comparison analysis, the software package Geomagic studio version 10.0 was used, which allowed the processing of the 3D point cloud, the generation of a triangulated surface (polygonal model), and plane representation of the object surface. To create the surface, several steps are needed, through the clean-up of a point object and its conversion to a polygon object.

The first step is to remove any point clusters that are disconnected (far away) from the main body of the point cloud. The next step is to remove outliers that are not part of the main cloud, usually caused by reflections (Geomagic, 2007). A lower value

limits selection to the farthest points, while a higher value includes a wider range of outliers. Then, the final step “wraps the model": surface wrapping is done for both parts of the two scans separately with a medium level noise reduction option. The process of comparing the surfaces of the road and building facade are explained in the following trials.

A. 3D surface comparison method using road surfaces

After a surface is created from each of the two scans acquired during continuous runs in opposite driving directions (see Figures 4.14 and 4.15), analysis of the 3D comparison will produce a 3D colour-coded mapping of the differences between the objects (Figure 4.16). If a portion of the test object has insufficient data for a valid comparison with the reference object, that portion of the results object will be grey (Geomagic, 2007). The 3D comparison of the different elevation models was also done with Geomagic Studio. This software has the ability to perform a 3D comparison between points-to-surface or surface-to-surface models using the TIN approach, as discussed below in the following tests.

The same five small areas used in section 4.2.1.1.2 (blocks 67, 45, 55, 36, 51) were also chosen for this test. The block numbers, point cloud for each scan, and triangle meshes for each surface are shown in Table 4.12.

Test area.	scans	Object’s Point cloud	Triangle meshes creating surface	GPS quality (ENH) m
Block 67	Pass 1 (scan. 4)	476 531	435 464	0.03
	Pass 2 (scan. 5)	463219	409 886	
Block 45	Pass 1 (scan. 4)	620 689	450 569	0.04 to 0.07
	Pass 2 (scan. 12)	376559	405 581	
Block 55	Pass 1 (scan. 11)	770 130	646 786	Over 0.10
	Pass 2 (scan. 12)	771 794	635 729	
Block 36	Pass 1 (scan. 4)	705 347	474 418	0.03
	Pass 2 (scan. 12)	392 156	424069	
Block 51	Pass 1 (scan. 4)	133 172	205 853	0.07 to 0.09
	Pass 2 (scan. 12)	227 812	328 182	

Table 4-12: Information on the selected blocks from the AOI.

Result and discussion

Block 67: A part of the road surface was taken from two drives passes in opposite direction from the point cloud, denoted as pass 1 and pass 2.

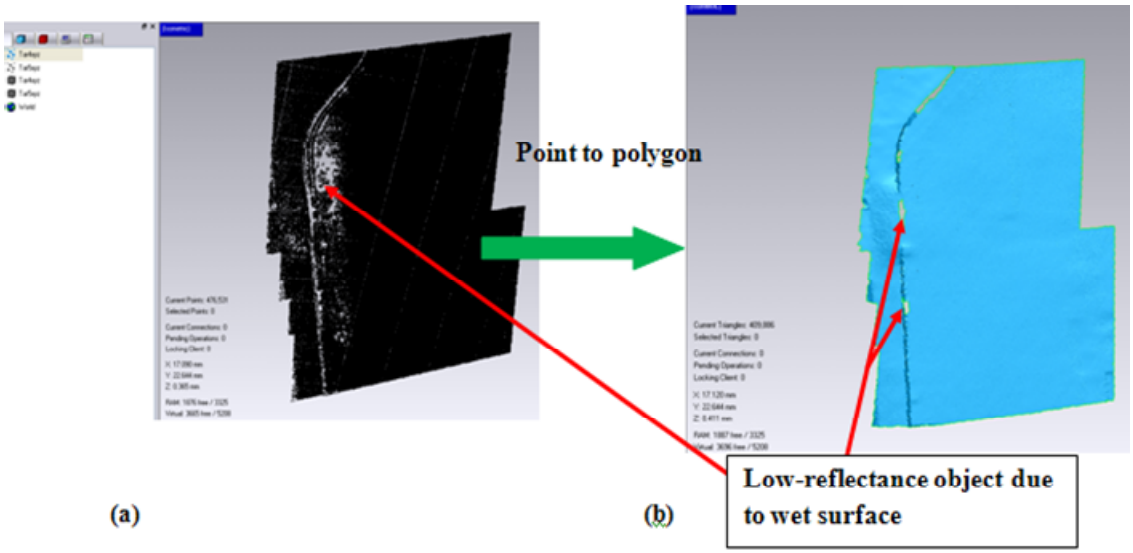

Figure 4-14: (a) Point cloud 1 of a part of the road surface (pass 1); (b) TIN created of a selected surface in pass 1 using Geomagic Studio software v.10 – Block 67.

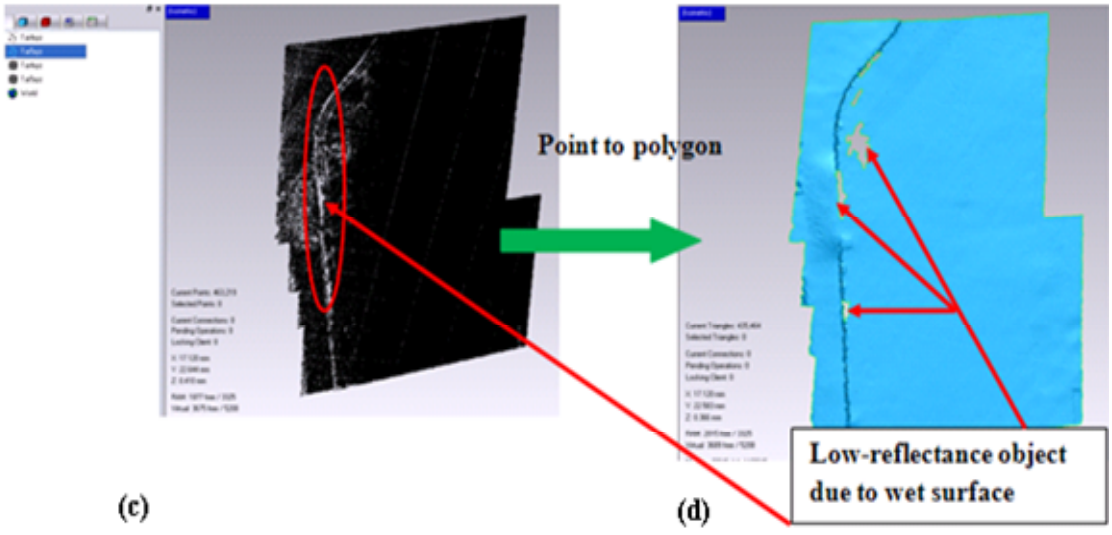

Figure 4-15: ((c) Point cloud 2 of the same part of the road surface (pass 2- Block 67); (d) TIN created of a selected surface in pass 2 using Geomagic Studio software v.10-Block 67.

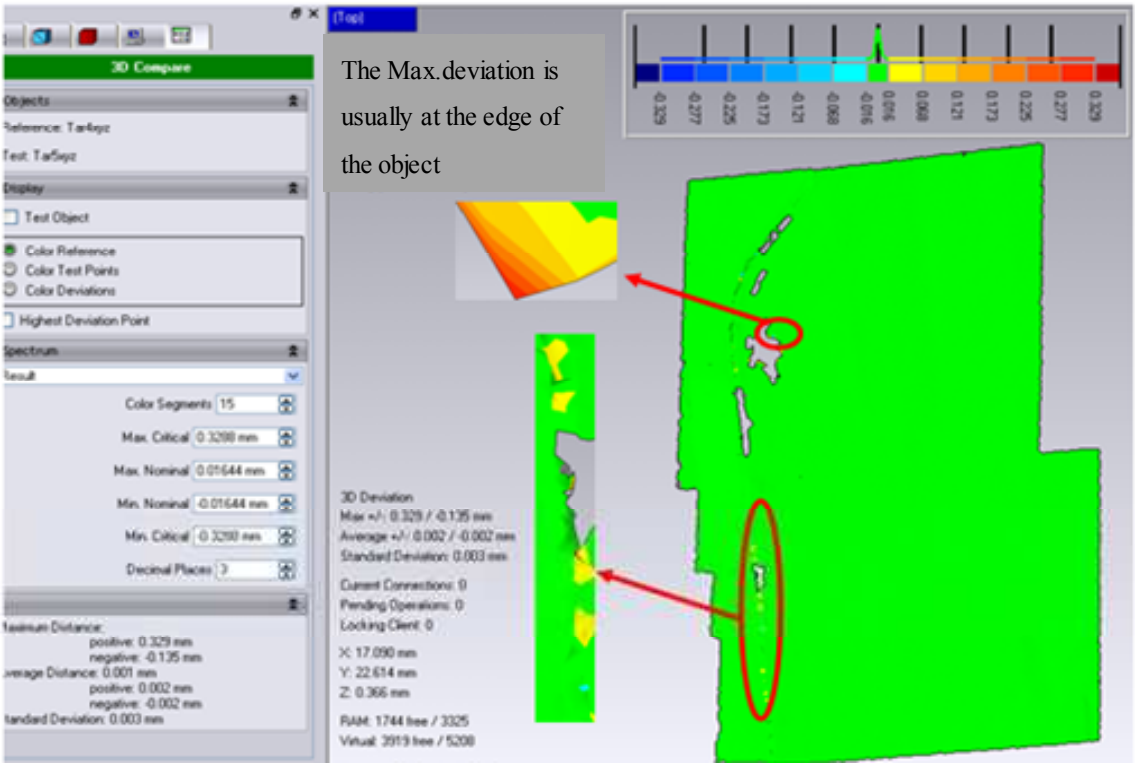

Figure 4-16: Result of deploying "3D surface compare" between two surfaces: object in Pass1 as a reference and pass 2 as a test surface.

The same procedure was performed on the road surfaces of blocks 55, 45, and 36, as depicted in Appendix G1. The statistical result of the 3D comparison for all the selected blocks is indicated in Table 4.13.

Block no.	Max. deviation (m)	Max. deviations (m)- accepted	Average distance		STDEV. (m)
			Deviation	Positive ; negative deviations (m)	
67	±0.3288	±0.0164	-0.0010	+0.002; -0.002	0.0030
45	±0.1730	±0.0086	-0.0010	+0.003; -0.002	0.0050
55	±0.1110	±0.0556	-0.0000	+0.003; -0.003	0.0040
36	±0.1240	±0.0062	-0.0010	+0.003; -0.002	0.0040
51	±0.4460	±0.0760	-0.0130	+0.013; -0.029	0.0310

Table 4-13: Statistical results of the 3D deviation of the two surfaces: one surface as a reference and the other as a test surface for all selected blocks.

Figure 4.16 shows the result of the deviation spectrum of "3D surface compare" in Geomagic software. A deviation spectrum is the distribution of colours to ranges of

surface deviation. The following parameters affect this form of spectrum on a one-time basis:

- **Colour Segments** specifies the number of deviation distances reported by this spectrum, each represented by a different colour.
- **Max. and Min. Critical** specifies the highest and lowest positive and negative differences reported by this spectrum, which in this test was ± 0.353 m.
- **Max. and Min. Nominal** specifies the highest and lowest positive and negative differences that are considered acceptable, or the region shown in green, which is ± 0.018 m.

In Geomagic Studio, the green colour appears when the comparison is performed. Blue indicates that the surface is directed towards the observer while yellow appears when in the wrong direction. This wrong direction can be resolved by using the flip option available in the "polygon" command.

The results in Table 4.13 present the following parameters:

- **Maximum Distance set** indicates the greatest differences (positive and negative) that are found anywhere in the comparison between the test and reference surfaces respectively (Geomagic, 2007).
- **Average Distance set** indicates the average difference (positive and negative) that is found anywhere in the comparison between two surfaces.
- **Standard deviation (std Dev.):** The std Dev of all differences see Table 4.13, column 6.

In Figures 4.14 and 4.15 (right) there were some gaps in the data due to wet surfaces and the low reflectance of objects. Figure 4.14 b was compared with Figure 4.15 d. For quality assessment of the surface model, a reference surface is often interpolated in the test surface to be checked (Akca, 2010). Evaluation is performed based on the height differences. This method is sub-optimal since in Figure 4.14 b surface discontinuities and surface modelling errors may lead to large height differences although the measurements are correct (Poli et al., 2004). For example, in Figure 4.16, if the frames of reference of the two surfaces differ, then again great differences occur, especially at discontinuities, although the height may be acceptable. In

Geomagic Studio (version 10.0), 3D analysis comparison between two surfaces was used based on ICP (Besl and McKay, 1992) to determine the 3D deviation of the two scans obtained from different runs of the same area.

Table 4.13 shows the statistical results of the "3D surface compare", where the nominal maximum deviation, average height and standard deviation of the spatial distance between the reference and test surfaces, after performing the 3D analysis, were computed as a range between ±0.017 m, -0.001 m and 0.009 m, respectively for block 67 (see Figure 4.16). The nominal deviation, as depicted in the result of the 3D surface analysis, degraded along the kerb by up to ±0.074 m (see the histogram at the top of Figure 4.16). The lowest deviation can be seen in blocks 36 and 45, where the nominal max deviations are 0.0062 m, 0.0086 m, respectively. The greatest deviation can be found in block 55, where the nominal max. deviation is 0.056 m. This could be because of the effect of the different satellite geometry on the first and second runs, creating different multipath environments. Calibration errors and measurement errors may also be behind this effect.

The nominal maximum deviation for the E, N, and H components in block 67, for example, was found to be 0.0083 / 0.0088 / 0.013 m, respectively. These are the maximum differences of the height deviation between the two surfaces after removing planimetric components. In planimetric form, this bias is because of the different orientation of the two driving passes, and it is only significant in the N direction.

In height, bias is possible, for the same reason as mentioned above. The differences are higher at surface discontinuities in kerbs up to ±0.074 m as depicted in yellow and blue spots along the kerb in Figure 4.16. This is possibly due to modelling errors (see also Appendix G, Figure G1). The surface comparison data shows a rise in the hump. The possible explanation is the change of fitting from the use of inappropriately calibrated data. The achieved maximum deviation of height differences was 0.056 m, and this discrepancy increases usually at the edge of the object (see Figure 4.16). It should be noted that this data needs to be improved. This will enable a new calibration procedure to be considered, in order to significantly reduce the maximum deviation to less than 0.01m anywhere in the MLS data.

B. For the building facade

In the same way, the test was applied on part of the building façade in block 51 (see Table 4.12). As shown in Figure 4.17, the highlighted point cloud of the facade was tested.

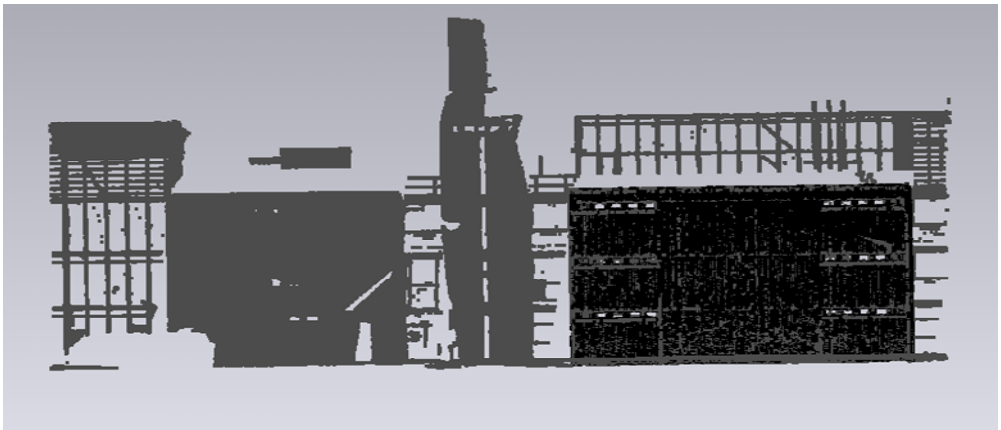

Figure 4-17: Point cloud of part of the facade of the building acquired from two passes.

After applying the same technique of TIN in Geomagic software on the two surfaces, the result obtained was inaccurate. This could be because there was insufficient data for a valid comparison with the reference object. This portion of the result object was indicated in grey. The result of the comparison is shown in Figure 4.18.

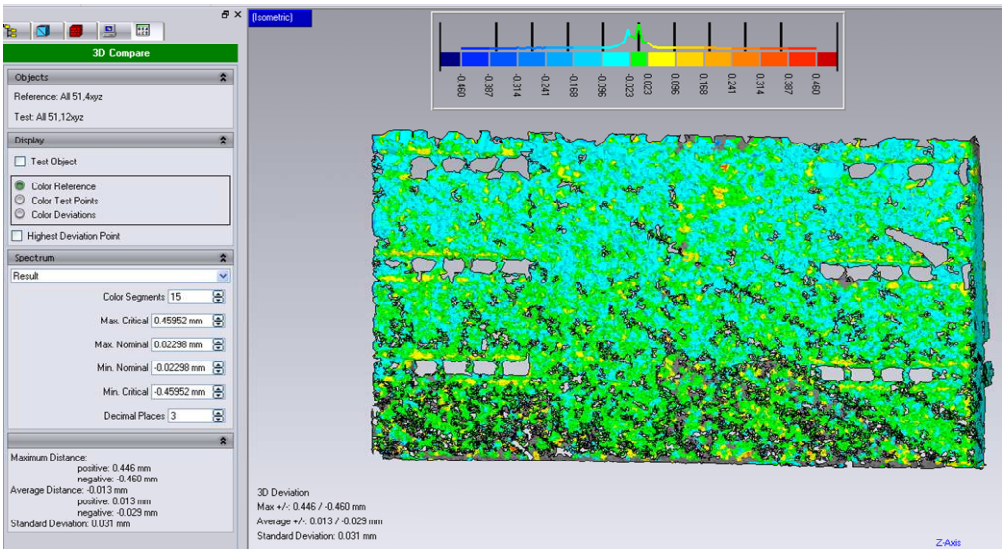

Figure 4-18: The result of 3D deviation between two TIN surfaces: pass 1 as a reference and pass 2 as a test surface-Block 51.

Figure 4.18 shows that only 49% of the points were far away from the model used in the computation. This means that 51% of the points were accepted; alternatively, the geometric plane features for the building facade was used instead of TIN, as explained in the next section.

Results of comparing planes on the building façade

In the previous test, the analysis of the "3D surface compare" method on the road surfaces was performed at four different places along the laser scanner trajectory with the aim of determining the value of tilt error between the surfaces. The road surfaces were represented by a TIN (Triangles Irregular Network), which is perfect for representing matching smooth surfaces. The TIN approach was also applied to the building facade, but poor results were obtained from the 3D surface analysis (see Figure 4.18). Therefore, the building facade is represented by geometric planes. There are two methods for fitting geometric planes, namely a best-fit algorithm and a mathematical model (parameters). The first method allows the software to fit a new 3D feature to the existing structure, while the latter requires a mathematical description. This involves a group containing the relevant parameters for user input. The first method was used for this work on the road surfaces and building facades.

In this test, the same part of the building façade as shown in Figure 4.17 was tested. A geometric plane for each façade was created (see Figure 4.19) and then an analysis was performed on the planes following the same approach as when using "3D surface compare". The same approach was applied on the other three blocks (46, 49 and 57), as depicted in blue (see Figure 4.13). The statistical results are shown in Table 4.14 and the graphical representations of blocks 46, 49 and 57 are shown in Appendix G-G2.

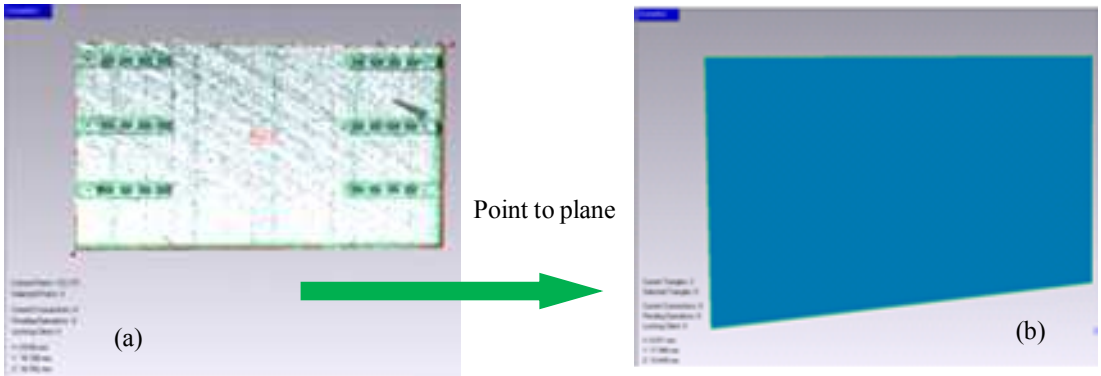

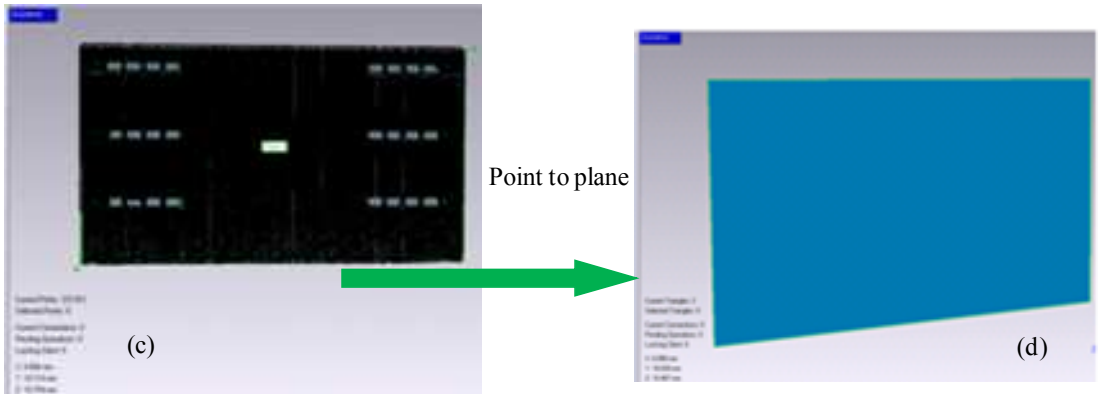

Figure 4-19: Point cloud data from two driving passes -Block 51 (a and c): point cloud 1 and 2 of pass 1and pass 2 respectively; (b and d): creating a plane for pass 1and pass 2 respectively.

Block no.	Max. deviation-accepted	Max. distance : positive; négative déviations (m)	Average distance deviations (m)	Positive; negative deviations (m)	Std. (σ) of all deviation points (m)
51	±0.0529	+0.0320 ; - 0.1060	-0.0120	+0.0050; -0.0150	0.0110
46	±0.0760	+0.3820 ; - 0.2300	+0.0760	+0.1510; -0.0790	0.1340
49	±0.0050	+0.0970 ; - 0.0990	+0.0270	+0.0120; -0.0320	0.0240
57	±0.0022	+0.0370 ; - 0.0440	-0.0400	+0.0800; -0.0120	0.0120

Table 4-14: Statistical results of the 3D deviation of the two planes: one plane as a reference and the other as a test plane of the entire selected block on the building façade.

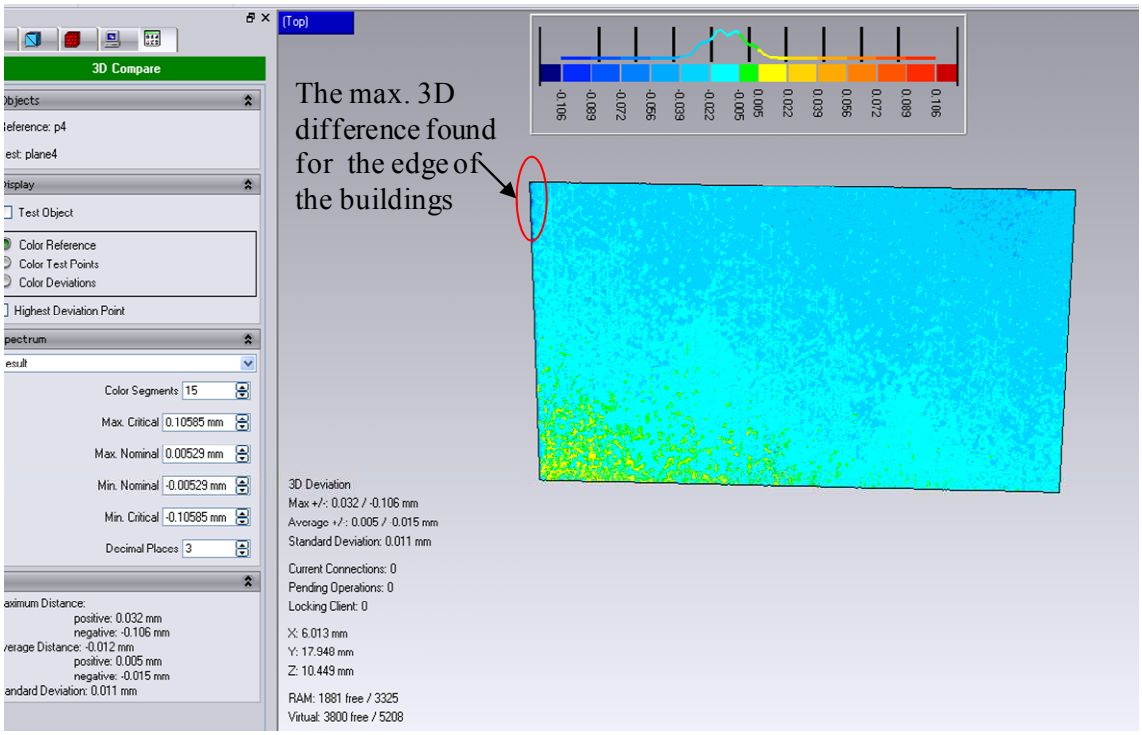

Figure 4-20: The result of 3D deviation between two planes of the building facade: plan1 pass1as a reference and plan 2 pass 2 as a test surface of block 51.

Figure 4.20 illustrates that the statistical results obtained from comparing the planes of the building facade is better than previously, as the maximum deviation of all corresponding points is 0.032 m and the maximum deviation obtained from the TIN surfaces was 0.44 m.

On the other hand, the difference in the coloured regions of acceptance (e.g. green), depicted on the colour bar shows that a few points were found not to be very good, with the deviation spanning from 0.005 m (green) to 0.032 m (cyan). This is due to calibration errors and measurement errors of the MLS system. These errors are based on random and systematic errors in the system measurement and parameters. Habib and Van Rens (2007) stated that the value of the random error depends on the precision of the system measurement and parameters, which contain position and orientation measurements from GPS/IMU, mirror angle and ranges. On the other hand, systematic errors are usually caused by biases in the bore-sight alignment parameters relating to the system components, and biases in the system measurements (e.g. mirror angle, ranges and drift in the position and orientation information).

In Table 4.14, the highest 3D deviation can be seen in block 46, where the nominal 3D maximum deviation value is 0.076 m. Also, this block has the highest standard deviation (0.134 m), because a few points were found not to be very good with the deviation ranging from 0.076 m (green) to 0.382 m in the deviation spectrum. The other two blocks (57 and 49) have the lowest standard deviation (0.012 m, 0.024 m) and slightly different nominal 3D deviation values (0.002 and 0.005 m, respectively). The possible reason for this is the effect of improper calibration parameters, and the fluctuating GPS position quality, as previously mentioned (see also Figure G2 in Appendix G).

The benefit from the geometric plane for the building facade was also used to solve the problem of the difficulty in measuring the exact point on the building corner. This is performed through the intersection of the fitted plane sides, as explained in the fitting geometric tests below.

C. Fitting tests for determining systematic errors:

1. Fitting the geometric plane on the building façade

In order to quantify the tilt error in the road surfaces and building facade, the planes are created for both parts of the building, and the correct corner is measured as a result of the intersection of the two planes, and then compared with the intersection planes of the other point cloud of the same area. Thus, the horizontal and vertical component error values between the two intersections are determined. Figure 4.21 describes the construction of planes from the point cloud of the building façade, and then the conversion of these planes into CAD for the intersecting process and measuring the exact points on the corners of the building.

The results of the measuring point for measuring the corner of the intersection of both passes can be seen in Table 4.15. A graphical representation of the other blocks (46 and 57) is shown in Appendix G, Figure G3.

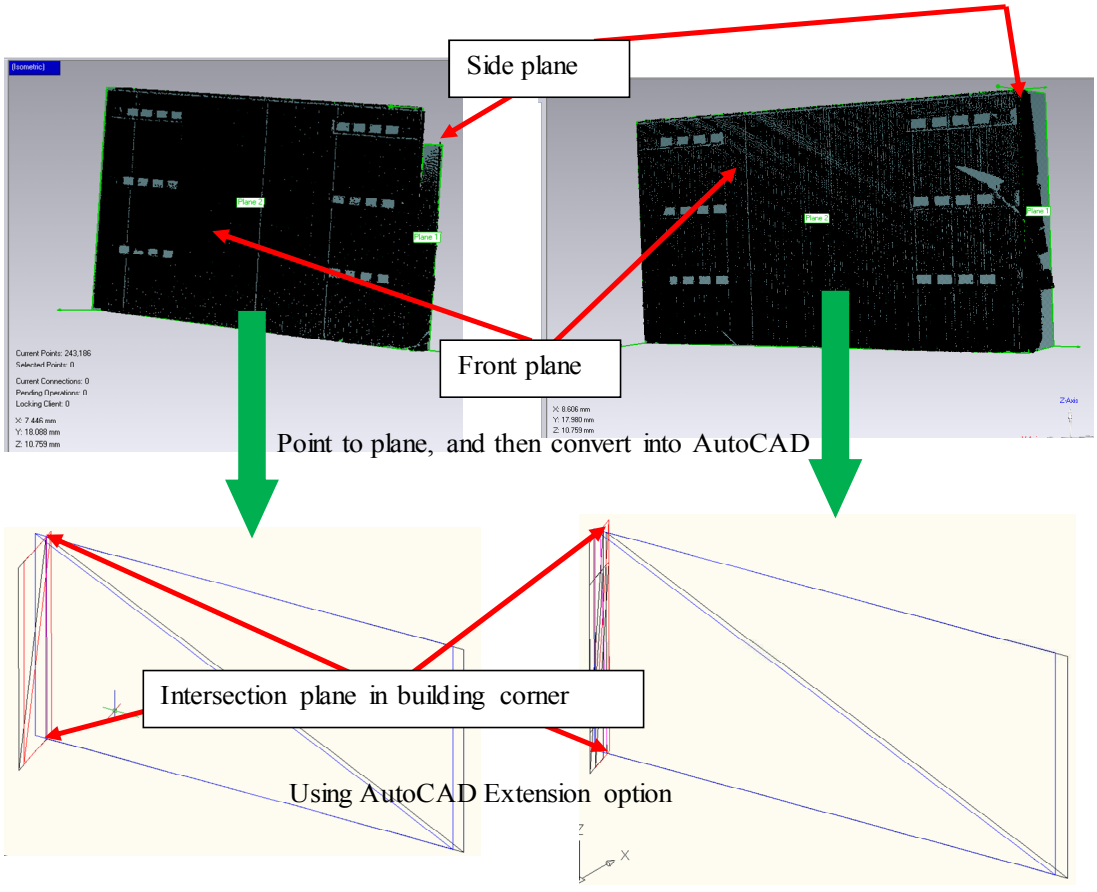

Figure 4-21: Point cloud data from two driving passes of block 51: Upper left and right: two plane surfaces (front and side) of point cloud 1 and point cloud 2 of the building façade from pass 1and pass 2 respectively; Lower left and right: the result of intersection of planes using AutoCAD software.

Block no.	Δ E m	Δ N m	Δ EN	Δ H m	GPS quality (ENH) m
51	0.0537	0.0509	0.0740	0.0056	0.070
46	0.0487	0.0341	0.0594	0.0109	0.050 to 0.030
57	0.0395	0.0544	0.0672	0.0295	0.070

Table 4-15: Planimetric and height errors in the measuring point on the building corner.

Table 4.15 shows that the planimetric and height effects are still significant after solving the problem of misidentifying the point on the building corner. In addition, the effect of horizontal position is greater than the vertical effect on the measured points on the building corner. A possible explanation is the change in coordinating measurements from the use of improperly calibrated data. Soininen (2010) illustrated in field trials that the effect of heading is greater than roll and pitch on the building facades and road surfaces. The effects of these parameters (HRP) are presented graphically in section 4.4.

2. Experimental results of fitting plane on the road surfaces

Four trials were undertaken to demonstrate the capabilities of the process of determining the planimetric error on road surfaces, and to identify the effect of tilt error between two fitted surfaces. Each trial was carried out in different positions from the AOI for blocks 55, 45, 36 and 67. Figure 4.22 shows the point clouds on the road surface from two separate drives taken in opposite directions. The plane for each surface was created, and the ICP approach was applied to fit the planes together.

In order to detect the value of the tilt errors, the two fitted planes were converted into AutoCAD, to identify and measure the effect. The absolute accuracy of the horizontal and vertical components was measured from four well-defined points in the overlap of the two scans, e.g. shown by dots in the specified area of Figure 4.22. These points were compared after fitting the two planes with their actual values obtained from TS. The result of the 3D deviation of the two planes and the accuracy of the model after fitting of the horizontal and height components, along with the value of the tilt error on the road surfaces, are illustrated in Table 4.16. This tilt error value is clearly shown between two rubber speed humps in Figure 4.23.

- **Block 55 planimetric impacts on the road surfaces.**

The planimetric and height deviation between two planes of MLS block 55 of part of the road from two passes was tested as shown in Figure 4.22. In addition, four well-defined points were measured at the edge of each plane and the humps to assess the quality of data and to determine good initial parameters for applying the ICP approach.

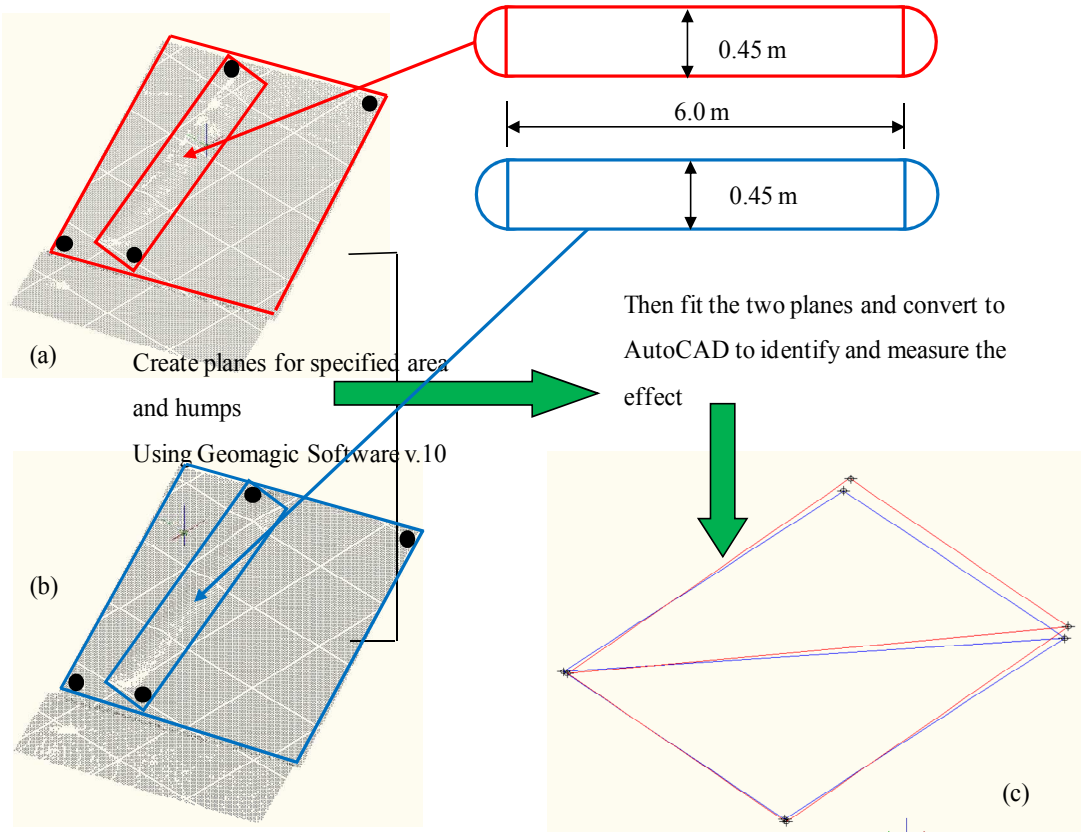

Figure 4-22: The planimetric and height deviation between two planes of block 55: (a) point cloud 1 of part of the road; (b) point cloud 2 of the same part; the top right figure indicates four well defined points measured at the edge of the plane and humps; (c) the planimetric and height deviation of the two planes obtained.

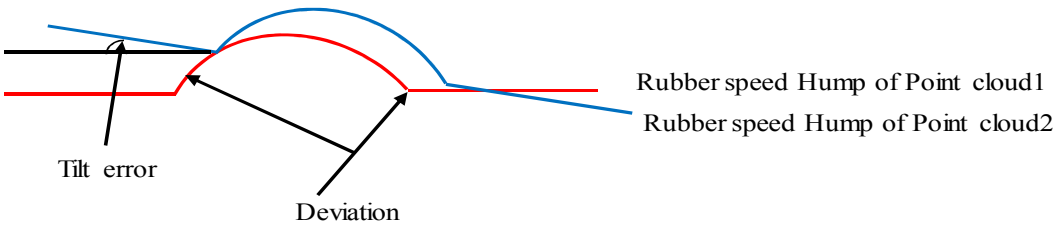

Figure 4-23: Profile visualising the effect of tilt between two surfaces on the road (not to scale).

In the same way, the planimetric and height effects were measured in blocks 45, 36 and 67 on the road surfaces, and the results are shown in Table 4.16.

Block no	Average (ΔE) m)	Average (ΔN) (m)	(Average ΔEN) m)	Average ΔH (m)	Tilt error (m)	GPS position quality (ENH) m
36	0.0216	0.0217	0.0306	0.0063	1.50^{o}	0.0300
67	0.0648	0.0215	0.0683	0.0256	0.65^{o}	0.0400 to 0.0700 m
55	0.1252	0.1090	0.166	0.1340	2.00^{o}	Over 0.1000 m
45	0.0679	0.0215	0.07122	0.0070	0.95^{o}	0.0800 cm

Table 4-16: The effect of planimetric and height deviations on the road surfaces compared with TS data, as well as tilt error between the two surfaces.

Table 4.16 shows that a clear systematic error existed between the two surfaces of the selected blocks. These errors arise from improper calibration of data, measurement errors and navigation error. The planimetric and height deviation between the two scans of the same area and the impact of the tilt error between two surfaces were measured in AutoCAD for each block. This effect varied depending on the slope distance of the road surface, and also calibration between the laser scanner and IMU; when the vehicle moves from the first run and turns back 180^{o} to collect data for the second run, the three axes (HRP) will then change and affect the results. This effect is presented graphically in Figure 4.28. Further evaluation of the quality of data was performed with an additional source of data using TLS. This assessment is introduced in the next section.

4.3.1.3 Additional source of data using TLS

In this section, another source of data was provided for assessing the quality of MLS data in urban areas. The MLS data were collected in 2009. The operating range of the MLS varied between 20 and 70 m depending on visibility. The system parameters used in the data collection from the Jubilee Campus are summarised in Table 4.17 (3DLM Ltd.).

MLS usually measures objects from a vehicle moving at a steady speed, providing a 3D point cloud with point spacing depending on the range between the point and the scanner. In this survey, the speed and orientation of the vehicle changed according to

the road network in the Jubilee Campus, giving different point densities. As an example, in narrow streets the vehicle moved slowly, leading to increased point density; when turning fast, the density decreased considerably, as shown in Figure 3.20 (chapter 3).

MLS StreetMapper	**Specification**
Scanner	2009: Riegl VQ-250
Effect. point measurement rate	50 to 300 kHz
Max. measuring range	500 m @ ρ>= 80% and 50 kHz:
	75 m @ ρ>= 10% and 300 kHz
Scanning frequency	100 line/sec
Sensor position from	135^{o} from forward and -40^{o} pitch from horizontal
horizontal level	level
Navigation system	Novatel oem v3 IGI imu iid 256hz
TLS	
Scanner	Faro Focus^{3D} 120
Point measurement rate	Max. to 976000 pts/second; typical
Point density	1 / 4 equivalent to (6 x 6) mm @ 10 m

Table 4-17: The Specification of MLS (source: 3DLM Ltd,) and TLS.

Faro Focus^{3D} 120 TLS provides reference data for verification of the MLS. This data was acquired with a high resolution setting of (6.0x6.0) sq. mm at 10.0 m range. The scanner was positioned at known points, as described in section 4.2.5.

Data processing and results

The workflow of data processing for accuracy assessment of the MLS data is shown in Figure 4.24. The profile laser data is transformed into three dimensions during the geo-referencing phase procedure of the mobile laser points with the appropriate time stamp. This is merged with the trajectory information on the scanner's position and attitude. This procedure was performed by 3DLM Ltd. The point cloud was geo-referenced using targets (see the section on registration and geo-referencing in chapter 3) with geo-referencing in three dimensions, in the UK national grid system.

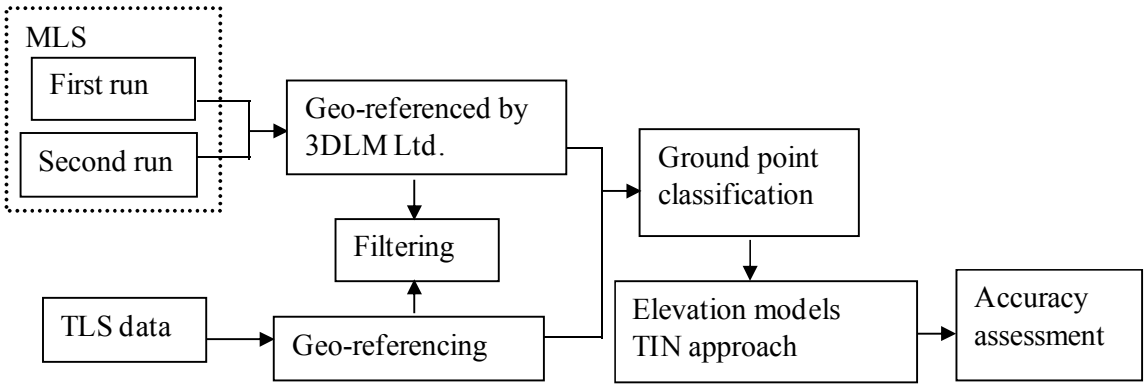

Figure 4-24: Workflow for point cloud data.

The point cloud data was filtered using Faro SCENE software. This is because with the phase-based TLS system technique the number of false points is higher than the pulse-based MLS system. The filtering was performed by removing points which had intensity values less than a defined threshold. This removed points from the air (normally dark) as well as some real hits from the target far from the scanner or with low reflectivity.

The ground point classification was performed in TerraScan (Soininen, 2010). The digital elevation model was formed from the classified ground points using both triangular irregular network (TIN) (Axelsson, 2000) and regular grid approaches (Vaaja et al., 2011). On the road surface, the ground point density was much higher than the building facade, where the dense low vegetation reduced the number of hits. Therefore, only the ground surface was investigated in this test, and with only the TIN approach.

The accuracy of the MLS was assessed by comparing the DEMs created from the laser point cloud of MLS data from two blocks (67, 55) with the reference points collected with stationary TLS measurements of the same blocks (see Table 4.18). These two blocks were chosen so as to investigate the accuracy under varying GPS qualities.

To validate the data, the selected reference areas were supported with several GCPs. The areas were close so as to provide a range of approximately 6-10 m between the vehicle trajectory and objects. The control points were used as a reference for

checking the quality of the surface model. The streets were selected to check how well the road surface could be mapped in urban areas.

The selected areas are shown in Figure 4.25. The quality parameter was calculated using elevations computed from MLS (H_{MLS}) and reference (H_{TLS}). TLS data served as the reference data.

$RMSE_H = [(sum\ (H_{MLS} - H_{TLS})^2/n\ ]^{0.5}$ .....(4.2.1.3.1)

Also, the systematic errors include the average deviation (bias) between the MLS and DEM of the reference in two selected areas, as shown in Table 4.18.

Results and analysis

Table 4.18 summarises the accuracy of the DEMs of the TLS as a reference compared with digital elevation models of MLS data. In point cloud 1 the best accuracies were obtained from areas 1, 2, 3 and 4, with RMSE ranging from 3.4 to 6.2 cm.

Target	Points Pass1	Points Pass2	Size (m)	MLS Point cloud 1/ Pass 1		MLS point cloud 2/ Pass 2	
				RMSE	Bias	RMSE	Bias
Block67	**476 531**	**463 219**		0.0680	-0.0350	0.0366	-0.0470
Area1	50056	50386	6 x 5	0.0345	-0.0309	0.0490	-0.0480
Area2	33736	34551	6 x 5	0.0444	0.0431	0.0391	0.0382
Area3	18991	19114	3.5x 7	0.0622	0.0593	0.0520	0.0346
Aerea4	83401	86926	3.5x 6	0.0512	0.0485	0.0486	0.0476
Block55	**770 130**	**771 794**		0.1686	-0.0831	0.1486	0.0820
Area1	25639	22364	6 x 3	0.0882	0.0751	0.1068	0.1028
Area2	23615	21456	6 x 3	0.1243	0.1223	0.0911	0.0884
Area3	24854	26266	2.5x6	0.0586	-0.0489	0.0864	-0.076

Table 4-18: DEM model accuracy obtained from laser data.

In MLS point cloud 2, block 67, the best accuracy was obtained for areas having an RMSE between 3.9 and 5.2 cm and a deviation (bias) of -4.8 to 4.8 cm. With point cloud 1, the corresponding errors for the areas were 3.4 to 6.2 cm and -3.1 to 5.9 cm. In block 67, the RMSE obtained was 6.8, 3.7 cm with a deviation of -3.5, 4.7 cm in point cloud 1 and point cloud 2 respectively.

The situation is different in block 55, with point cloud 1; the corresponding errors for the areas were 5.8 to 12.4 cm and -4.8 to 12.2 cm. However, in the second pass (point cloud 2), the accuracy obtained was between 8.6 and 10.7 cm and a deviation of -7.6 to 10.3 cm. For block 55, the RMSE obtained was 16.9 and 14.7 cm with a deviation of -8.3 and 8.2 cm in point cloud 1 and point cloud 2 respectively.

The above results show that the trajectory of the laser points in pass 1 was less accurate than pass 2, from comparison of each pass with the TLS data. The findings also showed that a clear systematic error existed in the MLS dataset. The error was derived from the computation of the GPS/IMU data of those blocks (67 and 55). After correcting the systematic error for each area separately (see equation 4.2.1.1.3.2), the RMSE was about 1 cm for the areas selected in block 67 and about 1 to 4 cm for block 55 in the first run. The corresponding figures for the pass 2 data were mostly below 1cm in block 67 and about 2 to 4 cm in block 55. Table 4.19 represents the surface model accuracies obtained after correction.

$$\text{Correction} = \sqrt{RMSE^2 - Bias^2} \quad \text{.....(4.2.1.1.3.2)}$$

Targets	First pass / (RMSE) m	Second pass / (RMSE) m
Block 67	0.0583	0.0315
Area 1	0.0153	0.0098
Area 2	0.0109	0.0084
Area 3	0.0187	0.0388
Area 4	0.0163	0.0096
Block 55	0.14.76	0.1239
Area 1	0.0461	0.0300
Area 2	0.0190	0.0220
Area 3	0.0322	0.0411

Table 4-19: MLS DEMs accuracy for areas selected (of block 67 and 55) after correction of the systematic error.

To validate the data used from small areas (A1.A2, A3 and A4) of block 67 and (A1, A2, A3) block 55, the Cyclone software was used for fitting points of each area to the plane. The standard deviation results of each fitted surface area are shown in Table 4.20. Also, the "3D surface compare" approach based on TIN through Geomagic software was used between two point clouds of each selected area. The overall standard deviation between surfaces that resulted from "3D surface compare"

analysis is shown in Table 4.20, columns 4 and 8 for the two blocks respectively. A graphical representation of the 3D surface analysis of each area can be seen in Appendix F.

Block 67	Std Dev σP1 (m)	σP2 (m)	σP1, P2 (m)	Block 55	Std Dev σP1 (m)	σP2 (m)	σP1, P2 (m)
Area 1	0.0032	0.0034	0.0040	Area1	0.0046	0.0044	0.0050
Area 2	0.0029	0.0029	0.0010	Area 2	0.0043	0.0041	0.0020
Area 3	0.0020	0.0034	0.0090	Area 3	0.0034	0.0044	0.0100
Area 4	0.0031	0.0033	0.0240				

Table 4-20: Standard deviation of each area using Cyclone software, and overall standard deviation resulting from "3D surface compare" analysis.

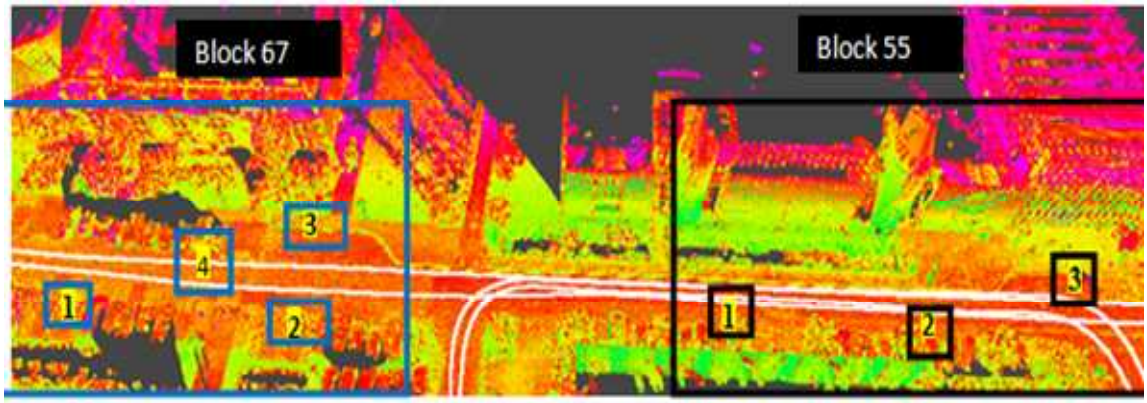

Figure 4-25: Point cloud of blocks 67 and 55. The marked area was selected for assessing the accuracy of the data on the road.

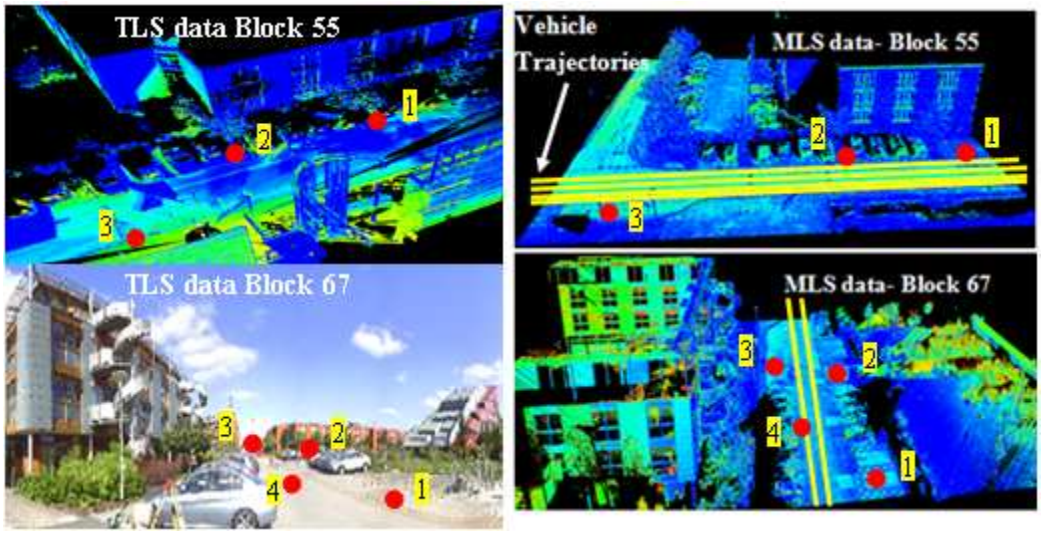

Figure 4-26: TLS obtained (left) with the marked areas indicated with red dots and MLS obtained (right) with trajectories overlain.

4.4 Evaluating calibration parameters

4.4.1 Methods for data calibration

After combining the position and orientation data, the resulting dataset is a collection of point clouds from different runs, covering the object surface several times. When analysing MLS data, misalignments between the IMU and the laser scanner will be shown.

In this section, Terrascan / TerraMatch was used to check the MLS calibration data. This method determines the misalignment angles (Δω, Δφ, Δk). Then, these parameters will be used for correcting the laser points.

The parameters provided by 3DLM Ltd. were used as initial values for determining the corrections to apply for the laser data of the selected areas, and the procedure continued until the convergence was achieved. Figure 4.27 shows the two workflows of the calibration procedure: match and tie line principles used with the TerraMatch algorithm (Rosell Polo et al., 2009).

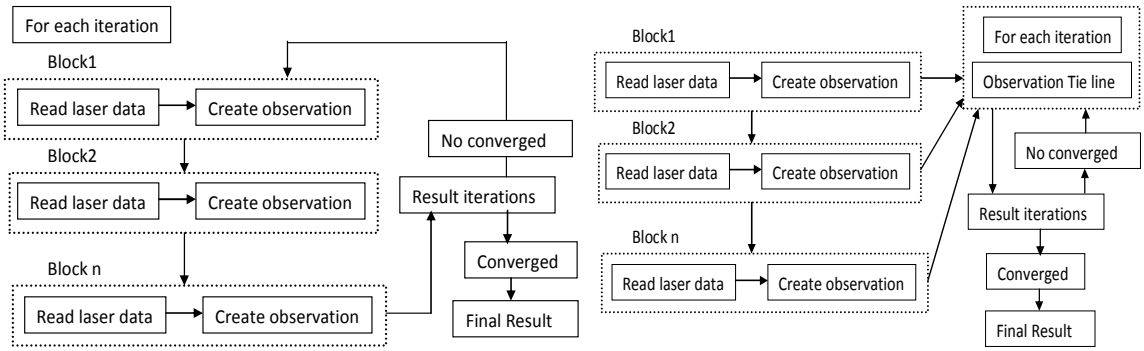

Figure 4-27: Find match and tie line principles (source: (Rosell Polo et al., 2009)).

The differences between match and tie line can be summarised as follows (Rosell Polo et al., 2009):

Find match	**Find tie lines**
1- Surface-to-surface matching	Feature-to-feature matching
2- Only one type of observation	Several types of observation

3-	More time-consuming adjustments	Less time-consuming adjustment
4-	New (better) observations for each iteration	Old observation for each iteration
5-	No manual observation	Manual observation possible

Alternative calibration, developed by Rieger et al. (2010b), relies on matching planar surfaces located in the three-dimensional point clouds. The process of identifying corresponding surfaces in overlapping scans and calculation of the misalignment values of the MLS system is similar to the procedures already known as "bore sight alignment" and "scan data adjustment" from airborne laser scanning (Skaloud and Lichti, 2006); (Morin, 2002), and MLS in the static position (Talaya et al., 2004), and in the laboratory (Graefe, 2007b), as described in section 2.2.1.

Rieger et al. (2010b) used determination of the relationship between corresponding planar surfaces using RiPROCES Riegl software to solve the problem of misalignment parameters.

$$d_1^i = \left(p_2^i - p_1^i\right).n_1^i \;; \quad d_2^i = \left(p_2^i - p_1^i\right).n_2^i \;\; : \sigma$$

$$= \sqrt{\frac{\sum_{i=0}^{n} \left(\frac{d_1^i + d_2^i}{2}\right)^2}{n}} \ldots\ldots\ldots (4.3.1.1)$$

σ : mean square residual distance of all corresponding planar surfaces.

d1, d2 : residual distance of corresponding planar surfaces.

n1, n2 : normal vectors.

p1, p2: location of plane and its centre of gravity.

4.4.2 Benefits of performing calibration

As mentioned previously, the quality of the point cloud derived from an MLS system is based on random and systematic errors in the system measurement and parameters. Systematic errors are usually caused by sensor misalignment parameters relating to the system components and the method of measurement (Habib and Van Rens, 2007). The determination of these parameters can then enable them to be used in calculating ground laser point coordinates (Barber et al., 2008; Habib and Van Rens, 2007; Talaya et al., 2004). These parameters must be checked in any project involving MLS.

In general, the effects of the three angles of heading, roll and pitch (HRP) are visible at longer distances from the mobile scanner, as shown in Figure 4.28. The heading error was also visible in point features (e.g. columns and building corners) along the road (see Figure 4.28 (1)). The effects of roll and pitch errors are visible as elevation differences on the ground and as leaning building walls. These effects are shown in Figure 4.28 (2 and 3). The roll effect is visible on the wall along the road (Figure 4.29 (3)). The pitch effect is visible on the wall across the road (Figure 4.29 (4)) (TerraSolid., 2009).

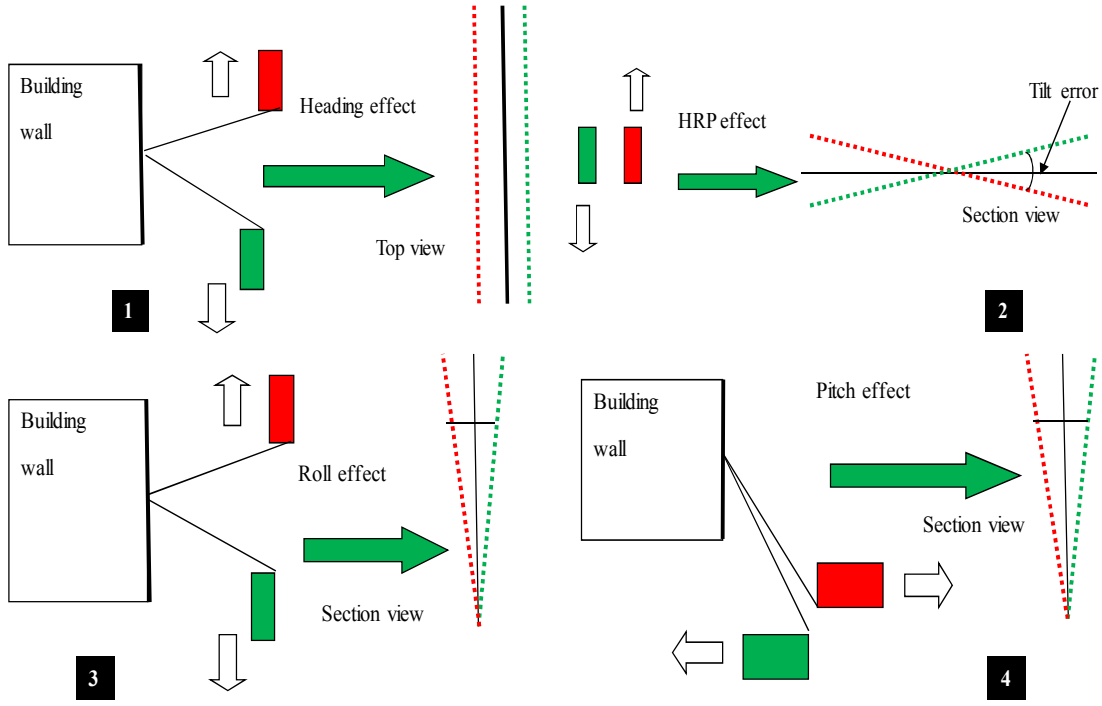

Figure 4-28 Mobile laser scanning of building facade and road surface from different driving and scanning directions. Top left (1): the heading angle effect along the building. Top right (2): effect of three angles (HRP) visible as elevation on the ground. Lower left (3): roll angle effect along the building. Lower right (4): effect of pitch angle across the building (TerraSolid., 2009).

4.4.3 Terra Match features

The main processing steps for the calibration dataset using TerraMatch features, as described in section 2.2, are data preparation, matching of profile laser lines, applying corrections and output of matching report.

4.4.3.1 Practical Tests

Checking calibration is important to remedy the misalignment between the laser scanner and IMU. Part of the laser results for block 55 was used to check the delivered data from 3DLM Ltd. The rest of the selected areas were used for correcting the effect of misalignment angles on the laser point data.

The calibration procedure was applied in the area of block 55 (Figure 4.25). The procedure allows common tie lines on the ground and walls to be found from the independent scans performed. The identification of these tie lines and calibration of the misalignment angles is performed automatically. The previous H, R and P results, which are 0.348, 0.044 and 0.299 respectively, were used as initial values. The final corrections for the calibration project produced by 3DLM Ltd. are presented in Table 4.21.

Correction for (HRP)	[degrees]
R shift	+0.044
P shift	+0.299
H shift	+0.348

Correction for (HRP)	[degrees]
R shift	-0.002
P shift	+0.013
H shift	+0.011

Table 4-21: Calibration result. Left: calibration 1 some days before survey at Jubilee Campus produced by 3DLM Ltd. Right: calibration 2 (recalibrated) in area of a block 55 after collecting data from Jubilee Campus, which is the correction for calibration 1.

From block 55, the laser data was filtered to get ground points. These ground points have been modeled “key points” and, then, matched using TerraMatch software to get misalignment between laser scanner and IMU. Figure 4.29 shows a profile of the segment before recalibration and after the recalibration.

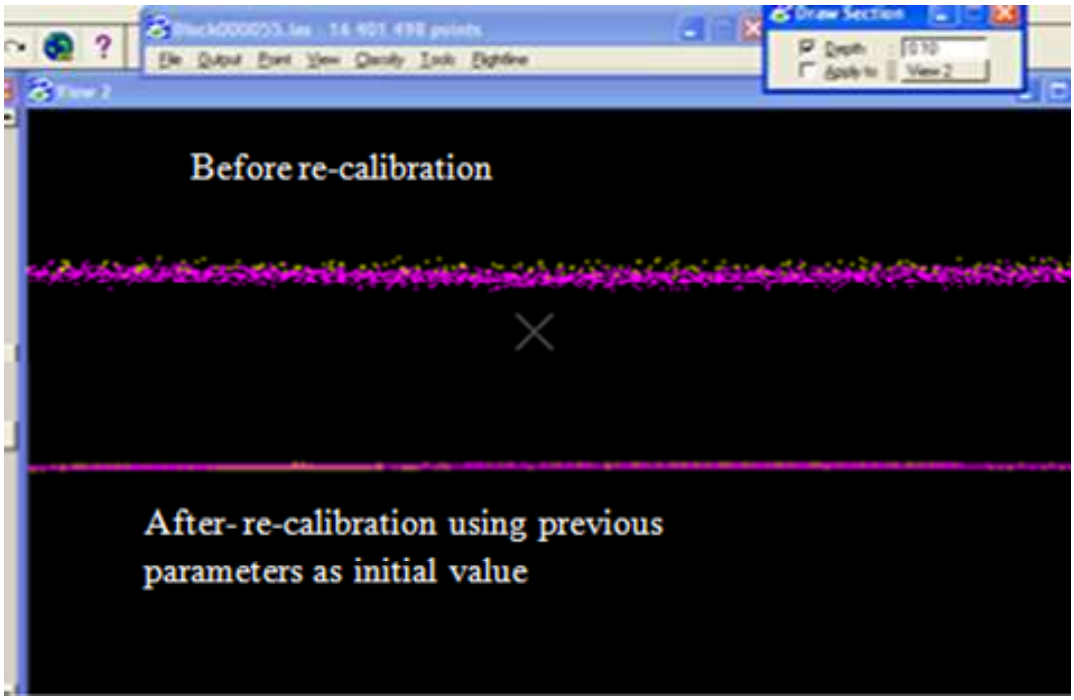

Figure 4-29: Profile of the ground surface before and after re-calibration of block 55 data

The effect of misalignment angles on the average 3D mismatch and the horizontal and vertical components for blocks 67 and 55, before and after the correction applied to the data in both areas are illustrated in Table 4.22 and Figures 4.30 and 4.31. These results were automatically provided by the software.

Test area	**Road surfaces**			**Building facade**	**Remarks**
	Average 3D mismatch	Average EN mismatches (m)	Average H mismatches (m)	Average wall lean (m)	
Block 67	0.0202	0.0188	0.0074	0.0485	Before correction
	0.0077	0.0056	0.0046	0.0174	After correction
Block 55	0.0421	0.0401	0.0116	0.0452	Before correction
	0.0085	0.0057	0.0064	0.0085	After correction

Table 4-22: Results of mismatches before and after misalignment.

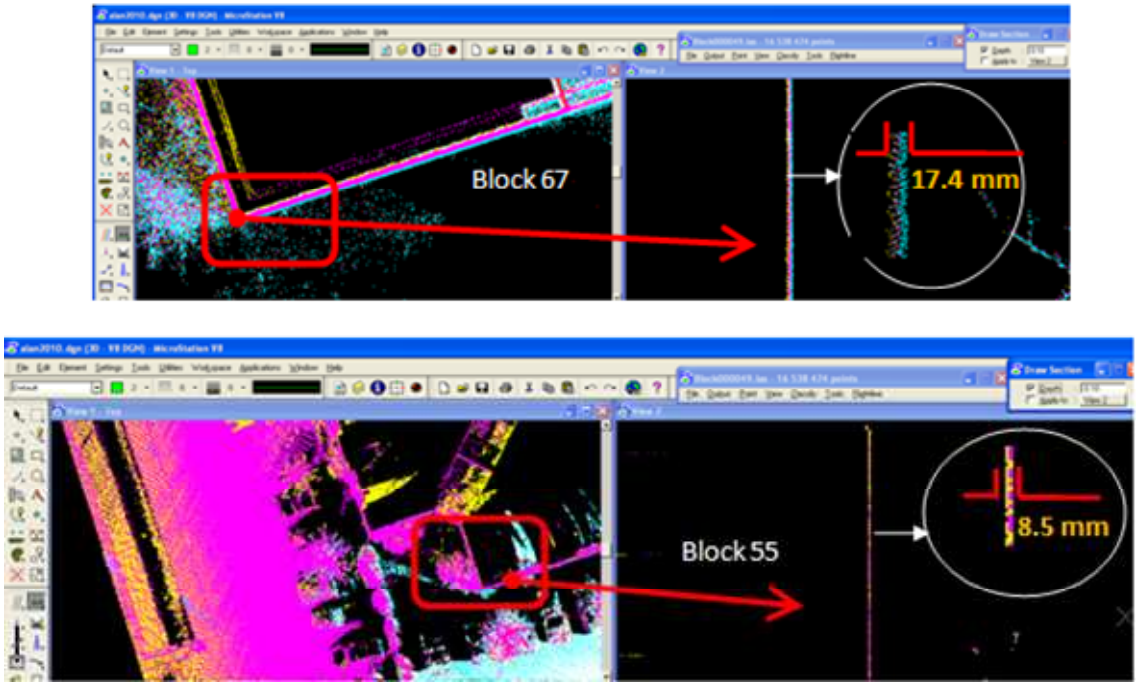

Figure 4-30: Profile of walls in blocks 67 and 55 after applying correction.

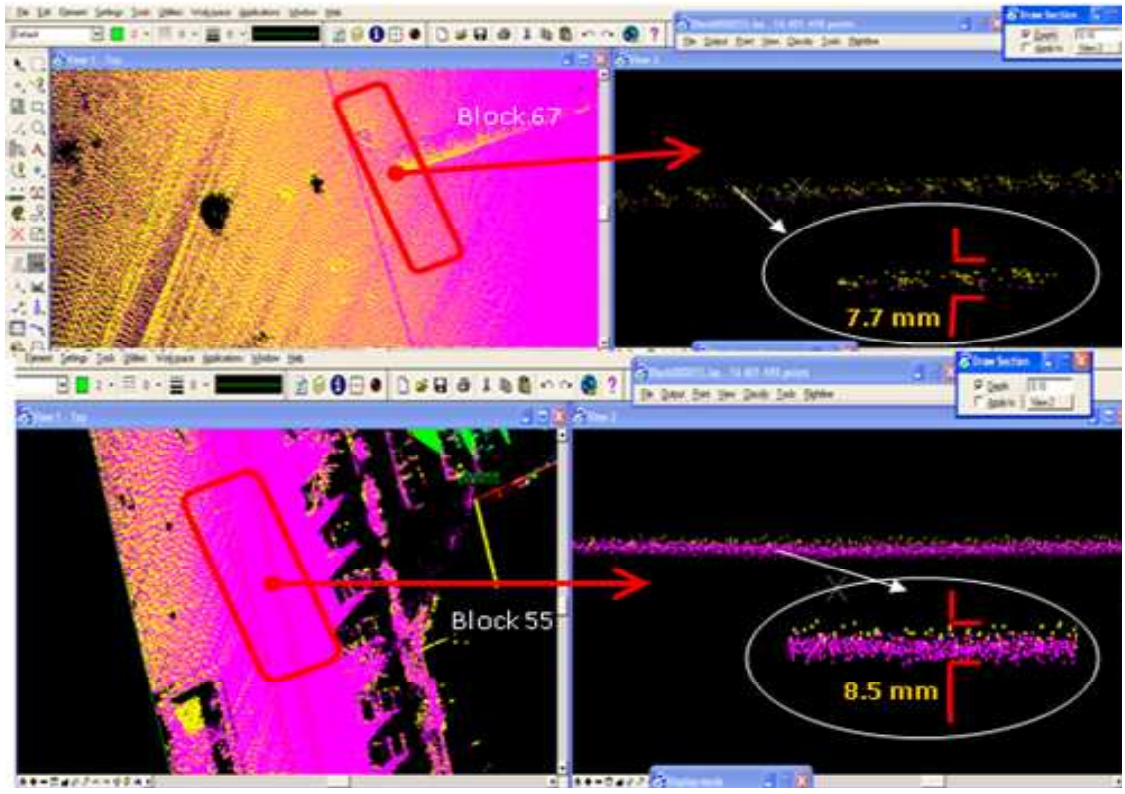

Figure 4-31: Profiles of ground surfaces of blocks 67 and 55 after applying correction.

4.4.3.2 Using the survey control point for improving misalignment angles

The main purpose of this test was to investigate the possibilities of reducing the HRP effect between the laser scanner and the IMU for the area of interest. The same areas were chosen from an open area (block 67) and a relatively urban canyon (block 55). These blocks feature different styles of building and narrow streets, and were scanned during two and seven passes respectively for block 67 and block 55. The area was flat (see Figure 4.32), and most of it, especially in block 55, was covered with trees in front of the buildings.

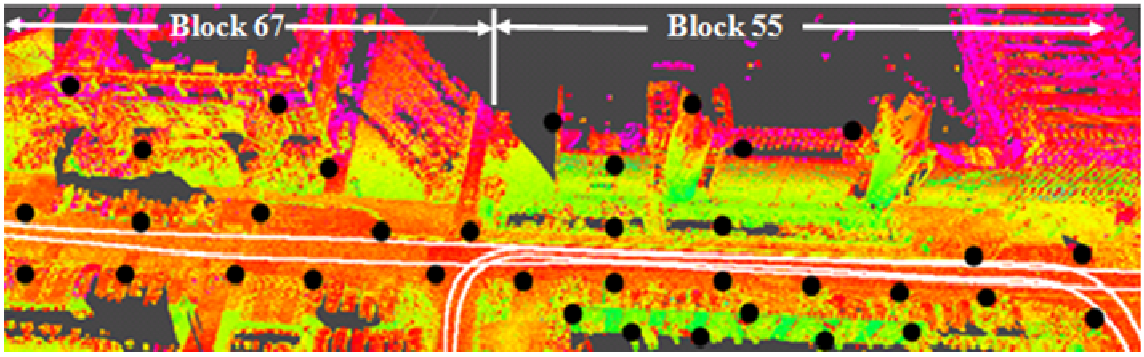

Figure 4-32: The two test areas. Left: Block 67. Right: Block 55. Black dots represent GCPs along the road and building facades.

The TerraMatch software was again employed to improve the misaligned HRP angles of the data collected using natural features and survey control points. Survey control points had previously been measured to a high level of accuracy in the study area at 10 m intervals starting from zone 1 and ending at zone 3, as described in section 4.2.2.

This was to assess the calibration parameters in the two tests, after which the corrections based on this optimal case were applied for the entire point cloud of the selected areas. The results (Table 4.23) show that when using ground control points with natural features, the HRP effect on the quality of the point cloud was improved. The achievable accuracy of the laser data also improved, as shown in Table 4.23 and Figure 4.33.

Test area	GCPs	No. of runs	Line	Deviation (m)		Test area
				EN	H	
Block 67	0	2	112 control line on the ground	0.0192	0.0095	Auto
			85 control line on the building	0.0285	0.0122	Auto
Block 55	0	7	280 control line on the ground	0.0451	0.0182	Auto
			126 control line on building	0.0411	0.0175	Auto
Block 67	5	2	112 control line on the ground	0.0187	0.0091	Auto+Manual
			85 control line on the building	0.0122	0.0112	Auto+Manual
Block 55	5	7	280 control line on the ground	0.0208	0.0177	Auto+Manual
			126 control line on building	0.0199	0.0163	Auto+Manual
Block 67	7	2	112 control line on the ground	0.0157	0.0086	Auto+Manual
			85 control line on the building	0.0110	0.0108	Auto+Manual
Block 55	7	7	280 control line on the ground	0.0198	0.0167	Auto+Manual
			126 control line on building	0.0189	0.0133	Auto+Manual
Block 67	20	2	Ground surface	0.0094	0.0054	Auto+Manual
			Building facade	0.0066	0.0073	Auto+Manual
Block 55	20	7	Ground surface	0.0100	0.0096	Auto+Manual
			Building facade	0.0092	0.0091	Auto+Manual

Table 4-23: GCPs with natural features increasing the accuracy of calibration parameters.

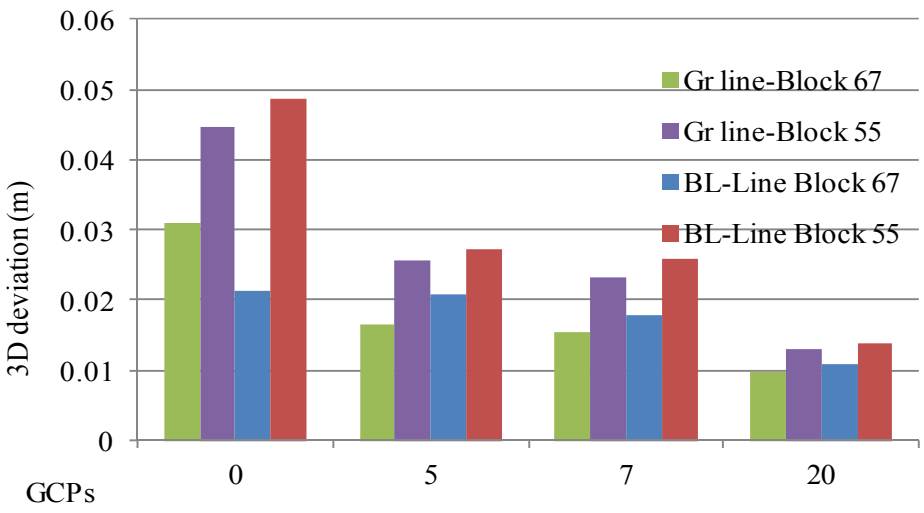

Figure 4-33: Experimental result of calibration using control points.

Figure 4.33 shows that as the number of GCPs increases, the accuracy of the data collected gets better. The figure also illustrates that the result of the 3D deviation of the ground surface was better than for the building façades in both blocks, while the same 3D deviation value (around 0.020 m) can be detected for the building façade and ground surface of block 67 using 5 ground control points. A 3D deviation of better than 1cm can be achieved with more than 20 GCPs, while with no GCPs the accuracy is degraded, especially in the urban area. In block 55, the RMSE was around 0.050 m on the building and up to 0.046 m on the ground surface (see Figure 4.33). In block 67, the accuracy was 0.030 and 0.022 on the ground surface and building facade, respectively. This is because of the HRP effect (see Figure 4.28).

4.5 Limitations of the method used

The problems and limitations of the method used for evaluating laser data can be summarised as follows:

Method of quality assessment:

1. **Nearest point**

- Difficulty in measuring the point exactly in the corner of the feature of interest.

- The data assessment procedure was based on the skill of the human operator in estimating the coordinates of points in both the MLS system and the Total Station data.
- The point clouds supplied were produced by 3DLM Ltd.
- The system used was calibrated by the commercial operator, and within the scope of the project, this cannot be considered.

2. **Surface-to-surface comparison (ICP) approach**

The disadvantages include the fundamental assumption of complete overlap of identical shapes and being provided with the theoretical point taken from the surface of the known geometry rather than measured (Besl and McKay, 1992).

3. **Additional source of data TLS**

- TLS as a reference source needs data to be collected from multiple viewpoints to cover a large area for MLS assessment. This is time-consuming and costly.

From the above limitations in the use of targets, it can be seen that there is great potential for improving MLS data to overcome the difficulties observed, by using natural features on the objects used for assessing the quality of the MLS results in urban environments.

4.6 General discussion

The horizontal and vertical position accuracy was tested on the road surfaces and building facades using survey control points along the study area and comparing the results with MLS data. The result achieved for road surfaces was within 2-4 and 3-4 cm respectively, and for building facades 2-6 and 3-5 cm respectively (see section 4.3.1.1, Table 4.7). The 3D surface analysis method was used for quality assessment of MLS data in selected blocks. The 3D deviation value obtained from TIN for block 67 was 0.018 m and changed along the kerb at ±0.074. This was explained by changes in the matching due to the use of inappropriately calibrated data. The situation was the same for blocks 55 and 36, where the 3D deviation value was 0.006

m and 0.009 m, but this value broke down to -0.058 m and 0.036, respectively, where the surface was discontinuous (e.g., along the kerb) and the largest 3D deviation is usually evident at the edge of the object (see Figure 4.16). In the case of the building façade, for example, the maximum deviation value was 0.032 m and decreased to -0.106 m at the edge of the building. The same situation occurred in the other blocks (45, 49 and 57), where the deviation value of the building facade from block 45 was continuously decreased by 0.10 m, while in blocks 49 and 57, it was decreased by 0.06 m and 0.05m, respectively (see Table 4.14). This is attributed to error in the measurement and system calibration. It should be noted that further system calibration of MLS is important to reduce the maximum deviation value to below 0.01 m anywhere in the MLS data.

On the other hand, additional sources of data such as TLS were analysed for the two blocks (67 and 55) from the AOI to assess the quality of the data captured by MLS. The mobile laser scanner data used in this work had proved to be useful when a close viewpoint, dense point cloud, and high ranging accuracy were needed.

The positioning accuracy of the GPS/IMU system is the most critical part in the error budget and thus ground reference data is needed. The accuracy of the MLS-based surface model, or DEMs, especially on the ground surface, TLS was used for reference data. The estimated precision of the reference method is, therefore, better than 1cm. The obvious reason for the better results achieved in the second runs compared to the first runs from the two selected blocks (67 and 55) (see Table 4.18) is that the scanner passed closer to the targets.

The accuracy assessment presented in section 4.3.1.3 takes into account the variation of errors by classifying the ground points. Table 4.19 shows the variations of the vertical error for the first run on a small area of block 67. It seems that the elevation errors have a connection with the scanning angle and range. The surface error also includes regular laser lines which are perpendicular to the direction of vehicle trajectory. These errors may also be linked to the computation of the navigation data, but future studies, dealing with spatial variation of MLS-based DEMs errors, are clearly needed in open areas such as mapping topography.

The calibration parameters for the misalignment angles (HRP) were tested from the two areas, blocks 67 and 55, using natural features (control line) and known points. The accuracy of parameters was improved with a significant number of known points, and 3D deviation below 1cm level was obtained (see Table 4.23 and Figure 4.33). This value is an approximate value and will not remain the same in the entire area due to navigation error and the difficulty of matching a natural point in the point cloud. This problem will be solved by designing new 3D targets to overcome the limitation cited above.

4.7 The importance of designing targets for improving the accuracy of MLS data

As mentioned in the previous sections, matching natural detail points from different point clouds manually or automatically is not always possible. This is because it is hard to measure exactly the same point in two scans or multi-scanning. Also, the dependency on the intensity value to match these points may not give good results. Therefore, using targets has great potential for performing the matching between any point clouds. This is because, when using targets, there is no need to measure exactly the same points where the centre of the targets can be determined from some surrounding points. Moreover, as clearly stated from the previous works, there is a significant issue with point identification, and there is a need, therefore, to design new 3D targets.

The frequently adopted nearest point method and the idea of fitting a plane on the building facade and road surfaces still do not fit exactly the same definable point or feature. Targets will overcome many problems, namely: misidentification of corresponding points in two or more scans, checking the quality assessment of the data, geo-referencing and solving the problems of navigation errors when GPS is unavailable in urban areas and providing a clearly, definable, unique point. Issues related to designing targets will be described in the next chapter.

4.8 Conclusion

In this chapter, a quality assessment of MLS data in urban areas has been discussed, which covers objective 1 and 2 of this thesis. The methods used for the quality assessment of MLS were considered from an initial survey over the AOI on Jubilee Campus. The complete trajectory started from an open area (good for GPS visibility) to an urban canyon, where the street width is reduced and the presence of tall buildings creates obstacles for sky visibility. In these environments, the positioning system relies only on the IMU sensor, which cannot provide a good trajectory for long distances. Therefore, the good areas and bad areas were extracted from the AOI, to evaluate the quality of results of MLS data for building facades and road surfaces in different environments. The previous trials assessed the accuracy of MLS data by measuring the point cloud in different ways. We also analysed the accuracy of MLS for elevation using TLS as a reference. The RMSE of the elevation level is better than 5 cm accuracy, as shown in section 4.3.1.3, Table 4.19. The results obtained indicate that MLS can provide accurate and precise information over large areas. However, data needs to be controlled for systematic errors, which significantly affect objects obtained from surface analysis requiring high accuracy measurement. A new target design is needed to overcome the difficulties encountered when using natural detail points on objects. This will be discussed in chapters 5 and 6.

CHAPTER 5: TARGETS DESIGN AND EVALUATION

In this chapter, a new target is designed and tested in order to overcome the limitations of the other targets such as Leica circular flat and faro sphere targets and broaden the variation of targets available. The design of target includes choosing the size, shape and colours. The design is then tested at different ranges, incidence angles and resolutions in order to evaluate the performance in each case. The work flow diagram can be seen in Figure 5.1.

This chapter also describes, in detail, trials undertaken to assess the registration of the point clouds using the available targets compared with the new designs. This allows evaluation of the quality of directly measured positions and orientations of the reference objects using different scanning resolutions, and to assess their effect on the results when multiple scans are combined. Finally, the advantages and disadvantages of the targets used are discussed, and a summary of the results, are given. This research aims to fulfil objective 3

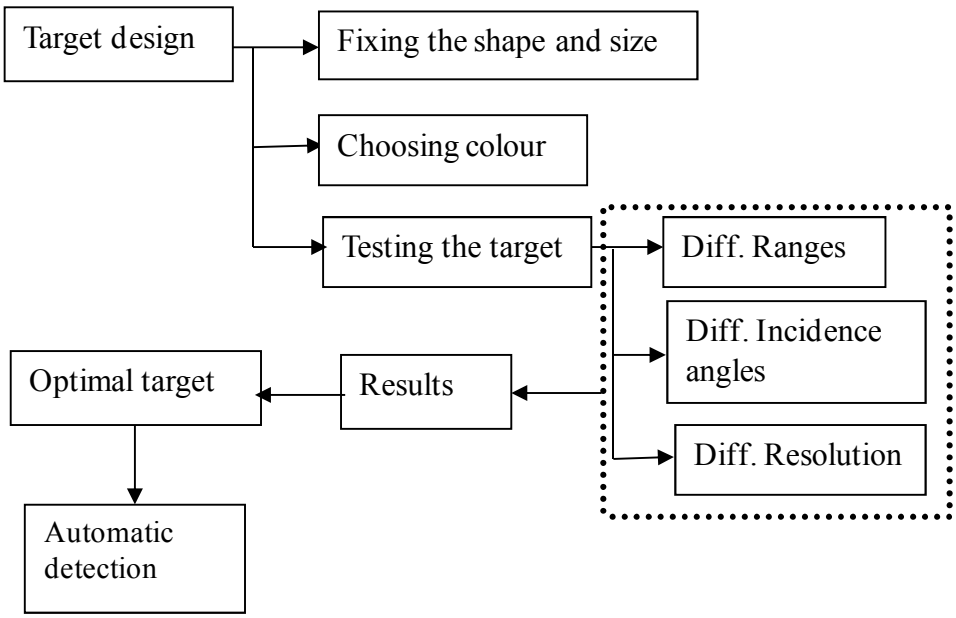

Figure 5-1: The flow diagram for the optimal designed target.

5.1 Software available

There are many commercial software packages available, as described in chapter three, for detecting predefined targets automatically. In the laser scanning workflow, Cyclone is initially used to control the laser scanner during scanning with a laptop connected to the scanner. The scan resolution and the distance to the object can be set, as well as the area selected for scanning. Scanning data is also displayed in the viewer in real time. Whilst, the SCENE software data is separately stored on a SD card from the Faro scanner device and then, downloaded manually or automatically by the software for processing and analysing data.

There are several ways for the Leica flat targets to be acquired. The first is when the scanner is still set up in surveying position just after a scan; the target can be detected in the "model space" either by detecting the point or by fencing each area around the target. The point are chosen which are within 4" from the target centre (Leica., 2010) The scanner then acquires the point cloud defining the target first by doing a coarse scan of the area selected. Following the coarse scan, a fine scan is done, which places a vertex in the model space at the centre of each target selected and is labelled. The accuracy, according to the manufacturer, is about 2mm precision (Leica., 2011).

This method is mainly adopted when using the HDS3000 TLS. The Faro scanner is different, the detected targets such as sphere, and natural reference targets, namely plane, point, line, rectangular etc., are automatically detected by the SCENE Faro software.

Registration, as describe in chapter 3, is the process of fitting scans together from different positions to build up one model. This requires at least three HDS targets or three sphere target to be scanned, using the HDS3000 or Faro scanner respectively. The same target should be seen from both measurement positions. The software measured the target and automatically performs a seven (7) parameters transformation, XYZ position, three rotations and scale.
The software uses least squares for the best fit to orient the two or more scans into the same coordinates system. This transformation can also be done without using

targets; which called point cloud registration (see chapter 3). It uses at least three common points in both scans point clouds to register them together. This tends to be less accurate than using target, the difficulty of detecting the same three points on each scan. Registration without targets can be useful in MLS, where less accuracy is required especially for urban modelling, and visualisation and land decision making or when scanning unstable structures, where it might be not safe to fix target in such area for example on a historical building and also at restricted area.

The delivered point clouds should be filtered to remove noisy and unwanted sections of the point cloud before a final product is created. The software allows the user to extract and measure information from the raw point cloud, such as distance and intensity values, planes or meshes, which allows further information to be extracted. Spheres and planes can be fitted and volume can be calculated, error reports are generated for each mesh or plane created, which shows how well the plane or mesh has been fitted.

For all their advantages, as mentioned in section 5.1, these software packages are unable to detect the custom made target. Therefore, for a new target design, an appropriate algorithm to detect the target and its centre must be developed and tested. This will be discussed in chapters six and seven

5.2 Specific Targets

Targets are used for scan registration, quality assessment and accurate geo-referencing of scans to a known survey control point. Leica HDS targets and Faro sphere are designed with the software to be automatically recognised; an algorithm detects the centre point by assessing the point cloud that makes up the target. The reflective differences between the different colours on some of the targets allow for very accurate target registration. Leica Geosystems quotes a target accuracy of 2mm. There are several different kinds of targets available, in the field trial, blue and white HDS 6” inches circular and (3”x3”) square inch targets were used with HDS 3000 data (see Figure 5.2). With Faro focus 120 trials, the same targets were used along with two kinds of sphere targets, 145 mm and 200 mm diameter, respectively. The

small spheres were specifically designed for registration of multiple scans, while the large one was used for assessing the accuracy of the scanner (see Figure 5.2).

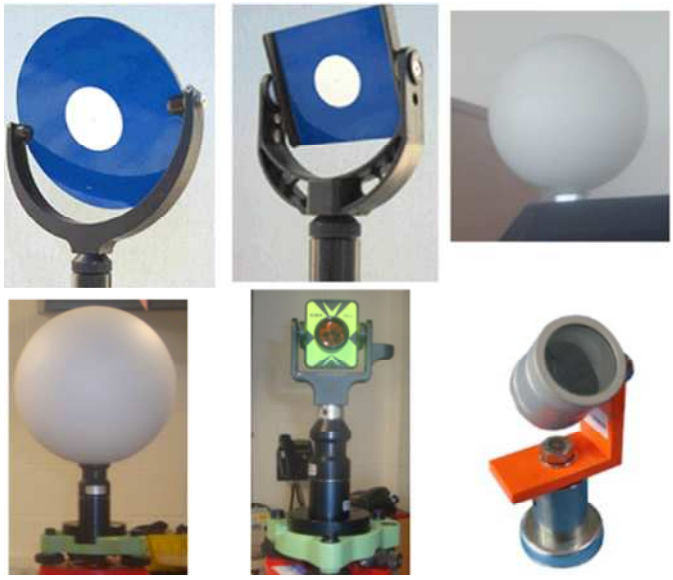

Figure 5-2: The HDS and sphere targets used in the field trial. Top left: 6" circular blue and white middle. Top middle: 3"x3" square blue and white. Top right: small sphere 145 mm dia., lower left: large sphere 200 mm dia., lower middle and right: mini prism for large and small sphere respectively.

Other types of these targets are available such as adhesive and magnetic targets, which can be attached to structures. See Figure 5.3. Some of the targets used in the field trials were attached to a tribrach so they could be levelled and to tripods so they could be centred over a known point. This means that they could be surveyed by a total station to accurately obtain target coordinates. Other targets are staked on structures via magnetic and sticky bases such as those of Leica HDS and Faro sphere, respectively. The appearance of Leica HDS and Faro sphere targets in laser point cloud can be seen in Figure 5.4.

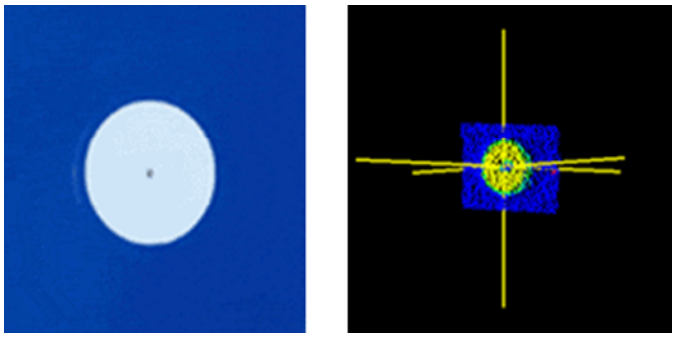

Figure 5-3: Leica Adhesive target and their appearance in the point cloud (source: (Leica., 2011)).

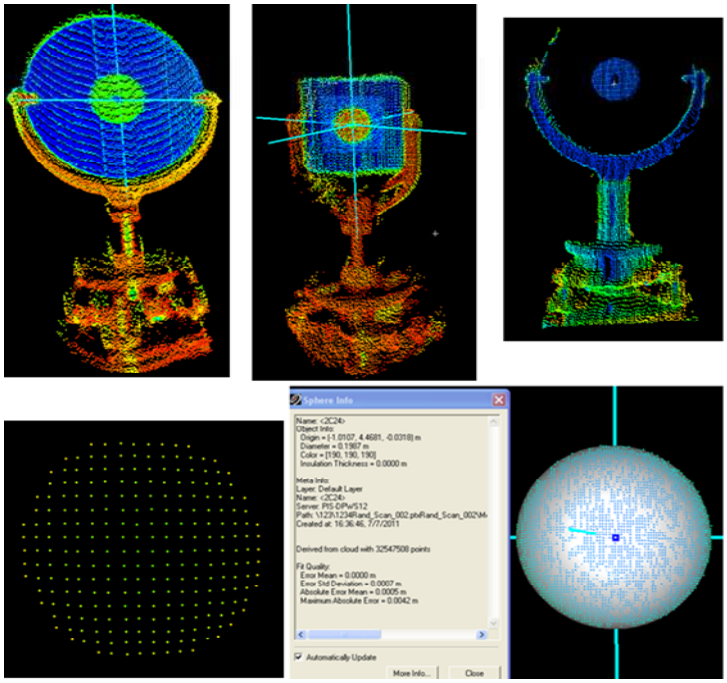

Figure 5-4: The appearance of Leica HDS and sphere targets in laser point cloud. Left and middle: A blue and white target scanned normally with the HDS3000. Right: Front view of a blue and white target scanned with the Faro scanner, with noisy and missing data. Lower left: sphere target scanned normally with Faro scanner. Lower right: sphere target scanned and fitted with a report showing the quality of fit using Cyclone software.

For the Faro scanner field trials, the blue and white HDS target gave noisy and erroneous data and could not be used in conjunction with the Faro scanner (see Figure 5.4 top right); the reason behind this blue section is the high reflectivity of this colour for the scanner. Large parts of the targets are missing, because the laser reflects back stronger when it hits the blue section than the surrounding objects. This means that when the internal sensor receives the laser pulse back, it perceives the phase change as shorter and the blue section is considered to be closer than it is. Therefore, this type of target failed in the trial for the range test and incidence angle with the Faro scanner. The same situation happens with the designed targets, where high reflectivity tape was used.

5.3 Summary

The manufacturer targets, such as Leica HDS and Faro sphere as mentioned before have some limitation in the field trial in terms of range, incidence angle, size and

signal response. Leica HDS target is affected by incidence angle over 45°. In addition, the precision of the centre can be estimated up to 2 mm at range 1-50 m (Lecia geosystem, 2011). Regarding Faro sphere target, the centre of sphere cannot be measured precisely, and need prism to measure its centre. This will introduce additional error beside the laser measurement errors. To overcome these limitations, it is important to design new targets, which can help to provide more accurate results. This will be discussed in the next section.

5.4 Design of 3D targets

5.4.1 Shape, dimensions and apex finding

Two types of 3D targets, pyramids and cones, were designed for improving the results quality of MLS data in urban areas. Each type was investigated, as detailed in the following sub-sections. Methods for defining the 3D target apex are defined on a mathematical basis and potential limitations identified. Based on a clear understanding of these issues, the following points should be considered:

- How to overcome the limitations in term of range, incidence angle and signal response.
- What are the benefits and limitations of the designed target?
- The accuracy of automatic target measurement, as well as the possibility of using these targets in calibration procedures.

All these issues were addressed, in order to identify the size and shape of a 3D target designed that is suitable for outdoors use, and before carrying out mobile laser scanning in different environments.

5.4.1.1 Pyramid target

Several sizes of pyramid target were designed and tested, starting with a three face triangular base, and up to an eight face. Each target had a height of (10 cm) and a radius of 15 cm. Each face was covered using optimal colours (black, white, dark grey, green and highly reflected colour (HRT)), as shown in Figure 5.5.

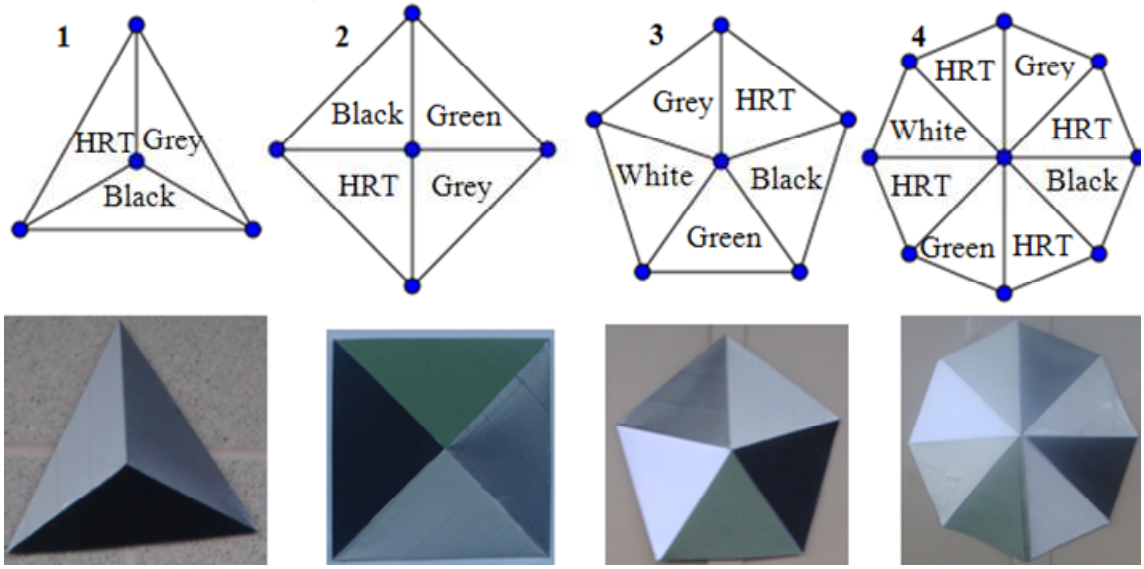

Figure 5-5: The different shape of pyramid targets from 3 to 8 faces used in the field trial: Top: 1) triangular base; 2) Square base; 3) pentagon base; 4) octagon base. Lower: Coating pyramid's faces by optimal colours.

The reason behind choosing the pyramid is that the apex can be easily defined by an intersection plane algorithm. This was based on trials conducted at the beginning of this research, which should the pyramid have significant potential, and is actually an easier geometric shape to work with. Choosing a colour for each face was based on tests carried out on a variety of coloured surface objects. These colour tests are discussed in the next section. The reason for investigating the optimal colour for 3D pyramid faces is to enable easy detection in an automatic process.

In terms of the height of these targets, several tests were carried out to determine the most optimal value. Each target was made with different heights starting from 2 cm up to 15 cm. In addition, a small size of a pyramid at height of 8 cm and base of 20 cm, in order to see the accuracy of the apex, when changing the base, as shown in Figure 5.6. These targets were tested under approximately perpendicular (0^{o}) incident angles at a range of about 10 m. The performance of the targets with different heights was investigated by comparing the position of the targets apex, achieved from the laser scanner, with the position achieved by Total Station measurement.

.

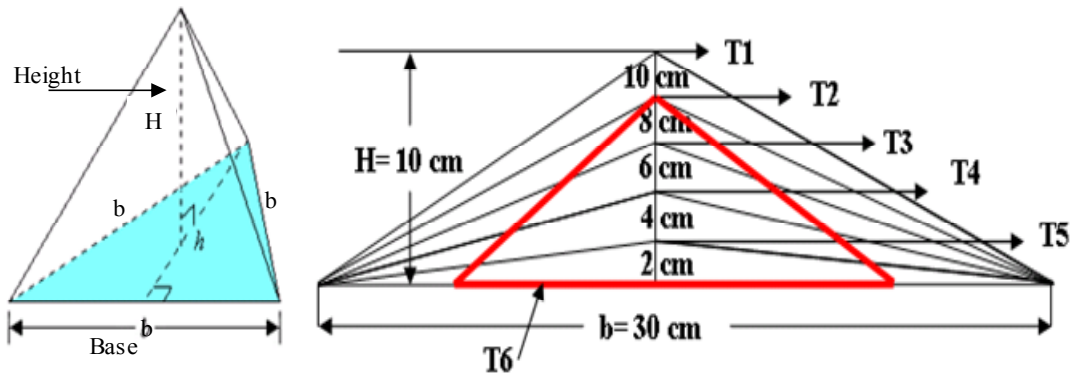

Figure 5-6: Pyramid triangular base. Left: sample of pyramid 3 faces; Right: position of various heights of triangular pyramid in proportion to the height and red line represents a small size of the pyramid.

The following methods were used to compute the apex of the various 3D pyramid targets, after filtering the target points manually from surrounding objects using cyclone software v.6.

- A developed algorithm and coded in Matlab
- Leica Cyclone software v.6

The first method, a script program was created, using Matlab functions, to compute the apex of the different size of pyramid target based on a plane equation in 3D space. The mathematical model of the program for computing the apex automatically can be summarised in four steps as follows:

Step1: Picking up random point, say **M,** from the filtered points on the surface target.

Step2: Find two closet points $\mathbf{N^m_1}$, $\mathbf{N_2^m}$ using distance equation which is:

$$\mathbf{d12=d21=}\sqrt{(x_2-x_1)^2+(y_2-y_1)^2+(z_2-z_1)^2} \quad \text{.....(5.4.1.1.1)}$$

Then, find two smallest values in [dm1, dm2, dm,..... dmn] for point **M** to $\mathbf{N^m_1}$ and $\mathbf{N_2^m}$

Step 3: From step 1 and step 2, solve the parameters (a, b, c) for point **M, (i.e. using (M, $\mathbf{N^m_1}$, $\mathbf{N_2^m}$) to solve (a, b, c) , by** using plane equation in 3D space as given below.

$$\left.\begin{aligned} &\mathbf{X1\ a+\ Y1b\ +\ Z1c=1}\\ &\mathbf{X2\ a+\ Y2b\ +\ Z2c=1}\\ &\mathbf{X3\ a+\ Y3b\ +\ Z3c=1} \end{aligned}\right\} \quad \text{.....(5.4.1.1.2)}$$

Where:

$$\mathbf{X1, Y1, Z1 = M;\ X2, Y2, Z2 = N^{m}_{1}\ ;\quad X3, Y3, Z3 = N_{2}^{m}}$$

Repeat step (1 and 2) for each raw data point (meaning each possible points for M): The output is sets of (a, b, c). Correlation, to find the most three popular appearing parameters (a, b, c) are applied. The sets of parameters (a, b, c) obtained are divided into three groups; each group has a number of sets of (a, b, c). The least squares method was applied to each group in order to determine a set of parameters (a, b, c). Consequently, the most popular three sets of parameters are obtained.

Step4: Using these three popular (a, b, c) sets to solve the apex of the target, using the equation given below.

$$\left.\begin{aligned} &\mathbf{a1X+b1Y+c1Z=1}\\ &\mathbf{a2X+b2Y+c2Z=1}\\ &\mathbf{a3X+b3Y+c3Z=1} \end{aligned}\right\} \text{.....(5.4.1.1.3)}$$

Express in matrix form from equation (5.4.1.1.1) to (5.4.1.1.3)

1- Distance matrix of the two smallest values to any point from selected target's points

$$\begin{bmatrix} 0 & d12 & d13 & \cdot & \cdot & \cdot & \cdot & d1n \\ d21 & 0 & d23 & \cdot & \cdot & \cdot & \cdot & d2n \\ d31 & d32 & 0 & \cdot & \cdot & \cdot & \cdot & d3n \\ . & . & . & \cdot & \cdot & \cdot & \cdot & . \\ . & . & . & \cdot & \cdot & \cdot & \cdot & . \\ . & . & . & \cdot & \cdot & \cdot & \cdot & . \\ . & . & . & \cdot & \cdot & \cdot & \cdot & . \\ dn1 & dn2 & dn3 & \cdot & \cdot & \cdot & \cdot & 0 \end{bmatrix}_{(nxn)} \quad \text{.....(5.4.1.1.4)}$$

2- Equation (5.4.1.1.2) for solving parameters (a, b, c) is based on least squares. It can be written in a matrix form.

Let $A=\begin{bmatrix} X1 & Y1 & Z1 \\ X2 & Y2 & Z2 \\ X3 & Y3 & Z3 \end{bmatrix}_{(3x3)}$, $X=\begin{bmatrix} a \\ b \\ c \end{bmatrix}_{(3x1)}$, $B=\begin{bmatrix} 1 \\ 1 \\ 1 \end{bmatrix}_{(3x1)}$ .....(5.4.1.1.5)

So it can be compacted as **AX=B.** The objective is to find a normal vector (a, b, c) for each small triangle. Parameters (a, b, c) are obtained:

The nth sets of parameter (a, b, c) were divided into three groups, each group has a number of sets and their parameters are close to each other. The average of each group represents one face of the pyramid. For example, pyramid T1= 84 pts / target, the programme calculates 84 set of parameters. Each group should take 28 set of parameters. Due to problem in the computation of each small triangle between three faces, each group took more or less, (e.g. 33 sets of parameters for group1were isolated, 27 pts for group2 and 24 for group 3). These changes affected the accuracy of calculating the apex

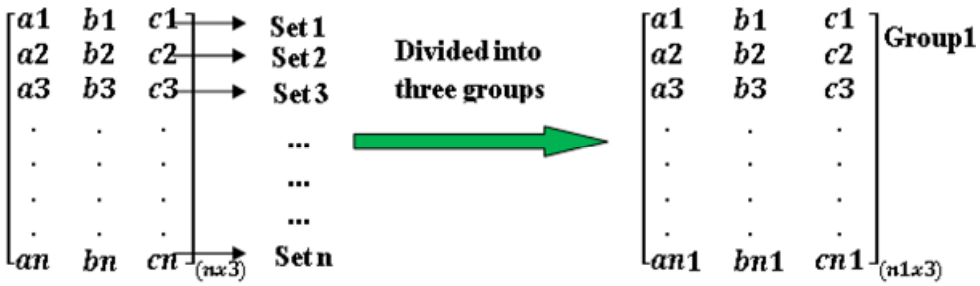

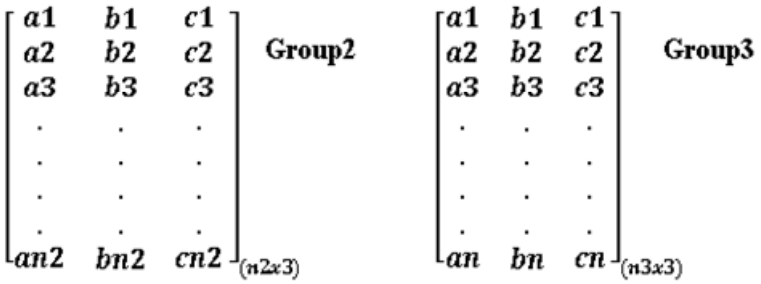

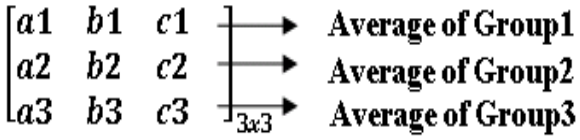

.

3- Re-visit equation (5.4.1.1.3) to compute the apex of the target.

$$\begin{bmatrix} a1 & b1 & c1 \\ a2 & b2 & c2 \\ a3 & b3 & c3 \end{bmatrix} . \begin{bmatrix} X \\ Y \\ Z \end{bmatrix} = \begin{bmatrix} 1 \\ 1 \\ 1 \end{bmatrix} \quad \text{.....(5.4.1.1.6)}$$

$$\begin{bmatrix} X \\ Y \\ Z \end{bmatrix} = \begin{bmatrix} a1 & b1 & c1 \\ a2 & b2 & c2 \\ a3 & b3 & c3 \end{bmatrix}^{-1} . \begin{bmatrix} 1 \\ 1 \\ 1 \end{bmatrix}$$

The programme was applied to 10 pyramid targets with various heights **(**T1 to T6**).** The result can be seen in Table 5.1, and the flow diagram of the programme script can be seen in Figure 5.7.

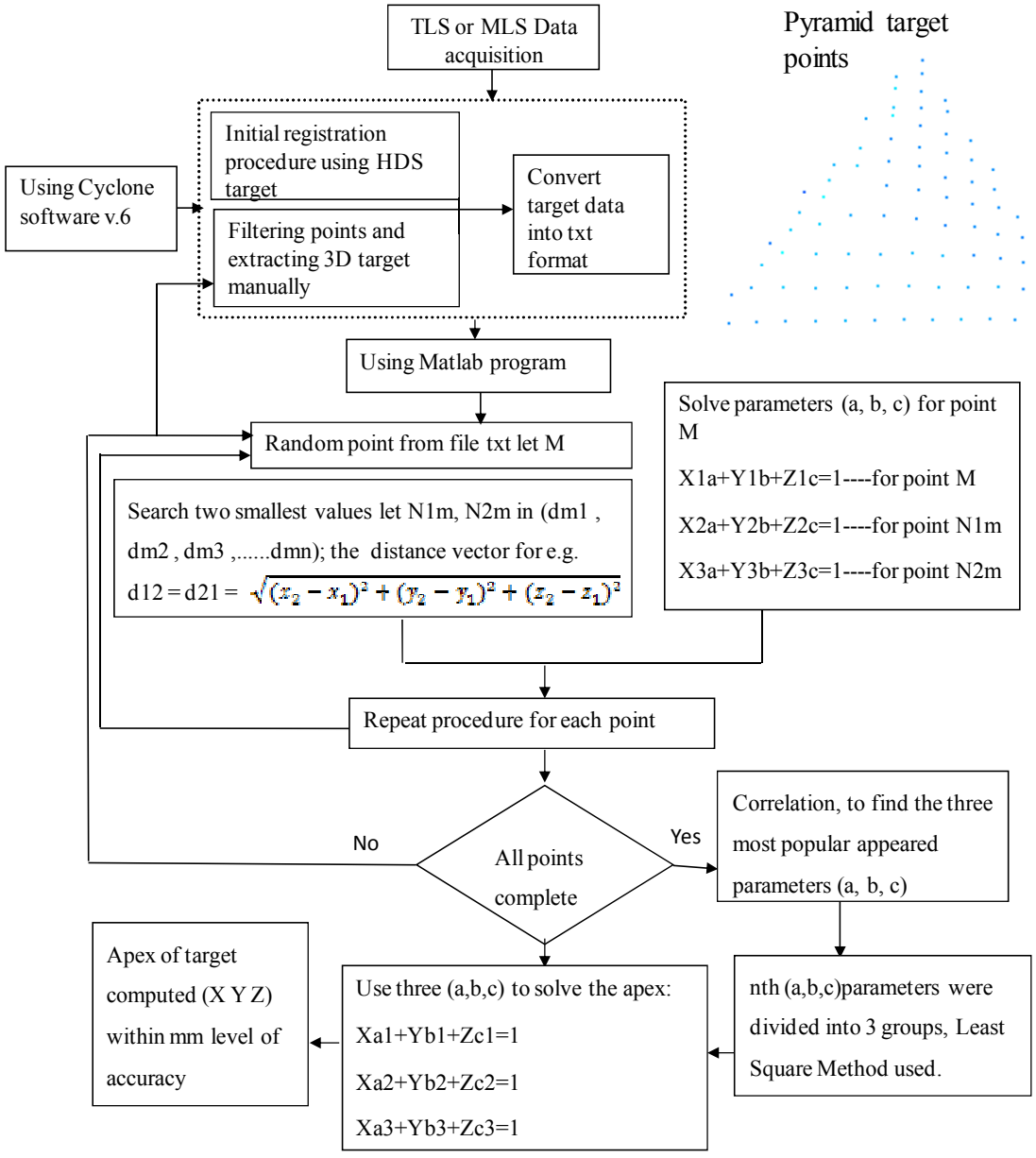

Figure 5-7: Automatic workflow for computing the apex of a pyramid target after manually filtered the target's points.

The second method, Leica Cyclone v.6 software was used to define the pyramid apex automatically, based on fitting planes to each side, and determining the vertex of these fitted sides (see Figure 5.8).

Leica HDS3000 scanner was used in this trial with the two point densities (1x1) cm and (2x2) cm. The results of each method can be seen in the Table 5.1.

Target	Height (m)	Accuracy (xyz) using Matlab algorithm (m)	Accuracy (xyz) using Cyclone
Point density : (1x1) cm – scan resolution			
T1	0.1000	0.0046	0.0031
T2	0.0800	0.0099	0.0037
T3	0.0600	0.0109	0.0073
T4	0.0400	0.0078	0.0077
T5	0.0200	0.0099	Fail
T6*	0.0800	0.0085	0.0027
Point density : (2x2) cm – scan resolution			
T1	0.1000	0.0065	0.0054
T2	0.0800	0.0092	0.0057
T3	0.0600	0.0085	0.0094
T4	0.0400	0.0073	0.0096
T5	0.0200	0.0100	Fail
T6*	0.0800	0.0089	Fail

Table 5-1: Result of targets position error of different heights using Matlab algorithm and Cyclone software with scan spacing (1x1 and 2x2) cm respectively.

*T6: small size of pyramid used in the trail, base of 20 cm and height of 8 cm.

In addition to the computational check of the positional accuracy of the pyramid targets from different height, the Figure 5.8 shows visual check was obtained from Cyclone software, and shows the accuracy of the pyramid target using two scan resolutions: (1x1) cm and (2x2) cm, respectively.

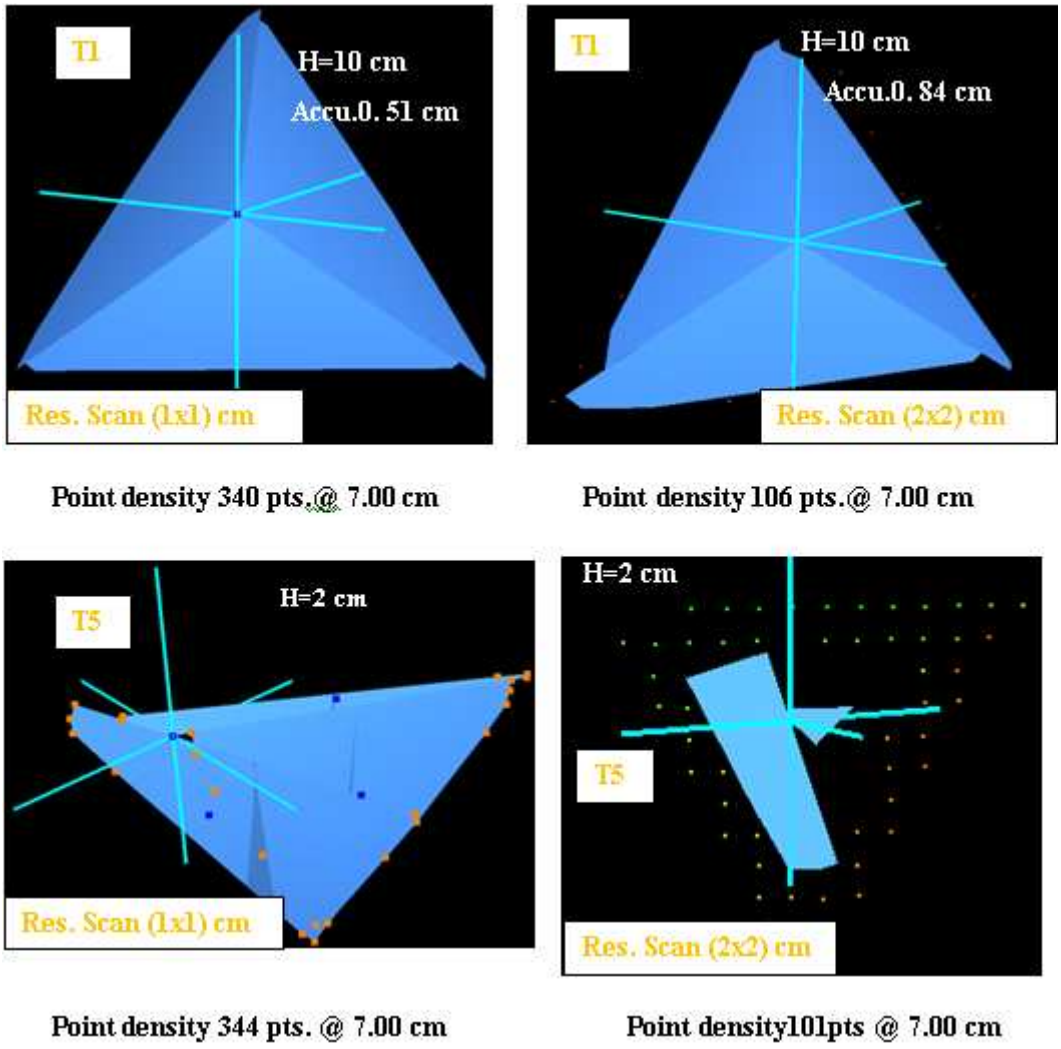

Figure 5-8: Apex accuracy of the pyramid targets using Cyclone software. Top left and right, scan resolution (1x1) sq. cm. Lower left and right, scan resolution (2x2) sq. cm.

5.4.1.2 *Result analysis*

From Table (5.1), according to the selected dimensions for a pyramid, the height is 10 cm with the length of 30 cm. The accuracy of the apex reduces with decreasing height (see Figure 5.9). The method used by the Cyclone software is based on fitting planes to each side, and determining the apex of these fitted sides. The precision of fitting plane is based on the number of point per target and height to base ratio (see Figure 5.8). The larger the size (i.e. in term of base and height), the better precision and accuracy can be achieved.

The Matlab program is not affected by height ratio, but it was affected by high point density, which delays the processing, and problems in computing parameters of a

normal vector for each small triangle, which clashes between faces affecting the accuracy of the apex.

The limitations of both methods and the need for further development can be summarised as follows:

1. The main limitation of Cyclone or other software is the inability to detect the custom made target automatically from surrounding points in the laser point cloud.
2. The use of Cyclone software is limited for no more than targets with three faces; an example of four faces can be seen in Figure 5.10b. This means that there is no redundancy in the computation of the apex via Cyclone, which is an important factor for hiding errors in apex determination, where the more faces, the better precession and accuracy of the apex can be achieved, is discussed in section 5.5.
3. With low point density, bad positioning accuracy can be obtained even with a proper height (see Figure 5.10a).
4. The Matlab program becomes slow with high density of points. This is beside the problems of calculating parameters of a normal vector for each small triangle which clashes between faces.
5. The Matlab program was written only for computing the apex of the target automatically at the first stage, and cannot isolate pyramid faces. Therefore, further development is needed.

These issues were solved and are discussed in the next chapter. The optimal size of the pyramid was chosen at height and base of 10 and 30 cm respectively, and other variations or parameters affected the targets are introduced in this chapter. These can be summarised as follows:

1. The scanning range and the incidence angles.
2. Number of points hitting the target, including range, size, surface reflectance, PRR, point density (resolution) and incidence angles.
3. Colour of the target (reflectance)

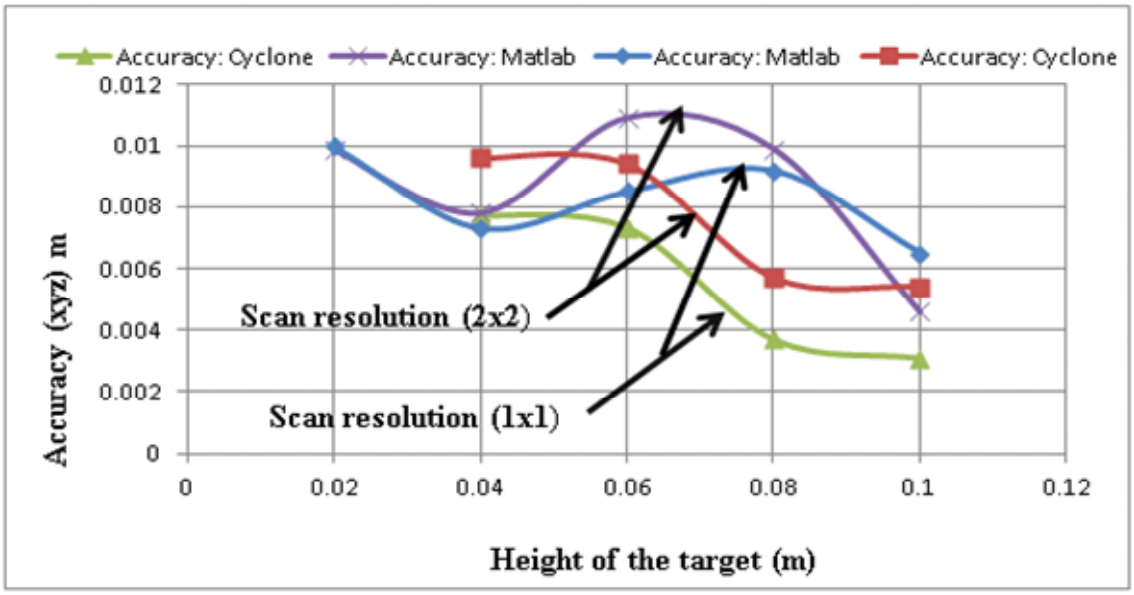

Figure 5-9: Accuracy of the apex Vs height.

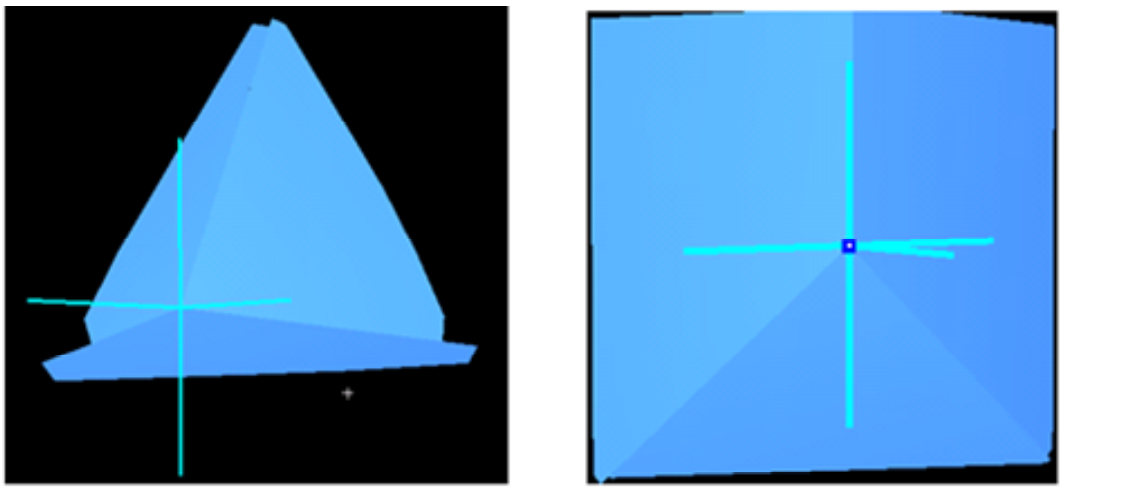

a). Bad positioning accuracy of the apex b). Failed intersection plane in cyclone

Figure 5-10: Failed case in Cyclone: a): Bad positioning accuracy (left), due to a low point density, b): Failed intersection in four sides of the pyramid target.

5.4.1.3 Validate the method used for defining the apex

Perfect data of a pyramid target were produced via AutoCAD software, to prove the computation method used for defining the apex of the pyramid target. The work flow for converting pyramid target to point cloud is as follows:

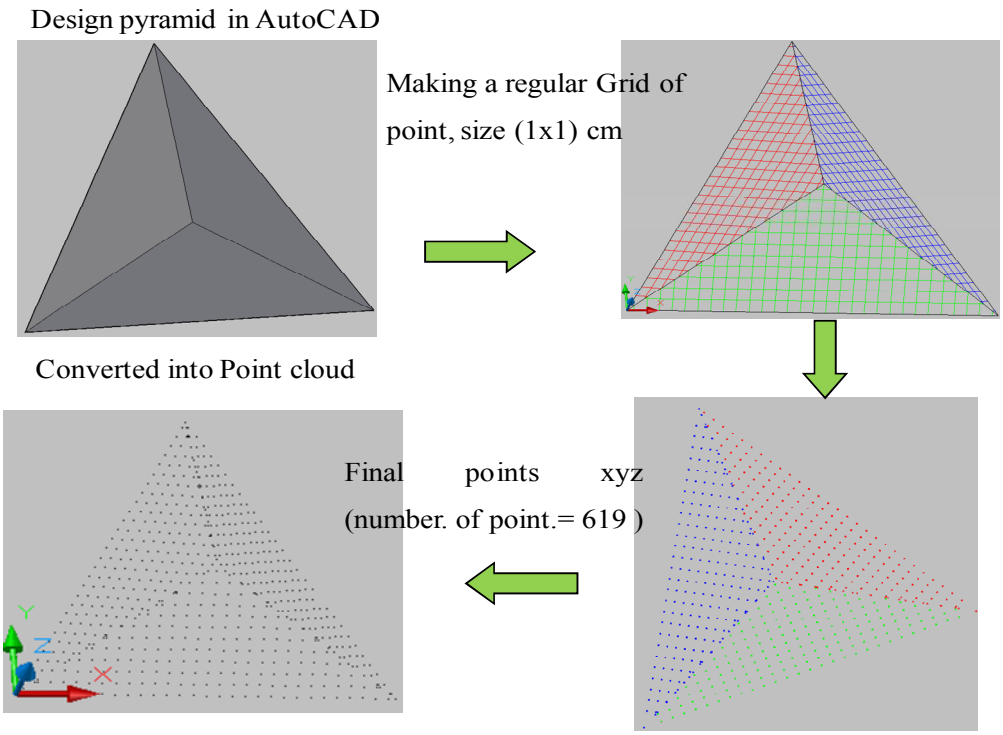

Figure 5-11: The process of creating perfect data.

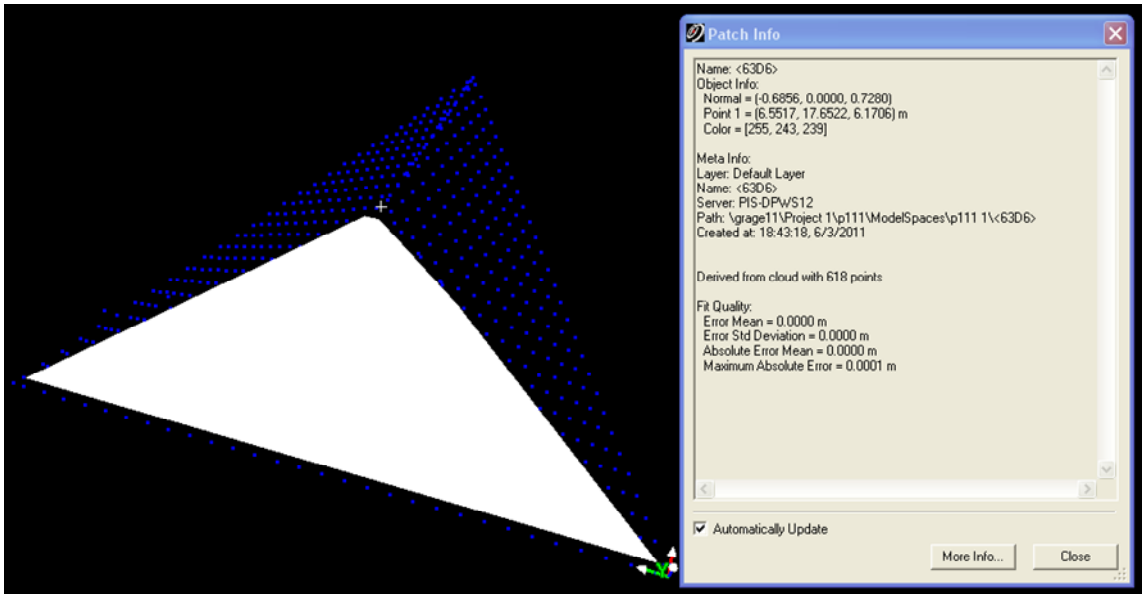

Figure 5-12: The statistical result of the quality of fitting one side of the perfect data without error.

The perfect data was applied to assess the method used. The Cyclone software was used and no error was obtained from fitting the plane to a perfect data, as shown in Figure 5.12. Regarding Matlab algorithm, the error was still around 2 to 4 mm, due to the problems for calculating normal vectors for each small triangle, which is overlapped between faces. With more than 500 points, the programme was slow in processing the data, as mentioned previously.

5.4.1.4 Cone target

Two sizes of a cone were designed and tested. The design was based on three dimensions, as follows:

- The vertical height (or altitude), which is the perpendicular distance from the top down to the base (h) see Figure 5.13
- The radius of the circular base (r)
- The slant height (S) which is the distance from the top, down side, to a point on the base circumference.

The same procedure, as used to find out the best height for the pyramid was used for the cone. Tests show that cone with dimensions of (r = 0.15 m, S=2r) does give the best results. This can be attributed to the relationship between the geometry and the intersection angle, where this later should be around 45 degree or more (see Figure 5.13 right)

The reason behind choosing the cone is to overcome the limitations of the pyramid mentioned before, such as (incidence angle, multi faces, etc). The cone can be seen at any incidence angle and has only one face.

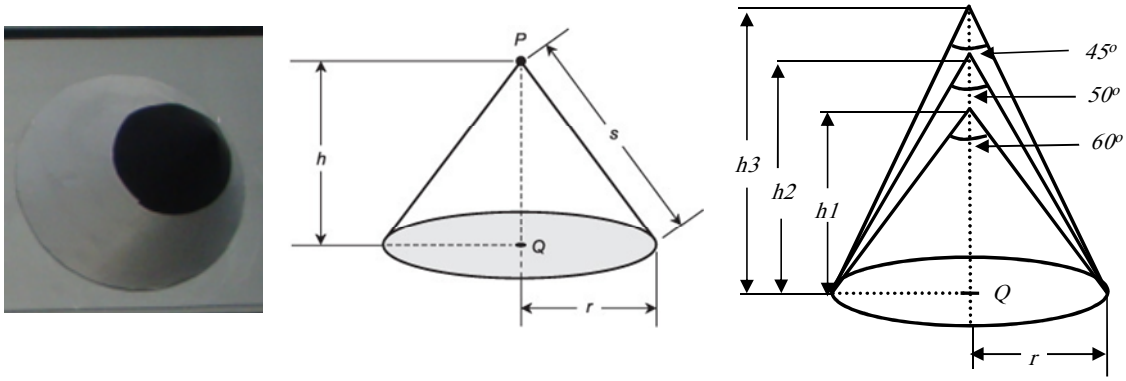

Figure 5-13: Cone shape: Left: sample of cardboard cone. Middle: Geometric shape of the cone. Right: different height with fixed radius.

Figure 5.13, left, represents two halves of cone, the first half covered with a black colour from the top, the other half covered with a white colour, in order to be easily distinguished from surrounding object in the points cloud. The reason behind choosing these colours is based on the return intensity of the coloured surface, and this is discussed in the next section.

5.4.1.5 Sample of other geometric target designs

Beside the 3D pyramid and the cone targets, other 2D geometric targets were designed and tested, namely are dot and circles targets. Least squares algorithm was used to calculate the centre of these targets. The achievable accuracy of their centre within mm level of accuracy obtained through automatic target detection and computation with normal incidence angle. This accuracy degraded with increasing incidence angle and has an impact on the range measurement, and hence the accuracy of the point cloud (Soudarissanane et al., 2009).

The testing of these targets was carried out at approximately perpendicular incidence angles to find out the proper size for dot radius and ring width. Based on the trials, the appropriate dots targets were fixed in a radius of 1.5 cm for each dot, and the space between the centres of dots was 5cm. The size of the entire target was 30 cm length and 20 cm wide, comprises two diagonal lines of dots and one perpendicular. Each line contains four dots (see Figure 5.14). The more dots in a line, the better the intersection can be achieved. The dots covered with different colours to be easily found in automatic detection.

The ring target contains three circles with the same centre. Each ring has a width of 1.5 cm radius. The radius distance between each circle from the centre is 5 cm. The design of these two targets can be seen in Figure 5.14. The ring target has been rejected due to its low accuracy and unreliable results, as each circle gave a different position for the target centre after the fitting process.

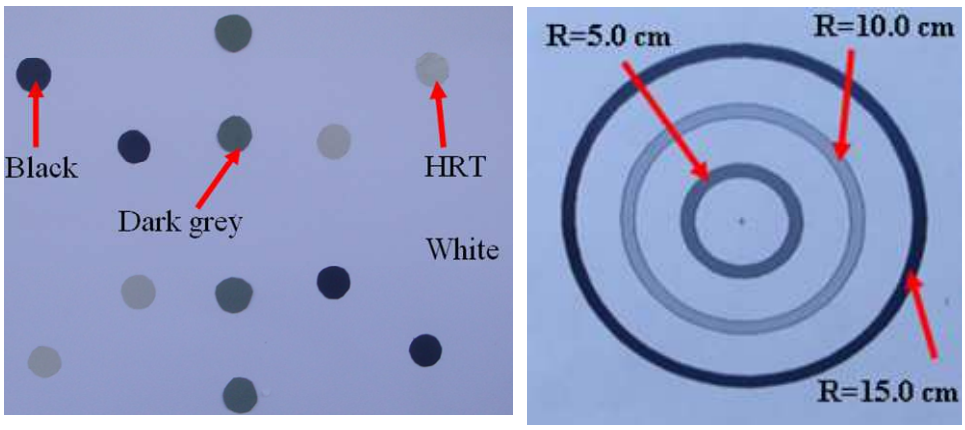

Figure 5-14: 2D target design: left dots target, Right: Rings target.

5.4.2 Return Intensity analysis

In this section, the intensity of several colours was investigated. It is important to see how the laser signal is reflected back to the scanner from different coloured surfaces, to find out the intensity range value of which colour and decided which can be used in the targets. The best reflector colours are used for pyramid faces and others designed target in order to be easily isolated automatically. In addition, the influence of range and incidence angle (IA) on the surface objects is discussed.

The main purpose of this test is to find the reflection of colour surfaces against white and black colours that were decided to be used for the targets, as mention in section 5.4. According to Boehler et al. (2003), the white colour has strong reflectivity, while black has a weak response among all colours. The objects under test were various square pieces of Cardboard (12.5x12.5) cm of the same material and different colours. The test was done in two different environments, inside and outside the laboratory. The reason for doing these two trials is to show the behaviour of a signal response in different brightness. This is useful for MLS, where data tends to be captured in different areas of illumination. This was done to challenge the colours and observe their differences with respect to white and black, in term of intensity value.

In this test, twelve different colours and three different materials have been tested to have a look on the reflectivity of each one as shown in Figure 5.15 showing, also, six tiles attached on a small wooden board, a black matt and gloss, white matt and gloss, a dark grey matt and a light grey gloss. Both tiles boards were held on the wall perpendicular to the scanner. This means that the laser beam hit the two boards at (perpendicular approximately 0◦) incidence angle. Different angle of incidence could be used to see the scanner behaviour, if the two boards are scanned at different rotation, as well as with different types of surfaces. This is investigated after selecting of the optimal colours used for the designed targets.

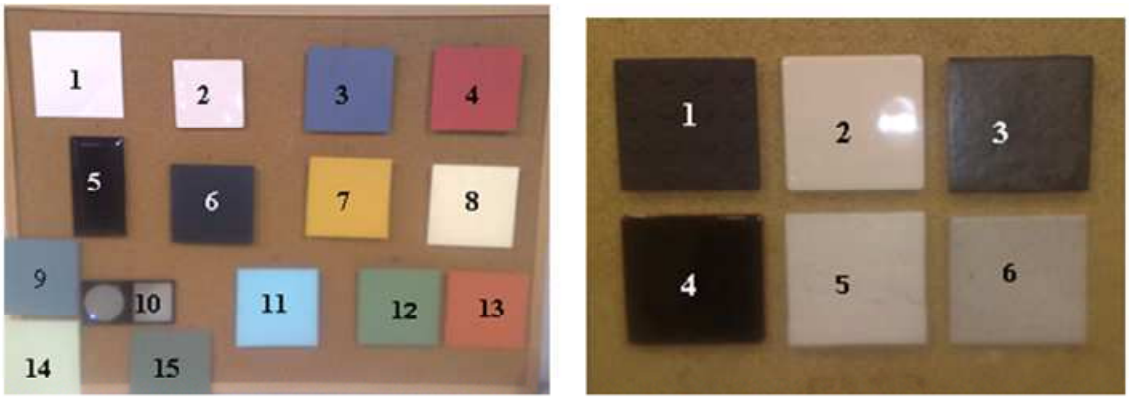

Wooden board 1 Wooden board 2

Figure 5-15: Different materials used in an indoor test for intensity return analysis. Left:: Wooden board 1 contains 12 pieces of cardboard with different colours and adding three tiles, gloss white and black with edge, and two small mirrors, circular on the left and square in the right. Right: Board2 contains six tiles, (Top left: Matte black (1); bottom left: Gloss black (4); top middle: Gloss white (2); bottom middle: Matte white (5); top right: Matte dark grey (3); bottom right: Gloss light grey (6).

Figure 5.15 shows the board of tiles that was made for the purpose of this test. The board was made from wood and the tiles used had different materials and colours. For example, Figure (5.15 left) represents each piece of cardboard used from the same materials. Figure (5.15-right) represents each tile with different textures and different materials. Both materials were available in NGI store.

Figure 5-16: Different tiles with various textures.

Figure 5.16, left (tile no.2): Gloss white tiles, it was chosen to show the effect of signal response compare with the white matte one.

Figure 5.16, middle (tile no.5), Gloss black with edges. This tile is made from the same material as gloss white tiles with the only difference of being black and with the edges slant. This tile was selected in order to see how the scanner behaves on the

targets that are slanted, and this effect is taken into account when extracting the suitable colour for the target.

Figure 5.16, right (tile no.10): Mirrors. This is a normal mirror with two different types, small square part and circular part. The former is an ordinary mirror while the later is magnifying mirror used to observe the signal response when coming from a highly reflective surface. This object was ignored, due to the high differences in the reflectivity between its points.

5.4.2.1 Data collection and processing

The data collection involved setting up the board and scanning at a normal incidence angle in two cases, indoor and outdoor the laboratory. Two laser scanners were used HDS3000 and FARO Focus^{3D}. The two boards were scanned at point density (1x1) sq.cm and at a distance of approximately 7 m. Both scanners were used on the same day. The Cyclone software was used for post-processing the amount of points involved that returned to the sensor and the intensity values (highest – lowest) of each piece of cardboard and tile in both cases (inside and outside lab.). The number of points, the intensity values for each tile in both cases, and the maximum and minimum intensity of each piece of cardboard and tile were recorded.

5.4.2.2 Data analysis and Result

The data was analysed in Cyclone using the intensity values given by the software. The intensity values are between 0 and 1, the value 1 represents a strong signal return (a reflective surface), shown in green or blue colour, which depends on the degree of reflectance, while value 0 represents a weak return (an absorbent surface) shown in red colour. The average intensity of each piece of cardboard and tile was determined through the software.

To compare the precision of different tiles surfaces, a plane ("patch") was fitted through the points of each piece of cardboard and tile of board 1 and board 2. The standard deviation, absolute error mean and maximum absolute error for each patch was found; these are presented in Table 5.2 and 5.3. To begin with, Table 5.2 shows the average intensity and statistical result for each tile in board 2. The statistical

result obtained on demand electronically using the object information tool in the Cyclone software, an error report of the patch's fit is produced. The statistical report of fit quality contains several factors:

The standard deviation (stdv.): the standard deviation of all the points compared to the patch.

The absolute mean: the average error of each point away from the patch.

The maximum absolute error: the maximum distance a point is located away from the patch.

Tile type: Board 2		Mean intensity outside	Mean intensity inside	Error stdv.(m)	Absolute error mean (m)	Max absolute error (m)
1	Matt Black	0.4326	0.4326	0.0025	0.0018	0.0138
2	Gloss white	0.5038	0.4982	0.0027	0.0018	0.0095
3	Matt dark grey	0.4510	0.4564	0.0020	0.0018	0.0080
4	Gloss Black	0.3852	0.3943	0.0039	0.0028	0.0204
5	Matt White	0.5097	0.5000	0.0019	0.0011	0.0066
6	Gloss light grey	0.4865	0.4941	0.0024	0.0021	0.0081

Table 5-2: Average intensity and statistical results of each tile in board 2 (inside and outside) lab.

Table (5.2) shows the intensity of return signal on various materials of board 2 with different colour and texture; the highest signal return was given by the matte white tiles. This surface gave the best precision with mean error of less than 2 mm, as the surface gives a strong diffusion reflection. It, also, has higher reflectivity, where measurements were taken inside the laboratory in normal conditions.

The weakest return signal was given by the gloss black tiles. This surface also gave the worst precision with a maximum deviation away from the fitted plane of 20.4 mm and an error standard deviation of over 3.5 mm. The reason for the poor precision, and low intensity value is that the dark surface absorbs much of signal, while the gloss gives specular reflection, as mention in section 3.6.4. The gloss black surface affected the signal so much that over half the points that hit the surface have not been recorded by the scanner as can be seen in Figure 5.17.

The results for the gloss black and matt white tiles were expected, research by (Kremen et al., 2006) reported similar results. Also gloss black surface has less reflectivity, when used inside the laboratory.

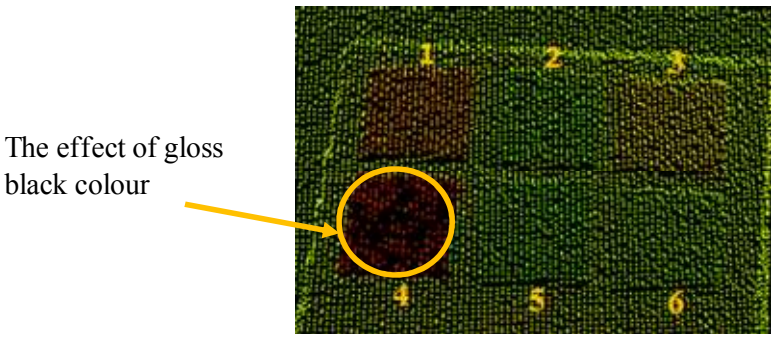

Figure 5-17: The point cloud of the scanned tiles, gloss black tile (no.4) large amount of data missing as depicted in yellow circle.

This effect can be seen very clearly in Figure 5.18, where the pyramid target tested with this colour has different brightness. The amount of return of gloss black colour has less effect, when scanning inside the laboratory compared with outdoor. This is because the surface is not affected by any external factors, such as the sunshine.

Generally, the results of the others tiles and cardboard show that the colour factor does affect the intensity return value more so than the surface type. This is because of the relationship between the absorbability of the signal and the colour. On the other hand, the surface finish seems to affect the precision more than the materials colour. This is because the type of reflectivity is dependant mainly on the finish of the material characteristics. This can be seen with the gloss light grey tile, which has worse precision than the dark matt grey tile, but not the lowest intensity return.

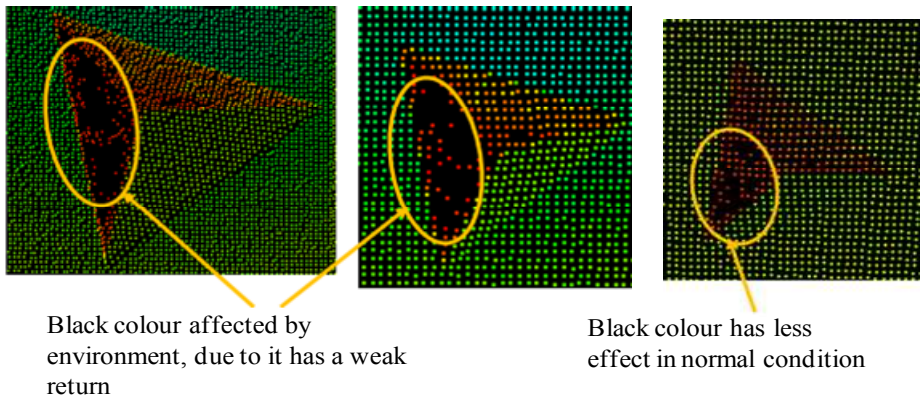

Figure 5-18: Shows the scan points of the pyramid target outdoor and indoor. Left and middle: Scan points of the target outdoor at point density (0.5x0.5) and (1x1) cm respectively, in both resolutions (note the gloss black, as one face of the target, large amount of data missing). Right: scan points inside the lab., at point density (1x1) cm, (note the gloss black has less amount of data missing than outdoor).

No. Of tiles	Type of pieces carton	Mean Intensity indoor	Mean Intensity outdoor	Error stdv. (m)	Abs. error mean (m)	Max Absolute error (m)
Wooden board1 1						
1	White	0.5156	0.5153	0.0020	0.0016	0.0043
2	Gloss white	0.4982	0.4967	0.0020	0.0016	0.0041
3	Blue	0.4657	0.4682	0.0020	0.0015	0.0053
4	Pink	0.4519	0.4526	0.0030	0.0022	0.0090
5	Gloss black with an edge	0.4072	0.4076	0.0030	0.0023	0.0080
6	Black light	0.4438	0.4567	0.0023	0.0018	0.0070
7	Yellow	0.4849	0.4853	0.0019	0.0015	0.0052
8	Near to white	0.5032	0.5074	0.0022	0.0017	0.0070
9	The blue fade	0.4726	0.4792	0.0017	0.0013	0.0052
10	Mirror	0.3990		0.0073	0.0052	0.0024
11	Blue sky	0.5021	0.5034	0.0017	0.0014	0.0052
12	Green fade	0.4830	0.4842	0.0019	0.0015	0.0047
13	Orange	0.4620	0.4599	0.0017	0.0014	0.0052
14	Light green	0.5076	0.5094	0.0018	0.0015	0.0044
15	Dark green	0.4715	0.4712	0.0023	0.0011	0.0069

Table 5-3: Average intensity and statistical results of each tile in board 1 indoor and outdoor.

From Table 5.3, it can be seen that the most return from the tiles under indoor and outdoor conditions have more or less the same intensity value. This means that the intensity value of the coloured surface will be slightly different under different conditions; for example, the intensity value of white in an indoor and outdoor scan is 0.5156 and 0.5153, respectively, where the different is only in the fourth decimal place. This is because the glossy white colour reflects more, when scanned outdoors compared with indoors. This is one of the favoured colours for use on designed targets, and is useful on a target surface in the MLS survey. The intensity return value of the other colours had a slightly increased value in outdoor compared to indoor scans. These differences can be clearly seen in Figure 5.19. This displays the maximum and the minimum intensity of the points on each tile surface on the two boards.

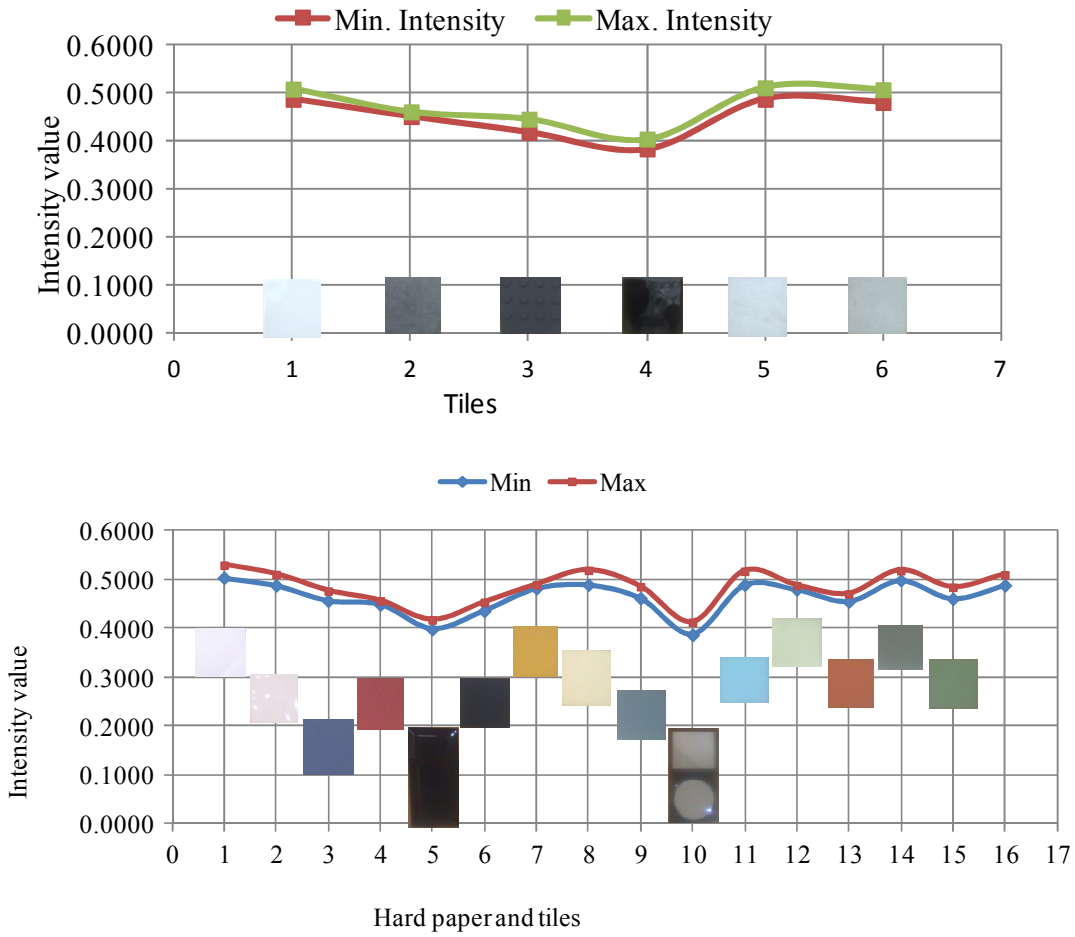

Figure 5-19: Minimum and maximum intensity return of the material used. Top: Tiles in board 2. Lower: Pieces of cardboard in board 1.

The optimal selected colour from the results of this test depends on the intensity range value. The initials colours fixed are Black, dark grey, orange, green and white as well as highly reflected tape (HRT). See Figure 5.20.

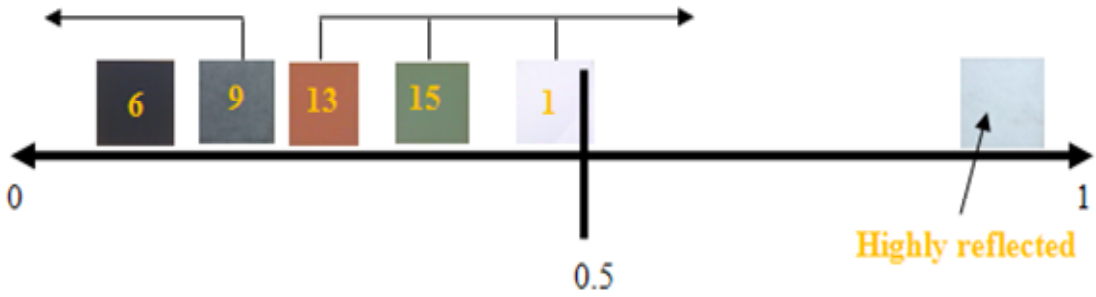

Figure 5-20: Intensity range of the optimal colour.

Figure 5.20 represents the maximum and minimum intensities of the optimal colour, which is to be used on the designed target. These colours were used on one of the designed target (triangular based pyramid target) in two cases, indoor and outdoor, in order to check the most favourable colour. The results of maximum and minimum intensities of the selected colour for target design from both cases can be seen in Figure 5.21 and 5.22.

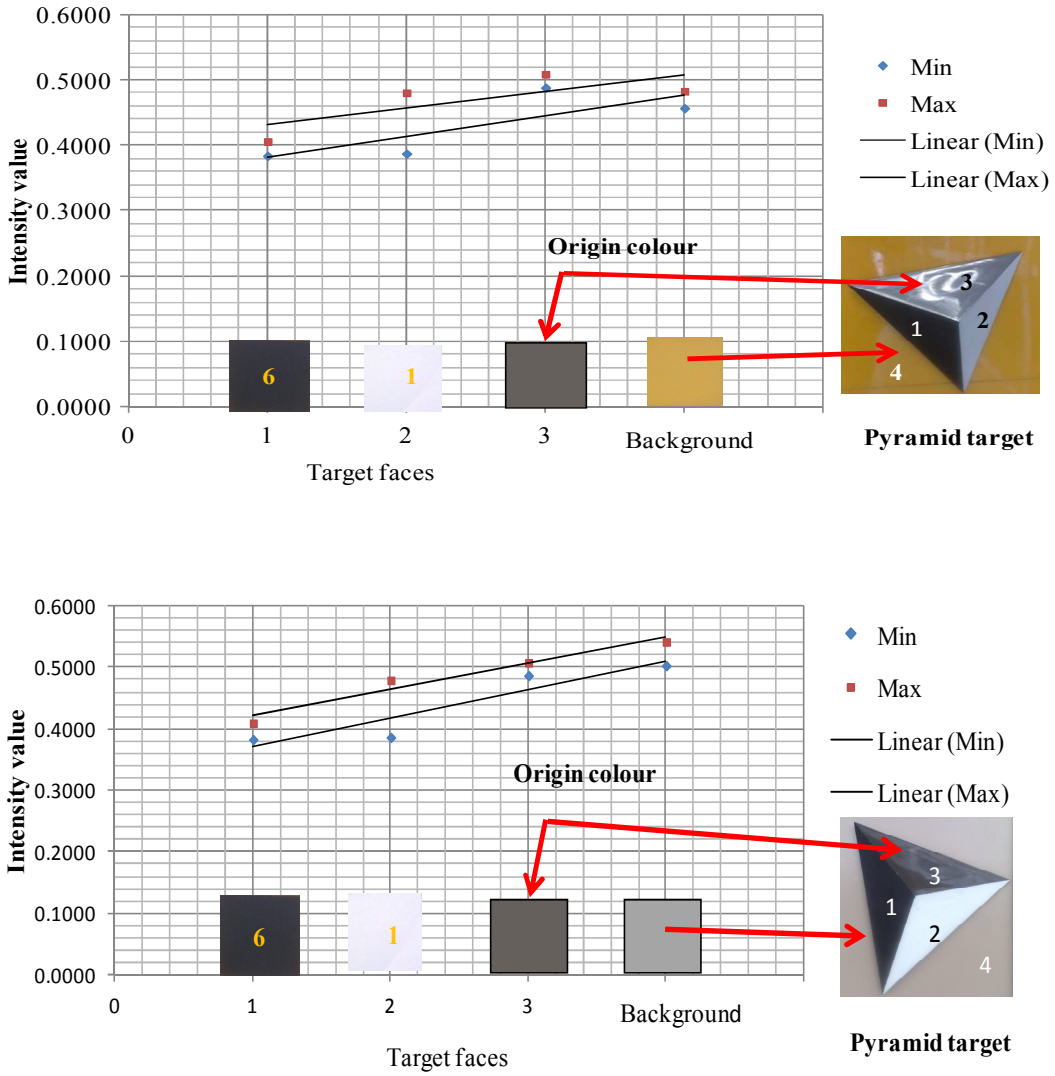

Figure 5-21: Target scanned inside the laboratory with chosen colour. Top (black, white and origin surface (gloss grey)), with a gloss yellow background. Bottom: (black, white and origin surface (gloss grey)), with brown background.

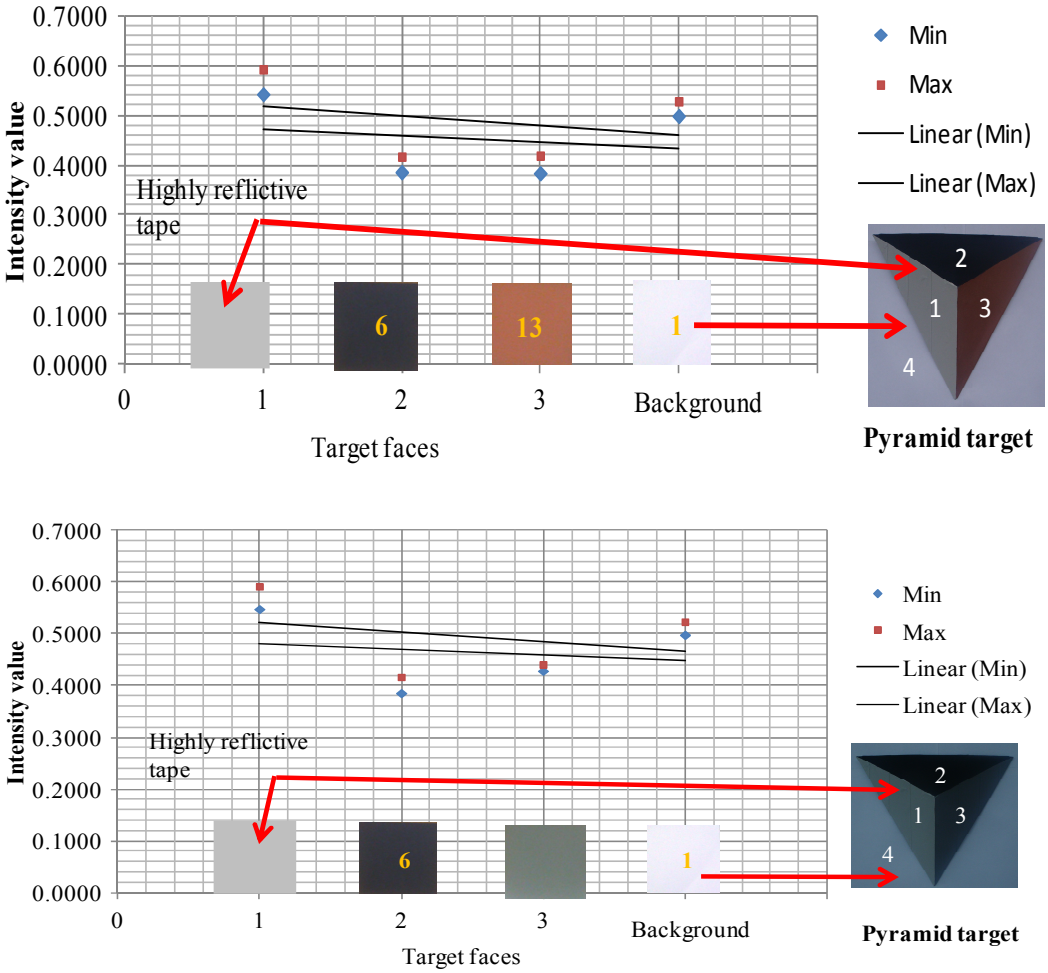

Figure 5-22: Target outside with chosen colours: Top (black, HRT and orange). Bottom: (black, HRT and dark grey), with white for its background.

The difference between the maximum and minimum intensity values tends to be small, when the surface scanned has the same colour distribution. Also, a closer look on the Figures reveals that the tiles with dark colour have unreliable points (see Table 5.2). In addition, by comparing tiles in different brightness, the difference between the maximum and the minimum intensity values seems to be greater in some surfaces such as white colour.

From the two Figures 5.21 and 5.22, it is clearly that there was an overlap between the intensity values of the return signal from the fixed colour for each face of the target. Only the last Figure (5.22, bottom) shows that the intensity values for each face are not involved with the neighbouring face.

These colours were selected for use in automatic target detection. The reason for each face having a separate colour is to be easily isolated from the others. The

selected colours are Black colour, highly reflective tape colour, Grey colour and White for the background. These colours can be easily detected from surrounding object in laser point cloud using automatic detection process, which is discussed in the next chapter.

5.5 The effect of range and incidence angle on the designed target

This section investigates the effects of range and incidence angles (IA) on the quality of 3D target accuracy in the point cloud. The IA can be described as the angle between the laser beam vector and the normal vector to the target surface, such as pyramid, cone, sphere and Leica flat target. The IA affects the individual point signal to noise ratio (SNR). This effect has been studied in TLS by many researchers such as (Kremen et al., 2006; Kaasalainen et al., 2008; Soudarissanane et al., 2009). The received signal level of the measurements decreases with increasing incidence angles.(Soudarissanane et al., 2009). As illustrated in Figure 3.18 in chapter 3, the returned signal level influences the precision of the distance determination.

To calculate incidence angle of each individual scan point; Let the vector P = [xi; yi; zi]

Where, i =1 to n, and P is defined by Soudarissanane et al. (2009) "*as the laser beam vector from the laser scanner to the surface in the direction of the transmitted laser beam"*. The incidence angle β, is the angle between the laser beam vector (P) and the normal vector (N) of the target surface can be expressed in the equation 5.5.1 (Soudarissanane et al., 2009).

$$\beta = \cos^{-1}\frac{P.N}{|PN|} \quad \text{..... (5.5.1)}$$

The theoretical IA contribution to the signal deterioration for each target surface was plotted as shown in Appendix H.

The range of Leica HDS3000 can reach up to 300 m on a 90 % reflective surface (Leica., 2009). On the other hand, FARO Focus^{3D} can reach up to 120 m also from a 90 % reflective surface (User manual, 2011).

This section is about the effect of ranges and incidence angles on the quality of the centre/apex of the designed targets compared with their estimated accuracy measured via Total Station (TS).

Two TLS Faro focus^{3D} 120 and Leica HDS300 were used for this test. The validity of the manufacturer's accuracy claims for both scanners was evaluated. Leica Geosystem gives errors of 4mm distance error over 1-50 m for HDS 3000 and 4 to 5mm distance over 1-50 m for the Faro focus^{3D}.

5.5.1 Experiment setup

Three tests were carried out to examine the effect of the incidence angle and range on the accuracy of the targets centre/apex such as (Cone, pyramid, sphere, and flat target). The specifications of these targets used are discussed in section 5.4. The first two trials were carried out with designed targets (i.e., Cardboard targets (cone and pyramids) and compared with the manufacture's one (sphere and leica targets). While, in the third trial the designed targets were made of aluminium by Faculty workshop at the University. In all trials, a total station (TS) has been used to determine the coordinates of the centre/apex of each target independently.
The first set of tests was performed to examine the incidence angle contribution at a fixed distance to the scanner. This test is performed on a 0.70 x1.20 white coated wood board. This board was mounted on a tripod via circular tribrach a screw clamp mechanism provided with a goniomete, which enables the mechanism to rotate the board horizontally with a precision of 1^{o}.

In the second test, the IA has been fixed on (0^{o}) and the range has been changed. The third test was used with a different range and a different incidence angle, in order to assess the effect of incidence angle on the range measurements, and how the effect can be removed.

5.5.2 Survey description

In the first test, four targets were attached on a wooden board, a cone, a pyramid; a sphere and flat target (see Figure 5.23). The board was placed at a distance of 10 m from the scanner. The board is rotated from (0^{o}) to (90^{o}) in step of (10^{o}). At each step, the board is scanned, as depicted in Figure 5.24. The analysis of data has been based on 10 scans, for example the cone contained between 667 and 181 points per scan depending on the incidence of the surface with respect to the laser beam.

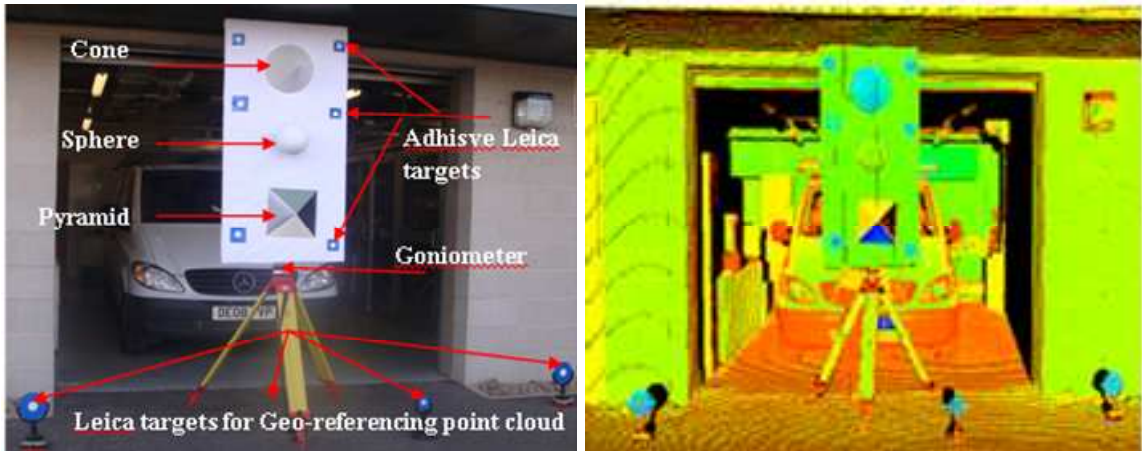

Figure 5-23: Board targets and the point cloud of the scanned board. Top: cone, Middle Sphere and bottom pyramid 4faces and surrounding 6 circular Leica targets) adding 3 circular Leica target for geo-referencing the point cloud.

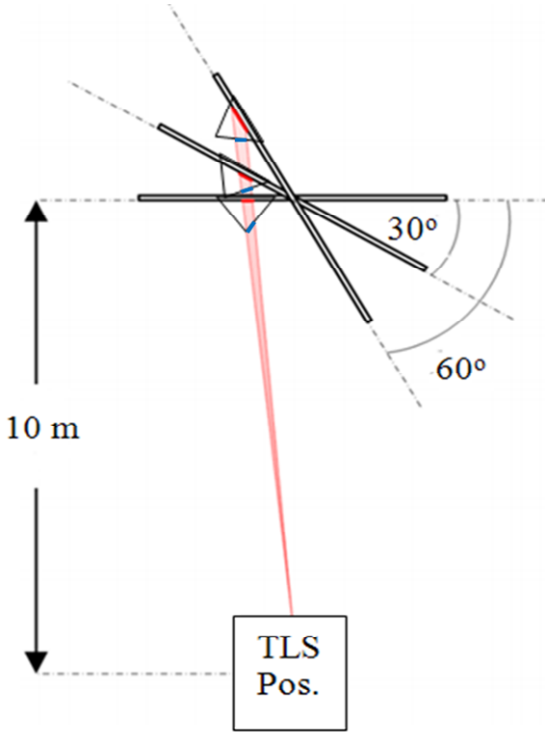

Figure 5-24: Front view of the measurement setup1, with the schematic illustration of horizontal rotation of the board using the goniometer. A representative laser beam is depicted in red on a board and blue on a cone target.

In the second test, the scanner was placed at distance ranging from 10 to 100 m in steps of 10 m from the targets (see Figure 5.25). This test contains 10 scans captured successively. However, only 3 scans are captured in a good quality. The point density of each target decreases with increasing the range as shown in Table 5.4 and 5.5. For higher ranges at normal incidence angles, the standard error (standard deviation of the residual"σ") for each target obtained was more than 5 mm is discussed in section 5.5.4.

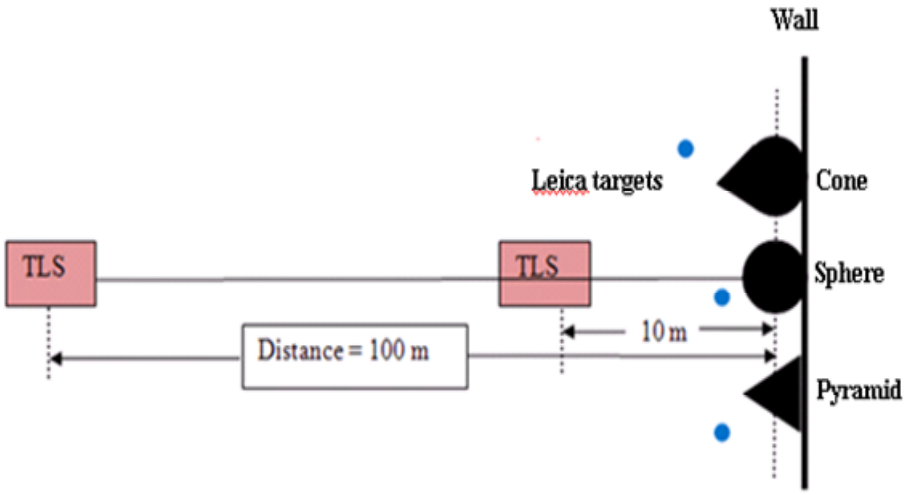

Figure 5-25: Plan view of the position of laser scanner setup 2 for the targets range trial using Faro focus^{3D} and HDS 3000.

In the third trial, the high quality specially made targets (pyramid and cone) were fixed on the tripod using magnetic mount kit (see Figure 5.26), and the scanner (HDS3000) placed at different incidence angle ranging from (0^o) to 80^o in step of (10^o) and at a distance from 10 to 50 m in step of 10 m. At short distances, the point density of cone target was between 181 and 667 points depending on the incidence angle. At the far distance, based on the incidence angle, the point density of each target can be seen in Table 5.7 and 5.8. For larger ranges and incidence angles, the standard error (standard deviation of the residual"σ") for each target was more than 5 mm are discussed in section 5.5.4.

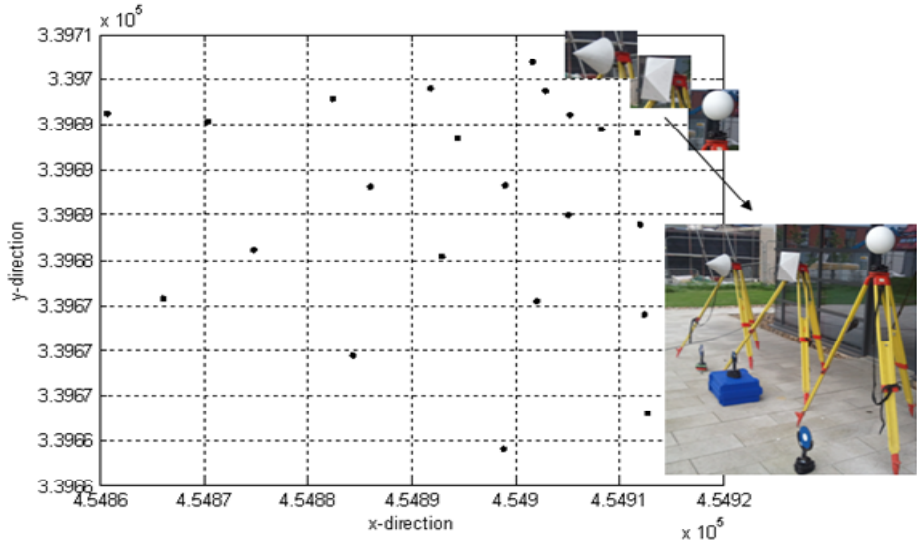

Figure 5-26: Plan view of the position of laser scanner setup3 for the targets range and incidence angles trials. Target's position rigidly fixed on the tripod using magnetic kit is depicted on the right picture.

5.5.3 Result and Analysis

The result of the test1 and test2 can be summarised as follows:

Test1: The effect of incidence angle at a fixed distance to the scanner

The effect of the IA at fixed range to the scanner on the accuracy of each target centre can be seen in Table 5.4 and Figure 5.27.

Incidence angle (o) Range=10 m	Accuracy[1] (ΔR) sphere radius (mm)	Accuracy[2] sphere centre (mm)	Accuracy[2] cone apex (mm)	Accuracy[2] pyramid apex (mm)	Accuracy[2] Leica flat target centre (mm)
(0°)	0.27	3.89	2.63	2.92	1.70
(10°)	0.47	3.02	2.81	4.22	1.89
(20°)	0.67	2.12	3.80	4.81	1.19
(30°)	0.87	2.63	4.26	5.11	1.86
(40°)	1.07	2.94	6.73	6.74	2.44
(50°)	0.85	3.37	7.79	8.61	6.25
(60°)	0.64	3.80	11.05	12.75	12.92
(70°)	-0.69	4.88	5.46	6.42	Fail
(80°)	-0.75	5.90	4.20	12.54	Fail
(90°)	0.46	6.11	4.02	Fail	Fail

Table 5-4: Accuracy of the apex Vs incidence angle with constant range.

Accuracy (1) is the difference between the estimated sphere radius and its actual radius provided by the manufacturer.

Accuracy (2) is the 3D difference between the estimated value of the target centre/apex achieved from laser scanner and TS coordinates of the same point.

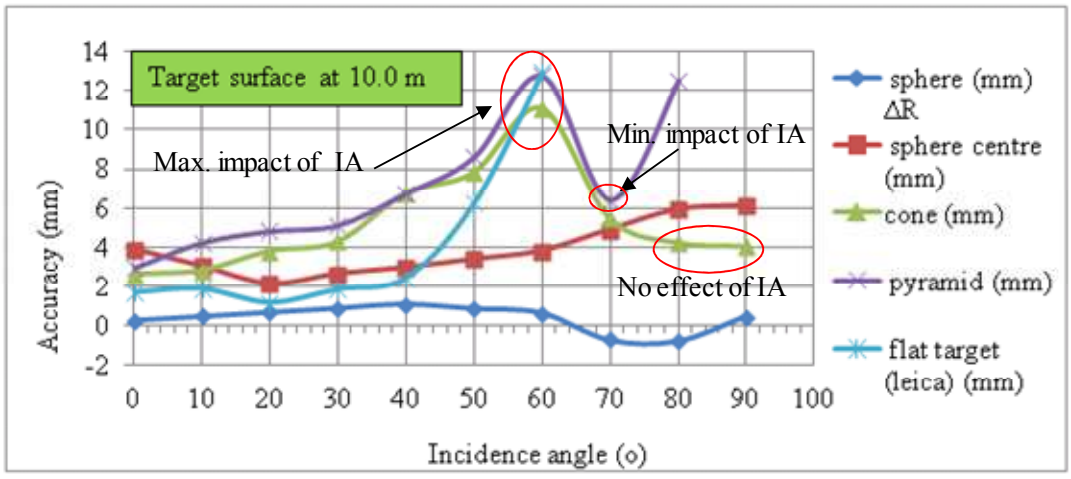

Figure 5-27: Accuracy Vs incidence angle with fixed range. And over 60°, the results of cone and pyramid target are fluctuated, due to its geometric shape.

Test2: The effect of range at a fixed IA (0^o)

The effect of the Range on the accuracy of each target centre/apex can be seen in Table 5.5 and Figure 5.28. The pyramid and flat targets are failed to register beyond the range of 60.0 m, whereas the accuracy of the sphere and cone targets is degraded beyond this range. At a range of 90 m, the sphere failed to register, as the number of points was less than required, while the cone is still worked (see Table 5.6). The full measurements of this test for both scanner HDS3000 and Faro focus can be seen in Appendix I.

Range (m) IA= (0^o)	Error sphere (mm) ΔR	Error sphere centre (mm)	Error cone (mm)	Error pyramid (mm)	Error flat target (Leica) (mm)
10	0.27	3.70	2.63	2.92	1.19
20	0.75	5.32	5.26	5.84	2.38
30	1.73	6.94	7.89	8.77	2.57
40	2.30	8.56	9.10	11.27	2.76
50	2.87	10.18	9.45	12.75	5.95
60	2.98	16.8	11.34	16.5	7.14
70	6.28	18.4	16.60	Fail	Fail
80	35.68	21.52	20.70	Fail	Fail
90	Fail	Fail	23.4	Fail	Fail

Table 5-5: Error Vs range with constant incidence angle and different ranges.

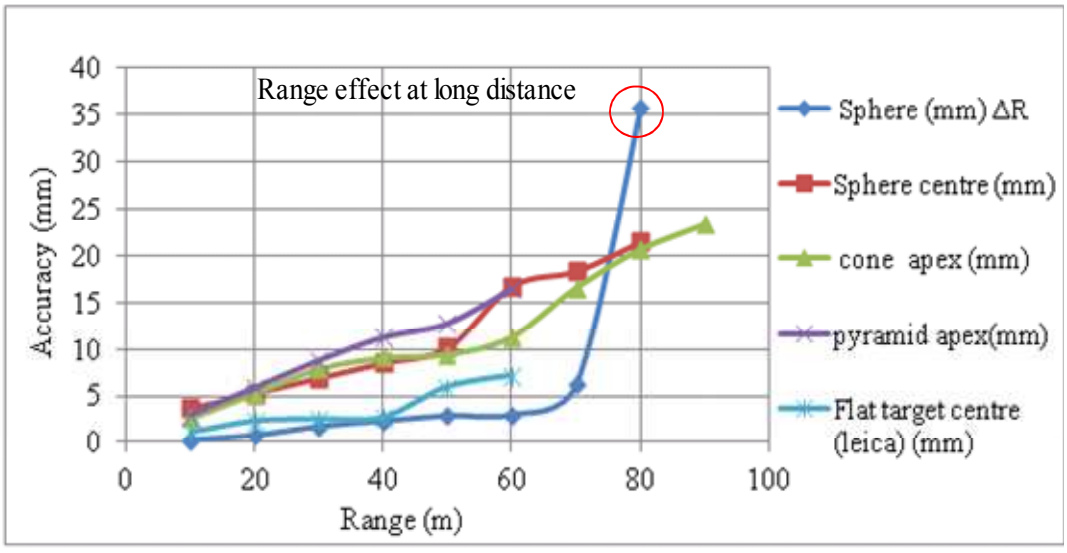

Figure 5-28: Accuracy Vs range with constant incidence angle of different targets.

The effect of range and IA on points per target can be seen in the Table 5.6 and Figure 5.29

Range with IA = 0	sphere pts/targ.	Cone pts/targ.	Pyramid pts/targ.	Leica flat pts/targ.
10	332	583	588	76
20	82	153	142	38
30	38	82	84	24
40	18	32	42	16
50	14	21	32	12
60	7	18	20	6
70	5	15	10	4
80	4	10	Fail	4
90	3	8	Fail	3
100	2	6	Fail	2

IA (deg.) with 10 m range	Sphere pts/targ.	Cone pts/targ.	Pyramid pts/targ.	Leica flat pts/targ.
0	307	667	818	56
10	307	667	796	56
20	307	667	775	56
30	307	627	753	56
40	307	587	731	56
50	307	576	664	52
60	304	564	598	40
70	301	533	346	Fail
80	296	435	70	Fail
90	222	181	Fail	Fail

Table 5-6: Range and IA Vs point per target. Left: Fixed IA (o) at different range Right: Fixed range at different IA.

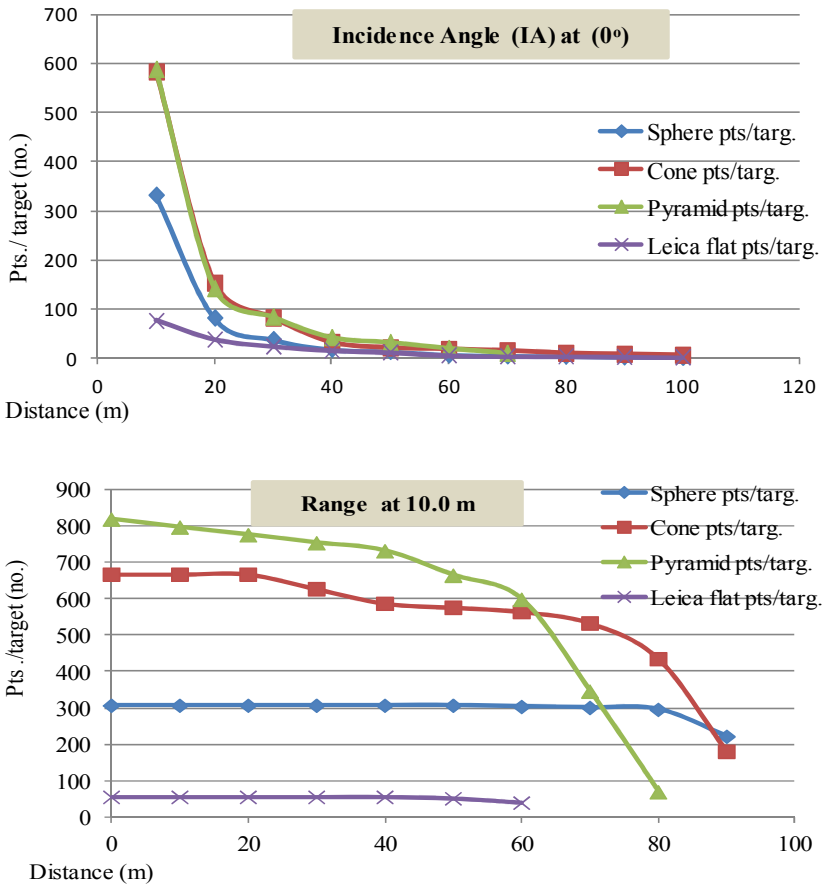

Figure 5-29: Range and IA Vs point per target.

Test3: The effect of IA in several distances from the scanner

In this test, different IA with different ranges, were investigated (see Figure 5.26). To begin with the effect of IA and range on the point per target, the result can be seen in Tables 5.7. The graphical representation of range placement of each target surface can be seen in Appendix J1. The effect of the IA at several ranges to the scanner in the accuracy of each target centre/apex can be seen in Figure 5.30.

Distance (m); IA = 0°	Cone	Pyramid	Sphere
10	711	900	332
20	182	225	84
30	82	100	38
40	44	63	21
50	32	53	14

Distance (m); IA = 20°	Cone	Pyramid	Sphere
10	702	895	333
20	178	226	84
30	80	100	33
40	40	51	21
50	28	39	14

Distance (m); IA = 40°	Cone	Pyramid	Sphere
10	658	782	333
20	138	194	84
30	62	74	34
40	34	49	22
50	26	37	15

Distance (m); IA = 60°	Cone	Pyramid	Sphere
10	514	570	332
20	136	189	84
30	61	69	39
40	27	33	21
50	19	21	14

Distance (m); IA = 80°	Cone	Pyramid	Sphere
10	443	373	333
20	129	166	84
30	53	41	32
40	19	Fail	21
50	12	Fail	14

Table 5-7: The effect of IA and range Vs point per targets.

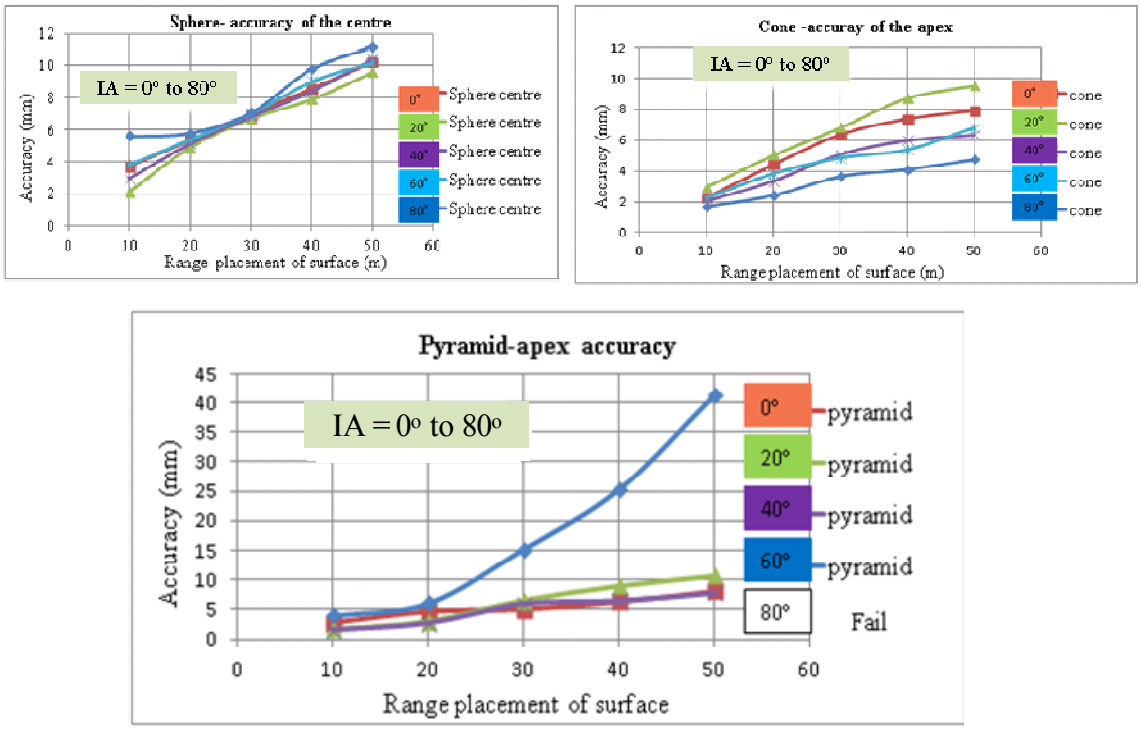

Figure 5-30: Accuracy Vs incidence angle at several distances to the scanner for different targets. Top left: Sphere surface, Top right: Cone surface, Lower: Pyramid 4faces.

Result analysis of test1

From Table 5.4 and Figure 5.27, the results show that the accuracy of the target centre/apex decreased with increasing the IA, except for the sphere target, which is not affected by IA.

The sub-millimetre error in sphere radius was obtained from a comparison between the computed radius and its actual value provided by the manufacture, as shown in Table 5.4, column 2. The sphere radius was computed using least squares fitting points to a target surface via different methods, such as average determination, Gauss Newton and Levenberg Marquedt (LM) algorithm. These methods are discussed in more details, in chapter 7.

For this test, the results of LM algorithm were used because they are more accurate than the others, which based on a combination of two methods (Steepest and Gauss method). The full statistical result obtained from this method can be seen in Appendix J2.

The reason behind using the radius of the sphere for comparison is the invisibility of the target centre. This is one of the limitations of the sphere target, where it has to be replaced manually with the prism kit, which can add an additional source of errors. In test 1, the sphere cannot be replaced by its prism accurately for measuring its centre, where it is fixed tightly on the board.

Test1 shows that the most accurate results were achieved by the sphere target. The cone is next with mm level even at 90^{o} IA, but its accuracy degraded with increasing the IA. The possible explanation is due to its geometric shape change, which might be affected by the laser beam, even in perpendicular IA. The pyramid comes next, and its accuracy fluctuated, where it failed at larger IA. The flat target provides high accuracy at small IA, but degraded with increasing IA and failed with IA greater than 50^{o}. Generally, the accuracy of Cone and Pyramid target are fluctuated, because of their geometric shape. As for flat target, the effect appears over 45^{o} where it failed at over 50^{0} IA (see Figure 5.27).

Result analysis of test2

The result of the second test shows that the further the range, the worst the accuracy achieved. The best targets were the sphere and the flat, while the cone and pyramid came next in this order. In other words, the pyramid and cone are slightly less accurate than sphere and flat target in term of normal IA and short range due to their shape properties. While at greater distances, of up to 70-80 m, all targets failed, except for the cone, which can be detected within 1-2 cm level of accuracy (see Figure 5.28).

From both Tables for the range accuracy results (see Appendix I, Tables I1-1 and I1-2), it can be seen that the error values (the difference between the laser scanning data for estimated target centres using a least squares surface fitting, with its considered actual value measured by total station readings) are negative. This indicates that the laser scanner considerers the target closer than it is. For the TOF HDS3000, the internal sensor is receiving the laser pulse in a shorter time than it should be for that distance. The Phase based Faro focus^{3D} is calculating a shorter shift in the phase than it should be. This could be down to a number of factors including the HRT, advance of the laser pulse due to the atmosphere, or an internal error in the range measurement system. The mathematical process of fitting laser point to target surface is introduced in chapter 7.

Result analysis of Test3

Table 5.7 shows that the point density of the cone and pyramid decrease with increasing the IA, while the sphere target has almost the same number of points at any IA. The further the range, the less the number of points can be obtained from each target surface. Figure 5.29 shows the accuracy of each target centre/apex separately (sphere, cone, pyramid) compared with its estimated value. As illustrated in the analysis of test1 and test2, the result of test3 for each target can be summarised as follows:

1. The flat target provides high accuracy at small IA between 0^o-40^o and at 10-30 m range but degraded with increasing IA failing at IA greater than 50^o. This is because the automatic detection of its centre was defined directly

through the laser scanner in the field. Over this range and IA the accuracy of its centre is degraded.

2. The cone is next at the same range and IA with mm level of accuracy even with 90 degree IA. The good result can be obtained.
3. The pyramid comes next with nearly 1 cm level accuracy, but degraded with increasing IA
4. The sphere target is the best one in all situations with sub-mm precision of its centre can be achieved, but it has less absolute accuracy in its invisible centre compared to cone target.

The cone target has been chosen as an optimal target to be used with MLS survey for the following reasons:

1. Easily calculated, where there is only one surface to be detected unlike the pyramid, in which each face must be detected individuality; this is discussed in chapter 6.
2. The cone can be detected and the apex can be calculated from any IA.
3. Only one colour can be used in the cone, making detection of the target easier (see chapter 6).
4. The cone shape is a combination of spheres and pyramid. Good fitting and intersection to identify its apex can be achieved, unlike sphere and pyramid. The pyramid is highly affected by IA, where each face needs to be fitted separately and then intersection of each fitted side determined, to get the apex accurately. This reduces the confidence in computing the apex. The more the series of operation, the more the error occurrence contribution in calculating the apex.
5. Finally, from an economic point of view, the cone is cheaper than the sphere and Leica target (e.g. the price of one 200 dia for normal sphere is approximately 500 GBP, whereas a cone is less than 150 GBP). In addition, the cone is more accurate than the sphere in term of absolute accuracy. However, in term of relative accuracy "precision of centre/apex", the quality of fitting of the sphere is more accurate than all targets used in this project (see Table 5.7), even after removing the effect of incidence angle from the targets used, such as cone, pyramid and flat target, the sphere is still the best.

6. The sphere could be more accurate than the cone if its centre measure by high precision survey technique leading to more cost, effort and time.

5.5.4 Removing incidence angle on the target surface

The effect of the IA in the precision of the target centre/apex, where the IA changes at a fixed distance can be seen in Table 5.8 and Figure 5.31.

The standard error (standard deviation of the residual "σ ") of fitting each target and define target centre/apex (see Table 5.8) was computed using the approach of least squares surface fitting, such as Levenberg Marqurdt, Gauss Newton and average determinations. These approaches are discussed in more details, in chapter 7. The range measurement deviation of each individual point from the estimated target surface can be calculated using the equation below (Soudarissanane et al., 2009).

$$ep = Rm \times N^T \quad \text{.....(5.5.4.1)}$$

Where, ep Represent the deviation of the range measurement of each individual point from the estimated target surface (This error includes the effect of range and IA).

Rm: Represent the mean deviation points to the plane defined by the normal vector (deviation between actual data and predicted data, i.e. surface residual).

N^T is the normal vector of the target surface. The standard error of fitting surface (σep) is calculated using Equation 5.5.4.2.

$$\sigma_{ep} = \sqrt{\frac{\sum ep^2}{n}} \quad \text{.....(5.5.4.2)}$$

Range=10m Incidence angle (o)	Sphere σxyz (mm)	Cone σxyz (mm)	Pyramid σxyz (mm)	Leica target σxyz (mm)
0°	0.54	0.48	3.1	1.36
10°	0.52	0.50	3.11	1.50
20°	0.50	0.53	3.13	1.65
30°	0.66	0.77	3.03	1.80
40°	0.83	1.01	2.93	1.95
50°	0.67	1.77	3.12	2.00
60°	0.52	2.54	3.32	2.05
70°	0.40	3.58	2.54	Fail
80°	0.41	5.48	2.01	Fail
90°	0.71	7.00	Fail	Fail

Table 5-8: Standard error of target centre/apex Vs incidence angle with constant range of different targets.

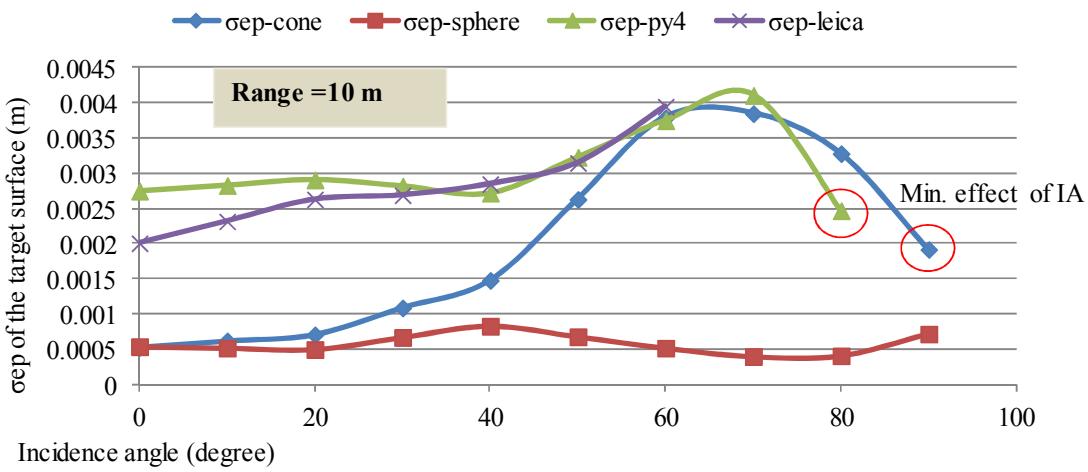

Figure 5-31: Standard error of the surface residual Vs incidence angle with constant range.

Figure (5.31) shows measurement precision with respect to the incidence angle of the targets surface, given a fixed scanner position, the standard total error of the targets (cone, sphere, pyramid and flat target) is plotted in blue, red, green and magenta, respectively. The incidence angle can be removed from the dataset depending on the IA coefficient (Cβ) of value ranging between 0 to 1 as defined in equation 5.5.4.3 (Soudarissanane et al., 2009).

$C\beta = \cos\beta; \quad 0 < C\beta < 1$ .....(5.5.4.3)

Where, cosβ is computed as expressed in Equation 5.5.1 for each individual point of each target used.

After removing IA from the dataset, the remaining effect is the range effect (ed) which was computed as expressed in equation 5.5.4.4.

The standard error of each individual point (ed) was computed following equation 5.5.4.5. (See Table 5.9 and Figure 5.32).

$$e_d = e_p \times cos\beta \quad \text{.....(5.5.4.4)}$$

$$\sigma_{ed} = \sqrt{\frac{\sum ed^2}{n}} \quad \text{.....(5.5.4.5)}$$

Range=10 m Incidence angle (o)	Cone after remove β (mm)	Sphere (mm)	Pyramid after remove β (mm)	Flat target after remove β (mm)
0°	0.48	0.54	2.10	1.36
10°	0.50	0.52	2.08	1.46
20°	0.53	0.50	2.06	1.57
30°	0.67	0.66	2.04	1.55
40°	0.81	0.83	2.01	1.45
50°	1.13	0.67	1.96	1.43
60°	1.45	0.52	1.94	1.60
70°	1.59	0.40	1.92	----
80°	1.65	0.41	2.01	----
90°	1.85	0.71	----	----

Table 5-9: The remaining standard error of the centre/apex after removing the incidence angle effect from each target surface.

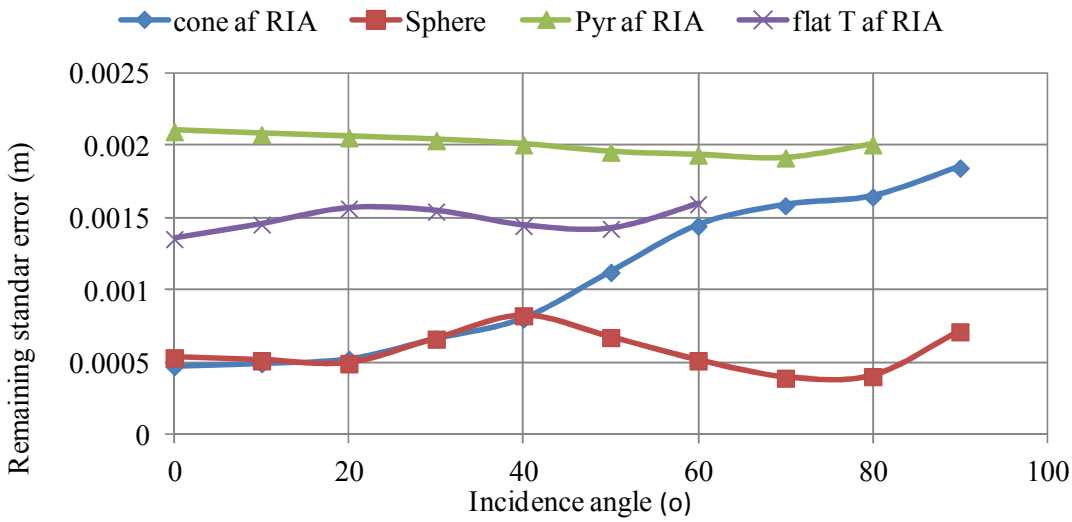

Figure 5-32: The remaining standard error of the surface residuals after removing the incidence angle (RIA) effect from each target surface at fixed range.

In the same way, the approach applied in test2 fixed IA with different ranges can be seen in Figure (5.33) and Table (5.10), and also applied in test3, the standard error of the effect of IA at several distances on the target surfaces can be seen in Figure (5.34).

Range (m) IA (deg.) = 0	Sphere σxyz (mm)	Cone σxyz(mm)	Pyramid σxyz(mm)	Leica target σxyz (mm)
10	0.54	0.48	3.10	1.36
20	0.86	1.49	5.30	2.95
30	1.82	2.12	6.65	5.44
40	2.42	2.83	7.58	6.85
50	3.64	6.38	8.54	8.16
60	23.25	6.81	10.24	Fail
70	Fail	8.10	Fail	Fail
80	Fail	10.89	Fail	Fail
90	Fail	22.08	Fail	Fail
100	Fail	Fail	Fail	Fail

Table 5-10: Standard error of the target centre/apex Vs range with constant incidence angle of different targets.

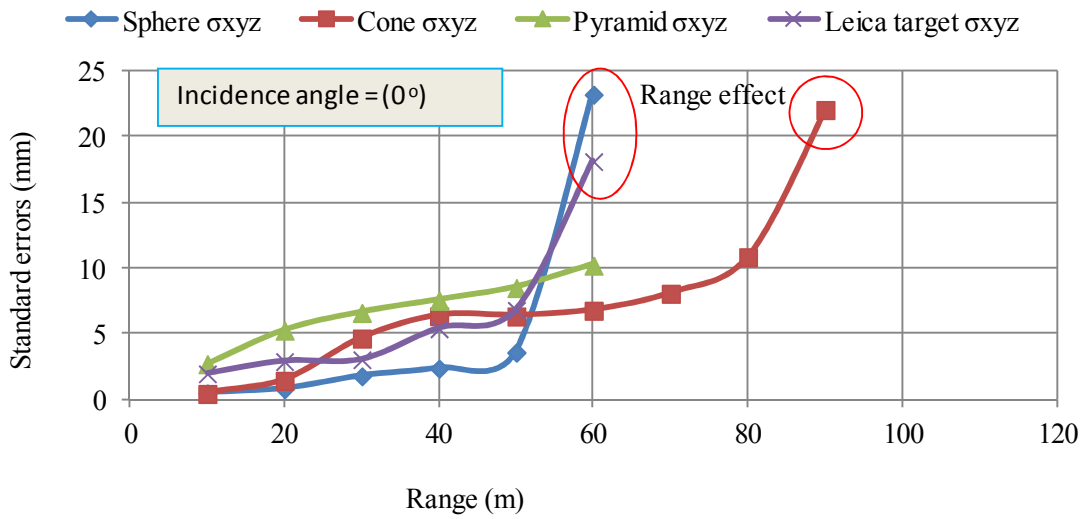

Figure 5-33: Standard error of the surface residuals Vs range with constant incidence angle.

The theoretical basis of target position accuracy and precision is introduced in more details in chapter 7.

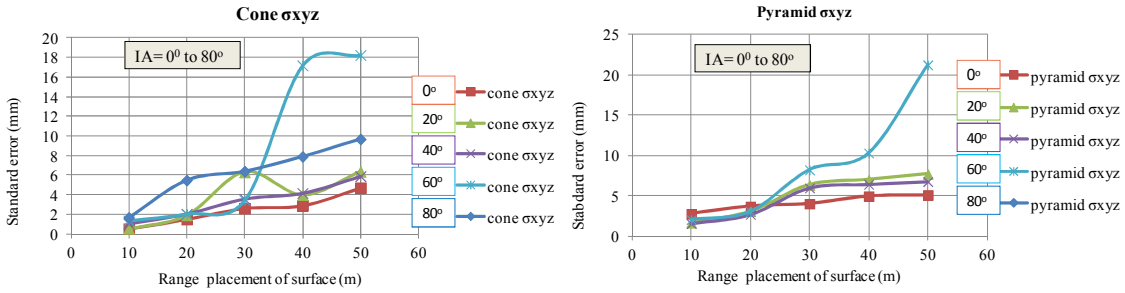

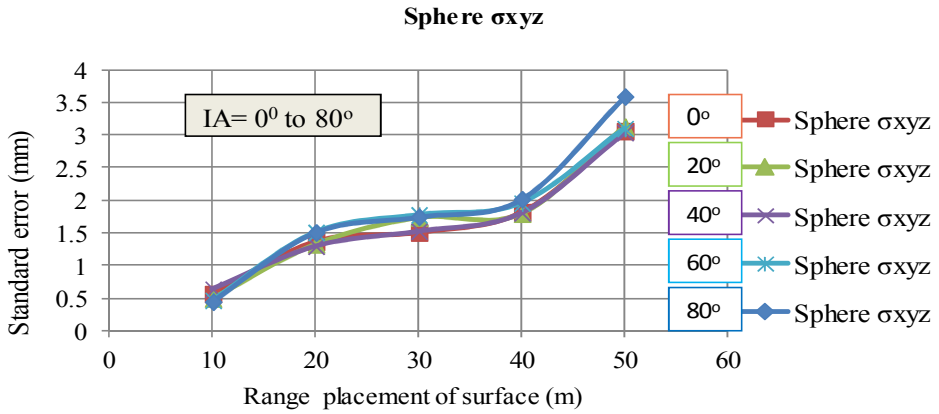

Figure 5-34: The effect of IA at several distances to the scanner Vs standard error of the target surface. Top: Sphere surface, Middle: Cone surface, Lower: Pyramid faces.

5.5.5 Result Discussion

The analysis of results of all three tests can be summarised as follows:

1. The results of different targets (cone, sphere, pyramid and Leica flat target) used in these tests shows

    a. The sphere target is the best, because is not affected by IA,

    b. The cone target is better than pyramid because it can be seen from any IA.

    c. The pyramid fails when IA equals the height angle of the target at (more than 50^{o} IA) and low points were obtained, which is negatively affected the quality of the apex determination (see Figures 5.27).

    d. The flat target is affected significantly with IA larger than 50^{o}. Figure 5.35 show the problem of IA with the Pyramid and Leica flat target.

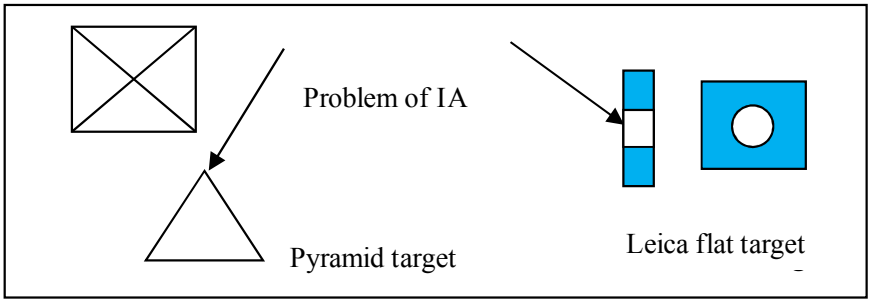

Figure 5-35: Problem of IA on the pyramid and flat target.

2. Although the targets cone and sphere would be seen from all rotation (0-80^{o}), the incidence angle of the beam from 45^{o} and more would be very steep, causing lower point density on the surface of the target and difficulty in automatic target centre identification (see chapter 6). As a result, the coordinate precision of this target would be poor as can be seen in (cone, pyramid and flat target, Figure 5.27 and Table 5.4). Flat target and pyramid with less than five faces will negatively affect the quality of self-calibration. For this reason, the cone and sphere are chosen, because they can be seen from any incidence angle, while the others should be placed somewhere to be scanned from approximately normal incidence angle.

The effect of incidence angle and range can be separated from dataset where they both occur at the same time. Due to the large incidence angle causes large measurement uncertainties (Soudarissanane et al., 2009). This was clearly showed in test3 achieved with different range and different IA using proper targets designed at the university, as mentioned in section 5.5.2.

5.5.6 The advantages and disadvantages of the target used

The advantages and disadvantages of the target used in this project can be summarised in Table 5.11

Target	Advantages	Disadvantages
Sphere	+ Is not affected by IA + Can be used for automatic registration of multiple scans with high accuracy at short distance + Only one colour needed, easy for detection and calculation + Only 4 point needed to determine its centre and radius + The solid surface is high reflective made it from "Spectralon" is a solid thermoplastic (e,g. Faro sphere)	- Invisible centre - Failed in automatic detection beyond the range 20 m by Faro SCENE software. - Very expensive - Noise measurements comes from the bottom of the sphere, because of its shape
Cone	+ Is not affected by high IA, good	-Need a highly reflective tape to cover

	intersection for its apex can be achieved at up to 90 m range and 90° IA. + Can be used in self calibration of MLS and merge multiple scans from different scans of the same area. + Only one colour needed, easy for detection and calculation + Only 7 points need to determine its apex, normal and angle between the normal and the direction to its apex.	its surface for automatic detection process. This can be solved by making it commercially using a solid thermoplastic like Faro sphere
Pyramid	+ Easy shape for computing apex, + Only 3 points from each face can define its apex (e.g., 3faces needs 9 points)	- Different colours needed for automatic detection, to separate each face. - Failed in high IA and high range up to 60 m and 60°
Flat target	+ For calibration and registration of point cloud at small range and areas. + The precision and accuracy of the estimated centre depends on the no., of points captured per target.	- Failed in steep IA greater than 45° - Needs a highly reflective tape to cover its surface for automatic detection process.
Others	+ Geometric primitives, such as (plane, point, line) give a good result at short distance and at normal IA	-All (plane, point, line) failed in steep IA and bad results in automatic registration of point cloud (see next section).

Table 5-11: The advantages and disadvantages of the target used in this project.

5.6 The advantage of multi-scans over single scan

In general, using multiple scans can solve many problems, for example, for image-based registration and for reconstructing high-quality textures for the output digital object to generate maps of high visual quality for the scanned objects (Bernardini et al., 2010). In addition, multiple scans can be useful for calibration of the MLS system to determine 3D offsets of the various sensors (typically known as lever arm offsets).

Another advantage of multi-scans is increasing the number of points; the more runs, the more points can be obtained, as described in chapter 4. It can also be used for joining scans together, where not all parts of the structure are visible from only one set-up (see section 3.4, and Figure 3.5).

In this test, the multiple scans approach was used for registering a point cloud based on a target and natural features from a single scan. The test was applied to investigate the accuracy of registration based on a target with multiple scans compared with a single scan.

5.6.1 Multiple scan trial

Two tests were undertaken with the TLS Faro Focus^{3D} to assess the registration of a point cloud based on natural reference points, such as a plane, line, corner point or rectangle and targets such as spheres, pyramids, Leica flat targets and a newly designed target cube with size 10x10 cm^2, and the effect on the results of combining multiple scans. The two tests were as follows:

1. Eight scans were used with different resolutions in different directions from the same position.
2. Three scans with the same resolution and quality were used from three different positions along the room.
3.

The method adopted for these tests was based on the perfect target with the centre known exactly, before and after carrying out the actual scan. Both tests were undertaken under favourable conditions, predominantly inside buildings at temperatures between 15◦ and 20◦C. These tests include common references, which are natural references and targets. A Trimble robotic total station (TRTS) was used to measure the local coordinates of the targets within ±1mm level of accuracy.

The scan settings for the cases were established to a different resolution, as shown in Table 5.12. The scanner does not allow the resolution to be set in terms of point spacing at a particular distance (e.g., resolution 1/4 is 6.136 mm at 10 m).

Considering that the ranges recorded were shorter, especially for manually fixed targets, a spot spacing of about 4 mm was obtained. The maximum distance from scanner to the target was 7 m, and the minimum was 3 m. This means that the spot spacing between the targets and the scanner varied, as shown in Figure 5.34.

Resolution	Quality	Speed (ktp/sec)	Net scan time (full scan)	pt/360°
1/4	3x	244	0:03:35	10,240
1/4	4x	122	0:07:09	10,240
1/5	4x	122	0:04:35	8,192
1/8	4x	122	0:01:47	5,120
1/8	6x	122	0:07:09	5,120
1/10	4x	122	0:01:09	4,069
1/16	4x	122	0:00:27	2,560
1/32	4x	122	0:00:07	1280

Table 5-12: Resolution and quality of each scan used in simulation.

The scan can contain several millions of points and with full resolution (1/1) a correspondingly large memory is required. Therefore, the maximum resolution was started in (1/4), and considered as full resolution, as shown in the first column of Table 5.12. The second column explains the quality of the scanned point; 4x indicates that the same point was scanned four times and the average of points was taken. The speed of measurement per second and the net time of the full scan in columns 3 and 4 depended on the resolution and quality settings selected. Scan per 360◦, as shown in column 5, refers to the points captured per revolution.

The reason for using eight scans instead of two was to evaluate the influence of different resolutions on the natural target and the designed target.

5.6.2 Test description

The experiments were established in two laboratories at NGI, University of Nottingham. The first test contains the reference objects, 7 spheres and 5 pyramids; 5 spheres had a diameter of 145 mm, and the others had a diameter of 200 mm. The smaller spheres were used for the registration of multi-scans, and Faro SCENE

software was used to detect the spheres automatically from each scan at different resolutions. Then, these scans were combined. The larger spheres were used as a control value with the other reference values to assess the quality of registration. The remaining reference object points such as cubes and pyramids are considered as check points (see the distribution of the spheres and other targets in Figure 5.36, top). The second test used the same targets, as shown in Figure 5.36, bottom.

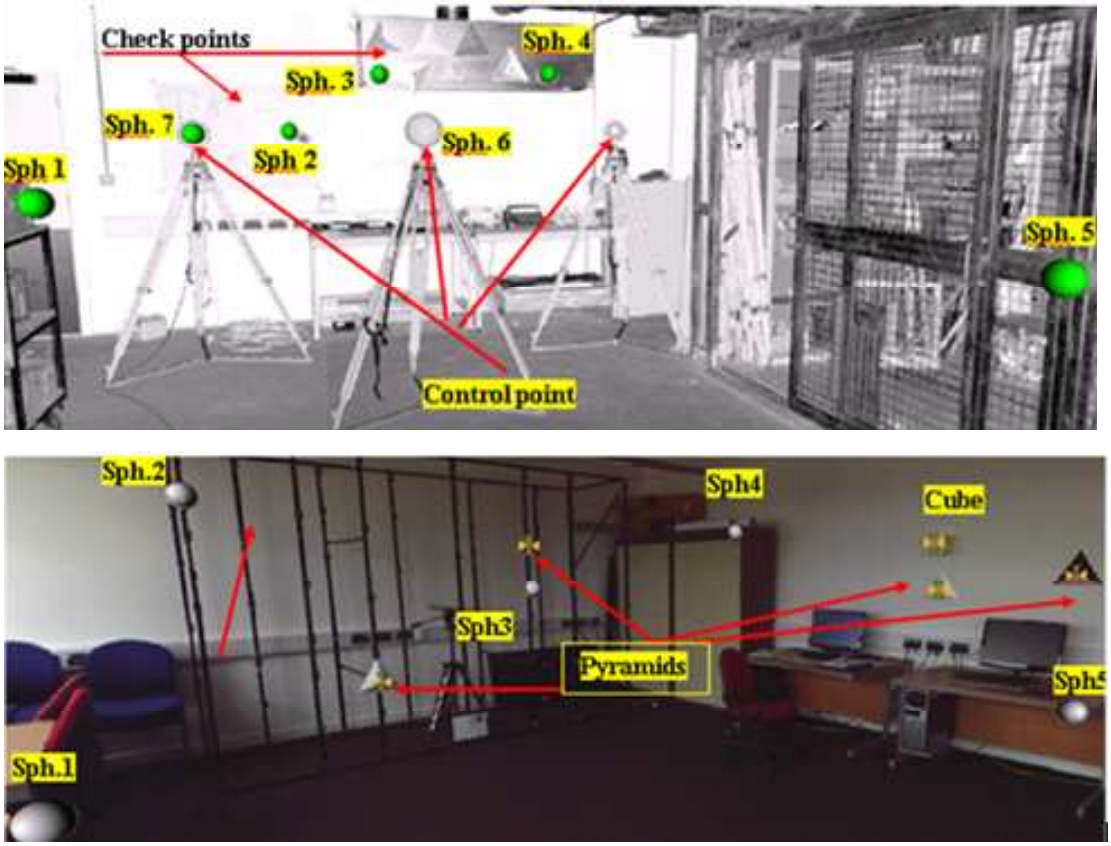

Figure 5-36: Distribution of targets in two locations. Top: test in the surveying lab includes spheres, control point and check point. Bottom: test in the photogrammetric lab with the same targets.

5.6.2.1 Test 1 - results and discussion

1. Accuracy of registration using sphere targets

In this test, the accuracy of the target centre/apex through the registration of eight scans at different resolutions and angles was investigated. Spherical targets (145

mm) were used for registration of eight scans. During the registration process, the laser scanning software (Faro SCENE) computes an optimal alignment between the point clouds based on the best fit of the common geometrical objects (spheres).

The registration accuracy depends on the geometry and the overlapping area, as described in chapter 3. The statistical results of the registration scans, obtained automatically on demand through Faro SCENE software, are given in Table 5.13.

Scan cluster	Resolution quality	Detected spheres	Mean residual (mm)	Object fit	Scan result (mm)
Scan1	1/4 – 3x	4	1.00	Scan fit	Mean residual = 0.80 Deviation Residual=0.90 Min.residual = 0.00 Max.residual = 4.10
Scan2	1/10-4x	5	0.80	Scan fit	
Scan3	1/16-4x	3	0.60	Scan fit	
Scan4	1/32-4x	3	1.10	Scan fit	
Scan5	1/4-4x	5	0.70	Scan fit	
Scan6	1/8-6x	5	0.70	Scan fit	
Scan7	1/5-4x	4	0.70	Scan fit	
Scan8	1/8-4x	5	0.70	Scan fit	

Table 5-13: Scan results.

In Table 5.13, the mean residual in column 4 is the average discrepancy in the overall coordinate systems between the position and orientation of all corresponding reference objects of each registration. The results of each registration scan were obtained at a millimeter level of precision up to 0.7 mm, except for scans 1 and 4, which were within one millimeter, as shown in column 4. So, scans 1 and 4 seem not to be optimal. This is attributed to the lower quality of data capture, low resolution of the scan and the number of detected targets. For example, the number of common objects (spheres) detected was less than in the other scans (column 3 in the table). The mean residual obtained for corresponding sphere targets is 0.8 mm, and the deviation of all corresponding objects is 0.9, while the maximum residual is 4.0 mm.

2. Accuracy of target centre/apex from single and multiple scans

Targets	No.	Scan1	Scan2	Scan3	Scan4	Scan5	Scan6	Scan7	
		1/4- 4x (4x4) mm	1/5- 4x (4.5x4.5) mm	1/8- 4x (7x7) mm	1/8- 6x (7x7) mm	1/10- 4x (11x11) mm	1/16- 4x (17x17) mm	1/32- 4x (22x22) mm	All scans
		σΔE, ΔN (mm)	σΔE, ΔN (mm)	σΔE, ΔN (mm)	σΔE, ΔN (mm)	σΔE, ΔN (mm)	σΔE, ΔN (mm)	σΔE, ΔN (mm)	σΔE, ΔN (mm)
Sphere	2	1.54	1.73	2.02	1.56	3.27	7.06	11.2	1.5
Pyramid	7	1.71	1.75	1.83	1.76	2.01	5.79	-----	1.75
Cube	1	2.11	2.32	2,59	2.16	2.54	2.69	-----	2.2
Circular target	1	1.44	1.57	1.93	1.52	1.99	-----	-----	1.30
Corner pt.	6	15.71	16.66	28.42	17.89	38.87	-----	-----	16.0

Table 5-14: Accuracy of the horizontal components of the centre/apex vs. single and multi-scans.

Targets	No.	Scan1	Scan2	Scan3	Scan4	Scan5	Scan6	Scan7	All scans
		1/4- 4x	1/5- 4x	1/8- 4x	1/8- 6x	1/10- 4x	1/16- 4x	1/32- 4x	
		σΔh (mm)	σΔh (mm)	σΔh (mm)	σΔh (mm)	σΔh (mm)	σΔh (mm)	σΔh (mm)	σΔh (mm)
Sphere	2	2.15	2.77	2.92	2.09	3.49	19.06	21.2	1.90
Pyramid	7	1.86	1.25	1.32	1.93	2.51	11.79	-----	1.80
Cube	1	1.21	1.62	2,21	1.18	2.19	5.69	-----	1.20
Circular target	1	1.44	1.57	1.93	1.52	1.99	-----	-----	1.40
Corner point	6	7.69	8.32	14.28	9.99	18.88	-----	-----	7.0

Table 5-15: RMS error of height on the target centre/apex at different resolution scans after geo-referencing.

5.6.2.2 Test 2 - results and discussion

Testing targets with registration of point clouds

a. <u>Registration using spheres</u>

In this test, the same size of sphere target was used for registration of three scans taken along the room in different positions (see Figure 5.36). In order to perform a

registration, it is necessary to identify common points between scans (see chapter 3). For this purpose, targets are placed in each scan. These targets are used to calculate the parameters of a 3D conformal transformation that will register the three scans to a local survey grid. The results can be seen in Table 5.16. The results for the corresponding sphere targets can be seen in Table 5.17.

Scan cluster	Mean residual (m)	Object fit	Scan result (m)
Scan1	0.0021	Scan fit	Mean residuals = 0.0021 Déviation residual = 0.0010 Min residual.=0.0000 Max residual.=0.0032
Scan2	0.0021	Scan fit	

Table 5-16: Scan result along the room.

References	Residual (m)	Scan	
Sphere 1	0.0032	Scan1	Scan2
Sphere 2	0.0026	Scan1	Scan2
Sphere 3	0.0023	Scan2	Scan1
Sphere 4	0.0023	Scan2	Scan1
Sphere 5	0.0021	Scan1	Scan2

Table 5-17: Results for the corresponding spheres.

b. Registration using sphere, pyramid and cube

Using the sphere, pyramid and cube, poor results were obtained from the automated algorithm because the selected targets (pyramid and cube) were not recognised by the software. Therefore, these were considered as objects and their centres were defined manually. The results can be seen in Table 5.18, and the detailed results can be found in Appendix M-M1.

References	Target detection in both scans		Correspondence view	References
	Scan 1	Scan 2		
Sphere	5	5	5	Mean residual = 0.0092 Deviation residual = 0.0068 Min. residual = 0.0000 Max. residual = 0.0232
Pyramid	7	7	7	
Cube	1	1	1	

Table 5-18: Scan results of mean residual values for three reference objects.

c. Registration using sphere and natural features

Using four geometric objects (sphere, corner point, line and rectangle) as a reference for registration of two or multiple scans, the quality of the result was reduced. Then, all the available reference objects were used, for automatic detection using Faro SCENE software, and poor results were obtained again, as shown in Tables 5.19 and 5.20. This is because the automatic search for targets detection was unsuccessful. The specification of Faro Focus^{3D} recommends avoiding using planes, lines, pipes, etc., for automatic registration scans (User manual, 2011). A screenshot of the results obtained electronically is shown in Appendix M-M2.

References	Target detection in three scans			Correspondence view	Scan result (m)
	Scan 1	Scan 2	Scan3		
Corner Point	70	70	70	8	Mean residuals = 0.0244
Rectangle	21	30	29	5	Deviation residuals = 0.0188
Sphere	All	All	All	All	Min residual.= 0.0000
Line	393	499	523	None	Max residual = 0.0539

Table 5-19: Scan result of mean residual value for four reference objects.

References	Target detection in both scans		Correspondence view	Scan result (m)
	Scan 1	Scan 2		
Corner Point	70	70	5	Mean residuals = 0.0240
Rectangle	30	4	1	Deviation residuals = 0.0240
Sphere	All	All	All	Min residual = 0.0000
Line	367	306	None	Max residual = 0.1049

Table 5-20: Scan result of mean residual value for all references available.

From the above results, it can be seen that with the automatic registration of the point cloud using the sphere as a reference point, a good result can be achieved (see Table 5.16). In order to determine the quality of the corner point, line, plane and rectangle, when used as reference objects in automatic detection for registration of the point cloud, these reference objects were tested separately and compared with the sphere. The results are shown in Table 5.21.

References		Target detection in three scans			Correspondence view	Scan result (m)
		Scan 1	Scan 2	Scan3		
Sphere	Corner point	70	70	70	8	Mean residuals = 0.0101 Deviation residuals = 0.0077 Max. residual = 0.0220
	Rectangle	21	30	29	5	Mean residuals = 0.0128 Deviation = 0.0097 Max. residual.= 0.0261
	Line-manually selected	10	10	10	10	Mean residuals = 0.0048 Deviation = 0.0037 Max. residual.= 0.0106
	Plane-manually selected	10	10	10	10	Mean residuals = 0.0032 Deviation = 0.0024 Max. residual.= 0.007

Table 5-21: Statistical results of each natural reference object with the sphere separately.

References	No. of detecting objects	Correspondence view	Mean value overall residual (mm)	Deviation overall residual (mm)	Min (mm)	Max. (mm)
Sphere	7	7	1.5	1.0	0.0	3.2
Corner Point	70	8	20.0	14.0	0.0	100.0
Rectangle	30	5	22.2	17.0	0.0	102.0
Planes	188	13	4.0	3.5	0.0	10.0
Lines	393	None				
Pyramids	7	None-7 manually	7.3	5.3	0.0	18

Table 5-22: Statistical results of each reference object used alone in registration.

Table 5.22 shows the result of registration with different reference objects. The average residuals of each registration are calculated as shown in the fourth column; the lower the value, the better the registration result.

In these results, the natural reference objects (corner point and rectangle) seem not to be optimal in the automatic registration process. The distance between the positions of the two reference points serves as input for the calculation of the residual value. Values close to zero indicate a good registration result. Reference pairs can be easily identified, which can cause problems in the registration. In the table, columns 4, 5 and 6 indicate the deviation, minimum and maximum of the overall residual, respectively.

5.6.3 Result discussion

In the accuracy tests, comparing different scan resolutions and different methods of registration were discussed. The relationship between accuracy and the resolution was tested; using different targets at different resolutions (see Tables 5.14 and 5.15).

Referring to the result of the registration process, an increase in the number of targets, over the minimum of three points normally required, improves the registration accuracy. The accuracy of registration deteriorates from 1 mm to 20 mm with 6x6 sq. mm and 30x30 sq. mm resolution, in that order.

5.7 Conclusion

This chapter discussed the use of different control targets, namely a cone, pyramids, dots and ring designed for improving MLS data in urban areas. A number of trials were performed to determine the most favourable target. The results confirmed that the optimal targets are the cone and sphere. The cone was chosen as an optimal target; its magnetic mount and the 15 cm radius (r) of its circular base and slant height equal to 2r compose a good intersection in the apex. This can provide sufficient accuracy from a point density of about minimum 9 pts / target at 90 m range (see Table 5.5).

The effects of incidence angle and range on the target design were investigated in a series of trials, and the results showed again that the cone and sphere are the most favourable targets to use for improving the MLS data. But analysis of the results shows that the sphere has less accuracy than the cone in terms of calculating its centre (see Tables 5.4 and 5.5).

The achievable positioning accuracies of the apex of the proposed pyramid and cone designs, obtained by testing different laser point densities, are around 2mm in the horizontal and vertical positions. The accuracy of the determined target position in the laser point cloud depends on the point density and point distribution as well as the height-to-base ratio (height/base). The accuracy of the apex fell by approximately 17% when the height of the pyramid was reduced by 1 cm (see section 5.4.1.2).

The surface reflectance test found that the best surface to scan was the matt white surface, which gave the highest signal return, and the precision standard deviation of the quality of fitting a point to a plane was 1.1mm (see section 5.4.2.2). The gloss black surface, on the other hand, gave the weakest signal return and the lowest precision. The return was so poor for the gloss black that large portions from the surface point were not recorded (see Figure 5.17).

The effect of the scan resolution on the quality of the scan points and registration was investigated using simulation tests in the NGI lab. The findings show that the registration of multiple scans achieves better quality results using targets. It is necessary to ensure that there are enough reference objects in the scans before actual scanning takes place; this prevents problems during registration of the point cloud. Although registration can be done purely on the basis of natural targets, enhancing the scanned environment by using additional 3D reference objects, such as cones, spheres, and pyramid targets, is necessary.

Moreover, it can be concluded that the spheres and other manually selected targets provide more registration information than planes or lines, corner points and rectangles (see the visual inspection in appendix M) as the automatic workflow cannot identify the exact location of the object of the same size in two or more scans. It is recommended to avoid using automatic correspondence search for planes (User manual, 2011). In addition, targets placed symmetrically, as in most trials, are not detected whether in automatic or manual search. Moreover, the distance between references should not be less than 1m in automatic detection using Faro SCENE software.

Generally, the registration process achieved more precise results when targets were manually placed in the vicinity of the overlapping area (see the tables of section 5.6.2). One major burden in the registration process is to find the corresponding objects. Therefore, at least four or five corresponding references in a scan should be available. However, a higher number of object matches per scan may improve the results of the correspondence search and will make registration easier and less error-prone.

CHAPTER6: AUTOMATIC DETECTION OF TARGETS

This chapter provides a detailed description of the proposed automatic workflow for detecting and analysing the results achieved for the three designed targets (cone, pyramid, and dot) and comparing these with the sphere target designed by the manufacturer. The main sections describe and analyse the algorithms for detecting a target automatically from the entire point cloud, as well as detecting targets of the same shape in the same cloud. The individual stages have been designed to address the issues introduced in the recognition criteria process, with the potential view to be fully automated. Finally, the advantages and disadvantages of the algorithm used and a summary of the results will be given.

6.1 Introduction

The creation of an automatic workflow (see Figure 6.1) to detect and measure the proposed 3D custom targets (pyramid, dot and cone) from surrounding objects in the laser point cloud is an essential task because a lot of commercial software packages such as Faro SCENE v. 4.1 (2011) and Cyclone software v. 6.0, are unable to detect and measure custom-made targets automatically.

Matlab-based algorithms have been produced to detect all the targets appearing in the point cloud and to calculate the centre/apex of each target automatically with a high level of accuracy.

6.2 Algorithm description

Two scripts programs (UNT1 and UNT2) were written using Matlab functions (see Appendix K). The algorithm contains two parts. The first part is automatic detection of the target from surrounding objects in the laser point cloud. The second part is computing the centre/apex of the detected target; this part is discussed in more detail in the next chapter.

The first part of the program is to detect the targets, specifically the pyramid, dot, cone and sphere, and any other target. This part is based on three criteria: intensity range values, distance between points and the size of the target. The distance between points should be equal to or less than the size of the target. The target itself should be one third of the background size. The reason for using the background is to make sure all points used to calculate the target centre/apex are located inside the target. These conditions are discussed in the next section.

The second part of the program, computation, uses the following algorithms:

- Plane intersection algorithm for use with the pyramid faces.
- Line intersection algorithm for use with the dots target.
- Least squares surface fitting using three methods for fitting the line, plane, cone and sphere, which are average determination (AD), and the Gauss Newton (GN) and Levenberg Marquardt (LM) algorithms.

The fitting process of the methods above is described in more detail in the next chapter.

6.3 How the algorithm can detect the target

The targets, the pyramids seen in Figure 6.1, have between three and eight faces. One face of each of them was covered with high reflectivity tape (HRT) except for the octagon-based pyramid, four faces of which were covered with HRT. The reason for using HRT is that this colour is rare and highly detectable from surrounding environments. Therefore, it can provide a good initial step in the detection process**.** Using four faces will ensure that this colour will be seen from any incidence angle (i.e. the orientation of the target relative to the laser scanner).

The first step is to detect the points with HRT from the point cloud. This detection is based on the range of the intensity of this colour which was determined previously (see section 5.4.2).

These points will be divided into groups, with each group including only those within a distance of 30 cm (the length of the target) from each other. From Figure 6.2, assume six groups will be found. Then, points in the other four colours (black (BC), dark grey (DC), green (GC) and white (WC)) will be tested to find which one is close to each HRT group within the same 30 cm range. If there are no points from the four colours surrounding the HRT or there is only one colour surrounding the HRT, these groups will be neglected because there is no possibility of them being a target (see Figure 6.2).

A further check involves the points in the other colours surrounding the HRT groups being tested to ensure that the distance between them is no greater than 30 cm (the length of the target). Points lying outside this range will be deleted.

Here, the benefit of the background of the target will be clear. If the target is used without the background, some point from outside the target might be used in the calculations to find the centre/apex, but the background helps to avoid that.

At the end and based on the number of points expected from the target, the detected groups will be specified as targets or not. The number of points depends on several factors, such as the density of the point cloud used in the laser scanner, the distance between the target and the laser scanner and the incidence angle, as described in the previous chapter.

The above procedure can be summarised as follows

- Find the points of HRT
- Divide these points into groups each of which could be a target (points of HRT)
- Find the other colours (BC, DC, GC and WC) surrounding the HRT within the length of the target for each group (30 cm)
- Apply the distance condition of 30 cm between the three colours
- Apply the conditions of the number of points per target that it is expected to capture from the laser scanner (see section 4.2.1)
- Calculate the centre/apex of the target.

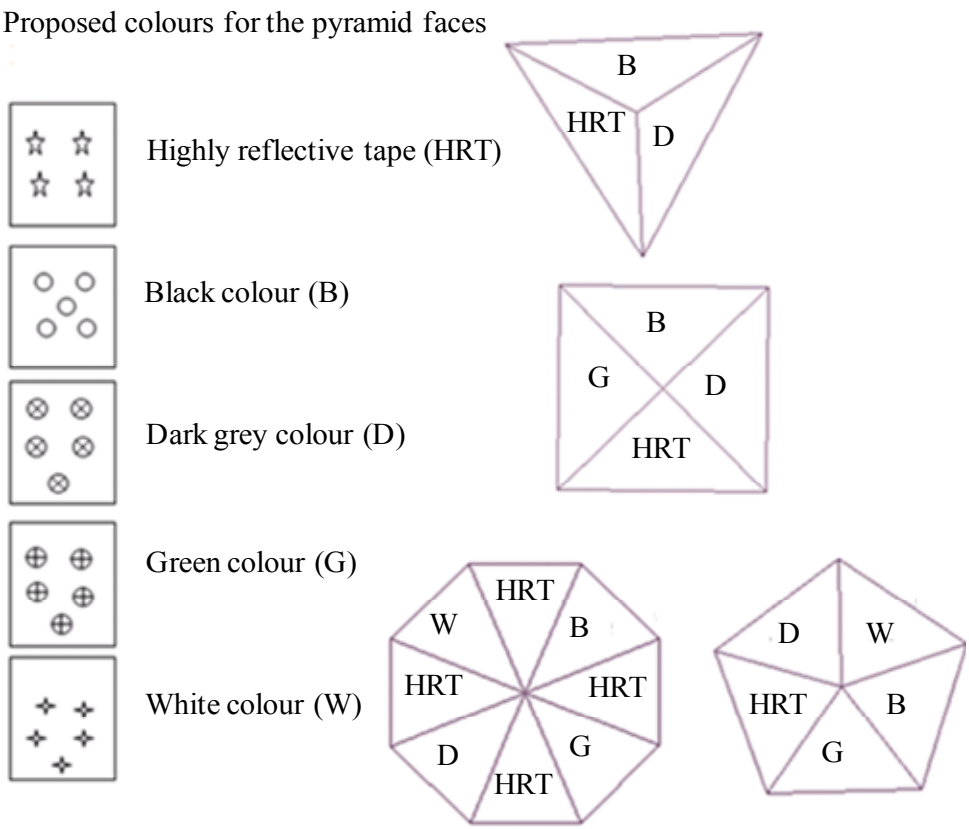

Figure 6-1: Regular pyramid targets. Left: target colours list (HRT, BC, DC, GC and WC). Right: triangular, square, pentagon and octagon based pyramids covered in different colours. One face of each target is covered by HRT except for the octagon, 4 faces of which are covered in HRT.

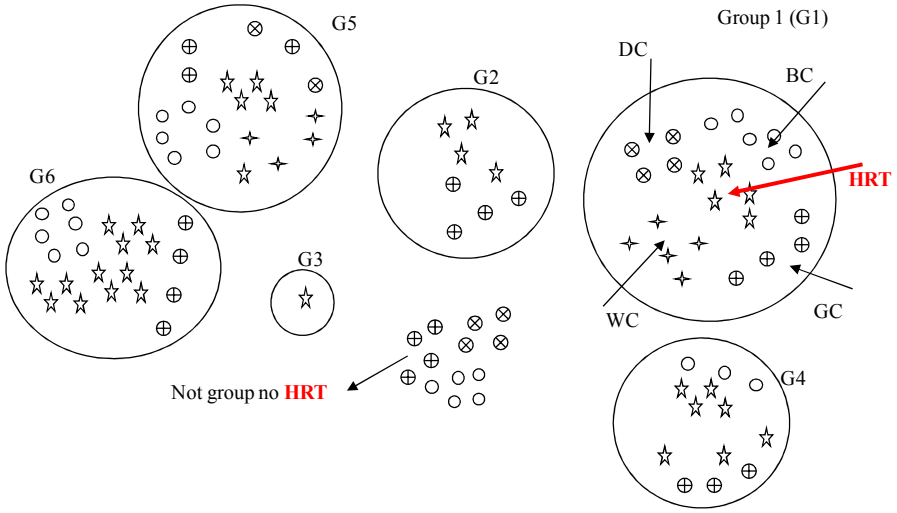

Figure 6-2: HRT group and its surrounding points in the laser point cloud.

Using the HRT can help to make the program faster than searching the entire point cloud to detect the target. In any direction, at least three faces can be obtained from the eight visible faces. The more faces, the better the accuracy that can be achieved. The disadvantage of this algorithm is that it fails with low point density on the target surface, when the number of points outside the target is greater than the number inside. Then, the algorithm detects the wrong target position. Therefore, even with eight faces the program will create a lot of groups and cannot predict exactly which group is a target or not. In this case, further development is necessary.

The program can work successfully:

- When the target is completely visible in scan data or a minimum of three faces are visible in the laser point cloud; the more faces, the better the accuracy that can be achieved.
- When the incidence angle is less than 50^{o}, particularly for flat targets and the triangular based pyramid.

The program fails:

- When the incident angle is very steep to the target, decreasing the number of detected points. As a result, the coordinate precision of this target will be poor, negatively affecting the quality of the apex determination.
- When the colour of the background clashes with the colour of the target; the target will fail in automatic detection.
- When each face of the target has less than three points, such that the target center/apex cannot be calculated.
- When only two faces of the target are visible, causing the program to fail to compute the apex.
- When the effect of light and shadows on the target surface and its background are different, especially when three faces are visible.

Statistical result

The precision estimate and external error determination of the target centre/apex are evaluated. This is achieved as follows:

- The standard deviation of each fitted side of the pyramid target is calculated.
- Least squares surface fitting of a best-fit plane/line to a set of data.

- Comparison of the computed apex with its control value.

The algorithm developed through Matlab functions was tested on two types of target: pyramid and dot. For the test, the following steps were performed:

Step 1: Data acquisition of an area using the Leica Terrestrial Laser Scanner (TLS HDS3000). The data was then converted and saved in a .txt file, containing (X, Y, Z) and coordinates, and the intensity value as reflected from the surface. The number of points in the cloud was 60801, at a scan resolution of 1x1 cm.

Step 2: Plotting the point cloud of an area containing the pyramid target (see Figure 6.3).

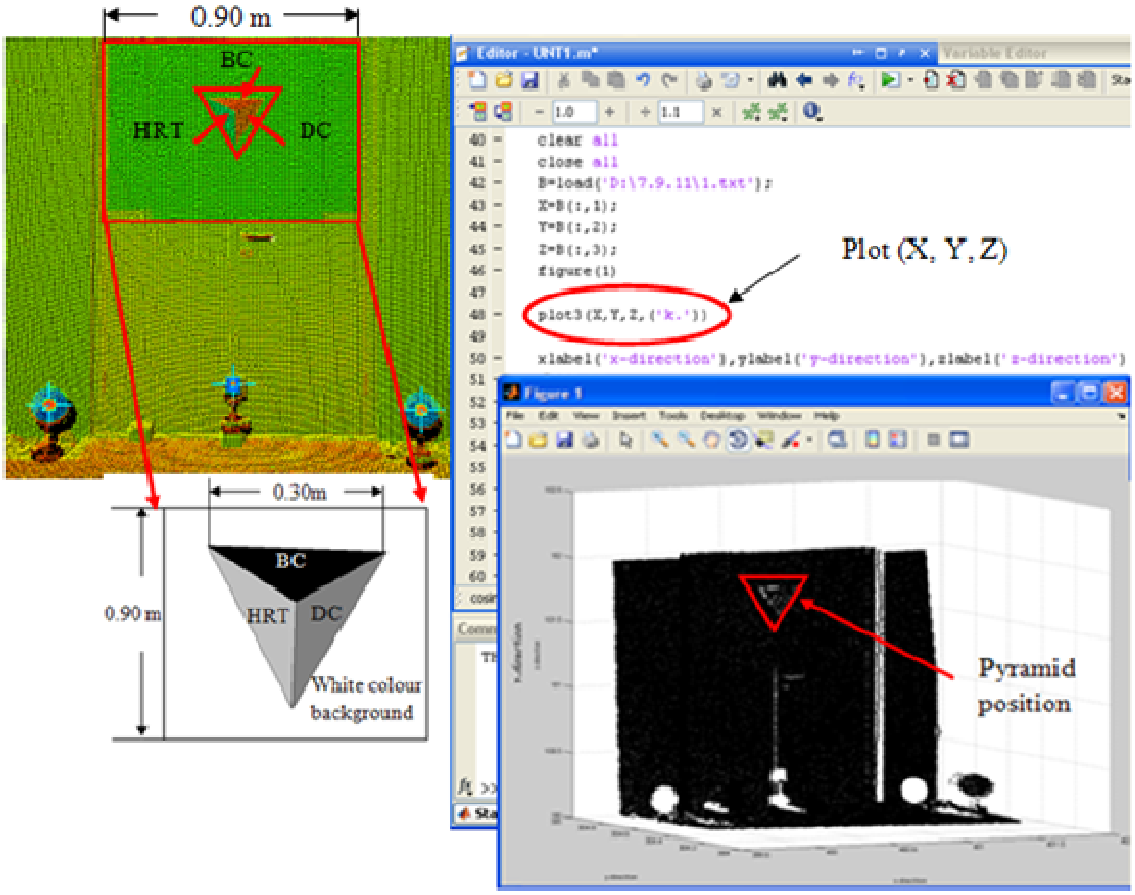

Figure 6-3: Point cloud of part of an area (top left) containing the pyramid target (bottom left), and its appearance in the point cloud using Cyclone software v.6; the figure on the right was drawn using Matlab functions.

Step 3: The points of the pyramid target and the surrounding point cloud are detected and isolated according to their intensity value. The program then finds the two initial points inside the target, as depicted in Figure 6.4.

```
clear all
close all
B=load('D:\7.9.11\1.txt');
X=B(:,1);
Y=B(:,2);
Z=B(:,3);
figure(1)
plot3(X,Y,Z,('k.'))
xlabel('x-direction'),ylabel('y-direct
grid on
figure(2)
B1=find(B(:,4)<-337&B(:,4)>-412);
C=B(B1,1:3);

plot3(C(:,1),C(:,2),C(:,3),'k.')
hold on
grid
B2=find(B(:,4)<-232&B(:,4)>-323);
D=B(B2,1:3);

plot3(D(:,1),D(:,2),D(:,3),'r.')
B3=find(B(:,4)>170&B(:,4)<280);
E=B(B3,1:3);

plot3(E(:,1),E(:,2),E(:,3),'b.')
xlabel('x-direction'),ylabel('y-direction'),zlabel('z-direction')

% finding the first point in the target
```

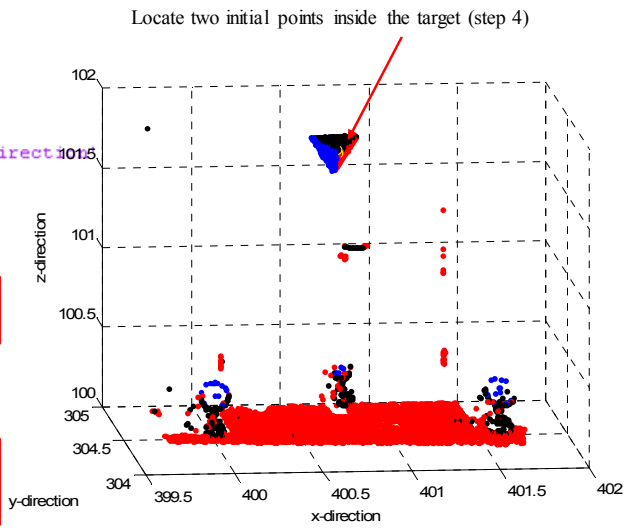

All 3D points in Matrices C, D and E are plotted

Figure 6-4: The target and surrounding point cloud with the two initial points located on the target.

Figure 6.4 shows a plot of all the points in matrices C, D and E for black, grey and highly reflective surfaces respectively; for example, plot 3 (C(:,1), C(:,2), C(:,3), 'k.'): This statement will plot the points on the target, and all other points which have the same intensity value. The symbols ‘k.’, ‘r.’ and ‘b.’ represent black, red and blue in the Matlab colour chart, respectively.

The three matrices of the point cloud with the same intensity values are created, such as C [ ] for black; D [ ], for dark green, presented in red and E [ ], for high reflective tape (HRT), presented in blue colour. These colours, reflected back to the scanner, contain blue, green and red (BGR) channel. These BGR were fixed by the manufactures of the HDS3000 scanner, where the single intensity value for a point has blue, green and red for high, medium and very low intensity values, respectively. The size of each matrix after filtering is as follows:

Size of C [ ] = 418*3

Size of D [ ] = 3235*3

Size of E [ ] = 185*3

Step 4: Finding the first point in the target in order to isolate points on the target from those which have the same intensity value, depending on the fact that the distance between the points with the different colours inside the target is equal to or less than the length of the pyramid target. This was achieved as follows:

1. Create an empty matrix, M [ ].

2. Compare each element in matrix C [ ] with those of matrix E [ ], whose sizes are (418*3) (185*3), respectively, through looping. The result will be arranged in matrix M (Figure 6.5, matrix M).

3. Create an empty matrix, say F [ ], which will show the index with its repetition obtained from the first column of matrix M (Figure 6.5 top, matrix F).

4. Find the maximum repetition, which is the second column in matrix F [ ], and display the values in matrix W (Figure 6.5 top, matrix W).

5. In matrix h [ ] (Figure 6.5, top), find the index numbers of the maximum redundancy in matrix F [ ].

6. Find the first point in the matrix h, say AM = (F (h, 1)). The first point was detected; let r be a black point inside the target and then plot the position of r (Figure 6.4).

7. The same procedure is then applied to matrices D [ ] and E [ ].

8. Find all the points inside the target (Figure 6.6).

9. After the two initial points are fixed inside the target, each colour can be easily detected separately, based on the intensity value and the limited range between them.

Matrix F: Shows the index and its repetition obtained in the first column of matrix M, while the second column is the number of the condition applied.

Matrix W: Shows only the max. repetition in matrix F in the second column.

Matrix h: Shows the index number of the maximum repetition from matrix F

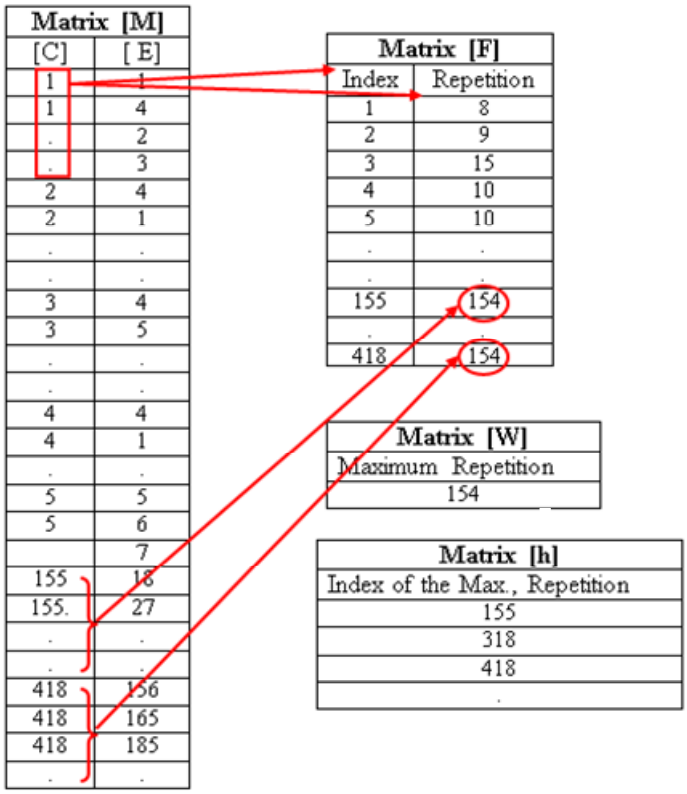

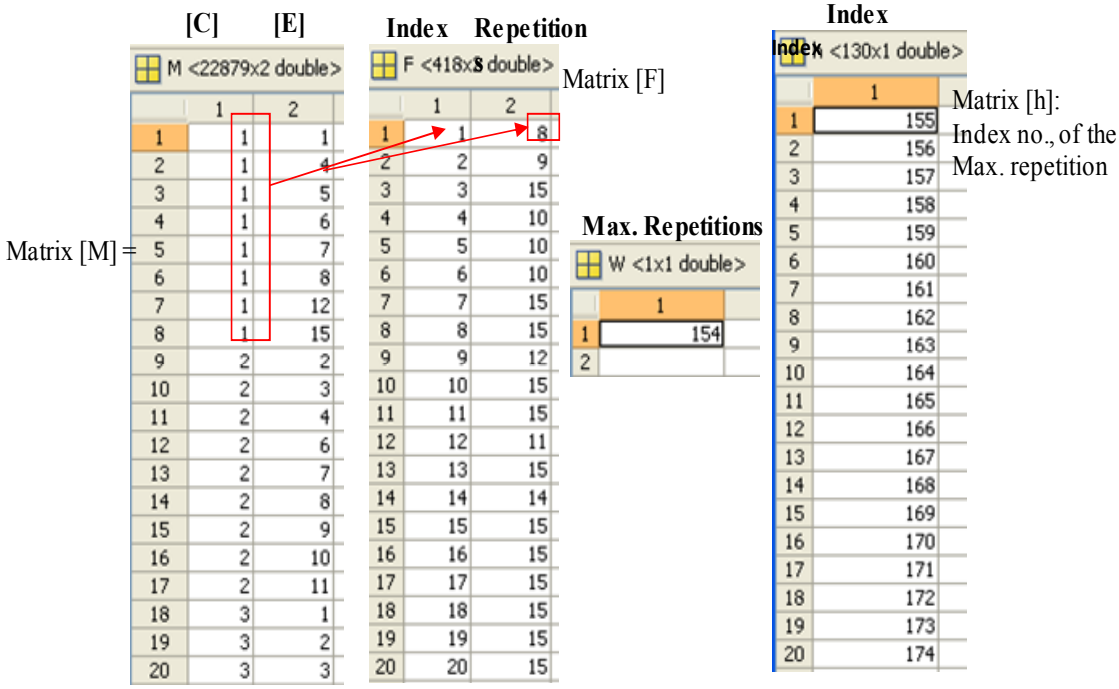

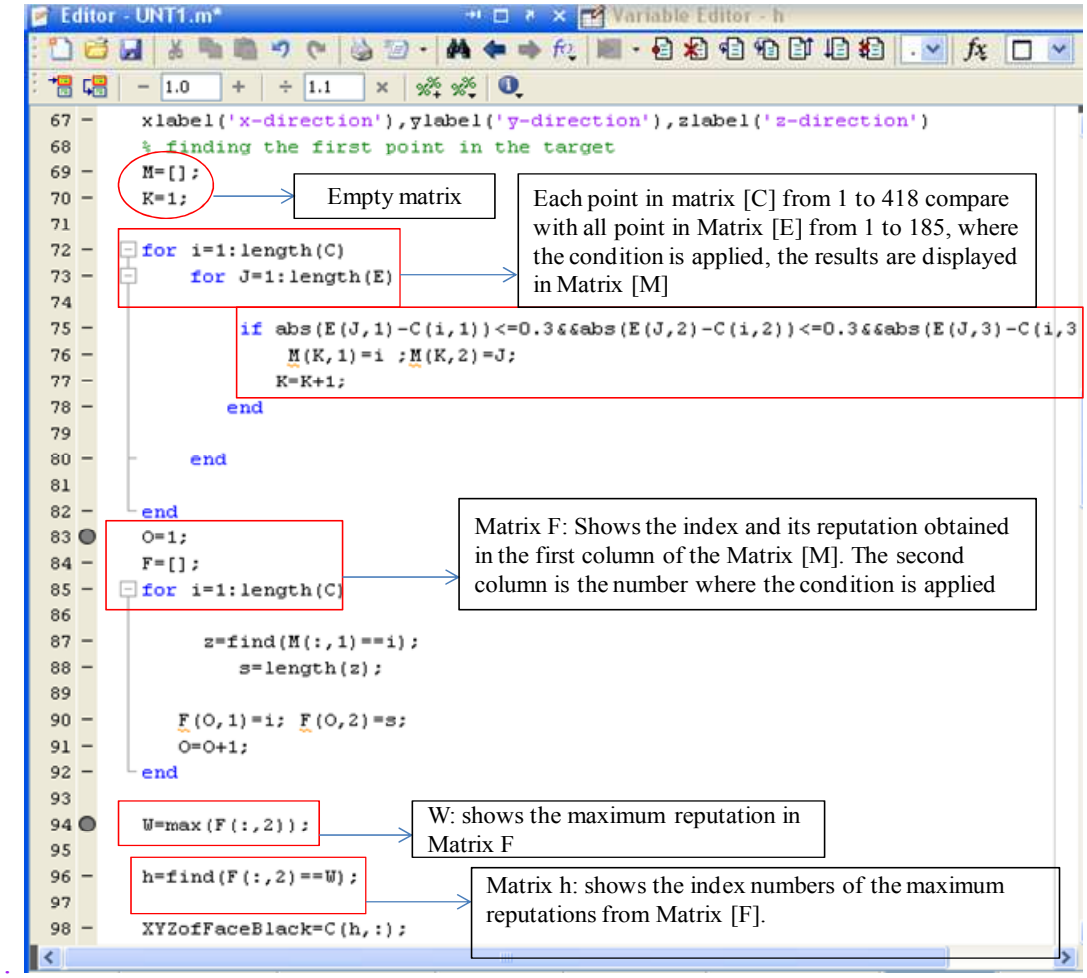

Figure 6-5: Target detection presented mathematically. Top: the process of isolating the target mathematically. Bottom: screenshot of the Matlab functions used.

The same procedure was applied with the other surfaces of the target with dark grey points (matrix D [ ]) and the HRT points of matrix E [ ]. The target was isolated successfully, as shown in Figure 6.6.

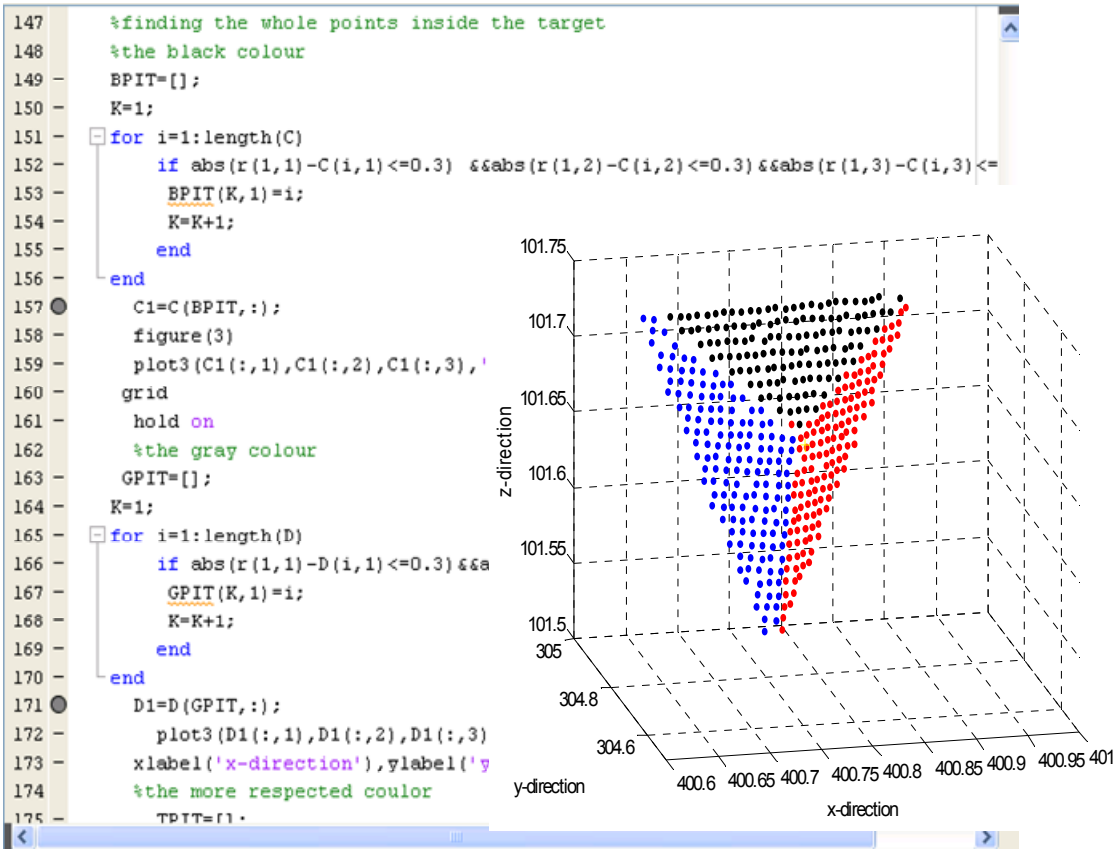

Figure 6-6: Target isolated successfully.

Figure 6.6 shows that the three colours (BC, DC, and HRT) were isolated. The full programme "UNT1" can be seen in the attached CD (see Appendix K).

10. Calculate the parameters of each separate face. The least squares method was applied to each colour face of the target, as shown in Figure 6.7. The calculation of parameters for each face is as follows:

The black C [ ], the dark grey D [ ], the HRT E [ ]

Par1 (a1.b1.c1) = $(C.C^T)^{-1}$. C^T.b .....For black

Par2 (a2, b2, c2) = $(D.D^T)^{-1}$. D^T.b.....For dark grey, presented in red

Par3 (a3, b3, c3) = $(E.E^T)^{-1}$. E^T.b .....For HRT, presented in blue

Then, the general equation of the plan intersection is:

$$\left.\begin{array}{l} a1x+b1y+c1z = 1 \\ a2x+b2y+c2z = 1 \\ a3x+b3y+c3z = 1 \end{array}\right\} \begin{bmatrix} a1 & b1 & c1 \\ a2 & b2 & c2 \\ a3 & b3 & c3 \end{bmatrix} \begin{bmatrix} X \\ Y \\ Z \end{bmatrix} = \begin{bmatrix} b \\ b \\ b \end{bmatrix} \quad \text{.....(6.3.1.1)}$$

```
183        %the black colour
184
185 -      b=ones(length(C1),1);
186 -      par1=inv(C1'*C1)*C1'*b % first parameters
187 -      standreddeviationofsurfaceC=std(C1);
188        %the dark grey colour, normal tape
189
190 -      b=ones(length(D1),1);
191 -      par2=inv(D1'*D1)*D1'*b  %second parameters
192 -      standreddeviationofsurfaceD=std(D1);
193        %the light grey colour, high reflectivity tape
194 -      b=ones(length(E1),1);
195 -      par3=inv(E1'*E1)*E1'*b  %third parameters
196 -      standreddeviationofsurfaceE=std(E1);
197 -      Q4=[par1';par2';par3'];
198
199        %THE INTERSECTION POINT
200 -      J=[1;1;1];
201 -      THEINTERSECTIONPOINT =inv(Q4)*J
202 -      T=THEINTERSECTIONPOINT;
203 -      plot3(T(1,1),T(2,1),T(3,1),'y+')
204 -      TS=[400.775;304.801;101.6570]
205 -      Diff=TS-T
```

Figure 6-7: Mathematical model for calculating the parameters of each face.

Figure 6.7 shows how the calculation parameters (a, b, c) of each face of the pyramid (BC, DC and HRT) were calculated. The apex of the pyramid target was computed based on the planes intersection algorithm (see equation 6.3.1.1).

11. Plot the position of the point resulting from the intersection of the three planes (see Figure 6.8).

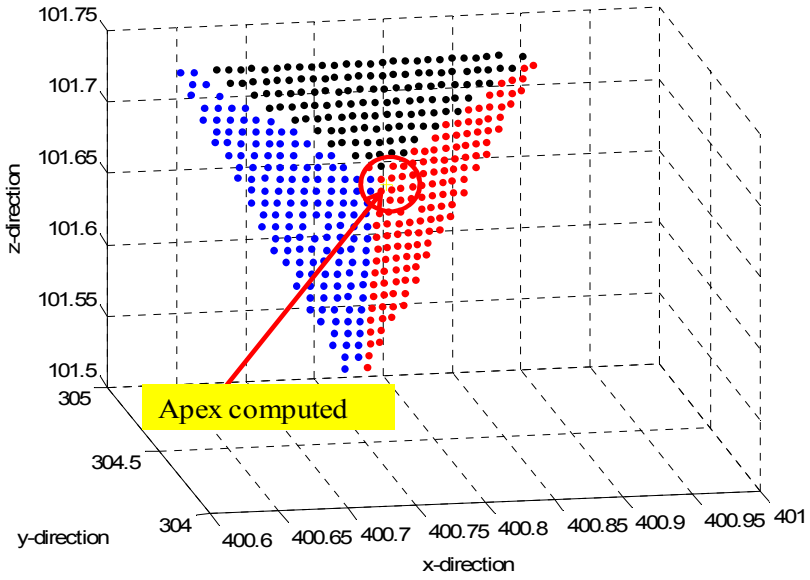

Figure 6-8: Apex of the pyramid target is computed.

The second part of the algorithm (UNT1) described was developed with support from Michael Lösler (2012b). The author used a combined algorithm, which estimates the plane parameters and the apex of the target together, formulated as a Gauss Helmert model with unknown in the restriction (see the algorithm in Appendix P). The mathematical mode of the algorithm is described in chapter 7. The reason for this update of the algorithm is that the previous solution estimated parameters on each plane in a single step and combined these solutions to compute the apex of the target. Therefore, it is not possible for an exact intersection point to be given by the three (or more) planes. The plane parameters could deviate from a single solution. As a result of this, the solution is to formulate the apex as a restriction and forcing an intersection. This developed algorithm was applied to the pyramid cases with different ranges and incidence angles, and the results can be seen in Appendix L.

Automatic dots target detection.

The algorithm UNT2 (see appendix K) was applied to the proposed dot target which involves a group of dots in a straight line in different directions (see Figure 6.9). The program can detect the target automatically, and then calculates the position of the target centre that results from the intersecting lines algorithm, which is based on the 3D line equation. The reason for using this type of target instead of a pyramid is that it is very cheap and can be more easily produced than a pyramid. In addition, the

returned laser beam energy cannot have an influence at a normal incidence angle, as in the pyramid target, which has a slant on its faces (see section 3.6.4 on surface reflectance and angle of incidence).

The same procedure that was applied to the pyramid target will be used for the dot target or any other targets, namely a pyramid with 4, 5, or 8 faces, cone, sphere, etc. It is important to say that this program is general for detecting any type of target automatically. The only change will be the method used for identifying the target's centre/apex. In this case, a line intersection will be used instead of the intersection of planes.

The following steps will explain how the algorithm detects the dots target and computes its centre.

Step 1: Data acquisition of an area using Leica Terrestrial Laser Scanner (TLS HDS300), then conversion of these data into a .txt file, containing (X, Y, Z, I, R, G, B). The number of points in the cloud was **62232**, and the scan resolution is 1x1 cm.

Step 2: Plotting the point cloud of a selected area, which contains the proposed dots target (see Figure 6.9).

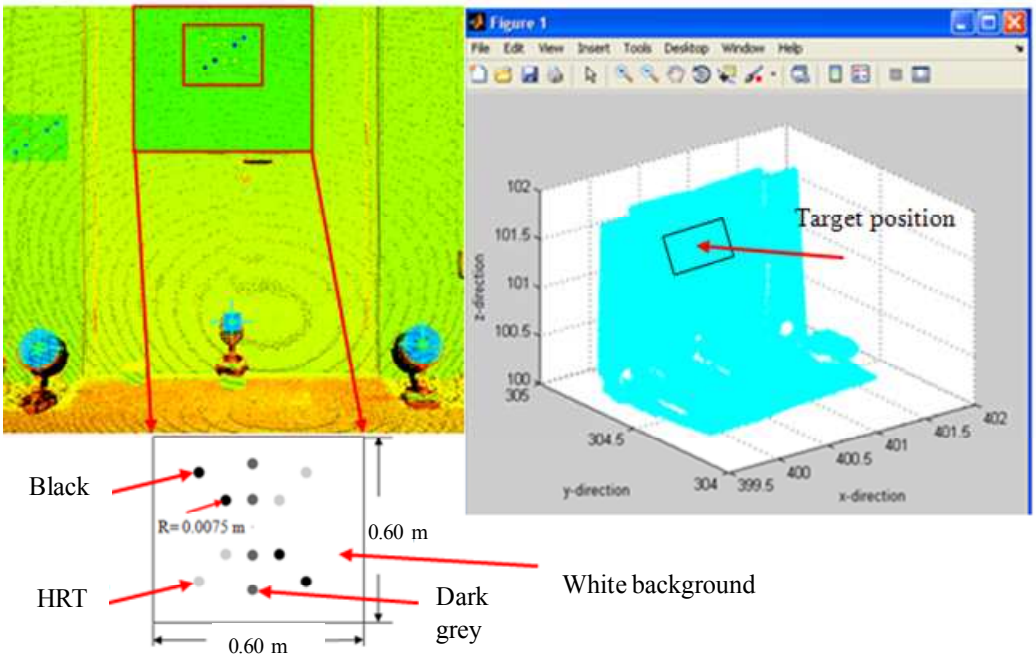

Figure 6-9: Displaying the point cloud of part of the area. Top left: point cloud plotted using Cyclone software, v.6. Bottom left: a sample of the proposed dots target. Right: points plotted using Matlab functions.

Step 3: The points of the dots target and surrounding point cloud are detected and isolated according to their intensity value. Then the program finds the two initial points inside the target, as shown in Figure 6.10.

Step 4: Finding the first point in the dots target. The same procedure is performed as with the pyramid target.

Step 5: Isolating dots from the surrounding point cloud into individual groups, as illustrated in Figure 6.11. Then the points of each dot are separated into a group (see Figure 6.12). In the next step, the program will isolate each dot (inner detection) using the same condition procedure.

Step 6: The centre of the target is calculated and plotted using two methods:

1. Calculating the mean point of each group, and then passing the lines through the mean of each one and intersecting them.
2. After isolating the points of the dots target, the process of fitting the line is been applied.

Step 7: Determining the 3D line equation of each line, and then calculating the centre of the intersection line using the line intersection algorithm.
The general 3D line equation passing through two 3D points is:

$$\frac{x-x1}{x2-x1}=\frac{y-y1}{y2-y1}=\frac{z-z1}{z2-z1} \quad \text{(6.3.1.2)}$$

where: (x2-x1, y2-y1, z2-z1) = parameters (a, b, c) respectively

$$\frac{x}{a1}-\frac{y}{b1}+\frac{z}{c1}=\frac{x1}{a1}-\frac{y1}{b1}+\frac{z1}{c1}\text{ ;} \quad \text{(6.3.1.3)}$$

where (x1/a1-y1/b1+z1/c1) = d1, and so on for d2 and d3)

$$\frac{1}{a1}x-\frac{1}{b1}y+\frac{1}{c1}z=d1 \text{--------1 for line1 ((BC) (C1 matrix))} \quad (6.3.1.4)$$

$$\frac{1}{a2}x-\frac{1}{b2}y+\frac{1}{c2}z=d2 \text{-------2 for line 2 ((DC) (D1 matrix))} \quad (6.3.1.5)$$

$$\frac{1}{a3}x-\frac{1}{b3}y+\frac{1}{c3}z=d3 \text{-------3 for line3 ((HRT) (E1 matrix))} \quad (6.3.1.6)$$

The equation above is linear, and the least squares method can be applied to calculate the target centre.

AX= d.....(6.3.1.7)

where: A= (1/a1-1/b1+1/c1, 1/a2-1/b2+1/c2, 1/a3-1/b3+1/c3);

X= (*x*, *y*, and *z*), and d = (*d1*, *d2*, *d3*), then the centre point of the intersecting line is:

X = inv (A).d.....(6.3.1.8)

Then, both sides of the of the equation (6.3.1.8) multiplying by the A^T to agree the inner matrix dimensions,

$X= (A^T A)^{-1}. A^T d$.....(6.3.1.9)

The equation above gives the coordinates of the intersections of lines.

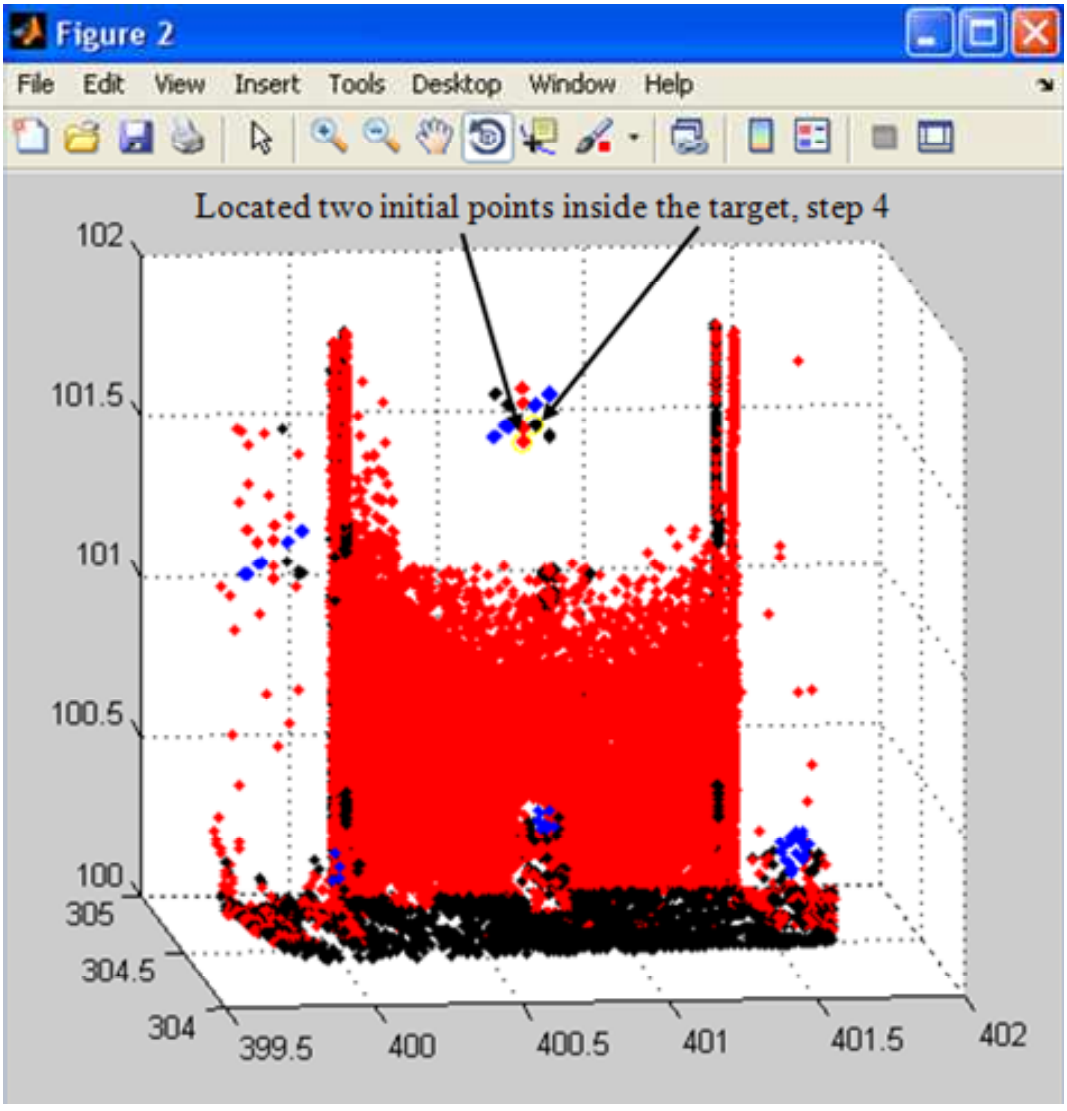

Figure 6-10: The target and surrounding point cloud with the two initial points located in the target.

```
173
174     % isolating ecach dot of black
175
176 -     D=load('f:\blackpointsinsidethetarget.TXT');
177 -     C1=D;
178 -     L=1;
179 -     s=[];
180 -     Z=[];
181 -     for i=1:length(C1)
182 -             if sqrt((C1(1,1)-C1(i,1))^2+(C1(1,2)-C1(i,2))^2+(C1(1,3)-C1(i,3))^2)>=0.015;
183 -               s(L,1)=i;
184 -               L=L+1;
185 -             end
186 -     end
187 -     Q=C1(s,:);
188 -     H=1;
189 -     for i=1:length(C1)
190 -         if sqrt((C1(1,1)-C1(i,1))^2+(C1(1,2)-C1(i,2))^2+(C1(1,3)-C1(i,3))^2)<=0.015;
191 -               Z(H,1)=i;
192 -               H=H+1;
193 -         end
194 -     end
195 -     DOT1B=C1(Z,:)
196 -     MD1=mean(DOT1B)
197 -     save('f:\DOT1B.txt','MD1','-ASCII')
198 -     figure(4)
199 -    plot3(MD1(1,1),MD1(1,2),MD1(1,3),'K.')
200 -    hold on
201 -    grid
202
203 -    save('f:\1000.txt','Q','-ASCII')
204
205 -    clear all
206 -    D=load('f:\1000.txt','Q','-ASCII');
```

Matrix for remaining dots

Matrix for isolating first group of dots

Matrix for remaining black dots

Mean of the first group of dot

Saving the remaining dots into a separate file

Loading the file and starts the same procedure for other black dots.

Then, the procedure will continue for the other colours (DC and HRT)

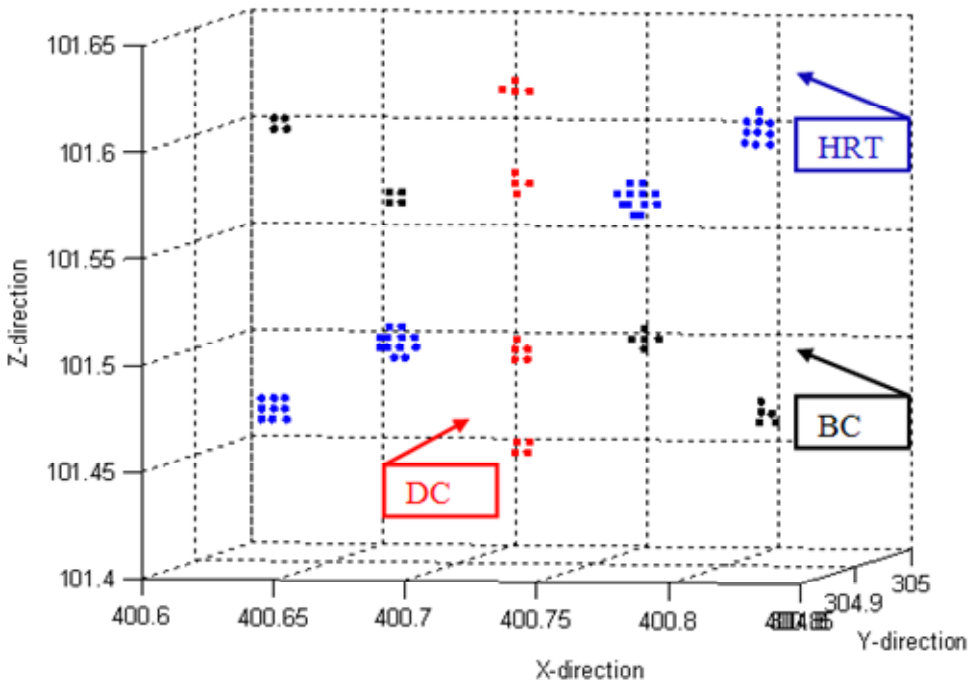

Figure 6-11: Isolating the dots target. Top: steps for isolating the dots target. Bottom: each dot isolated according to its colour.

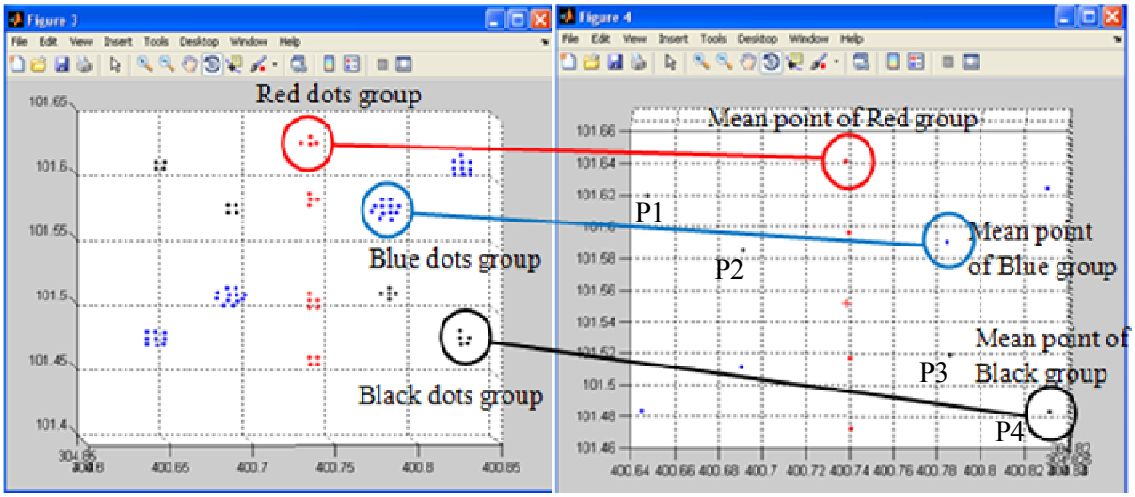

Figure 6-12: Dots isolated (left), and the mean point of each group computed (right).

In Figure 6.12, left, after isolating the points, the mean point of each group was computed, and the linear least squares equation (6.3.1.9) was applied to determine the centre of the target. Note: All points in a straight line have known coordinates (x, y, z). The first and end point of each line were chosen, where equation (6.3.1.9) uses just two points. For example, as shown in the BC dot (Figure 6.13), the line equation was applied with points (P1, P4), (P1, P3), (P2, P3), and P2, P4 and the same procedure was applied to the other lines. Consequently, the average intersection lines of the target centre were calculated (see algorithm UNT2 in the attached CD, Appendix K).

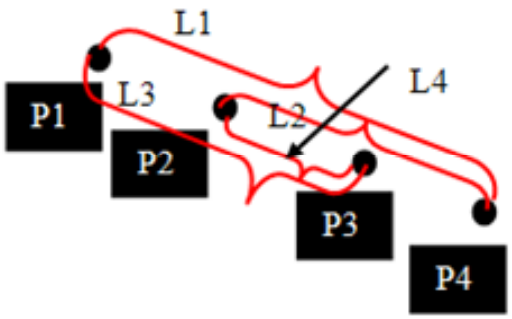

Figure 6-13: Shows the line equation of method 1: P1 to P4 refer to the mean point of each BC dot. L1 to L4 refer to the line passing through two known points (xyz) coordinates.

In the second method, the least squares fit algorithm was used to fit a best-fit line to the data for each group of dots. At the intersection of each fitted line, the accurate centre of the target was computed (see Figure 6.14), and compared with the actual value measured using TS.

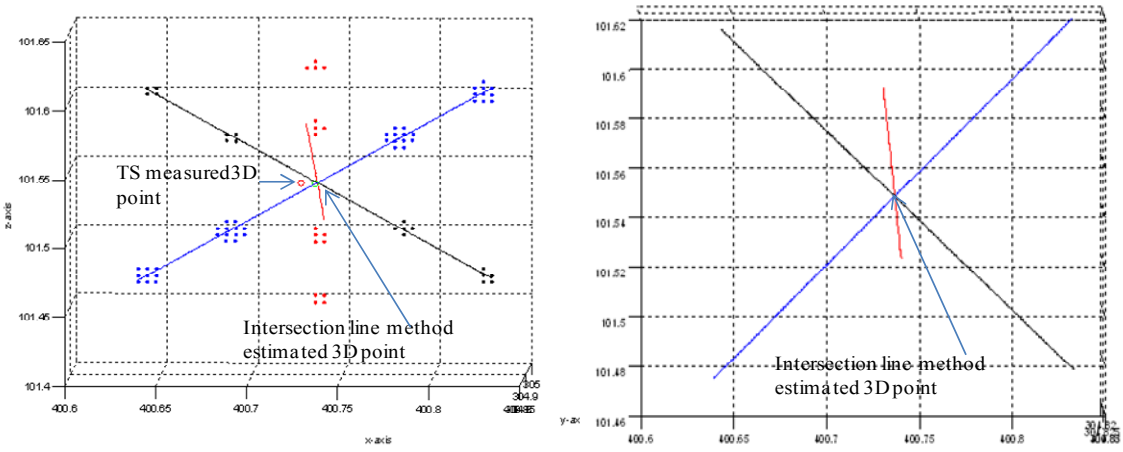

Figure 6-14: The centre of the target estimated through the intersection line after fitting each group of points to a line.

In the second method (Figure 6.14), the process of fitting a line to data was applied to each group and the residuals have been computed after fitting (see Appendix L, Figure L2-2). Then, the line intersection algorithm was applied to estimate the target centre. [See the application of UNT2 algorithm [UNT2.1 (UNT2.1.1 to UNT2.1.4), UNT2.2 and UNT2.3] files in the attached CD (see Appendix K.). The process of fitting will be described in the next chapter.

6.3.1 Results and analysis:

The accuracy of the two targets compared with their measured values using the Total Station are shown in Table 6.1.The accuracy of the surveyed value for each x, y and z component is ± 1mm in the local area.

	Absolute accuracy			Scan resolution	Note
Target	ΔE (mm)	ΔN (mm)	ΔZ (mm)		
Pyramid	4.00	3.00	3.00	2x2 sq. cm.	
Dots	Fail	Fail	Fail	Fail	
Pyramid	4.00	3.00	2.00	0.5x0.5 sq. cm.	
Pyramid	2.00	1.50	1.00	0.5x0.5 sq. cm.	After fitting
Dots	0.2	0.8	13	0.5x0.5 sq. cm.	
Dots	0.18	1.7	0.9	0.5x0.5 sq. cm.	After fitting

Table 6-1: Accuracy of the target centre compared with the actual value measured using TS.

Table 6.1 shows that good results can be obtained from the dots target at point spacing of 0.5x0.5 sq. cm and better than the pyramid at short range and normal incidence angle, but this target failed with point spacing of 0.2 x 0.2 sq. cm. This is because the scan resolution is larger than the size of each dot. Larger dots can be used, but this will affect the estimated centre of each dot, especially with bad distribution of scanned points inside the dot (see section 5.4). Consequently, poor accuracy and precision will be achieved. The accuracy of the pyramid apex depends on the accuracy of the compared data achieved from the Total Station, while the quality of the apex depends on the precision of the planar parameter of the surface normal. This also contributed error in apex determination, due to the effects of range and incidence angle (see section 5.5).

6.3.2 Workflow diagram

The work flow diagram of the two script programs (UNT1 and UNT2) was divided into two parts: detection and computation (see Figures 6.15 and 6.16) and was then used for the two types of the target: pyramids and dots.

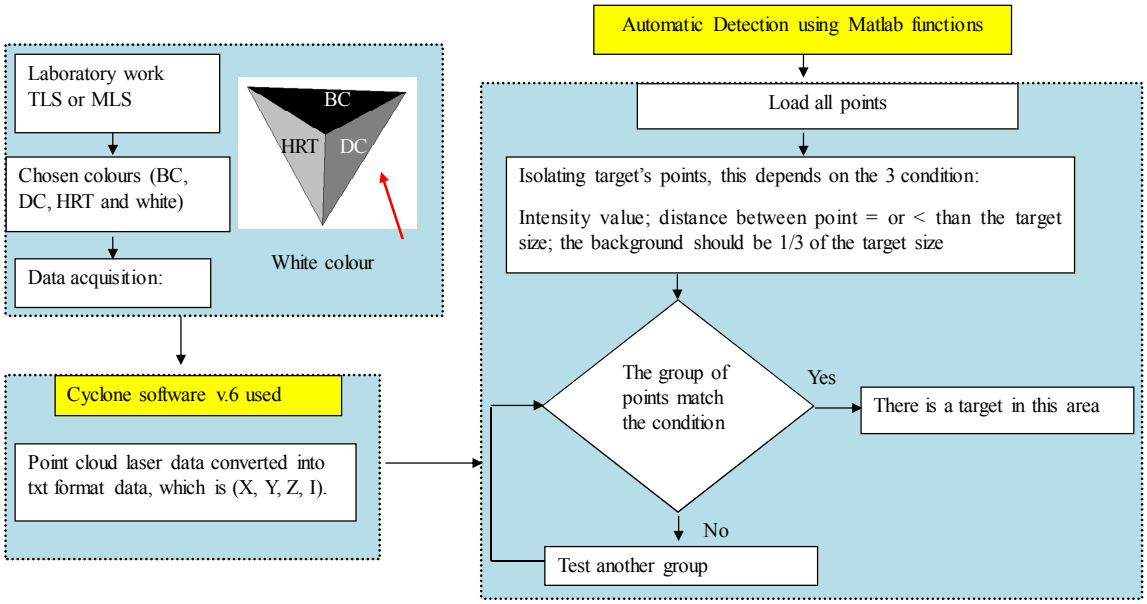

UNT1 algorithm for detection of pyramid targets

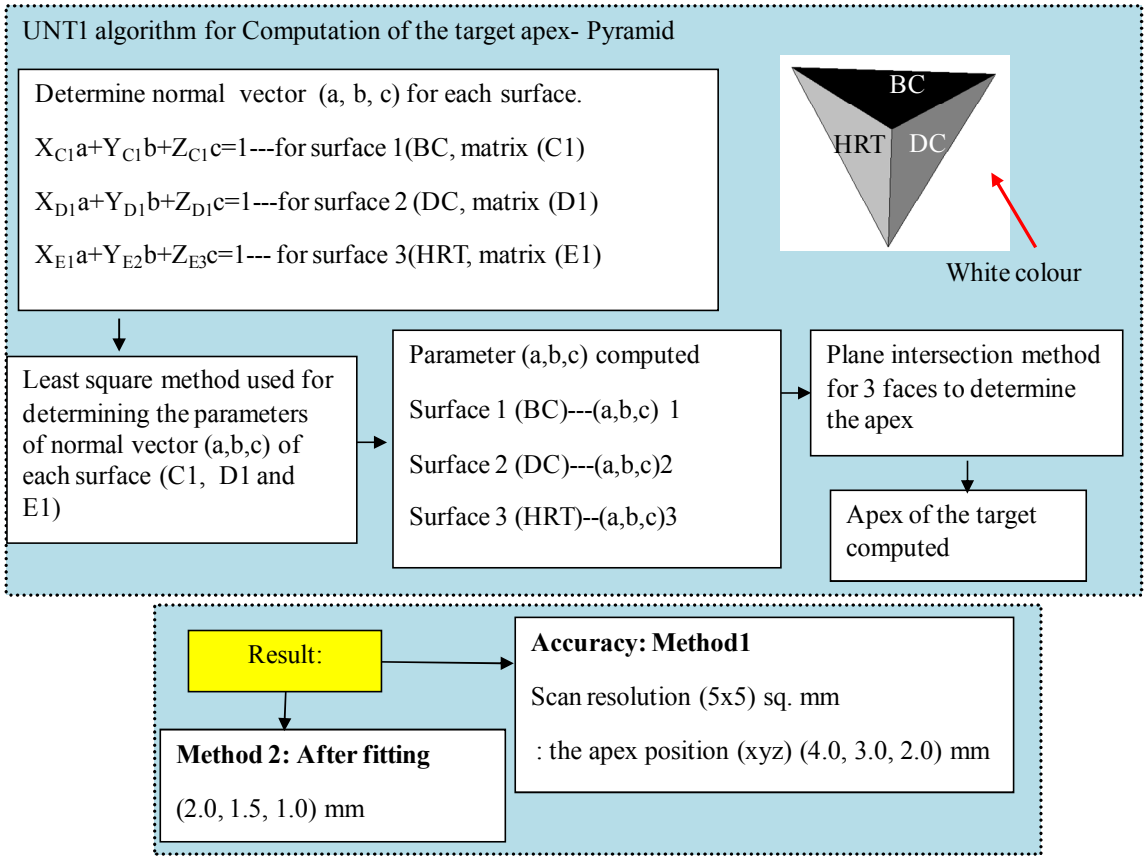

Figure 6-15: Automatic workflow diagram for detecting and computing the apex of the target. Top: detection of the target (any type of pyramid). Bottom: computation of the target apex using plane intersection method.

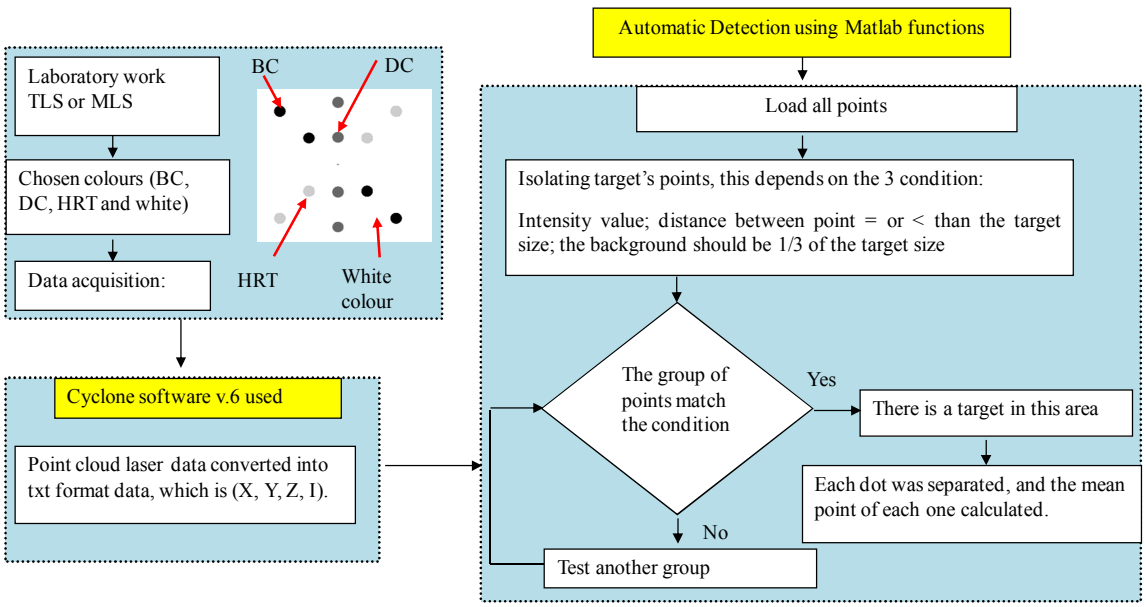

UNT2 algorithm steps of detection dots target.

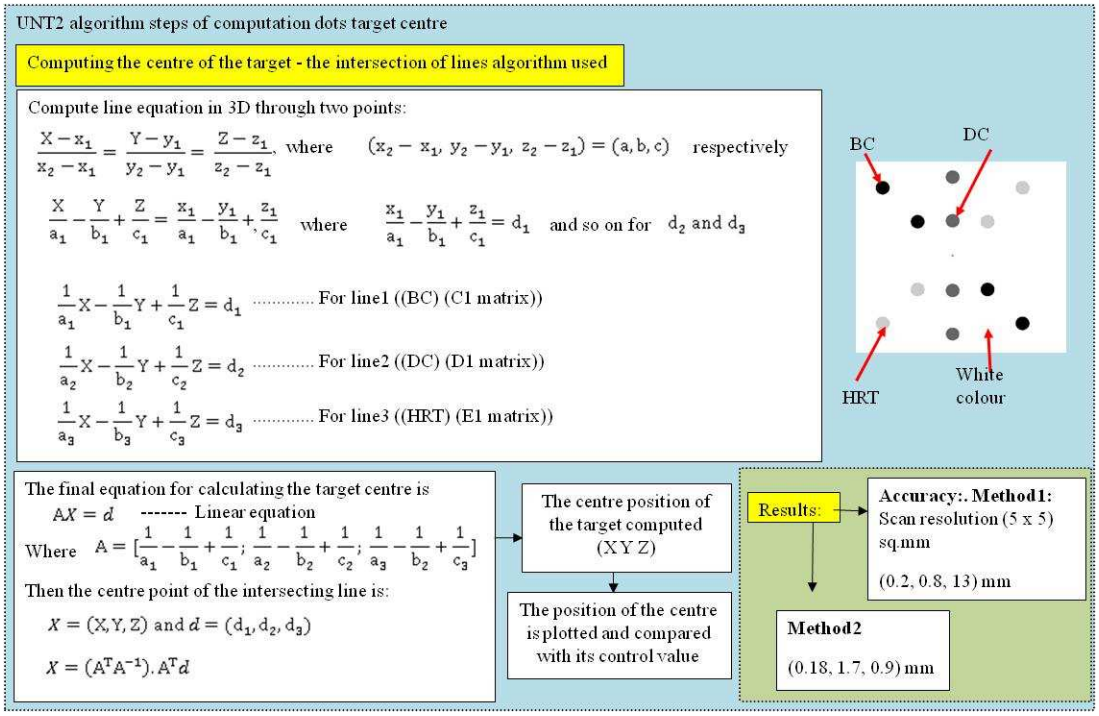

Figure 6-16: Automatic workflow diagram for detecting and computing the centre of the target. Top: detection of the target; Bottom: computation of the centre of the target using line intersection method.

The same program (UNT1) following the proposed workflow as described in Figure 6.15 was applied to detect and compute the apex of all types of pyramid targets (four, five and eight faces) at normal incidence angles and short range (see Appendix I3).

6.3.3 Limitations of the program

The limitations of the program can be summarised as follows:

- The targets must have a big background in order to be detected, which may negatively affect the overall view of buildings on which the target will be fixed. This is in addition to the difficulty of carrying out the targets when a number of them is needed.
- In some areas, the number of points outside the target is greater than inside, causing the program to detect the wrong object, as shown in Figure 6.17.

The above problems were solved by:

- Avoiding using the particular background; any flat surface can be used as a background, provided it is not in the range of the intensity values of the signal return from the target surfaces (see section 5.4.2 on intensity return analysis).

- Adding some criteria as follows:

1. The same procedure as discussed in section 6.3 will be followed, where the program finds the points from the three colours (BC, DC and GC) close to the HRT. So, if the points from these three colours are not close to any point from the HRT, this means that they are not located inside the target.
2. After getting the points, they will be divided into small groups, each having only points from the three colours which are close to each other, with a distance equal to or less than the length of the target.
3. These small groups will be divided into groups, each having the possibility of being a target. This division is based on the idea that the distance between the points in each target (points inside the target) is equal to or less than the length of the target. Within this step, each group has a number of repeated points, which should be filtered out.
4. The repeated points from step 3 will be removed from the list of each colour for each target and at the end a number of matrices will be obtained, each one of which could be a target, and for each group we have the number of points for each colour.
5. The program will detect the target's point among the groups by providing new conditions which are:
    a. A number of points per target that are expected to be captured by the laser scanner between minimum and maximum range.
    b. An approximate distance between targets within the whole point cloud, in order to detect each target separately.
6. After detecting the target points, the second part of the program will start as mentioned before.

The drawback of this algorithm is the long time required for processing. For example, one point cloud contains 88,600 points. The program needs several hours to complete working. The alternative solution for reducing the time is to increase the number of faces to eight, as described in section 6.3. This octagon target not only makes the program faster, but also overcomes the effect of the incidence angle. This led to creating a target as described in the previous chapter, "section 5.4 "section target design". The sphere targets are not affected by the incidence angle (IA), whereas a cone might be affected by the IA to some extent. Both of them can be seen

in any direction of scan. The effect of IA and range in automatic detection will be discussed in the next section.

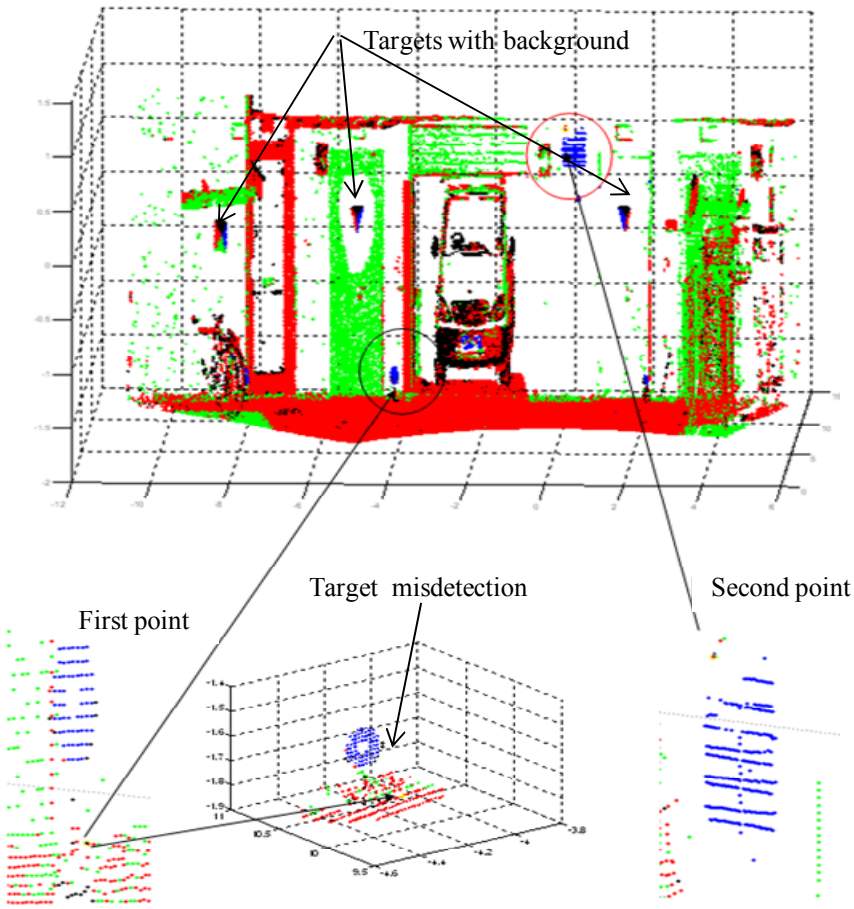

Figure 6-17: Detection of the wrong target.

6.4 The effect of incidence angle, range and scan resolution on automatic target detection

The effect of the incidence angle and range on the quality of apex determination was discussed in section 5.5. In this section, the effect of IA, range and scan resolution on the automatic detection will be discussed in an outdoor simulation test using two TLS HDS300 and Faro Focus^{3D} laser scanners.

6.4.1 Trials on pyramids and dots targets

Different types of pyramid targets, with 3, 4, 5 and 8 faces, were used and tested with different incidence angles and short ranges in from different positions, namely:

normal, steep and very steep IA. The pyramid targets were rigidly fixed on the wall and at each position the area of the targets was scanned, as shown in Figure 6.18. However, for the dots target only one position was taken from the previous test, due to the small dots size (see Figure 6.9).

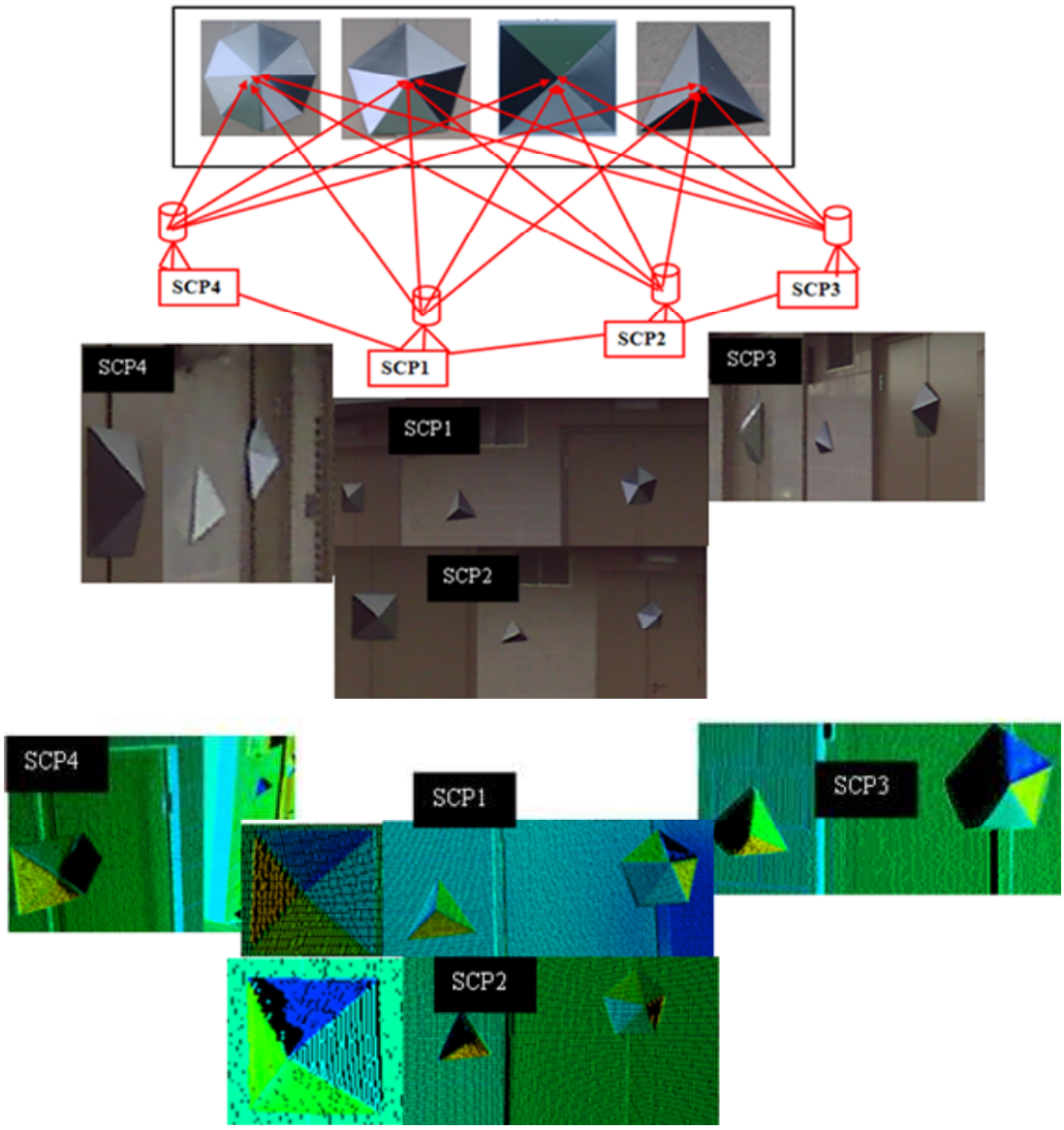

Figure 6-18: Position of the laser scanner on the pyramid targets. Top: the plan position of each scanner. Bottom: laser scanner point cloud of all positions.

This test contains 20 scans captured successively at around the same time with resolutions of 0.5x0.5, 1.0x1.0, 1.5x1.5, 2.0x2.0, and 2.5x2.5 cm. These were taken at each position cited above. However, only 10 scans (SCP1 and SCP2) were captured with a good quality. The program detects all targets automatically and computes their apexes using different methods. In the other 10 scans (SCP3 and

SCP4), the program was only able to detect one target from each scan, namely the square and pentagon targets from positions SCP3 and SCP4, due to the effect of IA, as described in the previous chapter, as well as the effect of scan resolution. The octagon pyramid target was detected from all positions; from each position, at least three faces could be detected (see section 6.3.2).

Tables 6.2 and 6.3 show the results of the dots and pyramid targets respectively. For the pyramids targets, only one scan resolution of 1x1 cm was taken from each position, as shown in Figure 6.19. The full results for all types of pyramids used in this trial, with their graph, can be seen in Appendix L, Figure L1-2. The application of the UNT1 algorithm (UNT1a1.m to UNT1a11) files with the data of this test can be found in the attached CD (see Appendix K).

Lines-fit	Point no	Accuracy (Δx, Δy, Δz) mm	Accuracy (Δx, Δy, Δz) mm	Std Dev (mm)	RMSE (mm)	RMSE (mm)
Black points	18			1.6		
Red points	17			0.4		
Blue points	43			4.5		
Intersection line at P	1	(-0.4, 8.0, -0.8) Method 1	(-0.3, 1.0, -0.4) Method 2	2.5	8.05	1.12

Table 6-2: Accuracy position of the point centre using intersection lines, and standard deviation of fitting line to data at point spacing of 10x10 sq. mm.

Scan position	Target type	Δx (mm)	Δy (mm)	Δz (mm)	RMSE(mm)	σxyz (mm)	Face missing
SCP1	8 sides	2.2	0.11	1.78	2.83	1.372	.....
	5 sides	4.2	-0.21	2.7	5.00	1.168	.....
	4 sides	-7.4	-0.3	5.6	9.29	3.296	.....
	3 sides	6.3	3.9	5.0	8.94	2.238	.....
SCP2	8 sides	3.1	0.47	2.54	4.04	1.236	3
	5 sides	4.5	1.11	3.84	6.02	1.084	2
	4 sides	6.1	-2.4	6.7	9.37	3.264	.....
	3 sides	-5.9	-4.1	-3.1	7.82	2.218	.....
SCP3	8 sides	5.10	2.1	1.18	5.64	1.268	3
	5 sides	4.23	2.1	2.22	5.22	2.032	2
	4 sides	8.0	11.8	-7.1	15.93	2.334	1
	3 sides	Fail: steep IA, 1 face missing				.....	1
SCP4	8 sides	3.33	0.28	3.10	4.56	3.692	4
	5 sides	Fail: very steep IA, 3 faces missing				.....	3
	4 sides	Fail: very steep IA, 2 faces missing				.....	2
	3 sides	Fail: very steep IA, 2 faces missing				.....	2

Table 6-3: Accuracy position of the apex using intersection planes, and uncertainties at point spacing of 10x10 sq. mm.

A resolution of 1x1 sq. cm was used and the full data can be seen in Appendix L-L3.

When using a scan resolution of 15x15 sq. mm for SCP1, the program failed to detect the required target. This was because the number of points outside was greater than those inside, and the program detected the wrong object (see Figure 6.17). This issue was solved by updating the program, as mentioned before.

6.4.2 Analysis of dots and pyramids results

From Table 6.2, it can be seen that the position of the intersection point for the dot target achieved via least squares surface fitting gives a better result than that obtained from the mean value method, as the RMSE for methods 1 and 2 are 8.05 and 1.12 mm, respectively. This is because if the points are not precise, the mean point might not be close to the centre.

Table 6.3 shows that the highest accuracy can be achieved from the 8-faced pyramid, as the more faces there are, the better the accuracy that can be achieved (see section 5.5). The larger standard deviation can be attributed to the increased number of observations from the different faces, which may include a number of bad points. The table also shows that the 8 faces can be seen from all positions, unlike the others. The pyramids with 3, 4 and 5 faces failed in position 4 and the accuracy of the apex reduced as the number of faces decreased.

Although the target can be seen from any IA angle, the range can have an effect on the detection of some colours such as black, which can be regarded as an absorbent surface, for which a weak return energy will be recorded. This effect increases with increasing range; at 50 m, there is no record from black with the HDS3000 scanner and at 40 m most of the points will not be detected. Therefore, the idea of one colour is important and this can be found in the cone and sphere targets.

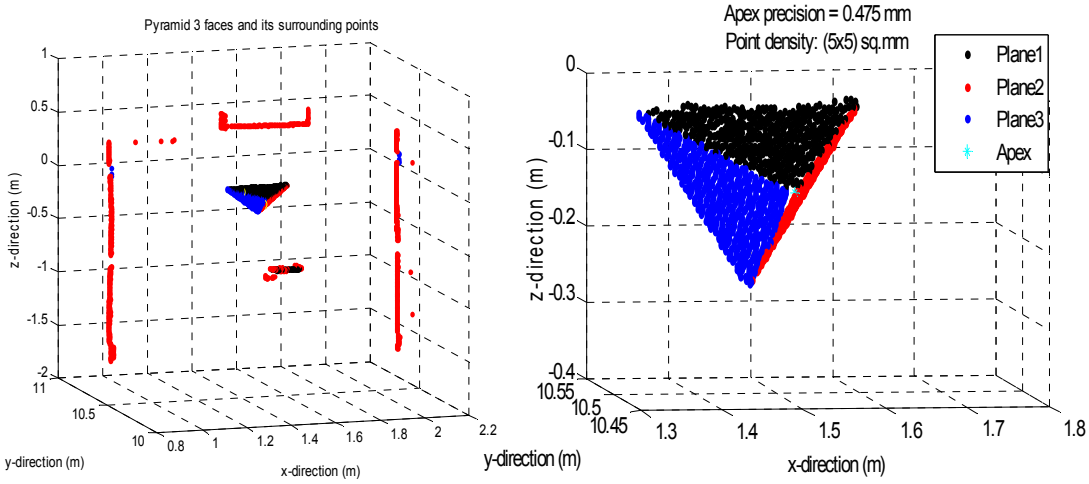
Pyramid 3 faces and its surrounding points
z-direction (m)
y-direction (m)
x-direction (m)
Apex precision = 0.475 mm
Point density: (5x5) sq.mm
Plane1
Plane2
Plane3
Apex
z-direction (m)
y-direction (m)
x-direction (m)

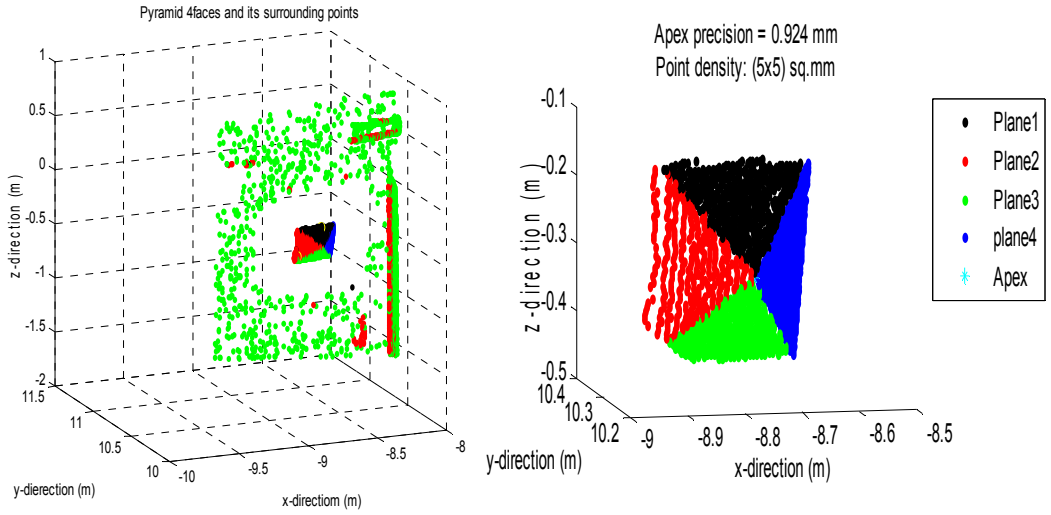
Pyramid 4faces and its surrounding points
z-direction (m)
y-dierection (m)
x-directiom (m)
Apex precision = 0.924 mm
Point density: (5x5) sq.mm
Plane1
Plane2
Plane3
plane4
Apex
z-direction (m)
y-direction (m)
x-direction (m)

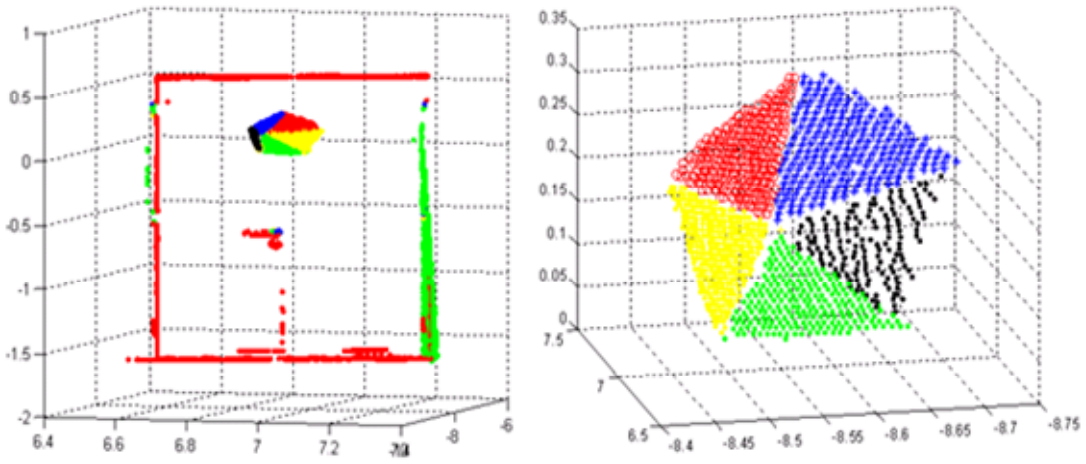

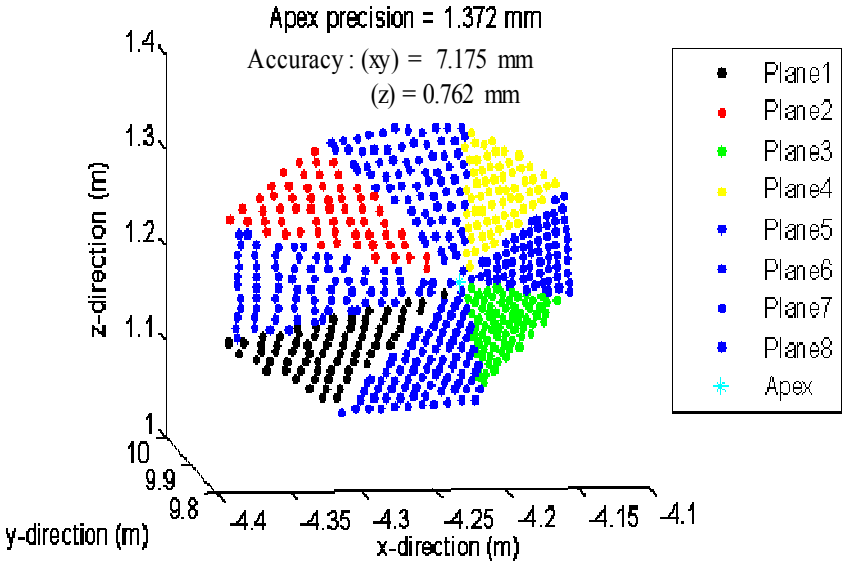

Figure 6-19: Sample detection of pyramid target at position SCP1: Top: three-faced pyramid; Middle: four faces. Bottom: five and eight faces respectively. The range is around 10-12 m. The point spacing was 5x5 mm. The entire point cloud comprised 62,649 points.

6.4.3 Trial on detecting sphere and cone

In this trial, the same detection procedure was applied to the cone and sphere target. In the case of the cone, two colours were used, highly reflective tape (HRT) and black (BC) The HRT covered the bottom and black was used for the top (see Figure 5.13). These two colours can be easily detected from the surrounding objects in the point cloud. Also, the sphere has a special unique highly reflective white colour made by Faro called Spectralon. This material is a solid thermoplastic that exhibits the highest diffuse reflectance. The sphere is not coated, but is rather a solid material. The degree of reflectance based on the Spectralon thickness is > = 7mm. In a thinner section, the reflectance of Spectralon decreases, e.g. falling from 99% to 93.3% at 1mm thickness @ 555 nm. The detection of these two targets can be described as follows:

Cone detection: As mentioned in the previous test, the detection of the cone follows the same procedure as that applied with the pyramids and line. The cone was tested in four positions (SCP1 to SCP4) (see Figure 6.20) at different IA and ranges from 5 to 13 m. The cone was detected in each position, except in SCP3, where the target was not able to pass due to the previously mentioned conditions. Therefore, a unique

colour was used. The algorithm UNT5 developed for detection of the cone can be found in the attached CD (see Appendix K).

The benefits of using one colour rather than different colours can be explained as follows:

- Calculation is easier where there is only one surface to be detected, unlike the pyramid, where each face must be detected separately.
- The cone can be detected, and the apex can be calculated from any IA.
- It makes the process of detection very easy and faster.

An example of processing cone data using the LM algorithm for calculating the apex can be seen in Figure 6.22, and Table 6.4 shows the statistical results for all positions.

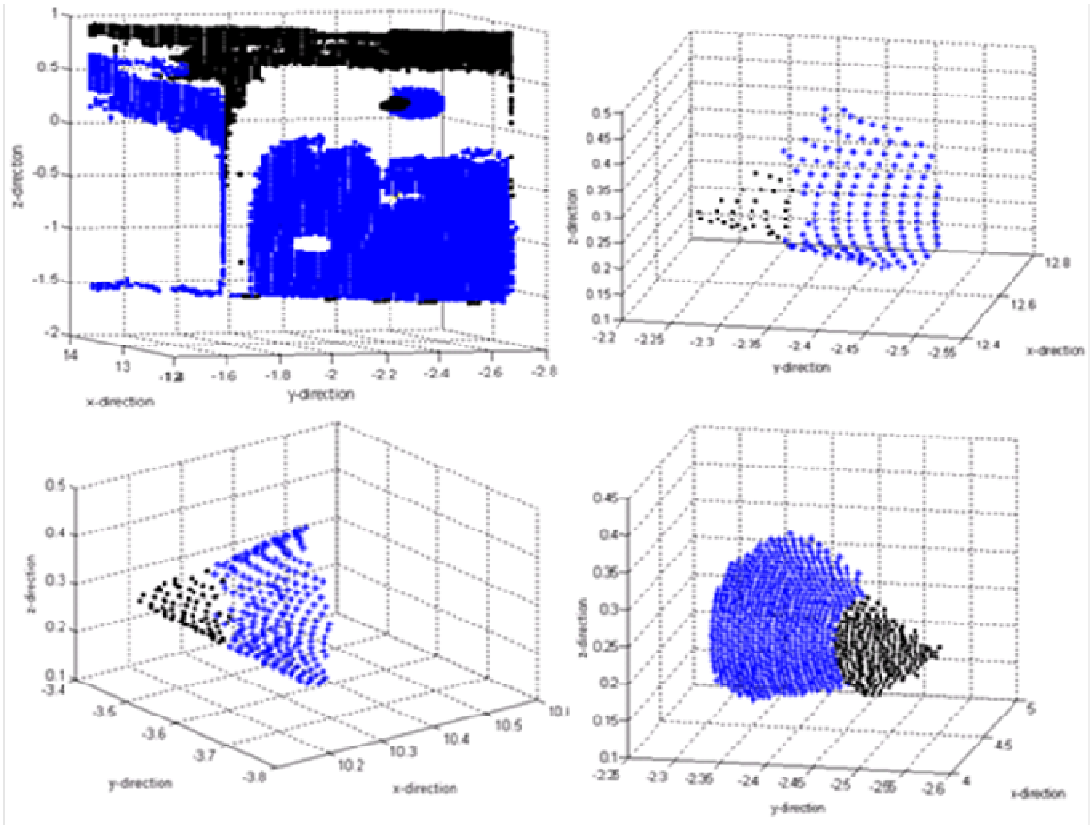

Figure 6-20: Cone detection and surrounding objects. Top left: SCP1 at range 12.65 m. Top right: SCP2 at 10.76 m. Lower left: SPC3 at 9.75 m: Lower right: cone detected at 5.0 m range and 80 IA.

Target	Position	Range	Points	Required	Redundancy	Accuracy (mm)	σxyz (mm)
Cone: size	SCP1	12.65	190	6	184	4.7501	1.822
Sh*[1]=300 mm	SCP2	10.76	225	6	219	4.922	1.543
α*[2] =60°	SCP3	9.75	300	6	294	2.201	1.341
r= 150 mm	SCP4	5.0	583	6	276	4.762	0.851

Table 6-4: Accuracy and precision vs. different ranges and incidence angle.

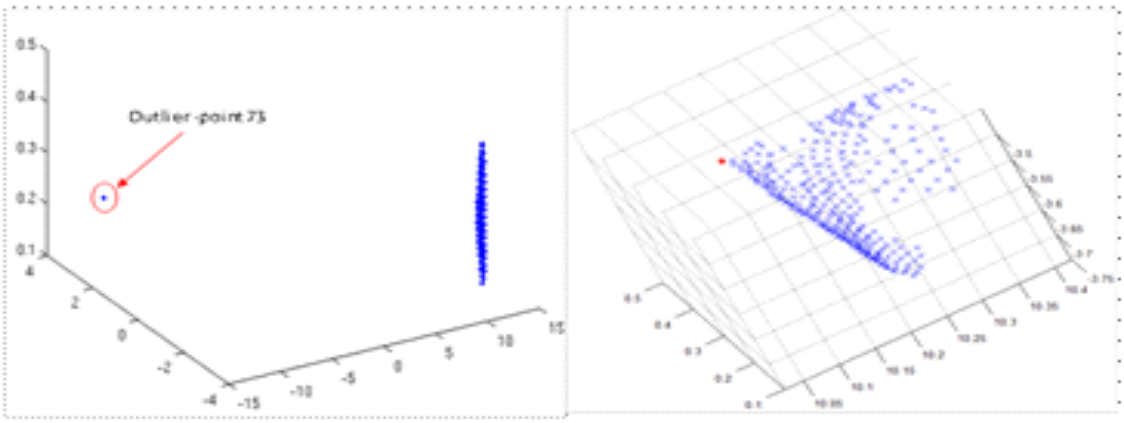

Figure 6-21: A sample of cone in position SCP1. Left: outlier detected. Right: apex determination, as depicted with a red dot, using the LM algorithm.

Sphere detection: Two spheres were used and tested, with different incidence angles in four positions (SCP1 to SCP4) (see Figure 6.22). One sphere was fixed horizontally on a steel door using a magnetic mount and the other one was mounted vertically on the tripod. The area was scanned with a 1x1 sq. cm resolution, as shown in Figure 6.22. The figure also shows the detection of the sphere at SCP1 and the computation of parameters as depicted in Table 6.5. This table includes the absolute accuracy of the centre and radius compared to the control values of the sphere at different positions (SCP1 to SCP4) using two methods, AD and Cyclone software. Figure 6.23 shows the accuracy of the sphere radius compared with its actual value.

The further statistical results include error standard deviation, error mean and absolute errors mean of positions (SPC1, SPC2, SPC3 and SPC4) and graph representation, and a table showing the computation of the radius, centres and residual errors of the sphere in the radial direction can be seen in Appendix I, I4 and I5. The algorithms UNT3 and UNT4 developed for fitting the sphere and computing its parameters can be seen in the attached CD (see Appendix K).

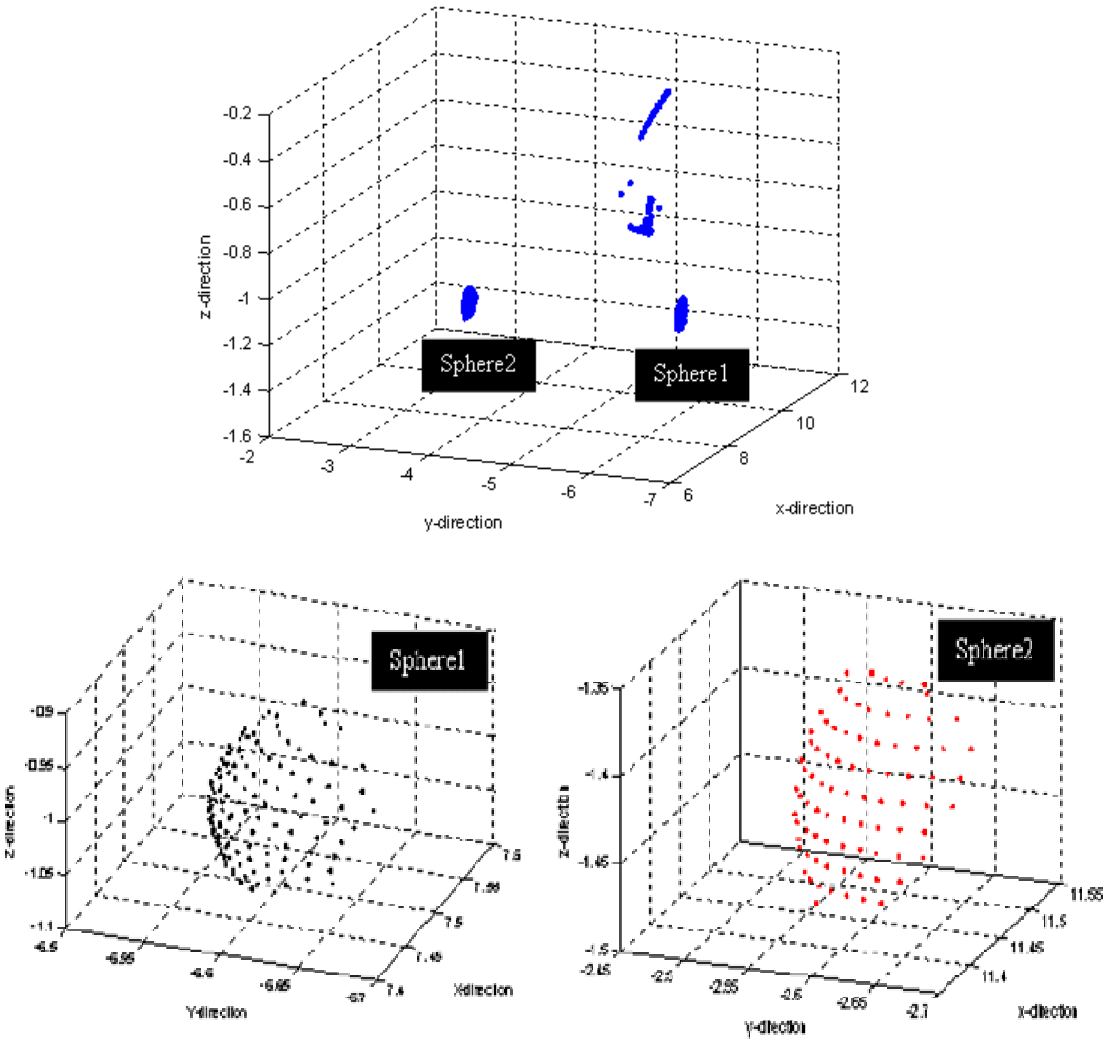

Figure 6-22: Sphere detection and surrounding objects. Left: sphere 1 detected at SCP1. Right: sphere 2 detected from the same position.

Position	Target	Δ Centre (mm)			R MSE	Radius (R) mm	ΔR (mm)	No.of pts	Dist. (m)
		ΔX	Δy	ΔZ					
SCP1	Sphere1	0.83	-2.38	2.97	3.90	96.10	3.90	133	10.00
	Sphere2	2.60	-0.87	2.48	3.7	96.30	3.70	83	11.77
SCP2	Sphere1	-1.50	-2.67	2.25	3.8	96.20	3.80	134	10.64
	Sphere2	1.53	-1.53	-0.77	2.97	97.70	2.30	149	10.12
SCP3	Sphere1	-5.11	-2.18	0.89	5.63	94.10	5.90	70	14.06
	Sphere2	1.50	-1.5	-1.50	2.60	97.40	2.60	142	10.47
SCP4	Sphere1	-1.21	-1.07	1.34	2.10	97.90	2.10	110	11.45
	Sphere2	0.20	-0.07	-0.67	0.70	99.30	0.70	481	5.96

Table 6-5: RMSE of the centre and error radius computation of spheres 1 and 2.

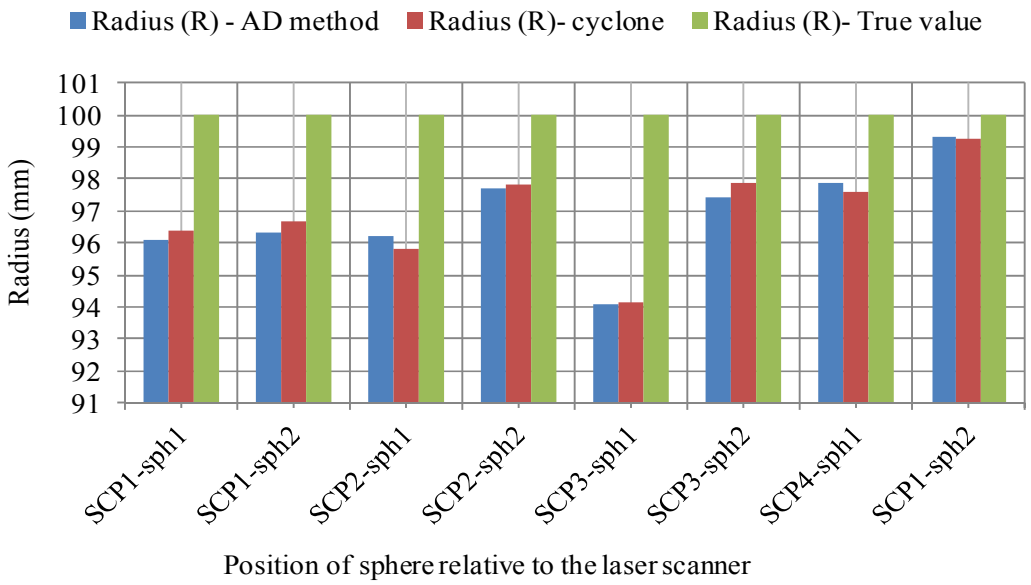

Figure 6-23: Position of sphere vs. radius compared with control values using Cyclone software and AD.

6.4.4 Analysis of cone and sphere results

The cone and sphere can be easily detected, and their centres are calculable as there is only one surface to be detected, unlike the pyramid, where each face must be detected individually. Both targets (cone and sphere) are unaffected by the incidence angle (IA). The sphere is much better than the cone in terms of IA because it has only one normal vector in the direction of its centre. Unlike the cone, each point has a normal vector, due to it geometric shape; only at a 90° IA one normal vector can be achieved.

Table 6.4 shows that the accuracy and precision of the cone apex fluctuated after the fitting process due to the effect of its geometric shape, as described in the previous chapter. For example, the best apex precision is achieved in position SCP 4. This is related to the effect of IA at that position, where it has only one normal vector, as previously mentioned. The accuracy of the cone apex depends on many factors, such as range, IA, point density, etc., as described in the previous chapter.

Table 6.5 shows the statistical results of fitting and calculating the sphere target centres. The worst accuracy of the sphere centre and radius can be detected in SCP3,

where the maximum range was 14.0 m and a low point density was also obtained. The RMSE and ΔR of that range were 5.60 mm and 5.90 mm, respectively. The greater the range, the worse the accuracy that is achieved. The best accuracy (sub-mm level) was achieved from SCP4, where the range is very close, and also there is no effect of IA on the sphere result, as mentioned in the previous chapter.

In general, the full statistical results of fitting both the cone and the sphere (see Appendix J2, Table J2-3) show that the cone is more accurate than the sphere. The possible explanation for this is that when capturing sphere data some unwanted points (noise) from the bottom are involved in the fitting process. These points cannot be detected by the algorithm as an outlier in order to remove them from the fitting process. The second issue is the invisibility of the sphere target's centre, adding additional error sources to the calculation steps.

6.5 Conclusion

In this chapter, automatic detection of the designed targets from surrounding points in the laser point cloud has been discussed. This covers the second part of objective 3 of this thesis.

The Matlab algorithm was improved to deal with many different cases, such as when the number of points outside the target is greater than that inside (see Figure 6.17). This issue was solved for the octagon-based pyramid by covering four of these faces with HRT as a good initial step. In addition, using this pyramid helps to ensure that at least three faces will be seen from any incidence angle, as described in section 6.3.

Fitting a best-fit line and plane to a set of data was discussed; the equations used can be seen in the next chapter. Absolute accuracy of the apex compared with its control value measured using TS at different resolutions between the maximum and minimum was presented in Appendix L. The accuracy of the measured value was within ± 1 mm.

For the sphere and cone, on the other hand, a good initial step in terms of detection and IA is to use a unique colour. Tests show that the cone and sphere are the best of all the targets used.

CHAPTER7: METHODS OF IDENTIFICATION OF TARGET CENTRE

This chapter complements the previous chapters in achieving the second part of the third objective of this research, and the subject of this chapter is to identify the quality of the centre/apex of the detected targets, as explained in the previous chapter.

This chapter will introduce the procedures for identifying a target's centre/apex in the laser point cloud, namely plane intersection, average determination and Gauss Newton. The mathematical models of these methods were used in Matlab to calculate automatically the centre/apex of different targets of the same shape in the same cloud. The Levenberg-Marquardt (LM) algorithm was used (from open source) as another option for fitting objects and calculating their centres. The full statistical results relating to the fitting process will be discussed. The workflow for the procedure can be seen in Figures 7.1 and 7.2, which show the processing steps using Matlab functions.

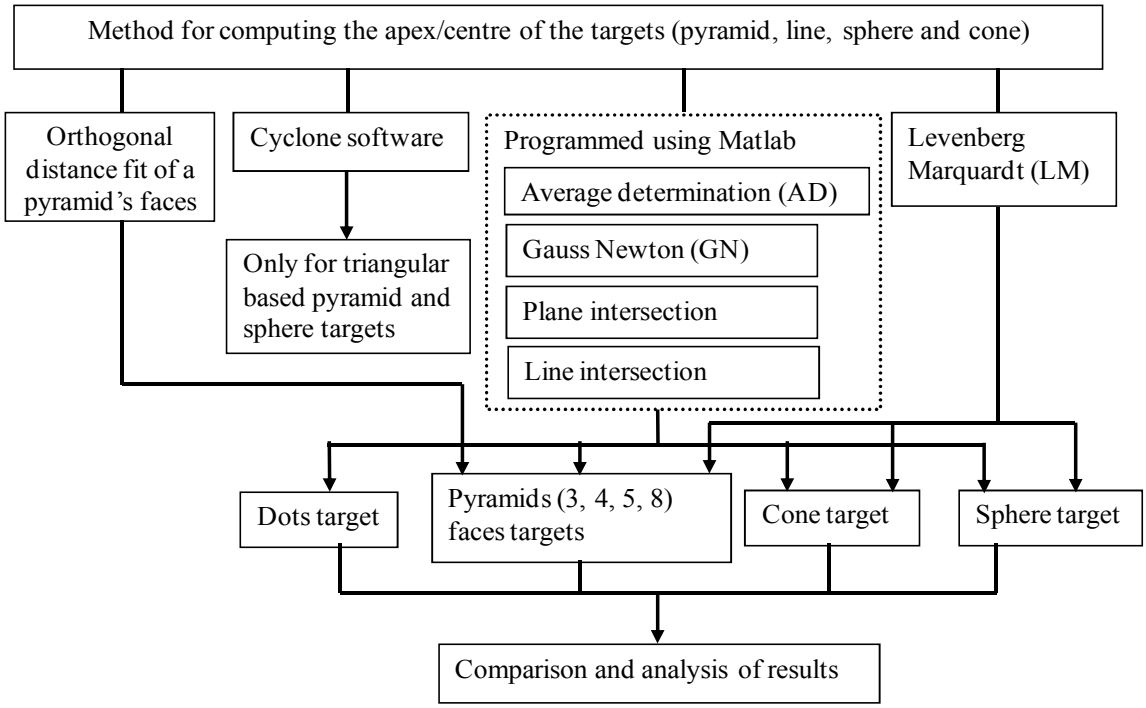

Figure 7-1: Flow diagram of the methods used for determining the centre or apex of the targets.

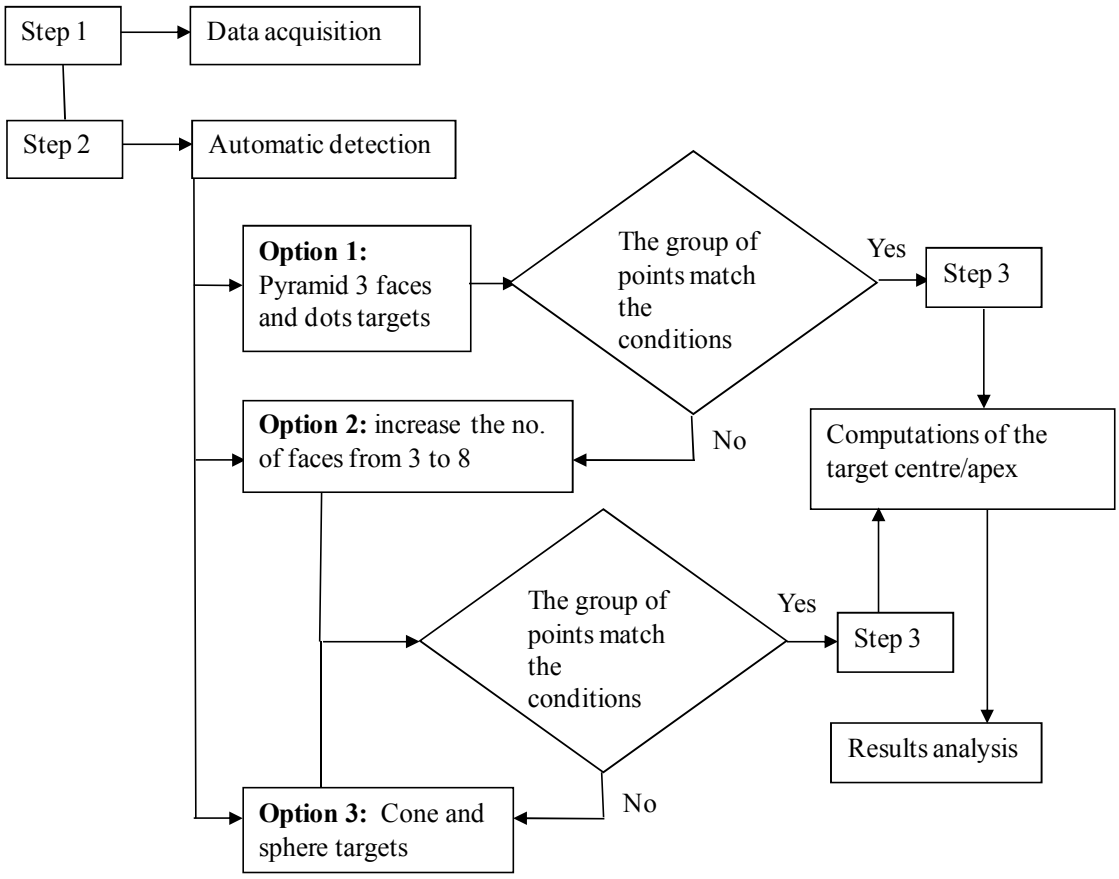

Figure 7-2: Flow diagram of automatic detection and identification of the target's centre/apex.

7.1 Introduction

The subject of this chapter is the use of algorithms for optimization of least squares best fitting of objects to a set of data of different geometric targets. This was tested using Matlab functions for the various geometric shapes of the targets, using real data points obtained from a static laser scanner (TLS) and/or MLS scanner. The geometric shapes investigated were a 3D line, planes (pyramid faces), spheres and a cone.

This chapter considers the problem of least squares surface fitting of spheres, a cone, plane and a line to 3D data. The motivation for this problem lies in identifying accurately the centre/apex of the shape, the actual target point. The problem can be decomposed into two logical steps: *Detection*, where the data points are grouped into sets each belonging to a different surface, as described in the previous chapter, and *fitting,* where the best surface of the appropriate type is fitted to each group of points. This chapter is mainly concerned with the problem of fitting, The geometric least

squares surface fitting of a cone, spheres and planes of a "simpler type" have also been studied by Luk´acs et al. (1997).

7.2 Least squares method

In general, the least squares technique for best-fitting of objects (line, plane, cone and sphere) uses the object that has the smallest sum of the deviations squared from a group of data.

The least squares technique uses a straight line. Consider fitting a straight line.

$y = a + bx$……(7.2.1)

According to the method of least squares, the best fit line has the property that:

$F = d_1^2 + d_2^2 + \cdots + d_n^2 = \sum_{i=1}^{n} di^2 = \sum_{i=1}^{n} (yi - f(x_i))^2 = a\ minimum$…(7.2.2)

The traditional method used in the standard books for least squares fitting of a straight line has been explained by many researchers, such as (Miller, 2006; Feller, 1971; Forbes, 1989).

7.2.1 Line fitting using least squares

Lines can be specified in 2D or 3D. The procedure is used to fit a line to a set of data points (xi,yi,zi). Any 3D point on the line can be expressed by equation (7.2.1.1). This can be specified by a point (x_o, $y_{o,}$, z_o) on the line and the direction cosine (a, b, c) (Delaware, 2008).

$(x, y, z) = (x_0, y_{0,,} z_0) + t(a, b, c)$……(7.2.1.1)

The value of t is the distance from a point to a line in 3D, denoted as d (Delaware, 2008).

$d = \sqrt{(x - x_0)^2 + (y - y_0)^2 + (z - z_0)^2}$……......(7.2.1.2)

In this thesis, two methods were used for fitting a line to a set of data.

1. Least squares fitting to a straight line in 2D, x and y axis, x and z axis and z and y axis, using a first order polynomial equation. This expresses the

dependent variable (y) as a polynomial in the independent variable (x) for a straight line y = a + bx (O'Haver, 2008).

2. Least squares fitting to a straight line in 3D, using singular value decomposition (SDV) for solving the parameters (a, b, c) (Delaware, 2008).

In both methods, the algorithms were developed using Matlab functions.

The first method, algorithm description: The best-fit line passes through the centroid (Xmean, Ymean, Zmean) of the data, and this is determined as follows:

- The coefficients *a* and *b* have to be found out from the linear equation (Y = a + bx), where y is a linear function of parameters (*a*, *b*).
- The initial step is to find the mean of the point's x_i, y_i and z_i. (i.e. $\bar{X}, \bar{Y}$ *and* $\bar{Z}$).
- The correlation coefficient R^2 needs to be determined. $R^2 = 1 - \frac{\sum_{i=1}^{n}(Y_i - a - bX_i)^2}{\sum_{i=1}^{n}(Y_i - \bar{Y})^2}$ This is a measure of the quality of fit (the fit is perfect when R^2 is exactly 1.00).

The application UNT2 (UNT2.1) algorithm for intersection lines in 2D, and UNT2.1.4 and UNT2.3 for 3D line intersection can be seen in the attached CD (see Appendix K).

The second method, algorithm description: The best-fit line passes through the centroid (x mean, y mean, z mean) of the data, and this is determined as follows (Delaware, 2008).

- A point on the line and the direction cosines (*a*, *b*, *c*) have to be found out,
- The initial step is to find the mean of the point x, y and z.

$$\bar{X} = \frac{\sum_{i=1}^{n} x_i}{n} ; \ \bar{Y} = \frac{\sum_{i=1}^{n} y_i}{n} ; \ \bar{Z} = \frac{\sum_{i=1}^{n} z_i}{n} \quad \text{.....(7.2.1.3)}$$

where, n is the number of point of each element (x, y, and z)

- The matrix A is formulated such that its first, second and third columns are $x_i - \bar{X}$, $y_i - \bar{Y}$ and $z_i - \bar{Z}$ respectively.
- This matrix A is solved by SVD via Matlab functions. The smallest singular value of A is chosen; the squares sum of residual points to the line distance and the corresponding singular vector is selected, which is the direction cosines (*a*,*b*,*c*).
- The suitable fit line is determined by $\bar{X}, \bar{Y}, \bar{Z}$, a, b and c.

7.2.2 Plane fitting using least squares best fit

The procedure of fitting a plane to a set of points (x_i, y_i, z_i) is given below. Any point (xyz) on the plane satisfies the equation below (Delaware, 2008).

$a(x - x_o) + b(y - y_o) + c(z - z_o) = 0$……...(7.2.2.1)

The distance between a point (x_i, y_i, z_i) and a plane can be determined by $x_o, y_o, z_o, a, b \text{ and } c$ and is given as follows (Delaware, 2008).

$di = a(x - x_o) + b(y - y_o) + c(z - z_o)$……(7.2.2.2)

A plane can be specified by a point (x_o, y_o, z_o) on the plane, and the direction cosine (a, b, c) of the normal to the plane.

The problem is to find the parameters (x_o, y_o, z_o) and (a, b, c) that minimize the sum of function F, which is the squares of the distances of each point to the plane following the equation.

$F = \sum_{i=1}^{n} d_i^2$……...(7.2.2.3)

where d_i^2 is the sum of the squares of distance of each point from the plane.

Two methods were used for plane fitting and determining the intersection point (three or more planes) to find the apex of a pyramid.

1. The same SVD approach was used to solve the parameters of each plane as a function of $\bar{X}, \bar{Y}, \bar{Z}, a, b \text{ and } c$. Then, the intersection of each fitted plane was used to calculate the apex of the target. The results can be seen in

Appendix L and the application of the UNT1 (UNT1.1) algorithm can be found in the attached CD (see Appendix K).

For the method referenced to SVD for fitting the line and plane, the precise analytical result is developed in two cases:

- Fitting a straight line in 3D (orthogonal distances between each point and the line).
- Fitting a plane in 3D (normal distances between the plane and each point).

This SVD method is not iterative, and the final output is achieved by only one run of computation via the Matlab algorithm.
A compendium of formulas is provided for the practical case of fitting to a straight line and the case of fitting to a plane. Numerical examples provided for the tests can be found in Delaware (2008).

2. The orthogonal distance fit of a pyramid faces (Lösler, 2012b).

The second method used for fitting and calculating the apex of the pyramid has been developed by in collaboration with Lösler (2012b). A combined algorithm was used, which estimates the plane parameters and the apex of the target together, formulated as the Gauss Helmert model with unknown in the restriction.

In the mathematical model for fitting a pyramid (for example, with four faces), the developed algorithm estimates the parameters of the four planes. The planes are parameterized as Hesse normal form (Wikipedia, 2012).

$$n_x x_i + n_y y_i + n_z z_i = d \quad \text{.....(7.2.2.4)}$$

with the secondary condition,

$$|n| = \sqrt{n_x^2 + n_y^2 + n_z^2} = 1 \quad \text{.....(7.2.2.5)}$$

For each plane, the unknowns are n_x, n_y, n_z and d. In the case of the square-based pyramid, the algorithm estimates 4×4 = 16 plane parameters. Up to this point, the algorithm produces the same results as a single fit of each plane (see section 6.2).

To estimate the intersection of the planes, the number of unknowns is increased by three, namely the coordinates of the intersection point. To force an intersection of the four planes, four additional conditions are introduced. If k is the intersection point, each plane has to contain k, or similar (Lösler, 2012b).

$n_x x_k + n_y y_k + n_z z_k = d$.....(7.2.2.6)

This mathematical model can be used in a common orthogonal distance fit algorithm.

This algorithm was applied to the pyramid cases using different ranges and incidence angles; the statistical results of each case can be seen in Appendix L-L1, L2 and R-R1 for the case of MLS.

7.2.3 Least squares best fit - sphere

Fitting of the sphere to the collected data using the three methods is illustrated in the following sub-sections.

7.2.3.1 Least squares fit - iteration method

A sphere is specified by four parameters. This means that four points are required for the sphere to be specified, namely the centre (a,b,c) and radius r. Any point on the sphere satisfies the equation (see the algorithm UNT4 in the attached CD). The mathematical model of this algorithm is as follows.

$(x - a)^2 + (y - b)^2 + (z-c)^2 = r^2$ ……(7.2.3.1.1)

Initial estimate of centre coordinates and radius

The function has to be reduced for a specific initial estimate of the centre and radius. Assume the function (Delaware, 2008).

$f = r_i - r$ ……...(7.2.3.1.2)

where

$r_i = \sqrt{(x_i - a)^2 + (y_i - b)^2 + (z_i - c)^2}$……(7.2.3.1.3)

The equation (7.2.3.1.2) can be expanded and gives

$f = r_i^2 - r^2$

$f = (\text{xi} - \text{a})^2 + (\text{yi} - \text{b})^2 + (\text{zi} - \text{c})^2 - r^2$

$= -(2axi + 2byi + 2czi) + (a^2 + b^2 + c^2) - r^2 + (xi^2 + yi^2 + zi^2)$

a,b and *c* are unknown parameters while all x_i, y_i and z_i are given. To obtain the initial values of the unknown parameters *a,b* and *c,* the equation needs to be linearized. In order to make the equation linear, the following approach can be used (Delaware, 2008).

$Let\ k = (a^2 + b^2 + c^2) - r^2$

$= -(2axi + 2byi + 2czi + k + (xi^2 + yi^2 + zi^2)$ ……..(7.2.3.1.4)

The equation (7.2.3.4) for n set of data points can be presented in a matrix form

$$\begin{bmatrix} f1 \\ f2 \\ .. \\ fn \end{bmatrix} = \begin{bmatrix} -2x1 & -2y1 & -2z1 & 1 \\ -2x2 & -2y2 & -2z2 & 1 \\ \cdots & \cdots & \cdots & \cdots \\ -2xn & -2yn & -2zn & 1 \end{bmatrix} \begin{bmatrix} a \\ b \\ c \\ k \end{bmatrix} + \begin{bmatrix} x1^2 + y1^2 + z1^2 \\ x2^2 + y2^2 + z3^2 \\ \cdots \\ xn^2 + yn^2 + zn^2 \end{bmatrix}$$

For the least squares solution, f i= 0, introduce the matrix notation.

$$\text{A}=\begin{bmatrix} -2x1 & -2y1 & -2z1 & 1 \\ -2x2 & -2y2 & -2z2 & 1 \\ \cdots & \cdots & \cdots & \cdots \\ -2xn & -2yn & -2zn & 1 \end{bmatrix};\ \text{P}=\begin{bmatrix} a \\ b \\ c \\ k \end{bmatrix} \text{ and B}=\begin{bmatrix} x1^2 + y1^2 + z1^2 \\ x2^2 + y2^2 + z3^2 \\ \cdots \\ xn^2 + yn^2 + zn^2 \end{bmatrix}$$

Solving the normal equation AP-B = 0 in least squares obtain parameters P. This means that P satisfies the normal equation as follows:

$A^T AP = A^T B$ ……..(7.2.3.1.5)

The initial estimates for parameters *a,b,c* and *k* are obtained from equation (7.2.3.1.5) for P. The initial estimates for the radius *r* can be obtained from the relation.

$k = (a^2 + b^2 + c^2) - r^2$

using the Gauss Newton method and building the Jacobian matrix (Delaware, 2008).

Gauss Newton method: The Gauss Newton method is used to reach the final values for the centre and radius, after obtaining the initial values of the centre *(a,b,c)* and radius *(r)*.

Minimizing function *f* : To minimize the function, the following equation can be expressed.

$d_i = r_i - r$ ……..(7.2.3.1.6)

where r_i is defined in equation (7.2.3.1.3).

Building the Jacobian matrix: The elements of the Jacobin matrix are expressed by differentiating of the function *di* with respect to (a, b, c and r) = J element matrix.

$$\begin{bmatrix} \frac{\partial d1}{\partial a} & \frac{\partial d1}{\partial b} & \frac{\partial d1}{\partial c} & \frac{\partial d1}{\partial r} \\ \frac{\partial d2}{\partial a} & \frac{\partial d2}{\partial b} & \frac{\partial d2}{\partial c} & \frac{\partial d2}{\partial r} \\ \cdots & \cdots & \cdots & \cdots \\ \frac{\partial dn}{\partial a} & \frac{\partial dn}{\partial b} & \frac{\partial dn}{\partial c} & \frac{\partial dn}{\partial r} \end{bmatrix} \quad \text{……..(72.3.1.7)}$$

The results are obtained for the various components of the Jacobian matrix and substituting in the matrix. The full mathematical algorithm can be found in (Eberly, 2008).

$$\begin{bmatrix} \frac{-(x1-a)}{r1} & \frac{-(y1-b)}{r1} & \frac{-(z1-c)}{r1} & -1 \\ \frac{-(x2-a)}{r2} & \frac{-(y2-b)}{r2} & \frac{-(z2-c)}{r2} & -1 \\ \cdots & \cdots & \cdots & \cdots \\ \frac{-(xn-a)}{rn} & \frac{-(yn-b)}{rn} & \frac{-(zn-c)}{rn} & -1 \end{bmatrix} \quad \text{…….(7.2.3.1.8)}$$

Solving the linear least squares system J^T. J P = J^T. (-d), where P= $\begin{bmatrix} pa \\ pb \\ pc \\ pr \end{bmatrix}$

The Increment parameters according to *(a1)* = *a*+*Pa*; *(b1*) = *b*+*Pb*; *(c1)* = *c*+*Pc*; *r1*= *r*+*Pr*

A convergence condition is applied based on the number of iterations and the condition is g = J^T . d is a minimum.

The practical application of this method can be seen in Tables 7.1 and 7.2 and a script algorithm UNT4 is presented in the attached CD (see Appendix K). The fitting

of the sphere was also investigated using the average determination method, which is discussed in the next section.

7.2.3.2 Least squares fit - average determination method

In this method, the average points of (x_i,y_i,z_i) of a sphere target are used. Then, the least squares surface fitting is used following the same equations, 7.2.3.1.2 and 7.2.3.1.3, as applied in the previous section.

The mathematical model for fitting of the sphere to a set of data was written using the Matlab function and the algorithm UNT3 (see the file in the attached CD). This method is based on the minimization of the function F. So, we minimize the equation 7.2.3.2.1, and solve the linear system for the normal equation.

$$F = \sum_{i=1}^{n}[(x_i - a)^2 + (y_i - b)^2 + (z_i - c)^2 - r^2]^2 \quad \text{.....(7.2.3.2.1)}$$

where *x*, *y* and *z* are the data, *a*, *b* and *c* are the centre of the sphere and r is the radius.

Algorithm description

The first step is to find the average of x, y and z following the previous equation 7.2.1.3 (section 7.2.1) giving $\bar{X}, \bar{Y}$ *and* $\bar{Z}$.

The second step is to set up two matrices A and B to determine the sphere's centre and radius. The two matrices are (Jennings, 2011).

A=

$$2 * \left[\frac{\sum_{i=1}^{n} x_i(x_i-\bar{X})}{n}, \frac{\sum_{i=1}^{n} x_i(y_i-\bar{Y})}{n}, \frac{\sum_{i=1}^{n} x_i(z_i-\bar{Z})}{n};\right.$$
$$\frac{\sum_{i=1}^{n} y_i(x_i-\bar{X})}{n}, \frac{\sum_{i=1}^{n} y_i(y_i-\bar{X})}{n}, \frac{\sum_{i=1}^{n} y_i(z_i-\bar{Z})}{n};$$
$$\left.\frac{\sum_{i=1}^{n} z_i(x_i-\bar{X})}{n}, \frac{\sum_{i=1}^{n} z_i(y_i-\bar{X})}{n}, \frac{\sum_{i=1}^{n} z_i(z_i-\bar{Z})}{n}\right] \quad \text{.....(7.2.3.2.2)}$$

$$B = \left[\frac{\sum_i^2[(x_i^2+y_i^2+z_i^2).(x_i-\bar{X}]}{n}, \frac{\sum_i^2[(x_i^2+y_i^2+z_i^2).(y_i-\bar{Y}]}{n}, \frac{\sum_i^2[(x_i^2+y_i^2+z_i^2).(z_i-\bar{Z}]}{n}\right]$$

.....(7.2.3.2.3)

Then, the centre of the sphere and the residuals in the radial direction are computed (see Appendix I, Figure I5).

Centre (a, b, c) = (A \ B)

Let $m_{xi} = (x_i - a)^2;\ m_{yi} = (y_i - b)^2; m_{zi} = (z_i - c)^2$

$$Radius = \sqrt{\frac{\sum_{i=1}^{n}(m_{xi}, m_{yi},\ m_{zi}),\ (m_{xi}+m_{yi}+m_{zi})}{n}} \quad \text{.....(7.2.3.2.4)}$$

Residual (k) = $Radius - \sqrt{m_{xi} + m_{yi} + m_{zi}}$ .....(7.2.3.2.5)

The statistical results of fitting the sphere are also calculated as follows:

Standard deviation (Std Dev) = $\sqrt{\frac{\sum_{i=1}^{n} k}{n-1}}$ .....(7.2.3.2.6)

Error Mean = $\frac{\sum_{i=1}^{n} k}{n}$ .....(7.2.3.2.7)

Absolute error Mean = $\left|\frac{\sum_{i=1}^{n} k}{n}\right|$ .....(7.2.3.2.8)

Maximum absolute error Mean = max $|k|$

Least squares were used to solve these equations and the results were compared using Cyclone software, as shown in Table 7.1. The full results from different positions can be seen in Appendix I4. Both the developed algorithms UNT3 for fitting (sphere) using the AD method and UNT4NEWFIT using the GN method can be seen in the attached CD (Appendix K).

7.2.3.3 Least squares fit - Levenberg Marquadt (LM) algorithm

To solve non-linear least squares problems, the Levenberg-Marquardt method is used as a standard technique. Least squares problems take place when fitting a parameterised function to a group of measured data points by reducing the sum of squared errors between the data points and function. Non-linear least squares

methods require iterations to reduce the summation of squares of errors between the measured data points and function (Gavin, 2011).

The Levenberg-Marquardt curve-fitting approach is a grouping of two minimisation methods: the gradient descent and the Gauss-Newton. In the first method, the summation of the squared errors is reduced by updating the parameters in the direction of the maximum reduction of the least squares objective (Gavin, 2011).
In the second method, the summation is the reduced square of errors, assuming that the quadratic function is locally least squares, and finding the minimum of the quadratic. The Levenberg-Marquardt method acts as a gradient-descent approach, when the parameters are far from their best possible value, and acts as the other method (Gauss-Newton) when the parameters are close to their optimal value (Gavin, 2011). This algorithm is already available from open source software JAG3D – a free program for network adjustment and deformation analysis. The algorithm developed by (Lösler, 2012a) is used for fitting objects such as the plane, line sphere and cone. The algorithm was applied in the tests described in section 5.5.5 and is discussed in the next sub-section. An example of fitting a sphere and cone from the tests described in section 5.5.5, using this approach, can be seen in Appendix J2.

Algorithm description

To apply the algorithm for fitting targets (cone, sphere and plane) and compute their statistical results, the following steps were performed:

Step 1: Data, from either TLS or MLS, should be converted and saved in a .txt file, containing (X, Y, Z) coordinates, and the point number. The main window of the software can be seen in Figure 7.3 (left). The geometric shape can be chosen from the settings shown in Figure 7.3 (right).

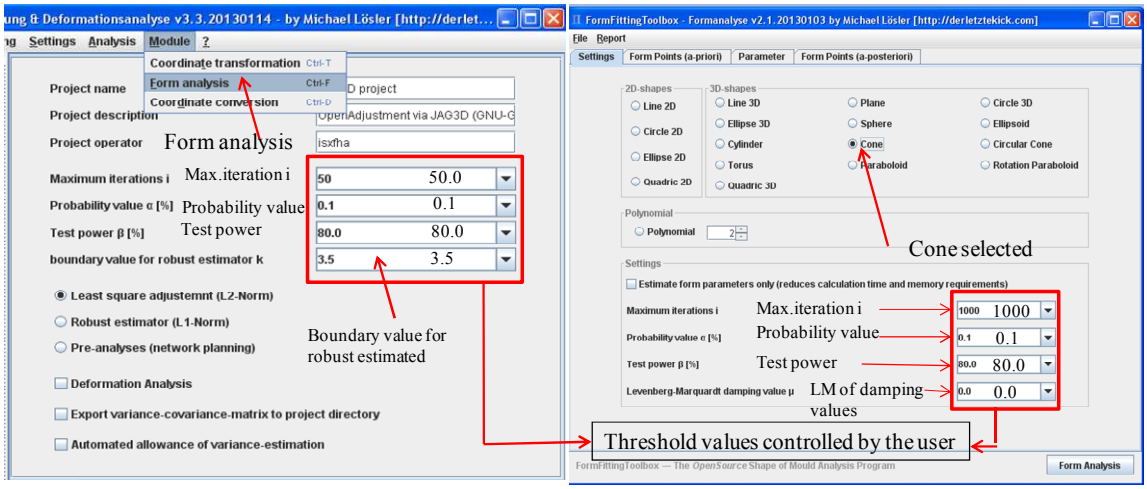

Figure 7-3: The LM algorithm. Left: the main window. Right: the list of the form objects that the algorithm provides for fitting.

The threshold values in Figure 7.3 control the capability of the algorithm using damping values, as can be seen in Figure 7.4.

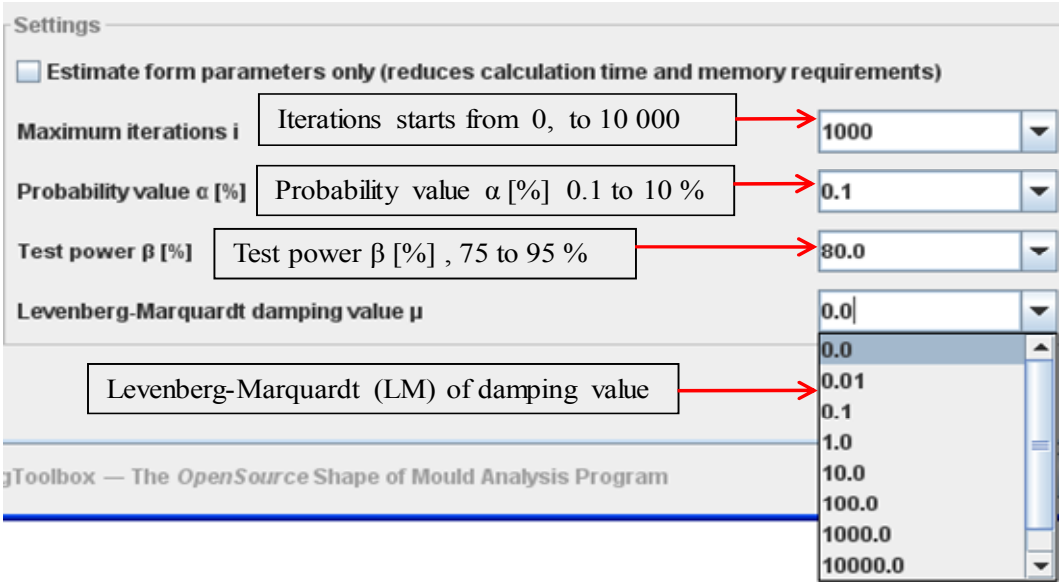

Figure 7-4: The LM algorithm of damping value and other control values.

Step 2: Load the data as shown in Figure 7.5, and the algorithm will then process the data to fit the object surface and adjust it to be error free. Here, the time of processing isimportant. The program is slow when the number of points increases to over 500.

Step 3: In this step, the algorithm computes the parameters of the selected target data (cone), and the variance and covariance matrix of the fitting are analysed automatically. The full statistical results of fitting the cone and sphere are shown in Appendix J2.

Step 4: After processing the data and adjusting the result, the report is saved in order to see the full statistical results (see Figure 7.6). A sample of the report can be found in Appendix J2, with an explanation of each element on the statistical results.

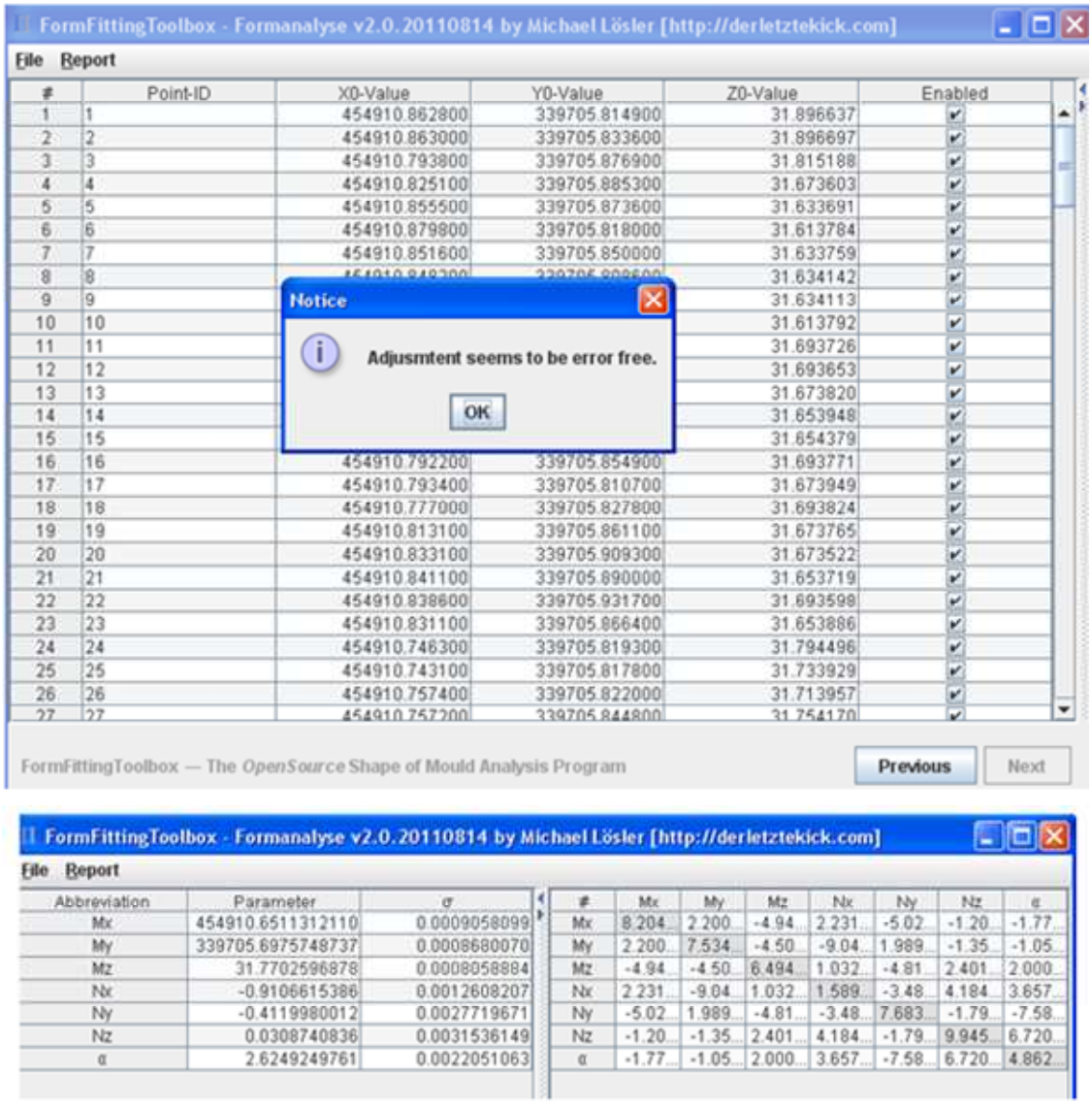

Figure 7-5: The process of point data and results. Top: the points and processing. Bottom: cone parameter solved, and variance covariance matrix determined.

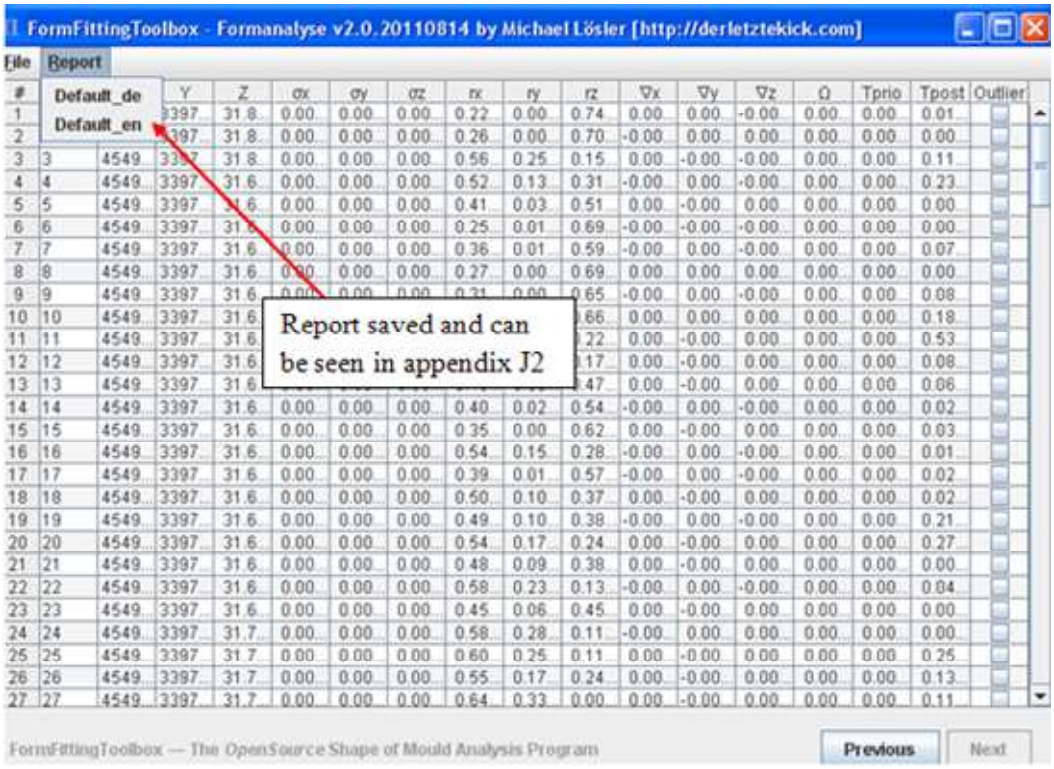

Figure 7-6: The statistical result of the cone fitting.

7.3 Results and analysis

Results for the sphere, cone and pyramid using Faro Focus^{3D} and HDS3000 laser scanners are presented below.

1. Using Faro Focus^{3D} 120 laser scanner

Target. Range= 10 m and IA =0^{o}	Point density	Pts/Tar	σpar. apex (m)	Accuracy apex (m)	Method
Sphere Size (0.100 m R)	(12*12) mm @ 10 m	149	0.0007 0.0004 0.0006 0.0016	-0.0023 -0.0036 -0.0021 -0.0039	AD LM Cyclone Gauss N
Cone Size (0.150 m R), and slant height=2R	(12*12) mm @ 10 m	300	-------* 0.0013 --------* 0.0075	-------* 0.0022 -------* 0.0064	AD. LM Cyclone Gauss N
Pyramid 8 faces Size (0.200 m R), and height= 0.100 m	(12*12) mm @ 10 m	447	0.0532 0.0016 0.0033 0.0090	-0.0021 -0.0081 -0.0029 -0.0080	AD. Orthogonal dist. Cyclone LM+Plane Int.

Table 7-1: Accuracy and precision of the targets using different methods.

2. Using HDS3000 laser scanner

Target. Range = 10 m and IA =0°	Point density	Pts/Tar	σpar. apex (m)	Accuracy apex (m)	Method
Sphere P1	(10*10)mm @ 10 m	332	0.0016	-0.0031	AD
			0.0005	-0.0037	LM
			0.0006	-0.0025	Cyclone
			0.0028	-0.0044	Gauss N
Cone P1	(10*10)mm @ 10 m	583	.....*	.....*	AD
			0.0005	-0.0026	LM
			.....*	.....*	Cyclone
			0.0044	-0.0051	Gauss N
Pyramid 8 faces P1	(10*10)mm @ 10 m	588	0.0053	-0.0092	AD
			0.0014	-0.0072	Orthogonal dist.
			0.0016	-0.0022	Cyclone
			0.0041	-0.0079	LM+Plane Int.

Table 7-2: Accuracy and precision of the targets (sphere, cone and pyramid) using different methods.

(*) The Cyclone software and AD algorithm were not used for fitting the cone.

Further variation results from different ranges and IAs can be seen in Appendix I1 and I2.

From Tables 7.1 and 7.2, it can be seen that all the error values of the difference between the parameters obtained from the fitting process and the control value (TS) are almost negative at a range of 10.0 m. This means that the laser scanner considers the target to be closer than it is, due to its highly reflective surface. For the time of flight (TOF) HDS3000, the internal sensor receives the laser pulse in a shorter time than it should. The Faro Focus^{3D} phase-based laser scanner calculates a shorter shift in the phase than it should. This could be due to a number of factors, including the high reflectivity of the target, advance of the laser pulse due to the atmosphere, or an internal error in the range measurement system.

The accuracy and precision decreased as the range increased for both scanners. The accuracy of the target position with the TOF HDS3000 laser scanner decreased

slowly, reaching 16 mm with a range of nearly 60 and 70 m for the sphere and cone respectively (see Appendix I, Tables I2-2 and I2-3). The specification given by Leica Geosystems for the HDS3000 gives a position accuracy of 6mm for a single measurement with 1-50 m for one sigma, but this specification was only met at 10 m in these tests using the phase-based Faro Focus^{3D}, while with the HDS3000 laser scanner, this accuracy was obtained with a range of nearly 30.0 m (see Appendix I, Tables I2 and I3) for the cone target and only using the LM method. The accuracy for the octagon pyramid apex at the same range using the LM method was 10.60 mm. This could be due to inaccuracy of the BM used for comparison. The sphere, cone and pyramid failed beyond the range of 40 m with the Faro Focus^{3D}, because they could not be recognised as targets in the automatic detection process, due to the large amount of data missing, as previously mentioned. With the HDS3000 laser scanner, the sphere and octagon pyramid failed beyond the ranges of 70 and 40 m respectively and the cone target remained working up to 90.0 m (see Appendix I, Table I2-1 to I2-4, and also Table 5.6)).

The precision of the modelled surface according to the specification given by Leica Geosystems for HDS3000 is 2mm, one sigma (Leica., 2010). In this test, results of fitting were better than the Leica specification, reaching about 0.5 mm for both the sphere and cone fitting, with the LM method using the HDS3000 laser scanner**.** This is because this algorithm is a combination of two minimisation methods: the gradient descent method and the Gauss-Newton method. In the gradient descent process, the sum of the squared errors is minimised by updating the parameters in the direction of the greatest reduction of the least squares objective (Gavin, 2011).

The fitting of the targets, especially the sphere, resulting from Cyclone software and AD (using Matlab functions), are nearly the same (see Tables 7.1 and 7.2, and also Table 6.5 or Figure 6.23); the only difference is that the Cyclone cannot detect the sphere or other targets automatically. Therefore, the Cyclone method was not used for further ranges in this test. The results obtained using the Gauss Newton method was also close to AD (see Tables 7.1 and 7.2). The reasons for using these methods are to compare each other in terms of the fitting process and computations of the target centre/apex. For example:

1. The average determination method was used to fit the sphere instead of using the optimization toolbox, the least squares fit used, and the average of the radii from the centroid (x, y, z). The centroid is calculated by an average, where the average can be considered the best fit (Miller, 2006).

2. The Gauss Newton method was used to fit the sphere by linearising a non-linear function using a Taylor series and using iterations to minimise the differences. Both methods were written in Matlab and combined with the detection part.

3. The LM method was used for fitting the geometric shapes of the cone, sphere, and plane. An example of fitting a best-fit cone and sphere to data is illustrated in Appendix J2.

4. The orthogonal distance fit of a pyramid's faces in collaboration with Lösler (2012b) was used for fitting pyramid faces (3,4,5 and 8), and the coordinates of the intersection planes and the estimated uncertainty of the apex were achieved to a high level of accuracy. The results obtained using this algorithm can be seen in Appendix L

Although the LM is a good least squares fit method, it has a number of disadvantages, such as that the algorithm is designed only for computation of the fitting process and cannot be used for target detection. For the dots and pyramid targets, an additional algorithm is needed for calculating the target centre/apex, such as the intersecting line and plane algorithm.

The accuracy and precision of the target position at different ranges can be summarised as follows:

- **Faro Focus^{3D} laser scanner - sphere and cone**

The accuracy obtained by the average determination and Gauss method at a minimum range (10 m), as shown in Table 7.1, is 2.30 and 3.9 mm for the sphere, and the precision of fitting at that range is 0.7 and 1.6 mm, one sigma, respectively, which is less than the specification given by the Faro Focus^{3D} product. The accuracy and precision of the target centre/apex obtained from the same range using the

Levenberg-Marquardt is better than the AD and Gauss methods by 0.9 and 2.2 mm. This is due to the LM algorithm iterating the values until reaching the convergence value. For these tests, the maximum number of iterations was 200 and precision of up to 0.5 mm could be obtained at a short distance.

The accuracy of the sphere centre obtained at maximum range (30.00 m) is 16 mm (see the full result in Appendix I Table I2-1), and the precision of fitting at that range is 5.80 mm. This accuracy and precision, obtained by the AD method, is better than that of the LM algorithm because the basis of the LM algorithm is a linear approximation of the function (f) in the neighborhood of the normal vector (Lourakis, 2005). This algorithm terminates when the value of residuals (observe – the estimate value) drops below a threshold, the relative change in the value of residuals of the second iteration is small, or the maximum number of iterations is completed without reaching the final value.

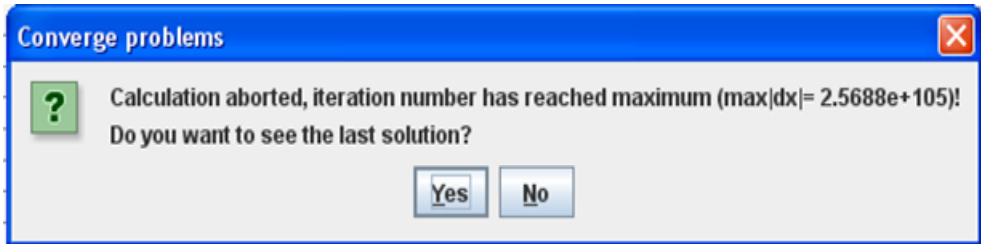

Figure 7-7: Screenshot report of the failed case.

This message shows that the program failed to fit the object and calculated parameters, due to a convergence problem.

This happened in the cone at (40 m) range at (0^{o}) IA, where the program failed to calculate the parameters (see Figure 7.7). This was solved by increasing the damping value (see Figure 7.4), which is less accurate than it should be. The precision and accuracy obtained in this case were 49.1 and 35.2 mm respectively (see Appendix I, Table I2-3).

- **HDS3000 laser scanner - sphere and cone**

The accuracy obtained by the average determination (AD) method at a minimum range (10 m) is -1.14 mm, and the precision of fitting at that range is 1.61mm**,** which is better than the specification given by Leica Geosystems. The accuracy obtained for

the same range using the LM is less than, and the precision is better than, that using AD by 1.14 mm, for the same reason as mentioned in the case of the sphere using the Faro Focus^{3D}120.

The accuracy obtained via the AD method at a range of 50.00 m is 13.00 mm (see the full results in Appendix I Table I2-2) and the precision of fitting at that range is 3.40 mm. 93.00 mm and 25.40 mm were obtained using LM for the same range due to its detection of outliers and its behaviour for the same reasons as mentioned above. After removing the outlier points, the accuracy and precision reduces to 10.18 and 3.64 mm respectively (see the results for the sphere at that range in Tables 5.5 and 5.10). Regarding the cone targets, the accuracy and precision of the apex were less than that of the same range, while the pyramid failed beyond the range of 40.0 m, as mentioned above.

7.4 Conclusion

This chapter discussed the mathematical model for determining the precision and accuracy of identifying the apex of the cone and pyramid and the centre of the sphere and Leica targets using least squares surface fitting of different methods, namely average determination, Gauss Newton, LM, and the commercial software package, Cyclone software v.6. The aim was to investigate the best fit capabilities of different algorithms and software.

The fitting process and computation of the target centre/apex from each technique were presented, showing that the best fit of the object to a set of data can be obtained from the LM algorithm at short range. The performance of this algorithm is degraded when a maximum number of iterations have been completed without reaching the final value. This can be solved by increasing the damping value, but this will affect the accuracy and precision of the apex or centre determination.

The LM is a technique that can be adapted to a wide variety of non-linear problems because it controls its own damping value (see Figure 7.4). It raises the damping if a step fails to reduce the sum of squares error; otherwise, it reduces the damping. In

this way, LM can negate difficult model non-linearities (although necessarily at low speed) (Lampton, 1997).

The least squares surface fitting using the average determination and Gauss Newton methods, developed by the author using Matlab functions, was also affected by noise measurements. The Gauss Newton method was used for fitting a sphere or cone, giving a cm level of accuracy, and the algorithm terminated in the second iteration. This is because the first iteration reaches the final value and the parameter value increases in the second iteration, which leads to termination of the program (see the algorithm in the attached CD of UNT4-GN method / UNT4NEWFIT.m). The benefit of the algorithm developed in this thesis is to detect the designed targets automatically from the surrounding point cloud and to calculate the centre/apex of these targets.

CHAPTER8: FINAL TESTING THE DESIGNED TARGETS WITH MLS

After the optimal design targets were selected, these were tested with MLS in an urban area, Figure 8.1 shows the optimal pyramid, cone and sphere targets, which were placed at various angles to the MLS scanning directions.

Targets are used in a number of ways in MLS, and are often chosen from natural detail points as discussed in chapter 2 section 2.2. These can be difficult to define particularly when high accuracy requirements need to be met; for example, in calibrating the system, matching scans together or fitting scans to existing surveys. This chapter begins with a brief description of the test, then, the accuracy of the result will be checked using both natural features and targets. Finally, the advantages and disadvantages of the method used, and a summary of the result will be given.

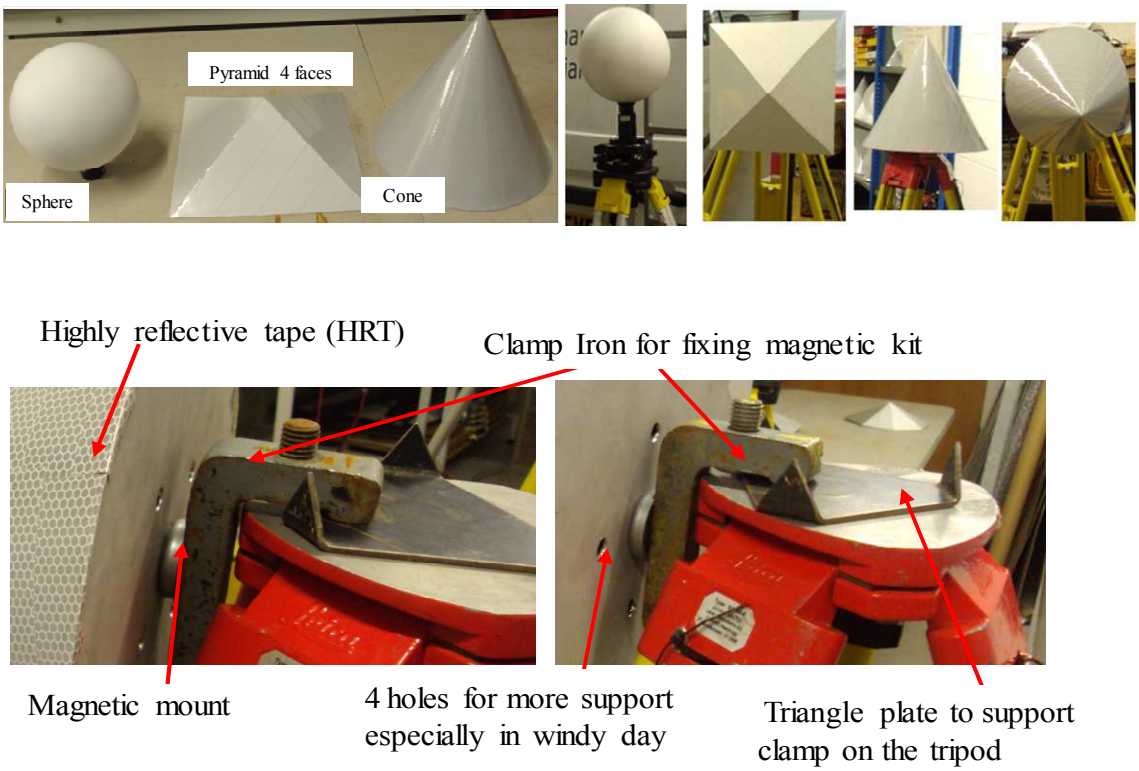

Figure 8-1: The proposed optimal targets and the way of fixing. Top: (Sphere, pyramid and cone) target. Middle: Target installing on the tripod using magnetic kits. Bottom: The way of installing the targets on the tripod.

8.1 Test description

This test aims to:

1. Compare the target coordinates achieved by MLS using designed targets and natural feature with those obtained from ground survey network adjustment.
2. Coordinate targets from multiple pass of scans to see how they compare.
3. Analyse the different types of targets used.

The above tasks were achieved through the following methodology.

1. MLS scanning the selected test site, including targets. Target coordinates are measured to high accuracy via ground survey using total station and level. The quality of the measured values are assessed using network adjustments, where the coordinates are measured several times from different fixed points, and all these observations are input to Trimble Geomatic Office (TGO) software to apply the adjustment. The results are compared after applying automatic target detection.

2. Matching the point cloud using natural features and targets. The Matlab algorithm is used for automatic detection (see Chapter 6 "the workflow of automatic target detection and measurement"), to compute the target centre/apex based on the least squares surface fitting (see Chapter 7). 3D transformation approach through the available software in NGI is used for matching using targets.
3. Comparing the result statistically from different target designs.

8.1.1 Test site

Two areas, with good and poor GPS visibility, have been selected (see Figure 8.2, left) for testing the designed target. Choosing these two areas was based on previous tests applied for assessing the quality of RTK in such areas.

8.1.2 Survey work

Some points have been fixed in both areas (see Figure 8.2, right) using a TRTS and based on three highly accurate GCPs (NGB10, NGB11 and NGB12). According to

the Nottingham Geospatial Institute (NGI) survey team, these point have been fixed with static carrier phase of 48 hours GNSS observation and about 3 to 5 mm level of accuracy of 1 sigma standard deviation, and considered being suitable for use as "true" coordinates. A level was used to determine the height and all observations were input to TGO software for applying the network adjustment, and the final coordinates of the two test area were computed, as given in (Table 8.1). The coordinates of the target centre/apex were measured several times from different fixed points in the two selected area, as shown in Figure 8.3. These observations were also input to TGO software to compute and adjust. The accuracy of target centre is based on the accuracy of points of the "true" GCPs. The full procedure of adjustment network can be seen in appendix O. It is worth mentioning that all coordinates used in the adjustments are in the National Grid OSGB36 coordinate system and the heights.

Point ID	Easting	Northing	Height	Note	Area
NBG10	454905.8200	339711.7890	30.1340	Previously adjusted by the NGI team and used as a "true" GCPs. at accuracy of 3 to 5 mm	Area1
NBG11	454893.2840	339700.2560	30.8140		
NBG12	454914.2120	339679.7200	29.9010		
T1	454887.6260	339685.7970	30.1180	Adjusted using survey network, and RMSE values are (1.0, 1.0, and 3.0) mm for E, N and Ht., respectively, (see appendix O).	
T2	454883.4240	339696.5870	29.9960		
T3	454882.8830	339708.8790	29.8540		
P1	454793.8126	339689.7516	29.9787	Adjusted using survey network, and RMSE values are (1.0, 1.0, and 3.0) mm for E, N and Ht., respectively , (see appendix O).	Area2
P2	454776.0763	339706.3035	29.4766		
P3	454770.3174	339743.8523	29.4959		
P4	454757.2604	339762.1003	29.4839		
P5	454757.3744	339782.5323	29.5119		
P6	454743.0744	339798.9743	29.5279		
P7	454749.3224	339810.2463	29.6499		
P8	454747.8836	339825.9370	29.8092		
P9	454856.5621	339850.0926	30.2153		
NBG11	454893.2840	339700.2560	30.8140		

Table 8-1: Adjusted GCPs of the two selected areas.

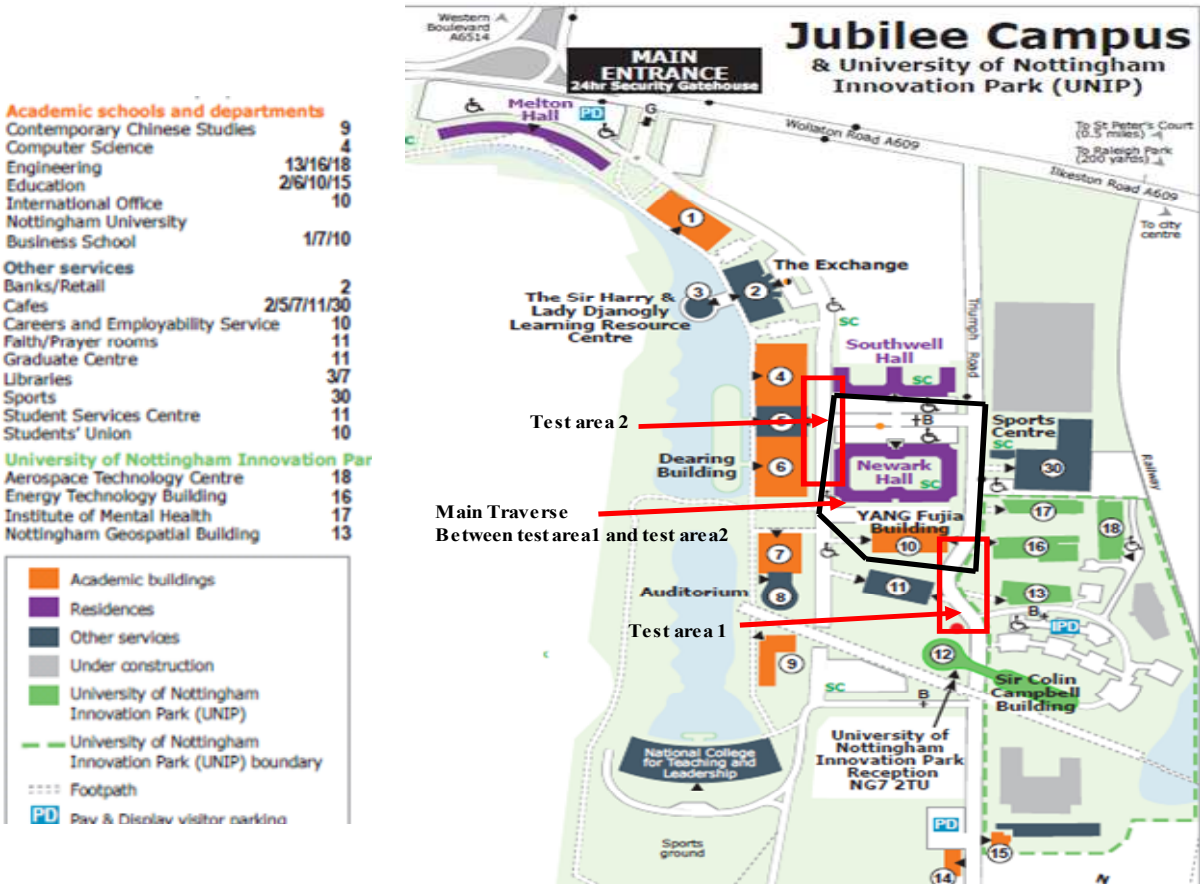

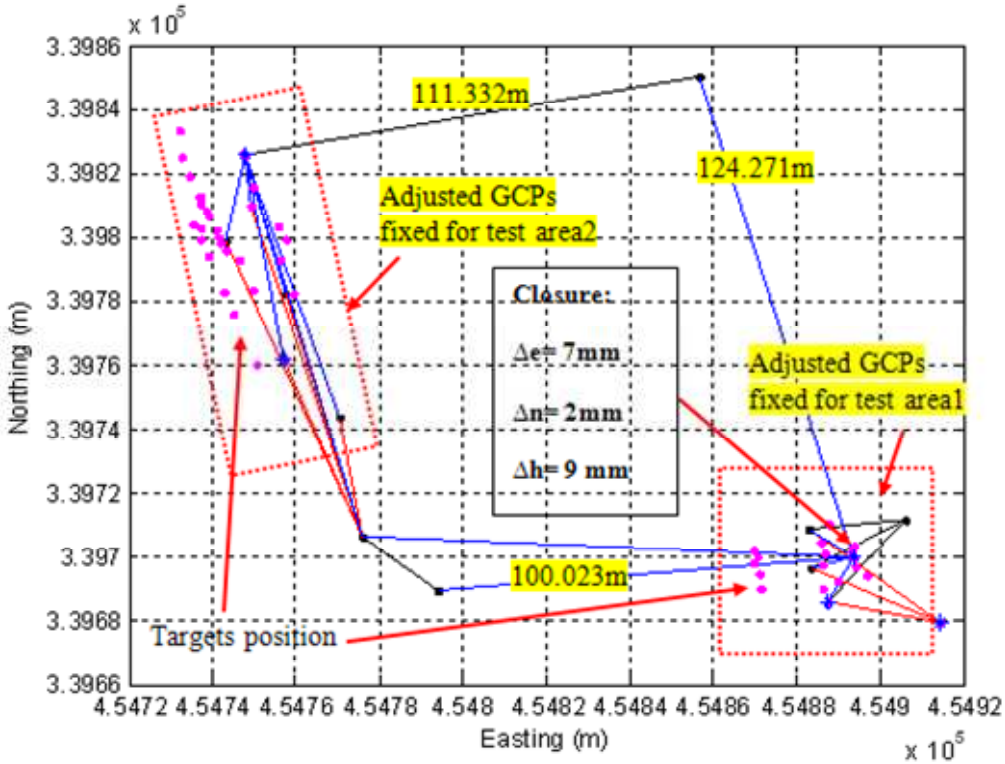

Figure 8-2: Test area and survey network. Top: Two test areas. Bottom: survey network for fixing the GCPs and the position of each target in two test areas drawn by Matlab algorithm.

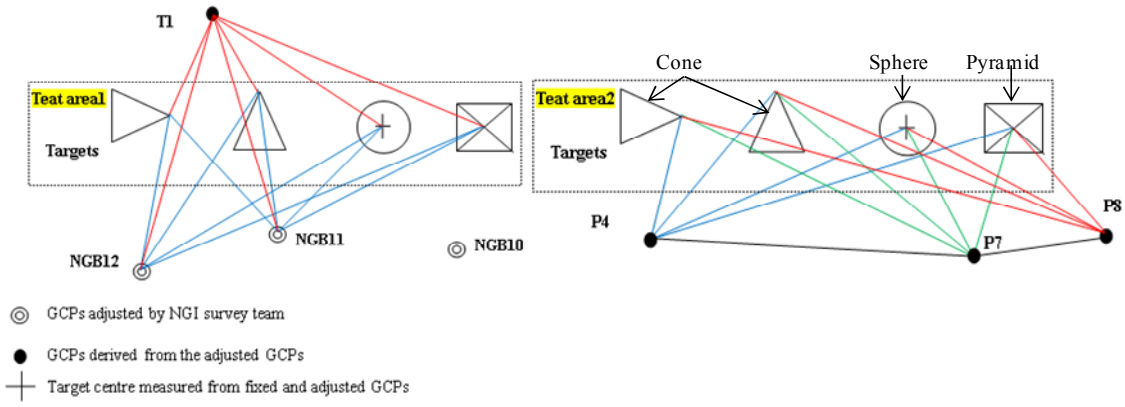

Figure 8-3: Traverse observation plan shows measuring the target centre/apex in area1 and area2 respectively.

8.1.3 MLS Data collection and processing

The MLS data were collected in December 2012. The applicable operating range of the MLS varied between 6 and 70 m depending on visibility. The system parameters used in the data collection from the Jubilee campus were previously summarised in chapter four, section 4.2.1.3, Table 4.17. The specifications of the system have been updated as can be seen in Table 8.2 (3DLM Ltd.).

MLS StreetMapper	**Specification**
Scanner	Riegl VQ-450: long range, high speed, high accuracy mobile mapping application
Effect point measurement rate	150 to 550 kHz
Max. the measuring range	800m @ ρ>= 80% and 150 kHz: 70 m @ ρ>= 10% and 550 kHz
Scanning Frequency	200 line/sec
Sensor position from horizontal level	135^{o} from forward and -40^{o} pitch from horizontal level
Navigation system	Novatel oem v3 IGI imu iie 400hz- S/N. 12-0175

Table 8-2: The specification of MLS (source: 3DLM Ltd.).

The MLS data was processed by 3DLM Ltd. where the trajectory of the vehicle was determined by post-processing using the permanent NGB2 reference station, which

located on the Nottingham Geospatial Building (NGB) to provide differential correction. Table 8.3 shows the standard deviation of (E, N and Ht.) of GPS position data in both areas. A summary report of the processing data can be seen in appendix Q, and another of calibrating the system using TerraScan / TerraMatch software is provided in appendix B.

GPS quality position – Area1			**GPS quality position – Area2**		
Std. E (mm)	**Std. N (mm)**	**Std. h (mm)**	**Std. E (mm)**	**Std. N (mm)**	**Std. h (mm)**
10 to 20	13 to 23	30 to 50	13 to 25	16 to 28	33 to 55
No., of satellite = 6 to 9 sat.			No. of satellite = 6 to 7 sat.		

Table 8-3: Standard deviation of the GPS position, and the number of satellite in area1 and area2.

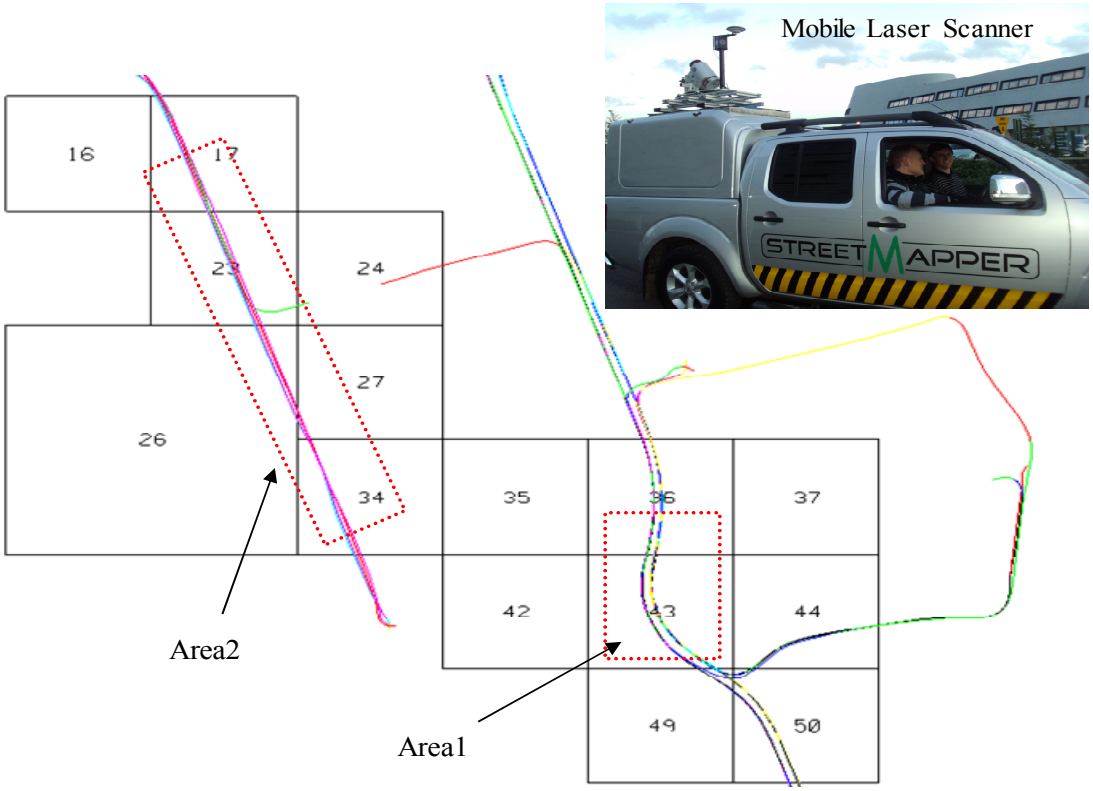

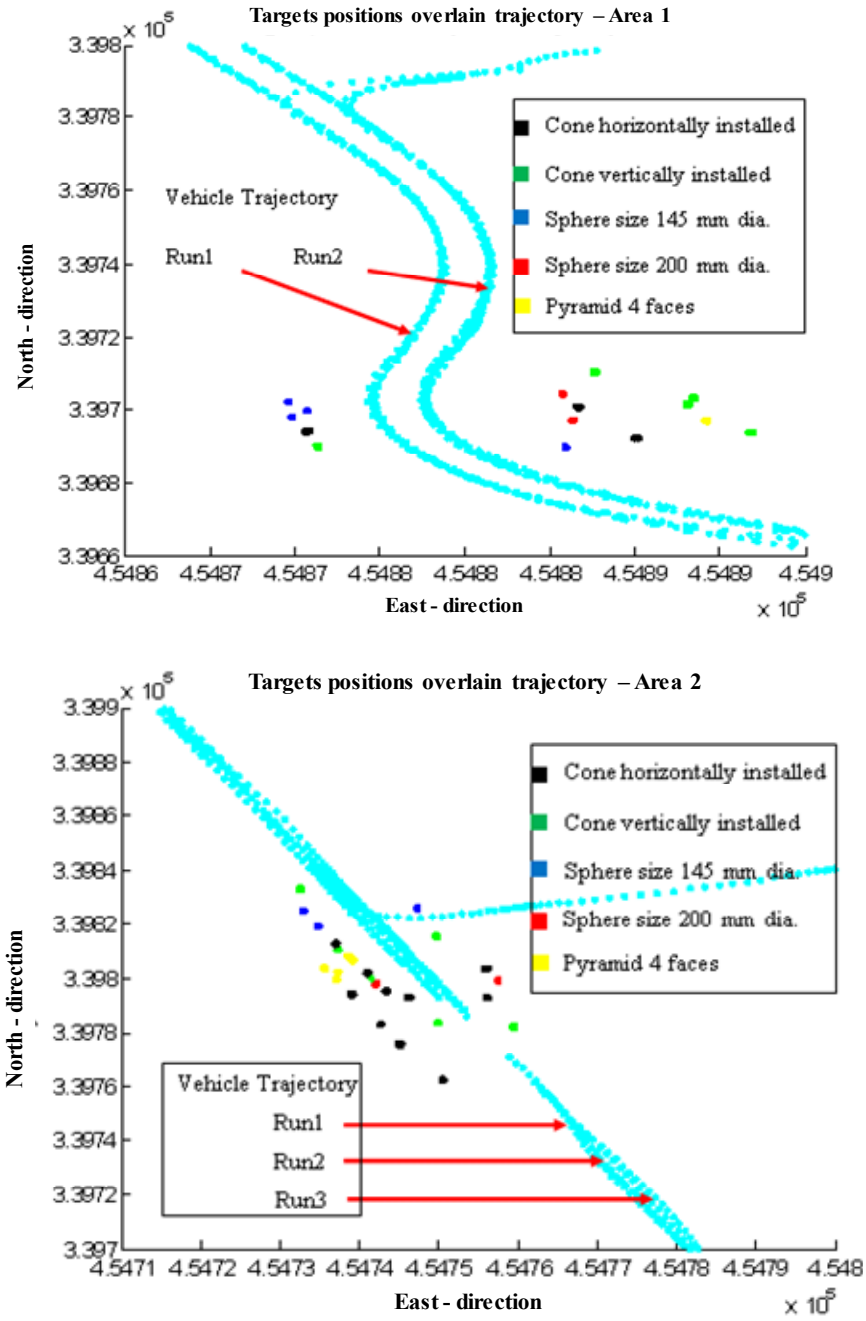

Figure 8-4: MLS survey in Jubilee campus. Top: Block of MLS point cloud with overlain trajectory solution shown in two test areas and in top right: MLS, StreetMapper (GPS, IMU and Riegle-VQ-450 laser scanner). Middle and Bottom: Targets positions overlain trajectory, area1and area2 respectively.

8.1.4 Result and analysis

After successfully running the TGO software to adjust the network, the adjustment result shows that to 95% confidence the maximum error ellipse is less than 2 mm for the adjusted coordinates of the target centre/apex. One of the output Figures from the TGO is the network geometry and error ellipse Figure of the adjusted point in both areas (See appendix O).

The 3D coordinates of each target, achieved using the TS and single and multi-scans of MLS, have been investigated. After detecting each target, the targets centre/apex have been estimated using the same approach of least squares surface fitting (LM, AD, and GN), discussed in Chapter 7. Then, the coordinates were compared with those of TS and the average deviation and RMS errors of the targets centre/apex with single and multi-runs from both areas (Area1 and Area2) were calculated. The results are shown in the following tables and figures. The full result of each target from both areas with single and multi-runs can be seen in appendix R-R2.

1. Using designed target- Cone : Area1 and Area2

Note- Area1: Cone Horizontally and vertically installed (H cone and V cone): Radius (r) = 0.15 m slant height = 2r : No. of (H Cone) = 3, average distance= 10.0 m. No. of V cone = 5, Average distance = 14.80 m.

Note- Area2: No. of H Cone. = 10, average distance = 8.15 m. No. of V cone = 6, average distance = 7.70 m.

Targets	Statistic	Pts.no.(R1,R2 and Multi-Runs)	Accuracy (Accur.) =TS Coord.- MLS estimated Coord; Area1								
			Run1 (mm)			Run2 (mm)			Multi-Runs (mm)		
			ΔE1	ΔN1	Δh1	ΔE2	ΔN2	Δh2	ΔE	ΔN	Δh
Cone H	Average Deviat.	(261,300, 562)	6.34	4.29	22.65	10.3	15.83	21.23	9.08	9.23	22.76
	RMSE		6.80	5.25	22.66	11.48	12.26	21.42	9.99	9.55	22.84
Cone V	Average	(134, 219,318)	20.06	9.50	22.4	16.60	14.57	13.51	12.96	13.89	16.67
	RMSE		21.69	11.99	23.54	17.23	14.59	16.33	13.83	14.82	18.19

Targets	Statistic	Pts.no.(R1,R2 and Multi-Runs)	Accuracy (Accur.) =TS Coord.- MLS estimated Coord; Area2											
			Run1 (mm)			Run2 (mm)			Run3 (mm)			Multi-Runs		
			ΔE1	ΔN1	Δh1	ΔE2	ΔN2	Δh2	ΔE3	ΔN3	Δh3	ΔE	ΔN	Δh
Cone H	Avera. Devia.	(289,367 ,54, 690)	6.13	6.28	24.69	5.18	-5.96	22.52	11.83	9.99	18.49	6.36	6.67	23.22
	RMSE		8.02	7.10	25.01	6.22	7.94	22.97	12.32	10.60	18.94	7.10	7.66	23.52
Cone V	Avera. Devia.	(287,336 ,186,800	16.03	7.18	8.15	12.85	8.60	11.15	18.40	10.44	12.47	14.52	7.32	9.09
	RMSE		19.39	8.72	9.06	15.44	10.90	14.07	20.09	11.19	13.34	17.87	8.64	12.58

Table 8-4: Average accuracy and RMSE of the cone apex vs single and multi runs in area1 and area2: Top: Area1. Bottom: Area2.

From both Tables, (8.4, top and bottom), it can be seen that average accuracy and Root Mean Square (RMS) error values for the apex of cone horizontally installed is better than vertically installed. This can be attributed to the number of scan points hitting the cone, which is more in the case of the H cone than V cone. This is because only half of the vertical cone can be seen during the test, while the other half is hidden from the laser beam. Even when the number of captured points increased for the V cone in the case of multi-scans, the accuracy has been less than achieved for the H cone. Also, it may be noted from Table 8.4 that the accuracy of the height of the V cone has been better than planimetric accuracy by 5.0 to 7.0 mm in each scan. This can be attributed to the fitting process, where the LM algorithm failed to calculate the parameters; it acts as a steepest descent method (see chapter 7 section 7.2.3.3.). This means that if the current step fails to reduce the error, the damping parameters have to be increased. Therefore, the LM is adaptive (Lourakis, 2005), and this may have contributed to reducing the error in height.

As can be seen from Figure 8.5, the planimetric accuracy in area1 is almost the same as in all scans (see Figure 8.5, top left). However, the planimetric accuracy has been better than the vertical in the processing of GPS position (see Table 8.3). It may also be noted from the result that the accuracy in east and west direction (ΔE)s were almost better than north and south direction (ΔN)s. This can be attributed to the number of satellites which were more in the E-W direction than N-S (see Table 8.3), due to its distributions (Bhatta, 2011).

Generally, the planimetric accuracy in area1 and area2 for H cone is (13 and 9.0) mm respectively; whereas, the vertical accuracy is (22 and 23) mm respectively. As for the vertical cone, the planimetric accuracy is (19.0 and 16.0) mm and the vertical accuracy is (16 and 9.0) in this order.

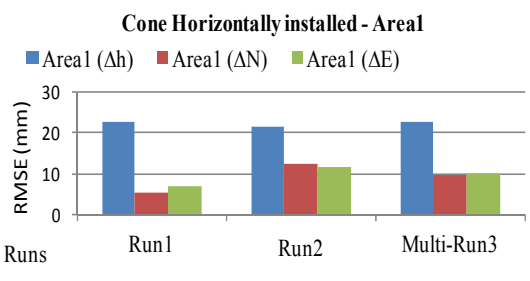

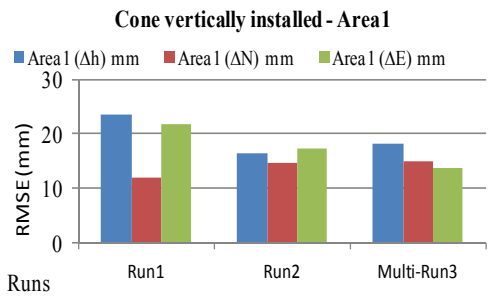

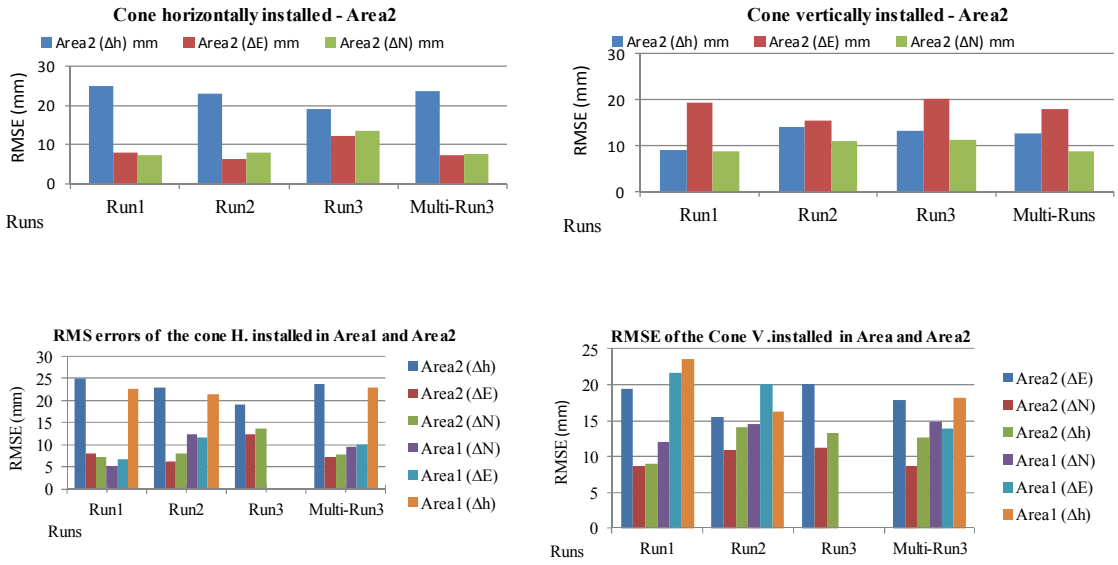

Figure 8-5: RMS error of the cone apex in two areas. Left: RMS error of the cone horizontally installed in both areas. Right: RMSE error of the cone vertically installed in both areas.

2. Using Faro manufactured target- Sphere : Area1 and Area2

Note Area1and Area2: Sphere 0.20 m dia. No. of the sphere. = 2, average distance = (10.60 and 8.15) m for Area1 and area2 respectively.

Target/ Area1	Pts.no.(R1,R2 and Multi-Runs)	Accuracy (Accur.) =TS Coord.- MLS estimated Coord./ Sphere								
		Run1 (mm)			Run2 (mm)			Multi-Runs (mm)		
		ΔE1	ΔN1	Δh1	ΔE2	ΔN2	Δh2	ΔE	ΔN	Δh
Average	(99, 169, 227)	7.18	3.94	28.87	5.39	24.62	26.31	4.32	17.13	26.31
RMSE		7.69	4.01	28.88	6.52	24.68	26.32	5.99	17.13	26.32

Target / Area2	Pts.no.(R1,R2, R3 and Multi-Runs)	Accuracy (Accur.) =TS Coord.- MLS estimated Coord / Sphere											
		Run1 (mm)			Run2 (mm)			Run3 (mm)			Multi-Runs (mm)		
		ΔE1	ΔN1	Δh1	ΔE2	ΔN2	Δh2	ΔE3	ΔN3	Δh3	ΔE	ΔN	Δh
Aver.	(137,146 ,27, 297)	8.66	-11.02	23.29	11.65	-3.97	24.5	4.02	4.9	20.9	10.60	6.95	23.54
RMS		8.91	11.06	23.31	12.20	4.60	24.58	5.60	5.46	20.94	10.97	7.00	23.55

Table 8-5: Average accuracy and RMSE of the sphere centre vs single and multi runs in area1 and area2: Top: Area1. Bottom: Area2.

From Table (8.5), the mean absolute error of ΔE and ΔN components show fluctuating results in both areas, for example the accuracy in east and west direction (ΔE)s, has been obtained in area1 (multi-scans) and area2 (run3) and the worst accuracy in run1 and run2 in that area, respectively. On the other hand, the best accuracy in north and south direction (ΔN)s in area1 (run1) and area2 (run2) has been up to 4 mm in both areas and this error increases inversely in that area up to 20 and 11 mm, respectively (i.e., it increases in area1(run2) and area2 (run2). The same case happened for east and west direction (ΔE).

These fluctuating results in both areas can be attributed to many factors: such as the satellites geometry where the number of satellites in E-W is more than that of N-S direction (see Table 8.3), the calibration of the system bore-sight alignment and lev`er arm offset between sensors (see chapter 2 section 2.3), and also geo-referencing error. As described in Chapter3, the error sources of the 3D points collected by MLS produce 14 parameters to calculate the coordinates of laser points (see chapter3 section 3.7). In addition, the fitting process of the sphere target itself produces errors.

Another factor is the TS reading of the sphere centre, might introduce error through replacing the sphere by the prism for observing. Another reason of getting absolute accuracy in N direction better than E direction in such area, the number of satellites in N-S direction, which might be equal or more than the E-W direction, where both sides of the area (E-W) are obscured by high buildings.

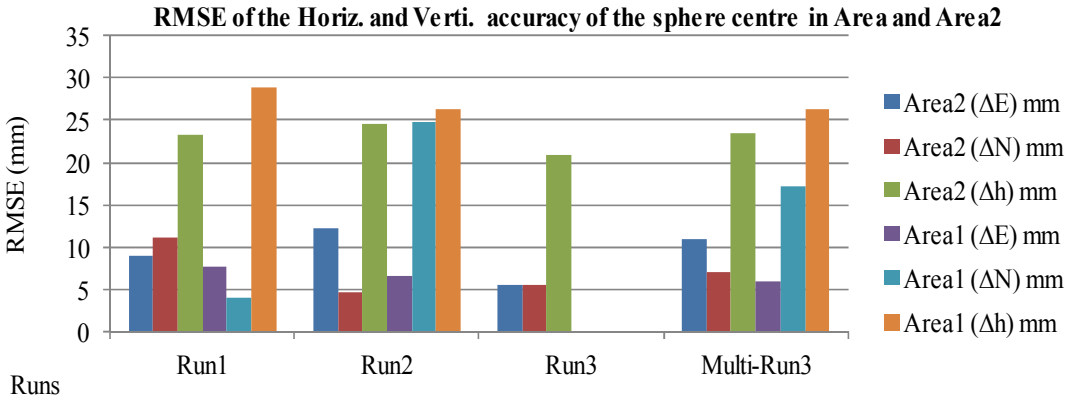

Figure 8-6: RMS error of the horizontal and vertical accuracy of the sphere centre in two areas.

3. Using designed target- Pyramids different faces: Area1 and Area2

Note-Area1: Pyramids: 4faces: length =300 mm and Ht = 0.10 m: No. of Pyramid = 1, dist = 17. 80 m.

Note-Area2: Pyramids: 3, 4, 4, 5, 8 faces: length = 0.30 m and Ht = 0.10 m; No. of pyramid = 5; Average distance = 9.0 m.

Targets/ Area1	Pts.no.(R1,R2 and Multi-Runs)	Accuracy (Accur.)-TS Coord.- MLS estimated Coord./ Pyramid								
		Run1 (mm)			Run2 (mm)			Multi-Runs (mm)		
		ΔE1	ΔN1	Δh1	ΔE2	ΔN2	Δh2	ΔE	ΔN	Δh
Pyramid 4 faces	(239, 298, 545)	-18..26	11.07	24.69	-17.25	22.21	20.60	-17.37	20.30	22.99

Targets/ Area2	Pts.no.(R1,R2 and Multi-Runs)	Accuracy (Accur.)-TS Coord.- MLS estimated Coord / Pyramids											
		Run1 (mm)			Run2 (mm)			Run3 (mm)			Multi-Runs		
		ΔE1	ΔN1	Δh1	ΔE2	ΔN2	Δh2	ΔE3	ΔN3	Δh3	ΔE	ΔN	Δh
Average	(264,303,f, 588)	12.56	-12.30	22.99	11.96	11.10	23.08	Fail	Fail	Fail	3.66	-8.62	22.41
RMSE		12.94	15.16	23.50	12.09	12.58	23.92	Fail	Fail	Fail	5.29	11.19	23.16

Table 8-6: Mean absolute accuracy and RMS error of the pyramid apex vs single and multi runs in area1 and area2: Top: Area1. Bottom: Area2.

From Table (8.6), it can be shown that the results obtained in area1 and area2 were less accurate than cone and sphere targets. This is because the intersection plane of each fitted side produces some error, and this will affect the calculation of the target apex determination; the greater the series of processes, the greater the error propagated. In addition, the matrix of the normal equation of the parameters is close to singular, due to the irregular points on the surface, and noise coming from neighbouring plan causes deviation in its apex. Figure 8.7 clearly shows the RMS error of each component of the target apex in both areas, and it shows the results in area2 were much better than area1 with single and multi-scans. This is because the trajectories of the laser scanner in area2 close to each other than area1 (see Figure 8.4, left).

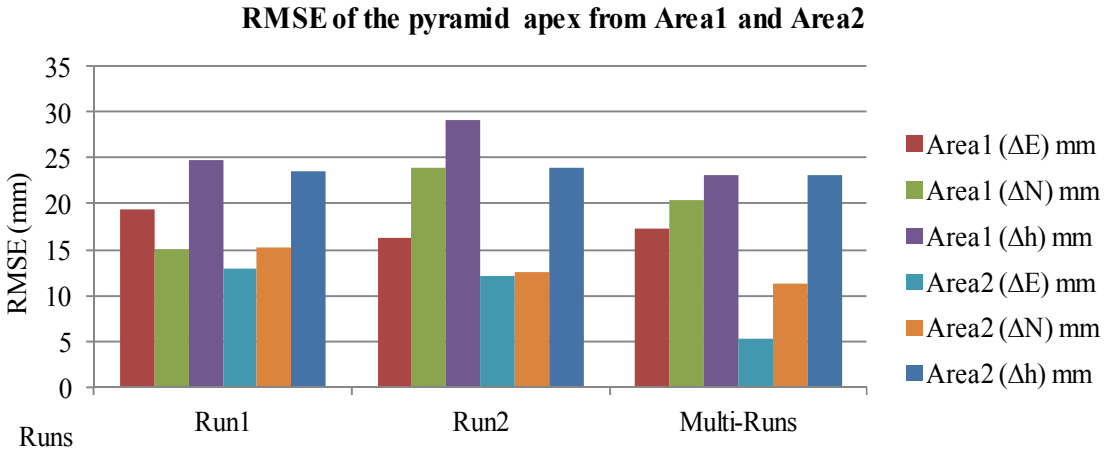

Figure 8-7: Figure: RMS error of the horizontal and vertical accuracy of the pyramid apex in two areas.

4. Sphere size 0. 145 m diameters: Area1 and Area2

Note area1and area2: Sphere size 0.145 m diameters: No. of sphere = 5, average dist. = 6.80 m in area1 and area2 respectively.

Targets / Area1	Accuracy	Accuracy (Accur.) ΔR =.Actual R – Estimated R			
		Pts.no.(R1,R2 and Multi-Runs)	Run1 ΔR (mm)	Run2 ΔR (mm)	All-Runs ΔR (mm)
Sphere	**Aver. accur.**	(62, 63, 127)	3.61	2.40	4.70
	RMSE		3.87	2.45	5.19

Targets / Area2	Accuracy	Accuracy (Accur.) ΔR =.Actual R – Estimated R				
		Pts.no.(R1,R2 and Multi-Runs)	Run1 ΔR (mm)	Run2 ΔR (mm)	Run3 ΔR (mm)	All-Runs ΔR (mm)
Sphere	**Average**	(66, 77, 82, 222)	3.30	2.56	1.24	2.26
	RMSE		3.67	3.01	1.81	2.44

Table 8-7: Average accuracy and RMSE of the sphere radius vs single and multi runs in area1 and area2: Top: Area1. Bottom: Area2.

Table (8.7) shows the comparison between the estimated sphere radius and its actual value with single and multiple scans in area1 and area2, as the prism was not available for measuring its centre.

It can be seen that the best average accuracy was given by area1 (run2) and area2 (run3). These two runs have the same point density. The worst average accuracy can

be found in area1 (multiple runs) and area2 (run1). This is because, in area1, the spherical targets in run1 are closer to the laser scanner than in run2 (see Figure 8.4, left). Therefore, when using the results of the two runs together in a multi-scan, the final accuracy will be affected by the poorer results of the second run.

Table (8.7) shows that, in area2, the better accuracy has been obtained with the multi-scans. This is because the trajectories of the laser scanner in all runs have been close to each other (see Figure 8.4, right). This means that range from each sphere target was the same, and combining scans would achieve a better result. This can be clearly shown in Figure 8.8.

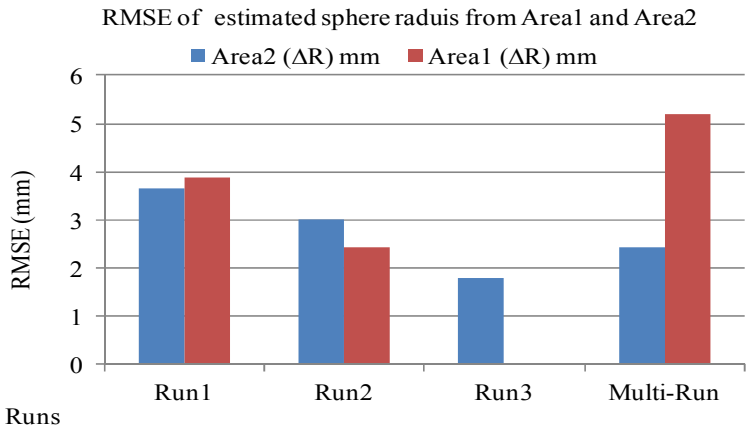

Figure 8-8: RMS error of the sphere radius vs single and multi-scans in both areas.

The results from different target designs used in this test are compared statistically following the same approach, i.e. Least squares surface fit, as discussed in (chapter 5, section 5.5.5). The mean standard deviation "σ enh" of each target centre/apex was computed in both areas, and the result is presented in table 8.8.

MLS Area1	**Sphere σenh (mm)**	**ConeH σenh (mm)**	**ConeV σenh (mm)**	**Pyramid σenh (mm)**	**MLS Area2**	**Sphere σenh (mm)**	**ConeH σenh (mm)**	**ConeV σenh (mm)**	**Pyra. σenh (mm)**
Run 1	1.863	1.799	7.078	1.308	Run 1	1.67	1.60	6.20	3.12
Run 2	1.713	2.348	6.695	1.392	Run 2	1.54	1.33	6.16	3.07
					Run3	2.69	2.49	7.05	Fail
All runs	2.365	2.412	6.7298	1.786	All runs	1.21	1.45	5.62	2.53

Table 8-8: Precision of the targets apex/ centre in area1 and area.2.

From Table (8.8), it can be seen that the highest precision has been achieved by pyramid in area1 (run1and run2) with an error uncertainty of the apex less than 1.4 mm. This is because the planes are parameterised as Hesse normal form, as described in chapter 7, which estimates the parameters of the 16 planes of the pyramid in the case of 4 faces. In addition, to estimate the intersection, the number of unknowns increased by 3, the coordinates of the intersection-point. To force an intersection of the 4 planes, 4 additional conditions are introduced (Lösler, 2012b). (See appendix P the algorithm developed for fitting pyramid faces and intersecting them to estimate the apex).

The weakest precision can be found in the V cone with the maximum uncertainty away from the apex of 7.08 mm in run1, because only one half of a cone was visible in scanning data collection, with poor fitting result. This error decreases by 1mm in run2 and multi-runs respectively. This improvement could be due to the high level of redundancy of the laser scanner data. While, the result of all targets have less precision, in the case of multiple scans (all runs), due to the effect of range from laser trajectory to the target as previously discussed.

In area2, the result can be found in H cone, sphere, pyramid and V cone in this order. All targets have good precision, in the case of multi-scans; due to all three passes close to each other as mentioned before. As can be seen in (Figure 8.9), the results of each target fluctuated starting from run1 to run3 and reduced in multi-runs. The pyramids failed in run3, because the points on each faces cannot be recognized by the detection process, due to the intensity of return signal of each face clashes with each other, and is regarded as one of the major disadvantages of the pyramid target (see chapter 5 sections 5.5.5).

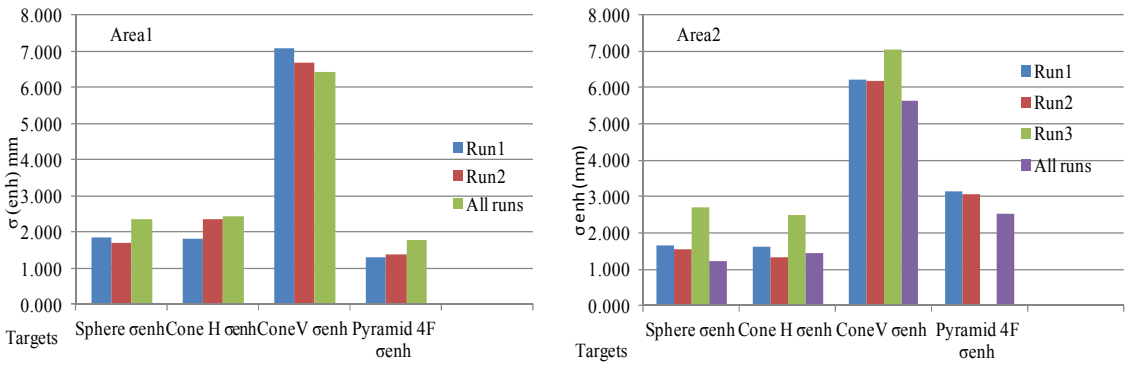

Figure 8-9: Precision of the apex/centre vs single and multi-runs in area1 and area2. Left: Area1.Right: Area2.

Target	Area 1		Area2	
	RMSE. Δ (en) (mm)	RMSE Δh (mm)	RMSE. Δ(en) (mm)	RMSE Δh (mm)
Cone (H)	8.15	27.29	14.43	22.61
Cone (V)	19.45	28.35	20.19	12.26
Sphere	17.18	28.30	12.02	22.99
Pyramid	19.77	23.97	17.62	26.29

Table 8-9: The average of the RMS errors of Horizontal and vertical accuracy of each target used in area1 and area2.

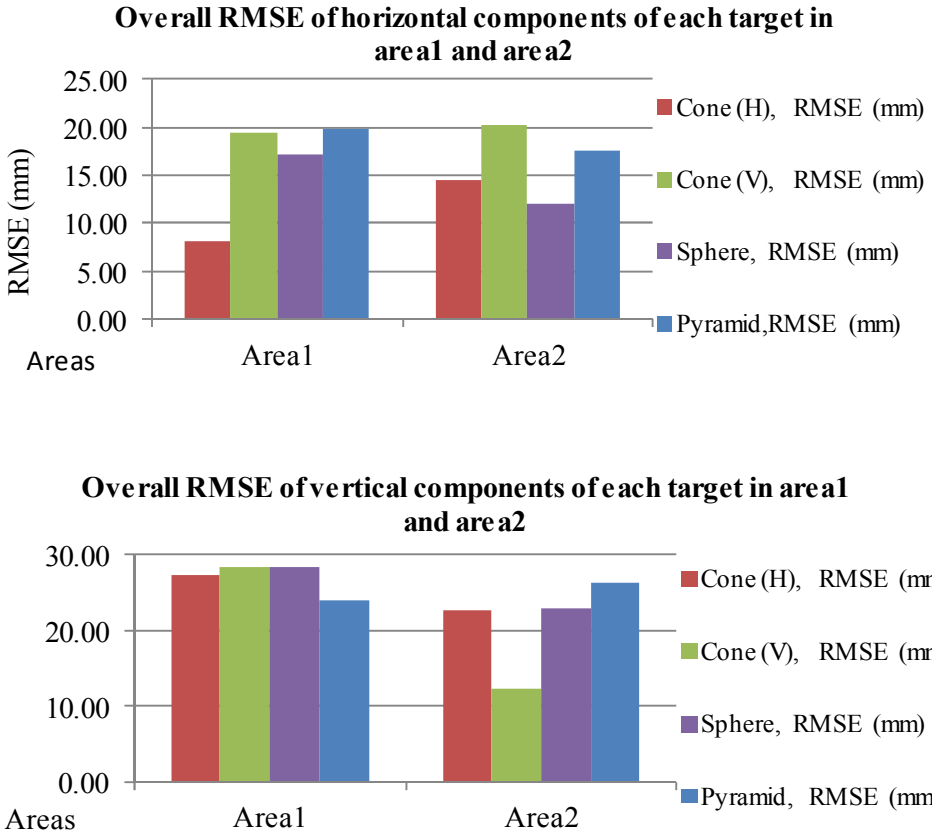

Figure 8-10: The average RMSE of Horizontal and vertical accuracy of the target apex/centre. Top: Horizontal accuracy. Bottom: Vertical accuracy.

Table 8.9 and Figure 8.10, top show the overall accuracy of the cone, sphere and pyramid in horizontal components in area1 and area2. In area1, the best horizontal accuracy can be found in H cone, sphere, V cone and pyramid, in this order.

In area2, the best one found was sphere, H cone, pyramid and V cone in this order. However, the sphere results were slightly better than H cone. This could be due to the low amount of redundancy, especially in run3, which affect the average accuracy

(see Table 8.4 and 8.5 or see appendix R). In addition, this error could be an error in the total station reading, reflector-less mode measurements were taken to the targets, which are less accurate than those taken of prism. Another factor is that the cardboard cone targets, which have low quality than manufacturer ones. Therefore, some unreliable cardboard cone targets were neglected.

In vertical components (Figure 8.10, bottom), almost all targets have the same accuracy in area1 expect the pyramid target has slightly better by 4 mm. whereas, in area2, the V cone found was better than the other targets, due to the same reasons mentioned before.

After removing the unreliable cone and pyramid targets, the obtained result were much better in both areas, and the overall RMS of the two areas can be seen in Table 8.10.

Target	Area 1		Area2	
	RMSE. Δ (en) (mm)	**RMSE Δh (mm)**	**RMSE. Δ (en) (mm)**	**RMSE Δh (mm)**
Cone (H)	8.10	22.30	8.80	23.10
Cone (V)	18.60	19.95	17.74	11.30
Sphere	17.18	28.30	12.02	22.99
Pyramid	19.77	23.97	13.61	26.06

Table 8-10: Horizontal and vertical accuracy of each target used in area1 and area2 after removing some unreliable cardboard targets.

Regarding the sphere targets size 145mm and also 200 mm, the comparison was performed using their known radius, where the prisms used for measuring their centres are not available. Three methods (LM, Cyclone and AD), as described in chapter 5 have been used for fitting sphere.

RMS of the comparison between estimated sphere radius values to that provided by the manufacturer was done after applying fitting using each method. In addition, standard deviation and absolute maximum error of the quality of fit were also estimated from each run separately in both selected areas, using only Cyclone software. The results can be seen in Table 8.11, and the full statistical results for each sphere with single and multi-scans can be seen in appendix R.

Area1	Sphere/ no.	ΔR-LM RMSE (mm)	ΔR-cyclone RMSE (mm)	ΔR-AD RMSE (mm)	RMSE Stdv.(mm)	RMSE Absul.Max. error (mm)
Run1	6	4.63	4.71	4.66	2.93	7.66
Run2	6	3.19	3.14	3.23	3.10	13.47
Multi-Runs	6	4.34	4.27	4.33	5.60	14.58

Area2	Sphere /no.	ΔR-LM RMSE (mm)	ΔR-cyclone RMSE (mm)	ΔR-AD RMSE (mm)	RMSE Stdv. (mm)	RMSE Absul.Max. error (mm)
Run1	7	3.68	3.74	3.74	2.96	7.99
Run2	7	3.46	3.47	3.39	2.99	7.20
Run3	7	4.31	4.28	4.26	3.18	7.84
Multi-Runs	7	3.21	3.23	3.25	3.91	12.77

Table 8-11: RMS error of the estimated sphere radius vs its actual value, and the mean standard deviation and the absolute maximum error of the quality of fit from each run in both areas. Top: Area1: bottom: Area2.

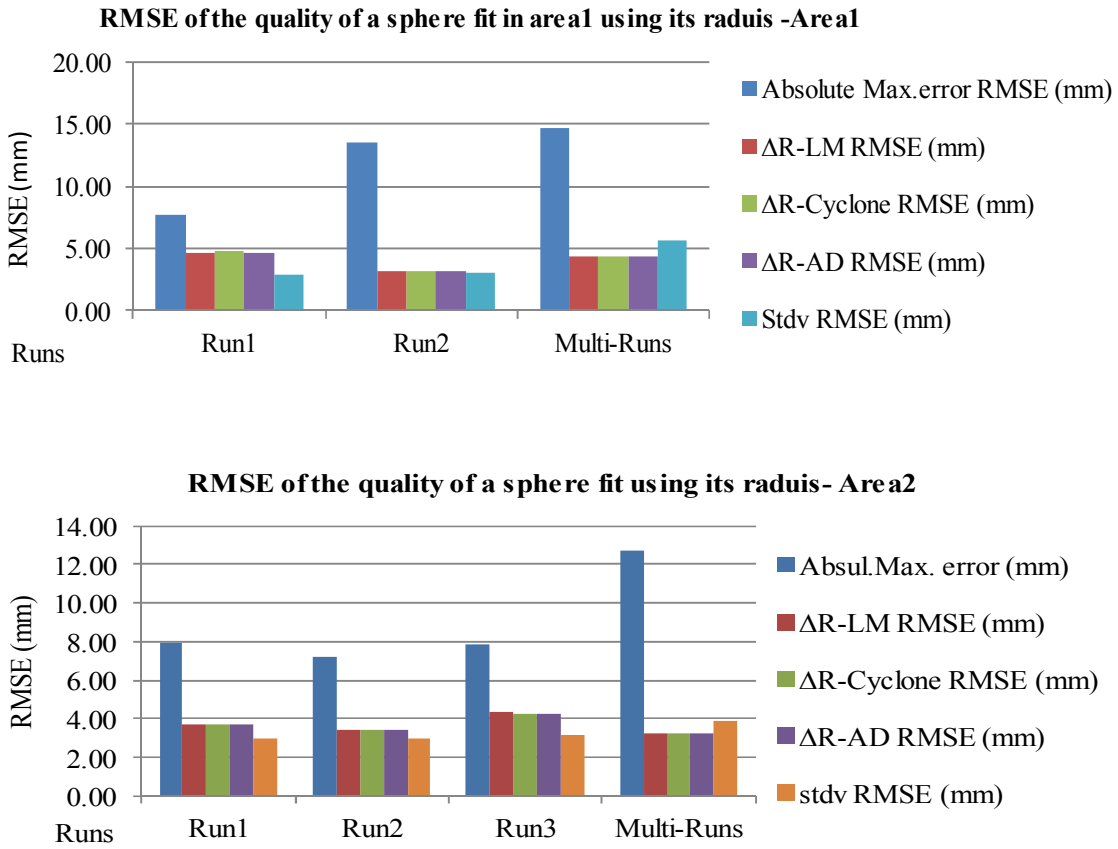

Figure 8-11: RMSE of the quality of fit of the sphere vs single and multi-runs in area1 and area2.

From Figure 8.11, it can be seen that the results of each method were almost the same in the comparison between predicted values of the sphere radius to their actual

values. Due to the fact that all of the three methods used follow the same approach of least squares surface fitting, only a small error up to 1.5 mm has been detected between run1 and run2 in area1, and less than 1 mm in area2 between run2 and run3. This small error could be due to the imperfect calibration of the system or sensitivity of the algorithm used in fitting process.

On the other hand, the maximum absolute errors of the fitting sphere in each run have increased in both areas, from (8 to 15) and (8 to 13) mm respectively, for the same reason mentioned above.

8.1.5 Summary and conclusion

Although the target (cone, sphere, and pyramid with 5 and 8 faces) would be seen from all vehicle directions (along, across and diagonal), the incidence angle of the beam from 45^{o} and more would be very steep, and causing lower point density on the surface of the target and difficulty in automatic target centre identification (see chapter 6). As a result, the coordinate precision of this target would be poor, as described in chapter 5 (cone, pyramid and flat target, Figure 5.27 and Table 5.4). This will negatively affect the quality of self-calibration using targets especially Leica flat targets (Reshetyuk, 2009). In addition, the large incidence angle causes large measurement uncertainty (Soudarissanane et al., 2009).

In this test, the targets were installed along the road on both sides, at different ranges from around 6 to 20 m from the laser scanner trajectory in both areas (see Figure 8.4, bottom left and right). All targets were approximately perpendicular to the direction of the laser scanner trajectory. This means that all targets were almost installed at 0^{0} incidences angle to the scanner. The effect of IA only will appear from the target itself due to its geometric shape especially in a cone and pyramid as described in chapter 5 sections 5.5.5. The quality of result of the target apex/centre achieved from this test can be summarised below.

Cone, sphere and pyramid targets in Area1 and Area2

The planimetric accuracy for the apex of the cone horizontally installed was better than vertically installed in all scans (see Table 8.4). This can be attributed to the achievable point density on the target's surface, which has been more in the case of

horizontally installed target. This also varies depending on a number of factors namely: measurement rate of the laser scanner, the scan speed, the range and the vehicle speed (Rieger et al., 2010a) (see chapter 4 section 4.2).

Generally, the planimetric and vertical accuracy of some of the targets in area1 was slightly better than area2, due to the GPS quality position in both area almost has the same quality (see Table 8.3). The specification given by RIEGL laser scanner for VQ-450 gives the range accuracy and precision (8 and 5) mm for 1.5 to 50 m at one sigma respectively. The accurate result of this test has only been met with H cone, and the result of precision has been below this specification.

The precision of all targets centre/apex (see Table 8.8) are less than the threshold value of the range laser scanner. While, the accuracy of the targets centre from the above tests, the result show that the cone is better than sphere and pyramid due to the same reason discussed before (see chapter 5 section 5.5.5).
It should be noted that the cone horizontally installed, and sphere are better than other targets to be used for matching multi-scans, to see how they can affect the result when multi- scans are combined together.

8.2 Point cloud registration using targets

Registration point clouds using natural features and targets, Matlab algorithm was used for automatic detection (see chapter 6 “the workflow of automatic target detection”) and to compute the target centre based on the least squares surface fitting (see chapter 7) for registration point clouds using natural features and targets. Least squares surface fitting approach through the available software in NGI was used for combining scans using targets and compared with registration using natural features. The main idea of using targets in a point cloud is to determine the relative orientation parameter (x, y, z and omega, phi and kappa) to register join the primary scan with another scan, while the targets are positioned in the overlap of the two or multiple scans (Harvey, 2004).

In this test, three type of target groups for matching multi-scans were compared namely: natural feature, all targets (cone, sphere and pyramid) and only targets specifically made for MLS such as cone.

The results of the three groups used (natural feature, targets and only H cone target) for matching point cloud can be discussed for each one separately.

1. Using natural feature:

Matching the point cloud using natural features was discussed in (chapter 3, section 3.4.3). Matching multiple scans from different driving and opposite directions in both areas was already achieved by the 3DLM Ltd. In order to validate their procedure, some check points in both areas (see Figure 8.12) were selected from the result of multi-scans matching and compared with their control value. The results were within 20 to 33 mm in area1 and within 20 to 28 mm in area2 (see Table 8.12).

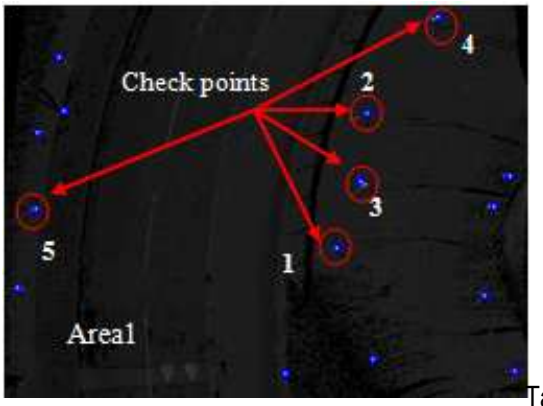

Check point	Area1 Δ (enh) m	Area2 Δ (enh) m
1	0.03331	0.02653
2	0.03153	0.02090
3	0.02341	0.02509
4	0.02776	0.02531
5	0.02781	0.02841

Table 8-12: The accuracy of matching multi-scan using natural feature.

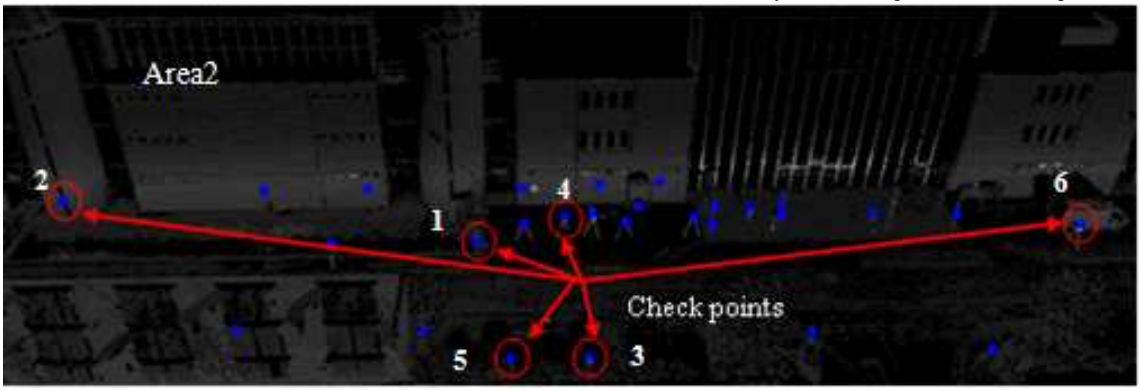

Figure 8-12: Matching process in area1 and area2 produced by 3DLM Ltd. using natural feature, .blue dot represents the centre/apex of each target in area1 and area2 respectively.

2. Using Targets

Target based registration is described in chapter3 is one of the most common registration approaches used to determine relative orientation parameters between any two scans or systems. In this test, targets have been used in two ways.

1. Register or transform each scan (run) separately to the TS coordinates system using targets in both areas (see Figure 8.13).

2. Matching multi-scans using targets in two cases. First using, all targets, visible in both scans and secondly using only H cone targets.

This is to test the quality of the target coordinates and their effect when multi-scans are combined together in area1 and area2.

8.2.1 Result of registration scan using targets

To register each scan to target coordinates system in both areas was done using Cyclone software (see chapter 5 section 5.2).

The mean absolute error of each scan using all targets in both areas was within 15 to 28 mm level of accuracy (see Table 8.13). While the mean absolute error of each scan when using optimal targets (only H cone) in both areas was within 5 to 8 mm level of accuracy (see Table 8.13) The accuracy of each scan after the fitting process was determined using 5 check points in both areas, as can be seen in Table 8.14, and Figure 8.13.

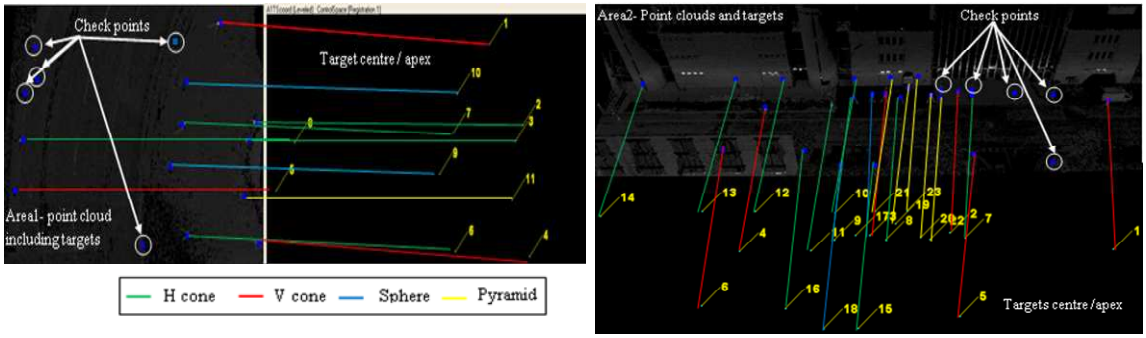

Figure 8-13: Fitting scan to the TS coordinates system in area1 and area2. Left: Area1: Right: Area2.

Target	No.	Area1- Mean Abs. Error (m)			No	Area2- Mean Abs. Error (m)			
		Run1	Run1	MR		Run1	Run2	Run3	MR
All targets	11	0.0284	0.0150	0.0152	23	0.0284	0.0150	0.0170	0.0152
only H cone	5	0.0053	0.0077	0.0078	10	0.0054	0.0061	0.008	0.0055

Table 8-13: The accuracy of 3D of the targets centre / apes per scan in area1 and area2.

Check point	Area1- Δ (enh) m			Check point	Area2- Δ (enh) m			
	Run1	Run2	MR		Run1	Run2	Run3	MR
5 /all target	0.0289	0.0153	0.0154	5/all target	0.0298	0.0162	0.019	0.0173
5/ only H cone	0.0103	0.0154	0.0156	5/ Just cone	0.0074	0.0083	0.012	0.0108

Table 8-14: The accuracy of fitting point cloud to targets vs single and multi-scans.

8.2.2 Matching multi-scans using targets

The quality result of matching scans together in area1 and area2 using all targets were within 11 to 18 mm respectively (see Table 8.15). This level of accuracy was better than using natural features. The results were improved when using only H cone targets in area1 and area2, and the results were within 6 to 7 mm respectively. The validation of matching multi-scans was done via the same check point used for the previous section (see Table 8.16).

Target	No.	Area1- Mean Abs. Error (m)	No.	Area2- Mean Abs. Error (m)
All targets	11	0.01797	23	0.01136
Only H cone	5	0.00678	10	0.00786

Table 8-15: The quality of matching multi-scans using all targets and specific cone targets in both areas.

Matching	Check points.	Area1- Δ (enh) m	No.	Area2- Δ (enh)
All targets	5	0.0183	6	0.0139
Only H cone	5	0.0109	6	0.0087

Table 8-16: The accuracy of matching multi-scans using 5 and 6 check points in area1 and area2 respectively.

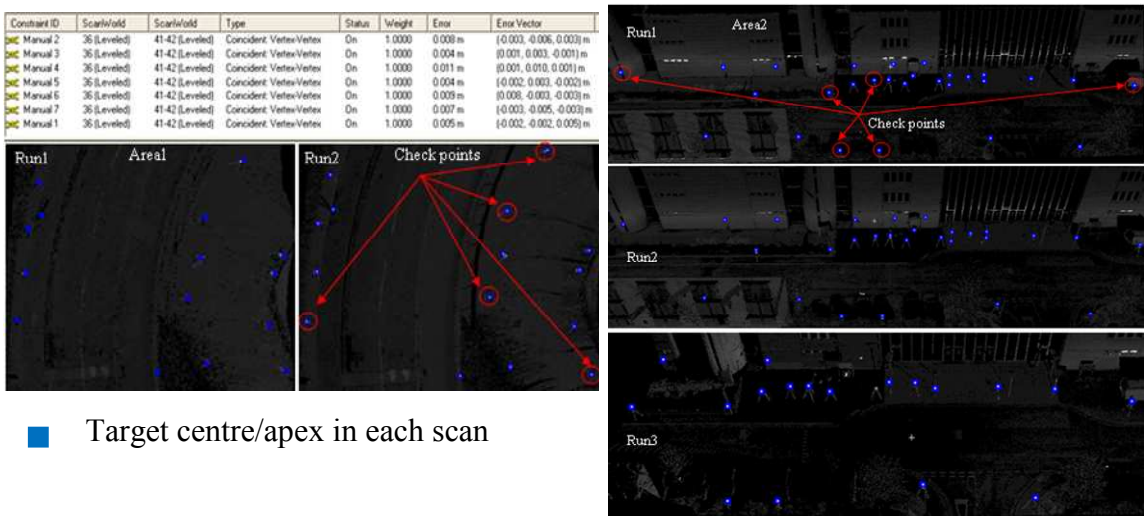

Figure 8-14: Matching multi-scans using targets in area1 and area2. Left: Area1. Right: Area2.

The above procedure work can be summarised in a flow diagram (see Figure 8.15).

1. The procedure of fitting each scan to the target coordinates system.

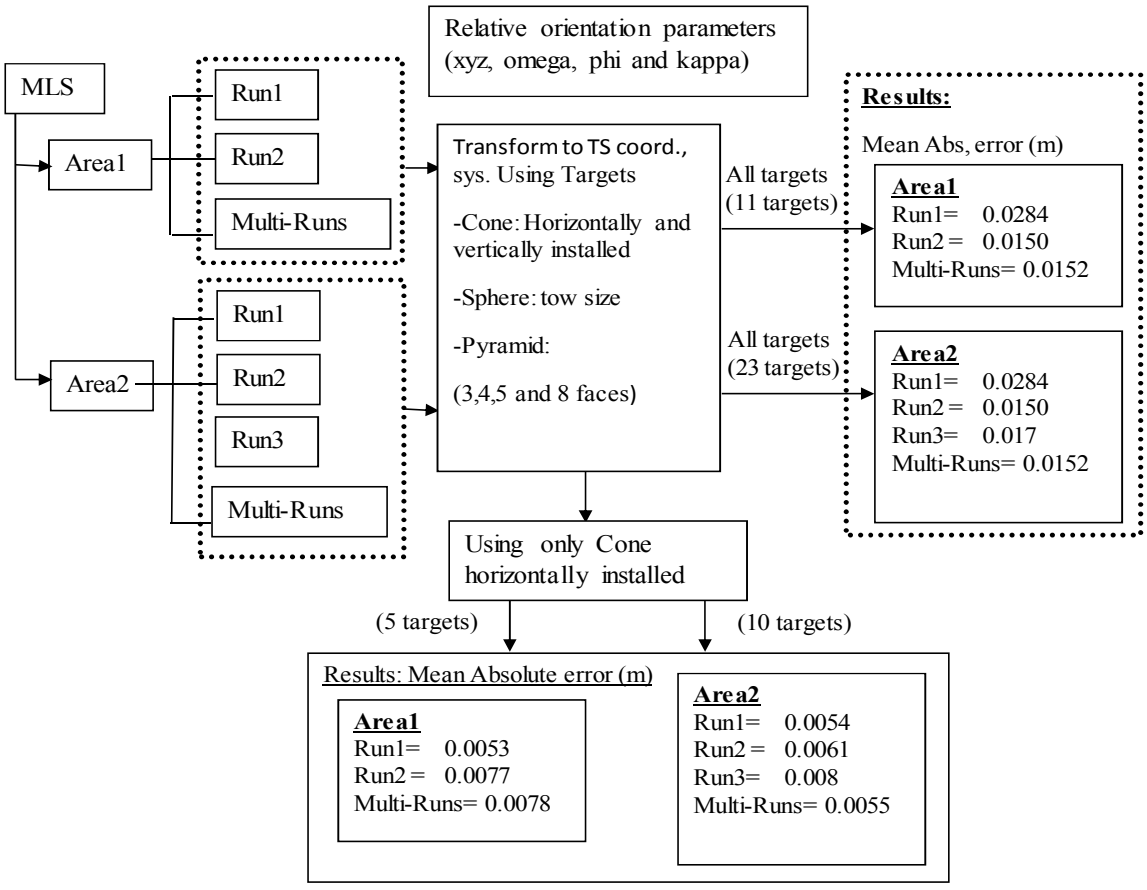

2. The procedure of matching multi-scan using targets.

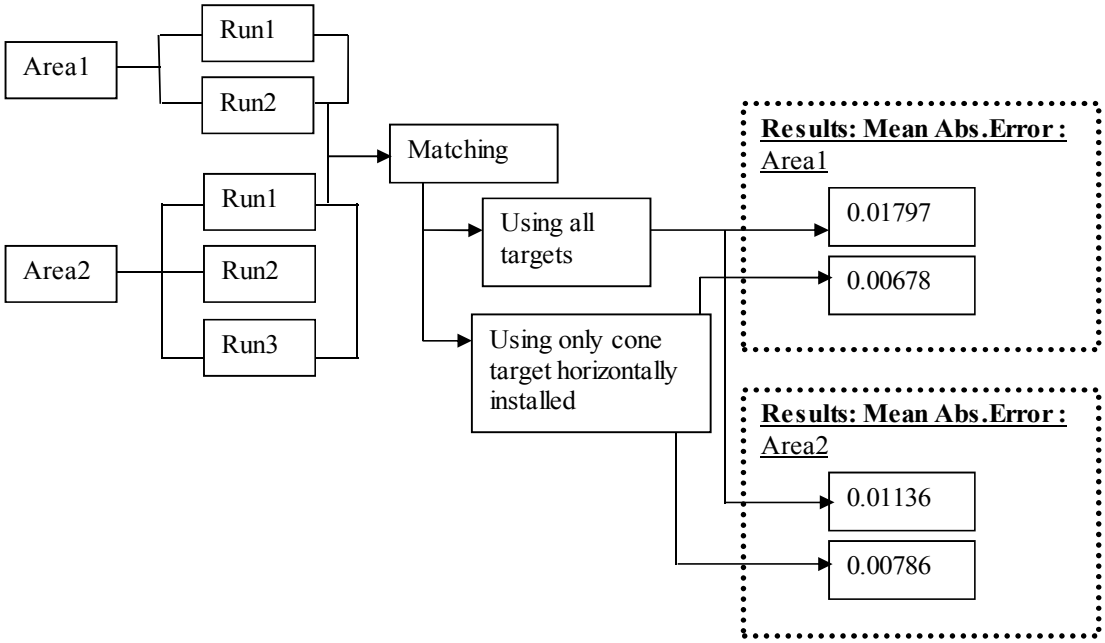

3. The procedure of comparing the result of matching using natural feature and targets.

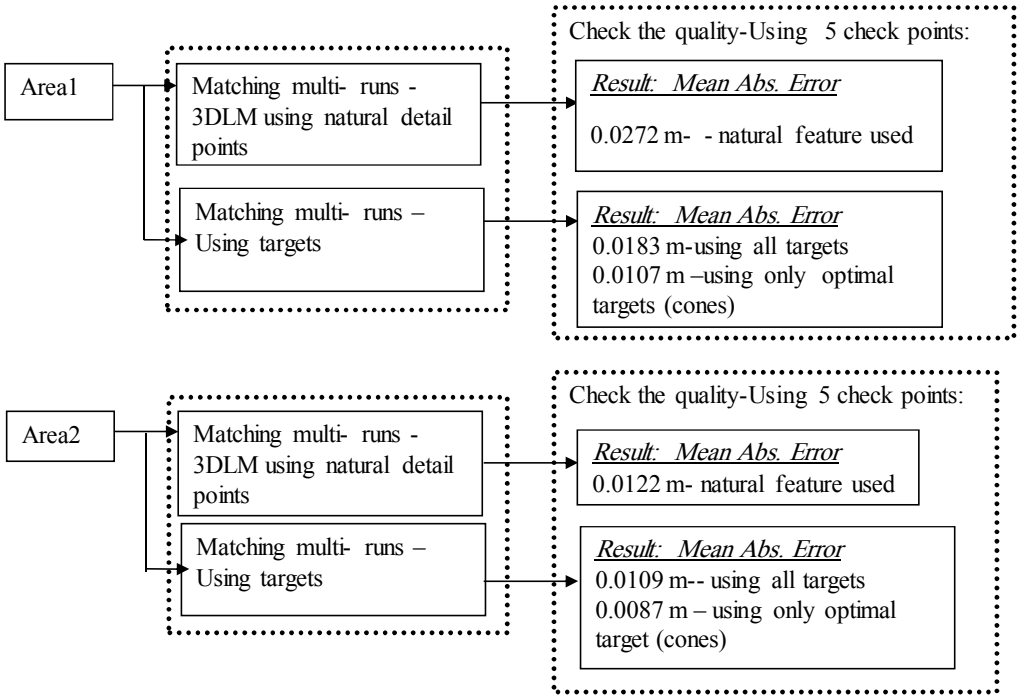

Figure 8-15: Flow diagram of the process of matching multi-scans using targets Top: Register each scan using corresponding targets. Middle: Matching scans together using corresponding target in both scans. Bottom: Compare the result of Matching using natural features and targets.

8.2.3 Comparison between three methods

Clear comparison between the three groups can be seen in Table 8.17.

Methods	Mismatches-Area1 (m)	Mismatches-Area2 (m)	Deviation (mm)
Natural feature	0.0272	0.0122	0.0150
All target	0.0183	0.0109	0.0074
Only H cones	0.0107	0.0087	0.0020

Table 8-17: The result of mismatches and the deviation of each method in both areas.

From Table 8.17, it can be seen that a better result of matching the multiple point cloud has been obtained using optimal target (cone). This is because the automatic detection and computing of the apex can be done with nearly 1mm level of accuracy.

The worst results have been achieved using natural features (see Table 8.17). This is because of the misidentifications of the corresponding points in multiple scans, whether automatically or manually. This problem could be reduced by improving system calibration, where some errors can still be presented in the MLS data, especially in direct geo-referencing. These errors are dominated by navigation errors and can be reduced using optimal targets. The use of both natural features and targets in the matching process gives a better result than the natural feature itself, due to the same reason and the result of this method. It may also, be taken into account and reliability improve the result quality of MLS "especially in the urban area", where insufficient number of optimal targets may be available in large areas.

As can be seen from Figure 8.16 the accuracy of matching multiple scans increases with an increased number of optimal targets. The more the number of targets or control points, the better the accuracy that can be achieved (see chapter 4 section 4.4.3.2).

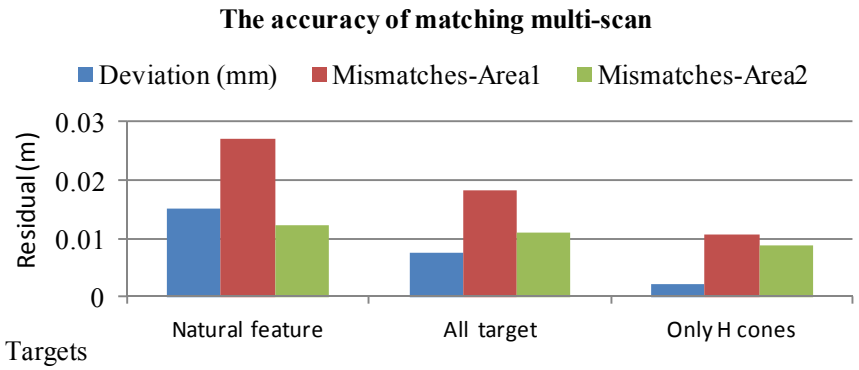

Figure 8-16: The achievable accuracy from each method.

As mentioned in section 8.2.3, the mismatches error has been minimised when using the optimal targets. The entire point cloud has then been moved or fitted according to the position of optimal target. Figure 8.17 shows the accuracy of the matching process for each method used and it also shows how well the check point fitted, where multi-scans were combined together with optimal target.

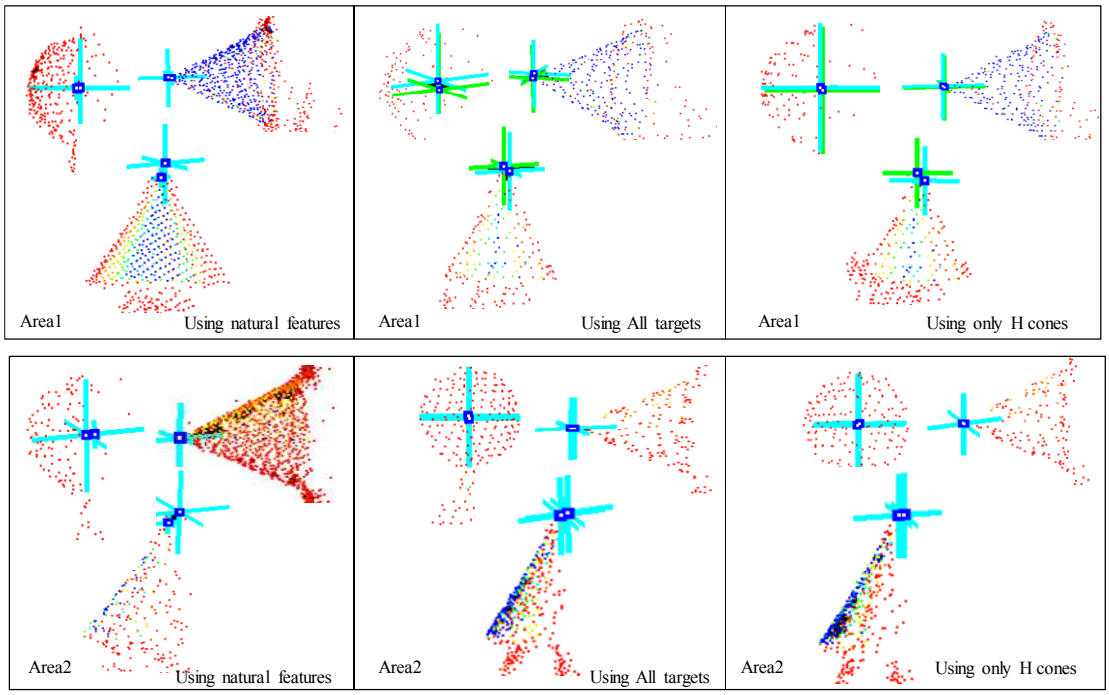

Scale = 1: 10; 1mm on a map = 10 mm on a ground

Figure 8-17: The accuracy of matching point cloud of three methods (using natural feature, using all targets, and using only optimal targets (H cones)) in both areas. Top: Area1. Bottom: Area2.

8.3 Conclusion

This chapter discussed the use of optimal target to improve the accuracy of MLS data in an urban area, where high accuracy requirements need to be met such as engineering scale mapping accuracy. The designed targets are portable targets and can be placed along the road and installed in the buildings or on the tripod using magnetic mount (see Figure 8.1) before MLS survey and their coordinates were surveyed using total station.

Based on the trials (see chapter 5), the optimal target was found to be cone shaped with 15 cm radius (r) and slant height to be 2r, Furthermore, for improved horizontal position accuracy, the target was covered by highly reflective tape (HRT) (see Figure 8.1). An efficient algorithm have been developed for accurate target position determination in the laser point cloud using intensity values, the length of the target and the approximate expected number of points per target. The target processing is highly automated, where the developed algorithm (Matlab) provides fast and robust processing. Only minimum human intervention is required; to select the optimal transformation for matching multiple scans based on the optimal targets. This level of automation leads to consistent target measurement than can be performed manually.

The result, based on multiple scan taken from different and opposite deriving directions has shown that the specifically designed targets can indeed validate mobile laser scanner data accuracy, and thereby improve road surface extraction accuracy from mobile data. Based on the designed target, up to 3 cm errors were detected in the MLS data collected over the urban area (Jubilee campus) that was corrected using targets. The results have shown that in MLS data, (6.8 and 7.9) mm, mean absolute error of the matching multi-scan using the designed targets (cone) can be achieved in both selected areas, respectively. To provide this high level of accuracy, or less a dense and well-distributed network of targets is needed.

The significant advantages of using targets specifically made for MLS is to increase the accuracy of data collected by a MLS particularly in an urban areas.
The experiments presented in the section 8.2.3 show examples of how combined targets and natural features for marching multi-scans perform more advantageously than the conventional methods for improving MLS data, especially in the urban area. The findings will contribute to easy, cheap, and accurate measures to enhance the quality of MLS data, and make it useful for applications, such as change detection, transportation corridors, and accurate 3D modeling.

CHAPTER9: CONCLUSIONS AND RECOMMENDATIONS

This chapter revisits the research aim and objectives, with outcome from this research. Recommendations for future research are also given.

9.1 Research aim and objectives re-visited

The overall aim of this research was to investigate methods to improve the accuracy of MLS data, particularly in areas of difficult GPS reception, typically in urban environments, by using targets instead of using natural features. The main aim behind the research background was to evaluate the factors affecting the MLS in urban areas, such as trajectory errors due to limited availability of satellite signal, and to investigate the difficulties of using natural features in the laser point cloud and the possibility of using a range of specially designed targets, instead of natural features for improving data quality.

Trials were carried out for testing designed targets from different ranges, incidence angles, point densities and brightness, and based on these trials; the optimal targets were fabricated at the University of Nottingham. Test results from multiple scanning drives using a Riegl laser VQ-450 MLS, system operated by 3DLM Ltd. (StreetMapper360), a vehicle-based laser mapping system, have shown that when using the optimal target, the MLS data accuracy for a variety of applications can be improved.

Section 1.2 lists a number of objectives that required addressing in order to achieve the research aim. These are summarised and revisited below, with a summary of the main conclusions for each one.

9.1.1 Assessing the quality of MLS's measurement in urban areas

The positioning accuracy of the GPS/IMU system is a critical part in the error budget and thus ground reference data is needed. Different methods for assessing the quality of MLS were applied, namely "Survey control points", "Surfaces comparison" and finally "Additional Source of data such as TLS". For the first assessment (see section

4.3.1.1), the RMSE values of the GCPS compared to the actual value measured by a Trimble robotic TS survey represent the external quality control of the data collected by a MLS. Adjusted GCPs residual were presented to examine systematic error in the survey network from the Bench mark control (MGB10, NGB11 and NGB12).

The Iterative Closest Point (ICP) method in Geomagic studio software was used to determine the 3D deviation and the tilt difference between two surfaces (see section 4.3.1.2). Tests show that the 3D differences between surfaces on the building facades and road surfaces fluctuated according to the GPS quality position; for example, in the case of the building facade, in test site blocks (55 and 67), the 3D difference was less than 3.2 cm and this value increased to more than 10 cm in the edge of the building (see Figure 4.20). In the road flat surfaces, the 3D difference was 0.9 cm and increased to 3.6 cm where surface discontinuity (e.g. across the kerb) was available (see Figure 4.16). The results show that a clear systematic error existed between trajectories of scan data of the selected blocks. These errors could come from the calibration of the system and GPS/IMU. The effect of tilt error between surfaces is varied depending on the slope distance of the road surface, and also calibration between laser scanner and IMU.

The third assessment, which is another source of data, was provided for assessing the quality of MLS data in the urban area. The accuracy of MLS based ground surface data was compared by an additional source of data, such as provided by TLS, used to reference data. The estimated precision of the reference method is, therefore, better than 1 cm. The results show that the scan points from MLS data in the pass1 has lower accuracy than pass2, when comparing each pass with TLS data. For example, the corresponding figures for the pass2 data were almost below 1 cm in laser block 67 and about 2 to 4 cm in laser block 55 (see section 4.3.1.3, Table 4.19). This can be attributed to the higher level of point density produced by the second pass, due to shorter laser distance measurement.

9.1.2 Discussing the factors affecting the accuracy of MLS in urban areas

The first factor is navigation solution (NS); the test result, section 4.3.1.1 of the point cloud in urban areas shows a higher RMS error than the point data in relatively open

areas (see Table 4.7 and Figure 4.12), due to the error in NS. A further factor is the quality of calibration of the MLS system mounting parameters (HRP and xyz) between the sensors, which can lead to introducing systematic error between two or more scans of the same areas. These errors could possibly be reduced by using an appropriate target to adjust the point cloud. The third factor is difficulty in measuring accurate natural detail points in the point cloud, such as building corners and the corner of a white road marking, due to no measurement being in able to the exact target point. This leads to misidentifying of the corresponding point in the matching process. This factor has been tested, (see section 4.3.1.3), and solved by creating a geometric plane for each side of the building facade and intersecting them to get the exact position of the points of interest. These positions were measured and compared with the TS value. The results show that the planimetric accuracy was influenced more than vertical position by this approach, and no improvements have been achieved in data quality. Therefore, specially designed targets are the best solution to overcome limitation of natural detail points.

The second part of this objective was checking the calibration produced by the 3DLM Ltd. company using the same approach of TerraMatch/TerraScan algorithm in two areas (block 67 and 55). This is proved more difficult than using targets, because it is hard to pick the same point between scans. It has been proven in section 4.4.3.1 that it is possible to detect the mismatch after applying correction between two or multi-scans with accuracy of around 1 cm on the wall and ground surface. Within the stated mismatch of 1cm by the 3DLM company, this was probably due to the good initial value of Heading Roll and Pitch used, and the close range of the scanner trajectory.

Another means for checking the calibration and reducing the error in data uses ground control points gathered along the study area, every 10 m, using an appropriate survey technique. Features visible in the laser point data, for example the corner of a white road marking, can be compared using GCPs and to assess it the calibration is acceptable. The test in section 4.4.3.2 found that the RMS error of block (67 and 55), less than 1 cm can be achieved with more than 20 GCPs in that area.

9.1.3 Using targets instead of natural features for improving the data quality

Designing different types of targets (pyramid, dot, ring and cone), and investigating the effect of range and incidence angles along with the effect of brightness and point density using two TLS, Faro focus^{3D} and HDS 3000, has been discussed. The designed targets (pyramid, dot and cone) and manufacturer targets (Faro sphere and Leica flat target) were evaluated in an indoor simulation to define the optimal target, including (size, shape, color reflectance, signal response (intensity), range, and incidence angle and point density.

Several tests were carried out to determine the most optimal height of the designed conical and pyramid target see section 5.4; the results show that the accuracy of the apex was reduced by approximately 17 % on decreasing the slant height of the cone and pyramid by 1cm. The second part of this objective was to determine the signal return and statistical measurements to different surface types. Tiles were scanned of all different colored surfaces to decide which colours can be used in the targets in order to be easily identified automatically. The findings from surface reflectance test found that the best surface to scan was the matt white surface, giving the highest signal return and a precision standard deviation of 1.1mm can be seen in section 5.4.2. The gloss black surface, on the other hand, gave the weakest signal return and the lowest precision.

The third part of this objective concerned the effects of incidence angle and range on the target design; these were investigated in a series of trials as presented in chapter 5. The results show that the cone is the most favourable target.

In order to investigate the possibility of detecting different targets of the same shape on the same cloud automatically, and the possibility of determining the centre of each target separately, the author implemented an algorithm. The programs scripts were written using Matlab and they detect and compute the apex of the target automatically. The detection was based on the criteria, such as intensity value, distance between points, and also the number of points expected to be captured from laser scanner example, given in chapter 6. The accuracy and precision of the target

centre/apex was tested from different ranges, IA and point density. The results show that the best target is chosen to be cone, (see section 5.5.5). This is attributed to the following reasons:

1. Easy for detection and computing, where there is only one surface to be detected, unlike for example, the pyramid, where each face must be detected individually.
2. Moreover, the cone can be detected, and the apex can be calculated from any incidence angle.
3. Only one colour needs to be used in the cone, making detection of the target easier.
4. Two colours can be used where the flat surface around the target cannot be found, see section 6.4.1.
5. Even with high angles of incidence sufficient radiation will be reflected back to the scanner (see chapter 5, section 5.5.5).
6. The actual target point used for measurement (apex) is physically visible from outside of the target so it can be easily observed by other survey techniques such as a Total Station.

9.1.4 Testing the designed target and checking the improvements in MLS data.

The investigation of improving the quality of MLS system results in matching multiple scans using targets instead of natural features was successfully and automatically performed. The results of using targets have been much better than the results obtained by matching natural features. See section 8.2.2.

The visual inspections of matching multiple scans show that using targets and natural features gave good results; the mean absolute error is up to 12 mm can be seen in section 8.2.2, Table 8.15. On the other hand, using only targets gives very good results in the matching process; the mean absolute error is up to 7 mm, see section 8.2.2, Table 8.15. However, when scanning unstable structures, and may not be safe to fix target in such area. Therefore, natural features with the target should be used to improve the accuracy of the matching process.

Using the optimal target design will not only increase data quality, but also enable the computing of laser scanner Exterior Orientation Parameters (EOP) to high accuracy, as natural features are often not suitable for matching multi-scans. However, using targets provides good accuracy for matching multi-scans rather than using natural features. Moreover, using targets in an automatic workflow for matching multiple scans has the potential to reduce the occurrence of systematic error with constant observing quality. The self-calibration parameters (offset and misalignment angle) of MLS system can also be achieved to high accuracy depending on the targets.

9.2 Recommendation for future research

The aim in the future should be to extend the potential of using the optimal target for improving accuracy, especially where navigation solutions tend to be degraded.

1. Exterior orientation parameters (EOP) of the laser scanner will be calculated using targets, where at least 3 targets should be available in the trajectory of the laser point cloud. The position will be determined based on intersection method using targets as a ground control point.
2. Another programming language is recommended to be used, such as FORTRAN and C# to detect the target and calculate the apex faster.

Not all topics related to the analysis of MLS data accuracy in urban areas were investigated in this research. For example, issues related to economical use (time and cost require for preparation, processing, and post-processing) have not been considered.

There are other prospects for future research activities in this area:

- It is recommended, to use of optimal target on large structures with MLS for rapid monitoring to detect the amount of geometric deformation in large engineering structures, such as bridges and dams. This will be useful for the applications, such as environmental hazards awareness including flooding and climate changes, change detection in 3D modelling and cultural heritage sites.

- An interesting avenue of future research in this area is to improve the IMU performance in urban areas, using a laser scanner and targets. In the urban area,

the GPS signal tends to be absent, where at that moment (when the GPS signal is out), the position and orientation are taken from GPS / IMU. However, the position of the pre-fixed target is also known from laser scanning. When the vehicle is moving, the IMU will still be working to provide orientation, but the position is not accurate. The idea behind this potential research area is to use the laser scanner itself to obtain the position depending on the targets detected from the previous known position. This could be calculated using basic mathematics (intersection method). The position data can also be used to determine the accelerometer errors, and therefore, when for example, the scanning is lost; a good position fix can be achieved from the IMU. Such application would be useful for in dense urban areas, as well as underground, for example, in mines and tunnels.

- Accuracy assessment of multi mobile laser scanning datasets using robust feature matching approach in overlapping scenes. Evaluating the quality of the positional accuracy of laser point clouds acquired from multi/overlapped data source. This should detect the bias in each relevant dataset by evaluating the relative and absolute accuracy of the selected matched primitives. Moreover, noise levels can be evaluated by quantifying the consistence between overlapping datasets. Although an accurate matching approach is required, a generic quality control measure could be achieved. This will be useful in the application of an integrated multi-source dataset, which can potentially produce more accurate results and more reliable information than one data source for a variety of applications, such as 3D city modelling, DTM generation, environmental hazard monitoring, etc.

REFERENCES

3D LASER MAPPING LTD. 2011. *Homepage of the company 3D laser mapping Ltd.* http://www.3dlasermapping.com [Online]. [Accessed 21 January 2011].

AKCA, D. 2010. Co-registration of Surfaces by 3D Least Squares Matching., Photogrammetric Engineering & Remote Sensing Vol. 76, No. 3, March 2010, pp. 307–318.

AKCA, D. & GRUEN, A. 2005. Fast correspondence search for 3D surface matching. International Archives of Photogrammetry, Remote Sensing and Spatial Information Sciences 36 (Part 3/W19), 186–191.

ALAMUS, R., BARON, A., BOSCH, E., CASACUBERTA, J., MIRANDA, J., PLA, M., SANCHEZ, S., SERRA, A. & TALAYA, J. 2004. On the accuracy and performance of the geomobil system. International Archives of Photogrammetry, Remote Sensing and Spatial Information Sciences 35 (Part 5), 262–267.

ALAMUS, R., BARON, A., BOSCH, E., CASACUBERTA, J., MIRANDA, J., PLA, M., SANCHEZ, S., SERRA, A. & TALAYA, J. 2005. GEOMOBIL: ICC land based mobile mapping system for cartographic data capture. Proceedings of XXII International Cartographic Conference of the ICA,9-16 July 2005, La Coruna,Spain; available at http://www.icc.es/pdf/common/icc/publications_icc/publication_techniques/fotogramefoto/bienni_2005_2006/geomobil.pdf.

AXELSSON, P. 2000. DEM generation fron laser scanner data using adaptive TIN model. *In proceeding of XIX ISPRS Congress,* Amsterdam, The Netherlands, 16-22/July /2000; Volume 33,Part B4,pp.110-117.

BAE, K. & LICHTI, D. 2008. Amethod for automated registration of unorganised point-coud., *ISPRS journal of photogrammetry and Remote Sensisng,* Volume (63).

BALIS, V., KARAMISTOS, S., KOTSIS, I., LIAPAKIS, C. & SIMPAS, N. 2004. 3D-Laser Scanning: Integration of Point Cloud and CCD Camera Video Data for the Production of High Resolution and Precision RGB Textured Models: Archaeological Monuments Surveying Application in Ancient Ilida. *In: Proceedings of FIG Working Week, Athens, Greece, May 22 – 27,* http://www.fig.net/pub/athens.

BALTSAVIAS, E. P. 1999b. Aiborne laser scanning: basic relations and formulas. *ISPRS J Photogramm and Remote Sens* 54: 199 – 214.

BALZANI, M., PELLEGRINELLI, A., PERFETTI, N. & UCCELLI, F. 2001. A terrestrial laser scanner: accuracy tests. In: Proceedings of 18th International Symposium CIPA 2001, Potsdam, Germany, September 18 – 21, pp 445 – 453.

BARBER, D., MILLS, J. & SMITH-VOYSEY, S. 2008. Geometric validation of a ground-based mobile laser scanning system. *ISPRS Journal of Photogrammetry and Remote Sensing,* 63**,** 128-141.

BARBER, D. M. 2003. Terrestrial laser scanning for the metric survey of cultural heritage structures. Thesis submitt to the Newcaslte University.

BECKER, S. 2009. Generation and application of rules for quality dependant facade reconstruction. *ISPRS journal od photogrammetry and remote sensing,* 64, 640-653.

BERNARDINI, F., MARTIN, L. M. & RUSHMEIER, H. 2010. High-Quality Texture Reconstruction from Multiple Scans. IBM T. J. Watson Research Center, P.O. Box 704, Yorktown Heights, NY 10598.

BESL, P. J. & MCKAY, N. D. 1992. A method for registration of 3D shapes. IEEE Transactions on Pattern Analysis and Machine Intelligence., vol. 14 (2), 239-256.

BHATTA, B. 2011. *Global navigation satellite systems : insights into GPS, GLONASS, Galileo, Compas and others.* , Leiden : CRC Press/Balkema, c2011., George Green Library G109.5 BHA.

BOEHLER, W., BORDAS VICENT, M. & MARBS, A. 2003. Investigating Laser Scanner Accuracy. i3mainz, Institute for Spatial Information and Surveying Technology, FH Mainz, Holzstrasse 36, 55116 Mainz, Germany.

BORNAZ, L., LINGUA, A. & RINAUDO, F. 2003. Multiple scan registration in LIDAR close-range applications. In: Proceedings of the ISPRS International Workshop WG V/4 and INTCOM III/V "Vision Techniques for Digital Architectural and Archaeological Archives". Ancona, Italy, July 1 – 3. http://www.commission5.isprs.org/wg4/workshop_ancona/proceedings.html.

BRENNER, C. 2009. Extruction of features from mobile laser scanning data for future driver assistance systems. Institute of Cartography and Geoinformatics, Leibiniz University Hannover. *Advances in GIScience.*

BURMAN, H. 2002. Laser strip adjustment for data calibration and verification. Internet archives of photogrammetry and remote sensing (IAPRS) Commession V1, WGV1/4.

CLARK, J. & ROBSON, S. 2004. Accuracy of measurements made with CYRAX 2500 laser scanner against surfaces of known colour. *ISPRS, Vol.XXXV. Commission* IV, part B4, pp.1031-1037.

CSANYI, N. 2007. Precision LiDAR Mapping of Transportation Corridors Using LiDAR-Specific Ground Targets.Department of Civil and Environmental Engineering and Geodetic Science The Ohio State University, 1216 Kinnear Rd, Columbus, Ohio 43212.

CSANYI, N. & TOTH, C. 2006. Improvement of LiDAR Data Accuracy Using LiDAR-Specific Ground Targets, *Photogrammetric Engineering & Remote Sensing*, (in press).

DEEMS, J. & PAINTER, T. 2006. LIDAR measurement of snow depth: accuracy and error sources. *In: Proceedings of International Snow Science* Workshop, Telluride, CO, pp 384 – 391. Available at http://www.avalanche.org/~issw2004/issw_previous/2006/proceedings/data/papers/050.pdf.

DELAWARE, S. 2008. *HESC 427.: LeastSquares-Course Hero* [Online]. Available: http://www.coursehero.com/file/5098441/LeastSquares/ [Accessed 12 Dec. 2012].

DIMSDAL, J. 2005. Feature: Laserscanner. Past, Present, and future. Professional Surveyor Magazine. Available at www.profsurv.com/magazine/article.

DUGGAL, S. K. 2004. *Surveying: Vo.II, New Delhi, Tata MCGRAW.*

EBERLY, D. 2008. Least squares fitting of data. http://www.geometrictools.com/ Copyright c 1998-2012. All Rights R LeastSquaresFitting.pdf p.p 6.

ELLUM, C. & EL-SHEIMY, N. 2002. Land-based mobile mapping systems. Photogrammetric Engineering and Remote Sensing 68 (1), pp.13–17 (and 28).

FARO 3DLS. 2011. *Homepage of the company FARO Technologies,Inc. http://www.faro.com*. [Online]. [Accessed 3th November 2011].

FELLER, W. 1971. *An Introduction to Probability Theory and Its Applications, 2nd edition, Vol. II, John Wiley & Sons, New York.*

FLI-MAP. 2011. *Homepage of FLI-MAP.* http://www.flimap.nl. [Online]. [Accessed 9th November 2011].

FORBES, A., B. 1989. Least Squares Best-Fit geometric elements, National Physical Labortaty (NPL) report April 1989. Mathematics-30 pages

GAVIN, H. 2011. The Levenberg-Marquardt method fornonlinear least squarescurve-fitting problems. Department of Civil and Environmental Engineering. Duke University.

GEOMAGIC, I. 2007. *Geomagic studio 10 user guide (2007_12_18_B). Available at* http://www.geomagic.com/. [Online]. [Accessed 18th August 2010].

GEOMATIC, I. 2007. *Introduction to the Geomatic office user guide. Available at http//* www.trimble.com/. [Online].

GERBER, B., JAZIZADEH, F., KAVULYA, G. & CALIS, G. 2010. Assessment of target types and layolus in 3D laser scanning for registration accuracy. University of Southern California, Department of Civil and Environmental Engineering.

GIM 2012. 3D Model for Queen's Jubilee Concert Planning. . *The Global Magazine for Geomatics (GIM), 26/06/2012.No.289.* Internet- www.GIM-International.com.

GIM 2013. New mobile indoor mapping system . The Global Magazine for Geomatics (GIM), 07/01/2013.No.318. Internet- www.GIM-International.com.

GLENNIE, C. L. 2007. Rigorous 3D error analysis of kinematic scanning LiDAR system. *Journal of Applied Geodesy,* 1(3), 147-157.

GORDON, S. J. 2005. *Structural Deformation Measurement Using Terrestrial Laser Scanners.*, PhD thesis, Curtin University of Technology, Department of Spatial Sciences, Australia.

GORDON, S. J. & LICHTI, D. 2004. Terrestrial laser scanners with a narrow field of view: the effect on 3D resection solutions. Surv Rev 37(292): 448 – 468.

GOTTWALD, R. 2008. Field procedures for testing Terresterial laser scanners- A contribution to a future ISO standard integrating generations FIG working Stockholm, Sweden.

GRAEFE, G. 2007a. High precision kinematic surveying with laser scanners. Journal of applied geodesy 1(2007), 185-199c de Gruyter 2007.DOI 10.1515/JAG.2007.021.

GRAEFE, G. 2007b. *Kinematische Anwendungen von Laserscannern im StraBenraum,*. PhD thesis, Kinematic applications of laser scanners in the street area, , Universitat der Bundeswehr Munchen, Institut fur Geodasie, Neubiberg. .

GRAEFE, G. 2007c. Quality management in kinematic laser scanning application. 3D Mapping Solutions GmbH, 82041 Oberhaching, Germany.

GRAEFE, G. 2008. Kinematic 3D laser scanning for road or railway construction surveys. Ist International conference on machine control and guidance2008, 3D mapping solutions GmbH, Genmeny.

GREJNER-BRZEZINSKA, D., LI, R., HAALA, N. & TOTH, C. 2004. From Mobile Mapping to Telegeoinformatics: Paradigm Shift in Geospatial Data Acquisition, Processing and Management. *PE and RS,* 70**,** 197-210.

HAALA, N., PETER, M., KREMER, J. & HUNTER, G. 2008. Mobile LiDAR Mapping for 3D Point Cloud Collection in Urban Areas - a Performance Test. IAPRS, Vol. 37, (B5), pp. 1119.

HABIB, A. 2010. *Integration of Photogrammetric and LIDAR data for Quality Assurance and Quality Control Purposes. Digital Photogrammetry Research Group.Department of Geomatics Engineering University of Calgary, Canada.*

Availabe at http://dprg.geomatics.ucalgary.ca, [Online]. [Accessed 5th February. 2010].

HABIB, A. & VAN RENS, J. Quality Assurance and Quality Control of LiDar System and Derived Data. Available at www.geotree.uni.edu/Resources2007/Lidar/AKAM_LIDAR_QC.pdf. 2007.

HARVEY, B. 2004. Registration and transformation of multiple site terrestrial laser scanning. *Geomatic Research Aust.,ISSN 1324-9983,No. 80 June 2004,pp. 33-50*.

HERITAGE., E. 2007. Laser scanning for National Heritage: Advice and guidence to users on laser scanning in technology and architecture.

HESSE, C. 2008. Hochauflosende kinematische objekterfassung mit terrestrischen laserscannern. PhD.thesis, Leibniz University of Hanover; Wissenschaftliche Arbeiten der fachrichtung Geodasie und Geoinformatik der Leibniz University Hannover, No.268. High-resolution kinematic object detection using terrestrial laser scanners. PhD.thesis, Leibniz University of Hanover, Scientific work of the Department of Geodesy and Geoinformatics, Leibniz University Hannover, No.268.

HIREMAGALUR, J., YEN, K. S., AKIN, K., BUI, T., LASKY, T. A. & RAVANI, B. 2007. Creating Standards and Specification for the use of Laser Scanners in Cultrans Peojects.University of California, Department of Transportation. Final report of contract IA 65A0210-Task order 06-21.

HOCK, C., CASPARY, W., HEISTER, H., KLEMM, J. & STERNBERG, H. 1995. Architecture and Design of the Kinematic Survey System KiSS. In Proceeding of the 3rd International Workshop on High Precision Navigation, pp. 569-576. Stuttgart, Germany.

HUNTER, G., COX, C. & KREMER, J. 2006. Development of A Commercial Laser Scanning Mobile Mapping System - StreetMapper, Processing of 2nd International Workshop of the future of Remote Sensing. .

INGENSAND, H., RYF, A. & SCHULZ, T. 2003. Performances and experiences in terrestrial laser scanning. In: Gruen A, Kahmen H (eds.) Optical 3-D Measurement Techniques VI. Available at http://www.geometh.ethz.ch.

JACOBS, G. 2005a. Registration and Geo-referencing. Prof Surv Mag, July. http://www.leicageosystems.com/hds/en/lgs_29445.htm.

JACOBS, G. 2005b. Registration and Geo-referencing. Professional Survey Magazine, July. http://www.leicageosystems.com/hds/en/lgs_29445.htm.

JAGER, R. R., MU¨ LLER, T. & SALER, H. 2005. Classical and robust compensate for submission procedures. A guide for training and practice of spatial data and geospatial professionals, Herbert Wichmann Verlag, Heidelberg, 2005.

JENNINGS, A. 2011. *File exchange "sphere fit least squares".. University of Dayton.* [Online]. Matlab Central: Mathworks. Available: http://www.mathworks.com/matlabcentral/fileexchange/34129-sphere-fit-least-squared/content/sphereFit.m. [Accessed 11 January 2011].

JOSHUA, I. 2011. *The effectiveness of the Riegl VMX-250 on a highway-rail vehicle. http://www.vmx250.rieglusa.com/*. [Online]. [Accessed 21 Nov. 2011].

KAASALAINEN, S., JAAKKOLA, A., KAASALAINEN, M., KROOKS, A. & KUKKO, A. 2011a. Analysis of incidence angle and distance effects on terrestrial laser scanner intensity: search for correction methods Remote Sensing, 3 (10) (2011), pp. 2207–2221.

KAASALAINEN, S., KAARTINEN, H., KUKKO, A., ANTTILA, K. & KROOKS, A. 2011b. Application of mobile laser scanning in snow cover profiling. Published by

copernicus publication on behalf of the European Geosciences Union- Published Murch 2011.

KAASALAINEN, S., KUKKO, A., LINDROOS, T., LITKEY, P., KAARTINEN, H., HYYPPÄ, J. & AHOKAS, E. 2008. Brightness measurements and calibration with airborne and terrestrial laser scanners. *IEEE Transaction on Geoscience and Remote Sensing*, 46(2), pp. 528-534.

KERSTEN, T. P., MECHELKE, K., LINDSTAEDT, M. & STEMBERG, H. 2008. Geometric accuracy investigations of the latest terrestrial laser scanning systems. Integrating generations FIG working. Stockholm, Sweden. .

KERSTING, A., ZHAI, R. & HABIB, A. 2008. Strip Adjustment Using Conjugate Planar and Linear Features in Overlapping Strips, *ASPRS 2008 Annual Conference*.

KREMEN, T., KOSKA, B. & POSPSIL, J. 2006. Verification of Laser Scanning systems quality. In: Proc. *In the XXIII FIG Congress,* Shaping the Change, Munich, Germany. October 8-13.

LAMPTON, M. 1997. Damping - Undamping strategies for the Levenberg-Marquardt non-linear least-square method. computers in physics.Journal 11 (1): pp. 110-115

LEICA 2010. Leica Geosystems (www.leica-geosystems.co.uk) accesed on the 20th August 2010.

LEICA. 2009. Leica Geosystems (www.leica-geosystems.co.uk) accesed on the 20th August 2009

LEICA. 2010. *HDS Trainning manual. www.leica-geosystem.com. Accessed 10 May 2010* [Online].

LEICA. 2011. *Homepage of the company Leica Geosystems. http://ww.leica-geosystems.com.* [Online]. [Accessed 10 November 2011].

LICHTI, D. D. & GORDON, S. J. 2004. Error Propagation in Directly Georeferenced Terrestrial Laser Scanner Point Clouds for Cultural Heritage Recording. In: Proceedings of FIG Working Week, Athens, Greece, May 22 – 27. http://www.fig.net/pub/athens.

LICHTI, D. D., GORDON, S. J. & TIPDECHO, T. 2005. Error models and propagation in directly georeferenced terrestrial laser scanner networks. Journal of Surveying Engineering 131 (4), 135–142.

LÖSLER, M. 2008. Reference point determination with a new mathematical model at the 20 m VLBI radio telescope in Wettzell. Journal ofApplied Geodesy 2 (2008), 233–238 6 de Gruyter 2008. DOI 10.1515/JAG.2008.026.

LÖSLER, M. 2012a. JAG3D – A free Program for Network Adjustment and Deformation Analysis. http://derletztekick.com/software/netzausgleichung (last access: 2012-12-02).

LÖSLER, M. 2012b. *Orthogonal Distance Fit of a Pyramid. http://forum.diegeodaeten.de/index.php?id=4083 (last access: 2012-12-02).* [Online].

LOURAKIS, M. I. A. 2005. A Brief Description of the Levenberg-Marquardt Algorithm Implemened by levmar. Institute of Computer Science Foundation for Research and Technology – Hellas (FORTH), 2005, available at: http://www.ics.forth.gr/~lourakis/levmar/levmar.pdf (accessed Sept. 18, 2012).

LUK´ACS, G., MARSHALLA, D. & MARTIN, R. 1997. Geometric least-squares fittingof spheres, cylinders, cones, and tori, in RECCAD Deliverable Documents 2 and 3. Copernicus Project No. 1068, Eds. R. R. Martin, T. Varady, Report GML 1997/5,

Computer and Automation Institute, Hungarian Academy of Sciences, Budapest,1997.

MÄÄTTÄ, K., KOSTAMOVAARA, J. & MYLLYLÄ, R. 1993. Profiling of hot surfaces by pulsed time-of-flight laser range finder techniques. Appl Opt 32(27): 5324 – 5347.

MILLER, S. J. 2006. The Method of Least Squares, Brown University, Providence, 2006.

MILLS, J. & BARBER, D. 2003. An Addendum to the Metric Survey Specifications for English Heritage – the collection and archiving of point cloud data obtained by terrestrial laser scanning or other methods.: Version 11/12/2003.

MORIN, K. W. 2002. Calibration of airborne laser scanners., master thesis, Department of Geomatics Engineering, University of Calgary, Alberta, Nov.2002.

NAYAR, S., IKEUCHI, K. & KANADE, T. 1989. Surface Reflection: Physical and Geometrical Perspectives. Technical Report CMU-RI-TR-89-7, The Robotics Institute, Carnegie Mellon University. http://www.ri.cmu.edu/pub_files/pub3/nayar_s_k_1989_1/nayar_s_k_1989_1.pdf.

O'HAVER, T. 2008. *A Pragmatic Introduction to Signal Processing with applications in Chemical Analysis-Curve fitting: Linear Least Squares* [Online]. Available: http://terpconnect.umd.edu/~toh/spectrum/IntroToSignalProcessing.pdf [Accessed 12 Nov. 2012].

OLYAZADEH, R., SETAN, H. & NIMA, F. 2011. Network Adjustment Program using MATLAB. Department of Geomatic Engineering, Faculty of Geoinformation and Real Estate, Universiti Teknologi Malaysia (UTM), 81310 UTM Skudai, Johor, Malaysia.

OPTECH. 2011. *Homepage of the company Optech. http://www.optech.ca (accessed November 2011)* [Online].

ORDNANCE SURVEY. 2012
. *Ordnancesurvey.co.uk/oswebsite/gps/osnetfreeservices/about/surveying_osnet.html. accessed April 2012* [Online].

OUDE EL-BERINK, S. J. 2008. Problem in automated building reconstruction based on dense airborne laser scanning data. *In*: ISPRS 2008: Proceeding of the XXI Congress: Silk road for information from imajery: The international socienty for photogrammetry and remote sensing 3-11July, Beijing, China. Comm. III, WGIII/3 Benjing: ISPRS, 2008.pp.93-98.

OUDE EL-BERINK, S. J. 2010. Acquisition of 3D topography: Automated of 3D road and building reconstruction using airborne laser scanner data and topographic maps, Delft, NCG, Nederlandse commissie voor Geodesie.

PFEIFER, N. & BRIESE, C. 2007a. Geomertic aspects of airborne laser scanning and treesterail laser scanning. International Archives of Photogrammetry, Remote Sensing and Spatial Information Sciences, IAPRS, Volume XXXVI, Issue Part 3/W52, p.311-319 (2007).

PFEIFER, N. & BRIESE, C. 2007b. Laser Scanning-Priniciple and application. Proceeding of Third International Scientific Conference " GEO-Sibirien-2007",. Novosibirsk, Russia.

PFEIFER, N. & LICHTI, D. D. 2004. Terrestrial Laser Scanning – developments, applications and challenges. GIM International 18(12): 50 – 53.

POLI, D., ZHANG, L. & GRUEN, A. 2004. SPOT-5/HRS stereo images orientation and automated DSM generation, International *Archives of Photogrammetry, Remote Sensing and Spatial Information Sciences*, 35(B1):421–432.

PRICE, W. & UREN, J. 1989. *Laser surveying. VNR International, London. p.40.*

PU, S. 2010. *Knowldege based building facade reconstruction from laser point cloud and images. ITC. Faculty of Geo-Information Science and Earth Observation of the University of Twente. PhD project.*

PUENTE, H., GONZAEZ-JORGE., ARIAS, P. & ARMESTO, J. 2011. Land based Mobile Laser Scanning System: A review, available at www.isprs.org/proceedings/XXXVIII/5/ls2011_submission_14.pdf. Commission V, WG V/3.

PUNMIA, B. C., ASHOK, K. J. & ARUN K, J. 2005. *"Surveying vo.1" Published by LAXMI PUBLICATIONS (p) LTD. 22, Golden HOUSE, Daryagan), New Delhi-110002*.

RESHETYUK, Y. 2009. *Self-calibration and direct georeferencing in terrestrial laser scanning. PhD thesis submited to the Universitetsservice US AB; Stockholm, Sweden, Department of Transport and Economics; Division of Geodesy; 100 44 Stockholm, January 2009. TRITA-TEC-PHD 09-001; ISSN 1653-4468; ISBN 978-91-85539-34-5.*

RIEGER, P., STUDNICKA, N. & PFENNIGBAUER, M. 2008. Boresight alignment method for mobile laser scanning systems, *RIEGL* Laser Measurement Systems GmbH.

RIEGER, P., STUDNICKA, N., PFENNIGBAUER, M. & ULLRICH, A. 2010a. Advances in mobile laser scanning data acquisition. FIG Congress 2010. Sydney, Australia, 11-16 April 2010.

RIEGER, P., STUDNICKA, N., PFENNIGHBAUER, M. & ZACH, G. 2010b. Boresight alignment method for mobile laser scanning systems, *Journal of applied Geodesy 4(2010) Vol 4 PT1*.

RIEGL. 2011. *Homepage of the company RIEGL Laser Measurement Systems GmbH. http://www.riegl.com (accessed November 2011)* [Online].

RIEGL. 2012. *Homepage of the company RIEGL Laser Measurement Systems GmbH. http://www.riegl.com.* [Online]. [Accessed 22 April 2012].

ROSELL POLO, J. R., SANZ, R., LLORENS, J., ARNÓ, J., ESCOLÀ, A., RIBES-DASI, M., MASIP, J., CAMP, F., GRÀCIA, F., SOLANELLES, F., PALLEJÀ, T., VAL, L., PLANAS, S., GIL, E. & PALACÍN, J. 2009. A tractor-mounted scanning LIDAR for the non-destructive measurement of vegetative volume and surface area of tree-row plantations: a comparison with conventional destructive measurements. *Biosyst. Eng.* vol (102), issue 2, p.p 128-134.

RUTZINGER, M., OUDE EL-BERINK, S., PU, S. & VOSSELMAN, G. 2009. Automatic extraction of vertical walls from mobile and airborne laser scanning data. In International Archives of Photogrammetry and Remote Sensing and Spatial Information Sciences; ISPRS: Vienna, Austria, 2009; Volume 38, Part 3 / W8, pp. 7–12.

RUTZINGER, M., PRATHAST, A. K., OUDE EL-BERINK, G. & VOSSELMAN, G. 2010. Detection and modelling of 3D trees from mobile laser scanning data. International archives of photogrammetry, remote sensing and special information, Vol. XXXXVIII, part5, Commission V symposium, Newcastle upon Tyne, UK. 2010.Commission V/ICWG_V/I.

SCHAER, P., SKALOUD, J., LANDTWIG, S. & LEGAT, K. 2007. Accuracy estimation for laser point cloud including scanning geometry. *International Archives of the Photogrammetry, Remote Sensing and Spatial Information Sciences*, 36 (part5 / C55), pp. 279-353.

SCHNEIDER, D. 2009. Calibration of a Riegl LMS-Z420i based on a multi-station adjustment and a geometric model with additional parameters. Commession V,WG V/3 Techisch University Dresden, Institite of Photogrammetry and Remote sensing. Germany.

SCHULZ, T. 2007. *Calibration of a Terrestrial Laser Scanner for Engineering Geodesy.* . PhD thesis, Eidgenössische Technische Hochschule (ETH) Zurich.

SCHWARZ, K. P., MARTELL, H., EL-SHEIMY, N.,, LI, R., CHAPMAN, M. & COSANDIER, D. 1993. VISAT- A Mobile Highway Survey System of High Accuracy. In Proceedings of the Vehicle Navigation and Information Systems Conference, pp. 467-481. Institute of Electrical and Electronics Engineers (IEEE), Ottawa, Canada.

SETAN, H. 2008. Lecture notes for Adjustment computations,Slide.1-24.

SHAN, J. & TOTH, C. K. 2008. *Topographic laser ranging and scanning: Prenciple and processing. Boca Rotana. CRC.* .

SICK. 2011. *Homepage of the company Sick Group. http://www.sick.com (accessed November 2011).* [Online].

SKALOUD, J. & LICHTI, D. D. 2006. Rigorous approach to bore-sight self - calibration in airborne laser scanning, ISPRS of Photogrametry and Remote Sensing 61 (2006), pp. 47-49.

SMITH, M. & TAHA, A. 2009. Photogrammetric Potential of the Canon EOS 5D MKII for Precise Still and Video Measurements. *The Institute of Engineering Surveying and Space Geodesy ,The University of Nottingham. September 2009*.

SMITH, M. J. 2010. Photogrammetry handouts. NGI. The University of Nottingham.

SMITH, M. J. & MOORE, T. 2010. Back to basic, plane transformation. The University of Nottingham. Handout, pp 240. From survey review, vol.34, No.266, october 1997.

SOININEN, A. 2010. *TerraScan User's Guide*; Terrasolid Ltd.: Helsinki, Finland, 29 January 2010; p. 308. .

SOUDARISSANANE, S., LINDENBERGH, R., MENENTI, M. & TEUNISSEN, P. 2009. Incidence angle infuluence on the quality of terrestrial laser scanning point. In *Proceeding of Laser sacnninr 2009, Paris, France, 1-2 Spetember 2009;* In *IAPRS; 2009*; Vol. 38, pp.83-88.

STERNBERG, H., KERSTEN, T., JAHN, I. & KINZEL, R. 2004. Terrestrial 3D Laser Scanning Data Aquisition and Object Modeling for Industrial as build Documentation and Architectural Application. Department of Geomatics, Hamburg University of Applied sciences.

STREETMAPPER360. 2009. *3D Laser Mapping Ltd, www.3dlasermapping.copm.* [Online].

TAIT, M., FOX, R. & TESKEY, W. 2004. A Comparison and Full Error Budget Analysis for Close Range Photogrammetry and 3D Terrestrial Laser Scanning with Rigorous Ground Control in an Industrial Setting. In: Proceedings of INGEO 2004 and FIG Regional Central and Eastern European Conference on Engineering Surveying, Bratislava, Slovakia, November 11 – 13.
http://www.fig.net/pub/bratislava/papers/ts_05/ts_05_tait_etal.pdf.

TALAYA, J., ALAMUS, R., BOSCH, E., SERRA, A., KORNUS, W. & BARON, A. 2004. Integration of a terrestrial laser scanner with GPS/IMU orientation sensors. In: International Archives of Photogrammetry and Remote Sensing, Vol. Commission 5, ThS 17, Istanbul, Turkey, July 12 - 23.
http://www.isprs.org/publications/archives.html.

TAO, C. V. & LI, J. 2007. *Advances in Mobile Mapping Technology. ISPRS Book Series, 4, Taylor and Francis, London,UK.*

TERRASOLID. 2009. *3D Laser Mapping Ltd, http://www.terrasolid.fi/ accesed December 2009.* [Online].

TERRASOLID. 2004 *TerraMatch user Guid, http://www.terrasolid.fi/system/files/tmatch.pdf.* [Online]. [Accessed 22 November 2009].

TERRASOLID. 2009. Processing Mobile Scanner Data -Calibration to Improve Positioning. Terrasolid European Users Event Vienna 17 – 20 February 2009.

TERRASOLID. 2010. *Processing of Airborne Laser Data and Images. 3D Laser Mapping Ltd, http://www.terrasolid.fi/ pdf, accesed July 2010.* [Online].

THIEL, K.-H. & WEHR, A. 2004. Performance capabilities of laser scanners – an overview and measurement principle analysis. In: Proceedings of the ISPRS working group VIII/2 "Laser- Scanners for Forest and Landscape Assessment", Freiburg, Germany, October 3 – 6. http://www.isprs.org/publications/archives.html.

TOPCON. 2011. *Homepage of Topcon Global Gateway. http://www.topconpositioning.com (accessed November 2011).* [Online].

TOPEYE. 2011. *Homepage of the BLOM GROUP. www.blomasa.com (accessed November 2011).* [Online].

TOPOSYS. 2011. *Homepage of the company TopoSys GmbH. http://www.toposys.com (accessed November 2011).* [Online].

TOTH, C. K. 2002. Calibrating Airborne LIDAR Systems, Proceedings of ISPRS Commission II Symposium, Xi'an, China, August 20–23, 2002, 475–480.

TRIMBLE. 2011. *Homepage of the company Trimble. http://www.trimble.com (accessed November 2011).* [Online].

TSAKIRI, M., LICHTI, D. D. & PFEIFER, N. 2006. Terresterial Laser scanning for deformation monitering. *In processdings of the 12th FIG symposium on deformation measurements and 3rd IAG symposium on geodesy for geotechnical and structure engineering,* Baden, Austria.

UREN, J. & PRICE, W. F. 2006. *"Surveying for engineers". Fourth edition.Basingstoke: Palgrave Macmillan*.

USER MANUAL 2011. FARO Laser Scanner Focus^{3D} manual, FARO Technologies Inc., December 2010.

VAAJA, M., HYYPPÄ, J., KUKKO, A., KAARTINEN, H., HYYPPÄ, H. & ALHO, P. 2011. Mapping Topography Changes and Elevation Accuracies Using a Mobile Laser Scanner**.** *Published: 17 March 2011*

VOSSELMAN, G. & MASS, H. G. 2010. *Airborne and terresterial laser scanning. Boca Raton, USA.*

VOSSELMAN, G. E. & MASS, H. G. E. E. 2010b. *Airborne and terresterial laser scanning. (eds) 2010b, Boca Rotan: CRC.* USA.

WAGNER, W., ULLRICH, A., DUCIC, V., MELZER, T. & STUDNICKA, N. 2006. Gaussian decomposition and calibration of a novel small-footprint full-waveform digitising airborne laser scanner. ISPRS Journal of Photogrammetry and Remote Sensing, 60.

WEICHEL, H. 1990. *Laser beam propagation in the atmosphere. SPIE Optical Engineering Press, Bellingham, Washington USA p.p 51-60.*

WIKIPEDIA. 2012. *Hesse normal form.* [Online]. Available:

http://en.wikipedia.org/wiki/Hesse_normal_form. [Accessed 23 December 2012].

WOLF, P. & DEWITT, B. A. 2000. *"Elements of Photogrammetry with applications in GIS". Mc Graw-Hill Higher.*

WOLF, P. & GHILANI, C. 1997. *Adjustment Computations: Statistics and Least Squares in Surveying and GIS. John Wiley & Sons, Inc., New York.*

ZOLLER+FROHLICH. 2011. *Homepage of the company Zoller+Fr¨ohlich GmbH. http://www.zofre.de (accessed November 2011).* [Online].

APPENDICES

Appendix A: Figures of vehicle trajectory Vs GPS position quality of the entire area of Jubilee campus using Matlab functions.

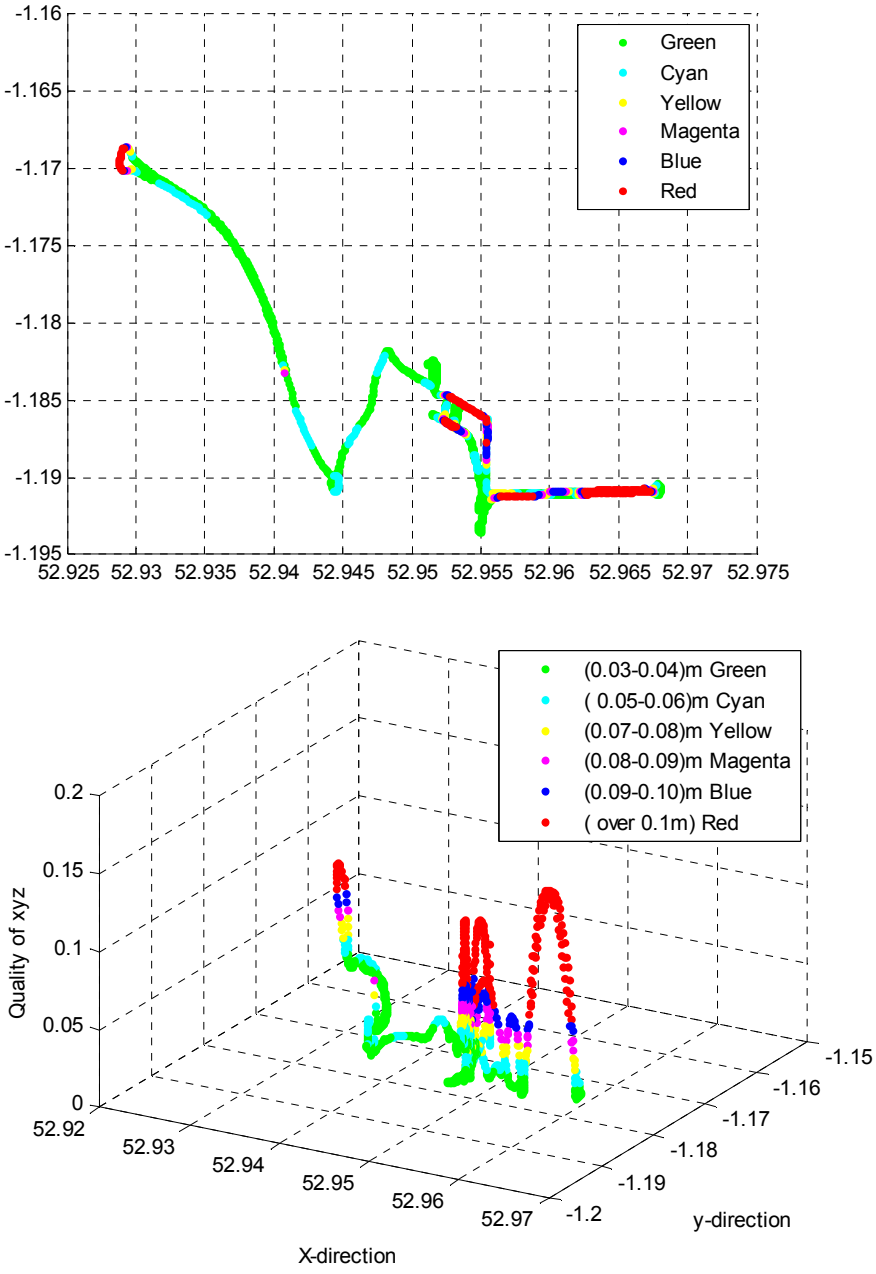

Figure A-1: Trajectory coloured according to GPS quality position in 2D (top), and 3D (bottom).

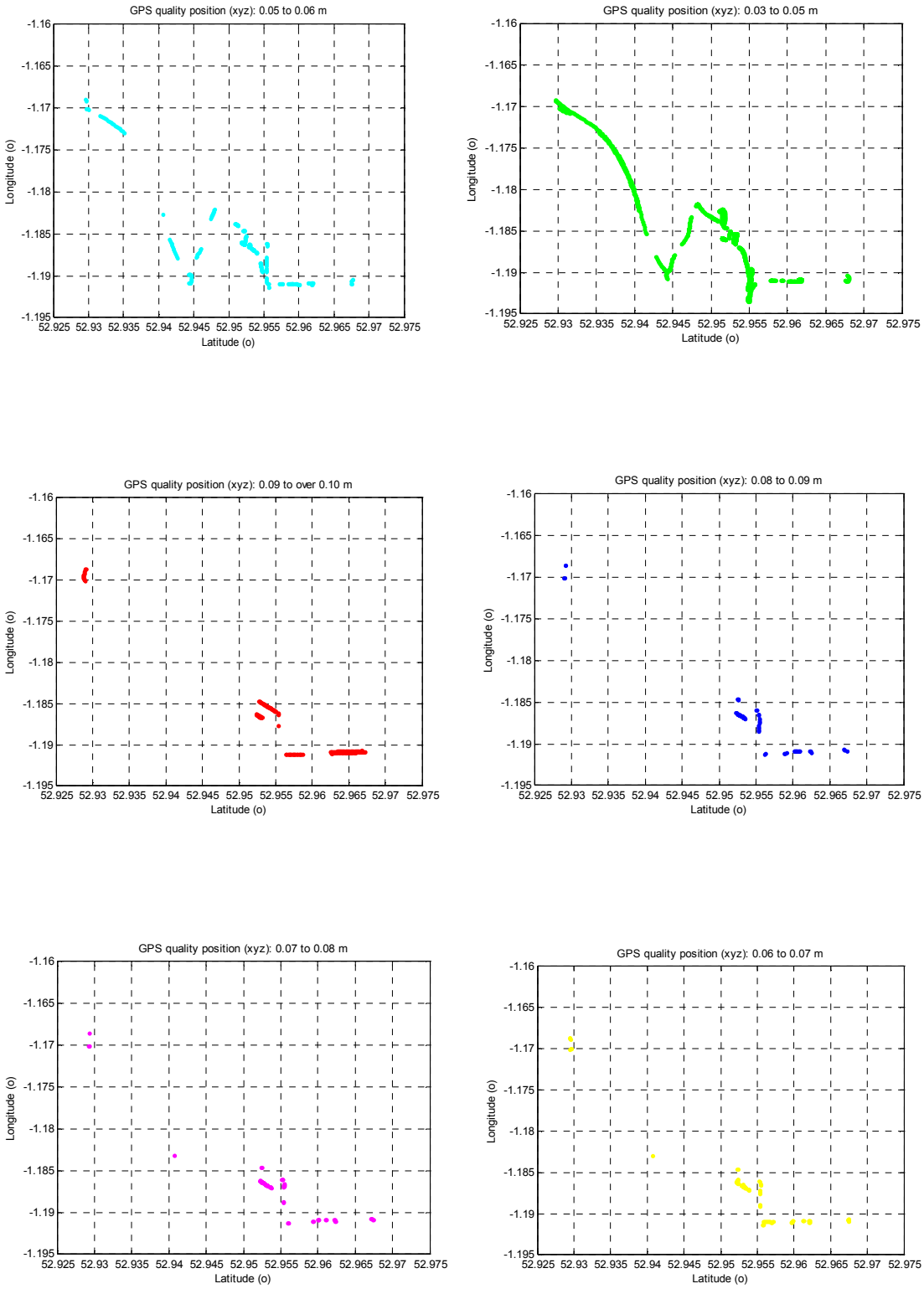

Figure A-2: Displaying trajectories coloured by RMS values (xyz).

Appendix B: MLS Calibration report in 2009 and 2012.

B1: Calibration report of the MLS data of first trial (November, 2009).

X= forward, Y= right, Z=down

Sensors	Lever arm offset			Misalignment angles		
	X (m)	Y(m)	Z (m)	Roll (o)	Pitch (o)	Yaw (o)
Scanner to IMU	-0.326	0.419	-0.096	0.044	0.299	0.348
GPS to IMU	-0.044	0.137	-0.166			

Table B1-1: Calibration of MLS system in November, 2009.

Note: Scanner was mounted 135 degrees from forward, and -40 degrees pitch from horizontal.

B2: Calibration report of the MLS data, October 2012.

Used loaded tie lines

Trajectories: E:\StreetMapper\StreetMapper - 2012-11-26 - 3DLM - Nottingham Jubilee Campus Calibration\traj\

Solution for whole data set

Solution per scanner

Starting average mismatches 0.01258 m; Final average mismatches 0.00901m

Execution time: 0.3 sec

Number of iterations: 21

Scanner H shift R shift P shift -0.206 -0.018 +0.032

Number of usable observations

Scanner Heading Roll Pitch 133 2120 1568

Mismatches

Average 3d mismatch: 0.01258

Average xy mismatch: 0.01674

Average z mismatch: 0.00955

Average wall lean: 0.01127

Statistics for internal observations

---

0 ground points; 0 xy points; 0 elevation points; 0 ground lines; 330 section lines, 0 roof lines

X Y Z

Average magnitude 0.013 0.006 0.010

RMS values 0.022 0.009 0.016

Maximum values 0.115 0.055 0.069

Observation weir 1121.0 1121.0 1539.0

Average magnitudes per line

Line	X	Y	Z
1	0.021	0.021	0.058
2	0.027	0.005	0.032
3	0.014	0.005	0.008
4	0.016	0.002	0.006
5	0.001	0.007	0.005
6	0.018	0.002	0.006
7	0.017	0.007	0.006
8	0.005	0.005	0.007
9	0.015	0.003	0.004
10	0.014	0.002	0.007
11	0.002	0.006	0.006
12	0.013	0.003	0.006
13	0.016	0.007	0.006
14	0.004	0.006	0.004
15	0.011	0.002	0.004
16	0.010	0.004	0.007
17	0.005	0.007	0.007
18	0.022	0.003	0.003
19	0.001	0.007	0.005
20	0.010	0.004	0.004
21	0.017	0.005	0.005
22	0.002	0.006	0.005
23	0.008	0.001	0.003
24	0.020	0.002	0.006
25	0.015	0.006	0.017
26	0.031	0.008	0.017
27	0.013	0.008	0.008
28	0.011	0.007	0.004
29	0.027	0.006	0.006
30	0.001	0.005	0.006
31	0.017	0.002	0.007
32	0.002	0.008	0.005
33	0.015	0.013	0.004

Appendix C: Figure of static GPS observation process.

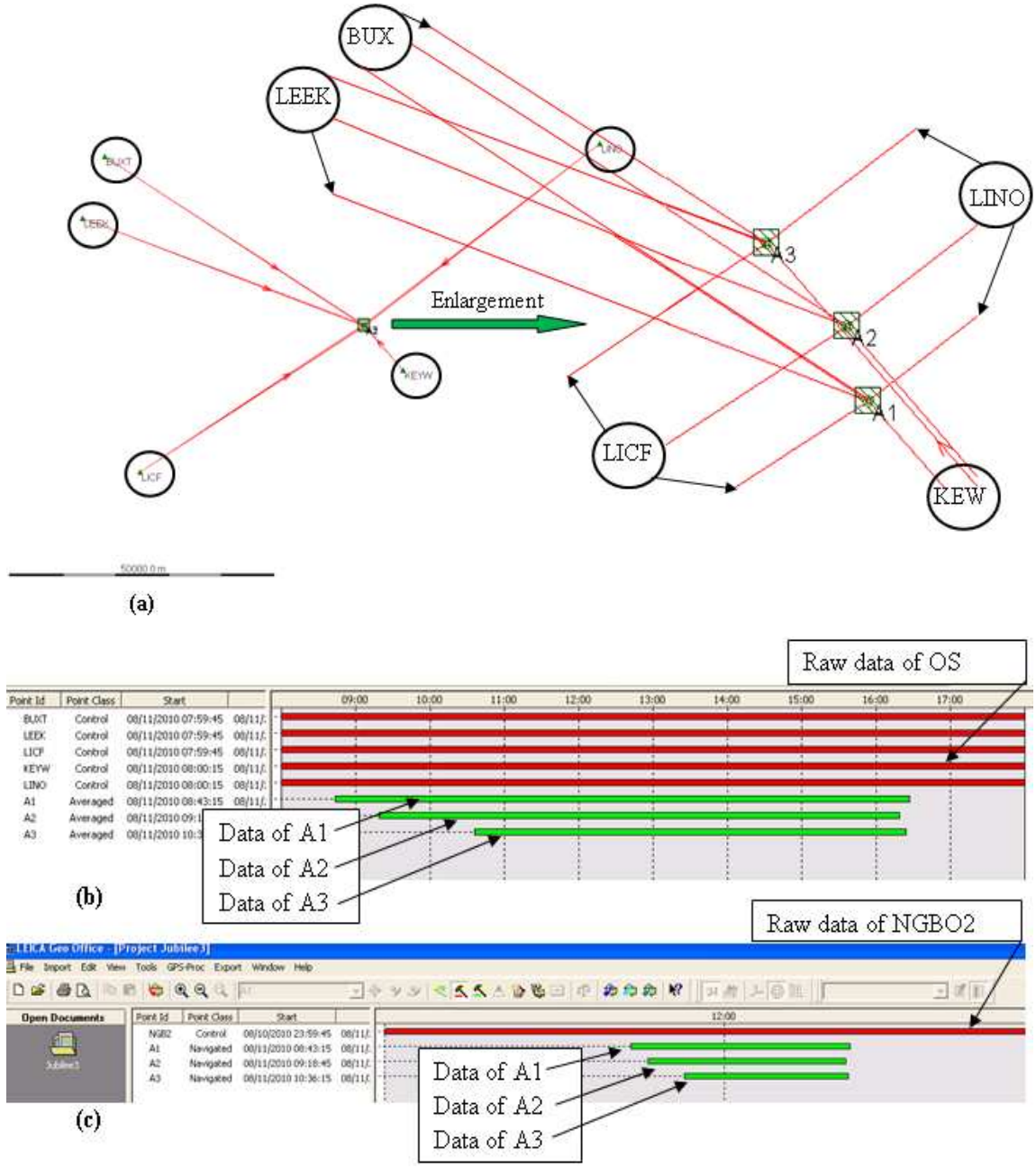

Figure C-1: (a) show the process of points (A1, A2, and A3) combined with five base stations. (b) The raw data of five base stations with three points; and (c) The raw data of three points with NGI base station (NGB2).

Appendix D: Tables of levelling closure and adjustment.

Point no.	Elevation from GPS (m)	Computed elevation from levelling procedure (m)	Different (m)	Remarks
From A1	**29.6572**			A1 fixed as a BM
To A2	29.6460	(29.6475)	-0.0015	
From A2				
To A3	30.2373	(30.2545)	-0.0172	
From A2				
To NGB11	30.8080	(30.7981)	0.0098	

Table D-1: Closure errors in levelling procedure of open loop

Point no.	Computed elevation	Elevation computed of the closed loop (m)	Different (m)	Distance (m)
From A2	29.6475			194.9240
To A1	**29.6572**	(29.6598)	0.0026	
From A3	30.2545			289.0580
To A2	29.6475	(29.6502)	0.0027	
From NGB11	30.7981			270.2070
To A2	29.6475	(29. 6491)	0.0016	

Table D-2: Closure errors in levelling process of closed loop.

Points	Distance (m)	Elevation H.P.C	Adjusted elevation	Correction
A2-TP*1	110.7110	31.2491	31.2483	-0.0007
TP1-TP2	81.4040	30.8795	30.8790	-0.0005
TP2-A1	2.8090	30.8122	30.8121	-1.8517E-05
Sum	**194.924**			

Table D-3: Levelling procedure from BM A1 to A2.

Points	Distance (m)	Elevation (H.P.C)	Adjusted elevation	Correction
A2-TP1	46.3440	30.8269	30.8266	-0.0002
TP1-TP2	74.9190	29.5751	29.5748	-0.0003
TP2-TP3	95.7240	29.5377	29.5372	-0.0004
TP3-A3	72.0710	29.6183	29.6180	-0.0003
Sum	**289.0580**			

Table D-4: Levelling procedure from BM A2 to A3.

Points	Distance (m)	Elevation (H.P.C)	Adjusted elevation	Correction
A2-TP1	58.1220	31.3687	31.3685	-0.0002
TP1-TP2	55.4730	31.6485	31.6483	-0.0002
TP2-TP3	108.8120	31.4774	31.4771	-0.0003
TP3-NGB11	47.8000	31.3126	31.3125	-0.0001
Sum	**270.2070**			

Table D-5: Levelling procedure from BM A2 to NGB11.

*TP: Turning point.

The simple formula generally used to compute the allowable closure is:

E= $c\sqrt{k}$

E: allowable closure in mm.

C: Accuracy constant.

K: the distance levelling in km.

Where, C has the specific constants are;

- C = 4mm for first order $\pm 4\sqrt{k}\ \ mm$
- C = 8.4mm for second order $\pm 8.4\sqrt{k}\ \ mm$
- C = 12mm for third order $\pm 12\sqrt{k}\ \ mm$

Error in levelling procedure equals computed last elevation minus known last elevation; the correction for elevation of point will be; the total correction divided by sum of levelling distance, and multiplied by the distance of the point from beginning. The formula can be simplified as,

$$\frac{\Delta E}{\sum S} = \frac{Cn}{\sum_{i=0}^{i=n} Si}\ ;\ \text{ then } Cn = \frac{\Delta E}{\sum S} * \sum_{i=0}^{i=n} Si$$

Where,

Cn Correction for elevation of point and,

ΔE / $\sum S$: Total correction and total distance of levelling work respectively

$\sum_{i=0}^{i=n} Si$: Distance of the point from beginning.

Appendix E: Figures of traversing procedure before and after adjustment along the study areas.

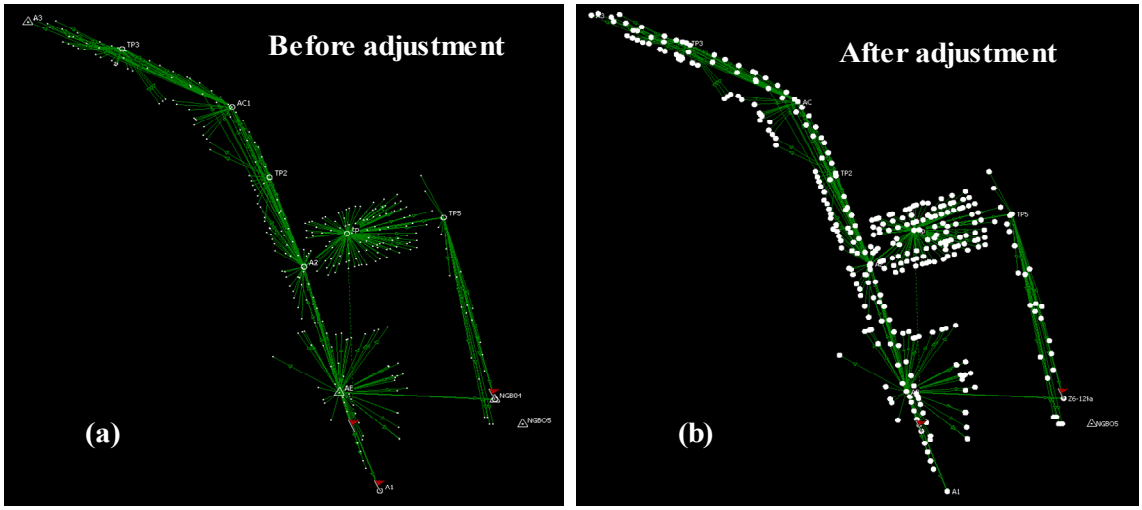

Figure E-1: Traverse field work procedure around study area-Jubilee campus: (a) before adjustment; (b) after adjustment.

Stat.	Direct.	Easting(m)	Northing(m)	Height(m)	ΔE(m)	ΔN(m)	Δh(m)
NGB 11	NGB12						
	AB	454776.052	339706.296	29.638	0.003	0.003	0.009
AB	NGB11	454893.272	339700.260	30.956	0.007	0.005	0.018
	A1	454806.509	339624.462	29.802	0.004	0.005	0.012
	A2	454749.295	339810.243	29.817	0.002	0.002	0.004
A2	AB						
	AC	454695.160	339942.559	29.738	0.002	0.003	0.010
	tp	454781.758	339837.899	30.747	0.002	0.002	0.005
AC	A2						
	A3	454541.280	340012.411	30.417	0.007	0.006	0.018
tp	A2						
	TP5	454854.726	339851.003	30.185	0.006	0.003	0.012
TP1	tp						
	NGB11	454893.287	339700.289	30.969	0.007	0.008	0.018
A2	AB						
	TP2	454723.343	339884.303	29.630	0.003	0.005	0.010
TP2	A2						
	AC	454695.134	339942.547	29.691	0.006	0.009	0.019
AC	TP2						
	TP3	454612.142	339989.986	29.767	0.005	0.006	0.017
TP3	AC						
	TP4	454572.561	339999.943	29.628	0.009	0.007	0.018
	A3	454541.280	340012.411	30.417	0.007	0.006	0.018
Stdv.(σ)					0.002	0.002	0.005
RMSE					0.005	0.005	0.013

Table E-1: The adjusted coordinates of the main traverse along the study area for the MLS data in 2009.

Appendix F: Figures of 3D surface analysis using TIN approach.

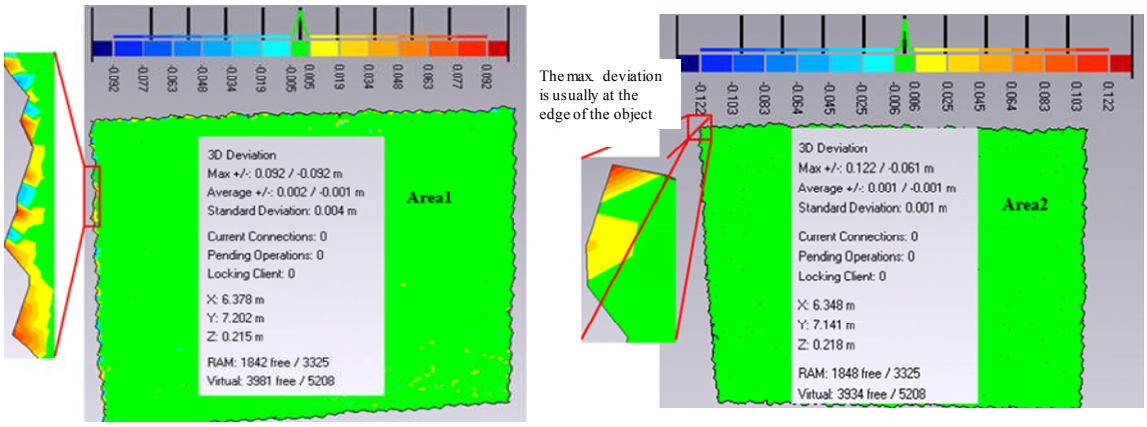

Figure F-1: 3D surface compare between two surfaces: Left: Area1 in pass1 and pass 2. Right: Area2 in pass1 and pass 2.

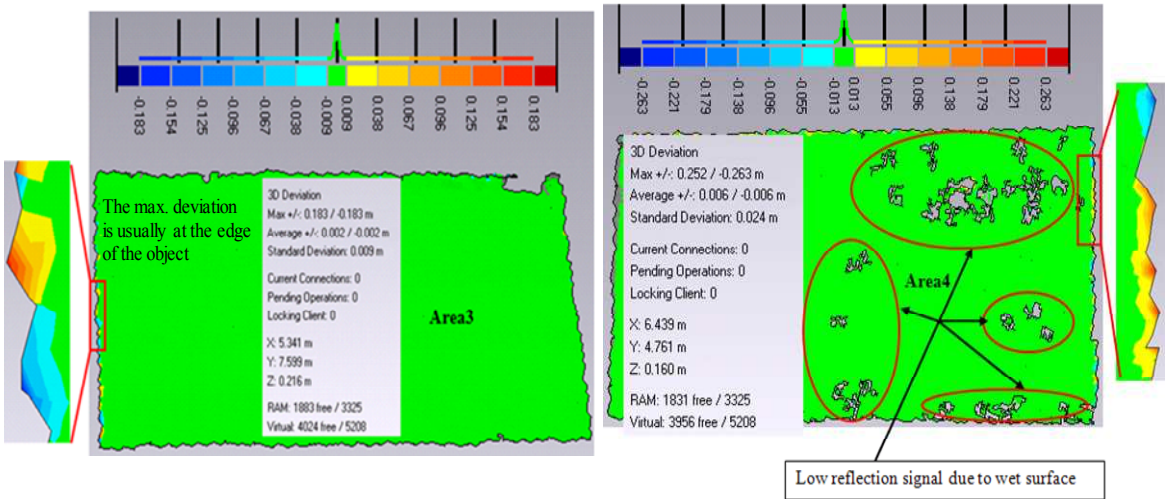

. Figure F-3: 3D surface compare between two surfaces. Left: Area 3 in pass1 and pass2. Right: Area 4 in pass1 and pass 2.

Appendix G: 3D surface analysis of different cases study

G1: Figures, Part1: Surface to surface compares.

1. MLS Block no. 55, the GPS quality position in this area is over 0.1m.

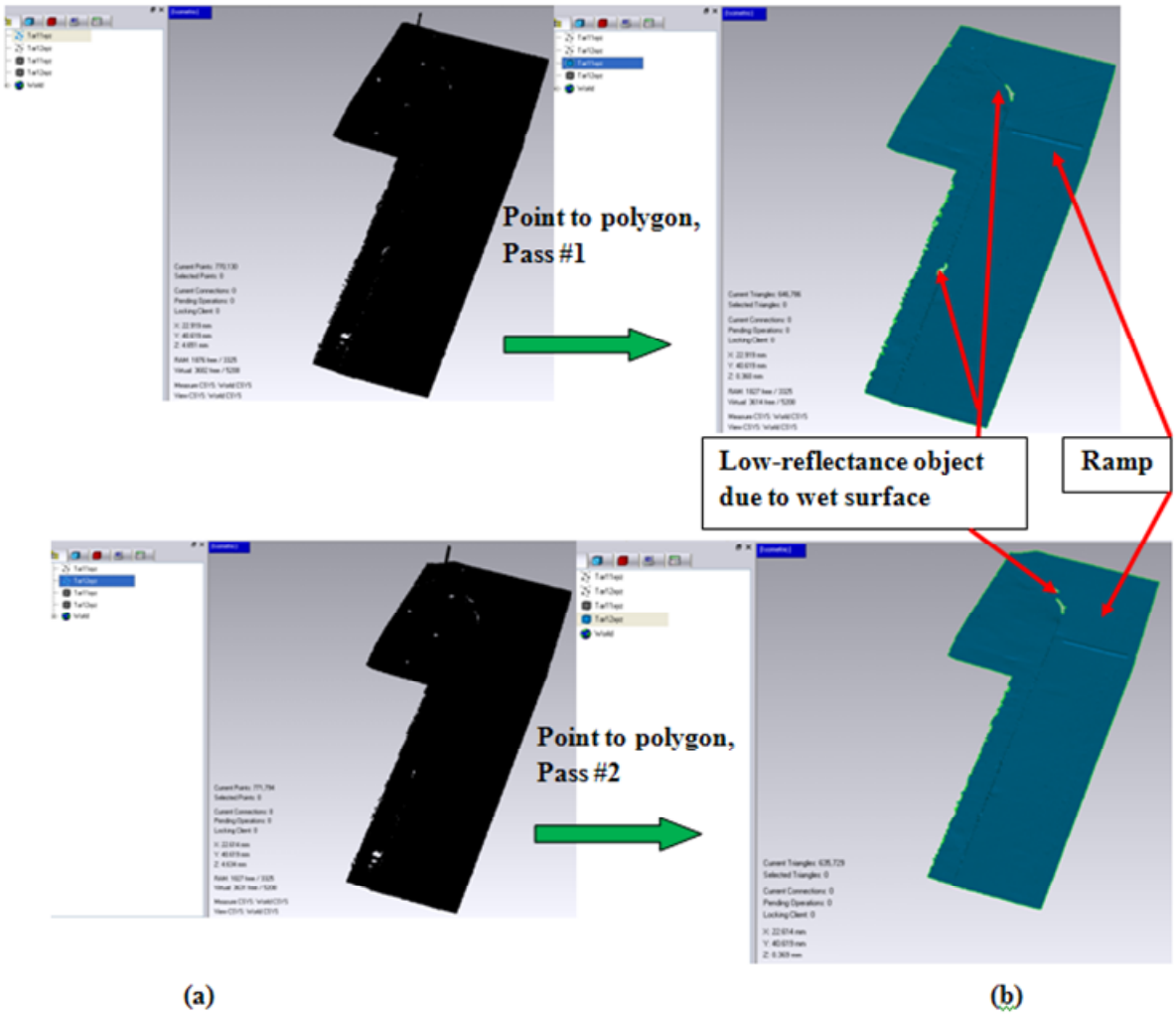

Figure G1-1: (a) Point cloud of a part of a road surface. Upper left: Point cloud of pass 1. Lower left: Point cloud of pass 2., (b) Represent TIN of a road surface of the pass1 and pass 2 respectively- Block55.

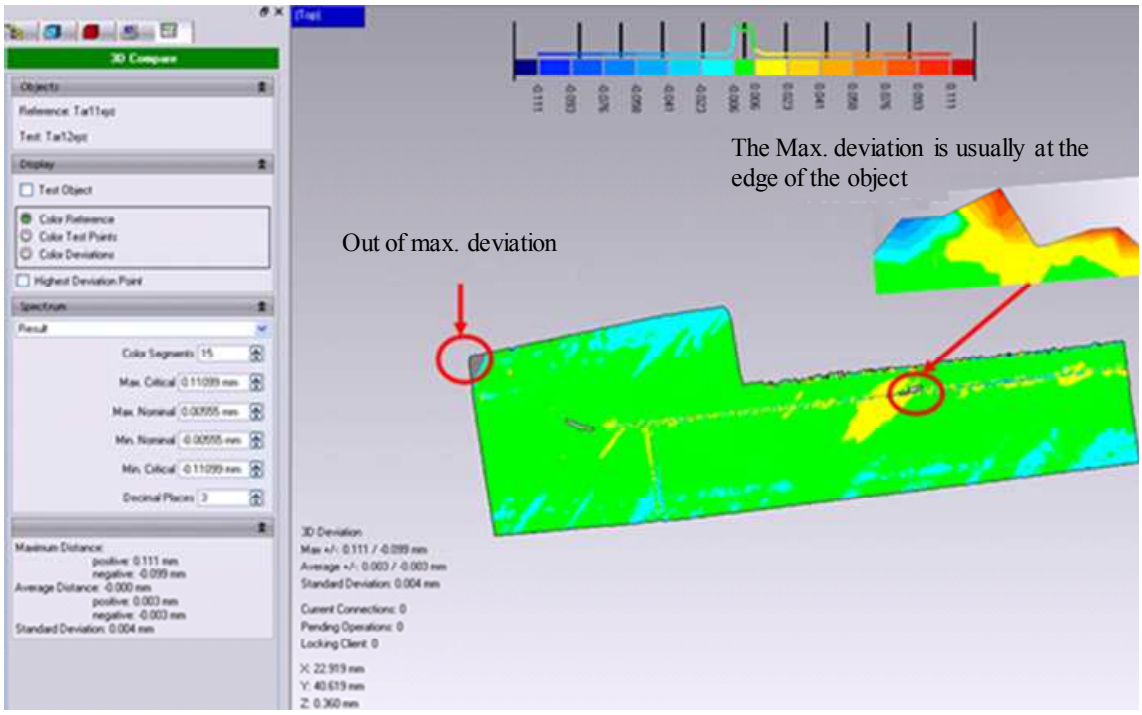

Figure G1-2: Show the result of 3D surface compare between two surfaces: one surface as a reference and the other as a test surface.

2. MLS Block no. 36, the GPS quality position in this area is 0.03 m.

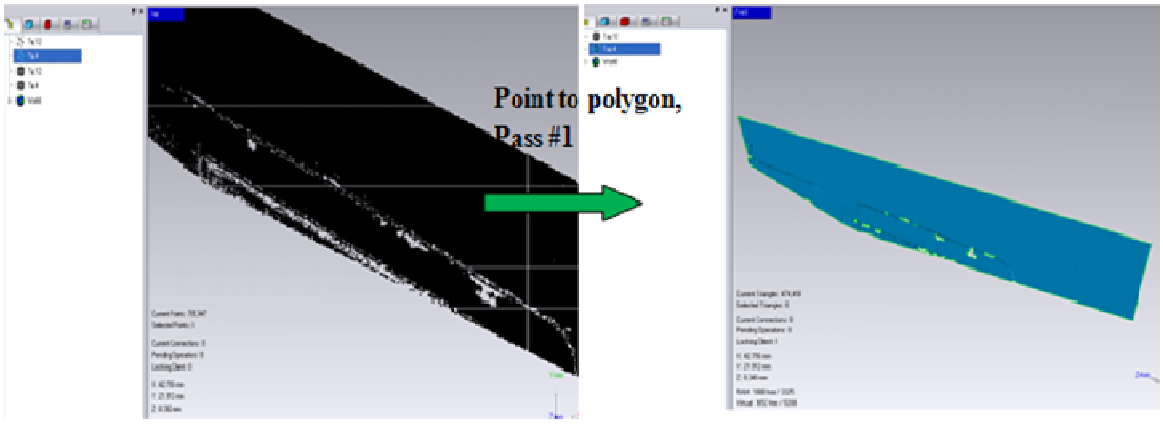

(a) (b)

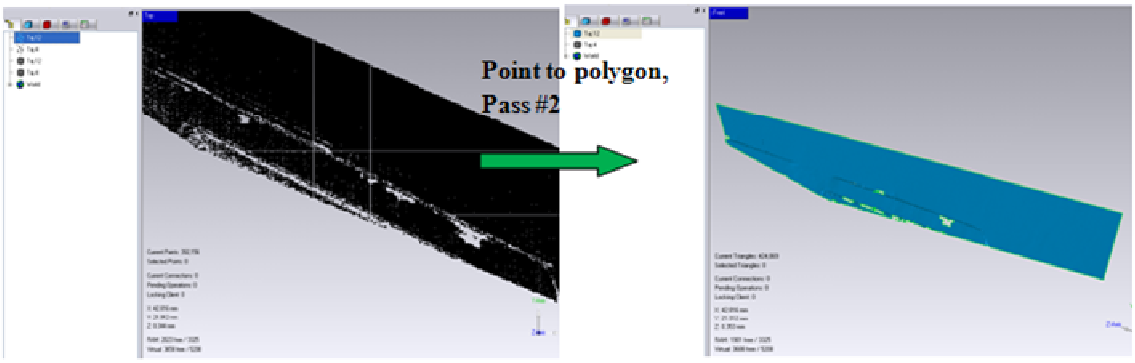

Figure G1-3: (a) Point cloud of a part of a road surface. Upper left: Point cloud of pass 1. Lower left: Point cloud of pass#2., (b) Represent TIN of a road surface of the pass 1 and pass 2 respectively- Block36.

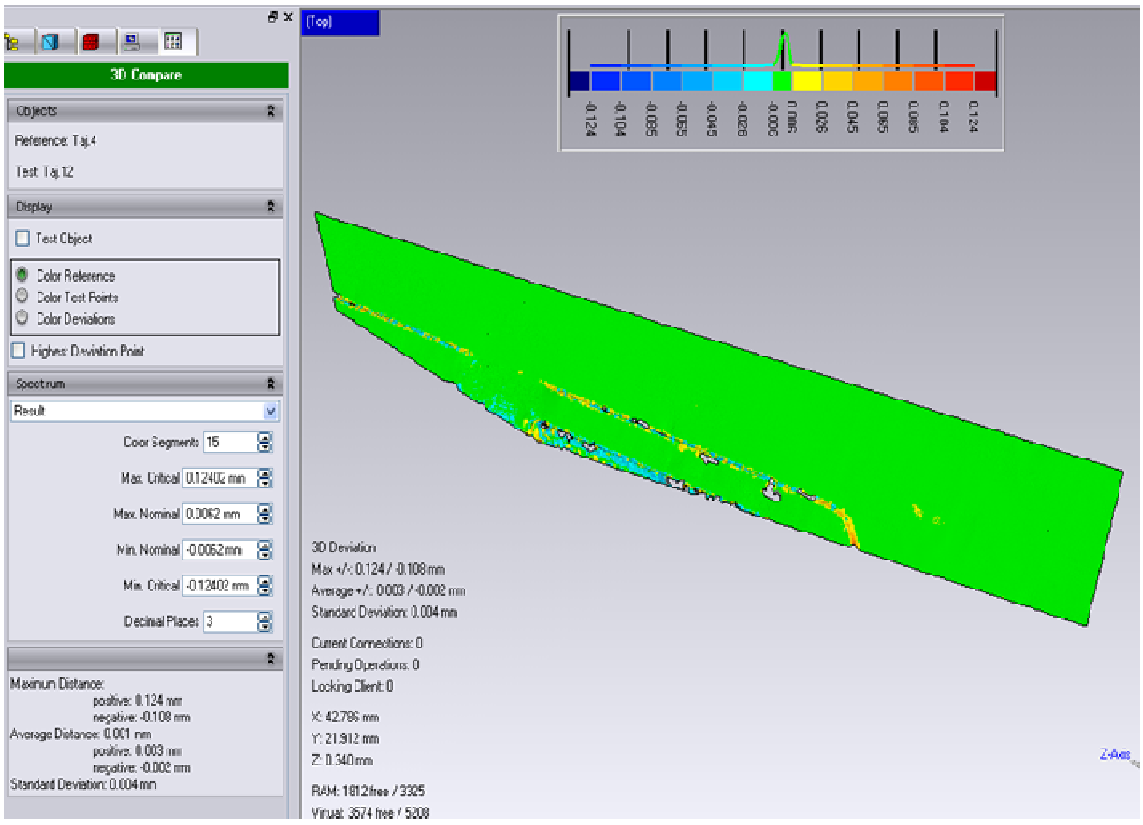

Figure G1-4: Show the result of 3D surface compare between two surfaces: one surface as a reference and the other as a test surface.

3. MLS Block no. 45, the GPS quality position (enh) in this area is 0.04 to 0.07m.

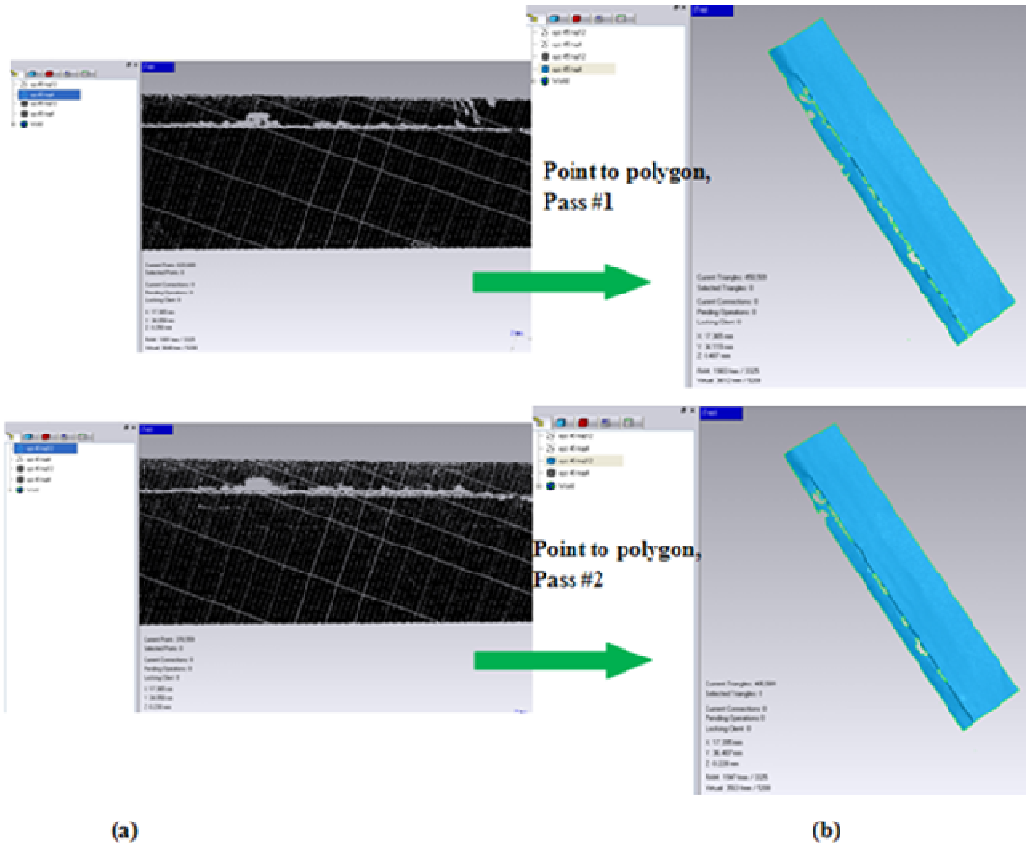

Figure G1-5: (a) Point cloud of a part of a road surface. Upper left: Point cloud of pass 1. Lower left: Point cloud of pass 2., (b) Represent TIN of a road surface of the pass1 and pass 2 respectively- Block45.

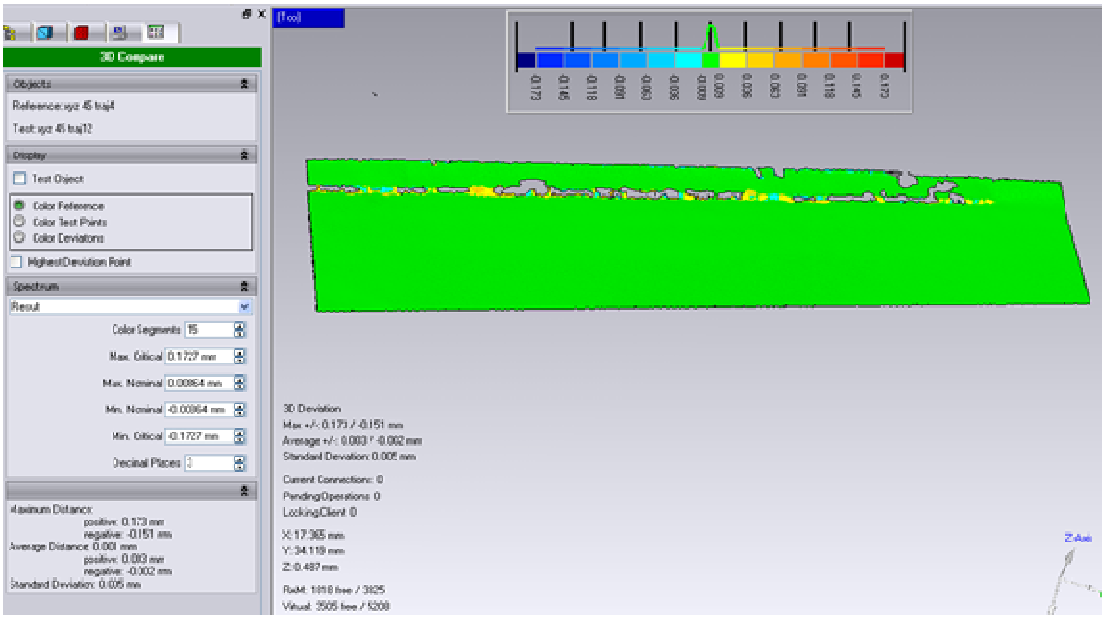

Figure G1-6: Show the result of 3D surface compare between two surfaces: one surface as a reference and the other as a test surface.

G2: Figures of geometric plane for building facade.

- Block 46, quality of GPS position in this area is 0.04-0.07 m.

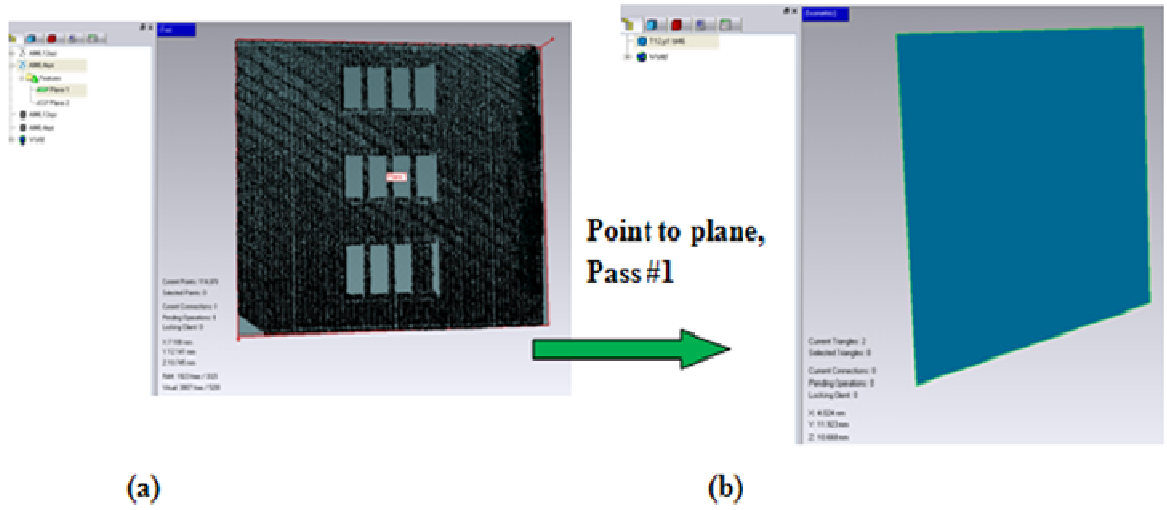

Figure G2-1: (a) Point cloud of a part of facade of the pass 1 (b) Plane created of the same facade.

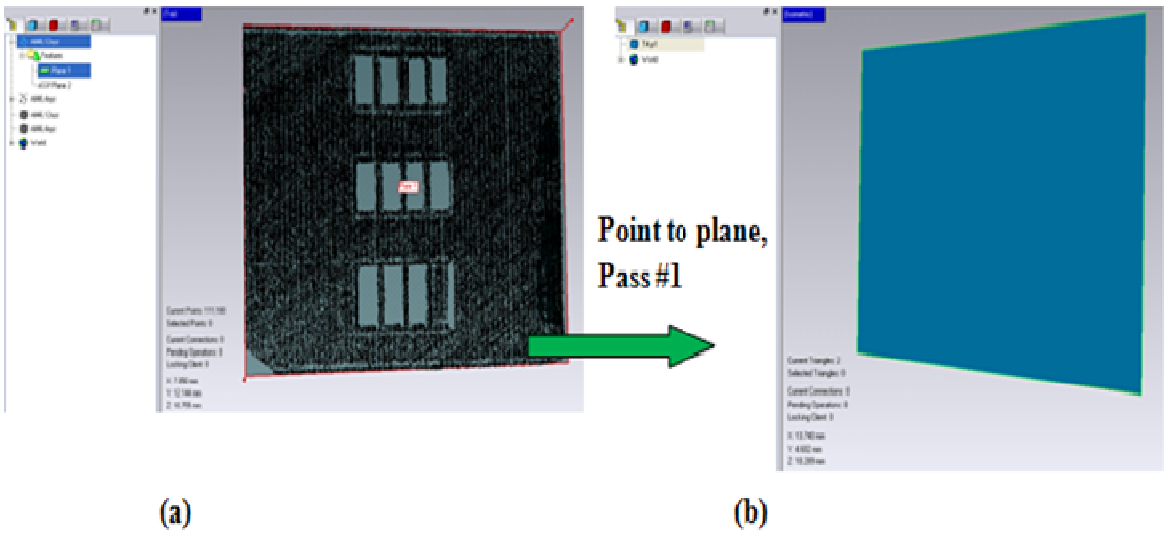

Figure G2-2: (a) Point cloud of a part of facade of the pass 2; (b) Plane created of the same facade.

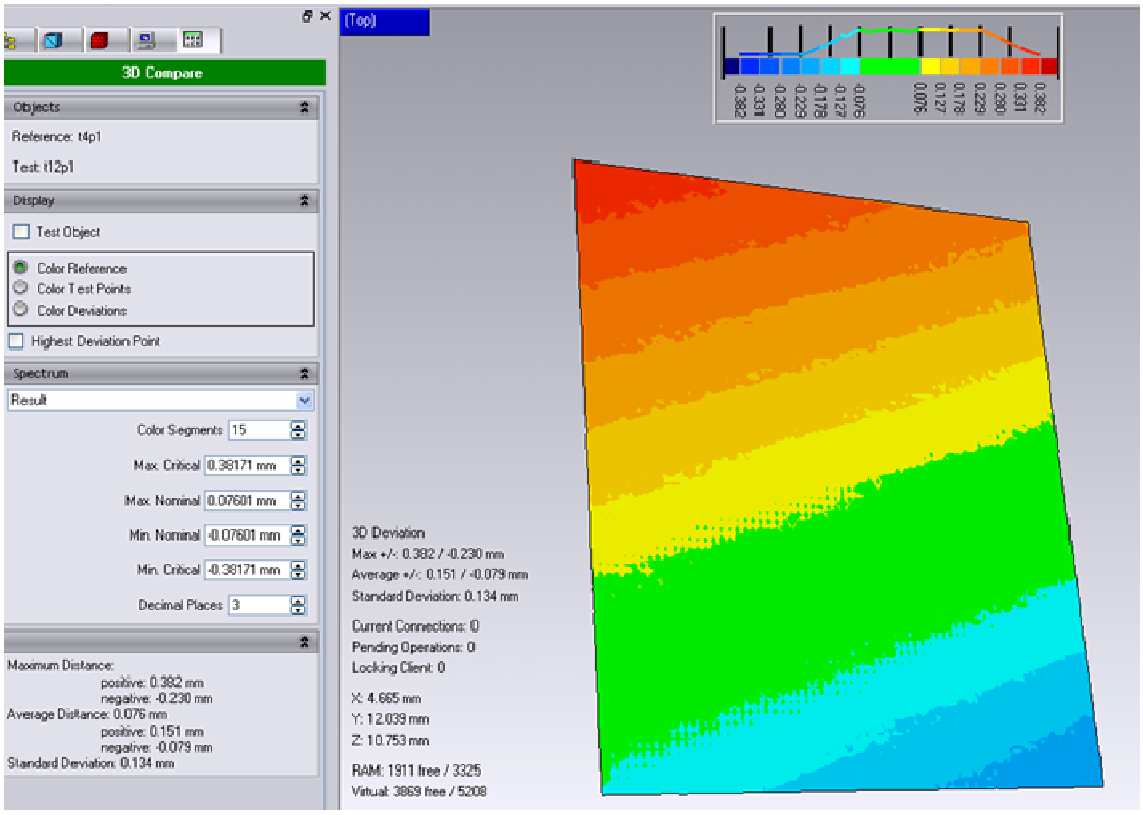

Figure G2-3: Show the result of 3D deviation between the two planes of building facade: Plane 1 as a reference and plane 2 as a test plane.

- **<u>Block 49, the GPS quality position in this area is 0.04m.</u>**

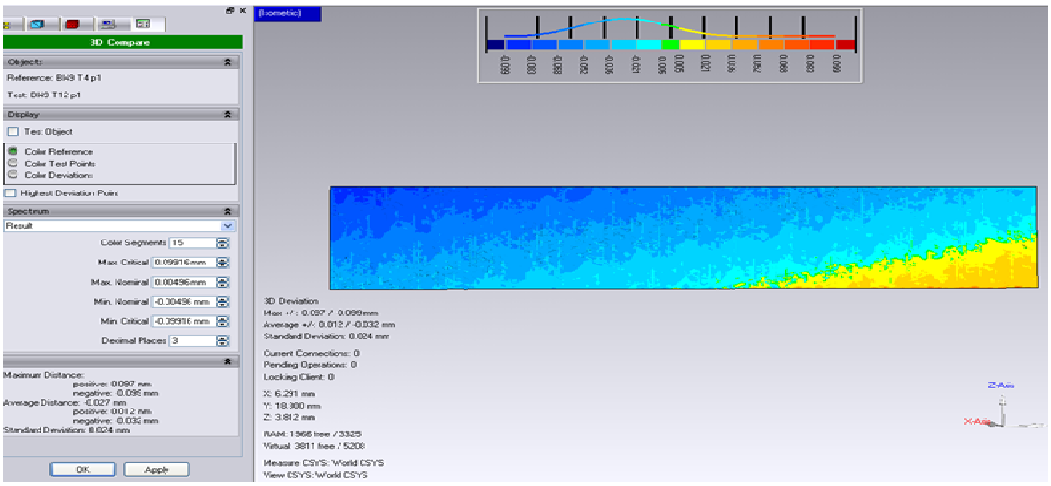

Figure G2-4: Show the result of 3D deviation between the two planes of building facade: Plane1 as a reference and plane 2 as a test plane.

- **Block 57, the GPS quality in this area is 0.07- 0.09 m.**

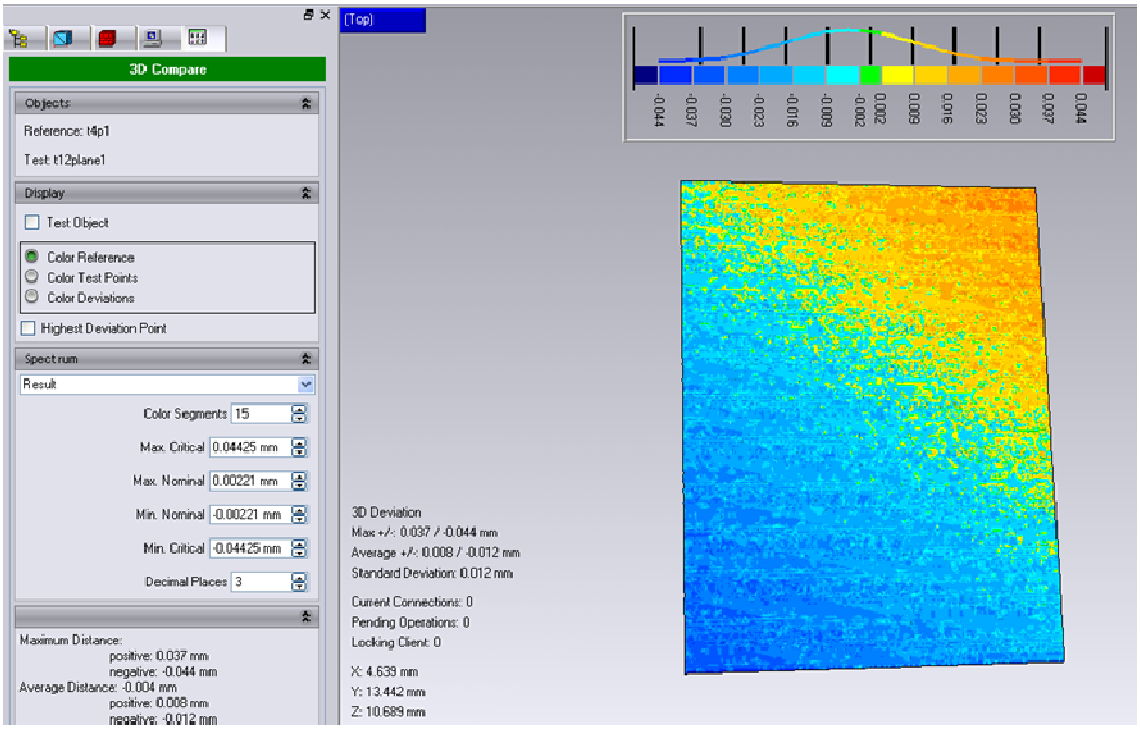

Figure G2-5: Show the result of 3D deviation between the two planes of building facade: Plane 1 as a reference and plane 2 as a test plane.

G3: Figures of plane intersection of building façade.

- **Block no.46, a part of building facade.**

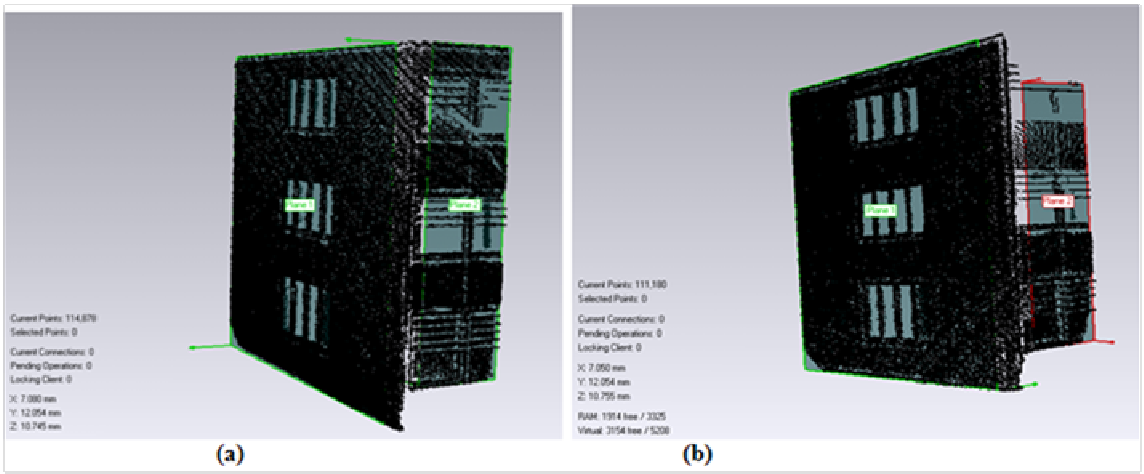

Figure G3-1: (a) show the creation of planes from the point cloud1 (front and side) of building façade; (b) shows the same planes on the point cloud 2- Block no. 46

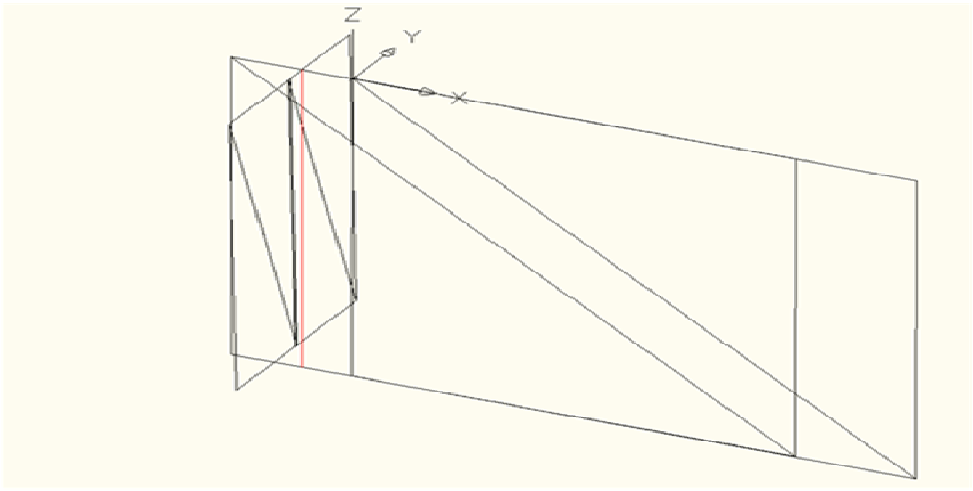

Figure G3-2: Show the intersection planes from the point cloud1 (front and side) of building facade of block no. 46 using AutoCAD software.

- **Block (51, 57) intersection planes.**

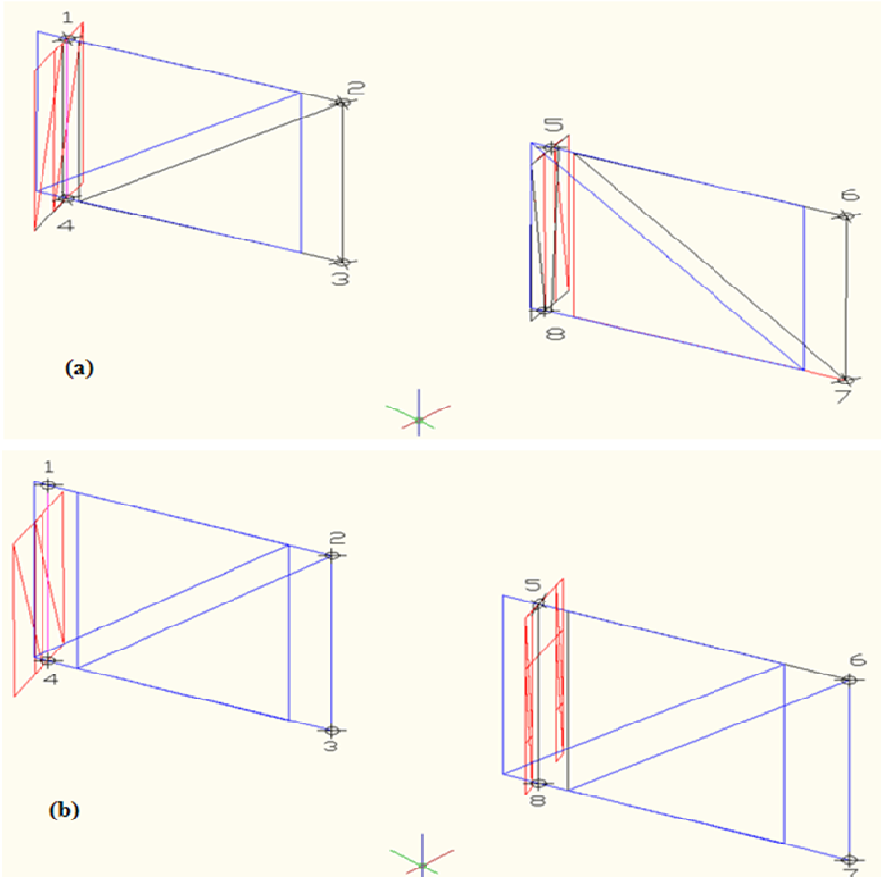

Figure G3-3: (a) intersection planes of point cloud 1; (b) Intersection planes of point cloud 2 of the same area of block 51, 57 respectively.

Appendix H: Figures of theoretical IA contribution to the signal deterioration for each designed target.

1. Pyramid 4 faces:

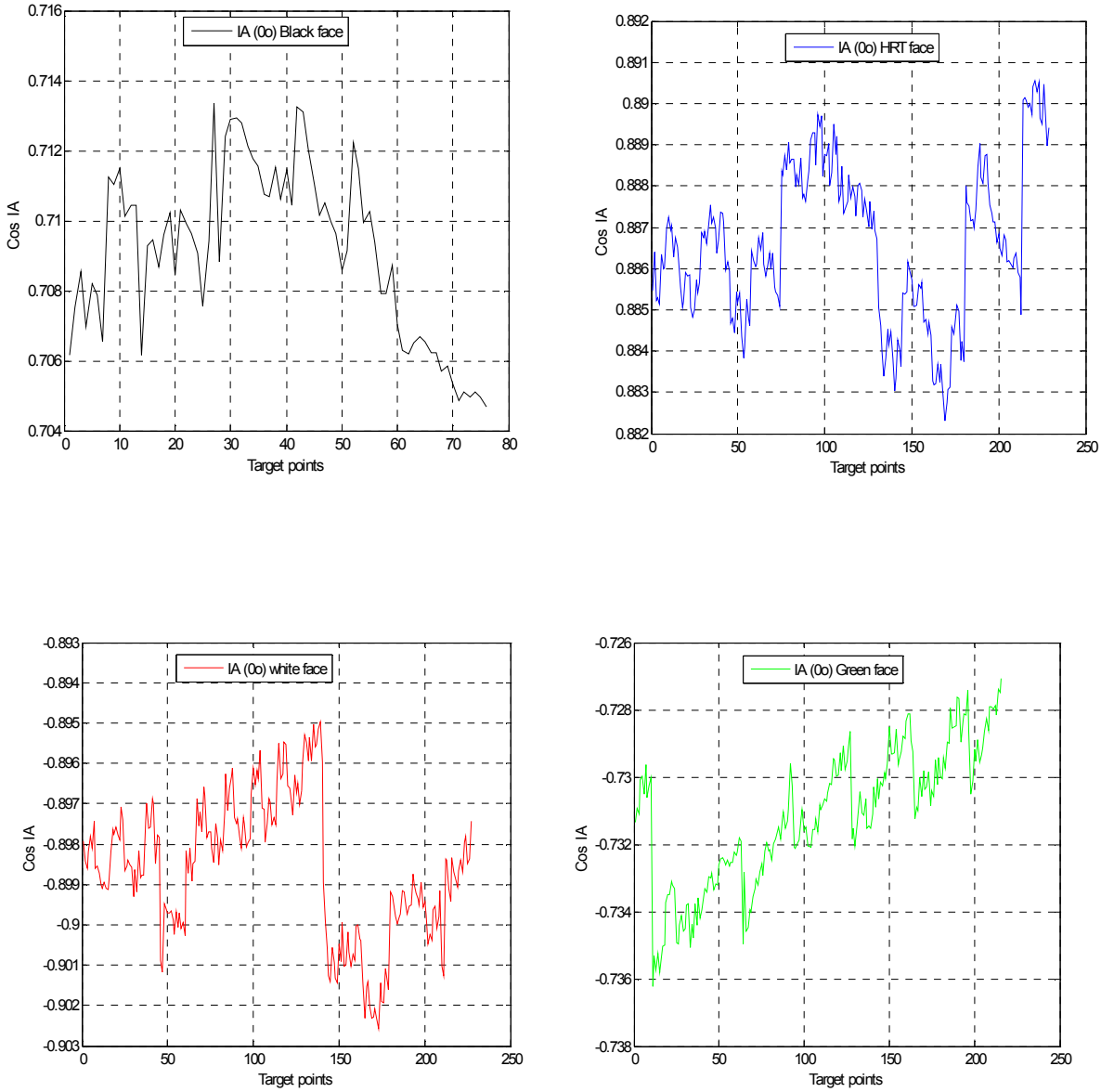

Figure H-1: Model of IA for each point of Pyramid faces.

2. Sphere- Model of IA

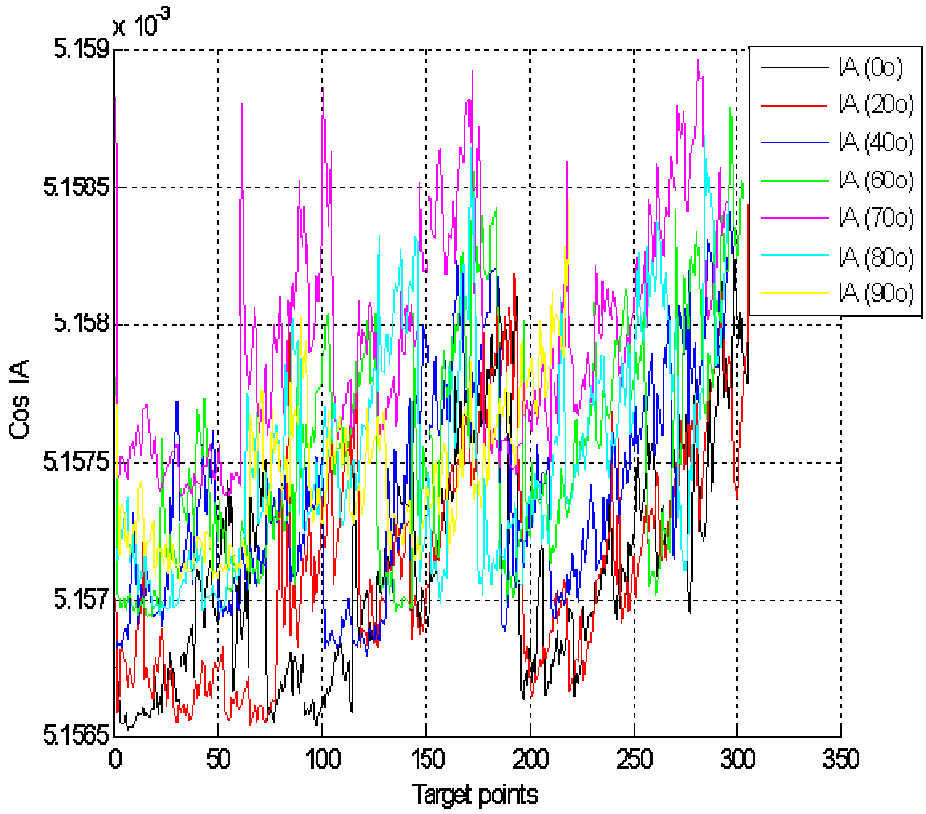

Figure H-2: Model of IA for each scan points of Sphere target.

3. Cone-Model of IA

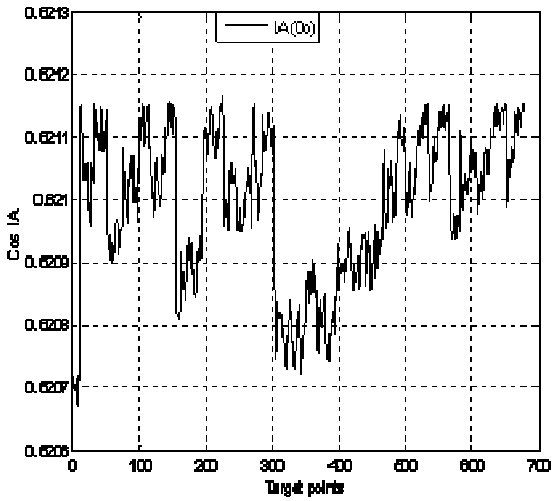

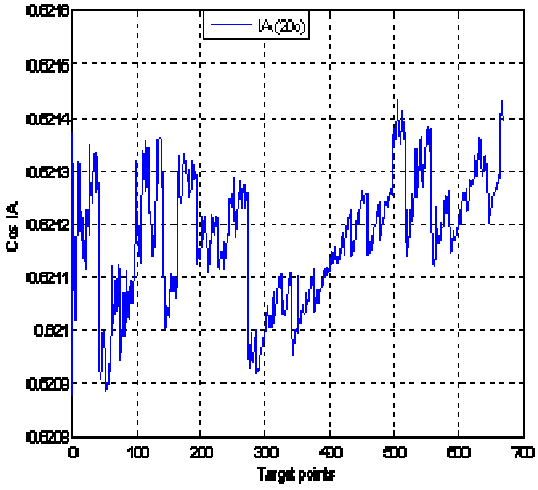

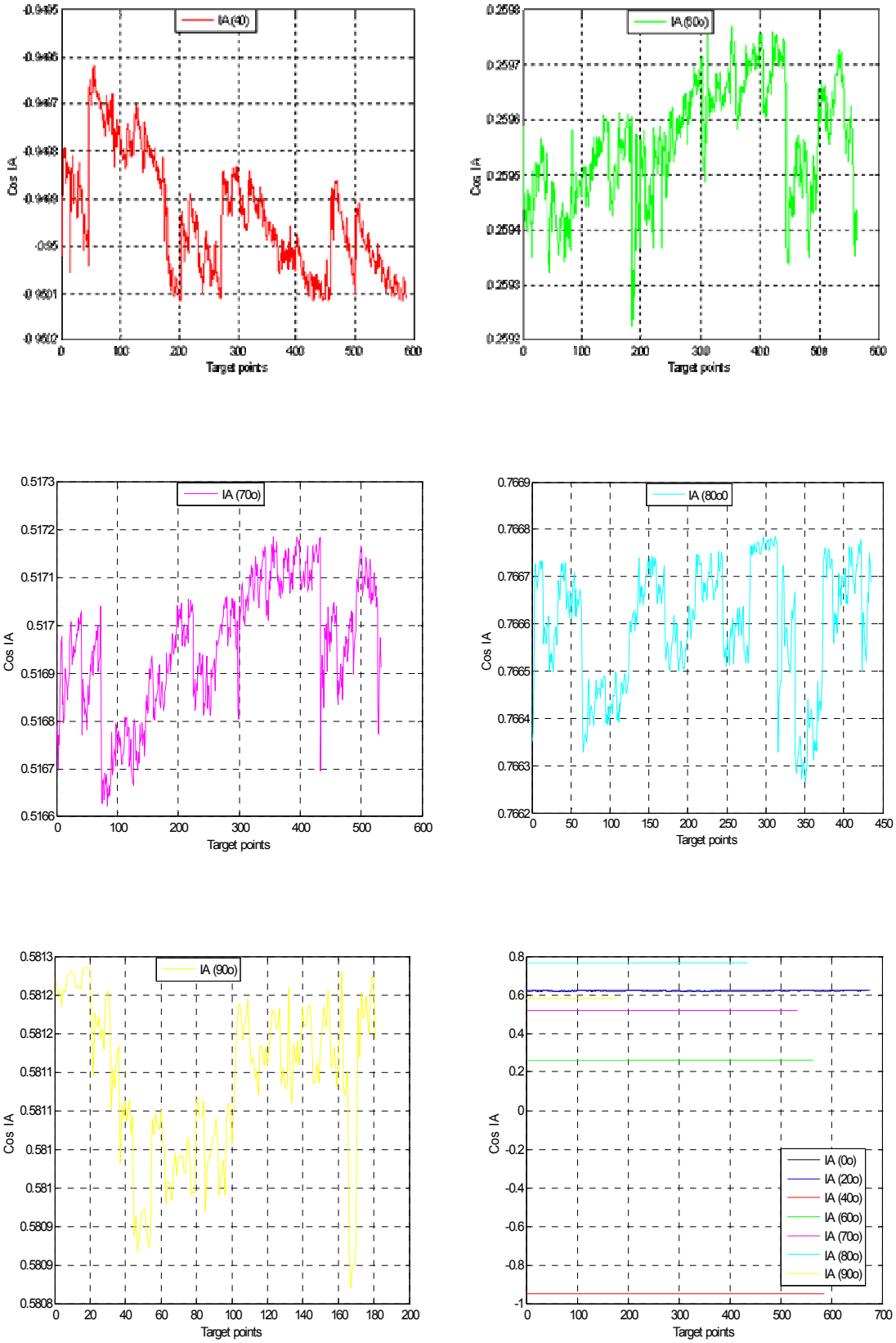

Figure H-3: Model of IA for each individual scan points of Cone target.

4. Leica flat target-Model of IA

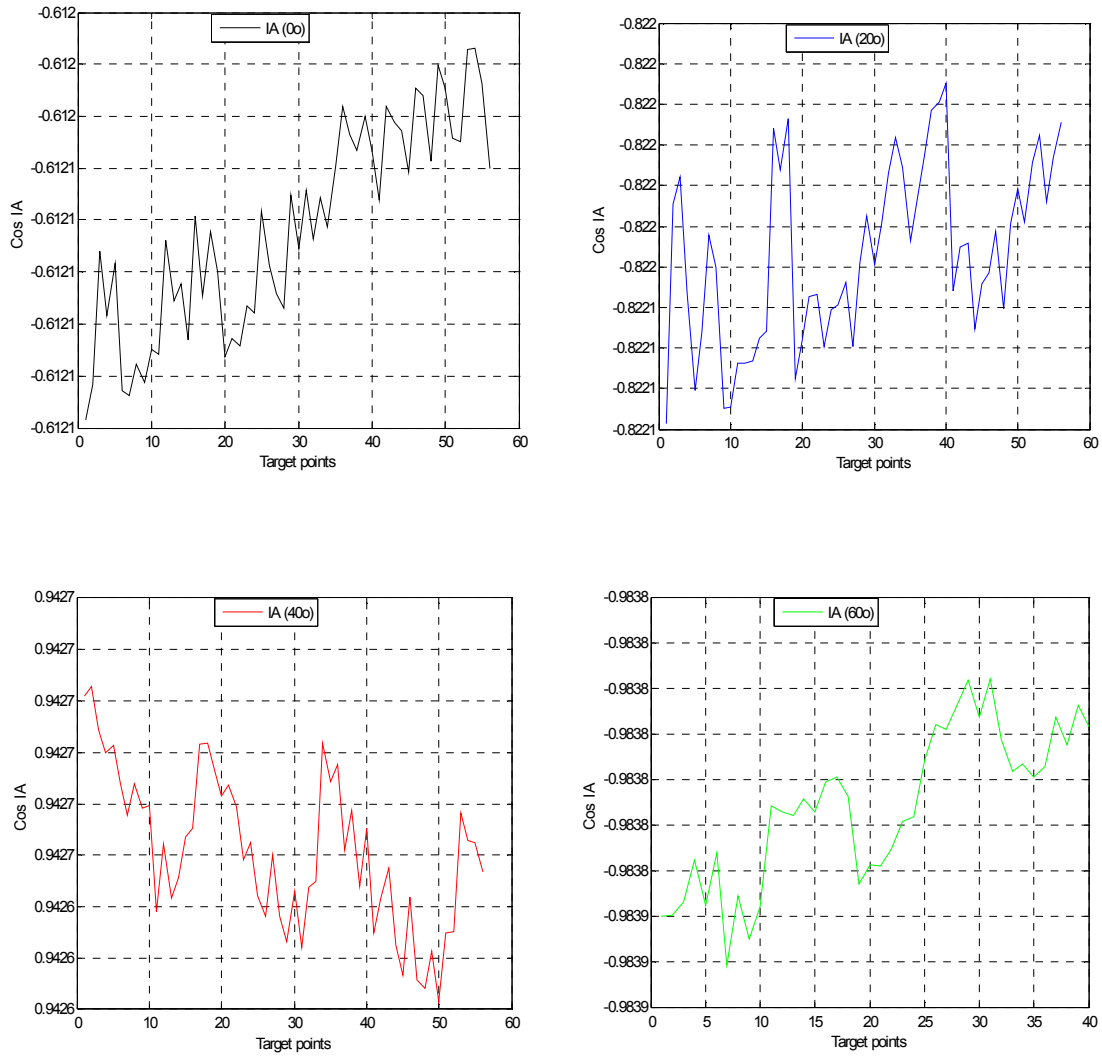

Figures H-4: Model of IA for each scan points of Leica flat target.

Note: The reader can refer to the script programs were written by the author using Matlab functions for each target. The files can be seen in the attached CD in this order as follows:

1. PyramidM.m. This program designed for the model of IA for pyramid target.
2. ConeM.m. This program designed for the model of IA for cone target.
3. SphereM.m. This program designed for the model of IA for sphere target.
4. LeicaM.m. This program designed for the model of IA for Leica flat target.

The mathematical models for computing IA of each scan points as follows

From the definition of the scalar vectors, the IA was computed for each scan points

$\vec{P}.\vec{N} = |\vec{P}|.|\vec{N}|\ cos\beta$,

Where $\vec{P}$ = Laser beam vector (xi, yi, zi); and $\vec{N}$= Normal vector (a, b, c) obtained from plane equation ax+by+cz=d. Thus, $\vec{P}.\vec{N} = d$

While the $|\vec{P}|$ = Magnitude of $\sqrt{\Delta x^2 + \Delta y^2 + \Delta z^2}$, and $|\vec{N}| = \sqrt{a^2 + b^2 + c^2}$

$\sqrt{a^2 + b^2 + c^2}$ Must be =1 as a unit length vector, and $\sqrt{\Delta x^2 + \Delta y^2 + \Delta z^2}$ is the mean range (R) from the scanner to the target surface; $R_{mean} = \sqrt{\frac{\sum(\Delta x_i^2 + \Delta y_i^2 + \Delta z_i^2)}{n}}$

Therefore, the cosine of IA can be computed following the equation below

$cos\beta = \frac{\vec{P}.\vec{N}}{|\vec{P}|.|\vec{N}|}$, this equation was applied to each scan point of the target used as follows.

$Cos\ IA = \frac{d}{\sqrt{\Delta x^2+\Delta y^2+\Delta z^2}.1}$. ; For each face of the pyramid and Leica flat target

$Cos\ IA = \frac{d}{\sqrt{\Delta x^2+\Delta y^2+\Delta z^2}.1}$. ; For cone target- each point has one normal vector except where, IA=90^o

$Cos\ IA = \frac{d}{\sqrt{\Delta x^2+\Delta y^2+\Delta z^2}.1}$. ; For sphere target, it has one normal vector from the radial direction to the centre.

Appendix I: Range effect.

I1: The range effect vs point per target at normal IA.

Using Faro focus 3D laser scanner.

Resolution and quality	Position	Range (m)	Pts/target	Min.pts require	Redundancy	Notes: The effect of black colour
1/8-4x (0.012 x 0.012) Sq.m @10 m) **Sphere:** size 0.200 m dia.	SCP1	10.000	149	4	145	
	SCP2	20.000	19	4	15	
	SCP3	30.000	9	4	5	
	SCP4	40.000	Fail			
Cone: size Sh*[1]=0.300 m α*[2] =60^{o}	SCP1	10.000	300	6	294	90 Bc*[3]
	SCP2	20.000	93	6	87	8 Bc
	SCP3	30.000	42	6	36	2 Bc
	SCP4	40.000	27	6	21	0 Bc
	SCP5	50.000	Fail		Fail.	
Pyramid (8 faces): size 0.300 m dia.	SCP1	10.000	447	9	438	28 Bc
	SCP2	20.000	57	9	48	4 **Bc**
	SCP3	40.000	46	9	37	0 Bc
	SCP4	50.000	Fail		Fail.	

Table I1-1: Range vs point per target, and redundancy using Faro focus^{3D} –TLS.

*[1]sh: slant height of the cone; *[2]α: the cone angle between the intersection of the two slant lines; *[3] Bc is the number of points received from black surface.

Using Leica HDS3000 laser scanner

Resolution	Position	Range (m)	Pts/ target	Min.pts require	Redundancy	Notes: The effect of black colour
(0.010 x 0.010) Sq. m **Sphere:** size 0.200 m dia.	SCP1	10.000	332	4	328	
	SCP2	20.000	82	4	78	
	SCP3	30.000	38	4	34	
	SCP4	40.000	18	4	14	
	SCP5	50.000	14	4	10	
	SCP6	60.000	7	4	3	
	SCP7	70.000	5	4	1	
	SCP8	80.000	4	4	0	
	SCP9	90.000	3	Fail		
	SCP10	100.000	2	Fail		
Cone : size 0.300 dia Sh*[2]=0.300 m α*[3]=60°.0	SCP1	10.000	583	6	577	132 Bc[*1]
	SCP2	20.000	153	6	147	47 Bc
	SCP3	30.000	82	6	76	8 Bc
	SCP4	40.000	32	6	26	2 Bc
	SCP5	50.000	21	6	15	1 Bc
	SCP6	60.000	18	6	12	1 Bc
	SCP7	70.000	15	6	7	0 Bc
	SCP8	80.000	10	6	4	0 Bc
	SCP9	90.000	8	6	2	0 Bc
	SCP10	100.000	6	6	0	0 Bc
Pyramid (8 faces): size a[*4]=0.1200 m Sh=0.1650 m	SCP1	10.000	588	9	579	.72Bc
	SCP2	20.000	142	9	133	15Bc
	SCP3	30.000	84	9	75	8Bc
	SCP4	40.000	42	9	33	4 BC
	SCP5	50.000	32	9	23	0 Bc
	SCP6	60.000	20	9	11	0 Bc
	SCP7	70.000	10	9	Fail	
2D Leica: size = 0.200 m dia	SCP1	10.000	76	Mean		Auto
	SCP2	20.000	38	Mean		Auto
	SCP3	30.000	24	Mean		Auto
	SCP4	40.000	16	Mean		Auto
	SCP5	50.000	12	Mean		Auto
	SCP6	60.000	6	Mean		Auto
	SCP7	70.000	4	Mean	Fail	
	SCP8	80.000	4		Fail	
	SCP9	90.000	3		Fail	
	SCP10	100.000	2		Fail	Beyond specific.

Table I1-2: Range vs point per target, and redundancy using Leica HDS3000-TLS.

*1: Bc refers to black colour; *2: Sh refers to slant height of the cone sides; *3: α refers to the angle between two slant lines of the cone target; *4: (a) and (sh) refer to the base and slant of each face of the pyramid respectively.

I2: Accuracy and precision for sphere; cone and pyramid.

1. Sphere size (100 mm Radius) –Using Faro 3D laser scanner

Target	Range (m)	σpar. (mm)	Accuracy (mm)	3D Laser scanner	Method for computation
SCP1	10.00	0.70 / 1.60	2.30 / -3.90	Faro focus	AD/Gauss Newton (GN)
SCP2	20.00	3.6 0/ 4.10	16.1/ 23.80		
SCP3	30.00	5.8 0/ 6.90	17.70 / 31.30		
SCP4	40.00	Fail	Fail		
SCP1	10.00	0.44	-3.68	Faro focus	LM
SCP2	20.00	8.10	-30.40		
SCP3	30.00	62.0	-61.40		
SCP4	40.00	Fail	Fail		

Table I2-1 Accuracy and precision of the sphere centre using different methods.

2. Sphere size (100 mm Radius) using HDS3000 3D laser scanner

Target	Range (m)	σpar. (mm)	Accuracy (mm)	3D Laser scanner	Method for computation
SphereP1	10.00	1.6 0 / 2.80	-1.14 / 4.40	HDS3000	AD / NG-auto detect.
SCP2	20.00	2.80 / 3.00	6.90 / 6.20		AD / NG-auto detect.
SCP3	30.00	2.50 / 3.20	8.10 / 7.20		AD / NG-auto detect.
SCP4	40.00	2.7 0 / 3.60	9.70/ 9.10		AD / NG-auto detect.
SCP5	50.00	3.40 /4.10	13.30 / 11..60		AD / NG-auto detect.
SCP6	60.00	3.80 /4.40	17.30 / 18.50		AD / NG-Manual
SCP7	70.00	0.00 / 0.00	-35.9 0/ 41.30		AD / NG-Manual
SCP8	80.00	0.00 / 0.00	-35.90 / 41.30		AD / NG-Manual
SCP9	90.00	Fail in calculation m>n			
Sphere P1	10.00	0.54	-3.70	HDS3000	LM-Auto
SCP2	20.00	1.50	5.32		LM-Auto
SCP3	30.00	1.82	6.94		LM-Auto
SCP4	40.00	2.42	8.56		LM-Auto
SCP5	50.00	25.40	92.90		LM-Auto
SCP6	60.00	23.25	16.78		LM-Manual
SCP7	70.00	64.33	-35.70		LM-Manual
SCP8	80.00	64.33	-35.70		LM-Manual
SCP9	90.00	Fail in calculation m>n			

Table I2-2: Accuracy and precision of the sphere centre using different methods.

3. Cone size (150.00 mm Radius and sh = 2Radius).

Target	Range (m)	σpar. (mm)			Accuracy (mm)	3D Laser scanner	Method
		σapex (mm)	σNormal (mm)	σα (mm)			
Cone	10.00	1.30	3.80	2.10	2.20	**Faro focus^{3D}**	LM-Auto.
	20.00	6.90	22.60	11.20	7.80		LM-Auto.
	30.00	16.20	53.80	27.60	18.10		LM-Auto.
	40.00	49.10	168.0	96.30	35.20		LM-Auto.
	50.00	Fail					LM-Auto.
Cone	10.00	0.50	2.10	1.00	2.63	**HDS 3000**	LM-Auto.
	20.00	1.60	5.40	2.70	5.26		LM-Auto.
	30.00	2.12	9.50	6.50	7.90		LM-Auto.
	40.00	2.80	19.20	8.60	9.10		LM-Auto.
	50.00	6.40	17.00	9.10	9.45		LM-Auto.
	60.00	6.80	19.90	10.00	11.34		LM-Auto.
	70.00	8.10	21.50	10.90	16.60		LM-Auto.
	80.00	10.90	22.30	11.15	20.70		LM-manual
	90.00	22.08	27.50	13.7	23.40		LM-manual
	100.00	Fail in calculation m>n					

Table I2-3: Accuracy and precision of the apex of the cone target using LM method.

4. Pyramid equilateral 8 faces size of each one (b =120.00 mm, sh =16.50 mm).

Target	Range (m)	σapex	Accuracy of the apex	3D Laser scanner	Method
Pyramid 8 faces	10.00	9.00	8.00	**Faro Focus^{3D}**	LM +Plane Int.
	20.00	12.00	13.00		LM +Plane Int.
	40.00	16.00	15.00		LM +Plane Int., manual
	50.00	.....	Fail	**Faro Focus^{3D}**	
	10.00	1.60	8.11		Orthogonal dist.fit
	20.00	4.30	9.20		Orthogonal dist.fit
	40.00	11.20	14.80		Orthogonal dist.fit
Pyramid 8 faces	10.00	4.10	7.92	**HDS 3000**	LM +Plane Int.
	20.00	6.30	9.80		LM +Plane Int.
	30.00	8.65	10.60		LM +Plane Int.
	40.00	10.60	14.80		LM +Plane Int., manual
	50.00	It cannot be recognized as a target			
Pyramid 8 faces	10.00	1.37	7.21	**HDS 3000**	Orthogonal dist. Py.,fit
	20.00	3.83	8.21		Orthogonal dist. Py.,fit
	40.00	10.89	14.40		Orthogonal dist. Py.,fit
	50.00	Fail			

Table I2-4: Accuracy and precision of the apex of the pyramid target using different methods.

I3: Figures represent the appearance of target in the laser point cloud.

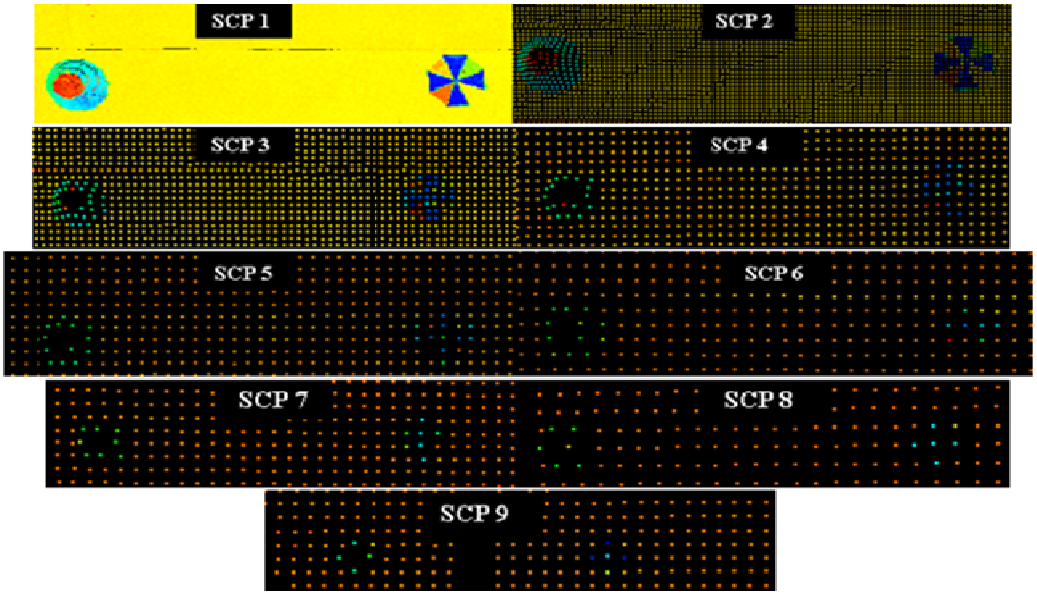

Figure I3-1: Range vs point per target in nine positions in step of 10 m.

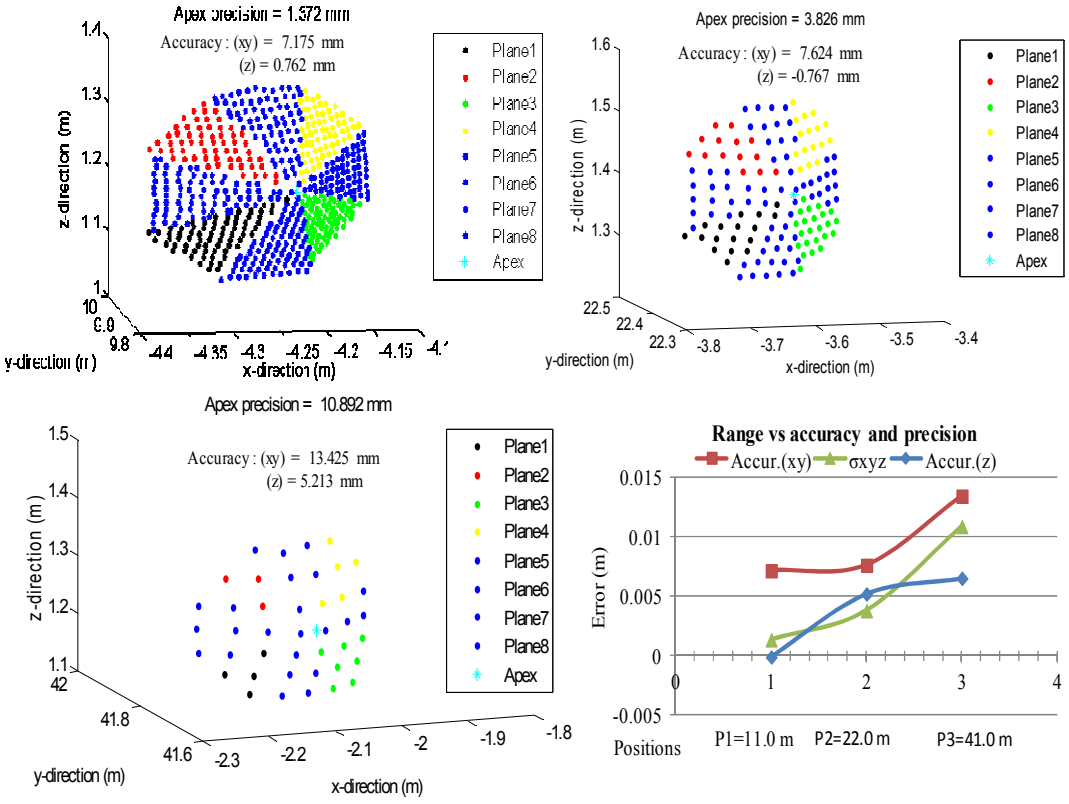

Figure I3-2: Range vs accuracy and precision of the pyramid 8 faces. Left: Pos.1, at range 10.0 m. Right: Pos.2 at range 20.0 m. Bottom left: Pos.3 at range 40.0m using orthogonal distance pyramid fit algorithm. HDS 3000 laser scanner used. Bottom right: Range effect vs accuracy and precision of the apex at three positions (10, 20, 40) m respectively.

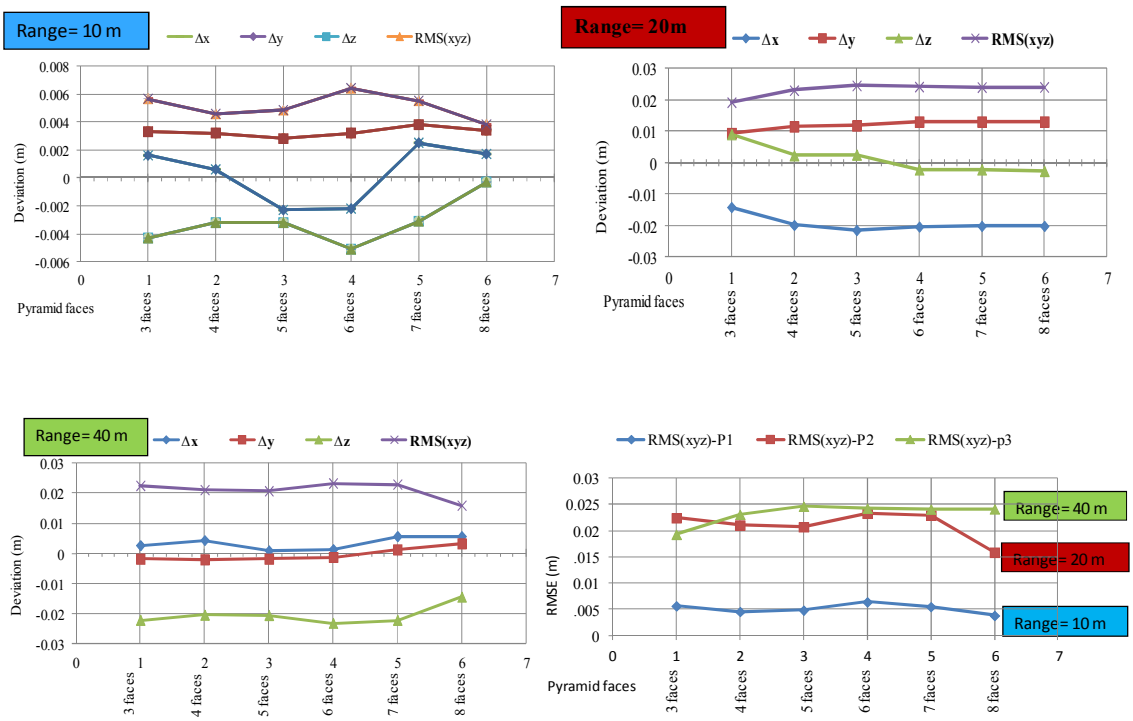

Figure I3-4: Rang effects vs accuracy of the apex from 3 to 8 faces at different ranges.

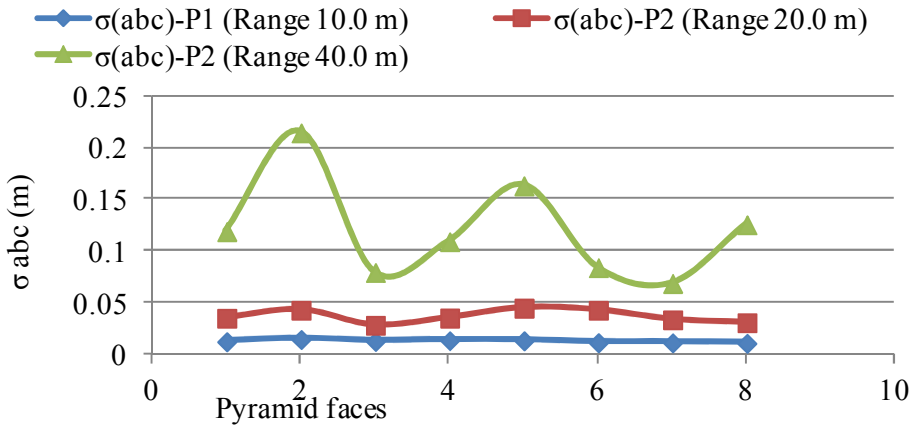

Figure I3-5: Pyramid faces vs precision of fitting at different ranges.

I4: Sphere targets detection and computations between two methods.

An example of sphere targets using, Cyclone software and average determination (AD) algorithm. The AD was programmed by the author using Matlab functions and combined with the detection part (see chapter 6.). The Cyclone software was used only for computation sphere parameters.

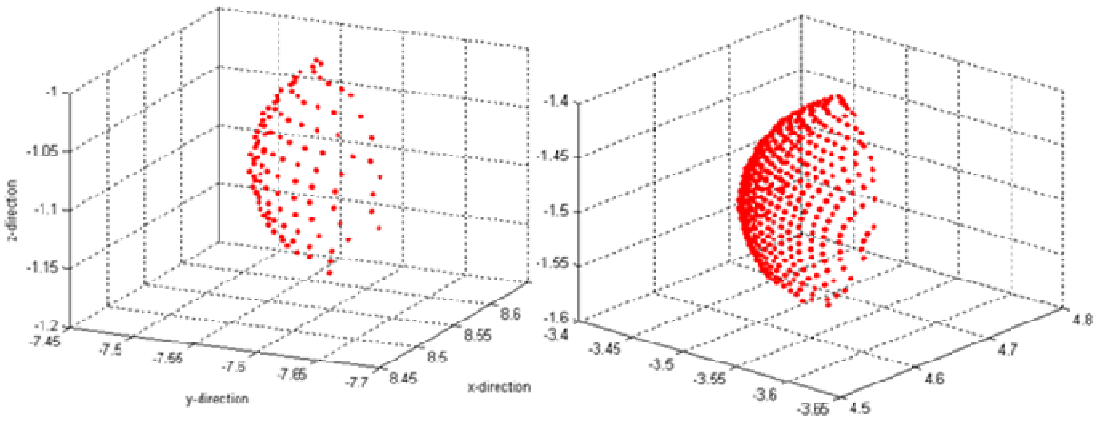

Figure I4-1 Sphere detection: Left sphere1,and right Sphere 2 at SCP4 respectively.

Statistical results of the sphere target parameters

1. The quality of fitting sphere target using Matlab functions. Auto -detection and computation of the sphere parameters (radius and centre) in four positions.

Position	Targets	Error stdv. (mm)	Absolute error mean (mm)	Max. Absolute error mean (mm)	Radius (R) mm	Diff. R (mm)	No.of pts	Distance (m)
SCP1	Sphere1	0.83	0.6	3.7	96.1	3.9	133	9.99
	Sphere2	1.9	1.02	11.50	96.3	3.7	83	11.77
SCP2	Sphere1	0.70	0.51	4..60	96.2	3.8	142	10.64
	Sphere2	0.73	0.53	3.30	97.7	2.3	149	10.12
SCP3	Sphere1	0.96	0.71	3.3	94.1	5.9	70	14.06
	Sphere2	0.58	0.47	2.0	97.4	2.6	142	10.47
SCP4	Sphere1	1.00	0.67	6.6	97.9	2.1	110	11.45
	Sphere2	0.66	0.44	7.8	99.3	0.7	481	5.96

Table I4-1: Statistical results (standard deviation error, absolute error mean and maximum absolute error mean), and residuals of the sphere radius - using Matlab functions.

2. The quality of fitting sphere target using Cyclone software, manually extracted, and sphere parameters (radius and centre) automatically computed in four positions.

Position	Targets	Error stdv. (mm)	Absl error mean (mm)	Max.Absl error mean (mm)	Radius (R) mm	Diff. R (mm)	No.of pts	Distance (m)
SCP1	Sphere1	0.70	0.53	4.4	96.40	3.6	160	9.99
	Sphere2	1.60	0.80	11.54	96.68	3.32	109	11.77
SCP2	Sphere1	0.71	0.53	4.51	95.78	2.22	142	10.64
	Sphere2	0.73	0.53	3.30	97.82	2.18	159	10.12
SCP3	Sphere1	0.94	0.70	3.30	94.12	5.88	72	14.06
	Sphere2	0.58	0.46	1.90	97.9	2.1	149	10.47
SCP4	Sphere1	1.00	0.68	6.66	97.62	2.4	125	11.45
	Sphere2	0.80	0.46	1.19	99.26	0.74	516	5.96

Table I4-3: Statistical results (standard deviation error, absolute error mean and maximum absolute error mean), and residuals of the sphere radius - using Cyclone software.

3. Comparison between two algorithms (Matlab and Cyclone).

Position	Targets	ΔX (mm)	ΔY (mm)	ΔZ (mm)	RMSE (mm)	Δ R (mm)
SCP1	Sphere1	0.14	-0.4	0.05	0.4267	-0.30
	Sphere2	0.42	-0.14	-0.4	0.5966	-0.38
SCP2	Sphere1	-0.18	-0.32	0.27	0.4557	0.42
	Sphere2	0.06	-0.06	-0.03	0.0900	-0.12
SCP3	Sphere1	-0.40	-0.22	0.07	0.4618	-0.02
	Sphere2	0.003	-0.003	0.003	0.0052	-0.50
SCP4	Sphere1	-0.18	-0.16	-0.2	0.3130	0.28
	Sphere2	0.03	-0.01	-0.1	0.1049	0.04

Table I4-4: The difference between the Matlab algorithm and Cyclone software the sphere parameters from different positions.

I5: Residual errors of the sphere in radial direction from different positions.

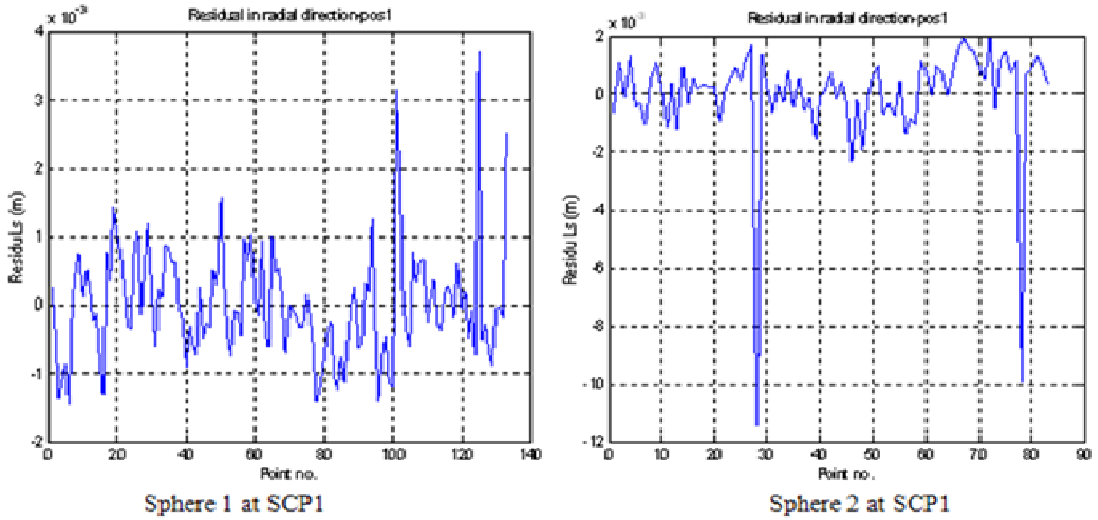

Sphere 1 at SCP1 Sphere 2 at SCP1

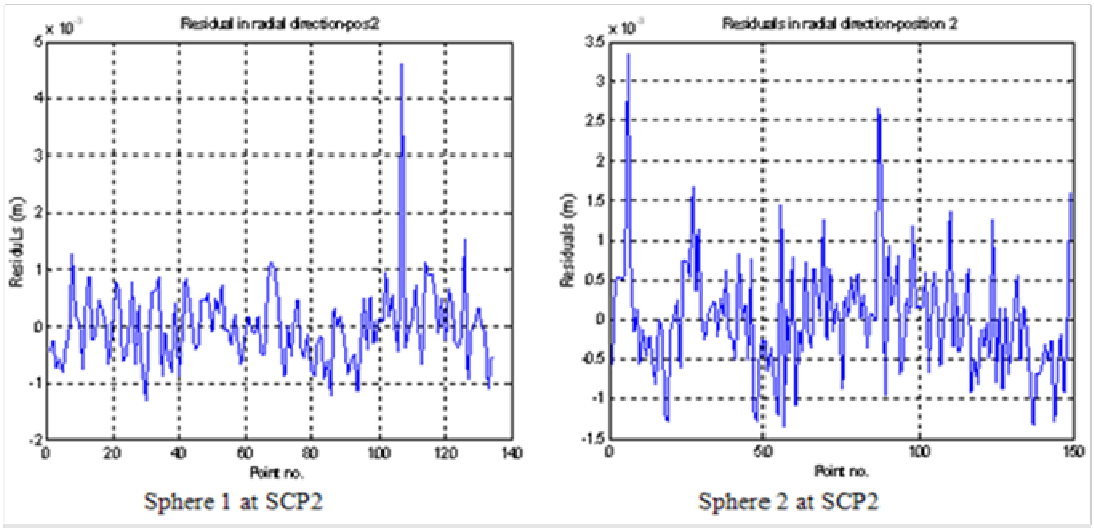

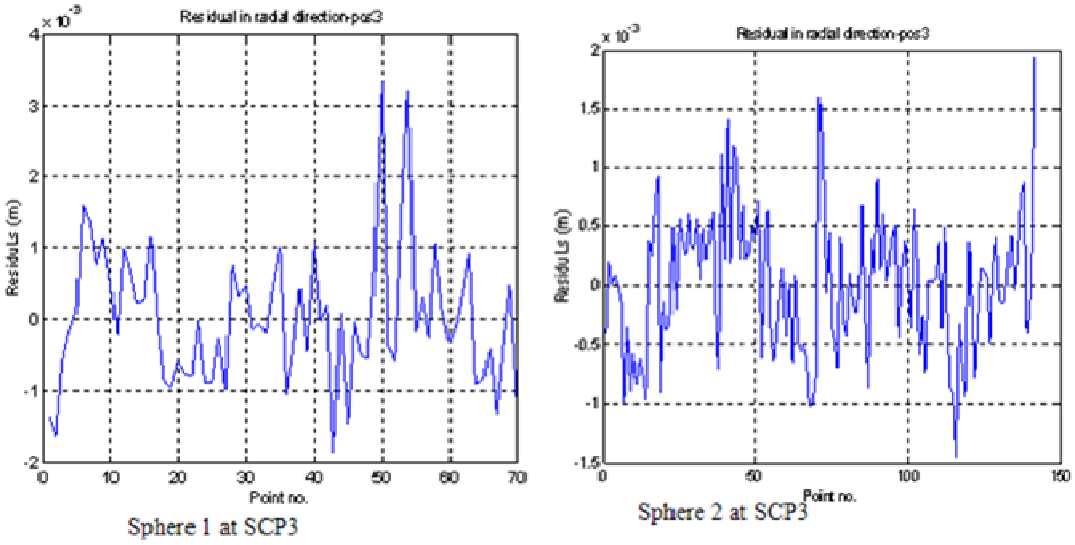

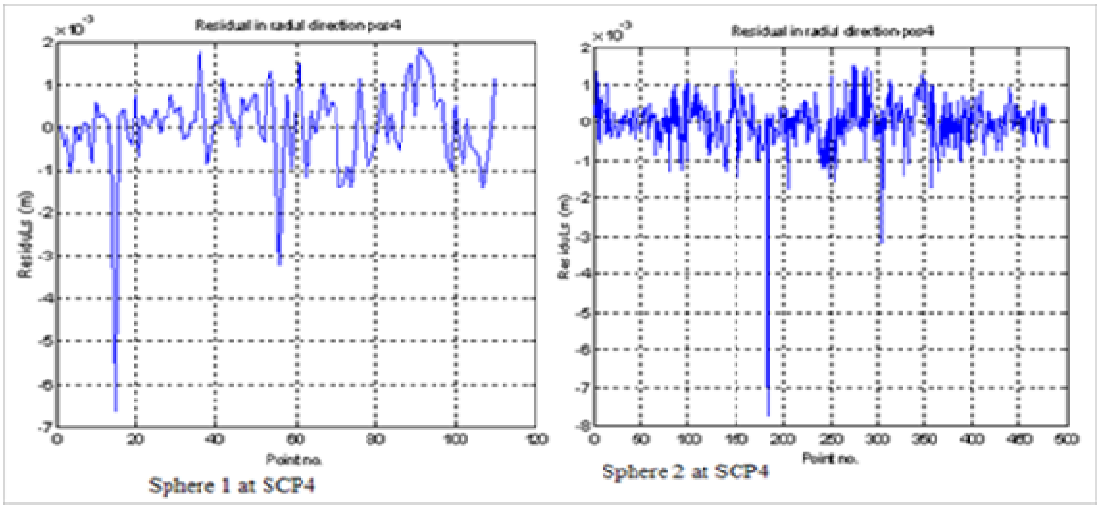

Figure I5-1: Residual errors in radial direction of the sphere from different positions.

Appendix J: Incidence angle effect at different distances.

J1: The effect of IA and Range on the number of points per target.

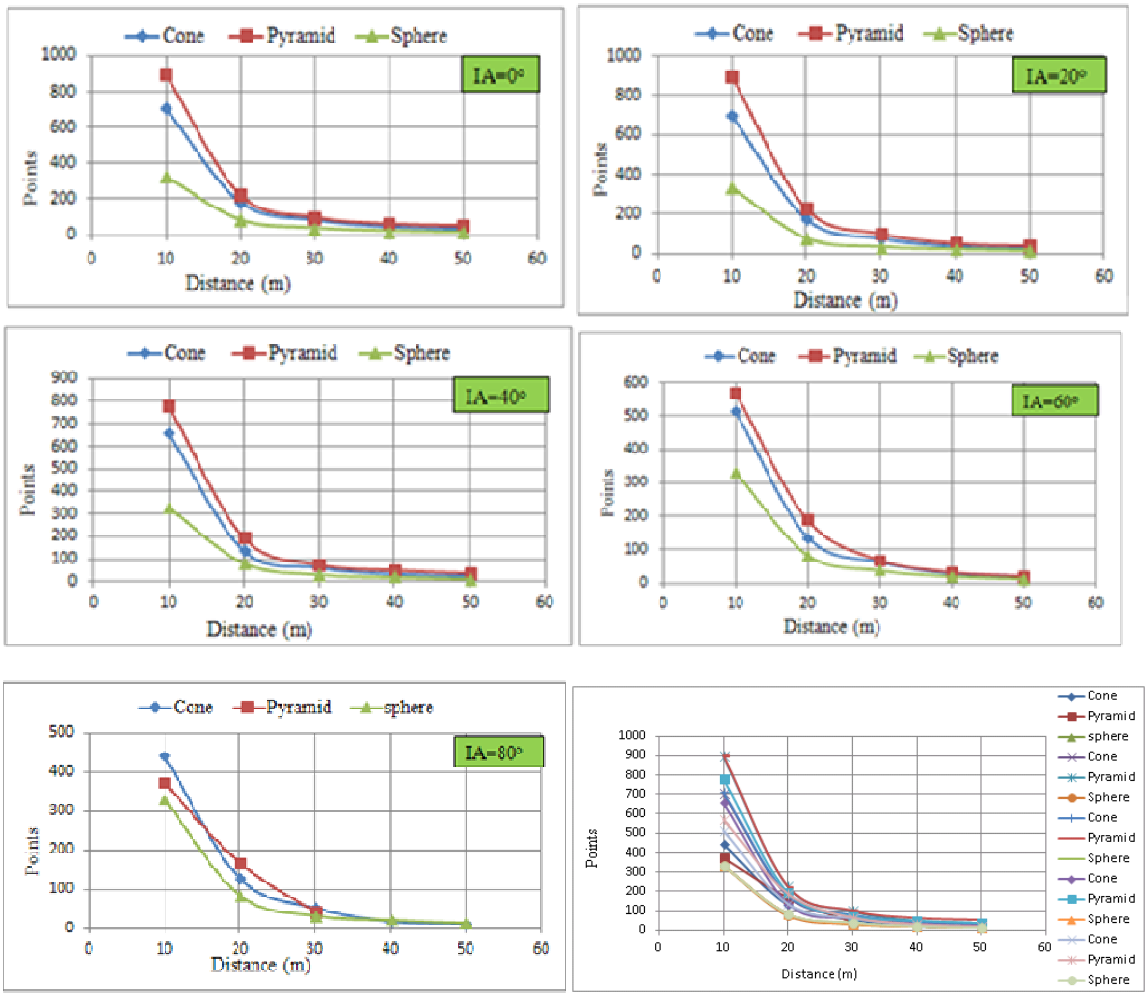

Figure J1-1: The effect of Incidence angle and range Vs point per targets.

J2: Statistical report of fitting cone and sphere using LM algorithm.

Two samples of statistical report of fitting cone and sphere targets -using Levnberg Marquadt (LM) algorithm. The reports for the fitting Cone and Sphere target at IA (0^o) with 20 m range are as following

- **<u>General information of the test targets: Cone and sphere</u>**

General information	**Cone**	**Sphere**
Form fitting Toolbox (FFT)	V2.0.20110814	V2.0.20110814
Name of regression form	Cone	Sphere
Date of calculation	12.07.2012 - 15:57:24	12.07.2012 - 16:17:14
Probability value α [%]	0.1	0.1
Test power β [%]	80.0	80.0
Sum of squares of errors Ω	0.000820926562	0.000200204375
Degree of freedom f = n-u+d = spur(R)	183 -7 = 176	178 - 4 = 74
$\sigma^2_{\text{a-priori}} : \sigma^2_{\text{a-posteriori}}$	1 : 0.000	1 : 0.000
Global test $T_{Global} \leq F_{f,\infty,1-\alpha} \mid H_0$	H_0 is *not* rejected, because $0.000 \leq 0.998$	H_0 is *not* rejected, because $0.000 \leq 1.061$

Table J2-1: Algorithm specification.

- **Form parameters of Cone and sphere:**

Name	Value	σPar
Mx	454910.6511	0.000906
My	339705.6976	0.000868
Mz	31.77025969	0.000806
Nx	-0.910661539	0.001261
Ny	-0.411998001	0.002772
Nz	0.030874084	0.003154
α	2.624924976	0.002205

Name	Value	σPar
Mx	454911.5046	0.000674
My	339703.0686	0.000379
Mz	32.07335338	0.000373
R	0.09991641	0.000477

Table J2-2: Cone parameters left, and Sphere parameters right with their standard parameter errors.

Table J2-2 shows that, the result of fitting seven and four parameters was obtained for cone and sphere respectively. Cone parameters are the three cone apex (Mx, My, Mz) and the vectors N (Nx, Ny, Nz) is the rotation-axis of the cone. This vector is also a unit-vector. The apex lies on N. The angle (α) describes the angle between the vector N and the curved surface area of the cone. The sphere parameters are the three sphere centre (Mx, My, Mz) and one radius R]

σPar: The standard error for each parameter as depicted in the second column of both tables.

- **Critical values for outlier detection**

K_{prio} ($F_{3,\infty,1-\alpha}$)	K_{post} ($F_{3,f-3,1-\alpha}$)
4.211	4.187

K_{prio} ($F_{3,\infty,1-\alpha}$)	K_{post} ($F_{3,f-3,1-\alpha}$)
4.211	4.154

Table J2-3: Critical value of outlier detection for cone right, and for sphere left.

Table J2-3 shows, critical value for outlier detection for cone and sphere fitting, and it shows also the "a posterior" of fitting cone is more effect than sphere, due to its geometric shape. The above critical values are the maximum error, and visually no measurement, should ever fall out site this values.

- . **Point :**

Point-ID	X_0	Y_0	Z_0	X	Y	Z	σ_X	σ_Y	σ_Z
1	454910.862800	339705.814900	31.896637	454910.862982	339705.814930	31.896304	0.001906	0.002153	0.001100
2	454910.863000	339705.833600	31.896697	454910.862879	339705.833604	31.896895	0.001856	0.002159	0.001179
3	454910.793800	339705.876900	31.815188	454910.794749	339705.876260	31.814692	0.001418	0.001860	0.001985
4	454910.825100	339705.885300	31.673603	454910.823787	339705.885977	31.672589	0.001492	0.002004	0.001792
5	454910.855500	339705.873600	31.633691	454910.855522	339705.873594	31.633715	0.001658	0.002122	0.001503
6	454910.879800	339705.818000	31.613784	454910.879798	339705.818000	31.613781	0.001869	0.002141	0.001196
7	454910.851600	339705.850000	31.633759	454910.850959	339705.850107	31.632946	0.001718	0.002149	0.001381
8	454910.848200	339705.808600	31.634142	454910.848332	339705.808623	31.634353	0.001841	0.002150	0.001192
9	454910.849100	339705.827200	31.634113	454910.848492	339705.827202	31.633239	0.001784	0.002160	0.001266
10	454910.874100	339705.834600	31.613792	454910.874967	339705.834667	31.615102	0.001817	0.002158	0.001248
11	454910.801000	339705.878100	31.693726	454910.803074	339705.876886	31.695020	0.001422	0.001939	0.001907

r_X	r_Y	r_Z	∇_X	∇_Y	∇_Z	Ω	T_{prio}	T_{post}	Outlier
0.220747	0.005804	0.740665	0.000188	0.000031	-0.000345	0.000000	0.000000	0.010544	☐
0.261208	0.000240	0.702158	-0.000125	0.000004	0.000205	0.000000	0.000000	0.003916	☐
0.568927	0.258363	0.155164	0.000966	-0.000651	-0.000505	0.000002	0.000001	0.111460	☐
0.522755	0.139204	0.311824	-0.001348	0.000696	-0.001041	0.000003	0.000001	0.232447	☐
0.410663	0.034973	0.515766	0.000022	-0.000007	0.000025	0.000000	0.000000	0.000079	☐
0.251320	0.016864	0.693106	-0.000002	-0.000001	-0.000003	0.000000	0.000000	0.000001	☐
0.367199	0.010324	0.591327	-0.000662	0.000111	-0.000840	0.000001	0.000000	0.078710	☐
0.273045	0.008564	0.695254	0.000136	0.000024	0.000216	0.000000	0.000000	0.004509	☐
0.317631	0.000003	0.656388	-0.000624	0.000002	-0.000897	0.000001	0.000000	0.081809	☐
0.291855	0.001747	0.666333	0.000903	0.000070	0.001365	0.000002	0.000001	0.181573	☐
0.566506	0.194221	0.220606	0.002113	-0.001237	0.001319	0.000007	0.000003	0.538348	☐

182

Point-ID	X_0	Y_0	Z_0	X	Y	Z	σ_X	σ_Y	σ_Z
1	454911.471200	339703.013700	32.150000	454911.471230	339703.013749	32.149932	0.001557	0.001394	0.001103
2	454911.470200	339702.974700	32.068724	454911.470257	339702.974854	32.068732	0.001550	0.000675	0.001643
3	454911.481000	339703.117300	31.988886	454911.481098	339703.117097	31.989237	0.001604	0.001461	0.000996
4	454911.403900	339703.064300	32.067468	454911.404948	339703.064344	32.067529	0.000324	0.001643	0.001642
5	454911.465400	339703.135100	32.008681	454911.465716	339703.134564	32.009202	0.001526	0.001274	0.001298
6	454911.442700	339703.111400	32.008329	454911.442425	339703.111590	32.008040	0.001308	0.001493	0.001268
7	454911.453600	339703.092300	31.988182	454911.454678	339703.091799	31.989982	0.001439	0.001602	0.000966
8	454911.456600	339703.053000	31.988181	454911.456156	339703.052856	31.987393	0.001450	0.001625	0.000900
9	454911.452900	339703.071800	31.988178	454911.452784	339703.071807	31.987987	0.001420	0.001644	0.000915
10	454911.433000	339703.089100	32.007942	454911.432435	339703.089262	32.007426	0.001161	0.001611	0.001254
11	454911.435300	339703.049700	32.007941	454911.433326	339703.049163	32.006078	0.001174	0.001615	0.001234

r_X	r_Y	r_Z	∇_X	∇_Y	∇_Z	Ω	T_{prio}	T_{post}	Outlier
0.104460	0.281800	0.549926	0.000032	0.000052	-0.000073	0.000000	0.000000	0.000993	
0.111699	0.831424	0.002022	0.000060	0.000163	0.000008	0.000000	0.000000	0.003384	
0.049457	0.210790	0.633262	0.000110	-0.000227	0.000393	0.000000	0.000000	0.023060	
0.961174	0.001726	0.003283	0.001085	0.000046	0.000063	0.000001	0.000000	0.135917	
0.138780	0.399677	0.377636	0.000345	-0.000585	0.000569	0.000001	0.000000	0.085385	
0.368028	0.176190	0.406047	-0.000290	0.000200	-0.000304	0.000000	0.000000	0.024359	
0.234850	0.050847	0.654857	0.001146	-0.000533	0.001914	0.000005	0.000002	0.599523	
0.222460	0.023393	0.700278	-0.000469	-0.000152	-0.000832	0.000001	0.000000	0.105186	
0.254563	0.000995	0.690801	-0.000122	0.000008	-0.000201	0.000000	0.000000	0.006224	
0.501407	0.041229	0.418414	-0.000588	0.000169	-0.000537	0.000001	0.000000	0.075514	
0.490816	0.036374	0.437225	-0.002047	-0.000557	-0.001932	0.000008	0.000003	0.977337	

78

Table J2-4: Statistical result of fitting points: Top fitting points to cone surface, Lower: fitting points to sphere surface.

Table J2-4 shows two samples of statistical result of the cone and sphere target with normal IA (0^o) at 20 m range, and with point density (1x1) sq. cm. The points collected per target were 182 and 78 for the cone and sphere respectively.

The definition of each element in the table provided by the software can be explained as follows:

X_0, Y_0 and Z_0: measured data; **X, Y and Z**: predicted data after fitting.

σ_X, σ_Y and σ_Z : Denote the uncertainties after adjustment. Because of the imperfection of the instrument, each observation gets a (small) residual during the adjustment. If for example, a perfect surface (or a perfect mathematical model), the

estimated uncertainties demonstrate the accuracy of the instrument. With σ (xyz), the uncertainties of a point are given. These values are taken from the estimated variance covariance matrix of the observation.

rx, ry and rz: Denotes the redundancy of the coordinate component of each point. The summation of [sum (rx, ry and rz)] is equal to the degree of freedom. The value is defined between $0 < r < 1$ or (similar 0-100 %). The recommended value is $0.4 < r < 0.7$ (Losler, 2012).

Δx, Δy and ΔZ: The deviation between measured data and the object fit function.

Ω: The minimisation of the sum of the weighted square errors (or weighted residuals) between the measured data (X_0, Y_0 and Z_0) and the object fit function.

T_{ptio}:, T_{post}: Both values are derived by a multiple tests to detect outlier. If the Null hypnotises H_0 rejected, the test observation will be deleted (Lösler, 2008). A detailed description of these two values is published by (Jager et al., 2005). The formulas are also given in equation (16) and (15) (Lösler, 2008).

Global test: It uses in test statistic, and to examine the compatibility of the posteriori estimated variance factor with the priori given variance factor. Also, is a key indicator of how well the observation fit together as shown in Table J2-1, last row

- **Covariance matrix for fitting cone and sphere**

#	Mx	My	Mz	Nx	Ny	Nz	α
Mx	+8.2049e-07	+2.2010e-07	-4.9445e-08	+2.2314e-07	-5.0224e-07	-1.2045e-07	-1.7741e-06
My	+2.2010e-07	+7.5344e-07	-4.5063e-08	-9.0453e-07	+1.9892e-06	-1.3510e-07	-1.0552e-06
Mz	-4.9445e-08	-4.5063e-08	+6.4946e-07	+1.0322e-07	-4.8181e-08	+2.4015e-06	+2.0008e-07
Nx	+2.2314e-07	-9.0453e-07	+1.0322e-07	+1.5897e-06	-3.4824e-06	+4.1850e-07	+3.6579e-07
Ny	-5.0224e-07	+1.9892e-06	-4.8181e-08	-3.4824e-06	+7.6838e-06	-1.7975e-07	-7.5817e-07
Nz	-1.2045e-07	-1.3510e-07	+2.4015e-06	+4.1850e-07	-1.7975e-07	+9.9453e-06	+6.7206e-07
α	-1.7741e-06	-1.0552e-06	+2.0008e-07	+3.6579e-07	-7.5817e-07	+6.7206e-07	+4.8625e-06

#	Mx	My	Mz	R
Mx	+4.5420e-07	+5.1279e-08	-1.3783e-08	+2.9483e-07
My	+5.1279e-08	+1.4382e-07	-2.5912e-09	+4.7993e-08
Mz	-1.3783e-08	-2.5912e-09	+1.3901e-07	-5.9266e-09
R	+2.9483e-07	+4.7993e-08	-5.9266e-09	+2.2770e-07

Table J2-5: Statistical result of Variance covariance matrix Top: Covariance matrix of fitting cone. Lower: Covariance matrix of fitting sphere.

Figure J2-5 shows the variance covariance matrix. Once the optimal object-fit (sphere and cone) parameters are determined, parameter statistics were computed via software for the converged solution.

The variance parameter errors (σ^2 par) are obtained in the diagonal values of the covariance matrix for the cone and sphere respectively.

The final standard error (σ par) for the coordinates of the apex such as normal vector and angle can be seen in Table J2-2, second column. This standard error (σ par) "*is a measure of how unjustified variability in the data propagates to variability in the solution, and is an error measure for the parameters"* (Gavin, 2011).
The standard error of the fit indicates how variability in the parameters affects the variability in the object-fit. The standard prediction error reflects the standard error of the object fit as well as the mean square measurement error.

2. Residual and summation of mean square error of cone fitting

(a)

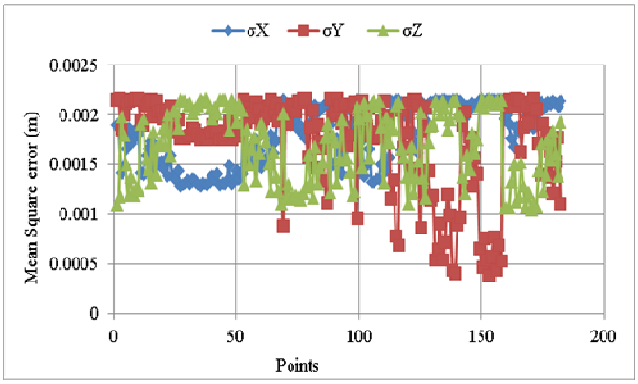

(b)

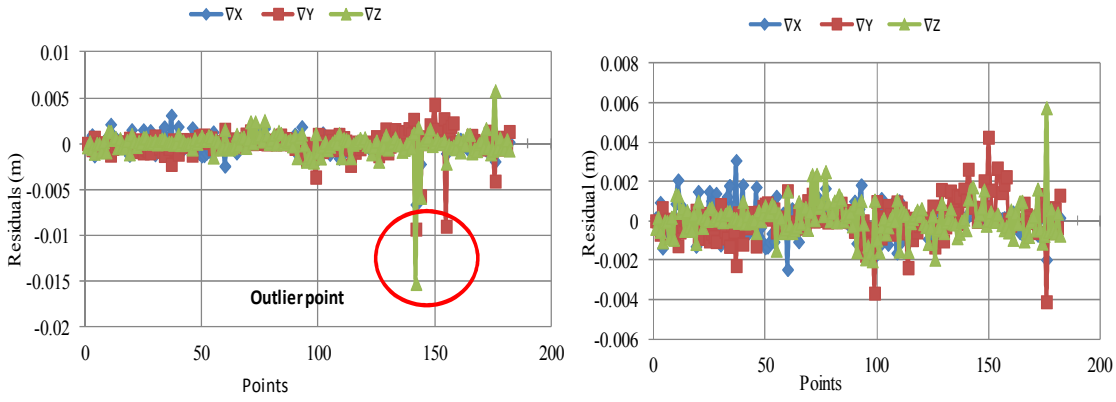

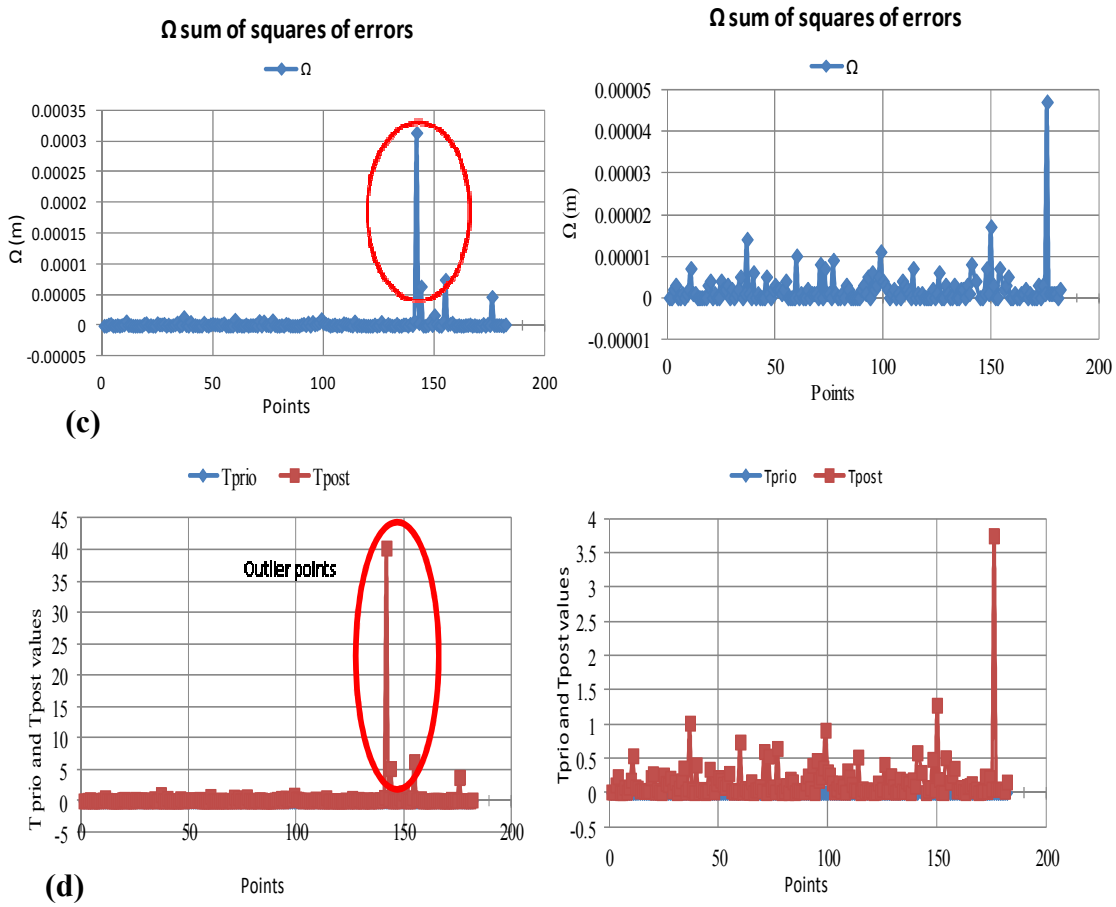

Figure J2-1: Statistical results of cone fitting. (a): Mean square error; (b): Residuals; (c): Sum of squares of errors; (d): a-priori and a-posteriori test values after adjustment. Figures (b), (c) and (d) right after removing outlier from the data.

3. Residual and mean square error of sphere fitting

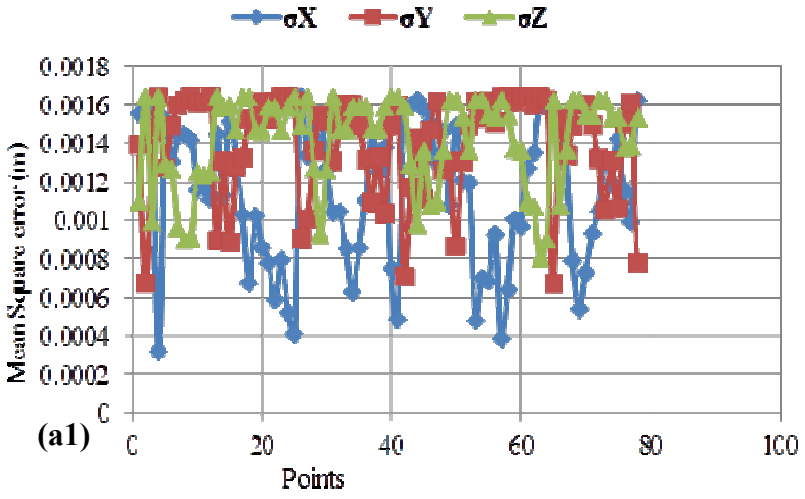

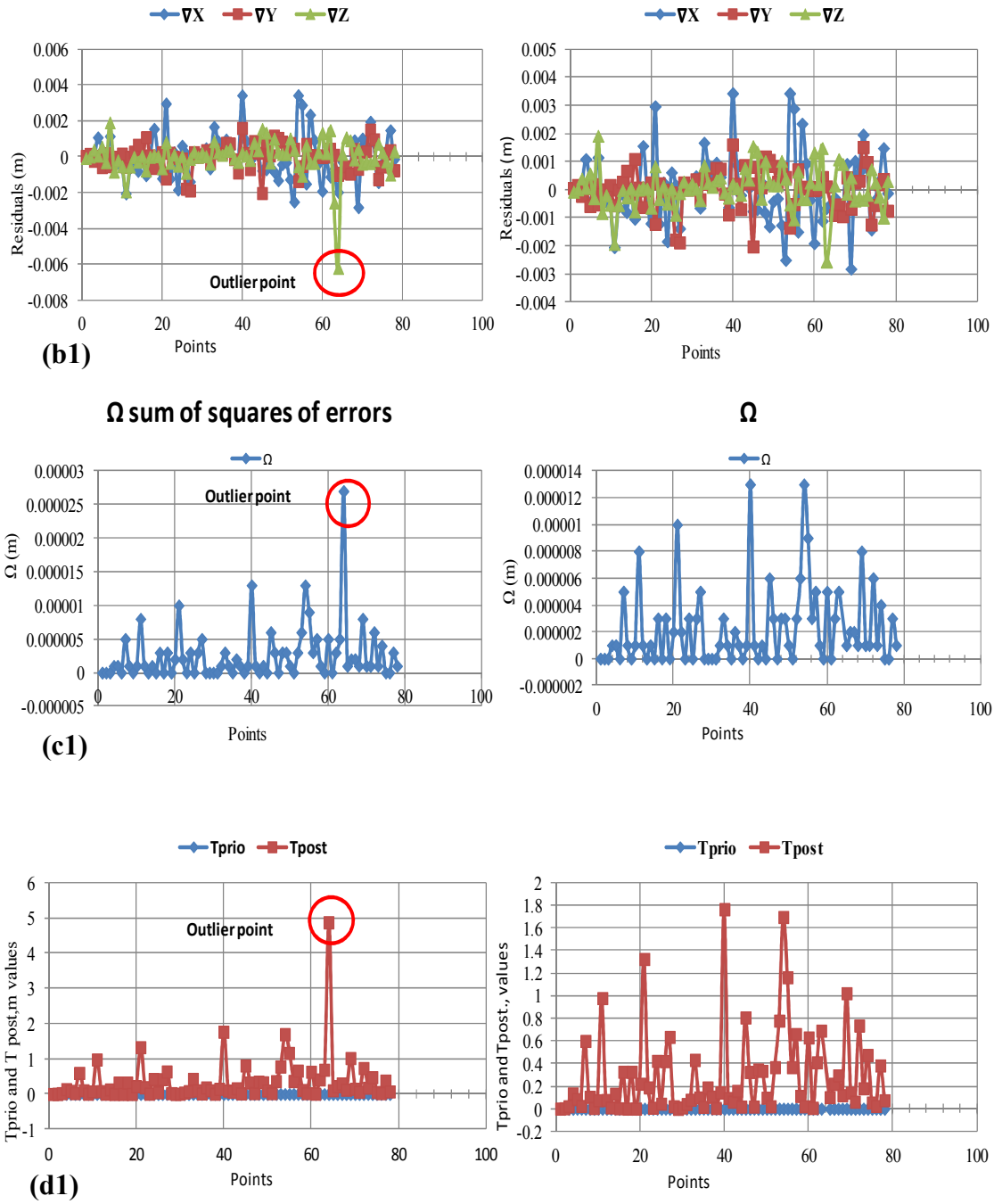

Figure J2-2: Statistical results of sphere fitting. (a1): Mean square error; (b1): Residuals; (c1): Sum of squares of errors; (d1): a-priori and a-posteriori test values after adjustment. Figures (b1), (c1) and (d1) right after removing outlier from the data.

Appendix K: Developed algorithm using Matlabe functions: Target detection, fitting and estimating their centre/apex.

Because of the long document of each developed algorithm, the author preferred to use CD for all scripts program written (enclosed CD). The names of each program with the data are as following:

Program 1 and 2 (UNT1, UNT2): For detection and computation (chapter 6): UNT1.m; UNT2.m: For pyramids and dots targets respectively.

Application of UNT1 algorithm: includes of three groups

Group1: This group contains 9 Matlab files, which are sub-programs developed for fitting pyramid faces (3 and 4) after detection from different positions and point densities. The sub-groups are UNT1.1 (UNT1.1.1 to UNT1.1.4) and UNT1.2 (UNT1.2.1 to UNT1.2.3).

Group2: This group contains 6 Matlab files developed for fitting pyramid 8 faces after detection from different positions and point densities. The sub-groups are UNT1.3, UNT1.3.1, UNT1.4, UNT1.4.1, UNT1.5 and UNT1.6.

Group3: This group contains 22 Matlab files developed only for detection and computation the apex from three different positions and scan resolution between (0.5 x 0.5 to 2.5 x 2.5) sq. cm:

Position1: Contains 13 Matlab files and it failed in UNT1a5 (see chapter 6), and it is very slow in UNT1Ap up to 4-5 hours because it checks each point on the target face with all point cloud (see chapter 6).

Position2: Contains 4 Matlab files and it failed in UNT1b2 and UNT1b3 (see chapter 6).

Position3: Contain 5 Matlab files and it is only successful in UNT1c1 and UNTc5 (see chapter 6).

Further applications of UNT1, applied on Board result test1, see section 5.5): Contains 7 Matlab files: Square based Pyramid from (0 to 80^o IA) at fixed rang (see chapter 5).

UNT1 algorithm Updated seconded part collaborated between the author and (Lösler, 2012b)**:** The orthogonal distance fit of a pyramid faces, (see appendix P). This algorithm applied for all pyramid faces and the final test with MLS in the field (see appendix R).

Application of Program UNT2: Contains 9 Matlab files, sub-programs developed for fitting a line to a set of points and intersecting each fitted line using two methods. (2D and 3D line)

1. Method 1 (2D): UNT2.1 [fitxy, fityz and fitxz); UNT2.1.1, UNT2.1.2, UNT2.1.3, UNT2.1.4 [(fitc1 (line1), fite1 (line2), fitd1 (line3)], and using intersection lines algorithm. Also, The UNT2.3 algorithm developed for fitting each line in 2D, and removes the noise.
2. Method 2 (3D) : UNT2.2 (line fit in3D) using SVD method (see chapter 7).

Program3 (UNT3 and UNT4): Developed for sphere detection and computation: Contain 4 Matlab files. These files are for sphere detection, fitting and computation its parameters (radius and centre) from different positions using two methods

- Average Determination (AD) method - Files UNT3 (UNT3.1 to UNT3.7).
- Gauss Newton (GN) method-. File UNT4 and UNT4.1.

Program4 (UNT5), for Cone detection and computation: Contain one Matlab files is UNT5. This file is for cone detection from different scanning positions.

Program5 (UNT7), for Model of IA of each target: Contains 4 Matlabe files (UNT7.1 to UNT7.4). These files are for the model of incidence angles (IA) for each target used (Cone, sphere, pyramid and leica flat target), (see appendix H).

Program6 (UNT8), for plotting Trajectory solution: Contain one Matlab file. This file just represents the survey data and solution error of GPS/IMU processed by 3DLM Ltd.

LM algorithm -result of the test1, 2, and 3: Contains full statistical results of cone, sphere, pyramid and leica flat target. (See result in chapter 5 and chapter 7).

Appendix L: Planes and lines fitting.

L1: Fitting a best-fit plane to data using Matlab functions (e,g., square based Pyramid using scan resolution (0.5 x 0.5) sq. cm at range 13.50 m and 40 IA m**.**

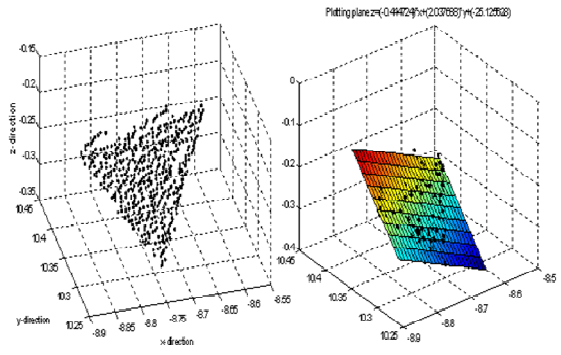

Black colour (BC) face

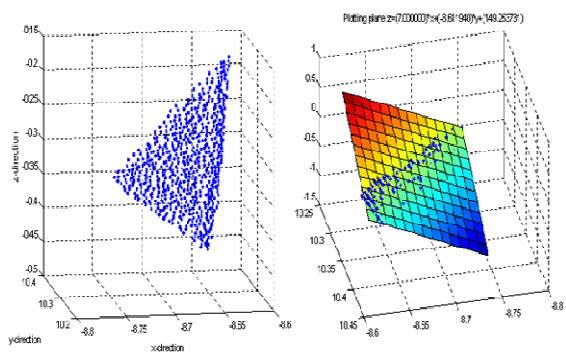

HRT colour face

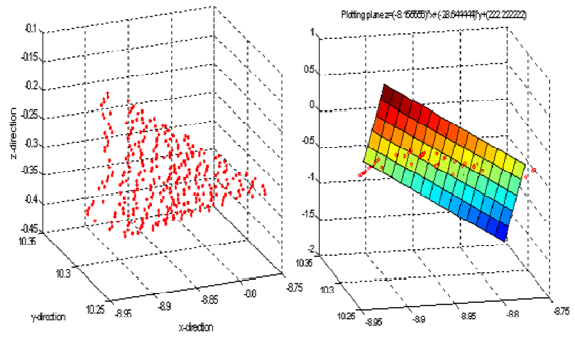

Red colour (DC) face

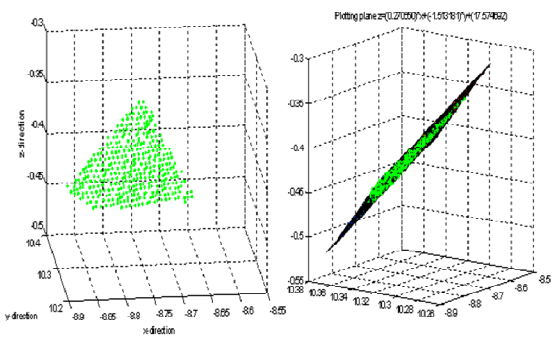

Green colour (GC) face

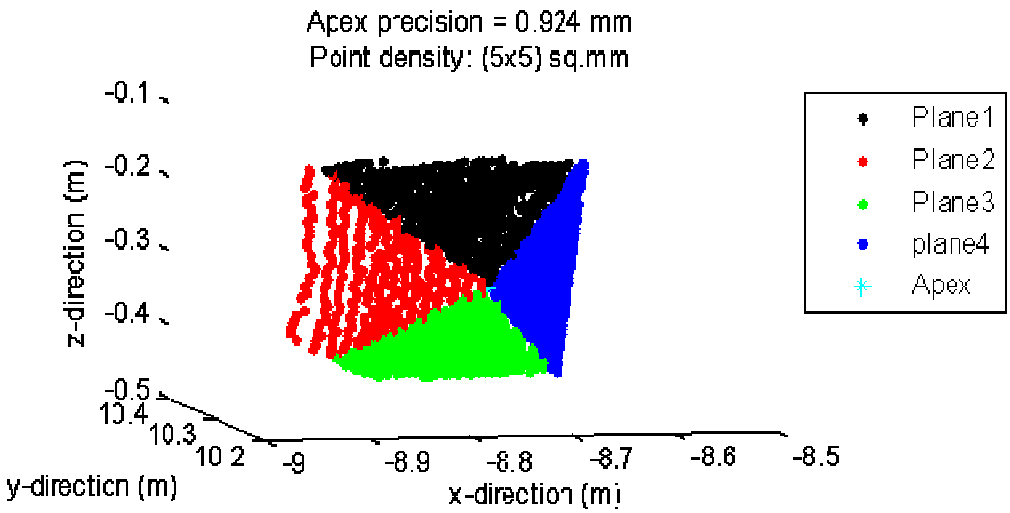

Figure: L1-1: Fitting a best fit plane to data and intersecting planes of each fitted side of square based pyramid.

Point density (Sq.mm)	Point no. for 3faces	Point no. for 4 faces	σapex (mm)		Range (mm)	
			3 faces	4 faces	3 faces	4 faces
(5x5)	1036	1777	0.475	0.924	10600	13500
(10x10)	79	107	2.238	3.296	IA = 27°	IA= 40°
(20x20)	78	105	2.218	4.062		
(25x25)	54	68	2.205	4.400		

TableL1-1: Apex precision Vs different resolutions.

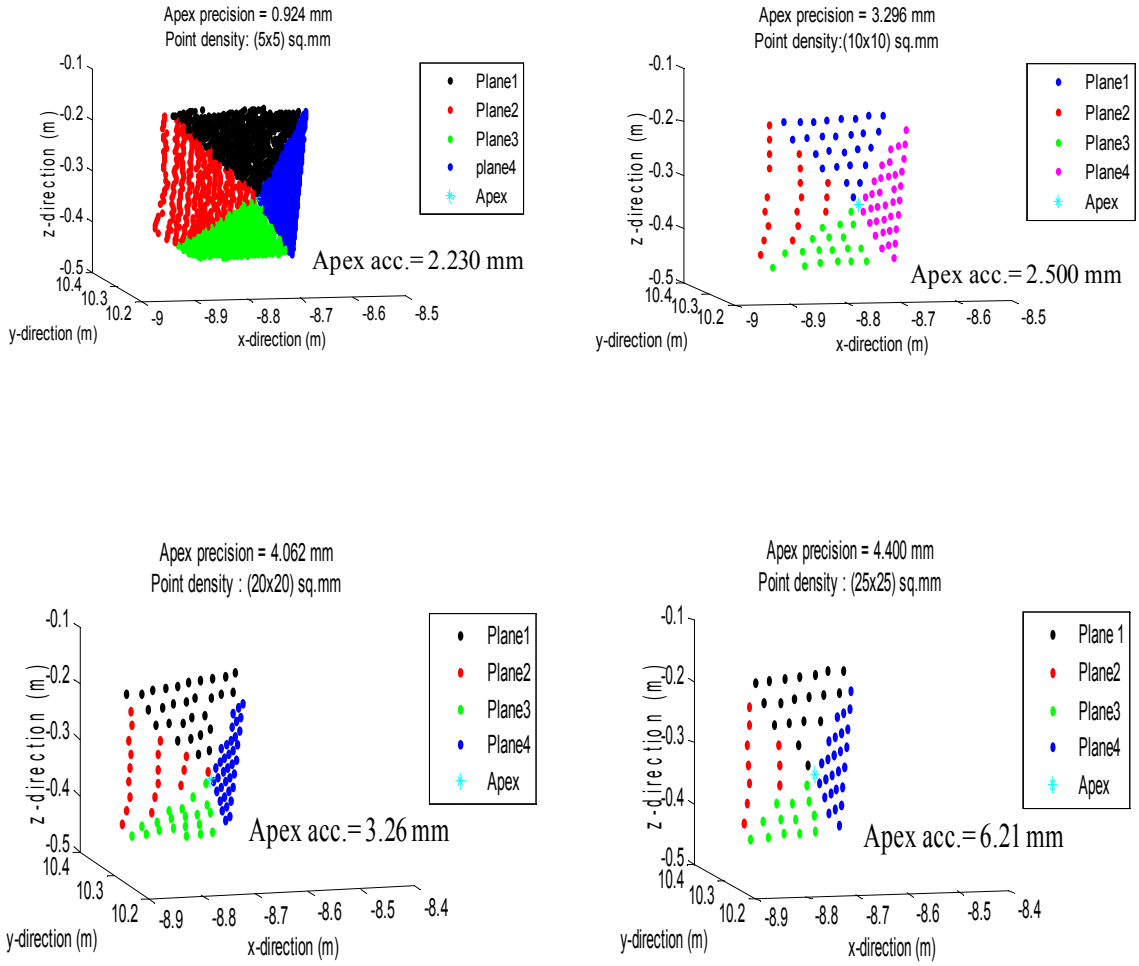

Figure: L1-2: Point density (scan resolution) vs precision and accuracy at around 13.5 m range and 40° IA.

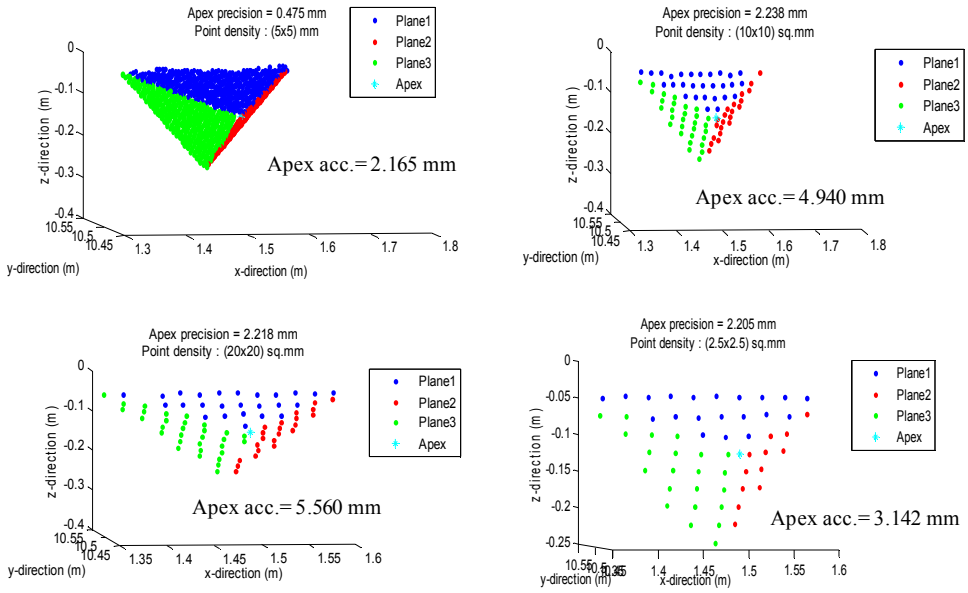

Figure: L1-3: Point density vs precision and accuracy at around 10.5 m range and 27° IA.

L2: The effect of IA at fixed range 10.0 m.

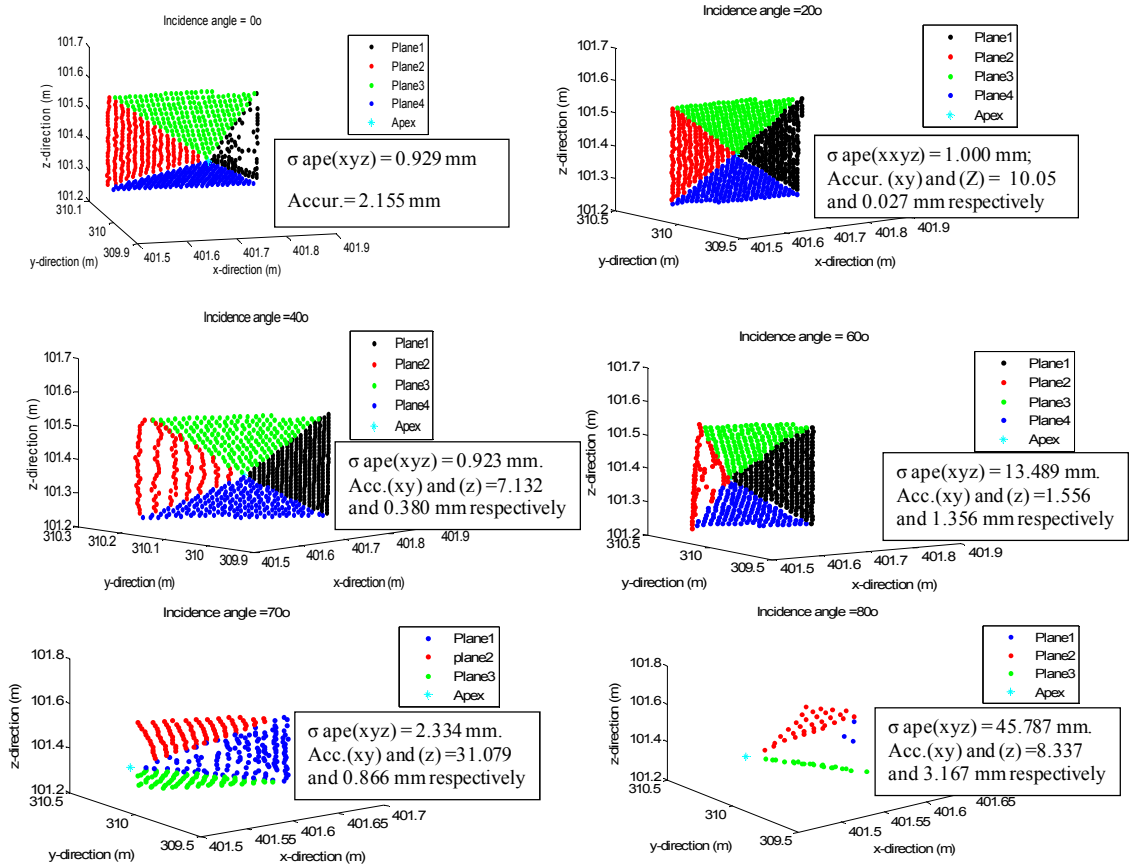

Figure: L2-1: Incidence angle vs precision and accuracy at fixed range 10.0 m.

L3: Fitting a best-fit line to data using Matlab functions- Scan resolution (5x5) mm at a range around 10.0 m at normal IA.

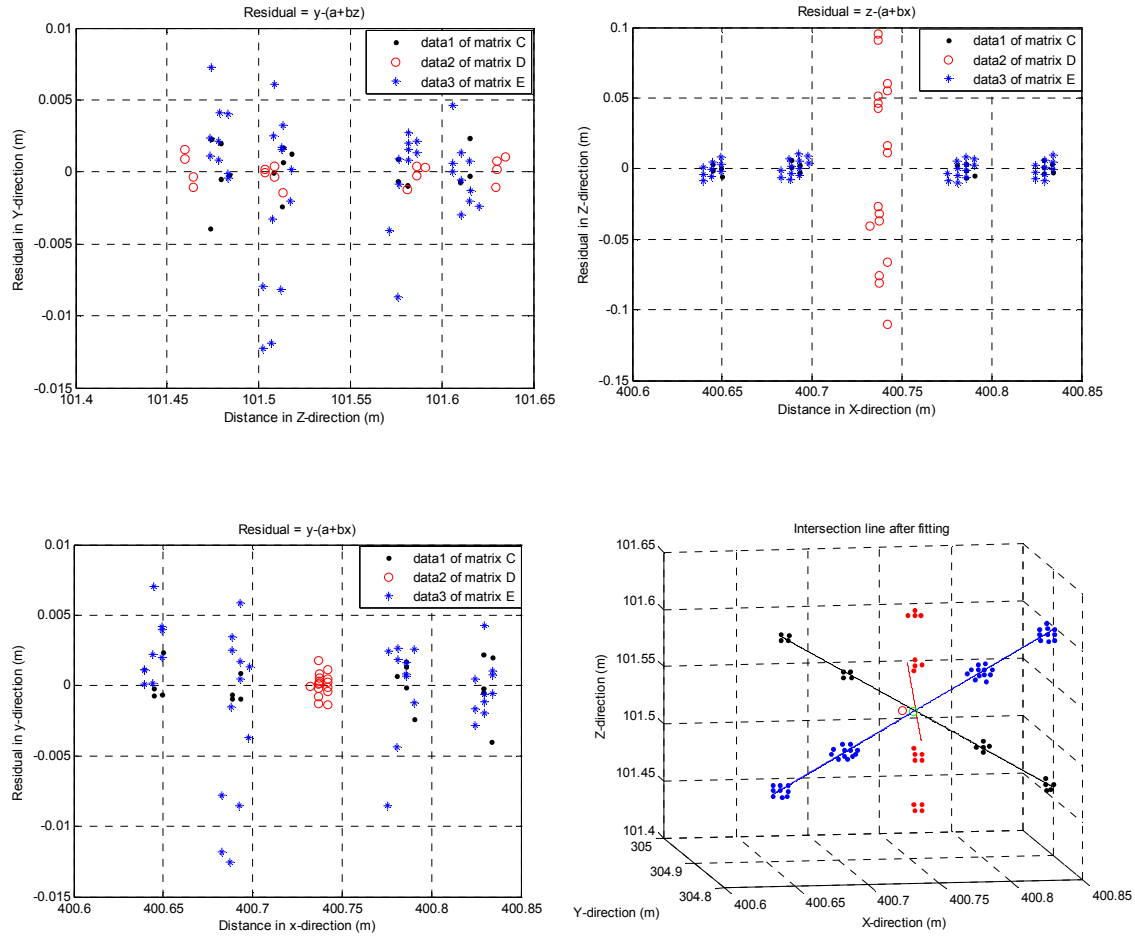

Figure L3-1: Residual of each point after fitting. Left: origin y along z-axis, (y (z)). Right: origin z along x-axis (z (x)). Bottom left origin y along x-axis, (y (x)). Bottom right: Intersection lines after fitting.

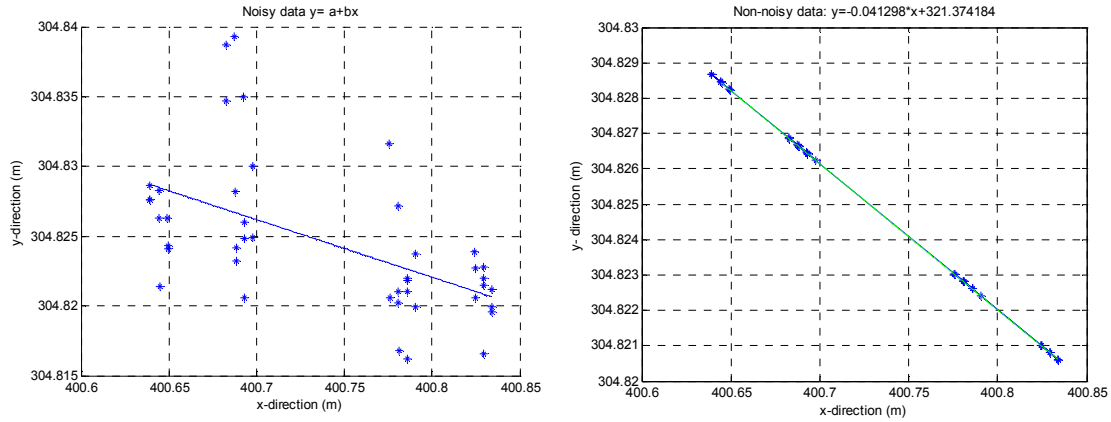

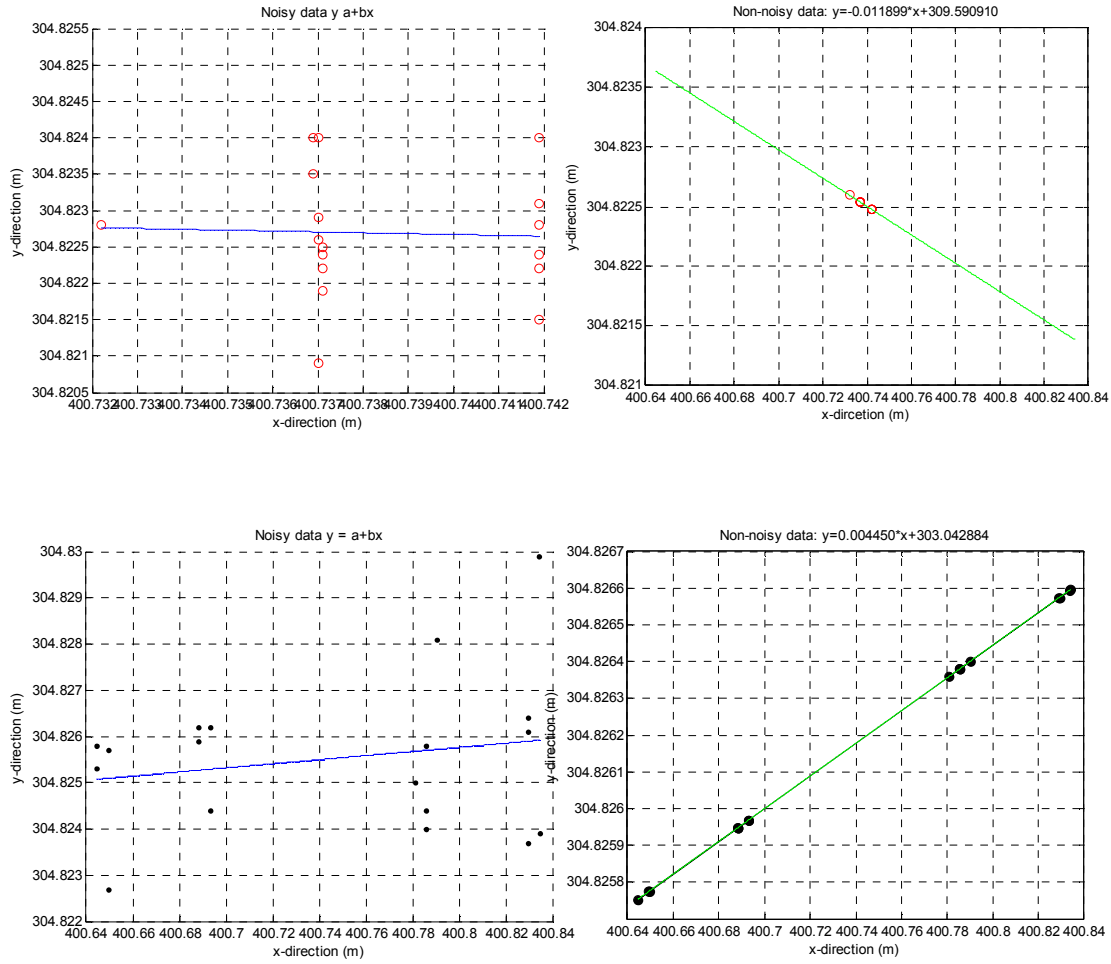

Figure L3-2: Fitting the best fit line to data. Top left: Noisy data of line1 (matrix E1) as depicted in blue dot. Top right: non noisy data after fitting. Middle Left : Noisy data of line 2 (matrix D1) as depicted in the red dot. Middle right fitting data Lower left: Noisy data of line 3 (matrix C1) as depicted on black dot. Lower right: fitting data. The detailed process of fitting line to data can be found in the attached CD.

L4: Accuracy of the pyramids apex.

Accuracy of the apex computed from different scan resolution and rages around 6.0 m to 15.0 m of SCP1, SCP2, SCP2 and SCP4.

Scan position 1 to 4 (SPC1-SPC4)

Scan position	Target type	Res(5x5) sq. mm	Res(10 x 10) sq. mm	Res(15x 15) sq. mm	Res(20x 20) sq. mm	Res(2.5x2.5) sq. mm	Missing Face
		RMSE1 (mm)	RMSE2 (mm)	RMSE3 (mm)	RMSE4 (mm)	RMSE5 (mm)	
SCP1	8 sides	2.41	2.83	2.88	4.46	5.11	-
	5 sides	2.68	5.00	4.65	6.02	8.13	-
	4 sides	6.80	9.29	Fail	11.67	12.63	-
	3 sides	6.50	8.94	Fail	9.46	6.14	-
SCP2	8 sides	2.81	4.04	4.76	6.10	8.02	3
	5 sides	5.30	6.02	Fail	11.68	11.90	2
	4 sides	4.93	9.37	7.82	9.98	10.83	-
	3 sides	5.26	7.82	9.15	12.01	12.91	-
SCP3	8 sides	4.61	5.64	7.20	9.50	10.10	3
	5 sides	4.20	5.22	Fail	8.10	8.25	2
	4 sides	6.74	9.23	9.65	11.47	11.74	1
	3 sides	Fail: very steep IA, 3 faces missing					1
SCP4	8 sides	6.60	8.24	Fail	9.35	10.15	4
	5 sides	Fail: very steep IA, 3 faces missing					3
	4 sides	Fail: very steep IA, 2 faces missing					2
	3 sides	Fail: very steep IA, 2 faces missing					2

Table L4-1: Shows RMSE vs resolution of the scanner for pyramid faces at different positions.

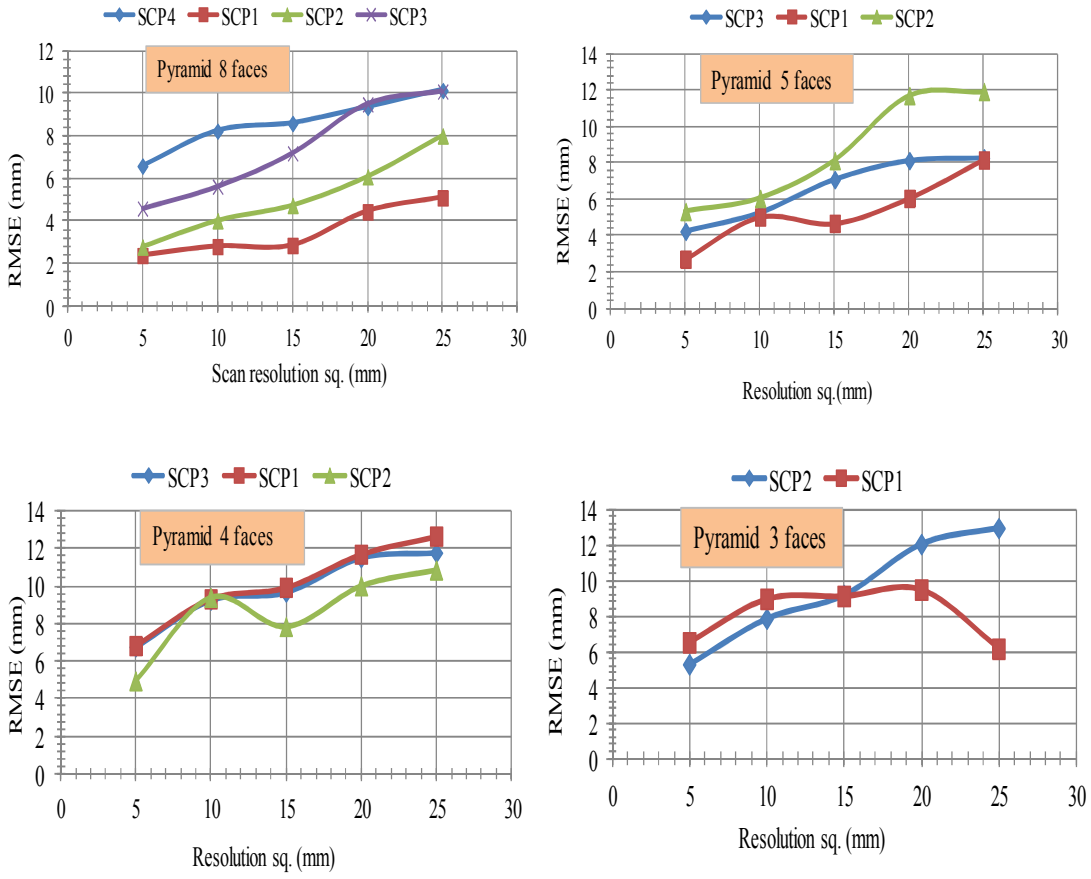

Figure L4-1: RMSE Vs Scan resolution between minimum (5x5) to maximum (25x25) mm of the pyramid (8, 5, 4 and 3) faces.

Appendix M: Registration process and Statistical results.

M1: Registration process

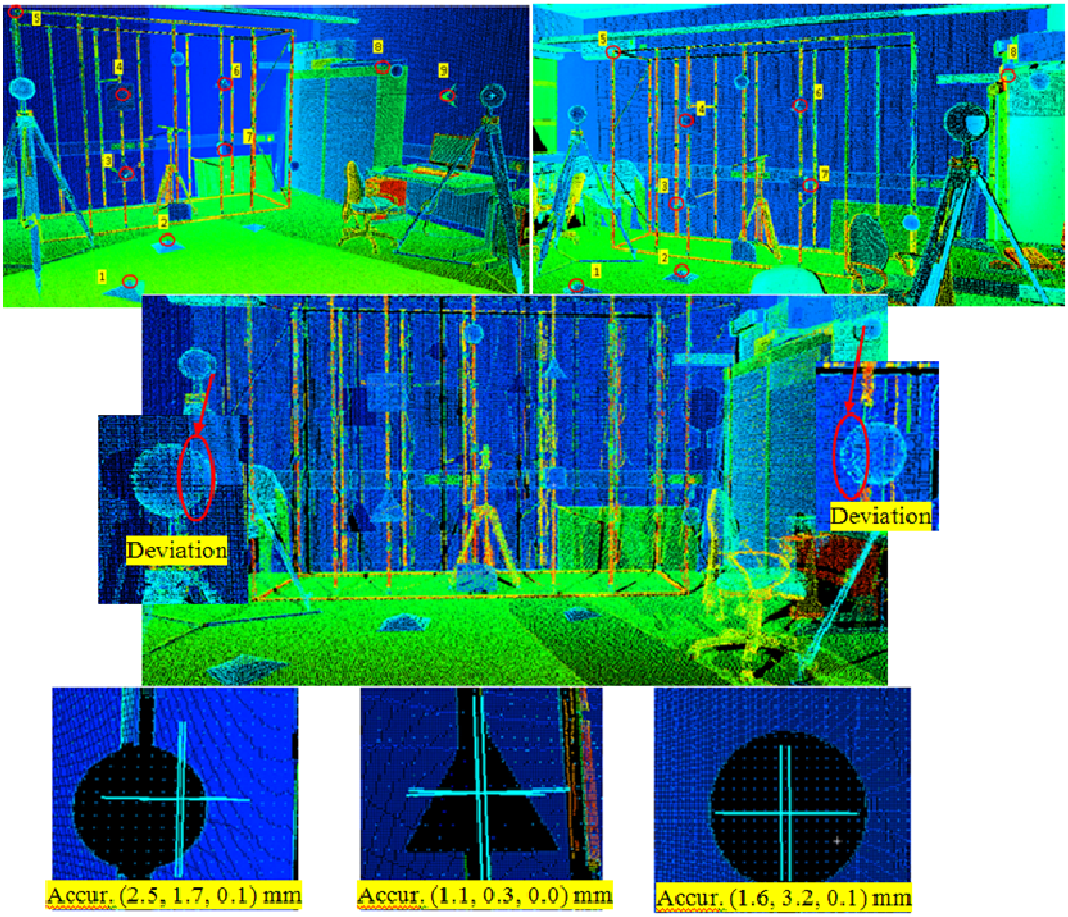

Figure M1-1: Point cloud to cloud registration based on natural feature.

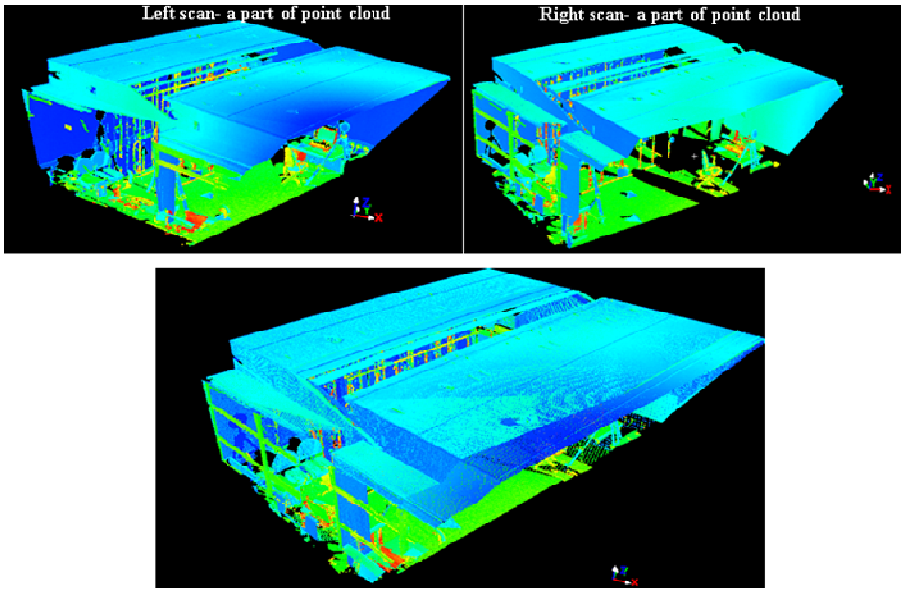

Figure M1-2: Registration of point cloud. Top left: Scan position 1, a part of point cloud. Top right: Scan position 2, a part of point cloud. Lower: Point cloud after registration.

M2: Registration of point cloud based on the sphere and designed targets (pyramids and cube).

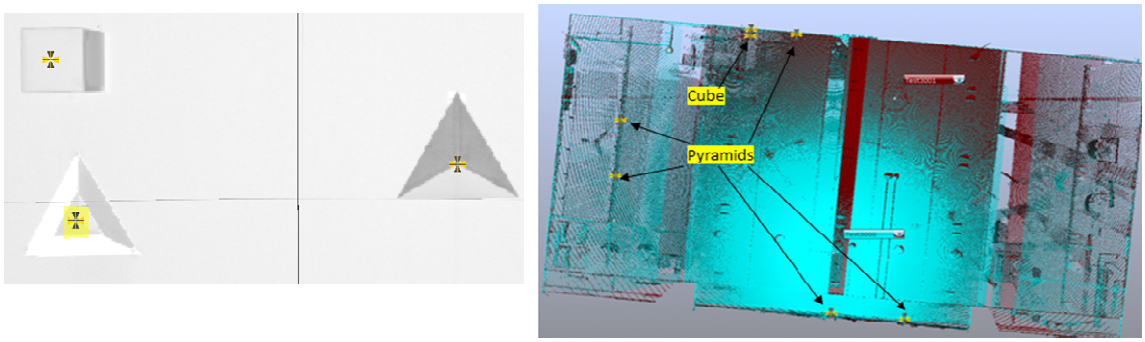

Figure M2-1: Different targets used in registration. Left: Cube and triangular based pyramid. Right.: Overall correspondence view with visible points of the pyramid and cube.

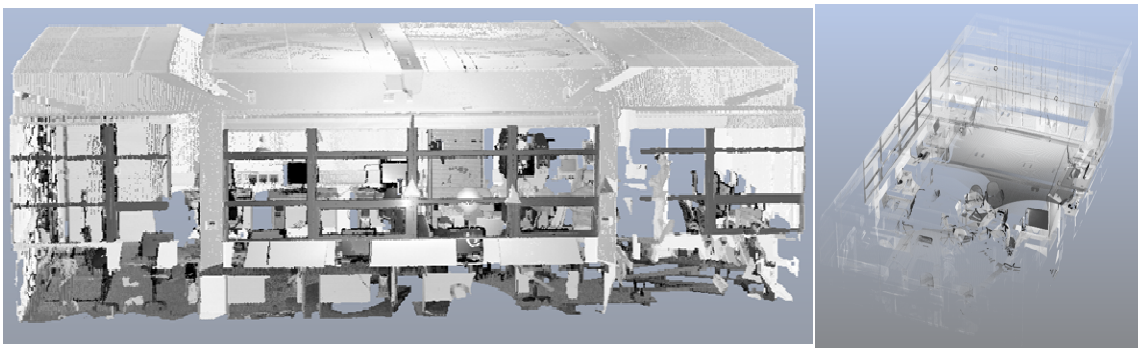

Figure M2-2: 3D view of the point cloud (left), and Clear view mode (right).

M3: Sphere and other targets (corner points) based Registration.

- **Sphere and corner point.**

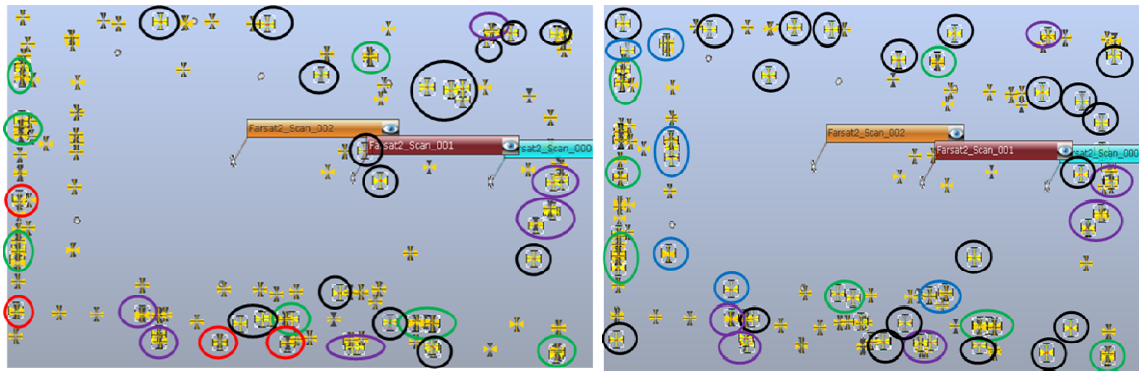

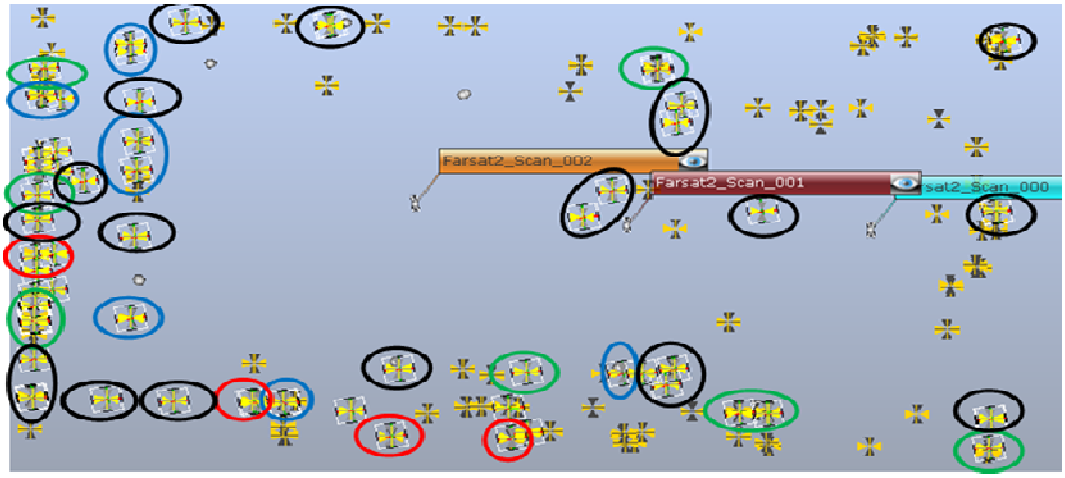

Figure M3-1: Registration of point cloud using sphere and corner point. All highlighted corner points are detected automatically from scan 1, 2 and 3. Green colour represents points detect in three scans. Purple, Red and blue represent point appeared in scan1, 2 and 3, respectively. Black represents point not corresponding in any two scans.

- **Sphere and rectangular object**

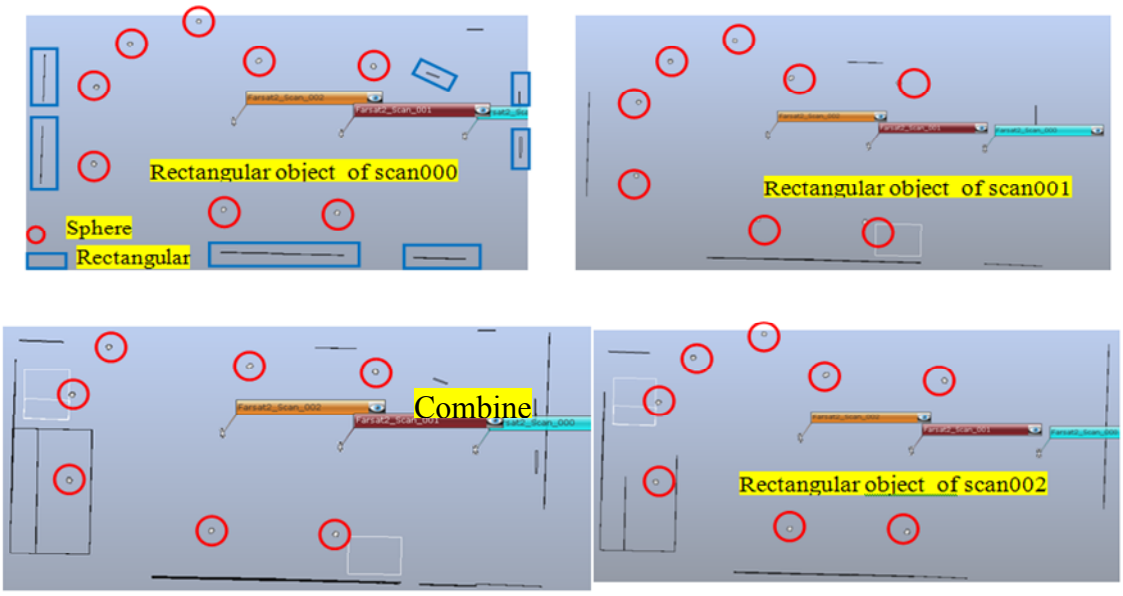

Figure M3-2: Registration point cloud based on sphere and rectangular. Top left, right and lower right for scan position 1, 2 and 3 respectively. Lower left: combined all three scan position.

Appendix N: Vehicle Trajectory of the StreetMapper360 system – GPS/IMU and Riegl laser scanner from the two period 2009 and 2012.

4. Figures of processing MLS data of 2009.

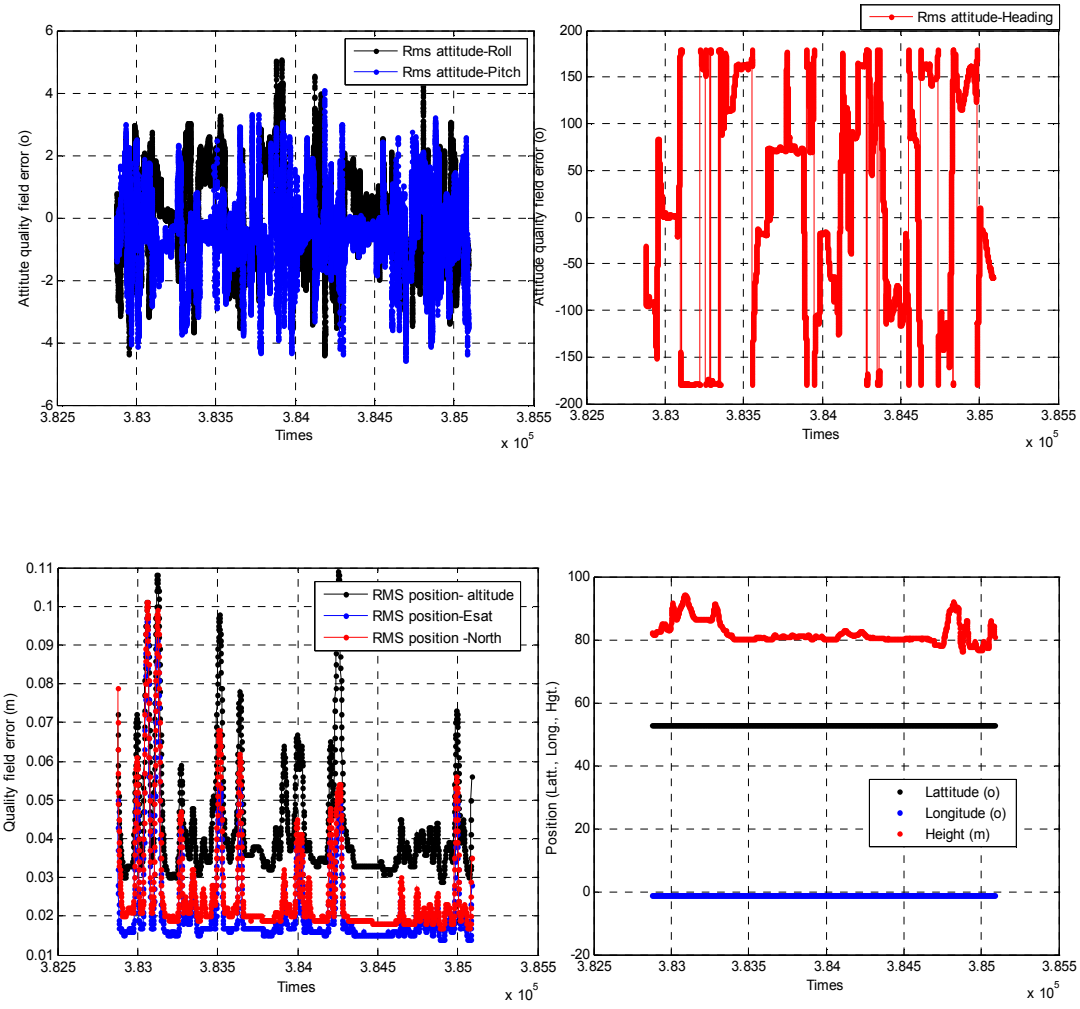

Figure N-1: Vehicle trajectory, position and attitude quality field errors. Top left: Attitude quality of field errors (RMS roll and pitch). Top right: RMS heading errors. Bottom left: RMS position (altitude, east and north) respectively. Bottom right: position (latitude, longitude and height) respectively.

1. Figure of processing MLS data, Nov. 2012

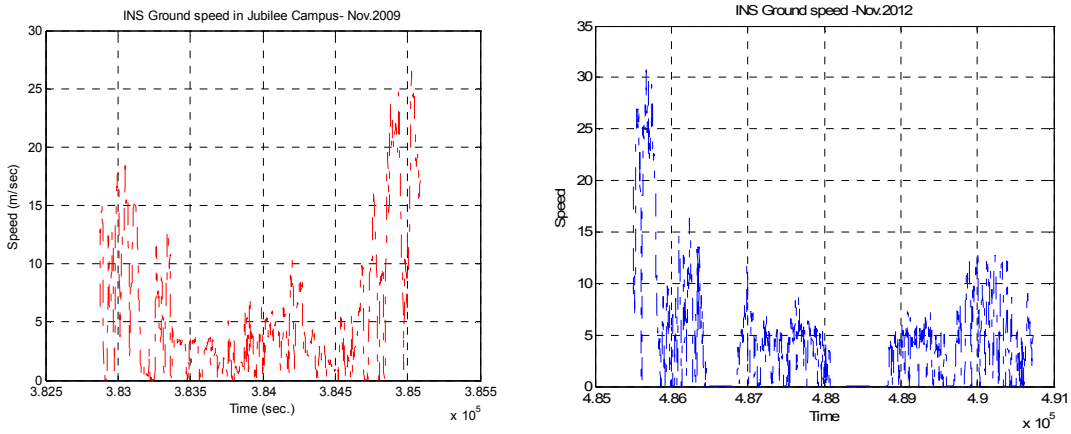

Figure N-2: INS Ground speed around Jubilee campus of 2009 and 2012. Left and right: INS Ground speed in November .2009 and November 2012 respectively.

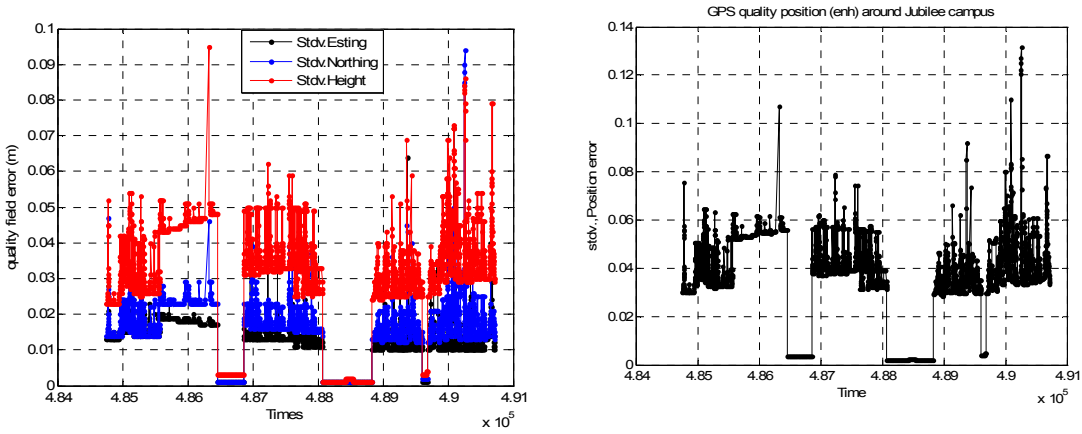

Figure N-3: Standard deviation of the GPS position quality in (E, N and H) direction around Jubilee campus. Left: stdv., of each components, and right: square root of the position (enh). 2009.

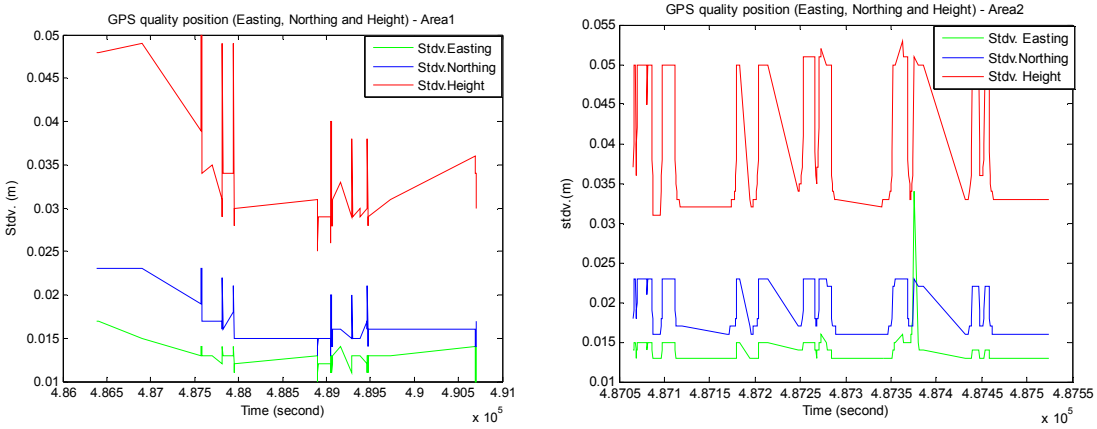

Figure N-3: Standard deviation of the GPS position quality in Area 1 and Area2. Left: Area1. Right: Area2-2012.

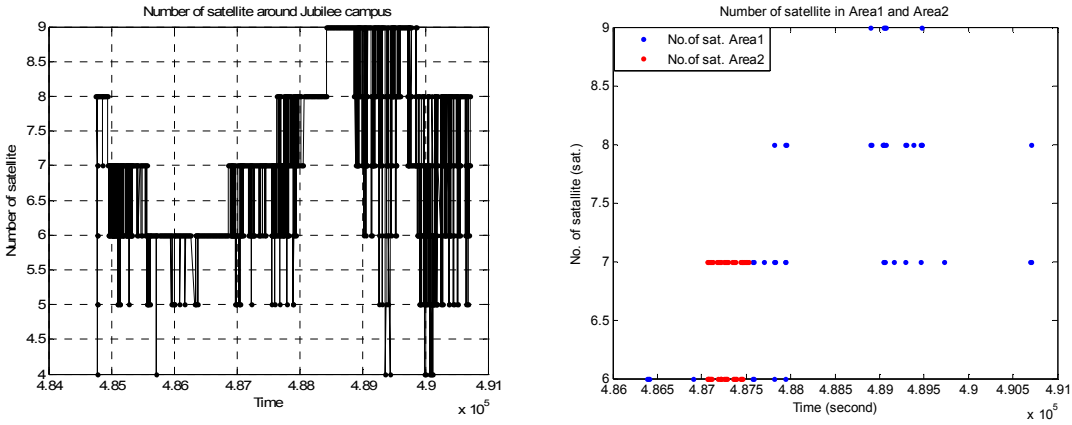

Figure N-4: Number of satellite visible in the entire Jubilee campus: Left: the entire area. Right in both areas, red dot and blue represent number of satellite in Area 1 and Area2 respectively-2012.

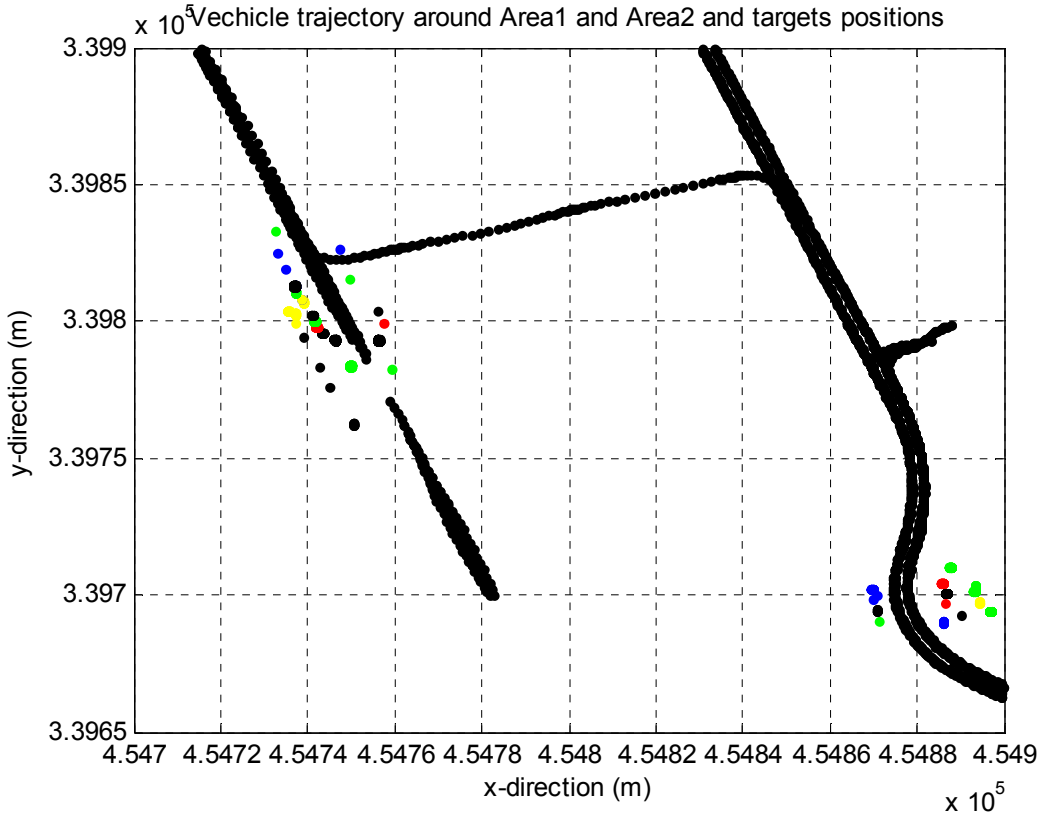

Figure N-5: Vehicle trajectory around area1 and area2 overlay, targets positions. Black and green colours represent cone targets horizontally and vertically installed respectively, red and blue represent sphere 200 and 145 mm dia., respectively, and yellow represents pyramid targets.

Appendix O: Network adjustment result and analysis.

After performing adjustment network using TGO software, the adjustment results show that Chi-square test was passed with 95% confidence with a maximum error ellipse of 3 mm for the adjusted coordinates. The result figures are the network geometry and error ellipses figure for the adjusted point in both selected area (Figure Ao-1). It is worth mentioning that all coordinates used in the adjustments are in the national Grid OSGB36 coordinate system.

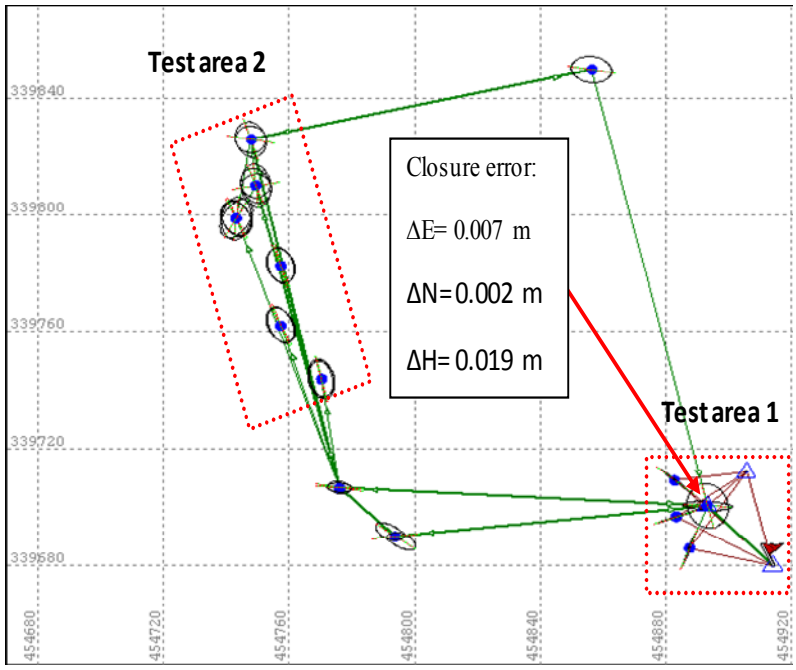

Figure Ao-1: Network geometry and error ellipse output from TGO.

Other output figures from TGO includes, vertical angles residuals, distance residuals, Northing residual, histogram of standardised residuals plot and distance and elevation a-posterior plot. For example, Figure Ao-2 shows Azimuth in different plots.

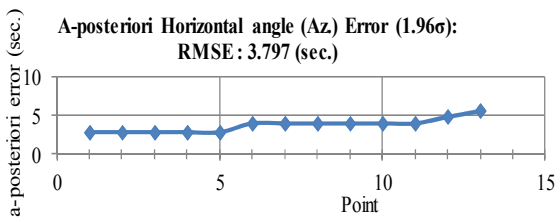

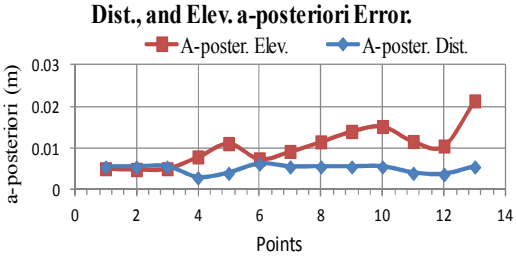

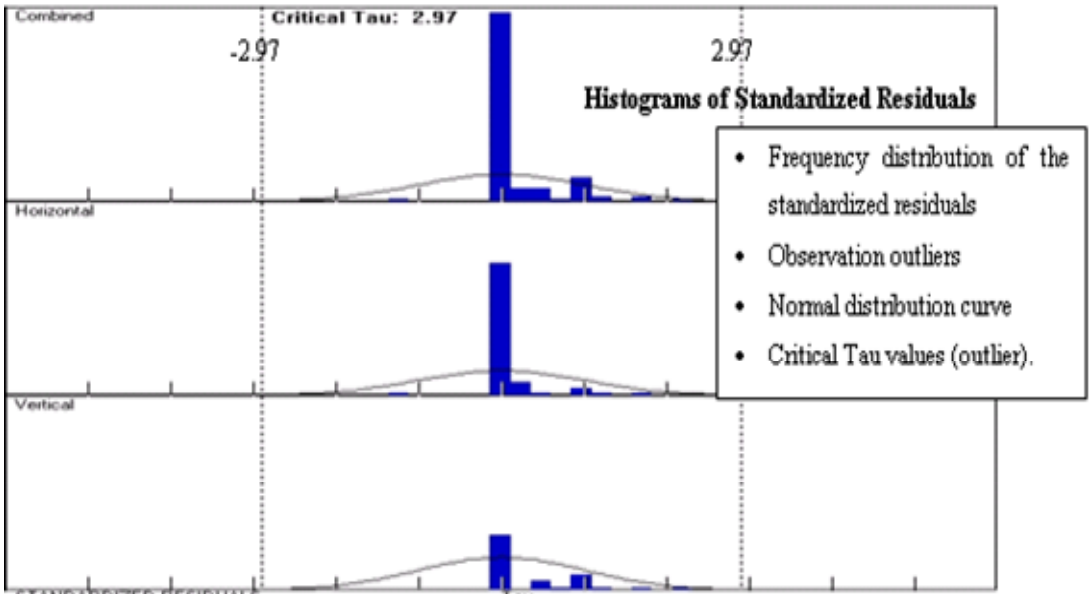

Figure Ao-2 Azimuth angle a-posterior error plot (left), distance and elevation a-posterior plot (right) and histogram residuals plot for Hor, Vert, components (bottom) for the adjusted network.

In general, most of the residuals of the total station observation (distance and angle) were found to be located within the normal distribution in the histogram plot. However, the observations were not found within the tails (alpha of 5%). The residual of the output adjusted coordinates (E, N and Ht) was found within the normal distribution in the histogram plot. These results illustrate the good quality of the observation as well as for the adjusted coordinates. The vertical dot line indicates the Critical Tau value. Residuals outside these lines are considered outlier. The local scale represents the sigma value. The Histograms show the frequency distribution of the observations standardized residuals from the most recent adjustment as shown in the (Figure Ao-2, bottom).

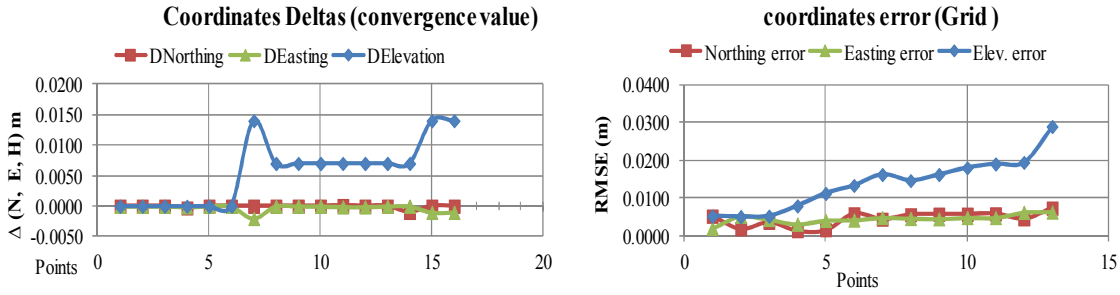

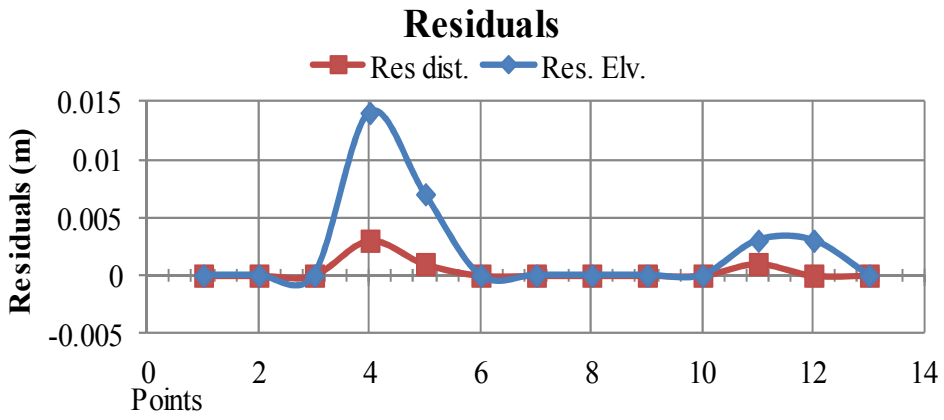

Figure Ao-3: Coordinates error deltas plot (top left) coordinates errors (top right) and residuals distance and elevation plot (bottom) for the two area network around Jubilee campus.

The standard deviation was found to be equal to 1.9 mm, 1.1mm and 5.0 mm for the error in Northing, Easting and height respectively. The deviations in Northing and Easting coordinates could be due to the use of different uncertainties in TGO software. In TGO, various uncertainties were used in the horizontal angles and distances. In addition, fixed uncertainties of the horizontal angles and distances of the GCPs (NGB10, NGB11 and NGB12) were used within adjustment. Also, one of the GCP (NGB10) has been rejected due to out of the tolerance fixed by the TGO (0.02 and 0.05) m for horizontal and vertical tolerance respectively. Another reason could be the adjustment of a combined network 3D network rather than 2D network. Within the 3D adjustment, the vertical angle can affect the height coordinates which as a result, can affect the slope distance. The error in the height might be due to the used of levelling procedure for measuring the height differences which is less accurate than the use of precise levelling technique (Duggal, 2004).

In general, it was decided that the adjusted coordinates of the network, result from TGO software, and were suitable for use as “truth” coordinates for the two selected areas in which the designed targets have been tested.

For comparison purpose, the network was adjusted using a simple linear distribution error as described in appendix D “levelling closure and adjustment”. The closure obtained from the traversed network is within the allowable accuracy of the first order traverse for horizontal control (see Table Ao-1). Since the permissible closure

for a traverse circuit (loop) is based upon length of lines and numbers of setups, it is logical to adjust each element (ΔE, ΔN and ΔH) on this basis.

The adjusted coordinates (E, N and H) from TGO compared with coordinates calculated from linear distribution errors (Figure Ao-4).

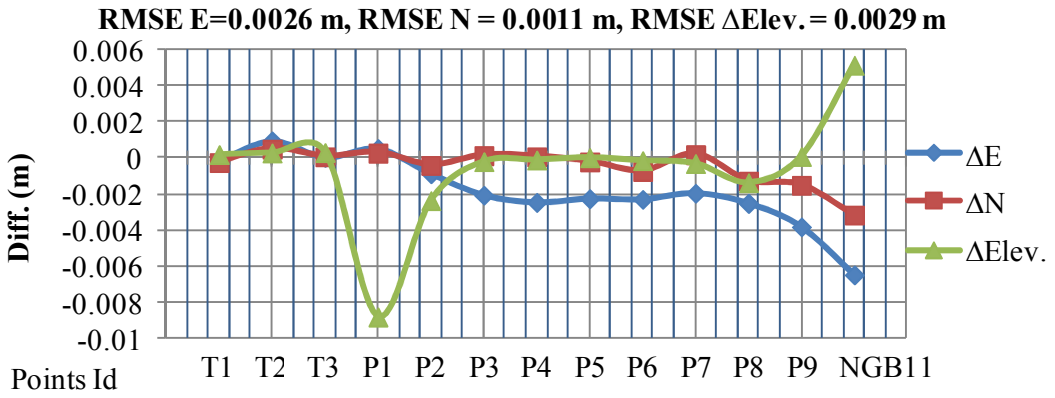

Figure Ao-4: 3D network, differences between TGO coordinates and linear distribution method in Horizontal and height coordinates.

The centre or apex coordinates of the designed target were also adjusted following the same procedure using TGO. The adjusted coordinates of the two areas were utilised as control values. The results of TGO adjustment show that Chi square test failed with 95% confidence with a maximum error ellipse of less than 2 mm for the adjusted coordinates (Figure Ao-6).

Type of Traverse	Angular error of closure	Total Linear error of closure
First **order traverse** for horizontal control	$6'' = \sqrt{N}$	1 in 25,000
Second **order traverse** for horizontal control and for important and accurate surveys	$15'' = \sqrt{N}$	1 in 10,000
Thrid **order traverse** for surveys of important boundaries etc.	$30'' = \sqrt{N}$	1 in 5,000
Minor theodolite **traverse** for detailing	$1'' = \sqrt{N}$	1 in 300
Compass **traverse**	$15'' = \sqrt{N}$	1 in 300 to 1 in 600

Table Ao-1: Errors of closure (source: (Punmia et al., 2005)).

A o2 Error Ellipse

In general, the 95% confidence region ellipses can be seen in Table Ao-2 (Olyazadeh et al., 2011):

Confidence region	39.4 (%)	86.5 (%)	95.0 (%)	98.9 (%)
Factor	1	2	2.477	3

Table Ao-2: Confidence region ellipses (source: (Olyazadeh et al., 2011)).

The factor 2.477 was used for the adjustment of GCPs in both areas and for testing the centre of the designed targets.

.

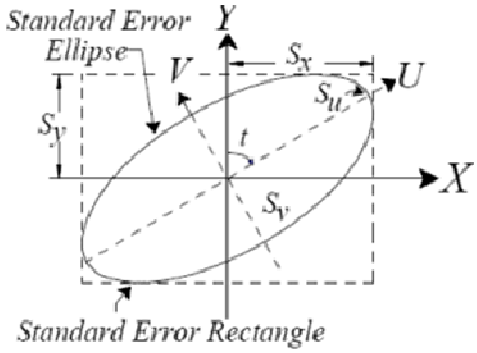

Figure Ao-5: Error ellipse (source:(Olyazadeh et al., 2011)).

Figure Ao-5 illustrates a standard error ellipse where (Wolf and Ghilani, 1997):

1. *t* is the rotation angle from Y axis to axis of largest error.
2. *Su and Sv* are the semi-major (largest error) and semi-minor (Least error).axes of ellipse respectively.
3. *Sx and Sy* are the standard deviation in X and Y coordinate respectively.

(Setan, 2008) explained that the 95% confidence region semi major axis and semi minor axis can be calculated following the equation below

Su = 2.447σ, sv = 2.447σ.

In the TGO adjustment, the point error Ellipses graphically obtained after adjustment (see Figure Ao-6) and show,

- The adjusted point's horizontal coordinate a posteriori errors consider these guidelines when viewing the error ellipses:
- The top of each plot is oriented to north.
- Arrows to the right of the ellipse represent the a-posterior errors for the heights and elevations.

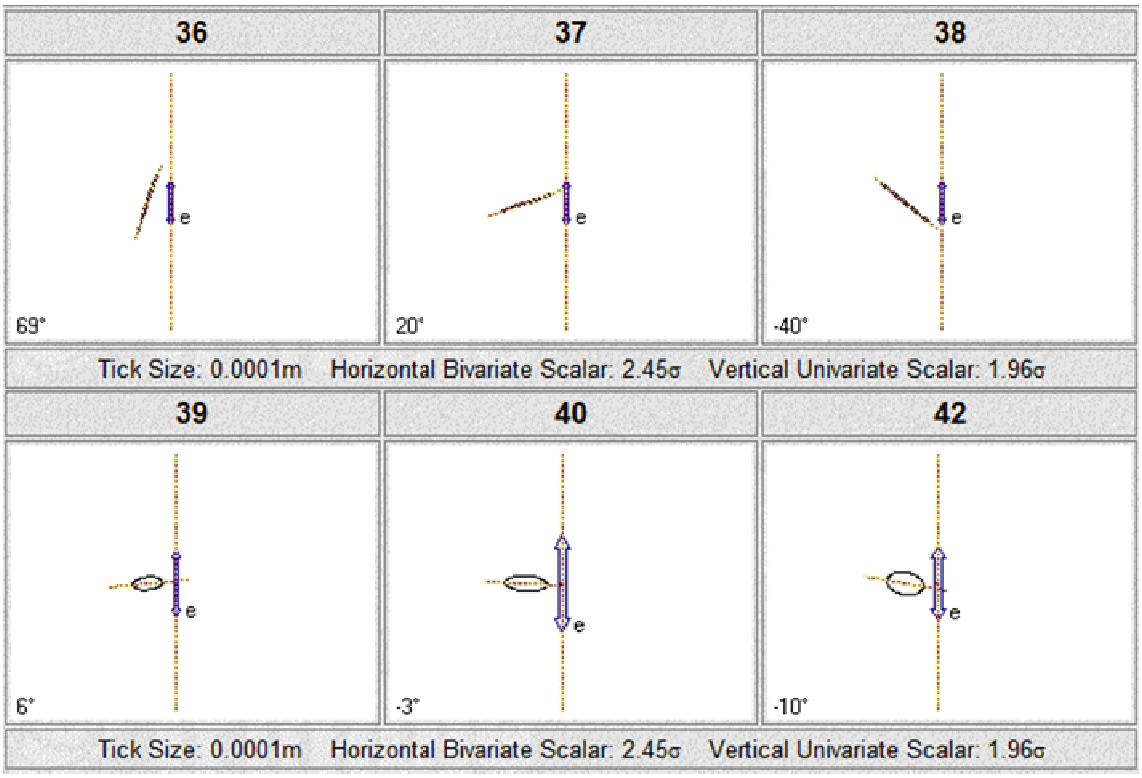

Figure (Ao-6): A sample of Point error ellipse obtained after adjustments.

Ao3: Network adjustments for coordinating of the targets apex/centre in two areas.

Area1:

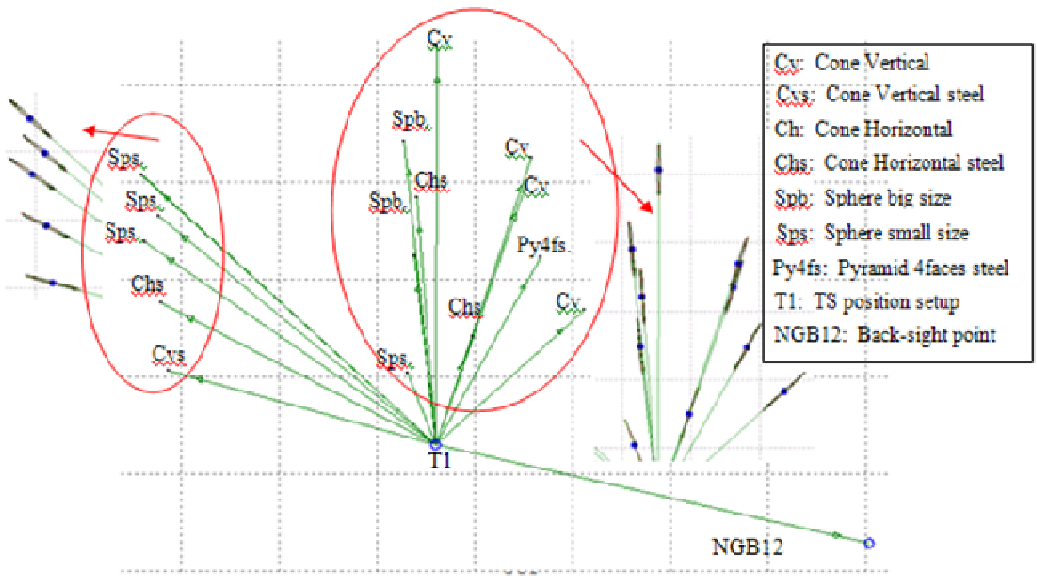

Figure Ao-.7: Testing- coordinating centre of different targets network geometry and error ellipse output from TGO.in Area1in one set up position.

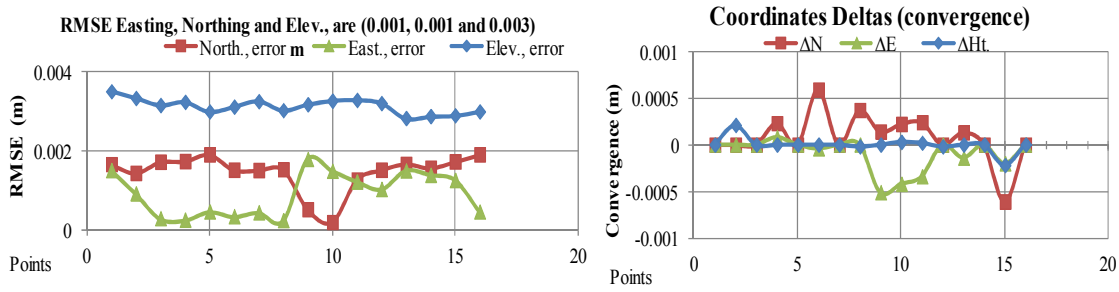

Figure Ao-.8: Easting, Northing and Elevation RMSE plot (top), Convergence for the testing-targets centre/apex in Area1.

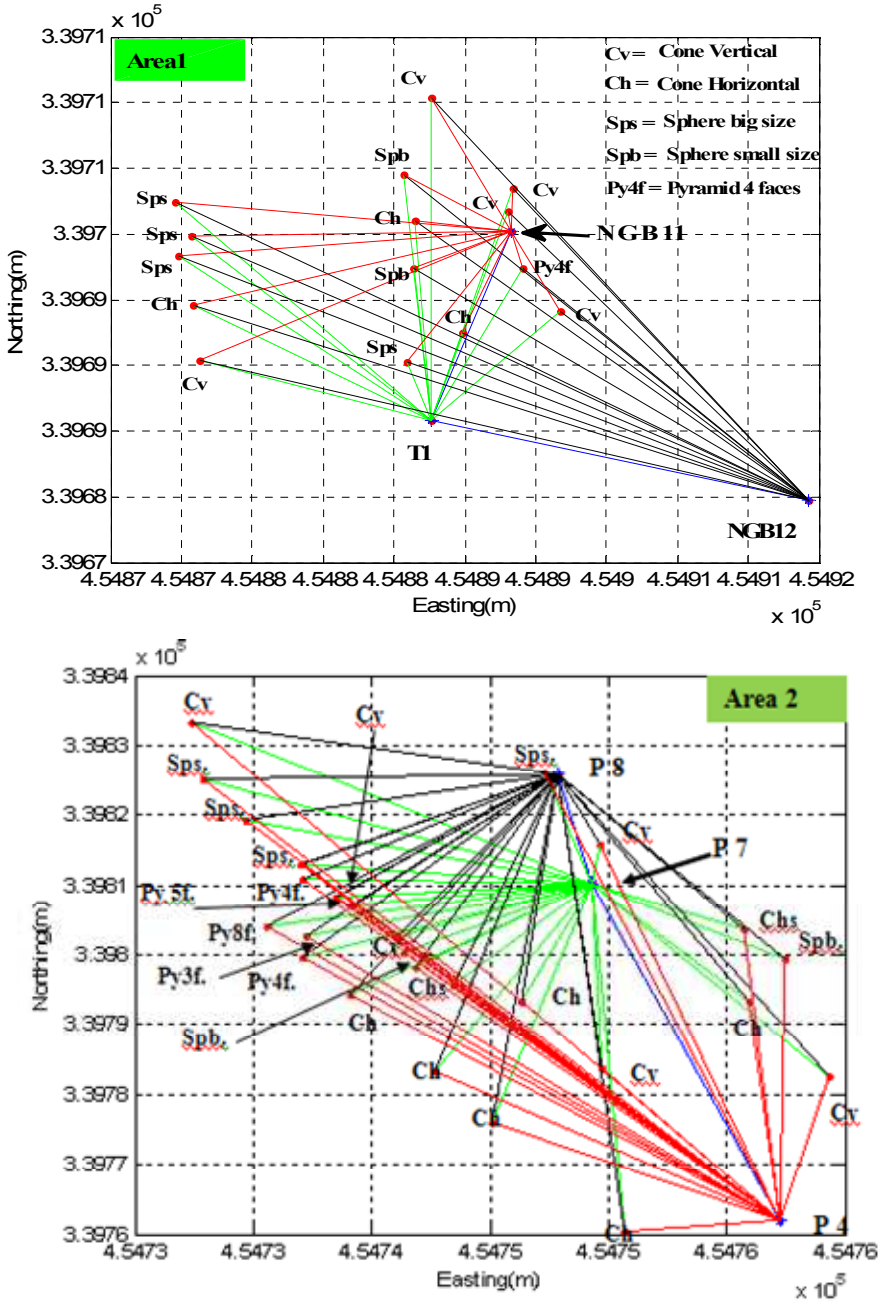

Figure Ao-9: Survey network for area1 and area2 drawn using Matlab functions.

Area2:

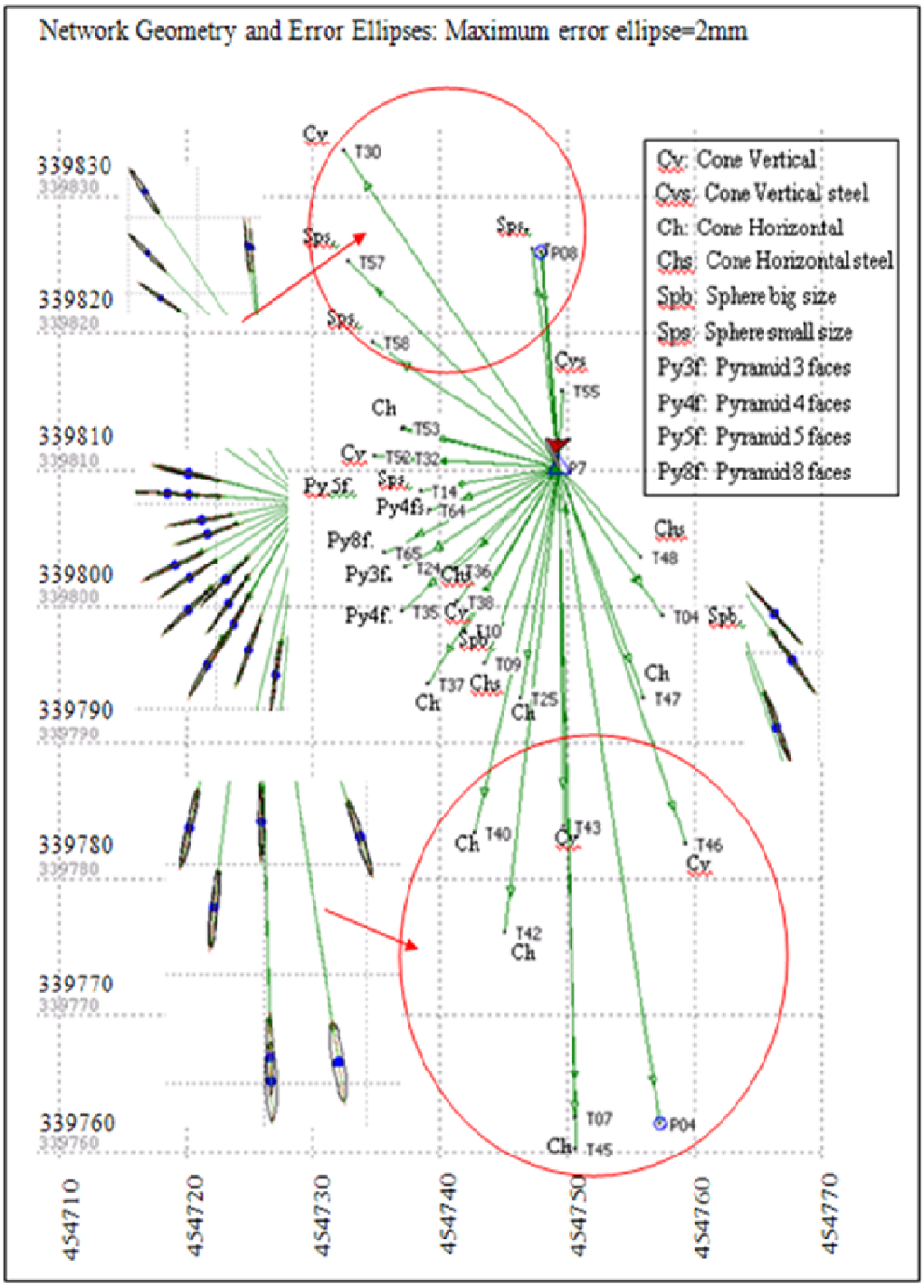

Figure Ao-.10: Testing- coordinating centre/apex of different targets network geometry and error ellipse output from TGO.in Area2 in one set up position.

The fail of chi square test poses the importance analysis of adjustments observation residuals. RMSE of Easting, Northing and heights, were plotted in different figures. These figures show the residuals,

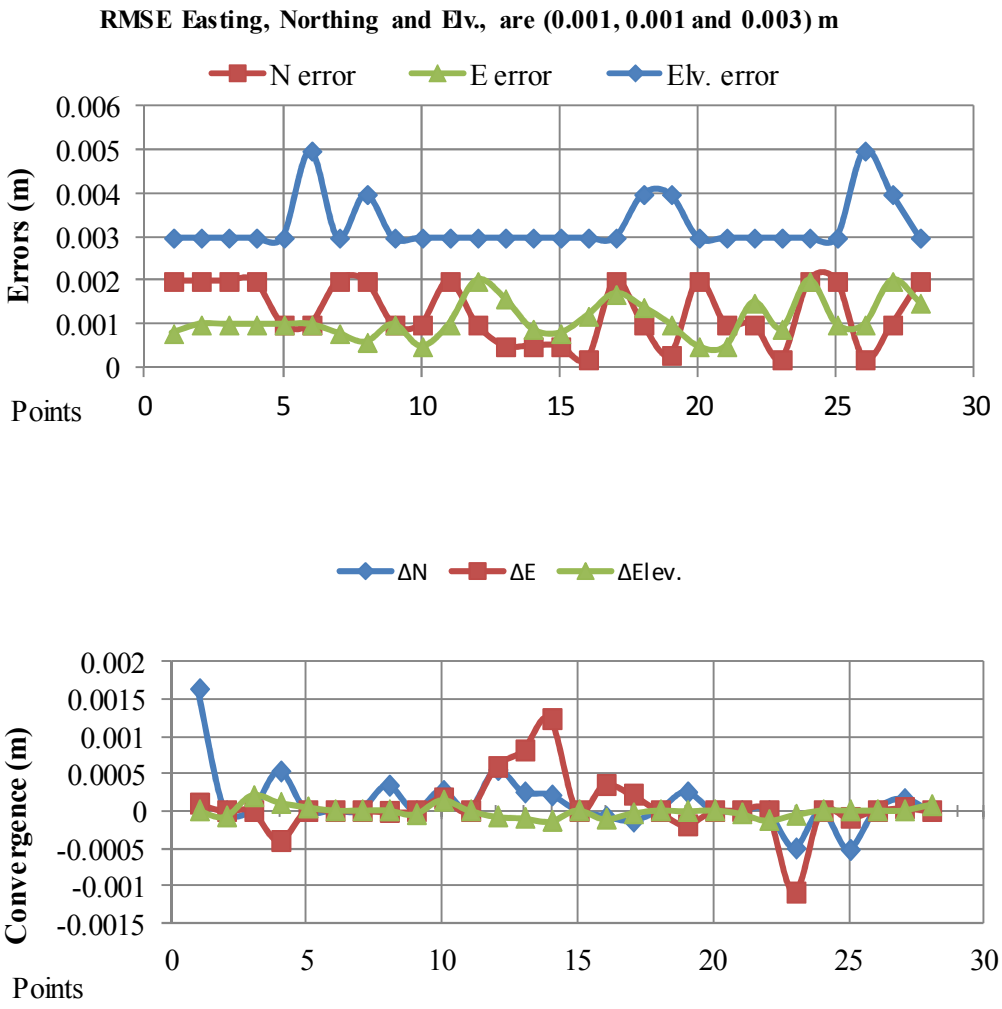

Figure Ao-.11: Easting, Northing and Elevation RMSE plot (top), Convergence for the testing-targets centre/apex (bottom) in Area2.

The results of 3D coordinates (E, N and Elev.,) obtained from TGO of testing target centre show that the RMSE values are (1.0, 1.0, and 3.0) mm for E, N and Elev., respectively. These differences could be due to the same reasons that found in TGO network adjustments. Based on these results, the adjusted 3D coordinates of the targets from TGO software were considered to be suitable for use as "truth" coordinates for all tests with MLS data.

Appendix P: Developed the second part of the UNT1 algorithm (see the file in the attached CD).

Appendix Q: Report summary of GPS/ IMU data processing provide by 3DLM Ltd. (see the file in the attached CD).

Appendix R: MLS data processing and figures.

R1: Fitting pyramid faces.

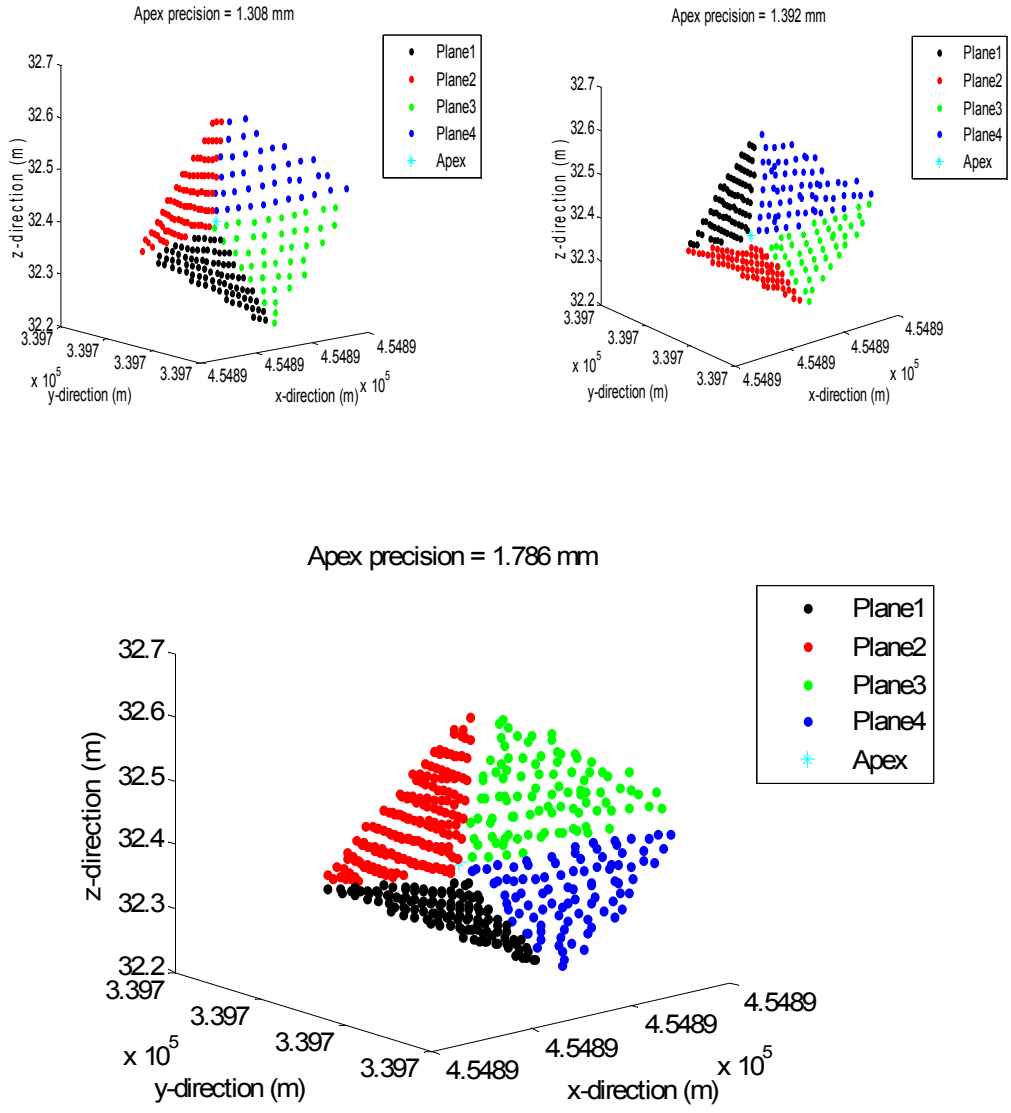

Figure R1-1: Precision of the apex vs single and multi-scans in area 1: Top left: Run1. Top right. Run2. Bottom: Multi-runs.

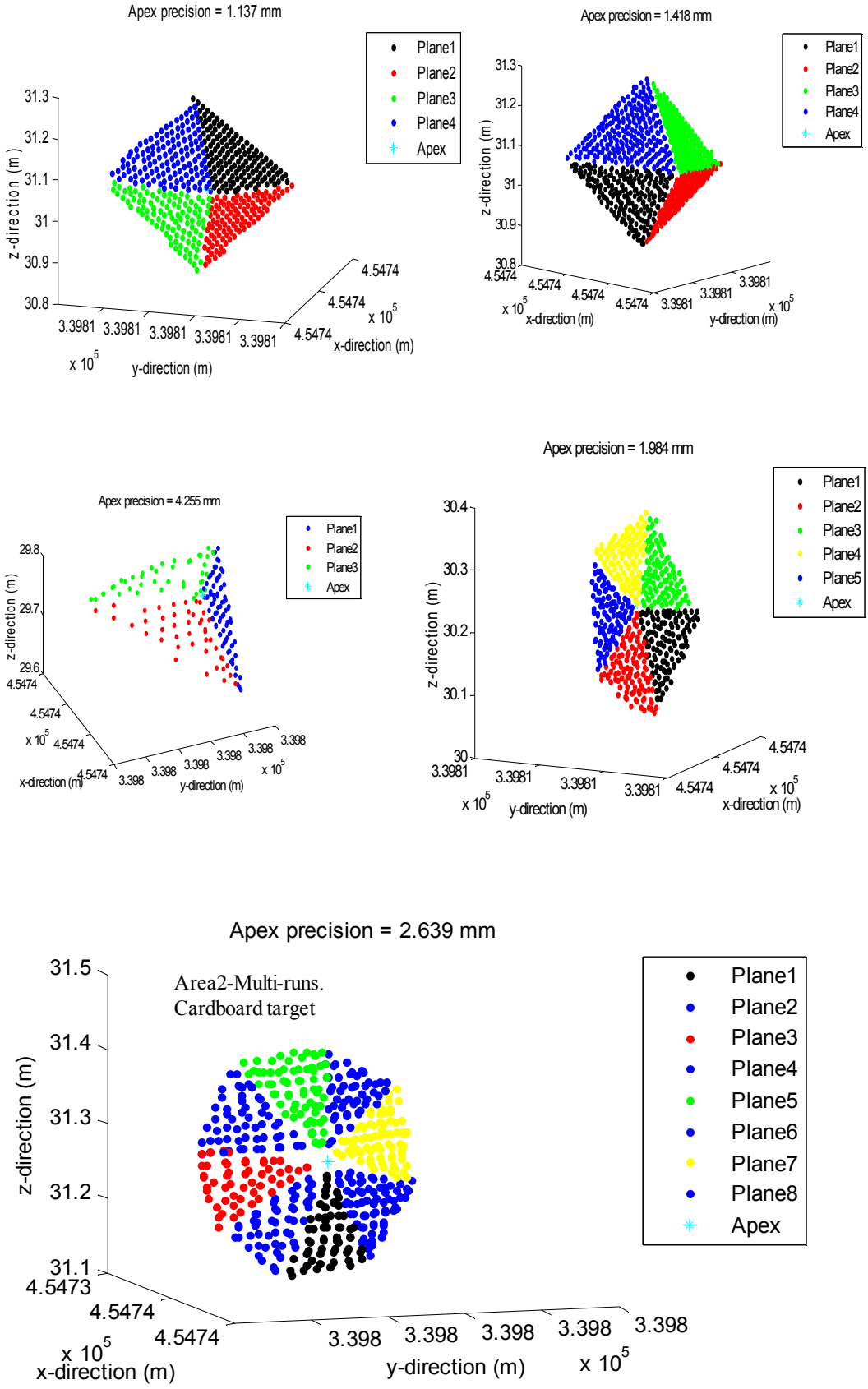

Figure R1-2: Precision of the apex vs multi-scans in area 2: Top left and right: pyramid square base, cardboard and aluminium respectively. Middle left and right: Pyramid triangular and pentagon base, aluminium and cardboard respectively. Bottom: Pyramid octagon base, cardboard.

Appendix S: Paper in preparation for this research

The importance of designing targets for improving the accuracy of MLS data in urban areas

In many application and processes in MLS there is a need to identify precise target points in the point cloud. This is not easily when you do not have an observation hitting exactly on the target point. This often tends to model the geometry of natural features, which can be very difficult. So introducing targets which have a known geometric shape is an easy and convenient way to obtain a target which can be recognised and an exact target point found.